

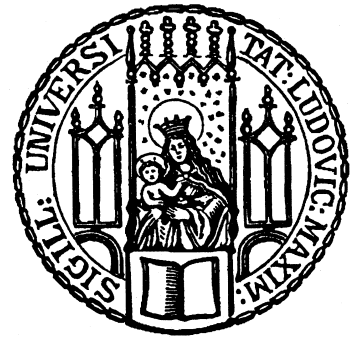
---

# GAUGE/GRAVITY DUALITY

## A ROAD TOWARDS REALITY

---

DISSERTATION BY PATRICK KERNER





---

# GAUGE/GRAVITY DUALITY

## A ROAD TOWARDS REALITY

---

DISSERTATION BY PATRICK KERNER

Dissertation  
an der Fakultät für Physik  
der Ludwig-Maximilians-Universität  
München

vorgelegt von  
Patrick Kerner  
aus Weingarten

München, den 22. Dezember 2011

# DISSERTATION

submitted to the faculty of physics of the  
Ludwig-Maximilians-Universität München

by Patrick Kerner  
born on November 13th, 1981 in Weingarten

supervised by PD Dr. Johanna Karen Erdmenger  
Max-Planck-Institut für Physik, München

1st Referee: PD Dr. Johanna Karen Erdmenger  
2nd Referee: Prof. Dr. Dieter Lüst

Date of submission: December 22nd, 2011  
Date of oral examination: February 23rd, 2012

# Zusammenfassung

In dieser Dissertation benutzen wir eine Dualität zwischen einer Eich- und einer Gravitationstheorie, um verschiedenartige Phänomene stark gekoppelter Systeme zu untersuchen. Im Besonderen betrachten wir Anwendungen der Dualität auf reale Systeme, wie zum Beispiel Systeme der kondensierten Materie und das Quark-Gluon-Plasma, das durch Schwerionenkollisionen am Relativistic Heavy Ion Collider (RHIC) und am Large Hadron Collider (LHC) erzeugt wird.

Die Dualität, die aus der Stringtheorie hervorgeht, bringt eine stark gekoppelte Eichtheorie in Beziehung zu einer schwach gekoppelten Gravitationstheorie, so dass nicht-perturbative Ergebnisse in der Feldtheorie durch störungstheoretische Rechnungen in der Gravitationstheorie erhalten werden können. Wie wir in den letzten Jahren gelernt haben, ist die Dualität besonders geeignet für die Beschreibung von heißen und dichten Plasmen sowie Echtzeitprozessen, die mit Transporteigenschaften oder Spektralfunktionen in Verbindung gebracht werden können.

Leider wurde bisher noch keine duale gravitative Beschreibung gefunden, die alle Aspekte eines stark gekoppelten Systems der realen Welt modelliert. Aber es gibt viele Gravitationsduale, die verschiedenartige Phänomene modellieren. Die grundlegende Idee dieser Doktorarbeit ist es unterschiedliche Gravitationsduale zu studieren, um eine entsprechende Beschreibung von heißen und dichten Plasmen zu entwickeln. Wir fokussieren uns insbesondere auf die Physik im thermischen Gleichgewicht oder nahe des Gleichgewichts.

Motiviert durch die experimentell beobachteten mesonischen Resonanzen im Quark-Gluon-Plasma, studieren wir zuerst Quasinormalmoden eines Gravitationsduals, das entsprechende Anregungen enthält. Die Quasinormalmoden auf der Gravitationsseite können mit den Polen der Greenschen Funktion auf der Feldtheorieseite identifiziert werden. Durch Untersuchungen der Quasinormalmoden beobachten wir wie Quasiteilchenresonanzen in einem heißen und dichten Plasma entstehen. Durch Variation der Temperatur und Dichte finden wir interessante Trajektorien der Quasinormalfrequenzen, die experimentell nachgewiesen werden können.

Außerdem finden wir eine Instabilität im Spektrum der Quasinormalmoden bei großen Werten des chemischen Potentials oder des magnetischen Feldes. Bei großem chemischem Potential löst die Instabilität die Kondensation eines Feldes aus, wobei eine Abelsche Symmetrie spontan gebrochen wird. Da die gebrochene Symmetrie global ist, beschreibt die kondensierte Phase eine Supraflüssigkeit. Bei großem ma-

gnetischem Feld erwarten wir, dass die Instabilität auf eine ähnliche Weise behoben werden kann.

Die gravitative Beschreibung dieser Supraflüssigkeiten steht im Focus dieser Arbeit. Im Besonderen konzentrieren wir uns auf Systeme, in denen außer der Abelschen Symmetrie auch die  $SO(3)$  Rotationssymmetrie spontan zu  $SO(2)$  gebrochen wird. Diese Systeme werden holographische p-Wellen Supraflüssigkeiten genannt. Wir konstruieren diese in einem bottom-up Gravitationsmodell sowie in einem top-down Stringtheoriemodell. Das Erstgenannte erlaubt die Beschreibung der Rückwirkung der supraflüssigen Dichte auf den Energieimpulstensor, während beim Letzteren die duale Feldtheorie explizit bekannt ist. Dieses Stringtheoriemodell ist die erste Beschreibung einer holographischen Supraflüssigkeit, die in die Stringtheorie eingebettet ist. In diesen holographischen Systemen studieren wir die Thermodynamik, die uns ermöglicht den Phasenübergang zur supraflüssigen Phase zu identifizieren, sowie einige Transporteigenschaften. Im bottom-up Gravitationsmodell finden wir ein nicht-universellen Quotienten aus Scherviskosität und Entropiedichte. Dies ist das erste Beispiel für einen nicht-universellen Wert für dieses Verhältnis in Eichtheorien bei großem  $N$  und unendlicher 't Hooft Kopplung.

Diese Arbeit basiert auf Ergebnissen, die am Max-Planck-Institut für Physik (Werner-Heisenberg-Institut) in München, Deutschland unter der Betreuung von PD Dr. J. K. Erdmenger erreicht wurden. Die relevanten Veröffentlichungen sind:

- [1] M. Ammon, J. Erdmenger, M. Kaminski and P. Kerner, *Superconductivity from gauge/gravity duality with flavor*, Phys. Lett. B **680**, 516 (2009) arXiv:0810.2316.
- [2] M. Ammon, J. Erdmenger, M. Kaminski and P. Kerner, *Flavor Superconductivity from Gauge/Gravity Duality*, JHEP **0910**, 067 (2009) arXiv:0903.1864.
- [3] J. Erdmenger, C. Greubel, M. Kaminski, P. Kerner, K. Landsteiner and F. Pena-Benitez *Quasinormal modes of massive charged flavor branes*, JHEP **1003**, 117 (2010) arXiv:0911.3544.
- [4] M. Ammon, J. Erdmenger, V. Grass, P. Kerner and A. O'Bannon, *On Holographic p-wave Superfluids with Back-reaction*, Phys. Lett. B **686**, 192 (2010) arXiv:0912.3515.
- [5] J. Erdmenger, P. Kerner and H. Zeller, *Non-universal shear viscosity from Einstein gravity*, Phys. Lett. B **699** (2011) 301 arXiv:1011.5912.
- [6] J. Erdmenger, V. Grass, P. Kerner and T. H. Ngo, *Holographic Superfluidity in Imbalanced Mixtures*, JHEP **1108** (2011) 037 arXiv:1103.4145.
- [7] M. Ammon, J. Erdmenger, P. Kerner and M. Strydom, *Black Hole Instability Induced by a Magnetic Field*, Phys. Lett. B **706** (2011) 94 arXiv:1106.4551.
- [8] J. Erdmenger, P. Kerner and H. Zeller, *Transport in Anisotropic Superfluids: A Holographic Description*, arXiv:1110.0007.

# Abstract

In this dissertation we use gauge/gravity duality to investigate various phenomena of strongly coupled systems. In particular, we consider applications of the duality to real-world systems such as condensed matter systems and the quark-gluon plasma created by heavy ion collisions at the Relativistic Heavy Ion Collider (RHIC) and the Large Hadron Collider (LHC).

Gauge/gravity duality which originates from string theory relates strongly coupled gauge theories to weakly coupled gravity theories. This duality allows for computations of non-perturbative results on the field theory side by perturbative calculations on the gravity side. As we have learned in the recent years, the duality is especially suitable to describe hot and dense plasmas as well as real-time processes related to transport properties or spectral functions.

Unfortunately, so far there is no dual gravity description modeling every aspect of a strongly coupled real-world system. However, there are many gravity duals which describe several phenomena. The general idea of this thesis is to study different gravity duals in order to develop a gravity description of hot and dense plasmas. In particular, we focus on physics in thermal equilibrium and close to equilibrium.

Motivated by the experimentally observed mesonic resonances in the quark-gluon plasma, we first study quasinormal modes of a gravity dual which contains such resonances. The quasinormal modes on the gravity side are identified with the poles of the Green's function on the field theory side. By studying these quasinormal modes, we observe how quasiparticle resonances develop in a hot and dense plasma. We find interesting trajectories of quasinormal frequencies which may be found experimentally as the temperature and density is varied.

In addition, we find an instability in the quasinormal mode spectrum at large chemical potential or magnetic field. At large chemical potential, this instability triggers the condensation of a field which breaks an Abelian symmetry spontaneously. Since the broken symmetry is global, the condensed phase describes a superfluid. At large magnetic field, we expect that the instability can be cured in a similar way.

The gravity description of these superfluids is in the main focus of this thesis. Especially, we concentrate on systems in which, in addition to the Abelian symmetry, the rotational symmetry  $SO(3)$  is spontaneously broken down to  $SO(2)$ . These systems are named holographic p-wave superfluids. We construct these in a bottom-up gravity model as well as in a top-down string theory model. The former allows us

to describe the back-reaction of the superfluid condensate on the energy-momentum tensor while the latter has the great advantage that we know the dual field theory explicitly. This string theory model is the first description of a holographic superfluid embedded in string theory. In these holographic models, we study the thermodynamics which allows us to identify the phase transition to the superfluid phase as well as some transport properties. In the bottom-up gravity model, we find a non-universal ratio of shear viscosity to entropy density. This is the first example for a non-universal value of this ratio in large  $N$  gauge theories at infinite 't Hooft coupling.

This thesis is based on results which have been obtained by the author under the supervision of PD Dr. J. K. Erdmenger at the Max-Planck-Institut für Physik (Werner-Heisenberg-Institut) in Munich, Germany during the time from January 2009 to December 2011. The relevant publications are listed below:

- [1] M. Ammon, J. Erdmenger, M. Kaminski and P. Kerner, *Superconductivity from gauge/gravity duality with flavor*, Phys. Lett. B **680**, 516 (2009) arXiv:0810.2316.
- [2] M. Ammon, J. Erdmenger, M. Kaminski and P. Kerner, *Flavor Superconductivity from Gauge/Gravity Duality*, JHEP **0910**, 067 (2009) arXiv:0903.1864.
- [3] J. Erdmenger, C. Greubel, M. Kaminski, P. Kerner, K. Landsteiner and F. Pena-Benitez *Quasinormal modes of massive charged flavor branes*, JHEP **1003**, 117 (2010) arXiv:0911.3544.
- [4] M. Ammon, J. Erdmenger, V. Grass, P. Kerner and A. O'Bannon, *On Holographic p-wave Superfluids with Back-reaction*, Phys. Lett. B **686**, 192 (2010) arXiv:0912.3515.
- [5] J. Erdmenger, P. Kerner and H. Zeller, *Non-universal shear viscosity from Einstein gravity*, Phys. Lett. B **699** (2011) 301 arXiv:1011.5912.
- [6] J. Erdmenger, V. Grass, P. Kerner and T. H. Ngo, *Holographic Superfluidity in Imbalanced Mixtures*, JHEP **1108** (2011) 037 arXiv:1103.4145.
- [7] M. Ammon, J. Erdmenger, P. Kerner and M. Strydom, *Black Hole Instability Induced by a Magnetic Field*, Phys. Lett. B **706** (2011) 94 arXiv:1106.4551.
- [8] J. Erdmenger, P. Kerner and H. Zeller, *Transport in Anisotropic Superfluids: A Holographic Description*, arXiv:1110.0007.

# Contents

<b>Zusammenfassung</b>	<b>iii</b>
<b>Abstract</b>	<b>v</b>
<b>1 Introduction and Overview</b>	<b>1</b>
<b>2 Introduction to String Theory</b>	<b>11</b>
2.1 Bosonic String Theory . . . . .	12
2.1.1 From Point Particles to Strings . . . . .	12
2.1.2 String Spectrum . . . . .	15
2.1.3 String Perturbation Theory . . . . .	18
2.1.4 Emergence of Gravity . . . . .	19
2.1.5 T-Duality and D-Branes . . . . .	21
2.2 Superstring Theory . . . . .	25
2.2.1 Worldsheet Fermions . . . . .	25
2.2.2 String Spectrum . . . . .	26
2.2.3 Physical States . . . . .	26
2.2.4 Emergence of Supergravity . . . . .	27
2.2.5 T-Duality and D-Branes . . . . .	29
2.2.6 $\mathcal{N} = 4$ Super-Yang-Mills Theory . . . . .	31
2.2.7 D-brane Intersections . . . . .	34
2.2.8 Brane Solutions in Type IIB Supergravity . . . . .	34
2.2.9 Anti-de Sitter Space . . . . .	36
<b>3 Gauge/Gravity Duality</b>	<b>39</b>
3.1 The Original AdS/CFT Correspondence . . . . .	40
3.1.1 The Maldacena Conjecture . . . . .	41
3.1.2 The Different Forms of the Correspondence . . . . .	43
3.1.3 Dictionary: Field/Operator Correspondence . . . . .	44
3.1.4 Holography . . . . .	45
3.1.5 Tests . . . . .	46
3.2 Generalizations Towards Real-World Systems . . . . .	48
3.2.1 Including Fundamental Matter: Flavor Branes . . . . .	49

<b>4</b>	<b>Holography at Finite Temperature</b>	<b>59</b>
4.1	Heating up the Correspondence . . . . .	61
4.1.1	Finite Temperature Field Theory . . . . .	61
4.1.2	Thermal AdS and Schwarzschild Black Hole . . . . .	64
4.2	Physics in Equilibrium . . . . .	66
4.2.1	Holographic Renormalization . . . . .	66
4.2.2	Thermodynamics of $\mathcal{N} = 4$ Super-Yang-Mills Theory . . . . .	68
4.2.3	Thermodynamics of Flavor Branes . . . . .	69
4.3	Physics close to Equilibrium . . . . .	76
4.3.1	Green's Functions from Gravity . . . . .	77
4.3.2	Green's Functions of $\mathcal{N} = 4$ Super-Yang-Mills theory . . . . .	85
4.3.3	Green's Functions from Flavor Branes . . . . .	88
4.4	Hydrodynamics . . . . .	107
4.4.1	Hydrodynamic Description . . . . .	108
4.4.2	Hydrodynamic Modes . . . . .	110
4.4.3	Kubo's Formula for Viscosity . . . . .	111
4.4.4	Transport in $\mathcal{N} = 4$ Super-Yang-Mills Theory . . . . .	112
4.4.5	Transport from Flavor Branes . . . . .	116
<b>5</b>	<b>Holography at Finite Baryon and Isospin Chemical Potentials</b>	<b>117</b>
5.1	Field Theory at Finite Chemical Potentials . . . . .	120
5.2	Physics in Equilibrium . . . . .	121
5.2.1	AdS Reissner-Nordström Black Hole . . . . .	121
5.2.2	Flavor Branes and Quark Chemical Potentials . . . . .	124
5.3	Physics close to Equilibrium . . . . .	135
5.3.1	Spectral Functions of Flavor Fields . . . . .	135
5.3.2	Quasinormal Modes of Flavor Field . . . . .	141
5.4	Hydrodynamics . . . . .	155
5.5	Instabilities . . . . .	156
<b>6</b>	<b>Condensed Phases and Hairy Black Holes</b>	<b>159</b>
6.1	Hairy Reissner-Nordström Black Hole . . . . .	165
6.1.1	Results at Zero Baryon Chemical Potential . . . . .	170
6.1.2	Results at Finite Isospin and Baryon Chemical Potential . . . . .	177
6.2	Fluctuations About the Hairy Black Hole . . . . .	185
6.2.1	Characterization of Fluctuations and Gauge Fixing . . . . .	185
6.2.2	Equations of Motion, On-shell Action and Correlators . . . . .	187
6.3	Transport Properties of the Hairy Black Hole . . . . .	190
6.3.1	General Remarks on Viscosity in Anisotropic Fluids . . . . .	190
6.3.2	Universal Shear Viscosity . . . . .	192
6.3.3	Thermoelectric Effect Perpendicular to the Condensate . . . . .	192
6.3.4	Non-Universal Shear Viscosity and Flexoelectric Effect . . . . .	196
6.4	Holographic Vector Meson Condensation . . . . .	202
6.4.1	Results at Zero Baryon Chemical Potential . . . . .	203

6.4.2	Results at Finite Baryon and Isospin Chemical Potential . . .	218
6.5	Fluctuations About the Vector Condensate . . . . .	225
6.5.1	Adapted Symmetrized Trace Prescription . . . . .	226
6.5.2	Expansion of the DBI Action . . . . .	228
6.5.3	Results and Comparison of the Two Prescriptions . . . . .	230
<b>7</b>	<b>Conclusion and Outlook</b>	<b>239</b>
7.1	Quasinormal Modes of Massive Charged Flavors . . . . .	239
7.2	Black Hole Instabilities . . . . .	240
7.3	Holographic p-wave Superfluids . . . . .	241
7.3.1	Hairy Black Hole Solution . . . . .	241
7.3.2	Holographic Vector Meson Condensate . . . . .	241
7.3.3	Holographic Superfluidity in Imbalanced Mixtures . . . . .	242
7.3.4	Transport in Anisotropic Superfluids . . . . .	242
7.4	Outlook . . . . .	243
7.4.1	Critical Phenomena . . . . .	243
7.4.2	Hydrodynamics . . . . .	244
7.4.3	Universality . . . . .	244
<b>A</b>	<b>Conventions</b>	<b>247</b>
A.1	Units . . . . .	247
A.2	Convention for Indices . . . . .	247
<b>B</b>	<b>General Procedures</b>	<b>249</b>
B.1	Schrödinger Potentials . . . . .	249
B.2	Constructing the Gauge Covariant Fields . . . . .	251
B.2.1	Residual Gauge Transformations . . . . .	251
B.2.2	Physical Fields . . . . .	254
B.3	Holographic Renormalization . . . . .	254
B.3.1	Asymptotic Behavior . . . . .	254
B.3.2	Counterterms . . . . .	256
<b>C</b>	<b>Numerical Recipes for Holography</b>	<b>259</b>
C.1	Numerics for Flavor Branes at Finite Temperature . . . . .	259
C.2	Numerics for Flavor Branes at Finite Chemical Potentials . . . . .	267
C.3	Shooting Method . . . . .	269
C.4	Relaxation Method . . . . .	270



# Introduction and Overview

Based on today's knowledge, matter interacts via four forces: gravity, electromagnetism, weak and strong nuclear force. The latter three are described by the standard model [9] at least to energies of up to a few TeV [10]. The standard model is a quantum field theory [11,12] and, thus, incorporates the ideas of field theory, special relativity and quantum mechanics. Gravity, however, is formulated as a classical field theory in Einstein's general theory of relativity [13] and does not contain the concepts of quantum mechanics.

*Gravity* has a special property: The maximum entropy in a region of spacetime is determined by the size of the boundary of this region [14]. The most famous examples are black holes whose entropy grows with the horizon area. This leads to the *holographic principle* (see e.g. [15–17]) which states the expectation that in quantum gravity all physics within some volume can be described in terms of degrees of freedom on the boundary of this volume. It is tempting to speculate that the information of the entire  $(3 + 1)$ -dimensional universe is stored on its  $(2 + 1)$ -dimensional boundary, the cosmological horizon.

In the *standard model* the three interactions are described by gauge theories, i. e. field theories with Lagrangians that are invariant under a continuous group of local symmetry transformations. The gauge symmetry of the standard model is given by the group  $SU(3)_C \times SU(2)_L \times U(1)_Y$ . The  $SU(3)_C$  part of the gauge group gives rise to quantum chromodynamics (QCD) which describes the strong nuclear interaction while the electroweak interaction is given by  $SU(2)_L \times U(1)_Y$ . At lower energy the gauge group  $SU(2)_L \times U(1)_Y$  is broken down, e. g. by the Higgs mechanism, to  $U(1)_{\text{em}}$  which describes quantum electrodynamics (QED). The Lagrangian of the standard model is the most general one invariant under the standard model gauge group with the specific matter content given in table 1.1.

The general belief in physics today is that there exists a fundamental theory which allows for a unified description of all forces known as the *theory of everything*. Historically the concept of unification has been very successful. For instance electricity and magnetism were combined to *electromagnetism* [18] by Maxwell. A direct consequence of this unification was the prediction of electromagnetic waves

Field (1. generation)		Gauge group representation	Electric charge
Left-handed leptons	$E_L = (\nu_L, e_L)$	$(\mathbf{1}, \mathbf{2}, -1/2)$	$(0, -1)$
Right-handed electron	$e_R$	$(\mathbf{1}, \mathbf{1}, -1)$	$-1$
Left-handed quarks	$Q_L = (u_L, d_L)$	$(\mathbf{3}, \mathbf{2}, 1/6)$	$(2/3, 1/3)$
Right-handed up quark	$u_R$	$(\mathbf{3}, \mathbf{1}, 2/3)$	$2/3$
Right-handed down quark	$d_R$	$(\mathbf{3}, \mathbf{1}, -1/3)$	$-1/3$
Higgs	$\phi = (\phi^+, \phi^0)$	$(\mathbf{1}, \mathbf{2}, 1/2)$	$(1, 0)$

**Table 1.1:** The first generation of matter fields of the standard model. In the gauge group representation, the first number denotes the representation of  $SU(3)_C$ , the second of  $SU(2)_L$  and the third number the charge of  $U(1)_Y$ . The electric charge of the fields is given by the charge of the  $U(1)_{\text{em}}$  symmetry which is unbroken at low energies.

and, therefore, the understanding of the nature of light. Above an energy of about 100 GeV, electromagnetism and the weak nuclear force merge into a single force, the electroweak force, which is incorporated in the *standard model*. At even higher energies the electroweak and strong nuclear force are expected to join further into the *grand unified theory* (GUT) [19]. The most challenging problem in physics today is the unification of gravity and the grand unified theory. For this purpose we need a description of gravity which also incorporates the ideas of quantum mechanics. A most promising candidate for this unified description is string theory [20–23]<sup>1</sup>.

*String theory* is a fundamental theory where the basic object is one-dimensional, a string, in contrast to field theories where the elementary object is zero-dimensional, a particle. These strings can be open or closed. Different oscillations of the string considered at low energy describe particles with different properties like spin, charge and mass. In addition to the one-dimensional objects, higher-dimensional objects also appear non-perturbatively. These objects are called branes, derived from the word membranes. In this way string theory allows one to describe all known fundamental forces and matter in a mathematically consistent framework.

By studying the higher-dimensional branes, Maldacena found an astonishing relation between gauge theories and gravity named *gauge/gravity duality* [25]. This duality emerges by identifying the two possible descriptions of branes. On the one hand, branes can be seen as solutions to supergravity, the low-energy theory of closed strings. On the other hand, the low-energy theory of open strings, attached to the branes, is a gauge theory living on the brane. Maldacena’s insight was that both theories should be equivalent since they describe the same objects, the branes. Especially, this duality is of value since it is a strong-weak duality. For instance, it relates strongly coupled gauge theories to weakly coupled gravity. Since the gauge theory describes higher-dimensional gravity, gauge/gravity duality realizes the idea of the holographic principle. Thus, the correspondence is also often denoted as

<sup>1</sup>Loop quantum gravity [24] is another attempt to describe quantum gravity.

holographic duality.

But let us now come back to lower energies. Even though the standard model is a very successful theory describing particle interactions at energies below a few TeV, there are fundamental questions remaining. In the electroweak sector, these questions are for instance: What is the exact nature of the neutrinos? How big are their masses? How is the electroweak symmetry broken? Is there a Higgs field? Also some properties of QCD are still not understood, e. g. the dynamical origin of confinement and the generation of the mass gap in hadronic matter.

## The Trouble with Strongly Coupled Systems

Let us now focus on quantum chromodynamics. It is an asymptotically free theory [26, 27], i. e. the coupling is weak at high energies but strong at low energies. Due to the strong coupling at low energies, the standard textbook methods for computing observables in quantum field theories cannot be applied since they rely on a perturbative expansion in the coupling constant.

A possible method to address strongly coupled gauge theories is *lattice gauge theory* in which the spacetime is a discrete lattice. Due to this discretization, the otherwise infinite-dimensional path integrals become finite-dimensional and can be calculated by, for instance, the Monte Carlo method. It is believed but unfortunately not proven that by sending the lattice spacing to zero the continuous gauge theory is recovered.

This method is very suitable for the study of systems in thermal equilibrium but fails for dynamical processes. Even for certain equilibrium states, lattice gauge theories face technical problems. For instance, it is not known how to simulate a state at finite chemical potential. In both cases the problem is essentially the same: Lattice gauge theories require Euclidean time so that the weight factor of the path integrals  $\exp(-I)$ , with  $I$  the Euclidean action, converges faster. For dynamical processes this is clearly a problem since they demand a real-time formalism. For finite chemical potential, the problem is more technical: The finite chemical potential introduces oscillations in the weight factor of the path integral which make numerical calculation practically impossible since the convergence becomes slow. Due to these problems, not only QCD at low energies but strongly coupled systems in general are not well understood. Especially in modern condensed matter physics, strongly coupled systems are common. Famous examples are cuprate superconductors [28], heavy fermion compounds [29] and ultra-cold Fermi gases [30].

Remarkably, string theory comes to the rescue with *gauge/gravity duality*. By using this duality, we may map strongly coupled gauge theories to weakly coupled gravity. In this sense we can use perturbation theory in gravity to obtain non-perturbative results in the gauge theory. Amazingly, as it turned out in the last few years, gauge/gravity duality is especially powerful in describing real-time processes, which can be translated into transport properties or spectral functions. In addition, chemical potentials can be turned on easily. For instance, we may introduce finite

baryon and isospin chemical potentials in the sense of QCD. Thus, gauge/gravity is in particular useful where lattice gauge theory has technical problems.

Unfortunately, there is also a drawback. So far, there has been no gravity dual discovered which describes all aspects of a real-world system. For instance the gravity dual of QCD has not been found. So naturally the question arises: What can we learn from gauge/gravity duality? The general idea in applying gauge/gravity duality is to construct and analyze different gravity duals which are suitable for specific questions. In this way important ingredients for describing real-world phenomena may be found. The final goal of course is to combine all ingredients such that at the end the system can be understood in full glory.

### What Does Gauge/Gravity Duality Tell Us About Strongly Coupled Real-World Systems?

After defining the goal of the application of gauge/gravity duality to real-world systems, we now state results which have already been obtained or are obtained in this thesis. Let us begin by presenting the original form of the duality, the *Anti-de Sitter/Conformal Field Theory (AdS/CFT) correspondence*, found by Maldacena [25]. This original form arises from the study of D3-branes in flat space. It states that the superconformal  $\mathcal{N} = 4$  Super-Yang-Mills theory with gauge group  $SU(N_c)$  in  $(3 + 1)$  dimensions is dynamically equivalent to type IIB superstring theory on  $AdS_5 \times S^5$ . In the large  $N_c$  limit and at strong 't Hooft coupling  $\lambda = N_c g_{\text{YM}}^2 \gg 1$ , the string theory side of the correspondence simplifies to type IIB supergravity on  $AdS_5 \times S^5$ . In contrast to string theory, supergravity is well-understood on this curved background. This in principle allows us to translate difficult questions in strongly coupled field theories to manageable problems in supergravity. A more detailed motivation of the correspondence can be found in section 3.1.

In contrast to QCD,  $\mathcal{N} = 4$  Super-Yang-Mills theory is conformal. Thus, in order to make contact to QCD, we have to generalize the correspondence to *non-conformal* field theories which have a renormalization group flow. Since the conformal symmetry of the field theory is matched to the isometry of AdS space, non-conformal field theories must be dual to less symmetric spaces. In general, it is known that asymptotically AdS spaces result in field theories with a conformal UV fixed point. In the topic named AdS/QCD correspondence, gravity backgrounds are designed to model features of QCD (for a status see [31]). For instance, by introducing a cutoff in the interior of AdS, an IR cutoff, confinement and the mass spectrum at low energy can be analyzed. There are two different ways to introduce this cutoff – by a hard wall [32] or by a soft wall [33].

Usually in addition to the degrees of freedom transforming in the adjoint representation of the gauge group, there are degrees of freedom which transform in the fundamental representation of the gauge group, the *matter*. These are e.g. the quarks of QCD. In the context of gauge/gravity duality, these fundamental degrees of freedom are introduced by the embedding of additional  $Dp$ -branes [34] (for a review see [35]).

For instance, the introduction of  $N_f$  D7-branes gives rise to  $\mathcal{N} = 4$  Super-Yang-Mills theory coupled to  $N_f \mathcal{N} = 2$  hypermultiplets in the fundamental representation of the gauge group  $SU(N_c)$ . If the D7-branes are coincident, they generate an  $U(N_f)$  symmetry under which the hypermultiplets also transform in the fundamental representation<sup>2</sup>. In analogy to QCD this symmetry is referred to as flavor symmetry. In the limit where  $N_f \ll N_c$ , the additional branes do not influence the metric of spacetime, so they only probe the AdS geometry. On the field theory side, this limit is denoted as the *quenched approximation*<sup>3</sup>.

In this theory the hypermultiplets can form *bound states* which transform in the adjoint representation of the flavor group  $U(N_f)$ . In analogy to QCD we denote these bound states as mesons. Their spectrum shows a mass gap of the order  $M_q/\sqrt{\lambda}$  where  $M_q$  is the quark mass [39]. In QCD, however, there is a dynamical mass scale generated by chiral symmetry breaking which ensures that the mesons are massive even at zero quark mass. In [40] this effect has been realized in the context of gauge/gravity duality. Flavor branes are studied in more detail in section 3.2.1.

Although we can holographically describe several aspects of QCD in the vacuum, from now on we take a different point of view. We study QCD at temperatures slightly above the deconfinement temperature  $T_{\text{dec}} = 170$  MeV. It is expected that QCD is still strongly coupled even though it is in the deconfined phase [41, 42]. This phase is known as *quark-gluon plasma* which is produced by heavy ion collisions at the Relativistic Heavy Ion Collider (RHIC) and the Large Hadron Collider (LHC). Furthermore, finite temperature breaks both supersymmetry as well as conformal invariance so that  $\mathcal{N} = 4$  Super-Yang-Mills and QCD at these temperatures become similar. On the gravity side, the thermal state is described by a black hole [43, 44].

So the natural question arises: Can we make *quantitative predictions* for the quark-gluon plasma by using gauge/gravity duality? Taking the microscopic differences of QCD and  $\mathcal{N} = 4$  Super-Yang-Mills into account, the answer is, surprisingly, yes. For instance the energy density normalized to the energy density at zero coupling determined by lattice QCD and by gauge/gravity duality agree up to an error of 10% [45–47]. Also, gravity calculations nicely confirm that heavy mesons, such as  $\eta_c$  and  $J/\psi$  containing the charm quark, survive the deconfinement transition and melt only at higher temperatures [40, 48–50].

The most famous result in the context of gauge/gravity duality is definitely the small and universal ratio between the shear viscosity and the entropy density [51–56]. The ratio is the same for all field theories which have an Einstein gravity dual, i. e. the field theory is a large  $N_c$  gauge theory at infinite 't Hooft coupling  $\lambda$ . Only small deviations from this universal value have been found if finite  $N$  and/or coupling is considered by for instance adding a Gauss-Bonnet term to the gravity action (see e. g. [57, 58]), or if the system is anisotropic as discussed below. The small value for this ratio is also found experimentally by analyzing the hydrodynamic evolution of the quark-gluon plasma [59]. A more detailed discussion of gauge/gravity duality at

---

<sup>2</sup>Non-coincident branes have been studied e. g. in [36, 37].

<sup>3</sup>A review for the unquenched flavors in gauge/gravity duality is given in [38].

finite temperature can be found in chapter 4.

In the context of heavy ion collisions, there are also attempts to describe the full evolution of the system in a gravity dual (for reviews see [60,61]). By colliding the ions, a “fireball” out of equilibrium is produced, which is expected to thermalize. This *thermalization* is described by the creation of a black hole horizon on the gravity side (see e. g. [62–64]). Since the quark-gluon plasma is strongly coupled, particle traveling through the plasma interact strongly with the plasma so that their energy is reduced significantly [59,65]. This energy reduction is called *jet quenching*. A review of gravitational studies of this effect can be found in [66]. Due to the expansion of the quark-gluon plasma, the energy density, and thus the temperature, get lowered so that the quarks and gluons form hadrons. This process is known as *hadronization* and has been studied by holographic methods in [67,68].

Motivated by the great success in applying gauge/gravity duality to hot plasmas, it is reasonable to consider also hot and *dense* plasmas. The state of these plasmas is usually controlled by the temperature and the *chemical potential*. For QCD it is very common to introduce a baryon as well as an isospin chemical potential. The baryon chemical potential favors quarks compared to antiquarks while an isospin chemical potential introduces an imbalance between the different flavors. By varying the control parameters, temperature and chemical potentials, the state of a system can change drastically. The system undergoes a phase transition. An overview of the preferred phases at a given set of control parameters is given in the *phase diagram*, which is usually difficult to obtain theoretically. For instance, the structure of the QCD phase diagram is still under debate (see e. g. [69]). Since gauge/gravity duality allows one to study field theories at finite temperature and chemical potentials, it may give some insight into the QCD phase diagram (see e. g. [70–74]). More details on chemical potentials in the context of gauge/gravity duality can be found in chapter 5.

A special kind of phase transition is the *quantum phase transition* [75] which occurs at zero temperature and is driven by quantum fluctuations instead of thermal fluctuations. Especially interesting are continuous quantum phase transitions which feature a *quantum critical point*. This quantum critical point influences the phase diagram also at non-zero temperature. In this influenced region, the *quantum critical region*, the system may be described by a critical theory even at finite temperature [76,77]. It is expected that many strongly coupled condensed matter systems such as e. g. cuprates and ultra-cold Fermi gases undergo this kind of phase transition. These systems show interesting and unexplained phenomena such as non-Fermi liquid behavior and high  $T_c$  superconductivity, especially in the quantum critical region. Since gauge/gravity duality is suitable to describe strongly coupled critical theories, it should help to understand these effects. For reviews on this subject see [78–81]. Indeed, remarkable progress has been made in the application of gauge/gravity duality towards the description of superfluids and superconductors following the results of [82], as well as of (non-) Fermi liquids [83–90].

Let us now focus on the description of *superfluids* and *superconductors* in the

context of gauge/gravity duality which we discuss in chapter 6 (for a review see [91]). The spontaneous breaking of continuous symmetries by black holes developing hair was first achieved in [92] and later used to construct holographic superconductors/superfluids by breaking an Abelian symmetry [82, 93–98]. The relation between a spontaneously broken  $U(1)$  symmetry and superconductivity/superfluidity is for instance explained in [12, sec. 21.6]. Since in the context of gauge/gravity duality the broken symmetry is usually global on the field theory side, the system describes a superfluid and not a superconductor.

P-wave superfluids have also been constructed [4, 99, 100] where, in addition to the Abelian symmetry, the rotational group is also broken since the condensate is a Lorentz vector<sup>4</sup>. These holographic p-wave superfluids gave rise to the first *string theory embedding* of holographic superfluids [1, 2, 102]. Later on additional embeddings into string theory followed [103–109]. The models embedded into string theory have an important advantage: The dual field theories are explicitly known. For instance, we know their microscopic degrees of freedom as well as their Lagrangians. This allows us to compare strong with weak coupling calculations. Also the condensation process may be understood in terms of the microscopic degrees of freedom.

The influence of a magnetic field on holographic superfluids was studied in [110–114] and it has been found that the superfluid phase disappears at large magnetic fields. This is a remnant of the *Meissner-Ochsenfeld effect*. In order to generate the current expelling the magnetic field, the spontaneously broken  $U(1)$  must be gauged. Zero temperature solutions of holographic superfluids have been obtained in [115–119] and have revealed an *emergent scaling invariance* in the IR. This shows that holographic superfluids are controlled by a quantum critical point as expected for high  $T_c$  superconductors.

The fermionic response of holographic superfluids has been studied in [120–125] and relevant structures have been found, e. g. the *peak-dip-hump* and the *collapsing of Fermi surfaces*. These structures are known from angle-resolved photoemission spectroscopy (ARPES) [126].

Due to the spontaneous breaking of a global symmetry, a Nambu-Goldstone mode appears in the spectrum of superfluids and must be included in the hydrodynamic description of the system. This mode leads to additional sound modes, the *second* and the *fourth sound* [127], which have been studied in holographic s-wave superfluids [128–131]. A *full* hydrodynamic description has been obtained in [132–134] via the fluid/gravity correspondence [135, 136]. These studies rely on the analytic results found in [128, 137].

For holographic p-wave superfluids, additional Nambu-Goldstone bosons appear due to the breaking of the rotational symmetry. Thus, more modes have to be included into the hydrodynamic description, which makes it more interesting. Explicit holographic studies of hydrodynamics in these anisotropic superfluids have been first done in my own work [5, 8]. The most important result found there is that the universality of the ratio between shear viscosity and entropy density is destroyed in

---

<sup>4</sup>D-wave superfluids were constructed in [101].

anisotropic fluids. This was the first known way to obtain a non-universal ratio of shear viscosity to entropy density at leading order in  $N_c$  and 't Hooft coupling  $\lambda$ , i. e. from an Einstein gravity dual. Another realization was found later in [138].

### Achievements of this Thesis

In this thesis a special focus lies on holographic p-wave superfluids. We discuss their construction in the  $U(2)$  Einstein-Yang-Mills theory as well as their embedding into string theory by considering the D3/D7 brane model. Furthermore, we study the response of the broken phase due to small perturbations and determine its transport properties. In addition, instabilities which trigger the condensation to holographic superfluids are discussed. In this context the study of quasinormal modes which are dual to the poles of the field theory Green's functions are very useful. We study these quasinormal modes at finite temperature and density, especially in the D3/D7 brane model. The foundation of this thesis is given by the results of my studies:

**Quasinormal Modes of Massive Charged Flavors** We analyze the quasinormal mode spectrum in the D3/D7 brane setup at finite temperature and baryon density. Amongst our findings is a new purely imaginary scalar mode that becomes tachyonic at sufficiently low temperature and baryon density. In the vector sector we study the crossover from the hydrodynamic to the quasiparticle regime. In addition, we find non-trivial trajectories of the quasinormal frequencies as we vary temperature and density. The results can be found in [3] and section 4.3.3 and 5.3.2.

**Black Hole Instabilities** We find a new black hole instability in asymptotically AdS spaces. On the field theory side, this instability is induced by a magnetic field or a finite chemical potential. On the gravity side, this corresponds to a spatial component or time component of the gauge field in  $SU(2)$  Einstein-Yang-Mills theory, which provides the crucial non-Abelian structure. Our analysis may provide supporting evidence for recent QCD studies of  $\rho$  meson condensation induced by a magnetic field [139–142]. For more details see [7] and section 5.5.

**Hairy Black Hole Solution** In [4] we numerically construct asymptotically Anti-de Sitter charged black hole solutions of  $(4 + 1)$ -dimensional  $SU(2)$  Einstein-Yang-Mills theory that, for sufficiently low temperature, develop vector hair. These solutions are holographic p-wave superfluids. Previous analyses have shown that in the so-called probe limit, where the gauge fields are ignored in Einstein's equation, the transition to the superfluid state is second order. We construct fully back-reacted solutions, where the gauge fields are included in Einstein's equation, and find that above a critical strength of the back-reaction, the transition becomes first order.

**Holographic Vector Meson Condensate** We embed holographic p-wave superfluids into string theory by considering a probe of two D7-branes embedded

in the AdS black hole background. This has been the first embedding of a holographic superfluid in string theory which is presented in [1, 2]. We find a critical temperature at which the system undergoes a second order phase transition. The new ground state may be interpreted as a  $\rho$  meson superfluid. The embedding into string theory allows for an explicit identification of the degrees of freedom in the dual field theory as well as for a dual string picture of the condensation process.

**Holographic Superfluidity in Imbalanced Mixtures** In [6] we construct superfluid black hole solutions at finite baryon and isospin chemical potentials in the two systems discussed above: the back-reacted  $U(2)$  Einstein-Yang-Mills theory and the D3/D7 brane setup. Studying the phase diagram, we find in both systems a quantum phase transition at a critical ratio of the two chemical potentials. However, the quantum phase transition is different in the two systems: In the D3/D7 brane setup we always find a second order phase transition, while in the Einstein-Yang-Mills theory, depending on the strength of the back-reaction, we obtain a continuous or first order transition. We comment on the origin of this differing behavior in these apparently very similar models and compare to phenomenological systems.

**Transport in Anisotropic Superfluids** We study transport properties of holographic p-wave superfluids in [5, 8]. Due to the spacetime anisotropy of the system, the tensorial structure of the transport coefficients is non-trivial in contrast to the isotropic case. In particular, there is an additional shear mode which leads to a non-universal value of the shear viscosity even in an Einstein gravity setup. In addition to the non-universal shear viscosity, we also investigate the thermoelectric effect, i. e. the mixing of electric and heat current. Moreover, we also find an additional effect due to the anisotropy, the so-called flexoelectric effect.

The latter four topics about holographic p-wave superfluids are presented in chapter 6.

## Structure of this Thesis

To conclude the above introductory remarks, we give an overview of the rest of this thesis. At the beginning of each chapter we discuss the main ideas and results of the chapter. The chapters cover the following subjects:

- The present chapter includes a general introduction as well as an overview of this thesis.
- Chapter 2 introduces the basic concepts of string theory. We especially focus on subjects needed in the construction of gauge/gravity duals.

- In chapter 3 the original AdS/CFT correspondence as well as some generalizations, in particular the introduction of fundamental matter, are presented.
- Chapter 4 is devoted to gauge/gravity duality at finite temperature and the comparison to the quark-gluon plasma.
- In chapter 5, in addition to the finite temperature, finite baryon and isospin chemical potentials are considered.
- Chapter 6 is dedicated to the investigation of holographic p-wave superfluids.
- Chapter 7 concludes this thesis by summarizing the results as well as giving an outlook on open questions and possible further developments.

## Introduction to String Theory

Initially in the 1960's, string theory was constructed to describe hadrons and the strong interaction since the experimentally found Regge trajectories (see e. g. [143]), which describe the relation between meson mass and spin, can be understood from rotating strings (see e. g. [144]). Later a massless spin two particle was discovered in the string theory spectrum. Since no massless spin two meson had been detected, string theory was considered to fail as a theory of hadrons and quantum chromodynamics (QCD) was recognized as the right description of the strong interaction. However, since then the massless spin two particle has been interpreted as the graviton and Einstein's equations of general relativity were derived from string theory [145]. This suggested that string theory is a theory of gravity and not a theory of hadrons. This insight induced the first string revolution which leads to the five consistent superstring theories known today. Subsequently, dualities between these theories were revealed which resulted in the discovery of higher-dimensional objects, the branes [146]. This stage is named the second string revolution. One conjecture stated as a consequence of this revolution was the AdS/CFT correspondence [25]. This correspondence is a concrete realization of the holographic principle (see e. g. [15–17]), and relates a gauge theory to a higher-dimensional gravity theory. It is discussed in the next chapter.

In this chapter we review the important developments in string theory which lead to the AdS/CFT correspondence. More detailed presentations are given e. g. in [20–23]. We first look at the bosonic string theory in order to build up the string theory machinery and later generalize it to superstring theory. In the following we discuss the action principle of string theory, the resulting equations of motion and the spectrum. In the spectrum the fundamental force carriers, gauge bosons and a graviton, are present. Considering the low energy limit of string theory, also their known dynamics, the (Super-)Yang-Mills theories and the (Super)Gravity theories, emerge. These theories are phenomenologically very interesting since experimentally well-tested theories, such as the standard model, are formulated in this context.

## 2.1 Bosonic String Theory

In this section we give an introduction to the bosonic string theory focusing on the material relevant for constructing the AdS/CFT correspondence. We follow the description of [21]. We start by generalizing the action of a point particle to an one-dimensional object, a string. In section 2.1.2 we determine the spectrum of the bosonic string theory and find a  $U(1)$  gauge boson in the open string sector and a graviton in the closed string sector. In addition, we obtain that the bosonic string theory must be formulated in 26 dimensions<sup>1</sup>. In section 2.1.3 we discuss the perturbative description of string theory and determine the string coupling constant. The low-energy theory of closed string theory in which general relativity coupled to a two-form, the Kalb-Ramond field, and a scalar, the dilaton emerges is investigated in section 2.1.4. In section 2.1.5 we consider toroidal compactifications and find a non-trivial symmetry in the spectrum of closed strings, the T-duality. Applying this duality in the open string sector leads to higher-dimensional dynamical objects, the Dirichlet branes or short D-branes.

### 2.1.1 From Point Particles to Strings

First we discuss the pathway from a relativistic point particle to a relativistic string which both move in  $D$ -dimensional curved spacetime with metric  $G_{MN}$ . The position of a point particle at a given time  $X_0$  is given by  $D - 1$  functions  $\mathbf{X}(X_0)$  which define the *worldline*. In order to show the covariance of the theory, it is better to parameterize the world line by the parameter  $\tau$  such that  $D$  functions  $X^M(\tau)$  define the worldline where two worldlines  $X'^M$  and  $X^M$  are the same if  $X'^M(\tau'(\tau)) = X^M(\tau)$  for any monotonic function  $\tau'(\tau)$ . The simplest action which is independent of the parameter  $\tau$  is given by the length of the worldline, i. e. the proper time,

$$S_{\text{pp}} = -m \int d\tau \sqrt{-G^{MN} \dot{X}_M \dot{X}_N}, \quad (2.1)$$

where  $g^{MN} \dot{X}_M \dot{X}_N$  is the induced metric on the worldline and  $m$  the mass of the particle. In order to write the action in a more useful form without the square root, we introduce an additional independent field, the worldline metric  $\gamma_{\tau\tau}(\tau)$  and define

$$S'_{\text{pp}} = \frac{1}{2} \int d\tau \left( \frac{G^{MN} \dot{X}_M \dot{X}_N}{\sqrt{-\gamma_{\tau\tau}}} - \sqrt{-\gamma_{\tau\tau}} m^2 \right), \quad (2.2)$$

which reduces to the action (2.1) by using the equation of motion  $\gamma_{\tau\tau} = \dot{X}^M \dot{X}_M / m^2$ .

Now we repeat this consideration for a one-dimensional object, a string, whose motion defines a two-dimensional *worldsheet*  $\mathcal{W}$  instead of the one-dimensional

---

<sup>1</sup>This is the critical dimension where flat, Lorentz invariant spacetime solutions exists. If the dimension is non-critical, a non-trivial target space with a spacetime depending vacuum expectation value of the dilaton has to be introduced.

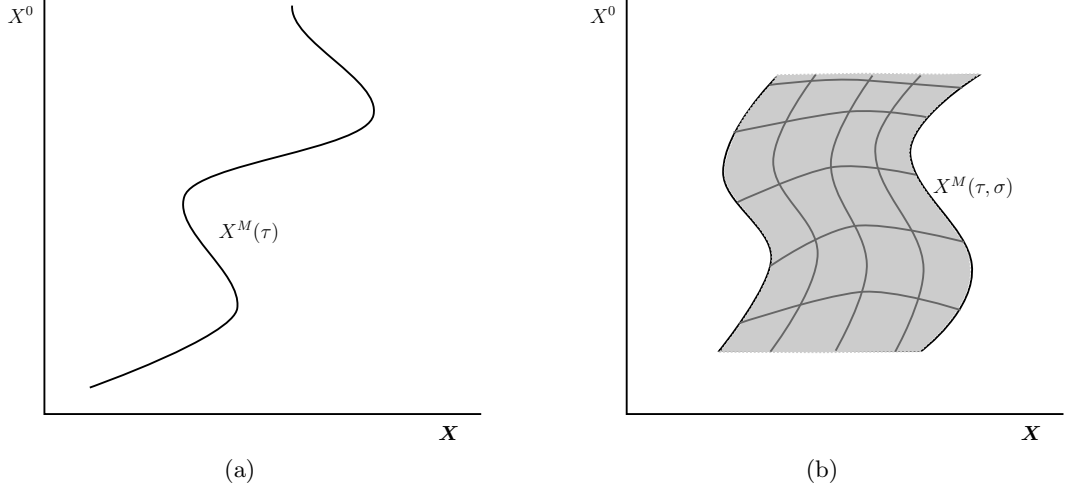


**Figure 2.1:** (a) Worldline  $X^M(\tau)$  of a point particle. (b) Worldsheet  $X^M(\tau, \sigma)$  of an open string.

worldline. We parameterize the worldsheet  $\mathcal{W}$  by  $X^M(\tau, \sigma) = X^M(\sigma^a)$  with  $a = 1, 2$ . The *Nambu-Goto action* is defined by the area of the worldsheet

$$S_{\text{NG}} = -\frac{1}{2\pi\alpha'} \int_{\mathcal{W}} d\tau d\sigma \sqrt{-\det(G^{MN} \partial_a X_M \partial_b X_N)}, \quad (2.3)$$

where  $h_{ab} = G^{MN} \partial_a X_M \partial_b X_N$  is the induced metric on the worldsheet and  $\alpha'$  the Regge slope which is related to the string tension  $T = 1/(2\pi\alpha')$ . In order to eliminate the square root in the string action, we introduce a metric  $\gamma_{ab}$  on the worldsheet. The action now reads

$$S_{\text{P}} = -\frac{1}{4\pi\alpha'} \int_{\mathcal{W}} d\tau d\sigma \sqrt{-\gamma} G^{MN} \gamma^{ab} \partial_a X_M \partial_b X_N, \quad (2.4)$$

which is known as the *Polyakov action* and where  $\gamma$  is the determinant of the metric  $\gamma_{ab}$ . Using the equation of motion  $h_{ab}(-h)^{-\frac{1}{2}} = \gamma_{ab}(-\gamma)^{-\frac{1}{2}}$ , the Polyakov action reduces to the Nambu-Goto action. Given the action for the string, we can now characterize the symmetries of the theory:

1.  $D$ -dimensional Poincaré invariance in flat space, i. e.  $G_{MN} = \eta_{MN}$ :

$$\begin{aligned} X'^M(\sigma^a) &= \Lambda^M_N X^N(\sigma^a) + a^M, \\ \gamma'_{ab}(\sigma^a) &= \gamma_{ab}(\sigma^a). \end{aligned} \quad (2.5)$$

2. Diffeomorphism invariance:

$$\begin{aligned} X'^M(\sigma'^a) &= X^M(\sigma^a), \\ \gamma'_{ab}(\sigma'^a) &= \gamma_{cd}(\sigma^a) \frac{\partial \sigma^c}{\partial \sigma'^a} \frac{\partial \sigma^d}{\partial \sigma'^b}, \end{aligned} \quad (2.6)$$

for new worldsheet coordinates  $\sigma'^a(\sigma^a)$

3. Two-dimensional Weyl invariance:

$$\begin{aligned} X'^M(\sigma^a) &= X^M(\sigma^a), \\ \gamma'_{ab}(\sigma^a) &= e^{2\omega(\sigma^a)}\gamma_{ab}(\sigma^a), \end{aligned} \quad (2.7)$$

for arbitrary worldsheet transformations  $\omega(\sigma^a)$ .

These symmetries, especially the Weyl invariance which is not present for the point particle, will play an important role when we quantize the theory. Before quantization we first have to understand the full classical action which has to be the most general action consistent with the above symmetries. Enforcing diffeomorphism invariance leads to the usual factor  $\sqrt{-\gamma}$  in the integral measure. To cancel its variation under the Weyl transformation, one more factor of  $\gamma^{ab}$  than  $\gamma_{ab}$  has to be included. The additional upper indices can only be contracted with derivatives, such that each term has precisely two derivatives. Thus, the additional term in the action beyond the Polyakov action is given by

$$\chi = \frac{1}{4\pi} \int_{\mathcal{W}} d\tau d\sigma \sqrt{-\gamma} \mathcal{R}, \quad (2.8)$$

where  $\mathcal{R}$  is the Ricci scalar constructed from  $\gamma_{ab}$ .  $\chi$  only depends on the topology of the worldsheet and is called the Euler number. The most general action invariant under the symmetries above is therefore

$$S'_P = S_P - \lambda\chi = - \int_{\mathcal{W}} d\tau d\sigma \sqrt{-\gamma} \left( \frac{1}{4\pi\alpha'} G^{MN} \gamma^{ab} \partial_a X_M \partial_b X_N + \frac{\lambda}{4\pi} \mathcal{R} \right), \quad (2.9)$$

where  $\alpha'$  and  $\lambda$  are the only free parameters. Later  $\lambda$  will be related to the string coupling such that there is only one dimensionful free parameter which defines the length scale of the theory.

By using the variational principle, we find the equations of motion as well as the boundary conditions for the strings. We exclusively consider the variation of  $X^M(\sigma^a)$  since these are the dynamical fields. For concreteness, we take the coordinate region to be  $-\infty < \tau < \infty$  and  $0 \leq \sigma \leq \ell$ , where we think of  $\tau$  as a time variable and  $\sigma$  as spatial. The variation of the action (2.9) is given by

$$\begin{aligned} \delta S_P &= \frac{1}{2\pi\alpha'} \int_{-\infty}^{\infty} d\tau \int_0^{\ell} d\sigma \sqrt{-\gamma} G^{MN} \nabla^2 X_M \delta X_N \\ &\quad - \frac{1}{2\pi\alpha'} \int_{-\infty}^{\infty} d\tau \sqrt{-\gamma} G^{MN} \partial^\sigma X_M \delta X_N \Big|_{\sigma=0}^{\sigma=\ell}, \end{aligned} \quad (2.10)$$

such that the equation of motion for  $X^M(\sigma^a)$  is the wave equation  $\nabla^2 X^M = 0$ . The boundary term vanishes either if we have Neumann boundary conditions

$$n^a \partial_a X^M = 0 \quad \text{on } \partial\mathcal{W}, \quad (2.11)$$

where  $n^a$  is the normal to the worldsheet boundary  $\partial\mathcal{W}$  or if the fields are periodic

$$X^M(\tau, 0) = X^M(\tau, \ell), \quad \partial^\sigma X^M(\tau, 0) = \partial^\sigma X^M(\tau, \ell), \quad \gamma_{ab}(\tau, 0) = \gamma_{ab}(\tau, \ell). \quad (2.12)$$

The Neumann boundary condition describes open strings whose endpoints move freely in spacetime while the periodic boundary condition describes closed strings. These two boundary conditions are the only possibilities which are consistent with  $D$ -dimensional Poincaré invariance of flat space. We will consider more complicated boundary conditions in section 2.1.5 where the  $D$ -dimensional Poincaré symmetry is broken by D-branes.

### 2.1.2 String Spectrum

In this section we discuss the mass spectrum of strings in flat space  $G_{MN} = \eta_{MN}$ . First we notice that string theory has an enormous symmetry group given by diffeomorphisms and Weyl symmetry which could lead to an enormous overcounting of the physical configurations. However, it is possible to fix a large amount of this gauge freedom (up to transformations of measure zero) by choosing a flat worldsheet metric  $\gamma_{ab} = \eta_{ab}$ . In this gauge, the equations of motion for  $X^M$  and  $\gamma_{ab}$  become

$$\begin{aligned} 0 &= (\partial_\tau^2 - \partial_\sigma^2) X^M, \\ 0 &= \partial_\tau X^M \partial_\sigma X_M, \\ 0 &= \partial_\tau X^M \partial_\tau X_M + \partial_\sigma X^M \partial_\sigma X_M. \end{aligned} \quad (2.13)$$

The constraints, known as *Virasoro constraints*, appear since we fix the gauge  $\gamma_{ab} = \eta_{ab}$ . In addition to the equations of motion, a solution must also satisfy the boundary conditions (2.11) and (2.12), respectively.

### Open String Spectrum

A solution to the wave equation which also satisfies the open string boundary condition (2.11) is given by

$$X^M(\tau, \sigma) = x^M + \frac{2\pi\alpha'}{\ell} p^M \tau + i\sqrt{2\alpha'} \sum_{n \neq 0} \frac{1}{n} \alpha_n^M \exp\left(-\frac{i\pi n \tau}{\ell}\right) \cos \frac{\pi n \sigma}{\ell}, \quad (2.14)$$

where  $x^M$  and  $p^M$  are the center of mass position and momentum.

We quantize the theory by imposing equal time canonical commutation relations,

$$[X^M(\tau, \sigma), \Pi^N(\tau, \sigma')] = i\eta^{MN} \delta(\sigma - \sigma'), \quad (2.15)$$

with the conjugate momentum  $\Pi^N(\tau, \sigma) = \partial_\tau X^N(\tau, \sigma)/2\pi\alpha'$ . This induces the canonical commutation relation for the center of mass position and momentum,

$$[x^M, p^N] = i\eta^{MN}, \quad (2.16)$$

and the commutation relation similar to the harmonic oscillator algebra for the coefficients  $\alpha_m^M$ ,

$$[\alpha_m^M, \alpha_n^N] = m\eta^{MN}\delta_{m,-n}. \quad (2.17)$$

In order to make the similarity explicit, we define

$$a_m^M = \alpha_m^M/\sqrt{m} \quad \text{and} \quad a_m^{M\dagger} = \alpha_{-m}^M/\sqrt{m} \quad (2.18)$$

for  $m > 0$  such that

$$[a_m^M, a_n^{N\dagger}] = \eta^{MN}\delta_{mn}. \quad (2.19)$$

Therefore, the Hilbert space of each open string mode distinguished by  $m$  is the Hilbert space of the harmonic oscillator. Their ground states  $|0\rangle$  are annihilated by the lowering operators  $a_m^M$  for  $m > 0$ . This Hilbert space has a severe problem: It contains negative norm states due to the commutation relations  $[a_m^0, a_m^{0\dagger}] = -1$ . This problem is already known from gauge theories and can be cured by fixing the gauge symmetries (see e. g. [11, sec. 8.2]). In string theory, the diffeomorphisms and Weyl symmetry have to be fixed by the Virasoro constraints (2.13) which leaves only  $(D-2)$  dynamical fields  $X^i(\tau, \sigma)$  and  $(D-2)$  raising operators  $a^{i\dagger}$  to generate physical states.

A general state  $|N\rangle$  can be build out of the vacuum  $|0\rangle$ ,

$$|N\rangle = \left[ \prod_{i=1}^{D-2} \prod_{n=1}^{\infty} \frac{(a_n^{i\dagger})^{N_{in}}}{\sqrt{N_{in}!}} \right] |0\rangle, \quad (2.20)$$

where  $N_{in}$  is the occupation number for each mode. The mass of the state  $m^2 = -p^M p_M$  is determined by

$$m^2 = \frac{1}{\alpha'} \left( N + \frac{2-D}{24} \right), \quad (2.21)$$

where  $N = \sum_i \sum_n n N_{in}$  and  $(2-D)/24$  is the operator ordering constant (see [21, sec. 1.3] for an explicit calculation). The level of the excitation determines the mass of the state. The lightest state is the vacuum

$$|0\rangle, \quad m^2 = \frac{2-D}{24\alpha'}, \quad (2.22)$$

which has a negative mass-squared if  $D > 2$ . This is a tachyonic mode and shows that the vacuum is unstable. So far, it is unknown if the bosonic string has a stable vacuum. However, in superstring theory which we study in section 2.2, this problem

is cured. Let us for now just ignore this problem and use the bosonic string theory as a toy model to develop the string technology.

The lowest excited states are obtained by exciting one of the  $n = 1$  modes,

$$a_1^{i\dagger}|0\rangle, \quad m^2 = \frac{26 - D}{24}. \quad (2.23)$$

These states transform as vector. Since we require Lorentz invariance, a vector with only  $D - 2$  states has to be massless such that the dimension of spacetime is restricted to  $D = 26$ . The same result can also be obtained by considering the Weyl anomaly which must be cancelled in string theory (see e. g. [21, sec. 3.4]).

In general, a massless vector can only couple to a conserved current (see e. g. [11, sec. 8.1]) and, thus, the theory has a gauge symmetry. In this simple case the gauge symmetry is just  $U(1)$ . However, we will also find non-Abelian gauge symmetries in section 2.1.5 by considering coincident D-branes.

## Closed String Spectrum

A solution to the wave equation which also satisfies the closed string boundary condition (2.12) is given by a combination of left- and right-moving waves,

$$X^M(\tau, \sigma) = X_L^M(\tau + \sigma) + X_R^M(\tau - \sigma), \quad (2.24)$$

with the mode expansion for the left- and right-movers are given by

$$\begin{aligned} X_L^M(\tau + \sigma) &= \frac{1}{2}x^M + \frac{\pi\alpha'}{l}p^M + i\sqrt{\frac{\alpha'}{2}} \sum_{n \neq 0} \frac{1}{n} \tilde{\alpha}_n^M \exp\left(-\frac{2\pi i n(\sigma + \tau)}{l}\right), \\ X_R^M(\tau - \sigma) &= \frac{1}{2}x^M + \frac{\pi\alpha'}{l}p^M + i\sqrt{\frac{\alpha'}{2}} \sum_{n \neq 0} \frac{1}{n} \alpha_n^M \exp\left(-\frac{2\pi i n(\tau - \sigma)}{l}\right). \end{aligned} \quad (2.25)$$

The equal time canonical commutation relations (2.15) again induces the canonical commutation relations for the center of mass position  $x^M$  and momentum  $p^M$  (see (2.16)) and commutations relation for  $\alpha_n^M$  and  $\tilde{\alpha}_n^M$  similar to the harmonic oscillator algebra (2.19),

$$[\alpha_m^M, \alpha_n^N] = m\eta^{MN} \delta_{m,-n}, \quad [\tilde{\alpha}_m^M, \tilde{\alpha}_n^N] = m\eta^{MN} \delta_{m,-n}. \quad (2.26)$$

For the closed strings, the Hilbert space is now a direct sum of two copies of the Hilbert space for the harmonic oscillators: one for the left-movers

$$\tilde{a}_n^M = \tilde{\alpha}_n^M / \sqrt{n}, \quad \tilde{a}_n^{M\dagger} = \tilde{\alpha}_{-n}^M / \sqrt{n}, \quad (2.27)$$

and one for the right-movers

$$a_n^M = \alpha_n^M / \sqrt{n}, \quad a_n^{M\dagger} = \alpha_{-n}^M / \sqrt{n}. \quad (2.28)$$

As in the open string, the closed string Hilbert space also seems to contain negative norm states. These states are projected out by satisfying the Virasoro constraints (2.13) such that now only  $D - 2$  creation operators  $a^{i\dagger}$  and  $\tilde{a}^{i\dagger}$  generate physical states.

A general state  $|N, \tilde{N}\rangle$  can be built from the vacuum  $|0, 0\rangle$ ,

$$|N, \tilde{N}\rangle = \left[ \prod_{i=1}^{D-2} \prod_{n=1}^{\infty} \frac{(a_n^{i\dagger})^{N_{in}} (\tilde{a}_n^{i\dagger})^{\tilde{N}_{in}}}{\sqrt{N_{in}! \tilde{N}_{in}!}} \right] |0, 0\rangle, \quad (2.29)$$

and its mass can be determined by  $m^2 = -p^M p_M$ ,

$$m^2 = \frac{2}{\alpha'} \left( N + \tilde{N} + 2 \frac{2-D}{24} \right). \quad (2.30)$$

In order to obtain gauge invariant states also the translation in the  $\sigma$  direction has to be canceled which leads to  $N = \tilde{N}$ .

The lightest state is the vacuum

$$|0, 0\rangle, \quad m^2 = \frac{2-D}{6\alpha'}, \quad (2.31)$$

which is again tachyonic. The first excited states are

$$a_1^i \tilde{a}_1^j |0, 0\rangle, \quad m^2 = \frac{26-D}{6\alpha'}, \quad (2.32)$$

and transform as a massless two-tensor if  $D = 26$ . It can be decomposed into a symmetric traceless tensor, an antisymmetric tensor and a scalar.

In general, a massless symmetric tensor must couple to a conserved symmetric tensor which is the energy-momentum tensor in our case. Thus, the massless symmetric tensor is the graviton and the theory must have spacetime covariance which should lead to gravity. We will explicitly find Einstein's equations for gravity in section 2.1.4. In addition, we find a gauge symmetry which is related to the antisymmetric two-tensor.

### 2.1.3 String Perturbation Theory

In field theory, Feynman diagrams are a very useful concept in determining perturbative results for amplitudes, e.g. in scattering processes. They can be obtained by perturbatively evaluating the Feynman path integral in the coupling constant. Applying this reasoning to string theory allows us to identify the string coupling constant and to find a diagrammatic form of the perturbation theory.

In the Euclidean path integral formalism, all paths which connect the initial and final configuration are summed up with the weight  $\exp(-I)$  where  $I$  is the Euclidean action evaluated on the path considered. In string theory this means

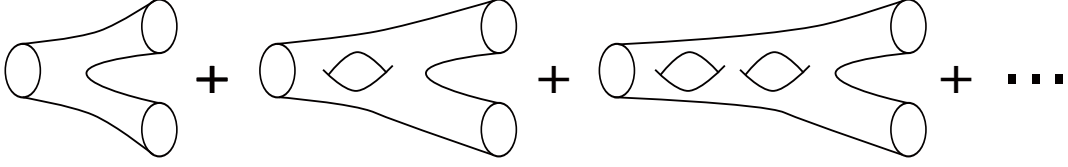


**Figure 2.2:** Worldsheets for the decay of a closed string into two closed strings.

that we have to sum over different worldsheets. For closed strings the sum contains all two-dimensional oriented surfaces without boundaries while for the open strings boundaries have to be included. These worldsheets can be distinguished by their topology. Especially, the number of handles counted by the genus  $g$  is used to distinguish them. Using this distinction, the path integral over all worldsheets  $\mathcal{W}$  decomposes into a sum over genera  $g$  and an integral over the worldsheets  $\mathcal{W}_g$  with genus  $g$ ,

$$\mathcal{Z} = \int_{\mathcal{W}} \mathcal{D}X^M \mathcal{D}\gamma_{ab} e^{-I'_P} = \sum_g \int_{\mathcal{W}_g} \mathcal{D}X^M \mathcal{D}\gamma_{ab} e^{-I'_P}, \quad (2.33)$$

where  $I'_P$  is the Euclidean version of the action (2.9). Since the Euler number  $\chi = 2 - 2g$  contained in the action (2.9) only depends on the genus of the worldsheet, the partition function  $\mathcal{Z}$  becomes

$$\mathcal{Z} = \sum_g e^{-\lambda(2-2g)} \int_{\mathcal{W}_g} \mathcal{D}X^M \mathcal{D}\gamma_{ab} e^{-I_P}, \quad (2.34)$$

where  $I_P$  is the Euclidean version of the Polyakov action (2.4). Thus, varying the genus of the worldsheet changes the relative weight in the path integral.

In order to identify a coupling constant, we consider a scattering process in string theory, e. g. the decay of one closed string in two closed strings. The worldsheets for this process are given in figure 2.2. In the first diagram the genus of the worldsheet is zero while it is one in the second such that the relative weight is changed by a factor  $\exp(2\lambda)$ . In the second worldsheet, the handle may be interpreted as an emission and reabsorption of a closed string such that there are two vertices and the coupling constant is given by  $g_{\text{closed}} = \exp(\lambda)$ . Similarly the coupling constant for the open string can be found and is related to the closed string coupling constant,

$$g_s = g_{\text{closed}} = g_{\text{open}}^2 = e^\lambda. \quad (2.35)$$

In the next section we will identify  $\lambda$  and hence the string coupling constant with the vacuum expectation value of the dilaton field.

#### 2.1.4 Emergence of Gravity

In section 2.1.2 we found a graviton in the closed string spectrum in flat space. The condensation of these gravitons lead to a curved metric. Let us now consider the

massless closed string states in such a curved metric  $G_{MN}(X)$ . In addition to the background metric, we consider an antisymmetric two-tensor  $B_{2MN}(X)$ , the Kalb-Ramond field, and a dilaton<sup>2</sup>  $\Phi(X)$  in the background which can be seen as the condensate of the antisymmetric two-tensor and the scalar found in section 2.1.2, respectively. In this situation, the bosonic string action (2.9) becomes

$$S = \frac{1}{4\pi\alpha'} \int_{\mathcal{W}} d^2\sigma \sqrt{\gamma} \left[ \left( \gamma^{ab} G_{MN}(X) + i\epsilon^{ab} B_{2MN}(X) \right) \partial_a X^M \partial_b X^N + \alpha' \mathcal{R}\Phi(X) \right], \quad (2.36)$$

where now  $\lambda$  is identified with the dilaton field  $\Phi$ . We already noticed in the determination of the string spectrum that enforcing the theory to be Weyl invariant on the worldsheet induces important constraints. This is also true in this situation, and we may achieve Weyl invariance by demanding a traceless energy-momentum tensor on the worldsheet,

$$0 = T^a_a = -\frac{1}{2\alpha'} \beta_{MN}^G g^{ab} \partial_a X^M \partial_b X^N - \frac{i}{2\alpha'} \beta_{MN}^B \epsilon^{ab} \partial_a X^M \partial_b X^N - \frac{1}{2} \beta^\Phi \mathcal{R}, \quad (2.37)$$

which induces

$$\begin{aligned} 0 &= \beta_{MN}^G = \alpha' \mathcal{R}_{MN} + 2\alpha' \nabla_M \nabla_N \Phi - \frac{\alpha'}{4} H_{3MLO} H_{3N}{}^{LO} + \mathcal{O}(\alpha'^2), \\ 0 &= \beta_{MN}^B = -\frac{\alpha'}{2} \nabla^L H_{3LMN} + \alpha' \nabla^L \Phi H_{3LMN} + \mathcal{O}(\alpha'^2), \\ 0 &= \beta^\Phi = \frac{D-26}{6} - \frac{\alpha'}{2} \nabla^2 \Phi + \alpha' \nabla_L \Phi \nabla^L \Phi - \frac{\alpha'}{24} H_{3MNL} H_3^{MNL} + \mathcal{O}(\alpha'^2). \end{aligned} \quad (2.38)$$

Notice that here  $\mathcal{R}_{MN}$  is the spacetime Ricci tensor and  $H_3$  is the field strength of the two-form  $B_2$ ,  $H_3 = dB_2$ . The field strength  $H_3$  is invariant under the gauge transformation  $\delta_\xi B_{2MN} = \partial_M \xi_N - \partial_N \xi_M$ . At zero order in  $\alpha'$ , we obtain that the spacetime dimension is fixed,  $D = 26$ . At first order in  $\alpha'$ , we obtain the equations of motion for the background fields which can be derived from the action

$$S = \frac{1}{2\kappa_{26}^2} \int d^{26}x \sqrt{-G} e^{-2\Phi} \left[ \mathcal{R} - \frac{1}{12} H_{3MNL} H_3^{MNL} + 4\nabla_M \Phi \nabla^M \Phi + \mathcal{O}(\alpha'^2) \right]. \quad (2.39)$$

This is an effective action for the massless closed string states  $G_{MN}$ ,  $B_{2MN}$  and  $\Phi$ . Since the first term in the action is an Einstein-Hilbert term, we find general relativity emerging as the low energy theory of closed strings. We can use the spacetime Weyl transformation,

$$\tilde{G}_{MN} = e^{-\frac{1}{6}\Phi} G_{MN}, \quad (2.40)$$

---

<sup>2</sup>Strictly speaking the dilaton involves both the diagonal part of the metric  $G_{MN}$  and the field  $\Phi$ .

to obtain a canonical Einstein-Hilbert term

$$S = \frac{1}{2\kappa_{26}^2} \int d^{26}x \sqrt{-\tilde{G}} \left[ \tilde{\mathcal{R}} - \frac{1}{12} e^{-\frac{1}{3}\Phi} H_{3MNL} \tilde{H}_3^{MNL} - \frac{1}{6} \nabla_M \Phi \tilde{\nabla}^M \Phi + \mathcal{O}(\alpha'^2) \right], \quad (2.41)$$

where tensors with a tilde are obtained by using the metric  $\tilde{G}_{MN}$ . The action (2.39) written in terms of the original fields is denoted as the *string-frame action* while the latter (2.41) is called the *Einstein-frame action*.

The low-energy theory of closed strings is an Einstein gravity theory coupled to the Kalb-Ramond two-form field  $B_{2MN}$  and the dilaton  $\Phi$ . Thus, string theory is a generalization of general relativity and the quantized version of string theory, therefore, contains a realization of *Quantum Gravity*.<sup>3</sup>

### 2.1.5 T-Duality and D-Branes

In the previous section we have determined the low-energy effective action for closed strings and found a theory which contains gravity. Now we focus on open strings. We have already obtained a  $U(1)$  gauge boson in the spectrum of open strings in section 2.1.2. In this section we will introduce hyperplanes, the Dirichlet-branes or short the D-branes, on which open strings end. These hyperplanes break  $D$ -dimensional Lorentz invariance. In the spectrum of open strings attached to D-branes, we will find non-Abelian gauge bosons.

#### T-Duality

T-duality denotes the equivalence between two string theories compactified on different backgrounds. For simplicity let us consider the bosonic string theory compactified on a circle,

$$X^{25} \sim X^{25} + 2\pi R. \quad (2.42)$$

First we consider closed strings. As in field theory, the center-of-mass momentum around the circle must be quantized,  $p = n/R$  with  $n \in \mathbb{Z}$  in order to have single valued string states. This is the *Kaluza-Klein mechanism*. In addition to this mechanism, closed strings can also wind around the compact direction,  $X^{25}(\sigma + 2\pi\ell) = X^{25}(\sigma) + 2\pi R w$  where  $w \in \mathbb{Z}$  is conserved and known as the *winding number*. The mass spectrum of the closed strings compactified on the circle is given by

$$m^2 = -p^M p_M = \frac{n^2}{R^2} + \frac{w^2 R^2}{\alpha'^2} + \frac{2}{\alpha'} (N + \tilde{N} - 2), \quad (2.43)$$

where the first term is the contribution due to the momentum in the compact direction, the second term is the contribution due to the potential energy of the winding string while the last term is the usual oscillator and zero-point energy contribution

---

<sup>3</sup>So far, it is unclear if this realization is the one we observe in our universe. An other approach to Quantum gravity is e. g. Loop Quantum Gravity [24].

(see section 2.1.2). In order to cancel translations in the  $\sigma$  direction, we obtain the constraint

$$nw + N - \tilde{N} = 0, \quad (2.44)$$

where the first term is new compared to the discussion in section 2.1.2.

We obtain that the spectrum is invariant under the transformation

$$R \rightarrow R' = \frac{\alpha'}{R}, \quad n \leftrightarrow w, \quad (2.45)$$

named *T-duality*. This equivalence extends also to the interactions. Therefore, the compactifications with radius  $R \geq \sqrt{\alpha'}$  are equivalent to the compactifications with radius  $0 \leq R \leq \sqrt{\alpha'}$ <sup>4</sup>. For instance the noncompact limit  $R \rightarrow \infty$  where the momentum is continuous and the winding modes become infinitely massive is equivalent to the limit  $R \rightarrow 0$  where the winding states approach a continuum and the momentum states become infinitely heavy. This is an effect which is only present in string theories but not in field theories such that we can conclude that strings see geometry very differently.

Now we consider open strings which will lead to the D-branes. In the open string sector, which contain a  $U(1)$  gauge boson in the spectrum, there is a possibility of a nontrivial Wilson line,

$$W_q = \exp \left( iq \oint dx^{25} A_{25} \right) = \exp(-iq\theta), \quad (2.46)$$

induced by the constant gauge field  $A_{25} = -\theta/2\pi R$ . Due to the coupling of the open string and the gauge field,  $-iq \int dx^M A_M$ , this Wilson line modifies the spectrum

$$m^2 = \frac{(2\pi n + q\theta)^2}{4\pi^2 R^2} + \frac{1}{\alpha'}(N - 1), \quad (2.47)$$

where  $n$  counts the momentum in the compact direction. The first term is the square of the gauge-invariant momentum  $-i\partial_{25} - qA_{25}$  in the compact direction while the second is the usual oscillator and zero-point energy contribution (see section 2.1.2).

In the limit  $R \rightarrow 0$  we observe that the nonzero momentum states become arbitrary heavy as in the closed sector. However, there is no other quantum number like the winding number  $w$  which would lead to a continuum of states. Thus, we observe the resulting states move in 25 dimensions. Since a theory of open strings always contains closed strings, it seems inconsistent that open strings move only in 25 dimensions while closed strings move in 26 dimensions.

In order to solve this problem, we have to focus on the endpoint of the open strings: Under T-duality the Neumann condition translates to Dirichlet condition such that the T-dual coordinate  $X'^{25}$  is fixed for each endpoint of the string. Indeed both endpoints are constrained on the same hyperplane which is the D-brane. By T-dualizing another orthogonal direction, we can also fix its T-dual coordinate. Thus, by T-dualizing  $25 - p$  orthogonal directions we end up with a  $p$ -dimensional hypersurface, the  $Dp$ -brane.

---

<sup>4</sup> $R = \sqrt{\alpha'}$  is the self-dual radius at which the gauge symmetry is enhanced.

## Chan-Paton Factors

Now the question arises: Can we also obtain different hyperplanes where the open string must end? This can be achieved by the *Chan-Paton* factors which are quantum numbers,  $i, j = 1, \dots, n$  associated to the endpoints of open strings. This of course lead to  $n^2$  gauge bosons in the open string spectrum, one for each combination of the Chan-Paton factors and it can be shown that this generates an  $U(n)$  gauge symmetry with generators  $\lambda_{ij}^a$ . Now let us generalize the Wilson line to this non-Abelian gauge group. A constant gauge field  $A_{25}$  can always be diagonalized,

$$A_{25} = -\frac{1}{2\pi R} \text{diag}(\theta_1, \dots, \theta_n), \quad (2.48)$$

and the open string spectrum becomes

$$m^2 = \frac{(2\pi l - \theta_j + \theta_i)^2}{4\pi^2 R^2} + \frac{1}{\alpha'}(N - 1), \quad (2.49)$$

where now the differences of the  $\theta$ 's appear. The gauge bosons  $A^a \lambda_{ij}^a$ ,  $N = 1$ ,  $l = 0$ , may now be massive,  $m^2 \propto (\theta_i - \theta_j)^2$ . In a generic setup only the diagonal ones, i. e.  $i = j$ , are massless such that the unbroken gauge symmetry is  $U(1)^n$ . If the  $n$   $\theta$ 's coincide in sets of  $r_i$ , the gauge group is enhanced to  $U(r_1) \times \dots \times U(r_s)$  with  $\sum_{i=1}^s r_i = n$ .

Due to T-duality it is still true that the endpoints of the open strings are fixed to the T-dual coordinate  $X^{25}$ . But in contrast to the Abelian case, the string may now end on different hyperplanes denoted by the Chan-Paton factor. These hyperplanes are separated by a distance proportional to the difference in the  $\theta$ 's. In a generic setup we obtain  $n$  distinct hyperplanes. But if some  $\theta$ 's are equal, the hyperplanes coincide and in the spectrum we find non-Abelian gauge fields.

## D-Branes

Let us now study these hyperplanes in more detail. We will find that they are dynamical objects named Dirichlet-branes or short D-branes. We have seen above that the diagonal elements of the gauge field correspond to the positions of the branes. A spacetime dependent value of these gauge field components changes the shape of the brane and a fluctuation in the gauge field translate into an oscillation of the brane. Thus, the shape of the brane is dynamical and it must be determined by an action.

An effective action for a single D $p$ -brane can be written in terms of the massless fields on its worldvolume. They are a  $U(1)$  gauge field  $A_\alpha(\xi)$  with  $\alpha = 0, \dots, p$  and  $25 - p$  transversal scalars  $X^{\mathcal{A}}(\xi)$  with  $\mathcal{A} = p + 1, \dots, 25$  which describe the shape of the brane where  $\xi^\alpha$  are the coordinates on the brane. The effective action of the D $p$ -brane is given by

$$S_p = -\mu_p \int d^{p+1}\xi e^{-\Phi} \sqrt{-\det(\mathcal{P}[G + B_2] + 2\pi\alpha' F_{\alpha\beta})}, \quad (2.50)$$

where  $\mathcal{P}$  is the pullback on the worldvolume of the  $Dp$ -brane,

$$\mathcal{P}[G] = \frac{\partial X^M}{\partial \xi^\alpha} \frac{\partial X^N}{\partial \xi^\beta} G_{MN} \text{ and } \mathcal{P}[B_2] = \frac{\partial X^M}{\partial \xi^\alpha} \frac{\partial X^N}{\partial \xi^\beta} B_{2MN}. \quad (2.51)$$

This action is the *Dirac-Born-Infeld action*. The appearance of the induced metric is easy to understand since  $\int d^{p+1}\xi \sqrt{-\det G_{\alpha\beta}}$  just determines the worldvolume of the brane and is therefore a generalization of the Nambu-Goto action. The contribution of the field strength  $F_{\alpha\beta}$  can be understood by T-duality [21, sec. 8.7] which also fixes the appearance of  $B_{2\alpha\beta}$  since only the combination  $B_{2\alpha\beta} + 2\pi\alpha' F_{\alpha\beta}$  is invariant under the gauge transformation found below (2.38). Since the action is determined by open string tree-level amplitudes, its dependence on the dilaton is fixed to be  $e^{-\Phi} = g_{\text{open}}^{-2}$ .

For  $n$  separated  $Dp$ -branes, the action is given by  $n$  copies of this action. However, if the  $n$   $Dp$ -branes coincide, we have observed that there are  $n^2$  massless fields which generated the non-Abelian  $U(n)$  gauge symmetry and the fields  $X^A$  and  $A_\alpha$  have to become  $n \times n$  matrices. The meaning for the gauge field is obvious, it is the non-Abelian  $U(n)$  gauge field, while the meaning of the matrix-valued scalars is more mysterious. They lead to noncommutative geometry which plays an important role in the dynamics of D-branes (see e. g. [147, 148]). Due to the non-Abelian gauge symmetry, the partial derivative  $\partial_\alpha X^A$  must be replaced by a covariant derivative and, therefore, contain commutators like  $[A_\alpha, X^A]$ . In addition, the field strength contains the commutators  $[A_\alpha, A_\beta]$  which in the T-dual picture gives rise to the commutators  $[X^A, X^B]$ . In order to obtain a gauge invariant action, we need to perform a trace over the gauge indices. It is proposed that the trace must be taken in a symmetrized way, i. e. first symmetrize the gauge indices and then take the trace. Using this approach there are still some discrepancies between string scattering amplitudes and the effective action beyond the fifth order in the field strength [149, 150]. Neglecting these problems, the action for coincident  $Dp$ -branes is given by [151]

$$S_p = -\mu_p \text{STr} \int d^{p+1}\xi e^{-\Phi} \sqrt{\det Q} \left[ \det(E_{\alpha\beta} + E_{\alpha A} (Q^{-1} - \delta)^{AB} E_{B\beta} + 2\pi\alpha' F_{\alpha\beta}) \right]^{\frac{1}{2}}, \quad (2.52)$$

with

$$E_{\alpha\beta} = \mathcal{P}[G + B_2] \quad \text{and} \quad Q^A_B = \delta^A_B + i2\pi\alpha' [X^A, X^C] E_{CB}. \quad (2.53)$$

We will later make extensive use of this action and will deal there with the problems of this action. Important to notice is that if the fields only carry values within the Cartan subalgebra the non-Abelian DBI action reduces to the form (2.50).

The tension of the  $Dp$ -brane  $\mu_p$  can be calculated by string amplitudes. Two separated D-branes can feel each other's presence by exchanging closed strings. This exchange can also be written as a loop of an open string. Comparing the two amplitudes, we can read off the  $Dp$ -brane tension [21, sec. 8.7],

$$\mu_p = \frac{\sqrt{\pi}}{16\kappa_{26}} (4\pi^2 \alpha')^{(11-p)/2}. \quad (2.54)$$

## 2.2 Superstring Theory

In this section we generalize the discussion of the previous section to the superstring which we obtain by demanding supersymmetry on the worldsheet. We follow the description of [22]. It turns out that worldsheet supersymmetry leads to supersymmetric spacetime theories which naturally contains fermions in contrast to the bosonic string theory. In total there are five consistent superstring theories. However, we will only focus on two of them, the Type IIA and IIB theory.

### 2.2.1 Worldsheet Fermions

In order to obtain an action which is invariant under worldsheet supersymmetry, we have to include *worldsheet fermions*  $\psi^M$  in the worldsheet action (2.4),

$$S = -\frac{1}{4\pi\alpha'} \int d\sigma^1 d\sigma^2 \sqrt{-\gamma} (\partial_a X^M \partial^a X_M + \bar{\psi}^M \Gamma^a \partial_a \psi_M), \quad (2.55)$$

where  $\psi^M = (\psi_-^M, \psi_+^M)$  is a two-component Majorana spinor and  $\Gamma^a$  are  $2 \times 2$  Dirac matrices. This action is invariant under superconformal transformations which contain the conformal transformation already present in the bosonic string and additional supersymmetry transformations.

The fermions have to satisfy the Dirac equations  $\partial_+ \psi_-^M = 0$  and  $\partial_- \psi_+^M = 0$  with  $\sigma^\pm = \tau \pm \sigma$  and the boundary conditions  $(\psi_+^M)^2 = (\psi_-^M)^2$  for  $\sigma = 0, \ell$ . At  $\sigma = 0$  we fix the overall sign of the components  $\psi_+^M(\tau, 0) = \psi_-^M(\tau, 0)$ . However, at  $\sigma = \ell$  we have two possible solutions named Ramond (R) and Neveu-Schwarz (NS) sector,

$$\begin{aligned} \text{R: } \quad & \psi_+^M(\tau, \ell) = +\psi_-^M(\tau, \ell), \\ \text{NS: } \quad & \psi_+^M(\tau, \ell) = -\psi_-^M(\tau, \ell). \end{aligned} \quad (2.56)$$

These determine the mode expansion of both sectors

$$\begin{aligned} \text{R: } \quad & \psi_\pm^M(\tau, \sigma) = \frac{1}{\sqrt{2}} \sum_{n \in \mathbb{Z}} d_n^M e^{-\frac{2\pi i n \sigma_\pm}{\ell}}, \\ \text{NS: } \quad & \psi_\pm^M(\tau, \sigma) = \frac{1}{\sqrt{2}} \sum_{r \in \mathbb{Z} + \frac{1}{2}} b_r^M e^{-\frac{2\pi i r \sigma_\pm}{\ell}}, \end{aligned} \quad (2.57)$$

where  $d_n^M$  and  $b_r^M$  must satisfy  $\{d_n^M, d_m^N\} = \eta^{MN} \delta_{n,-m}$  and  $\{b_r^M, b_s^N\} = \eta^{MN} \delta_{r,-s}$ , respectively. For the bosons we have the same mode expansion as in the bosonic string.

In addition to the D worldsheet scalars  $X^M$ , there are D worldsheet fermions  $\psi^M$  in superstring theory. These contribute to the calculation of the Weyl anomaly. By demanding the Weyl anomaly to vanish, we obtain the critical dimension  $D = 10$  for the superstring theory.

### 2.2.2 String Spectrum

As for the bosonic string, we may use the expansion coefficient  $d_n^M$  and  $b_r^M$  to build a Hilbert space. Let us start with the open string.

For the NS sector the ground state is defined by  $b_r^M|0\rangle_{\text{NS}}$  for  $r > 0$ . Then the modes  $b_r^M$  with  $r < 0$  act as raising operators. Since the  $b_r^M$ 's are anticommuting, each mode can only be excited once.

In the R sector we also define the ground state such that it is annihilated by  $d_n^M$  with  $n > 0$ . However, in the R sector this ground state is degenerated due to the  $d_0^M$ 's since  $\{d_n^M, d_0^N\} = 0$  for  $n > 0$ , i.e. the  $d_0^M$  take a ground state into another ground state. Since  $d_0^M$  satisfy the Clifford algebra  $\{d_0^M, d_0^N\} = \eta^{MN}$ , the ground state is a spacetime spinor with spacetime spin 1/2. We denote the ground state by  $|\mathbf{s}\rangle_{\text{R}}$ . In  $D = 10$  this representation has dimension 32 and can be decomposed into the different chiralities,  $\mathbf{16} + \mathbf{16}'$ . The different chiralities can be defined using the operator  $\exp(i\pi F)$ .  $F$  is the worldsheet fermion number. Since  $\exp(i\pi F)$  anticommutes with  $d^M$ , it satisfy the same properties as  $\Gamma = \Gamma^0 \dots \Gamma^9$  of the Clifford algebra. In addition, every state excited by  $d_n^M$  for  $n < 0$  from this ground state has half-integer spacetime spin since the raising operators  $d_n^M$  for  $n < 0$  are spacetime vectors and, thus, increase the spacetime spin by an integer.

For closed strings we may combine the R and NS sector to obtain the right- and left movers. The NS-NS states as well as the R-R states have integer spacetime spin since the spins are additive and the two half-integer spins from the two R sectors combine to an integer spin. On the other hand, the NS-R and R-NS states have half-integer spin.

### 2.2.3 Physical States

In the bosonic theory we have already seen that the physical fields have to satisfy the Virasoro constraints and the level matching for the closed strings. In the superstring there are additional constraints due to supersymmetry.

We begin with the open strings. The NS sector is similar to the bosonic string. The lowest state  $|0; k\rangle_{\text{NS}}$  is a tachyon with mass  $m^2 = -1/2\alpha'$  and has  $\exp(i\pi F) = -1$ . The first excited mode  $b_{-1/2}^M|0, k\rangle_{\text{NS}}$  is a massless vector with  $D - 2$  spacelike polarizations, i.e. it is the vector representation  $\mathbf{8}_v$  of the little group  $SO(8)$  for  $D = 10$ . The unphysical polarizations are again removed by the constraint. It has  $\exp(i\pi F) = +1$ .

In the R sector the lowest states are  $|\mathbf{s}; k\rangle_{\text{R}}$  which have to satisfy the massless Dirac equation. This constraint projects out half of the states such that the physical states are given by spinor representations  $\mathbf{8}$  with  $\exp(i\pi F) = +1$  and  $\mathbf{8}'$  with  $\exp(i\pi F) = -1$  of  $SO(8)$ .

For the closed strings we obtain the lowest states from two copies of the open string states. Note that we have to fulfill the level matching condition for the left- and right moving states as in the bosonic string. Since the NS- sector is the only sector where the lowest state is not generated by any  $b^M$  or  $d^M$ , we cannot combine

Sector	Rep. of $SO(8)$	$m^2$
NS+	$\mathbf{8}_v$	0
NS-	$\mathbf{1}$	$-1/2\alpha'$
R+	$\mathbf{8}$	0
R-	$\mathbf{8}'$	0

**Table 2.1:** Lowest open string states: The sectors are labeled by the different periodicity (NS, R) and the worldsheet fermion number  $\exp(i\pi F)$  ( $\pm$ ).

Sector	Rep. of $SO(8)$	$m^2$
(NS+, NS+)	$\mathbf{8}_v \times \mathbf{8}_v = \mathbf{1} + \mathbf{28} + \mathbf{35}$	0
(NS-, NS-)	$\mathbf{1}$	$-1/2\alpha'$
(R+, R+)	$\mathbf{8} \times \mathbf{8} = \mathbf{1} + \mathbf{28} + \mathbf{35}_+$	0
(R-, R-)	$\mathbf{8}' \times \mathbf{8}' = \mathbf{1} + \mathbf{28} + \mathbf{35}_-$	0
(NS+, R+)	$\mathbf{8}_v \times \mathbf{8} = \mathbf{8}' + \mathbf{56}$	0
(NS+, R-)	$\mathbf{8}_v \times \mathbf{8}' = \mathbf{8} + \mathbf{56}'$	0
(R+, R-)	$\mathbf{8} \times \mathbf{8}' = \mathbf{8}_v + \mathbf{56}_t$	0

**Table 2.2:** Lowest closed string states: The sectors are labeled by the different periodicity (NS, R) and the worldsheet fermion number  $\exp(i\pi F)$  ( $\pm$ ). The representations  $\mathbf{28}$ ,  $\mathbf{56}_t$  and  $\mathbf{35}_\pm$  are antisymmetric two, three and four tensors where the four tensors satisfy a self-duality condition. The  $\mathbf{35}$  is a symmetric traceless two tensor. The  $\mathbf{56}$  and  $\mathbf{56}'$  are vector-spinors.

it with any other sector due to the level matching condition. In the other cases this condition is always fulfilled for the massless states. The lowest closed string states are collected in table 2.2.

#### 2.2.4 Emergence of Supergravity

In the previous section we presented the physical and massless states generated by open and closed strings. However, not all of these states can be present in a consistent theory such that some of the states have to be projected out of the spectrum (for more details see [22, sec. 10.6]). First we consider the closed string spectrum. In the bosonic string we have seen in section 2.1.4 that the closed string sector describes gravity. This will also be true for the superstring. However, due to supersymmetry we will obtain *supergravity*.

Supergravity is a theory which combines supersymmetry and general relativity. It can be constructed by demanding local supersymmetry which also leads to local Poincaré symmetry and therefore to general relativity. Supergravity theories can be formulated in any dimension less or equal 11. The lower-dimensional theories may be obtained by compactifying the unique eleven-dimensional theory whose UV completion is called *M-theory*.

The projection which gives us consistent closed string theories is known as the *Gliozzi-Scherk-Olive (GSO) projection*. In total there are four different possible projections leading to four different consistent string theories in ten dimensions which contain the following sectors:

$$\begin{aligned}
\text{Type 0A:} & \quad (\text{NS+}, \text{NS+}) \quad (\text{NS-}, \text{NS-}) \quad (\text{R+}, \text{R-}) \quad (\text{R-}, \text{R+}), \\
\text{Type 0B:} & \quad (\text{NS+}, \text{NS+}) \quad (\text{NS-}, \text{NS-}) \quad (\text{R+}, \text{R+}) \quad (\text{R-}, \text{R-}), \\
\text{Type IIA:} & \quad (\text{NS+}, \text{NS+}) \quad (\text{R+}, \text{NS+}) \quad (\text{NS+}, \text{R-}) \quad (\text{R+}, \text{R-}), \\
\text{Type IIB:} & \quad (\text{NS+}, \text{NS+}) \quad (\text{R+}, \text{NS+}) \quad (\text{NS+}, \text{R+}) \quad (\text{R+}, \text{R+}).
\end{aligned}$$

The type 0 theories have both a tachyon and there are no spacetime fermions. Therefore, we focus from now on onto the more interesting type II superstring theories<sup>5</sup>. By using table 2.2 we can read off the physical state for each sector in order to obtain the physical states of the type II theories,

$$\text{Type IIA: } \mathbf{1} + \mathbf{8}_v + \mathbf{28} + \mathbf{56}_t + \mathbf{35} + \mathbf{8} + \mathbf{8}' + \mathbf{56} + \mathbf{56}', \quad (2.58a)$$

$$\text{Type IIB: } \mathbf{1}^2 + \mathbf{28}^2 + \mathbf{35} + \mathbf{35}_+ + \mathbf{8}'^2 + \mathbf{56}^2. \quad (2.58b)$$

Since the spinors  $\mathbf{8}$ ,  $\mathbf{8}'$  and  $\mathbf{56}$  and  $\mathbf{56}'$  have different chirality, we see that the type IIA theory is nonchiral while the type IIB theory is chiral. In addition, both theories contain two gravitinos, the  $\mathbf{56}$  and  $\mathbf{56}'$  which is the reason for calling them type II theories<sup>6</sup>. Since the gravitinos are the superpartners of the gravitons, the  $\mathbf{35}$ , we expect to have  $\mathcal{N} = 2$  supersymmetry meaning 32 conserved spacetime supercharges. Indeed the massless spectrum of the closed superstrings which we have obtained above is exactly the same as the one of the type IIA and IIB supergravity.

## Type IIB Supergravity

Above we have seen the emergence of type II supergravity as the low energy limit of superstring theory, i. e. considering the massless closed superstring states. Since the type IIB theory plays an important role in the AdS/CFT correspondence we will discuss this theory in more detail.

The states of type IIB supergravity are listed in (2.58) and table 2.3. The bosonic fields are a metric  $G_{MN}$  transforming as a  $\mathbf{35}$ , the axion  $C_0$  and the dilaton  $\Phi$  transforming as  $\mathbf{1}$ , two two-forms  $B_{2MN}$  and  $C_{2MN}$  transforming as  $\mathbf{28}$  and a self-dual four-form  $C_{4MNRS}$  transforming as  $\mathbf{35}_+$ . The fermionic fields are two gravitinos  $\psi_{M\alpha}^{1,2}$  transforming as  $\mathbf{56}'$  and two dilatinos  $\lambda_{\alpha}^{1,2}$  transforming as  $\mathbf{8}'$ . As mentioned above the theory is chiral and parity violating.

The existence of the self-dual five-form field strength obstructs a covariant formulation of an action. However, we may write an action involving both dualities

<sup>5</sup>Note that there are more consistent string theories, e. g. the heterotic string which is a combination of the type II and the bosonic string and type I which is an unoriented version of the type IIB theory.

<sup>6</sup>The type 0 theories do not contain any gravitinos.

Field	Rep. of $SO(8)$	Description
$G_{MN}$	<b>35</b>	metric - graviton
$C_0 + i\Phi$	<b>1</b> <sup>2</sup>	axion - dilaton
$B_{2MN} + iC_{2MN}$	<b>28</b> <sup>2</sup>	two-form
$C_{4MNR}$	<b>35</b> <sub>+</sub>	self-dual four-form
$\psi_{M\alpha}^I \ I = 1, 2$	<b>56</b> <sup>/2</sup>	Majorana - Weyl gravitinos
$\lambda_\alpha^I \ I = 1, 2$	<b>8</b> <sup>/2</sup>	Majorana -Weyl dilatons

**Table 2.3:** Field content of type IIB supergravity

and then impose the self-duality constraint by hand. Doing so, we obtain

$$\begin{aligned}
S_{\text{IIB}} = & \frac{1}{4\kappa_{10}^2} \int d^{10}x \sqrt{-G} \left[ e^{-2\Phi} (2\mathcal{R} + 8\partial_M \Phi \partial^M \Phi - |H_3|^2) \right. \\
& \left. - \left( |F_1|^2 + |\tilde{F}_3|^2 + \frac{1}{2} |\tilde{F}_5|^2 \right) \right] \\
& - \frac{1}{4\kappa_{10}^2} \int C_4 \wedge H_3 \wedge F_3 + \text{fermions},
\end{aligned} \tag{2.59}$$

where we use the notation  $\int \sqrt{-G} |F_p|^2 = 1/p! \int \sqrt{-G} G^{M_1 N_1} \dots G^{M_p N_p} \bar{F}_{M_1 \dots M_p} F_{N_1 \dots N_p}$  with  $\bar{F}$  denotes the complex conjugate of  $F$ ,  $\kappa_{10}^2 = 2^6 \pi^7 \alpha'^4$  is the ten-dimensional gravitational constant and the field strengths are defined by

$$\begin{aligned}
F_{n+1} &= dC_n, & H_3 &= dB_2, \\
\tilde{F}_3 &= F_3 - C_0 H_3, & \tilde{F}_5 &= F_5 - \frac{1}{2} C_2 \wedge H_3 + \frac{1}{2} B_2 \wedge F_3.
\end{aligned} \tag{2.60}$$

The self-duality constraint is given by  $*\tilde{F}_5 = \tilde{F}_5$ .

### 2.2.5 T-Duality and D-Branes

In section 2.1.5 we have studied toroidal compactifications of the bosonic string theory which lead to D-branes. In this section we consider the effects of a toroidal compactification in type II superstring theory. Now the coordinate  $X^9$  is compactified,  $X^9 \sim X^9 + 2\pi R$ . In the limit  $R \rightarrow 0$  it can be shown that the considered theory and its dual have different chirality in the right-moving R sector [22, sec. 13]. This means that T-duality reverses the relative chiralities of the right- and left-moving ground states. Thus, if we start with type IIA theory which is nonchiral and T-dualize we obtain type IIB theory which is chiral and vice versa. This gives us a nice relation between the type II theories. In addition, since the IIA and IIB theories have different R-R fields,  $C_i$ , T-duality transforms them into each other.

As in the bosonic theory (see section 2.1.5), D-branes can be introduced in the superstring by demanding the open string spectrum to be T-dual. In addition to the

spontaneous breaking of the translation invariance, the D-brane also spontaneously breaks half of the spacetime supersymmetry which results in 16 conserved supercharges or  $\mathcal{N} = 1$  in  $D = 10$ . Thus, the D-brane is a 1/2 BPS (Bogomolnyi–Prasad–Sommerfield) state where the charge must be equal to the mass. In section 2.1.5 we have seen that the D-brane has tension and, therefore, is massive. Thus, it must be charged.

The  $Dp$ -brane naturally couples to a  $(p+1)$ -form, the R-R fields  $C_i$ . These R-R charges may be defined in analogy to the electric charge in electrodynamics. There the one-form  $A = A_M dx^M$  couples to the one-dimensional worldline of a pointlike electric charge  $\Sigma_1$ . The gauge invariant action for this interaction is given by

$$S_0 = \mu_0 \int_{\Sigma_1} A, \quad (2.61)$$

where  $\mu_0$  is the electric charge. We can generalize this interaction to any  $(p+1)$ -form  $C_{p+1}$  which couples to  $(p+1)$ -dimensional surface  $\Sigma_{p+1}$ ,

$$S_p = \mu_p \int_{\Sigma_{p+1}} C_{p+1}. \quad (2.62)$$

Thus, a  $(p+1)$ -dimensional hypersurface  $\Sigma_{p+1}$ , the  $Dp$ -brane, can be charged under a  $(p+1)$ -form  $C_{p+1}$ . The charge of the  $Dp$ -brane is  $\mu_p$ . The flux of the field strength  $F_{p+2} = dC_{p+1}$  is conserved,

$$\int_{S^{8-p}} *F_{p+2} = N, \quad (2.63)$$

where  $S^{8-p}$  is a sphere surrounding  $N$   $Dp$ -branes.

For each  $(p+1)$ -form  $C_{p+1}$ , there is also a magnetic dual  $C_{7-p}^{\text{magn}}$  which is a  $(7-p)$ -form and whose field strength is the Hodge dual of the field strength  $F_{p+1} = dC_{p+1}$ ,

$$dC_{7-p}^{\text{magn}} = *dC_{p+1}. \quad (2.64)$$

Consequently, each  $Dp$ -brane has also a magnetic dual, which is a  $D(6-p)$ -brane and couples to the field  $C_{7-p}^{\text{magn}}$ .

## D-Brane Action

The coupling of the D-brane to the NS-NS closed string fields is the same as in the bosonic theory. It is given by the Dirac-Born-Infeld action (2.50). For coinciding D-branes the non-Abelian version (2.52) has to be used. As seen above, in addition to the NS-NS background, the metric  $G$  and the  $B_2$  field, also the R-R background, the forms  $C_i$ , couple to the D-brane. The precise form of the coupling can also be found by using T-duality [22, sec. 13.3] and is given by a *Wess-Zumino (WZ) term*

$$S_{\text{WZ}} = \mu_p \text{Tr} \int_{\Sigma_{p+1}} \sum_q \mathcal{P}[C_q] \wedge \exp(\mathcal{P}[B_2] + 2\pi\alpha' F), \quad (2.65)$$

where the integral picks out the form proportional to the volume form of the  $Dp$ -brane. So far, we have only studied the bosonic fields on the brane. In addition, there are also fermionic fields which satisfy an action of the Dirac form. However, we will not study these fermionic fluctuation any further.

Due to the different structure of the superstring theory as compared to the bosonic string theory, the coupling constant  $\mu_p$  of the  $Dp$ -brane has a different value as in the bosonic theory [22, sec. 13.3],

$$\mu_p = \frac{\sqrt{\pi}}{\kappa_{10}} (4\pi^2 \alpha')^{\frac{3-p}{2}} = (2\pi)^{-p} \alpha'^{-\frac{p+1}{2}}, \quad (2.66)$$

and is related to the  $Dp$ -brane tension if the dilaton is constant  $g_s = \exp(\Phi)$ ,

$$T_p = \frac{\mu_p}{g_s} = \frac{1}{g_s (2\pi)^p \alpha'^{\frac{p+1}{2}}}. \quad (2.67)$$

For small field strengths  $2\pi\alpha'F \ll 1$  and constant dilaton, the DBI action reduces to an Yang-Mills action in  $(p+1)$  dimensions. The kinetic term of the gauge field is given by

$$\frac{T_p (2\pi\alpha')^2}{4} \int_{\Sigma_{p+1}} d^{p+1}\xi \operatorname{Tr}(F_{\alpha\beta} F^{\alpha\beta}), \quad (2.68)$$

which determines the Yang-Mills coupling constant  $g_{\text{YM},p}$ ,

$$g_{\text{YM},p}^2 = \frac{1}{T_p (2\pi\alpha')^2} = g_s (2\pi)^{p-2} \alpha'^{\frac{p-3}{2}}. \quad (2.69)$$

If we specialize this result to a stack of  $N_c$  coincident D3-branes, we find an  $\mathcal{N} = 4$  Super-Yang-Mills theory in  $(3+1)$  dimensions, i. e. 16 conserved super charges, with gauge group  $SU(N_c)$ <sup>7</sup> and coupling constant  $g_{\text{YM}} = 2\pi g_s$  in the low-energy limit. We will discuss this theory in the next section.

### 2.2.6 $\mathcal{N} = 4$ Super-Yang-Mills Theory

The field content of the  $\mathcal{N} = 4$  Super-Yang-Mills theory consists of the  $\mathcal{N} = 4$  gauge multiplet containing one gauge field  $A$ , four left handed Weyl fermions  $\lambda^a$  with  $a = 1, \dots, 4$  and six real scalars  $X^i$  with  $i = 1, \dots, 6$  which are in the adjoint representation of the gauge group. The supercharges are related by an  $SU(\mathcal{N} = 4)_R$   $R$ -symmetry under which the gauge field  $A$  transform as a singlet, the Weyl fermions  $\lambda^a$  as a **4** and the real scalars  $X^i$  as a **6**. In  $\mathcal{N} = 1$  superspace formalism, the  $\mathcal{N} = 4$  gauge multiplet can be written as vector multiplet  $W_\alpha$  and three chiral superfields  $\Phi_1, \Phi_2, \Phi_3$  (see table 2.4).

<sup>7</sup>The overall  $U(1) = U(N_c)/SU(N_c)$  factor actually corresponds to the overall position of the branes and may be ignored when the dynamics on the branes is considered.

$\mathcal{N} = 1$ Multiplet	Components	Spin	Rep. of $SU(4)_R$	$\Delta$
$\Phi_1, \Phi_2$	$X^1, X^2, X^3, X^4$	0	<b>6</b>	1
	$\lambda_1, \lambda_2$	1/2	<b>4</b>	3/2
$\Phi_3, W_\alpha$	$X^5, X^6$	0	<b>6</b>	1
	$\lambda_3, \lambda_4$	1/2	<b>4</b>	3/2
	$V_\mu$	1	<b>1</b>	1

**Table 2.4:** Fields of the  $\mathcal{N} = 4$  Super-Yang-Mills theory and their quantum numbers under the global  $R$ -symmetry group as well as their conformal dimension  $\Delta$ .

The Lagrangian is unique and given by

$$\begin{aligned}
\mathcal{L}_{\mathcal{N}=4} &= \text{Im} \left[ \tau \int d^4\theta \text{Tr} (\bar{\Phi}_I e^V \Phi_I e^{-V}) \right. \\
&\quad \left. + \tau \int d^2\theta \left( \text{Tr} (W^\alpha W_\alpha) + \text{Tr} (\epsilon_{IJK} \Phi_I \Phi_J \Phi_K) \right) + \text{h.c.} \right] \\
&= \text{Tr} \left[ -\frac{1}{4g_{\text{YM}}^2} F_{\mu\nu} F^{\mu\nu} + \frac{\Theta_I}{8\pi^2} F_{\mu\nu} * F^{\mu\nu} - \sum_a i\bar{\lambda}^a \bar{\sigma}^\mu D_\mu \lambda^a \right. \\
&\quad \left. - \sum_i D_\mu X^i D^\mu X^i + \sqrt{2} g_{\text{YM}} \sum_{a,b} C_i^{ab} \lambda_a [X^i, \lambda_b] \right. \\
&\quad \left. + \sqrt{2} g_{\text{YM}} \sum_{a,b,i} \bar{C}_{iab} \bar{\lambda}^a [X^i, \bar{\lambda}^b] + g_{\text{YM}}^2 \sum_{i,j} [X^i, X^j]^2 \right], \tag{2.70}
\end{aligned}$$

where  $\tau = \Theta_I/2\pi + i4\pi/g_{\text{YM}}^2$ , the trace is performed over the gauge indices,  $D_\mu$  is the gauge covariant derivative and  $F = dA + A \wedge A$  is the field strength tensor. In addition,  $\Theta_I$  denotes the instanton angle,  $C_i^{ab}$  and  $C_{iab}$  are related to the Clifford matrices for the  $SU(4)_R$   $R$ -symmetry and  $g_{\text{YM}}$  is the coupling constant. This Lagrangian may be obtained as a dimensional reduction on  $T^6$  of the ten-dimensional Super-Yang-Mills theory. The theory is classically scale invariant which we easily recognize by determining the mass dimensions of the fields and constants

$$[A] = [X^i] = 1, \quad [\lambda_a] = \frac{3}{2}, \quad [g_{\text{YM}}] = [\Theta_i] = 0. \tag{2.71}$$

Combined with the Poincaré invariance, we obtain that the theory is invariant under the *conformal symmetry*. Remarkably, this conformal symmetry is not broken by quantum correction.

### Global Symmetries of $\mathcal{N} = 4$ Super-Yang-Mills Theory

Let us now have a closer look at the global symmetries of the  $\mathcal{N} = 4$  Super-Yang-Mills theory in four dimensions. As mentioned above the theory is invariant under:

**Conformal symmetry** which is generated by Lorentz transformations  $L_{\mu\nu}$ , translations  $P^\mu$ , dilatations  $D$  and special conformal transformations  $K^\mu$ . They form the group  $SO(2,4) \simeq SU(2,2)$ .

**R-symmetry** which is given by the possible rotation of the supercharges in each other. This forms the group  $SO(6)_R \simeq SU(4)_R$ .

$\mathcal{N} = 4$  **Poincaré supersymmetry** which is generated by the supercharges  $Q^a$  with  $a = 1, \dots, 4$ .

These three symmetries can be combined into the *superconformal symmetry* group which in addition contains generators of the conformal supersymmetry, the fermionic supercharges  $S_a$  with  $a = 1, \dots, 4$ . The supercharges  $S_a$  have to be included to close the algebra and are defined as the commutator of the supercharges  $Q^a$  and the special conformal transformations  $K_\mu$ . Thus, the total global symmetry group is given by the superconformal symmetry group  $SU(2,2|4)$ . Its bosonic subalgebras are the conformal group  $SO(2,4)$  and the R-symmetry group  $SU(4)_R$ .

### Physical Relevant Representations and Correlators

In a conformal field theory, we may distinguish different operators by its scaling dimension  $\Delta$ . The scaling dimension is related to the eigenvalue of the scaling transformation  $D$ . From the algebra of the conformal group, it can be seen that  $P^\mu$  raises the scaling dimension while  $K^\mu$  lowers it. In unitary field theories, there are operators of lowest dimension named primary operators. Since they have the lowest scaling dimension, they have to be annihilated by  $K^\mu$ . For superconformal theories, the superconformal primary operators may be defined in a similar way. They must be annihilated by the supercharge  $S_a$ . It can be shown that the superconformal primary operators are gauge invariant scalars involving only  $X$  in a symmetrized way (see e.g. [152]). From the superconformal operators, we may construct the superconformal descents by applying the supercharge  $Q^a$ .

Conformal invariance is remarkably restrictive on correlators with 1, 2, and 3 conformal operators. For superconformal primary operators, which are scalars, the one point function

$$\langle \mathcal{O}(x) \rangle = c \delta_{\Delta,0}, \quad (2.72)$$

the two point function

$$\langle \mathcal{O}_1(x_1) \mathcal{O}_2(x_2) \rangle = \frac{\tilde{c} \delta_{\Delta_1, \Delta_2}}{x_{12}^{2\Delta_1}}, \quad (2.73)$$

and three point function

$$\langle \mathcal{O}_i(x_i) \mathcal{O}_j(x_j) \mathcal{O}_k(x_k) \rangle = \frac{c_{ijk}}{x_{12}^{\Delta_1 + \Delta_2 - \Delta_3} x_{13}^{\Delta_1 + \Delta_3 - \Delta_2} x_{23}^{\Delta_2 + \Delta_3 - \Delta_1}} \quad (2.74)$$

with  $x_{ij} = |x_i - x_j|$  are determined up to a constant. For  $n$  point functions with  $n > 3$ , we may construct combinations of  $x_{ij}$ 's which are conformally invariant, such that the correlation function can be any function of these combinations.

Name	Magnetic dual	Field
D(-1)-instanton	D7-brane	$C_0 + i\Phi$
F1-string	NS5-brane	$B_2$
D1-string	D5-brane	$C_2$
D3-brane	D3-brane	$C_4$

**Table 2.5:** Possible branes in type IIB supergravity and the field which is sourced by them.

### 2.2.7 D-brane Intersections

As discussed above, a stack of D-branes breaks half of the supersymmetry and gives rise to a gauge theory on the worldvolume of the brane. In this section we consider stacks of different kinds of D-branes, e. g.  $Dp$ -branes and  $Dp'$ -branes. For this configuration we split the coordinates according to their boundary conditions on the branes. There are four different conditions: Dirichlet-Dirichlet, Dirichlet-Neumann, Neumann-Dirichlet and Neumann-Neumann on the  $Dp$ -branes and  $Dp'$ -branes. The amount of unbroken supersymmetry depends on the number  $\#_{\text{ND}}$  of Dirichlet-Neumann and Neumann-Dirichlet coordinates. In [22, sec. 13.4] it is shown that if  $\#_{\text{ND}}$  is a multiple of four, a quarter of the supersymmetry, i. e. 8 supercharges, are preserved.

In the considered configuration an open string can have both ends on the same stack of D-brane or one on each stack. The  $p - p$  and  $p' - p'$  spectra are the same as before and give rise to gauge theories while the  $p - p'$  strings are new. They transform in the bifundamental representation of the gauge groups generated by the stacks of D-branes. By separating the stacks of D-branes, the states described by these open strings become massive due to the string tension  $1/2\pi\alpha'$ . Their mass  $m$  is given by

$$m = \frac{L}{2\pi\alpha'}, \quad (2.75)$$

where  $L$  is the distance between the stacks.

### 2.2.8 Brane Solutions in Type IIB Supergravity

In this section we consider D-brane solutions in supergravity. In section 2.2.5 we have seen that R-R fields are sourced by D-branes. From table 2.3 we know that type IIB supergravity contains R-R tensor fields of rank 0, 2 and 4 and their magnetic duals, a field of rank 8, 6 and 4. Accordingly, the possible D-branes are D(-1)-, D1-, D3-, D5- and D7-branes. In addition, the NS-NS field  $B_2$  can also source a 1-brane which is just the fundamental string  $F1$ . Its magnetic dual is called NS5-brane. We summarize the possible  $p$ -branes in type IIB supergravity in table 2.5.

Since the D-branes have tension and, thus, are massive, they contribute to the energy-momentum tensor and appear in Einstein's equations which determine the

spacetime metric. So in addition to a non-zero flux of the field strength, we expect the spacetime to be curved if we include these branes.

Let us now calculate the metric and the field strength for a  $Dp$ -brane. First we describe the geometry of  $Dp$ -brane solutions. It has a  $(p + 1)$ -dimensional flat hypersurface which is Poincaré invariant. The transverse space is  $(9 - p)$ -dimensional and rotational invariant. Therefore,  $Dp$ -branes are solutions with a symmetry group  $\mathbb{R}^{p+1} \times SO(1, p) \times SO(9 - p)$ . It is convenient to denote the coordinates as follows

$$\begin{aligned} \text{coordinates parallel to the brane:} & \quad x^\alpha & \quad \alpha = 0, \dots, p \\ \text{coordinates orthogonal to the brane:} & \quad y^{\mathcal{A}} = x^{p+\mathcal{A}} & \quad \mathcal{A} = 1, \dots, 9 - p. \end{aligned} \quad (2.76)$$

Due to the Poincaré invariance in  $(p + 1)$  dimensions, the metric in the directions parallel to the brane has to be a rescaling of the flat Minkowski metric, while rotational invariance in the transverse space forces the metric in those directions to be a rescaling of the flat Euclidean metric. Furthermore, the metric rescaling factors must be independent of the coordinates parallel to the brane,  $x^\alpha$  for  $\alpha = 0, \dots, p$ . Substituting an ansatz with the above restrictions into the field equations, we find that the solution can be expressed in terms of a single function  $H$ ,

$$ds^2 = H(\mathbf{y})^{-\frac{1}{2}} dx^\alpha dx_\alpha + H(\mathbf{y})^{\frac{1}{2}} d\mathbf{y}^2 \quad \text{and} \quad e^\Phi = H(\mathbf{y})^{\frac{3-p}{4}}, \quad (2.77)$$

where the function  $H$  must be harmonic with respect to  $\mathbf{y}$ . Using the rotational symmetry  $SO(9 - p)$  in the transverse space and the fact that the metric should become flat as  $y = |\mathbf{y}| \rightarrow \infty$ , the most general solution becomes

$$H(y) = 1 + \frac{R^{7-p}}{y^{7-p}}. \quad (2.78)$$

The factor  $R$  has dimension length and must therefore be proportional to the square root of the inverse string tension  $\sqrt{\alpha'}$  since  $\alpha'$  is the only dimensionful parameter of the theory. For  $N_c$  coincident  $Dp$ -branes the exact relation is given by

$$R^{7-p} = N_c g_s (4\pi)^{\frac{5-p}{2}} \Gamma\left(\frac{7-p}{2}\right) \alpha'^{\frac{7-p}{2}}. \quad (2.79)$$

**D3-branes** are worth to consider in more detail since they have a  $(3 + 1)$ -dimensional worldvolume as the observed universe surrounding us. Let us now look at the result for D3-branes. We obtain

$$ds^2 = H(y)^{-\frac{1}{2}} dx^\mu dx_\mu + H(y)^{\frac{1}{2}} (dy^2 + y^2 d\Omega_5^2), \quad (2.80)$$

with

$$H(y) = 1 + \frac{R^4}{y^4}, \quad R^4 = 4\pi N_c g_s \alpha'^2. \quad (2.81)$$

Furthermore, we find that the D3-brane solution has constant axion and dilaton fields, the two-forms  $B_2$  and  $C_2$  are zero and the field strength of the four-form  $C_4$  is given by

$$F_5 = (1 + *)dx^0 \wedge dx^1 \wedge dx^2 \wedge dx^3 \wedge dH^{-1}. \quad (2.82)$$

Since we consider here the supergravity approximation of string theory we have to determine the parameter region in which this approximation is valid. For this purpose, we compare the string length  $l_s \propto \sqrt{\alpha'}$  with the radius  $R$  of the D3-brane solution. Their ratio is given by

$$\frac{R^4}{\alpha'^2} = 4\pi g_s N_c. \quad (2.83)$$

For  $g_s N_c \ll 1$ , the radius  $R$  is much smaller than the string length  $l_s$  and, thus, full string theory has to be considered in this region, while for  $g_s N_c \gg 1$ , the radius  $R$  is much bigger than the string length  $l_s$  and the supergravity approximation is valid. In the following we only consider the region  $g_s N_c \gg 1$ .

To study this geometry further, we take two different limits into account. For  $y \gg R$ , we recover flat space  $\mathbb{R}^{1,9}$  and  $F_5 = 0$ . Next we consider the *near-horizon region*  $y \ll R$ . Its geometry is often denoted as the throat. In this limit the solution becomes

$$\begin{aligned} ds^2 &= R^2 \left( \frac{dx^\mu dx_\mu + dz^2}{z^2} + d\Omega_5^2 \right), \\ F_5 &= -4 \frac{R^4}{z^5} (1 + *)dx^0 \wedge dx^1 \wedge dx^2 \wedge dx^3 \wedge dz. \end{aligned} \quad (2.84)$$

where we use the coordinate  $z = R^2/y$ . The first term is the metric of a five-dimensional *Anti-de Sitter space*  $AdS_5$  while the second term is the metric of a five sphere  $S^5$ . In conclusion, the geometry close to a stack of D3-branes, i. e.  $y \ll R$ , may be summarized as  $AdS_5 \times S^5$  where both components have the identical radius  $R$ .

## 2.2.9 Anti-de Sitter Space

Anti-de Sitter space is a maximally symmetric Lorentzian manifold of constant negative curvature and is a vacuum solution to Einstein's field equations of general relativity with negative cosmological constant. The  $(d + 2)$ -dimensional Anti-de Sitter space ( $AdS_{d+2}$ ) can be represented by the  $(d + 2)$ -dimensional hyperboloid

$$X_0^2 + X_{d+2}^2 - \sum_{i=1}^{d+1} X_i^2 = R^2, \quad (2.85)$$

which is embedded in the flat  $(d + 3)$ -dimensional space.  $R$  is called the AdS radius. The metric on this space reads

$$ds^2 = -dX_0^2 - dX_{d+2}^2 + \sum_{i=1}^{d+1} dX_i^2. \quad (2.86)$$

By construction, this space has the isometry  $SO(2, d+1)$  and it is homogeneous and isotropic. A parameterization of equation (2.85) is given by

$$\begin{aligned} X_0 &= R \cosh \xi \cos \tau, \\ X_{d+2} &= R \cosh \xi \sin \tau, \\ X_i &= R \sinh \xi \Omega_i \quad \text{for } i = 1, \dots, d+1 \quad \text{with } \sum_i \Omega_i^2 = 1. \end{aligned} \quad (2.87)$$

By inserting this parameterization into equation (2.86), we obtain the  $AdS_{d+2}$  metric

$$ds^2 = R^2 \left( -\cosh^2 \xi d\tau^2 + d\xi^2 + \sinh^2 \xi d\Omega_d^2 \right). \quad (2.88)$$

The parameterization (2.87) covers the entire hyperboloid once if we take  $0 \leq \xi$ ,  $0 \leq \tau < 2\pi$ . Hence, these are global coordinates. Near  $\xi = 0$ , the above metric behaves as  $ds^2 \simeq R^2 (-d\tau^2 + d\xi^2 + \xi^2 d\Omega_d^2)$  and has the topology  $S^1 \times \mathbb{R}^{d+1}$ . Thus, this metric has closed timelike curves in the  $\tau$  direction which violate causality. To obtain a causal spacetime, we unwrap the circle  $S^1$  by taking  $-\infty < \tau < \infty$  without identification. This is the universal covering of the hyperboloid without closed timelike curves which we call from now on AdS space.

In order to obtain the metric of AdS space which appears in (2.84), we need to study some different parametrization of the  $AdS_{d+2}$  metric. In addition to the global coordinates defined in (2.87), there is a set of local coordinates  $(u, t, \mathbf{x})$  with  $0 < u$ ,  $-\infty < t < \infty$ ,  $\mathbf{x} \in \mathbb{R}^d$ . They are defined as follows

$$\begin{aligned} X_0 &= \frac{1}{2u} \left[ 1 + u^2 (R^2 + \mathbf{x}^2 - t^2) \right], & X_{d+2} &= Rut, \\ X_{d+1} &= \frac{1}{2u} \left[ 1 - u^2 (R^2 - \mathbf{x}^2 + t^2) \right], & X_i &= Rux_i \quad \text{for } i = 1, \dots, d. \end{aligned} \quad (2.89)$$

These coordinates, named Poincaré coordinates, cover only one half of the hyperboloid specified in (2.85). Inserting them into (2.86), the  $AdS_{d+2}$  metric becomes

$$ds^2 = R^2 \left[ \frac{du^2}{u^2} + u^2 dx_\mu dx^\mu \right]. \quad (2.90)$$

By applying the transformation  $z = u^{-1}$ , we find the form which appears in (2.84),

$$ds^2 = \frac{R^2}{z^2} (dz^2 + dx_\mu dx^\mu). \quad (2.91)$$

Another useful parameterization is given by  $r = R^2 u$  which leads to

$$ds^2 = \frac{r^2}{R^2} dx_\mu dx^\mu + \frac{R^2 dr^2}{r^2}. \quad (2.92)$$



## Gauge/Gravity Duality

In 1973 't Hooft found an interesting connection between  $SU(N_c)$  gauge theories in the *large  $N_c$  limit*, i.e.  $N_c \rightarrow \infty$ , and string theory [153]. After over twenty years, Maldacena first found an explicit realization of this connection in 1997 [25]. From this example we learn a general lesson: A gauge theory is related to a higher-dimensional string theory which is approximated by gravity in a particular limit. This suggests the name gauge/gravity duality. Since gravity is matched to a *lower*-dimensional gauge theory, these dualities also explicitly realize the *holographic principle* [15–17]. The holographic principle is a general feature of gravity and states that the amount of information contained in a volume is bounded by the area of its boundary. Therefore, the gravitational description of the dual gauge theory is often also denoted as the holographic description.

Let us now begin by considering the large  $N_c$  limit of a simple toy model. The large  $N_c$  limit is motivated by the fact that this limit allows for perturbative calculations with the expansion parameter  $1/N_c$ . The Lagrangian of the toy model is given by

$$\mathcal{L} \propto \text{Tr} \left[ \partial\Phi_i \partial\Phi_j + g_{\text{YM}} c^{ijk} \Phi_i \Phi_j \Phi_k + g_{\text{YM}}^2 d^{ijkl} \Phi_i \Phi_j \Phi_k \Phi_l \right], \quad (3.1)$$

where the fields  $\Phi_i$  may stand for any bosonic field  $X^i$  and  $g_{\text{YM}} A_\mu$  of the  $\mathcal{N} = 4$  Super-Yang-Mills theory (see section 2.2.6). Note that the three point vertices are proportional to  $g_{\text{YM}}$  while the four point vertices are proportional to  $g_{\text{YM}}^2$ . After defining the fields  $\tilde{\Phi}_i = g_{\text{YM}} \Phi_i$  and the 't Hooft coupling  $\lambda = g_{\text{YM}}^2 N_c$  which is fixed as  $N_c \rightarrow \infty$ , the Lagrangian becomes

$$\mathcal{L} \propto \frac{N_c}{\lambda} \text{Tr} \left[ \partial\tilde{\Phi}_i \partial\tilde{\Phi}_j + c^{ijk} \tilde{\Phi}_i \tilde{\Phi}_j \tilde{\Phi}_k + d^{ijkl} \tilde{\Phi}_i \tilde{\Phi}_j \tilde{\Phi}_k \tilde{\Phi}_l \right]. \quad (3.2)$$

Since the fields  $\Phi_i$  are in the adjoint representation denoted by the matrix  $(\Phi_i)^a_b$  with  $a, b = 1, \dots, N_c$  of the gauge group, the propagator has the following  $SU(N_c)$  index structure

$$\langle (\Phi_i)^a_b (\Phi_j)^c_d \rangle \propto \left( \delta^a_d \delta^c_b - \frac{1}{N_c} \delta^a_b \delta^c_d \right). \quad (3.3)$$

In the large  $N_c$  limit, the second term can be ignored which suggests a double line notation for the adjoint fields in the Feynman diagrams. Thus, each Feynman diagram is a network of double lines which defines a polyhedron.

We can now calculate the dependence on  $N_c$  and  $\lambda$  for such Feynman diagrams by simply writing down the Feynman rules. From the form of the Lagrangian (3.2), we see that each vertex introduces a factor  $N_c/\lambda$ , each propagator a factor  $\lambda/N_c$ , and each loop a factor  $N_c$  (from the sum over the gauge indices). Thus, a digram with  $V$  vertices,  $E$  propagators (= edges of the graph) and  $F$  loops (= faces of the graph) is proportional to

$$N^{V-E+F} \lambda^{E-V} = N^\chi \lambda^{E-V} = N^{2-2g} \lambda^{E-V}, \quad (3.4)$$

where  $\chi = V - E + F$  is the Euler character of the Riemann surface corresponding to the diagram. For closed surfaces, the Euler character  $\chi$  is given by the genus  $g$  of the surface,  $\chi = 2 - 2g$ . Thus, the perturbative expansion of any diagram can be written as a double expansion of the form

$$\sum_{g=0}^{\infty} N_c^{2g-2} \sum_{i=0}^{\infty} c_{g,i} \lambda^i = \sum_{g=0}^{\infty} N_c^{2g-2} f_g(\lambda). \quad (3.5)$$

Every amplitude can be decomposed into diagrams ordered by their genus  $g$ . In the large  $N_c$  limit it is clear that every amplitude is dominated by surfaces with minimal genus, which are surfaces topologically equivalent to a sphere. These *planar diagrams* contribute at order  $N_c^2$  while for any other diagram the contribution is suppressed by a factor  $N_c^{2g}$ . In figure 3.1 we see two examples: The first figure is planar and proportional to  $N_c^{2-3+3} = N_c^2$  while the second is not planar and proportional to  $N_c^{4-6+2} = N_c^0$ .

The expansion of Feynman graphs in  $1/N_c$  is equivalent to a topological expansion of the corresponding surfaces. In string theory, the same topological expansion is obtained in perturbation theory of closed, oriented strings where the expansion parameter is the string coupling  $g_s$  (see section 2.1.3).

Accordingly, we expect a connection between an  $SU(N_c)$  gauge theory in the large  $N_c$  limit and a perturbative string theory describing closed, oriented strings. The string coupling  $g_s$  and the number of colors  $N_c$  are related by  $g_s \propto 1/N_c$ . This analogy between a large  $N_c$  field theory and a perturbative string theory is a strong evidence that field theories and string theories are in general related. This relation is explicitly realized in the AdS/CFT correspondence which we state in the next section. In section 3.2 we discuss some generalization towards the application of the AdS/CFT correspondence to real-world systems.

### 3.1 The Original AdS/CFT Correspondence

The Anti-de Sitter/Conformal Field Theory (AdS/CFT) correspondence, as originally conjectured by Maldacena in 1997 [25], describes the remarkable equivalence

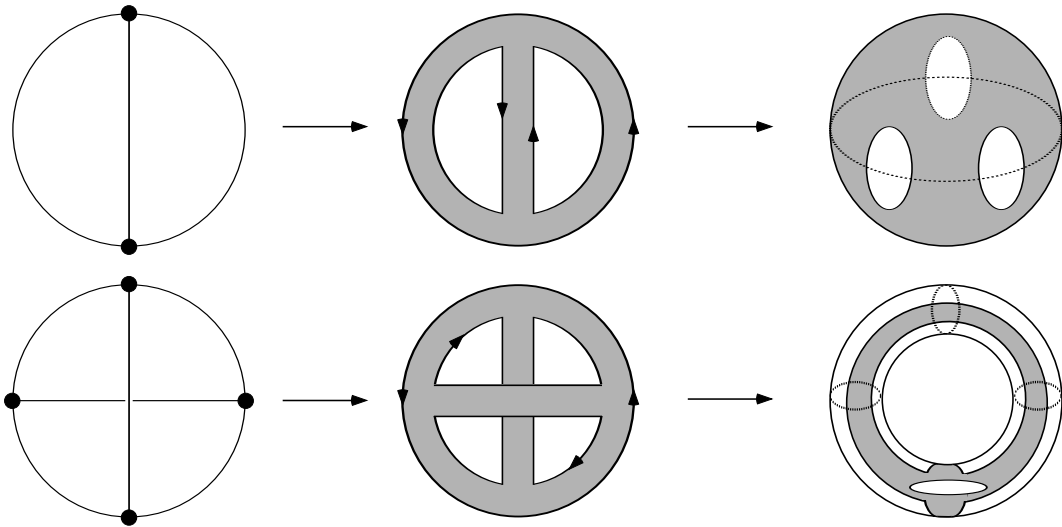


**Figure 3.1:** Feynman diagrams (left) may be translated in double line diagrams (middle). These double line diagrams define a Riemann surface with given topology. These surfaces are shown on the right.

between two apparently unrelated theories: Type IIB Supergravity described in section 2.2.4 and  $\mathcal{N} = 4$  Super-Yang-Mills theory described in section 2.2.6. In this section the original AdS/CFT correspondence is presented. For this purpose we follow the arguments of [152, 154].

By considering the low energy limit of a stack of D3-branes in two different ways, we illustrate the origin of the AdS/CFT correspondence out of string theory. After the two theories which are dual to each other are identified, we give a map between the natural objects in both theories, the operators of the field theory and the fields of supergravity. Afterwards the connection between the holographic principle and the AdS/CFT correspondence is presented. Since the conjecture is not proven, we close this section by listing some tests of the conjecture.

### 3.1.1 The Maldacena Conjecture

The origin of the AdS/CFT correspondence is the equivalent low energy descriptions of a stack of  $N_c$  D3-branes in flat space in terms of closed and open strings. The action for a stack of D3-branes is given by three terms: the bulk action  $S_{\text{bulk}}$ , the action for the branes  $S_{\text{branes}}$  and interactions  $S_{\text{int}}$  between the bulk and the branes,

$$S = S_{\text{bulk}} + S_{\text{branes}} + S_{\text{int}}. \quad (3.6)$$

Let us first consider this action in the low energy limit. We perform this limit by keeping the energy and all dimensionless parameters fixed and sending the string length to zero,  $\alpha' \rightarrow 0$ . In this limit, the bulk action becomes the type IIB supergravity action (2.59). The interaction between the bulk and the branes is determined

by including the bulk fields in the DBI and WZ action (see (2.50) and (2.65)) in order to obtain a covariant action. This leads to an energy-momentum tensor contributing to the supergravity equations of motion. However, since the coupling of the branes is given by  $\kappa_{10}^{-1}$  (2.66), the energy-momentum tensor scales as  $\kappa_{10} \propto \alpha'^2$ . Thus, the back-reaction of the branes vanishes in the limit  $\alpha' \rightarrow 0$  and we obtain type IIB supergravity in flat space. As seen in (2.68) and below that equation, the action of the branes simplifies to the  $\mathcal{N} = 4$   $SU(N_c)$  Super-Yang-Mills on the  $(3 + 1)$ -dimensional worldvolume of the branes. Summarized we obtain **type IIB supergravity in flat space and  $\mathcal{N} = 4$   $SU(N_c)$  Super-Yang-Mills action on the  $(3 + 1)$ -dimensional worldvolume of the branes** in the limit  $\alpha' \rightarrow 0$ .

Next we consider the supergravity solution of a stack of D3-branes as discussed in section 2.2.8. Notice that the  $g_{tt}$  component of the metric is not constant such that energies  $E_y$  measured at a distance  $y$  and energies  $E_\infty$  measured at a distance  $y \rightarrow \infty$  away from the branes are related by a redshift factor,

$$E_y = \left(1 + \frac{R^4}{y^4}\right)^{\frac{1}{4}} E_\infty. \quad (3.7)$$

As a result an observer at infinity observes a lower energy if an object is closer to the branes. This means that all kind of excitations close to the branes survive the low energy limit. Away from the branes, only massless particles with large wavelengths are allowed at low energies. Due to the large wavelength which is bigger than the gravitational size of the branes, these bulk modes decouple from the modes close to the branes such that we can study these two regions separately. In section 2.2.8 we have studied the supergravity solution in this two regions: far away from the branes we obtain flat space while close to the branes the space is  $AdS_5 \times S^5$ . To summarize, we obtain **type IIB supergravity in flat space in the bulk and type IIB supergravity on  $AdS_5 \times S^5$  with radius given by  $R^4 = 4\pi g_s N_c \alpha'^2$  close to the branes where  $N_c$  is given by the quantized flux  $\int_{S^5} *F_5 = N_c$ .**

We observed that in both low energy descriptions the dynamics away from the branes decouples and is governed by type IIB supergravity in flat space. Since the theories away from the branes coincide and decouple in both descriptions, it is natural to identify also the theories close to the brane. This leads to the conjecture that  **$\mathcal{N} = 4$   $SU(N_c)$  Super-Yang-Mills theory in  $(3 + 1)$  dimensions and type IIB supergravity on  $AdS_5 \times S^5$  with radius given by  $R^4 = 4\pi g_s N_c \alpha'^2$  where  $N_c$  is given by the quantized flux  $\int_{S^5} *F_5 = N_c$  are equivalent.** The parameters of both theories are related by

$$2\pi g_s = g_{\text{YM}}^2 \quad \text{and} \quad \frac{R^4}{(\alpha')^2} = 2g_{\text{YM}}^2 N_c. \quad (3.8)$$

In order to have a consistent classical supergravity approximation, the string coupling  $g_s$  must be small and the number of D3-branes  $N_c$  must be large such that  $R^4/(\alpha')^2 \propto N_c g_s \gg 1$ . On the gauge theory side, this corresponds to large number of colors and large 't Hooft coupling  $\lambda = g_{\text{YM}}^2 N_c \gg 1$ . This is known as the

Field theory side	String theory side
$\mathcal{N} = 4$ SYM for all $N_c, g_{\text{YM}}$	Full quantum IIB string theory
't Hooft limit of $\mathcal{N} = 4$ SYM expansion in $1/N_c$	Classical IIB string theory string loop expansion in $g_s$
Large $\lambda$ limit of $\mathcal{N} = 4$ SYM expansion in $\lambda^{-1/2}$	Classical IIB supergravity expansion in $\alpha'$

**Table 3.1:** The three different forms of the AdS/CFT correspondence

*weakest* form of the correspondence. It is, however, expected that the correspondence also holds for arbitrary values of these parameters. The different forms of the correspondence are presented in the next section.

### 3.1.2 The Different Forms of the Correspondence

The AdS/CFT correspondence states the equivalence between two theories:

- Type IIB superstring theory on  $AdS_5 \times S^5$  where both  $AdS_5$  and  $S^5$  have the same radius  $R$ , the five-form flux is quantized,  $N_c = \int_{S^5} *F_5$ , and the string coupling constant is  $g_s$ ,
- $\mathcal{N} = 4$  Super-Yang-Mills theory in four-dimensional Minkowski spacetime with gauge group  $SU(N_c)$  and Yang-Mills coupling  $g_{\text{YM}}$ ,

where the parameter of both theories are related by (3.8). This is the *strongest* form of the conjecture as it holds for any value of  $N_c$  and  $g_{\text{YM}}$ . Unfortunately, so far full quantum string theory is not understood in curved spacetimes. This strongest form of the conjecture may help to understand quantum string theory in terms of gauge theories. In order to get to weaker forms of the conjecture which are more under control, we consider certain limits.

First we perform the 't Hooft limit where we send  $N_c \rightarrow \infty$  while keeping  $\lambda = g_{\text{YM}}^2 N_c$  fixed. This limit corresponds to a topological expansion of the Feynman diagrams on the field theory side. On the string side, the 't Hooft limit may be interpreted as a weak-coupling limit of perturbative string theory since the string coupling  $g_s \propto \lambda/N_c$  is small. Thus, we replace non-perturbative string theory by perturbative string theory. In this *strong* form of the conjecture the 't Hooft coupling  $\lambda$  is the only free parameter. Perturbation theory on the field theory side is valid for  $\lambda \ll 1$  which corresponds to a small radius on the string side  $R^4/(\alpha')^2 \propto \lambda$ . Thus, in this limit, we have to consider classical string theory since there are modes which can wind around the geometry.

In order to simplify the string side even more, we consider the limit of a large radius  $R$  such that stringy modes decouple and only point-like objects remain. This is achieved by sending the 't Hooft coupling to infinity,  $\lambda \rightarrow \infty$ , which translates

into the supergravity limit of sending  $\alpha' \rightarrow 0$ . In this limit the string side simplifies to classical supergravity which is nicely under control while on the field theory side we obtain a strongly coupled quantum field theory.

Non-perturbative results are difficult to obtain and very rare. Since this weak form of the conjecture allows to obtain non-perturbative results by classical calculations in gravity, it is very powerful. Later in this thesis, we will use this form of the conjecture to obtain new results for strongly coupled field theories which may describe real-world systems such as the quark-gluon plasma or certain condensed matter systems (more on that in the following chapters).

### 3.1.3 Dictionary: Field/Operator Correspondence

In the last section we have proposed the equivalence between a conformal theory,  $\mathcal{N} = 4$  Super-Yang-Mills theory, and type IIB supergravity on  $AdS_5 \times S^5$ . In a conformal field theory, the natural objects to consider are operators  $\mathcal{O}$  since there are neither asymptotic states nor an S-matrix while in supergravity we have fields  $\phi$ . In order to match states in both theories to each other, we need a dictionary which relates the fields  $\phi$  to the operators  $\mathcal{O}$ .

First we study an example where the field  $\phi$  is the dilaton field  $\Phi$ . Its expectation value is related to the dynamical string coupling  $g_s$  and is determined by the boundary condition for the dilaton field at the AdS boundary,  $\Phi_{\text{bdy}}$ . We use the coordinates defined in (2.84), where the boundary is at  $z = 0$ . By the correspondence between the couplings (3.8), a change in the string coupling  $g_s$  by varying the boundary value of the dilaton field  $\Phi_{\text{bdy}}$  induces a change in the gauge coupling  $g_{\text{YM}}$ . On the gauge theory side, a change in the gauge coupling is achieved by the deformation of the Lagrangian by the marginal operator  $\mathcal{O} = \text{Tr}(F_{\mu\nu}F^{\mu\nu})$ . This deformation may be written as  $\int d^4x \Phi_{\text{bdy}}(x)\mathcal{O}(x)$ .

By studying the case of the dilaton field, we learn the general lesson that changing the boundary value of the field  $\phi$  leads to a deformation of the Lagrangian by an operator  $\mathcal{O}$  in the dual field theory. Therefore, the boundary value  $\phi_{\text{bdy}}$  acts as a source for the dual operator  $\mathcal{O}$ . More precisely, as discussed in [155], we propose that

$$\left\langle e^{\int d^4x \phi_{\text{bdy}}(x)\mathcal{O}(x)} \right\rangle_{\text{CFT}} = Z_{\text{string}} \left[ \phi(x, z) \Big|_{z=0} = \phi_{\text{bdy}}(x) \right], \quad (3.9)$$

where the left hand side is the generating function of correlation functions in the gauge theory. The right hand side is the full partition function of string theory with the boundary condition that the field  $\phi$  has the value  $\phi_{\text{bdy}}$  on the boundary of the AdS space. This statement should hold for all supergravity fields  $\phi$  and operators  $\mathcal{O}$  which gives an one-to-one correspondence between the fields  $\phi$  and the operators  $\mathcal{O}$ .

The operators  $\mathcal{O}$  in the conformal field theory are characterized by their transformation under the superconformal group  $SU(2, 2|4)$ . Especially, they are labeled by their scaling dimension  $\Delta$  (see section 2.2.6). We will now see that the scaling dimension of the operator  $\mathcal{O}$  is given by the mass  $m$  of the dual field  $\phi$ . In order to

obtain this relation, we consider the wave equation in Euclidean AdS space for the scalar field  $\phi$  with mass  $m$ ,

$$(\square_g - m^2)\phi = 0. \quad (3.10)$$

Using the metric (2.91), the radial part of this equation becomes

$$\left(\partial_z^2 - \frac{3}{z}\partial_z - \frac{R^2 m^2}{z^2}\right)\phi = 0, \quad (3.11)$$

which has two independent solutions. For small  $z$  these solutions behave as  $z^{4-\Delta}$ , named the *non-normalizable* solution, and  $z^\Delta$ , the *normalizable* solution, where

$$\Delta = 2 + \sqrt{4 + R^2 m^2}. \quad (3.12)$$

Therefore, the boundary condition for massive fields has to be regularized. In general, it should be changed to

$$\phi(x, z) = z^{4-\Delta}\phi_{\text{bdy}}(x) \quad \text{for } z \rightarrow 0. \quad (3.13)$$

Since the minimal coupled scalar  $\phi$  is dimensionless in our convention,  $\phi_{\text{bdy}}$  has dimension of  $[\text{length}]^{\Delta-4}$ . Then equation (3.9) implies that the dual operator  $\mathcal{O}$  has dimension  $\Delta$ . Since the normalizable solution has dimension of  $[\text{length}]^\Delta$  it may be related to the vev of the dual operator  $\langle \mathcal{O} \rangle$  [155].

For non-scalar fields, the relation between the mass and the scaling dimension of the dual operator changes since the equation of motion for the gravity field changes. The relation between the mass  $m$  and the scaling dimension  $\Delta$  are given by (cf. e. g. [152])

$$\begin{array}{ll} \text{scalars} & m^2 R^2 = \Delta(\Delta - 4), \\ \text{spin } 1/2, 3/2 & |m|R = \Delta - 2, \\ p\text{-form} & m^2 R^2 = (\Delta - p)(\Delta + p - 4), \\ \text{spin } 2 & m^2 R^2 = \Delta(\Delta - 4). \end{array} \quad (3.14)$$

### 3.1.4 Holography

In optics, holography is a technique to store information of three-dimensional objects on two-dimensional photographic plates [156]. Quantum gravity shares a similar property. The maximum entropy in a region of spacetime is determined by the size of the boundary of this region [14]. This leads to the holographic principle (see e. g. [15–17]) which states that in quantum gravity all physics within some volume can be described in terms of degrees of freedom on the boundary of this volume. The AdS/CFT correspondence gives an explicit realization of this idea. In order to see this in more detail, let us discuss the causal structure of AdS space.

For this purpose we rewrite the metric (2.88). It is convenient to introduce a new coordinate  $\theta$  defined by  $\tan \theta = \sinh \xi$  ( $0 \leq \theta < \pi/2$ ) leading to

$$ds^2 = \frac{R^2}{\cos^2 \theta} (-d\tau^2 + d\theta^2 + \sin^2 \theta d\Omega_d^2). \quad (3.15)$$

Up to a conformal rescaling, the metric is the same as the Einstein static universe,

$$ds^2 = -d\tau^2 + d\theta^2 + \sin^2 \theta d\Omega_d^2 \quad , \text{ with } 0 \leq \theta < \pi/2 \quad -\infty < \tau < \infty . \quad (3.16)$$

Let us now compare this metric with the conformal compactification of  $(d+1)$ -dimensional Minkowski space. The Minkowski metric in spherical coordinates is given by

$$ds^2 = -dt^2 + dr^2 + r^2 d\Omega_{d-1}^2 , \quad (3.17)$$

where  $d\Omega_{d-1}$  is the line element of the  $(d-1)$ -dimensional unit sphere  $S^{d-1}$ . We may rewrite this metric by the following transformations

$$\begin{aligned} ds^2 &= -du_+ du_- + \frac{1}{4} (u_+ - u_-)^2 d\Omega_{d-1}^2 , & u_{\pm} &= t \pm r \\ &= \frac{1}{\cos^2 \tilde{u}_+ \cos^2 \tilde{u}_-} \left( -du_+ du_- + \frac{1}{4} \sin^2 (\tilde{u}_+ - \tilde{u}_-) d\Omega_{d-1}^2 \right) , & u_{\pm} &= \tan \tilde{u}_{\pm} \\ &= \frac{1}{4 \cos^2 \tilde{u}_+ \cos^2 \tilde{u}_-} (-d\tau^2 + d\theta^2 + \sin^2 \theta d\Omega_{d-1}^2) , & \tilde{u}_{\pm} &= \frac{\tau \pm \theta}{2} . \end{aligned} \quad (3.18)$$

Up to a conformal rescaling, we obtain again the Einstein static universe with  $0 \leq \theta \leq \pi$ ,  $-\infty < \tau < \infty$ .

However, the range of the coordinate  $\theta$  in the conformal compactification of AdS is only half of the range as in the conformal compactification of Minkowski space  $\mathbb{R}^{1,d}$ . This means that the conformally compactified  $AdS_{d+2}$  only covers one half of Einstein's static universe and has a boundary located at the equator of  $S^{d+1}$  at  $\theta = \pi/2$ . The topology of this boundary is  $\mathbb{R} \times S^d$  which is the same as conformally compactified  $(d+1)$ -dimensional Minkowski space. Thus, we may identify the space in which the conformal field theory lives, i. e.  $(d+1)$ -dimensional Minkowski space, with the conformal boundary of the  $AdS_{d+2}$  on which supergravity is defined. This implies that the information of the supergravity theory in  $(d+2)$  dimensions can be stored in the boundary field theory in  $(d+1)$  dimensions and we obtain an explicit realization of the holographic principle discussed above. Hence, the AdS/CFT correspondence is also known as the holographic duality.

### 3.1.5 Tests

Although the AdS/CFT correspondence is still a conjecture, it has passed many non-trivial tests of its validity. In the following we discuss three of them: matching of the global symmetries, agreement of correlation functions and the conformal anomaly.

### Symmetry Matching

A key ingredient of the AdS/CFT correspondence to hold is that the global symmetries of both theories match since the symmetries do not depend on the coupling. The symmetries of  $\mathcal{N} = 4$  SYM theory are discussed in section 2.2.6. The symmetry group is the superconformal group  $SU(2, 2|4)$  whose maximal bosonic subgroup

is a product of the four-dimensional conformal group  $SU(2, 2) \simeq SO(2, 4)$  and the  $R$ -symmetry group of the  $\mathcal{N} = 4$  Poincaré supersymmetry  $SU(4)_R \simeq SO(6)_R$ . This bosonic group is immediately recognized as the isometry group of the  $AdS_5 \times S^5$  background since  $SO(2, 4)$  is the isometry group of  $AdS_5$  as discussed in section 2.2.9 and  $SO(6)$  is the isometry group of  $S^5$ . Considering the fermionic generators of the Poincaré supersymmetries on the AdS side, it can be shown that the full supergroup  $SU(2, 2|4)$  is also the symmetry group of the  $AdS_5 \times S^5$  background such that the global symmetries match on both sides of the AdS/CFT correspondence [152].

## Correlation Functions

As a second test, we may compare correlation functions, e. g. two and three point functions, which are calculated in both theories. In the gauge theory we can only calculate these correlation function for a small 't Hooft coupling  $\lambda \ll 1$ , while on the AdS side the supergravity approximation is only valid in the large 't Hooft limit  $\lambda \gg 1$ . Thus, we may only consider correlation functions of 1/2 BPS operators since their correlation functions do not receive perturbative corrections and are independent of the 't Hooft coupling  $\lambda$ .

The structure of the two and three point correlation functions is determined by the conformal symmetry up to a constant as shown in section 2.2.6. Since we do not know how a specific normalization in the gauge theory is related to a normalization in the gravity theory, we use the two point function to normalize the operators and gravity fields, such that

$$\langle \mathcal{O}_i(0) \mathcal{O}_j(x) \rangle = \frac{\delta_{ij}}{|x|^{2\Delta}}. \quad (3.19)$$

After the normalization is fixed, the three point functions obtained in both theories coincide,

$$\langle \mathcal{O}_1(x_1) \mathcal{O}_2(x_2) \mathcal{O}_3(x_3) \rangle_{\text{AdS}} = \langle \mathcal{O}_1(x_1) \mathcal{O}_2(x_2) \mathcal{O}_3(x_3) \rangle_{\text{CFT}}. \quad (3.20)$$

On the gravity side, Witten diagrams which are analogous to Feynman diagrams are used to calculate these correlation functions. The detailed calculation may be found e. g. in [152].

## Conformal Anomaly

An additional test is the agreement of the conformal anomaly calculated on the field theory and gravity side. In a conformal theory, the vev of the energy-momentum tensor is traceless. The conformal anomaly is the anomaly due to quantum effects which does not allow the tensor to be traceless anymore. For  $\mathcal{N} = 4$  Super-Yang-Mills theory, the conformal anomaly is given by (see e. g. [152])

$$\langle T^\mu_\mu \rangle = \frac{N^2 - 1}{32\pi^2} \left( \mathcal{R}^{\mu\nu} \mathcal{R}_{\mu\nu} - \frac{1}{3} \mathcal{R}^2 \right) \xrightarrow{N \rightarrow \infty} \frac{N^2}{32\pi^2} \left( \mathcal{R}^{\mu\nu} \mathcal{R}_{\mu\nu} - \frac{1}{3} \mathcal{R}^2 \right), \quad (3.21)$$

where  $\mathcal{R}_{\mu\nu}$  and  $\mathcal{R}$  are the Ricci tensor and Ricci scalar of the manifold on which the field theory lives. On the gravity side, the result is [152]

$$\langle T^\mu_\mu \rangle = \frac{R^3}{8\kappa_5^2} \left( \mathcal{R}^{\mu\nu} \mathcal{R}_{\mu\nu} - \frac{1}{3} \mathcal{R}^2 \right), \quad (3.22)$$

where  $\kappa_5^2 = \kappa_{10}^2 / R^5 \text{Vol}(S^5)$  is the five-dimensional gravitational coupling. Using the relation (3.8), we obtain

$$\kappa_{10}^2 = \frac{4\pi^5 R^8}{N_c^2} \quad \text{and} \quad \kappa_5^2 = \frac{4\pi^2 R^3}{N_c^2}, \quad (3.23)$$

such that (3.21) and (3.22) indeed agree. Thus, we have an amazing agreement of the field theory and gravity calculation. The important point in this calculation is that the anomaly coefficient does not depend on the coupling constant such that a weak coupling calculation on the field theory side can be compared with a strong coupling calculation on the gravity side.

## 3.2 Generalizations Towards Real-World Systems

In the following we aim at generalizing the AdS/CFT correspondence to relate strongly coupled real-world systems to weakly coupled gravity theories. If we succeed, perturbative gravity calculations describe the strongly coupled real-world system. These generalizations go under the name of *gauge/gravity duality* and are variations of the original AdS/CFT correspondence. These variations are divided into two different categories named *top-down* and *bottom-up* approaches. In this thesis we will use both kinds to shape the correspondence in such a way that it is suitable to describe real-world systems.

### Top-down Approach

In the top-down approach, the string theory setup which leads to the correspondence is changed. A similar discussion as for the original AdS/CFT correspondence results in an explicitly known field theory and gravity setup. One example is the *D3/D7 brane intersection* which is discussed in detail below. The additional D7-branes generate extra degrees of freedom as discussed in section 2.2.7. Another way to include additional degrees of freedom is to study *gauged supergravities*. These theories emerge if we spin the D3-branes in their transverse directions. Reduced to five dimension, these theories contain an additional Yang-Mills theory with a Chern-Simons term. The gauge group is given by the symmetry group of the transverse space, in the usual case  $SO(6)$ . On the field theory side, these gauge fields corresponds to  $R$ -charge currents.

Another kind of deformation is the mass deformation of the  $\mathcal{N} = 4$  Super-Yang-Mills theory which is obtained by deforming the superpotential  $W$  by a mass term

for the chiral superfields,

$$\delta W = \frac{m}{g_{\text{YM}}^2} \text{Tr} (\Phi_1^2 + \Phi_2^2) \quad \text{or} \quad \delta W = \frac{m_{IJ}}{g_{\text{YM}}^2} \text{Tr} \Phi_I \Phi_J. \quad (3.24)$$

The first preserves  $\mathcal{N} = 2$  supersymmetry and thus, is called  $\mathcal{N} = 2^*$  theory. Its gravity dual can be found in [157]. The latter is known as  $\mathcal{N} = 1^*$  since it preserves  $\mathcal{N} = 1$  supersymmetry. Its gravity dual is given in [158]. In both cases on the gravity side a field has a non-trivial profile in order to source the corresponding operators on the field theory side (see section 3.1.3).

From these examples, we learn how the AdS/CFT correspondence may be deformed in general. We may add new degrees of freedom on both sides of the correspondence and/or give a field a non-trivial profile on the gravity side in order to source an operator.

### Bottom-up Approach

From the top-down approaches, we learn some general ways to deform the correspondence. However, in the bottom-up approach, the procedure is less strict in the sense that we do not care about a string theory embedding of the setup. Instead we suppose that the correspondence is true in a much more general context. We may expect that every gravity theory with asymptotically AdS space is dual to a field theory with a conformal  $UV$  fixed point living on the boundary. According to the dictionary, every field included into the gravity setup corresponds to a new operator on the field theory side and a gauge symmetry in the bulk is identified with a global symmetry on the field theory side. This allows us to include several new fields into the correspondence. In addition, we may generate non-trivial gravity solutions, i. e. some fields have non-trivial profiles, in order to source various different operators.

The advantage of this bottom-up approach is that it is much easier to model real-world systems. For instance in [32], the authors present a simple model which nicely reproduces the meson mass spectrum of QCD. However, the disadvantages of the bottom-up approach is that since there is no string theory origin, the explicit field theory is not known. Therefore, the correspondence is much less under control as in the top-down approach.

#### 3.2.1 Including Fundamental Matter: Flavor Branes

The original AdS/CFT correspondence exclusively contains fields in the adjoint representation of the gauge group. In the terminology of QCD, this represents the gluons. However, in QCD there are also fields transforming in the fundamental representation of the gauge group, the quarks. In order to describe QCD holographically, it is useful to include these fundamental fields, the flavors, into gauge/gravity duality. In section 2.2.7 we have observed that two stacks of D-branes induce two gauge groups and the string stretching between the two stacks transforms in the bi-fundamental, i. e. in the fundamental or antifundamental of one gauge group. These

strings give rise to the fundamental matter. In addition, the open strings ending on the new stack of flavor branes transform in the adjoint of the flavor symmetry and thus, naturally describe mesonic degrees of freedom, bound states of the fundamental matter. On the supergravity side, these states are obtained by fluctuations of the flavor D-branes in the background geometry.

As discussed in section 2.2.8, the possible D-branes in type IIB string theory, we discussing here, are D1-, D3-, D5-, D7- and D9-branes. Let us discuss the different D-branes intersecting with a stack of D3-branes (see section 2.2.7):

**D9-branes** are spacetime filling branes. Thus, it is never possible to separate them from the D3-branes in order to obtain massive flavors.

**D7-branes** can fill all directions of the D3-branes in a supersymmetric embedding. In addition, there are two directions perpendicular to the D3-branes and D7-branes in which we may separate the two stacks in order to get massive flavors [34].

**D5-branes** fill at most only two spatial directions of the D3-branes in a supersymmetric embedding. Thus, we obtain a defect theory where the flavors live in  $(2 + 1)$  or  $(0 + 1)$  dimensions. In this intersection it is also possible to get massive flavors (see e. g. [159–161]).

**D3-branes** fill only one spatial direction of the D3-branes in a supersymmetric embedding. Thus, the flavors only move in  $(1 + 1)$  dimensions and can get massive [162].

**D1-branes** can only fill a direction perpendicular to the D3-branes in a supersymmetric embedding and thus, cannot give rise to flavors.

According to this list, only the D3/D7 brane intersection allows massive flavors in  $(3 + 1)$  dimensions if we restrict our discussion to supersymmetric embeddings. We will use this intersection from now on to introduce flavors into the correspondence. For the discussion of this intersection we follow [35].

We consider a stack of  $N_c$  coincident D3-branes along the 0123 directions and a stack of  $N_f$  coincident D7-branes along the 01234567 directions (see table 3.2). This embedding is a 1/4 BPS state, i. e. preserves 8 supercharges, and breaks the  $SO(6)$  isometry in the directions transverse to the D3-branes down to  $SO(4) \times SO(2)$ . The  $SO(4)$  rotates the 4567 directions while the  $SO(2)$  rotates the 89 directions.

### Field Theory of the D3/D7 Brane Interaction

The field theory of the D3/D7 brane intersection corresponds to  $\mathcal{N} = 4$   $SU(N_c)$  Super-Yang-Mills theory coupled to  $N_f$   $\mathcal{N} = 2$  hypermultiplets transforming in the fundamental representation of the gauge group.

The  $\mathcal{N} = 4$  vector multiplet is generated by massless open string modes on the stack of the  $N_c$  coincident D3-branes while the  $N_f$   $\mathcal{N} = 2$  hypermultiplets descent

	0	1	2	3	4	5	6	7	8	9
$N_c$ D3-branes	X	X	X	X						
$N_f$ D7-branes	X	X	X	X	X	X	X	X		
$N_f$ D7-branes	X	X			X	X	X	X	X	X
$N_f$ D5-branes	X	X	X		X	X	X			
$N_f$ D5-branes	X				X	X	X	X	X	
$N_f$ D3-branes	X	X			X	X				
$N_f$ D1-branes	X				X					

**Table 3.2:** The supersymmetric embeddings of the D3/D $p$  brane intersection in  $(9 + 1)$ -dimensional flat space.

Multiplet	Components	Spin	$SU(2)_\Phi \times SU(2)_R$	$U(1)_R$	$\Delta$	$U(N_f)$	$U(1)_B$
$\Phi_1, \Phi_2$	$X^1, X^2, X^3, X^4$	0	$(1/2, 1/2)$	0	1	1	0
	$\lambda_1, \lambda_2$	1/2	$(1/2, 0)$	-1	3/2	1	0
$\Phi_3, W_\alpha$	$X^5, X^6$	0	$(0, 0)$	2	1	1	0
	$\lambda_3, \lambda_4$	1/2	$(1/2, 0)$	1	3/2	1	0
	$V_\mu$	1	$(0, 0)$	0	1	1	0
$Q, \tilde{Q}$	$q, \bar{q}$	0	$(0, 1/2)$	0	1	$N_f$	1
	$\psi, \bar{\psi}^\dagger$	1/2	$(0, 0)$	$\mp 1$	3/2	$N_f$	1

**Table 3.3:** Fields of the low energy field theory originated from the D3/D7 brane intersection and their quantum numbers under the global symmetries.

from the strings stretching between the D3-branes and D7-branes, the D3–D7 strings (see section 2.2.7). The D7–D7 strings decouple in the limit  $\alpha' \rightarrow 0$  since the eight-dimensional 't Hooft coupling  $\lambda'$  on the D7-branes is given by

$$\lambda' = N_f g_{\text{YM},7}^2 \stackrel{(2.69)}{=} N_f g_s (2\pi)^5 \alpha'^2 \stackrel{(3.8)}{=} \frac{N_f}{N_c} \lambda (2\pi)^4 \alpha'^2. \quad (3.25)$$

Thus, the D7–D7 strings do not interact with the D3–D3 strings and the D3–D7 strings. The  $U(N_f)$  gauge symmetry on the D7-branes becomes a global symmetry in the  $(3 + 1)$ -dimensional theory.

The field content of this theory can be written in  $\mathcal{N} = 1$  superspace formalism. In addition to the vector multiplet  $W_\alpha$  and the three chiral superfields  $\Phi_1, \Phi_2, \Phi_3$  of the  $\mathcal{N} = 4$  gauge multiplet, the theory contains the chiral superfields  $Q^r, \tilde{Q}_r$  where  $r = 1, \dots, N_f$ . The components of the  $\mathcal{N} = 1$  superfields and their quantum numbers under the global symmetries are summarized in table 3.3. The global symmetries of this field theory is composed of the  $SO(4) \simeq SU(2)_\Phi \times SU(2)_R$  and the  $SO(2) \simeq U(1)_R$  isometry rotating the directions transverse to the D3-branes and the  $U(N_f)$  flavor symmetry rotating the multiplets  $Q^r, \tilde{Q}_r$ . The  $U(1)_R$  symmetry corresponds to an  $R$ -symmetry in the field theory. By introducing a finite mass for the flavors, this symmetry is explicitly broken. The  $SU(2)_\Phi$  symmetry rotates

the scalars in the adjoint representation while the  $SU(2)_R$  symmetry is the  $\mathcal{N} = 2$   $R$ -symmetry. The baryonic  $U(1)_B$  is the diagonal subgroup of the  $U(N_f)$  flavor symmetry. Only the flavors  $Q^r, \tilde{Q}_r$  carry charge under  $U(1)_B$ .

Due to the transformation properties of the fields, the Lagrangian is uniquely given by

$$\begin{aligned} \mathcal{L}_{\mathcal{N}=2} = \text{Im} \left[ \tau \int d^4\theta \left( \text{Tr} (\bar{\Phi}_I e^V \Phi_I e^{-V}) + Q_r^\dagger e^V Q^r + \tilde{Q}_r^\dagger e^{-V} \tilde{Q}^r \right) \right. \\ \left. + \tau \int d^2\theta \left( \text{Tr} (W^\alpha W_\alpha) + W \right) + \text{h.c.} \right], \end{aligned} \quad (3.26)$$

where  $\tau$  is the complex gauge coupling given in section 2.2.6. The superpotential  $W$  is given by

$$W = \text{Tr} (\epsilon_{IJK} \Phi_I \Phi_J \Phi_K) + \tilde{Q}_r (M_q + \Phi_3) Q^r, \quad (3.27)$$

where  $M_q$  is the quark mass.

### Probe Brane Approximation

The simplest way to analyze the D3/D7 brane intersection is in the probe limit in which the D7-branes do not influence the metric of the spacetime. The back-reaction of the D7-branes is determined by their contribution to the energy-momentum tensor. The contribution of the DBI action of  $N_f$  D7-branes is proportional to

$$2\kappa_{10}^2 N_f T_7 \stackrel{(3.8)}{=} \frac{\lambda N_f}{8\pi N_c}, \quad (3.28)$$

and, thus, can be neglected in the limit  $N_f \ll N_c$ . Note that the contribution to the source term in the equations of motion for the dilaton and axion is suppressed in the same way. Since we consider  $N_c \rightarrow \infty$ , the limit is satisfied for any finite  $N_f$ . On the field theory side, this limit corresponds to dropping the flavor loops and is known as the *quenched approximation*.

In the probe limit the D7-branes are embedded into  $AdS_5 \times S^5$  which describes the  $\mathcal{N} = 4$  degrees of freedom. For this purpose we write the  $AdS_5 \times S^5$  metric in the form

$$ds^2 = \frac{v^2}{2R^2} dx_\mu dx^\mu + \frac{R^2}{v^2} (dr^2 + r^2 d\Omega_3^2 + dW_5^2 + dW_6^2), \quad (3.29)$$

where we used the coordinate system given in (2.90) with  $v = \sqrt{2}uR^2$  and

$$dv^2 + v^2 d\Omega_5^2 = dr^2 + r^2 d\Omega_3^2 + dW_5^2 + dW_6^2, \quad (3.30)$$

with  $r^2 = W_1^2 + W_2^2 + W_3^2 + W_4^2$  and  $v^2 = r^2 + W_5^2 + W_6^2$ . Since the D7-branes wrap topologically trivial cycles in the internal space, there are no tadpoles.

The embedding of the D7-branes is determined by specifying its position in the  $W_{5/6}$  direction. Due to the  $SO(2)$  symmetry in these directions, we fix  $W_6 \equiv 0$ .

The rotational symmetry  $SO(4)$  and a constant mass in the field theory allow us to choose  $W_5$  to depend only on  $r$ . In addition, we use the  $U(N_f)$  gauge symmetry to rotate the field  $W_5$  into the  $\lambda^0 = \mathbb{1}$  direction. Then the pullback of the metric on the worldvolume of the D7-branes is given by

$$ds^2 = \frac{r^2 + W_5^2}{2R^2} dx_\mu dx^\mu + \frac{R^2}{r^2 + W_5^2} \sqrt{1 + W_5'^2} dr^2 + \frac{R^2 r^2}{r^2 + W_5^2} d\Omega_3^2. \quad (3.31)$$

This embedding generates new low energy degrees of freedom which correspond to massless open string fluctuations on the D7-branes and are described by the DBI action (2.52) and the WZ term (2.65). To simplify the calculation we consistently set the gauge field to zero such that the WZ term is always zero and the DBI action becomes

$$S_7 = -N_f T_7 \int d\xi^8 r^3 \sqrt{1 + W_5'^2}. \quad (3.32)$$

Using the Euler-Lagrange equation, the equation of motion for the embedding function  $W_5$  of the D7-branes is given by

$$\partial_r \left( \frac{r^3 W_5'}{\sqrt{1 + W_5'^2}} \right) = 0. \quad (3.33)$$

Close to the boundary  $r \rightarrow \infty$ , the solution to this equation has the asymptotic form

$$W_5 = L + \frac{c}{r^2} + \dots. \quad (3.34)$$

In section 2.2.7 we have seen that the distance  $L$  between the D3-branes and D7-branes is related to the quark mass  $M_q$ . Due to the additional factor of 2 in the metric of the Minkowski directions, the relation between the distance  $L$  and the quark mass  $M_q$  is

$$M_q = \frac{L}{2\sqrt{2}\pi\alpha'}. \quad (3.35)$$

Thus, the operator dual to the field  $W_5$  must contain the bilinear quark operator  $\tilde{\psi}\psi$ . The dual operator is (see e. g. [72, Appendix A])

$$\mathcal{O}_{M_q} = -\partial_{M_q} \mathcal{L}_{\mathcal{N}=2} = i\tilde{\psi}\psi + \tilde{q} \left( M_q + \sqrt{2}X^5 \right) \tilde{q}^\dagger + q^\dagger \left( M_q + \sqrt{2}X^5 \right) q + \text{h.c.}, \quad (3.36)$$

and the coefficient  $c$  determines the vev of this operator,

$$\langle \mathcal{O}_{M_q} \rangle = -2\sqrt{2}\pi^3\alpha' N_f T_7 c. \quad (3.37)$$

In order to obtain a supersymmetric embedding,  $c$  must be zero since the vev of this operator would break supersymmetry. Thus, the supersymmetric embedding is given by the constant embedding function  $W_5 = L$ . The induced metric on the D7-branes is then given by

$$ds^2 = \frac{r^2 + L^2}{2R^2} dx_\mu dx^\mu + \frac{R^2}{r^2 + L^2} dr^2 + \frac{R^2 r^2}{r^2 + L^2} d\Omega_3^2, \quad (3.38)$$

which is the metric of  $AdS_5 \times S^3$  at the boundary for  $r \rightarrow \infty$ . For  $r = 0$ , i.e.  $v^2 = L^2$ , the radius of the  $S^3$  shrinks to zero and the probe branes do not extend any further into the AdS space. For  $L = 0$ , the space is  $AdS_5 \times S^3$  everywhere and the dual field theory is still conformal. It can be shown that the  $\beta$ -function of the dual theory in this case is given by  $\beta \propto \lambda^2 N_f / N_c$  and, thus, vanishes in the probe limit.

The configuration we discussed so far is stable. Since the scalar field  $W_5$  is dual to the operator  $\mathcal{O}_{M_q}$  with  $\Delta = 3$ , the mass of the field  $W_5$  is given by  $R^2 m^2 = \Delta(\Delta - 4) = -3$ . At first view this seems to be unstable. However, in  $AdS_{d+1}$ , modes are stable if their mass is above the Breitenlohner-Freedman bound [163,164],  $R^2 m_{BF}^2 = -d^2/4$ . Thus, the mass of  $W_5$  is above the bound which guarantees stability.

### Mesonic Spectrum

After we embedded the D7-branes, we study the spectrum of the mesonic excitations. There are scalar and vector mesons with arbitrary  $R$ -charge. For this purpose we study the fluctuations of the D7-branes about the configuration discussed above [39]. There are the fluctuations of the scalars,

$$W_5 = L + 2\pi\alpha' w_5^a \lambda^a \quad \text{and} \quad W_6 = 0 + 2\pi\alpha' w_6^a \lambda^a, \quad (3.39)$$

and of the gauge field,

$$A = 0 + a_\alpha^a \lambda^a dx^\alpha, \quad (3.40)$$

where  $\lambda^a$  are the generators of the  $U(N_f)$  gauge symmetry on the D7-branes. Due to the non-Abelian structure, the pullback of the metric is given by

$$\mathcal{P}[G] = G_{\alpha\beta} + G_{88} D_\alpha W_5 D_\beta W_5 + G_{99} D_\alpha W_6 D_\beta W_6, \quad (3.41)$$

where  $D_\alpha$  is the covariant derivative. To calculate the mesonic spectrum, it suffices to work to quadratic order in the fluctuations,

$$\mathcal{P}[G] = G_{\alpha\beta} + (2\pi\alpha')^2 \frac{R^2}{v^2} (\partial_\alpha w_5 \partial_\beta w_5 + \partial_\alpha w_6 \partial_\beta w_6) + \dots. \quad (3.42)$$

Since the background metric is diagonal,  $Q = \mathbf{1}$  and the non-Abelian DBI action (2.52) becomes

$$S_7 = T_7 \text{STr} \int d^8 \xi \sqrt{-\det[\mathcal{P}[G] + 2\pi\alpha' F_{\alpha\beta}]}. \quad (3.43)$$

The contribution at second order in the fluctuations is given by

$$S_7^{(2)} = (2\pi\alpha')^2 T_7 \text{Tr} \int d^8 \xi \sqrt{-\det G_{\alpha\beta}} \left[ \frac{R^2 G^{\alpha\beta}}{2v^2} (\partial_\alpha w_5 \partial_\beta w_5 + \partial_\alpha w_6 \partial_\beta w_6) + \frac{1}{4} f_{ab} f^{ab} \right], \quad (3.44)$$

where  $f_{\alpha\beta} = \partial_\alpha a_\beta - \partial_\beta a_\alpha$ . In addition, there is also a contribution from the WZ term (2.65)

$$S_{WZ} = \frac{(2\pi\alpha')^2 T_7}{32R^4} \int v^4 dx^0 \wedge dx^1 \wedge dx^2 \wedge dx^3 \wedge \text{Tr}(F \wedge F), \quad (3.45)$$

which at second order becomes

$$\begin{aligned} S_{WZ}^{(2)} &= \frac{(2\pi\alpha')^2 T_7}{32R^4} \int v^4 dx^0 \wedge dx^1 \wedge dx^2 \wedge dx^3 \wedge \text{Tr}(f \wedge f) \\ &= \frac{(2\pi\alpha')^2 T_7}{8R^4} \int r(r^2 + L^2) dx^0 \wedge dx^1 \wedge dx^2 \wedge dx^3 \wedge dr \wedge \text{Tr}(a \wedge da). \end{aligned} \quad (3.46)$$

Using the Euler-Lagrange equation, the equations of motion are given by

$$\begin{aligned} 0 &= \partial_\alpha \left( \frac{\sqrt{-\det G_{\gamma\delta}} G^{\alpha\beta}}{r^2 + L^2} \partial_\beta w_{5/6} \right), \\ 0 &= \partial_\alpha \left( \sqrt{-\det G_{\gamma\delta}} f^{\alpha\beta} \right) - \frac{r(r^2 + L^2)}{4R^4} \epsilon^{\beta AB} \partial_A a_B, \end{aligned} \quad (3.47)$$

where  $A, B$  runs over the coordinates of the  $S^3$ . The second term in the equation of motion for the gauge field only contributes if  $\beta$  is one of the  $S^3$  indices. Notice that the different flavor components satisfy the same equations of motion as we expect for an  $U(N_f)$  invariant background.

Let us now focus on the equations of motion for the scalars. They can be expanded to

$$0 = \partial_r^2 w_{5/6} + \frac{3}{r} \partial_r w_{5/6} + \frac{2R^4}{(r^2 + L^2)^2} \partial_\mu \partial^\mu w_{5/6} + \frac{1}{r^2} \nabla^A \nabla_A w_{5/6}. \quad (3.48)$$

Due to the translation invariance in the Minkowski directions, we decompose the fluctuations in its Fourier coefficients. In addition, the  $SO(4)$  symmetry allows also to decompose the fluctuations into spherical harmonics  $Y^\ell$  such that we can write

$$w_{5/6} = \phi(r) e^{ik_\mu x^\mu} Y^\ell(S^3). \quad (3.49)$$

For a scalar in the representation  $(\ell/2, \ell/2)$  of  $SO(4)$ , the spherical harmonics satisfy

$$\nabla^A \nabla_A Y^\ell = -\ell(\ell + 2) Y^\ell. \quad (3.50)$$

It is convenient to define the dimensionless quantities

$$\tilde{r} = \frac{r}{L}, \quad \tilde{M}^2 = -\frac{2k^2 R^4}{L^2}, \quad (3.51)$$

in which the equation of motion becomes

$$0 = \partial_{\tilde{r}}^2 \phi + \frac{3}{\tilde{r}} \partial_{\tilde{r}} \phi + \left( \frac{\tilde{M}^2}{(\tilde{r}^2 + 1)^2} - \frac{\ell(\ell + 2)}{\tilde{r}^2} \right) \phi. \quad (3.52)$$

In [39] the solution to this equation is given as

$$\phi = \tilde{r}^\ell (\tilde{r}^2 + L^2)^{-\alpha} {}_2F_1 \left( -\alpha, -\alpha + \ell + 1, \ell + 2; -\frac{\tilde{r}^2}{L^2} \right), \quad (3.53)$$

where  $2\alpha = -1 + \sqrt{1 + \tilde{M}^2}$  and  ${}_2F_1$  is the Gauss hypergeometric function. In order to obtain a normalizable solution at the boundary  $\tilde{r} \rightarrow \infty$ , the series expansion of the hypergeometric function must terminate in such a way that its highest order term is suppressed by the prefactor  $\tilde{r}^{\ell-2\alpha}$ . This is ensured by [165, sec. 15.1]

$$\alpha = n + \ell + 1 \quad \text{for } n \in \mathbb{N}_0, \quad (3.54)$$

which determines the mass spectrum of the two scalar mesons  $w_5, w_6$  to be,

$$\begin{aligned} M_s &= \frac{L\tilde{M}}{\sqrt{2}R^2} = \frac{\sqrt{2}L}{R^2} \sqrt{(n + \ell + 1)(n + \ell + 2)} \\ &= \frac{2\sqrt{2}\pi M_q}{\sqrt{\lambda}} \sqrt{(n + \ell + 1)(n + \ell + 2)}. \end{aligned} \quad (3.55)$$

In the last equality we translate the gravity quantities to field theory quantities.

The gauge field fluctuations can be decomposed in four different representations of the symmetry group  $SO(4)$ . While  $a_\mu$  and  $a_r$  can be decomposed into scalar spherical harmonics  $Y^\ell$ ,  $a_A$  has to be decomposed into vector spherical harmonics,  $Y^{\ell,\pm}$ .  $Y^{\ell,\pm}$  transforms as  $(\frac{\ell\mp 1}{2}, \frac{\ell\pm 1}{2})$  under  $SO(4)$ . To summarize, we find scalars with respect to the four-dimensional Lorentz group in the representation  $(\frac{\ell-1}{2}, \frac{\ell+1}{2})$ ,  $(\frac{\ell+1}{2}, \frac{\ell-1}{2})$  and  $(\ell/2, \ell/2)$  of  $SO(4)$  and an additional vector in  $(\ell/2, \ell/2)$ .

In [39, 166] it is explicitly shown that the mesonic modes fill an  $\mathcal{N} = 2$  massive gauge supermultiplet. Its mass is given by (3.55). For  $\ell \geq 2$  it contains three real scalars and one vector in  $(\ell/2, \ell/2)$ , two real scalars in  $(\ell/2, \ell/2 \pm 1)$  and two Dirac fermions, one in  $(\frac{\ell}{2}, \frac{\ell+1}{2})$  and one in  $(\frac{\ell}{2}, \frac{\ell-1}{2})$ . For  $\ell = 0$  the supermultiplet consists of two real scalars and one vector in  $(0, 0)$ , one scalar in  $(0, 1)$  and one Dirac fermion in  $(0, 1/2)$  while for  $\ell = 1$  it consists of three scalar and one vector in  $(1/2, 1/2)$ , one scalar in  $(1/2, 3/2)$  and two Dirac fermions, one in  $(1/2, 0)$  and one in  $(1/2, 1)$ .

The meson spectrum shows a mass gap which is equal to the mass of the lightest meson

$$M_{\text{gap}} = \frac{4\pi M_q}{\sqrt{\lambda}}. \quad (3.56)$$

This means that for  $\lambda \gg 1$ , which is the regime we consider, the meson mass is much smaller than the quark mass  $M_q$ . The mesons are, therefore, together with the excitations of the  $\mathcal{N} = 4$  multiplet, the degrees of freedom which dominate the physics at low energy.

In the perturbative regime, i. e.  $\lambda \ll 1$ , the binding energy is small,  $E_b^{\text{weak}} = 2M_q - M_{\text{gap}} \propto \lambda^2 \ll 1$ . In contrast to this, the binding energy almost cancels the rest mass of the quarks in the strong coupling regime, i. e.  $\lambda \gg 1$ ,  $E_b^{\text{strong}} \approx 2M_q$ .

This becomes clear if we consider the “formation” of mesons in the bulk. The quark and antiquark which build the meson are represented by two opposite oriented strings stretched between the D3- and D7-branes. If the quarks are massive, the strings have a non-zero length  $L$  corresponding to the non-zero quark mass  $M_q \propto L$ . However, if we allow the D3–D7 strings to recombine, we obtain D7–D7 strings which may have arbitrarily short length. Since the D7–D7 strings correspond to the mesons, we obtain an arbitrarily small meson mass such that this simple picture matches nicely with above result.



# Holography at Finite Temperature

At zero temperature the difference between the  $\mathcal{N} = 4$  Super-Yang-Mills theory and QCD is enormous: QCD is a confining theory with a dynamically generated scale, the QCD scale, given by  $\Lambda_{\text{QCD}} \approx 200 \text{ GeV}$ , while  $\mathcal{N} = 4$  Super-Yang-Mills theory is a conformal theory and does not have any scale. Moreover,  $\mathcal{N} = 4$  Super-Yang-Mills theory is highly supersymmetric while QCD is not at all.

So how can we possibly learn anything about QCD by applying gauge/gravity dualities? The answer is to focus on a different phase of QCD. For temperatures slightly above the deconfinement temperature  $T_{\text{dec}} \approx 170 \text{ MeV}$ , QCD is believed to be in a deconfined but still strongly coupled phase known as the *quark-gluon plasma* [41,42]. Moreover, any finite temperature breaks both supersymmetry and conformal invariance such that  $\mathcal{N} = 4$  Super-Yang-Mills theory becomes similar to QCD. Thus, we may use gauge/gravity duality to understand the quark-gluon plasma produced at the Relativistic Heavy Ion Collider (RHIC) and the Large Hadron Collider (LHC).

In this spirit we must heat up the duality and introduce a finite temperature as described in section 4.1. For this purpose we use the concept of *finite temperature field theory* on the field theory side (see section 4.1.1) and consider *black holes* on the gravity side (see section 4.1.2). A thermal state on the field theory side is matched to an asymptotically AdS spacetime containing a black hole in the sense that the field theory temperature is given by the Hawking temperature of the black hole. Using the well-established methods to calculate thermodynamic quantities for asymptotically AdS black holes [167], we determine the thermodynamics of the strongly coupled  $\mathcal{N} = 4$  Super-Yang-Mills theory and its  $\mathcal{N} = 2$  flavored version in section 4.2.

We may compare these results to the ones which are obtained from lattice QCD [46]. For instance in figure 4.1, the energy density normalized to its value at zero coupling versus the temperature is presented. The curves obtained by lattice calculations have a very similar behavior. They rise sharply at the deconfinement transition and are constant afterwards. The plateau is at  $\epsilon/\epsilon_0 \approx 0.8 - 0.85$ . Gauge/gravity duality predicts a ratio of  $3/4$  (see section 4.2.2). This is remarkably close to the lattice QCD results taking their microscopic differences into account. Therefore, we expect that various aspects of strongly coupled plasmas are universal

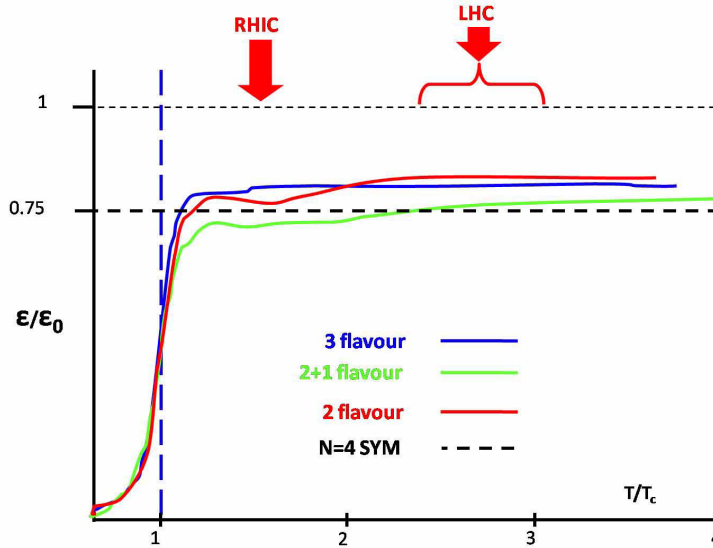


**Figure 4.1:** Energy density of QCD and  $\mathcal{N} = 4$  Super-Yang-Mills as a function of temperature. The energy density  $\epsilon$  is normalized to its value at zero coupling  $\epsilon_0$ . The temperature  $T$  is shown in units of the critical temperature  $T_c$ . The figure is taken from [45].

and so might be understandable by means of gauge/gravity duality.

After we have investigated the equilibrium state, we study the response of the systems due to small perturbations in section 4.3. On the field theory side, we use the concept of *linear response theory*. A perturbation  $\phi$  which sources an operator  $\mathcal{O}$  is related to the corresponding vacuum expectation value  $\langle \mathcal{O} \rangle$  in terms of Green's functions. In order to make use of the gravity dual, we need a recipe to determine the Green's functions from a gravity calculation. We discuss this recipe in section 4.3.1 and use it to calculate the Green's functions in the strongly coupled regime in section 4.3.2 and 4.3.3.

In the quark-gluon plasma there are still quasiparticle bound states present, even though the system is in the deconfined regime. These bound states are the mesonic excitations  $\eta_c$  and  $J/\psi$  which contain the heavy charm quark. We observe this phenomenon also in the context of gauge/gravity duality. In section 4.2.3 we find stable mesons up to a critical temperature  $T_{\text{crit}}$  which is larger than the deconfinement temperature  $T_{\text{dec}}$ . In this case the critical temperature scales with the quark mass,  $T_{\text{crit}} \propto M_q$ . Thus, we expect that mesons that contain heavy quarks survive to larger temperatures. This is in agreement with the  $\eta_c$  and  $J/\psi$  resonances found in the experiment.

The response of a system in the low energy and long wavelength limit is covered by *hydrodynamics* which can be seen as an effective field theory. We discuss hydrodynamics in section 4.4 by presenting the hydrodynamic description of an isotropic viscous fluid in section 4.4.1. This description allows for several propa-

gating modes, the hydrodynamic modes, which are examined in section 4.4.2. The system-dependent transport coefficients such as the shear viscosity may be determined in terms of Green's functions by Kubo's formulae. For the shear viscosity the Kubo's formula is presented in section 4.4.3. Finally, using this framework we investigate the transport properties of the  $\mathcal{N} = 4$  Super-Yang-Mills theory and its  $\mathcal{N} = 2$  flavored version in section 4.4.4 and 4.4.5.

Certainly the most famous result in the context of gauge/gravity duality is the universality of the ratio of the shear viscosity  $\eta$  to the entropy density  $s$  which we derive in section 4.4.4. This result is of particular interest since lattice QCD is not capable of describing real-time processes. At weak coupling, perturbative QCD calculations predict that the ratio is large,  $\eta/s \sim 1/\lambda^2$  for  $\lambda \ll 1$  (see e.g. [51]). Extrapolating to  $\lambda \sim 1$ , one finds  $\eta/s \sim 1$  which is much bigger than the result which we have obtained from gauge/gravity duality,  $\eta/s = 1/4\pi$ . Astonishingly, the measured value at RHIC for this ratio is small [59]. It is the smallest value ever measured, making the quark-gluon plasma the most ideal fluid ever observed. Since the analysis of the hydrodynamic evolution has large systematic uncertainties, the ratio is located between 0 and 0.2, so the gauge/gravity result fits much better than the perturbative QCD result.

Surprisingly, the quark-gluon plasma is not the only strongly coupled system which has a ratio of shear viscosity to entropy density in this ballpark (see e.g. [168]). Another example is cold atoms at unitarity. The universality of this ratio suggest again that strongly coupled systems may have universal features which can be predicted via gauge/gravity duality. In this sense the observed structures in the Green's functions of flavor fields presented in my own work [3] and section 4.3.3 are predictions for strongly coupled field theories and could perhaps be found experimentally.

## 4.1 Heating up the Correspondence

### 4.1.1 Finite Temperature Field Theory

At zero temperature any physical system allows quantum fluctuations. In the path integral formalism, the suppression of these fluctuations is determined by the action. For instance, the partition function is given by

$$Z_{\text{qm}} = \int \mathcal{D}\phi e^{iS[\phi]}, \quad (4.1)$$

and the vacuum expectation value of an operator  $F$  by

$$\langle F \rangle = \frac{\int \mathcal{D}\phi F[\phi] e^{iS[\phi]}}{Z_{\text{qm}}}, \quad (4.2)$$

where  $\mathcal{D}\phi$  is the measure on the field configuration space. The transition amplitude from an initial field configuration  $\phi_i$  at time  $t_i$  to a final field configuration  $\phi_f$  at

time  $t_f$  in this formalism is given by

$$\langle \phi_f(t_f) | \phi_i(t_f) \rangle = \int_{\phi=\phi_i}^{\phi=\phi_f} \mathcal{D}\phi e^{iS[\phi]}. \quad (4.3)$$

In the Hamiltonian formalism, it translates to

$$\langle \phi_f(t_f) | \phi_i(t_f) \rangle = \langle \phi_f(t_f) | e^{-iH(t_f-t_i)} | \phi_i(t_i) \rangle. \quad (4.4)$$

In addition, at finite temperature there are also thermal fluctuations. Any quantum mechanical system at finite temperature can be found in different energy eigenstates  $|n\rangle$  with energy  $E_n$ . The probability of finding the eigenstate  $|n\rangle$  is suppressed by the Boltzmann factor  $\exp(-\beta E_n)$  where  $\beta = 1/T$  is the inverse temperature. The partition function is given by

$$Z_{\text{thermo}} = \text{Tr} e^{-\beta H} = \sum_n \langle n | e^{-\beta H} | n \rangle = \sum_n e^{-\beta E_n}, \quad (4.5)$$

where  $H$  is the Hamiltonian of the system. In equilibrium, the system is described by the density matrix

$$\rho = \frac{e^{-\beta H}}{Z_{\text{thermo}}}, \quad (4.6)$$

and the expectation value of an observable  $A$  in the thermal ensemble can be calculated by

$$\langle A \rangle = \text{Tr}(\rho A) = \frac{\text{Tr}(A e^{-\beta H})}{Z_{\text{thermo}}}. \quad (4.7)$$

Using the *imaginary time formalism*, the path integral formalism (4.1) reproduces the thermal equilibrium partition function (4.5). In this prescription, we analytically continue the time coordinate into the complex plane and introduce a new time coordinate  $\tau = it$  by a Wick rotation. Then the path integral becomes

$$Z_{\text{qm}} = \int \mathcal{D}\phi e^{-I[\phi]}, \quad (4.8)$$

where  $I$  is the Euclidean action. In addition, we exclusively consider periodic field configurations along the imaginary time direction  $\tau$ . The period is given by  $\beta$ . According to (4.3) and (4.4), the transition between periodic states formulated in terms of the path integral and in the Hamiltonian formalism can be identified,

$$\int_{\substack{\beta\text{-periodic} \\ \text{states}}} \mathcal{D}\phi e^{-I[\phi]} = \sum_{\substack{\beta\text{-periodic} \\ \text{states}}} \langle \phi_\beta | e^{-\beta H} | \phi_\beta \rangle. \quad (4.9)$$

The right hand side of the equation is the thermal partition function  $Z_{\text{thermo}}$  as defined in (4.5) if we identify the period  $\beta$  with the inverse temperature. The left hand side of the equation then describes the path integral representation of the thermal partition function,

$$Z_{\text{thermo}} = \int_{\substack{\beta\text{-periodic} \\ \text{states}}} \mathcal{D}\phi e^{-I[\phi]}. \quad (4.10)$$

It is important to notice that the result does not depend on the real time anymore and that we need to enforce the periodic boundary conditions. The elimination of the time dependence is in agreement with the system being in equilibrium, i. e. observables do not change with time.

So far, we described the system statistically. From this description we may extract thermodynamic properties of the system. For instance we can calculate the expectation value of the energy,

$$\langle E \rangle = \text{Tr}(\rho H) = -\frac{1}{Z_{\text{thermo}}} \partial_{\beta} Z_{\text{thermo}} = -\partial_{\beta} \ln Z_{\text{thermo}}. \quad (4.11)$$

Another interesting thermodynamic quantity is the entropy  $S$  which can be expressed in terms of the density matrix  $\rho$ ,

$$S = \langle -\ln \rho \rangle. \quad (4.12)$$

Using (4.6), the entropy can be written as

$$\begin{aligned} S &= -\text{Tr}(\rho \ln \rho) = \frac{1}{Z_{\text{thermo}}} \text{Tr} \left[ e^{-\beta H} (\beta H + \ln Z_{\text{thermo}}) \right] \\ &= \beta \langle E \rangle + \ln Z_{\text{thermo}}, \end{aligned} \quad (4.13)$$

which implies

$$F = \langle E \rangle - TS = -T \ln Z_{\text{thermo}}. \quad (4.14)$$

The *free energy*  $F$  measures the amount of work which can be done by the system. It is the thermodynamic potential of the *canonical ensemble* which we consider here since the system is at constant temperature, volume and particle density. The system tends to lower the free energy and the equilibrium is given at its minimum.

From the free energy  $F(T, V, N)$  as function of temperature  $T$ , volume  $V$  and number density  $N$ , we may derive any other thermodynamical quantity. The entropy  $S$ , for instance, is given by

$$S = \left( -\frac{\partial F}{\partial T} \right)_{V, N}, \quad (4.15)$$

where the label  $V, N$  on the bracket means that the derivative with respect to the temperature  $T$  must be taken at constant volume  $V$  and number density  $N$ . In general, variations of the free energy can be expressed in the compact form

$$dF = -pdV - SdT + \mu dN, \quad (4.16)$$

where  $p$  is the pressure and  $\mu$  the chemical potential.

### 4.1.2 Thermal AdS and Schwarzschild Black Hole

In this section we focus on the thermal states on the gravity side. For this purpose we consider the  $(d+1)$ -dimensional global AdS space with metric

$$ds^2 = - \left( 1 + \frac{r^2}{R^2} \right) dt^2 + \frac{dr^2}{1 + \frac{r^2}{R^2}} + r^2 d\Omega_{(d-1)}^2, \quad (4.17)$$

where  $R$  is the AdS radius and  $d\Omega_{d-1}$  is the metric on the unit sphere  $S^{d-1}$ . This metric is a solution to Einstein's equations with negative cosmological constant  $\Lambda = -d(d-1)/2R^2$ . In contrast to the Poincaré patch considered in section 2.2.9, the boundary of this space has an  $\mathbb{R} \times S^{d-1}$  topology. According to the last section, we may Wick-rotate the system,  $\tau = it$  and consider periodic states,  $\tau \sim \tau + \beta$ , in order to obtain a finite temperature  $T = 1/\beta$ . The boundary has now an  $S^1 \times S^{d-1}$  topology.

This is not the only solution of the Einstein equations with negative cosmological constant. The other possible solution is the AdS Schwarzschild black hole. Its Euclidean metric reads

$$ds^2 = f(r)d\tau^2 + \frac{dr^2}{f(r)} + r^2 d\Omega_{d-1}^2 \quad \text{with } f(r) = 1 + \frac{r^2}{R^2} - \frac{2m}{r^{d-2}}, \quad (4.18)$$

where  $m$  is related to the ADM mass  $M$  of the black hole,

$$M = \frac{(d-1)\text{Vol}(S^{d-1})}{\kappa_5^2} m. \quad (4.19)$$

The event horizon of this black hole is at  $r_h$ , where  $f(r_h) = 0$ , which implies

$$m = \frac{r_h^{d-2}}{2} + \frac{r_h^d}{2R^2}. \quad (4.20)$$

By considering quantum fields in a black hole geometry, Hawking found that the black hole radiates a black body spectrum. The temperature of this spectrum is determined by the surface gravity of the black hole. Another possibility to calculate the temperature of a black hole is given by studying its Euclidean metric. Close to the horizon,  $r \approx r_h$ , the metric becomes

$$ds^2 = f'(r_h)(r - r_h)d\tau^2 + \frac{dr^2}{f'(r_h)(r - r_h)} + r_h^2 d\Omega_{d-1}^2, \quad (4.21)$$

and has a conical singularity as long as  $f'(r_h)\tau$  is not periodic in  $4\pi$ . Since the temperature  $T$  is related to the period in  $\tau$ , we obtain

$$T = \frac{f'(r_h)}{4\pi} = \frac{(d-2)R^2 + dr_h^2}{4\pi r_h R^2}. \quad (4.22)$$

The temperature is minimal,  $T^{\min} = \sqrt{d(d-2)}/2\pi R$ , for the horizon radius  $r_h^{\min} = R\sqrt{(d-2)/d}$ .

Since we have two possible solution for the temperatures  $T > T^{\min}$ , we must determine the ground state of the system, i. e. the state with less free energy. We calculate the free energy by using the saddle point approximation,

$$F = T I_{\text{on-shell}}, \quad (4.23)$$

where  $I_{\text{on-shell}}$  is the Euclidean on-shell action. The difference in the free energy between the AdS Schwarzschild black hole and the thermal AdS is given by

$$\Delta F = \frac{\text{Vol}(S^{d-1})r_h^{d-2}}{2\kappa_5^2 R^2} (R^2 - r_h^2). \quad (4.24)$$

For  $r_h > R$ , the result is negative and the AdS black hole is the ground state, while for  $r_h < R$ , the thermal AdS is thermodynamically favored. At  $r_h = R$  or  $T = (d-1)/2\pi R$ , there is a phase transition between these two spaces. This transition is known as the *Hawking-Page phase transition* [167]. The result of this discussion is that large black holes are stable in AdS space while small black holes decay into the thermal AdS space. The energy of this black hole is given by the ADM mass,

$$\langle E \rangle = \partial_\beta I_{\text{on-shell}} = M, \quad (4.25)$$

while the entropy is given by the area of the horizon  $A$ ,

$$S = \beta \langle E \rangle - I_{\text{on-shell}} = \frac{2\pi A}{\kappa_5^2} = \frac{2\pi r_h^{d-1} \text{Vol}(S^{d-1})}{\kappa_5^2}. \quad (4.26)$$

Let us now come back to gauge/gravity duality. Since the global AdS space has an  $S^1 \times S^{d-1}$  topology at the boundary, this space is expected to be dual to a field theory on  $S^1 \times S^{d-1}$ . The radius of the  $S^1$  is the inverse temperature  $\beta$  while the radius  $\beta'$  of the  $S^{d-1}$  determines the spatial geometry of the spacetime. Since the two radii are independent, we can discuss their ratio. On the gravity side, we found the Hawking-Page transition at  $\beta/\beta' \approx 1$ . The natural question is now: How can we see this phase transition on the field theory side? In [43, 44] it is argued by considering Wilson loops and the mass spectrum that on the field theory side, this phase transition describes the transition from a confining at low temperature to a deconfining phase at high temperature. In order to study  $\mathcal{N} = 4$  Super-Yang-Mills theory on  $S^1 \times \mathbb{R}^3$ , we decompactify the  $S^3$  by sending  $\beta' \rightarrow \infty$  which leads to the ratio  $\beta/\beta' \rightarrow 0$ . Thus, the theory on  $S^1 \times \mathbb{R}^3$  at any finite temperature is mapped

to the high temperature phase of the theory on  $S^1 \times S^3$ , i. e. the deconfining phase. The limit  $\beta' \rightarrow \infty$  corresponds on the gravity side to considering a black brane with the horizon topology  $S^1 \times \mathbb{R}^3$  in AdS space in contrast to a black hole with horizon topology  $S^1 \times S^3$ .

To summarize, we can study  $\mathcal{N} = 4$  Super-Yang-Mills theory on  $S^1 \times \mathbb{R}^3$  at finite temperature by studying black branes with horizon topology  $S^1 \times \mathbb{R}^3$  in AdS space. Since the partition functions of the gauge theory and the gravity theory are identified according to the AdS/CFT dictionary, the thermodynamic potentials of both theories also coincide. In addition, we identify the temperature on the field theory side with the Hawking temperature of the black hole.

## 4.2 Physics in Equilibrium

In this section we study the two described theories, the  $\mathcal{N} = 4$  Super-Yang-Mills theory and its  $\mathcal{N} = 2$  flavored version, at finite temperature. In order to determine the thermodynamics of these theories, we need a method to renormalize the divergences which are present in the calculation of the partition function. These divergences are the usual UV divergences known from any field theory calculation. In the context of gauge/gravity duality, the procedure is called *holographic renormalization* which we discuss in section 4.2.1. After renormalization, the partition function may be determined and we can extract the thermodynamics. We study the thermodynamics of the  $\mathcal{N} = 4$  Super-Yang-Mills theory in section 4.2.2 and of the flavor branes in section 4.2.3.

### 4.2.1 Holographic Renormalization

In gauge/gravity duality the partition function of the gauge theory is identified with the partition function of the corresponding string theory as described in (3.9). In the large  $N$  limit, we use the saddle point approximation in order to simplify the string partition function,

$$Z_{\text{string}} \approx e^{-I_{\text{on-shell}}}, \quad (4.27)$$

where  $I_{\text{on-shell}}$  is the Euclidean supergravity on-shell action. However, this on-shell action is usually divergent for instance due to the infinite volume of AdS space. Thus, in order to extract physical quantities out of the on-shell action we need a way to regularize it. This method is known as holographic renormalization which we discuss in the following. A lecture note on this subject can be found in [169].

In general, quantum field theories suffer from UV divergences. According to the discussion in section 3.1.1, the high energy fluctuations in the supergravity descriptions are far away from the D3-branes. This suggests that the UV divergences are mapped to IR divergences (long distance divergences) on the gravity side. This connection between UV and IR is a general phenomenon in gauge/gravity duality [170]. In quantum field theory we cancel the UV divergences by counterterms which do not

depend on the IR physics. This suggests that on the gravity side the counterterms should only depend on the IR region, i. e. the near-boundary geometry.

In order to regularize, we introduce a cut-off parameter  $\epsilon$  close to the AdS boundary. In the following we will use the coordinate system defined in (2.91) where the boundary is at  $z = 0$ , i. e. the cut-off parameter is small  $\epsilon \ll 1$ . Any bulk field  $\Phi(x, z)$  has an asymptotic expansion close to the boundary of the form

$$\Phi(x, z) = z^m \left( \phi_0(x) + z\phi_2(x) + \dots + z^n \left( \phi_{2n}(x) + \tilde{\phi}_{2n}(x) \ln z + \dots \right) \right). \quad (4.28)$$

Since the field equations are second order differential equations in  $z$ , there are two independent solutions with asymptotic behavior  $z^m$  and  $z^{m+n}$ , respectively. By expanding the equations of motion in  $z \ll 1$ , the coefficients  $\phi_k(x)$  may be determined in terms of two independent coefficients which we choose to be  $\phi_0(x)$  and  $\phi_{2n}(x)$ . According to the AdS/CFT dictionary discussed in section 3.1.3,  $\phi_0(x)$  is related to the source of the dual operator  $\mathcal{O}$  while  $\phi_{2n}(x)$  is related to the vev of the dual operator  $\langle \mathcal{O} \rangle$ .

By inserting the asymptotic expansion (4.28), the on-shell action restricted to the range of integration,  $z \geq \epsilon$  is given by

$$I_{\text{reg}}[\phi_0; \epsilon] = \int d^d x \sqrt{g_0} \left( \epsilon^{-\nu} a_0 + \epsilon^{-\nu+1} a_2 + \dots - a_{2\nu} \log \epsilon + \mathcal{O}(\epsilon^0) \right) \Big|_{z=\epsilon}, \quad (4.29)$$

where  $\nu$  is positive number and  $a_k$  are local functions of the independent coefficient  $\phi_0(x)$  but independent of  $\phi_{2n}(x)$ . The logarithmic divergence is related to the conformal anomaly which we discussed in section 3.1.5. By inverting the relation between the  $\Phi$  and  $\phi_0$ , we determine the divergent pieces  $a_k$  in terms of the field  $\Phi(x, \epsilon)$ . The counterterm action is then defined as

$$I_{\text{ct}}[\Phi(x, \epsilon)] = -\text{divergent terms of } I_{\text{reg}}[\phi_0, \epsilon], \quad (4.30)$$

which leads to the subtracted action at the cut-off,

$$I_{\text{sub}}[\phi_0, \epsilon] = I_{\text{reg}}[\phi_0, \epsilon] + I_{\text{ct}}[\Phi(x, \epsilon), \epsilon]. \quad (4.31)$$

By this definition the subtracted action has a finite limit as  $\epsilon \rightarrow 0$ . The renormalized action is defined by the limit

$$I_{\text{ren}}[\phi_0] = \lim_{\epsilon \rightarrow 0} I_{\text{sub}}[\phi_0, \epsilon], \quad (4.32)$$

and is a functional of the source  $\phi_0$ . By varying this functional we obtain the vev of the dual operator  $\langle \mathcal{O} \rangle$ ,

$$\langle \mathcal{O} \rangle = \frac{1}{\sqrt{g_0}} \frac{\delta I_{\text{ren}}}{\delta \phi_0}, \quad (4.33)$$

while higher  $n$ -point functions are calculated in the same fashion. We will use the procedure of holographic renormalization generally discussed here at several occasions throughout this thesis. For instance in the next section we discuss the holographic renormalization of AdS black branes.

### 4.2.2 Thermodynamics of $\mathcal{N} = 4$ Super-Yang-Mills Theory

Let us now discuss the thermodynamics of the  $\mathcal{N} = 4$  Super-Yang-Mills theory which is identified with the thermodynamics of black D3-branes [47] on the gravity side. The Euclidean metric of the black D3-branes is given by (cf. (2.80))

$$ds^2 = H(y)^{-\frac{1}{2}} (f(y)d\tau^2 + d\mathbf{x}^2) + H(y)^{\frac{1}{2}} \left( \frac{dy^2}{f(y)} + y^2 d\Omega_5^2 \right), \quad (4.34)$$

where the blackening factor is given by  $f(y) = 1 - (y_h/y)^4$ . In the near horizon limit  $y/R \ll 1$  and defining  $z = R^2/y$ , this metric becomes

$$ds^2 = \frac{R^2}{z^2} \left[ \left( 1 - \frac{z^4}{z_h^4} \right) d\tau^2 + d\mathbf{x}^2 + \frac{dz^2}{1 - \frac{z^4}{z_h^4}} \right] + R^2 d\Omega_5^2, \quad (4.35)$$

where  $z_h = R^2/y_h$ . Enforcing a regular Euclidean metric close to the horizon determines the Hawking temperature (see (4.22))

$$T = \frac{f'(z_h)}{4\pi} = \frac{1}{\pi z_h}. \quad (4.36)$$

In order to proceed further it is useful to integrate out the dependence on the  $S^5$  and exclusively consider the  $AdS_5$  space. The five-dimensional Euclidean action is given by

$$I = -\frac{1}{2\kappa_5^2} \int d^5x \sqrt{g} \left( \mathcal{R} + \frac{12}{R^2} \right) - \frac{1}{\kappa_5^2} \int_{\partial AdS_5} d^4x \sqrt{\gamma} \mathcal{K}, \quad (4.37)$$

where  $\kappa_5^2$  is given in (3.23). The second term in this action is a *Gibbons Hawking term* which is needed to obtain a well-defined variational principle.  $\mathcal{K}$  denotes the trace of the extrinsic curvature,

$$\mathcal{K}_{MN} = \nabla_M n_N, \quad (4.38)$$

where

$$\gamma_{\mu\nu} = \frac{R^2}{z^2} (f d\tau^2 + d\mathbf{x}^2) \quad (4.39)$$

is the induced metric on the boundary  $z \rightarrow 0$  and  $n_M dx^N = -Rz^{-1} f^{-1/2} dz$  an outward pointing unit normal vector on the boundary. In order to evaluate the on-shell action, we introduce a cut-off  $z = \epsilon \ll 1$  as described in section 4.2.1. The regularized on-shell action then reads

$$I_{\text{reg}} = \frac{VR^3}{T\kappa_5^2} \left( \frac{3}{\epsilon^4} - \frac{2}{z_h^4} + \mathcal{O}(\epsilon) \right), \quad (4.40)$$

where  $V$  is the volume of  $\mathbb{R}^3$ . This leads to the counterterm action

$$I_{\text{ct}} = \frac{3}{R\kappa_5^2} \int_{\partial AdS} d^4x \sqrt{\gamma} = \frac{3VR^3}{T\kappa_5^2} \left( -\frac{1}{\epsilon^4} + \frac{1}{2z_h^4} \right) + \mathcal{O}(\epsilon), \quad (4.41)$$

and to the renormalized action

$$I_{\text{ren}} = -\frac{VR^3}{T\kappa_5^2} \frac{1}{2z_h^4} = -\frac{VR^3\pi^4 T^3}{2\kappa_5^2} = -\frac{\pi^2}{8} V N_c^2 T^3. \quad (4.42)$$

The free energy of the  $\mathcal{N} = 4$  Super-Yang-Mills theory at strong coupling is therefore given by

$$F_{\text{strong}} = -\frac{\pi^2}{8} V N_c^2 T^4, \quad (4.43)$$

while at weak coupling the result is [171]

$$F_{\text{weak}} = -\frac{\pi^2}{6} V N_c^2 T^4 = \frac{4}{3} F_{\text{strong}}. \quad (4.44)$$

From the free energy, all other thermodynamic quantities may be derived. For instance the entropy  $S$  is given by

$$S_{\text{strong}} = -\frac{\partial F_{\text{strong}}}{\partial T} = \frac{\pi^2}{2} V N_c^2 T^3, \quad (4.45)$$

which coincides with the *Bekenstein-Hawking entropy* of the black hole

$$S_{\text{BH}} = \frac{2\pi A}{\kappa_5^2} = \frac{2\pi V R^3}{\kappa_5^2 z_h^3}, \quad (4.46)$$

where  $A$  is the area of the horizon. Another interesting quantity is the energy

$$\langle E \rangle = F + TS = \frac{3\pi^2}{8} V N_c^2 T^4. \quad (4.47)$$

The energy density, however, is also given by the vev of the energy-momentum tensor  $\langle T_{\mu\nu} \rangle$  which is the dual operator of the metric  $g_{\mu\nu}$ . Using the result of section 4.2.1, we obtain [172]

$$\langle T_{\mu\nu} \rangle = \frac{2}{\sqrt{\delta}} \frac{\delta I_{\text{ren}}}{\delta \delta^{\mu\nu}} = \frac{2R^2}{z^2 \sqrt{\gamma}} \frac{\delta I_{\text{reg}}}{\delta \gamma^{\mu\nu}} \Big|_{z=0} = \frac{R^2}{\kappa_5^2 z^2} \left( \mathcal{K}_{\mu\nu} - \mathcal{K} \gamma_{\mu\nu} - \frac{3}{R} \gamma_{\mu\nu} \right) \Big|_{z=0}, \quad (4.48)$$

where  $\delta_{\mu\nu} = z^2/R^2 \gamma_{\mu\nu}|_{z=0}$  is the flat Euclidean metric, the source. As expected this leads to  $\langle E \rangle = \langle T_{tt} \rangle V$  and  $F = -\langle T_{xx} \rangle V = -pV$ . Additionally, the trace of the energy-momentum tensor is zero,  $\langle T_t^t \rangle + 3\langle T_x^x \rangle = 0$ , as expected for a conformal theory.

### 4.2.3 Thermodynamics of Flavor Branes

In section 3.2.1 we added fundamental degrees of freedom to the  $\mathcal{N} = 4$  Super-Yang-Mills theory by embedding D7-branes into the AdS space. These new degrees of freedom contribute to the thermodynamics of the system. In this section we calculate this contribution [49]. The D7-branes are now embedded into the black brane background (4.34).

### Embedding at Finite Temperature

The simplest way to embed the D7-branes is to use similar coordinates as in the zero temperature case. For this purpose, we transform the metric of the black D3-branes (4.35) to the coordinates defined in (3.29),

$$ds^2 = \frac{1}{2} \left( \frac{v}{R} \right)^2 (-f dt^2 + dx^2) + R^2 \frac{dv^2}{v^2 f} + R^2 d\Omega_5^2, \quad (4.49)$$

with  $f = 1 - v_H^4/v^4$ . The black hole horizon is at  $v = v_H$ . In order to get the metric of the six-dimensional flat space in the 456789-directions, we transform the coordinates by

$$\frac{d\varrho}{\varrho} = \frac{dv}{v\sqrt{f}} = \frac{v dv}{\sqrt{v^4 - v_H^4}}, \quad (4.50)$$

which is solved by

$$2\varrho^2 = v^2 + \sqrt{v^4 - v_H^4}. \quad (4.51)$$

The black hole metric becomes then

$$ds^2 = \frac{1}{2} \left( \frac{\varrho}{R} \right)^2 \left( -\frac{f^2}{\tilde{f}} dt^2 + \tilde{f} d\mathbf{x}^2 \right) + \left( \frac{R}{\varrho} \right)^2 (d\varrho^2 + \varrho^2 d\Omega_5^2), \quad (4.52)$$

where  $f = 1 - \varrho_H^4/\varrho^4$  and  $\tilde{f} = 1 + \varrho_H^4/\varrho^4$ . The black hole horizon is now at  $\varrho = \varrho_H$ . The temperature  $T$  of the black hole, which is determined by demanding regularity of the Euclidean section, is in this metric convention given by  $T = \varrho_H/(\pi R^2)$  (cf. (4.36)). In the following we may use the dimensionless coordinate  $\rho = \varrho/\varrho_H$ , which covers the range from the event horizon at  $\rho = 1$  to the boundary of the AdS space at  $\rho \rightarrow \infty$ .

In a similar way to (3.30), we introduce spherical coordinates  $\{r, \Omega_3\}$  in the 4567-directions and polar coordinates  $\{L, \phi\}$  in the 89-directions [72]. The angle between these two spaces is denoted by  $\theta$  ( $0 \leq \theta \leq \pi/2$ ). The metric on the six-dimensional space in the 456789-directions reads

$$\begin{aligned} d\varrho^2 + \varrho^2 d\Omega_5^2 &= dr^2 + r^2 d\Omega_3^2 + dL^2 + L^2 d\phi^2 \\ &= d\varrho^2 + \varrho^2 (d\theta^2 + \cos^2 \theta d\phi^2 + \sin^2 \theta d\Omega_3^2), \end{aligned} \quad (4.53)$$

where  $r = \varrho \sin \theta$ ,  $\varrho^2 = r^2 + L^2$  and  $L = \varrho \cos \theta$ . Due to the symmetry, the embedding of the D7-branes only depends on the radial coordinate  $\varrho$  and  $r$ , respectively.

The two different coordinate systems  $\{\theta, \varrho\}$  and  $\{L, r\}$  are needed to describe the two possible embeddings of the D7-branes. The D7-branes may fall into the horizon of the black hole where we use the coordinate system  $\{\theta, \varrho\}$ . This embedding is called *black hole embedding*. The other possible embedding does not reach the horizon and is named *Minkowski embedding*. In this case the coordinate system  $\{L, r\}$  is the suitable one. There is a first order phase transition between these two different embeddings [40, 48]. We discuss this phase transition later.

Let us first discuss the black hole embedding with coordinates  $\{\theta, \varrho\}$ . Defining  $\chi = \cos \theta$ , we parametrize the embedding by  $\chi = \chi(\varrho)$  and choose  $\phi = 0$  using the  $SO(2)$  symmetry in the 89-direction. In addition, we use, as at the zero temperature, the  $U(N_f)$  symmetry to rotate the embedding into the  $\lambda^0 = \mathbf{1}$  direction. The induced metric  $\mathcal{P}[G]$  on the D7-brane probes is then

$$ds^2 = \frac{\varrho^2}{2R^2} \left( -\frac{f^2}{\tilde{f}} dt^2 + \tilde{f} d\mathbf{x}^2 \right) + \frac{R^2}{\varrho^2} \frac{1 - \chi^2 + \varrho^2 (\partial_\varrho \chi)^2}{1 - \chi^2} d\varrho^2 + R^2 (1 - \chi^2) d\Omega_3^2. \quad (4.54)$$

For zero gauge fields, which is a consistent solution, the WZ term (2.65) is zero and the DBI action (2.52) reduces to

$$S_{\text{DBI}} = -\frac{T_{D7}}{4} \int d^8 \xi \varrho^3 f \tilde{f} (1 - \chi^2) \sqrt{1 - \chi^2 + \varrho^2 (\partial_\varrho \chi)^2}. \quad (4.55)$$

Using the Euler-Lagrange equation, we obtain the equation of motion for the embedding function  $\chi$ ,<sup>1</sup>

$$\partial_\rho \left[ \frac{\rho^5 f \tilde{f} (1 - \chi^2) \partial_\rho \chi}{\sqrt{1 - \chi^2 + \rho^2 (\partial_\rho \chi)^2}} \right] + \frac{\rho^3 f \tilde{f} \chi (3(1 - \chi^2) + 2\rho^2 (\partial_\rho \chi)^2)}{\sqrt{1 - \chi^2 + \rho^2 (\partial_\rho \chi)^2}} = 0, \quad (4.56)$$

which implies the asymptotic behavior of the embedding function  $\chi$  near the boundary is

$$\chi = \frac{m}{\rho} + \frac{\tilde{c}}{\rho^3} + \dots. \quad (4.57)$$

According to the AdS/CFT dictionary, the parameters  $m$  and  $\tilde{c}$  are related to the quark mass  $M_q$  and the chiral condensate  $\langle \mathcal{O}_{M_q} \rangle$  as in the zero temperature case (see (3.35) and (3.37)). The relations are now given by

$$m = \frac{L(\varrho \rightarrow \infty)}{\varrho_h} = \frac{2M_q}{\sqrt{\lambda T}} \quad \text{and} \quad \tilde{c} = \frac{c}{\varrho_h^3} = -\frac{8\langle \mathcal{O}_{M_q} \rangle}{\sqrt{\lambda} N_f N_c T^3}. \quad (4.58)$$

For Minkowski embeddings, the equation of motion can be recast in terms of the coordinates  $\{L, r\}$ ,

$$\partial_{\tilde{r}} \left[ \left( 1 - \frac{1}{(\tilde{r}^2 + \tilde{L}^2)^4} \right) \frac{\tilde{r}^3 \partial_{\tilde{r}} \tilde{L}}{\sqrt{1 + (\partial_{\tilde{r}} \tilde{L})^2}} \right] - 8 \frac{\tilde{r}^3 \tilde{L} \sqrt{1 + (\partial_{\tilde{r}} \tilde{L})^2}}{(\tilde{r}^2 + \tilde{L}^2)^5} = 0, \quad (4.59)$$

where we use the dimensionless coordinates  $\tilde{r} = r/\varrho_H$  and  $\tilde{L} = L/\varrho_H$ . The asymptotic behavior of the embedding function  $L$  is given by

$$\tilde{L} = m + \frac{\tilde{c}}{\tilde{r}^2} + \dots. \quad (4.60)$$

<sup>1</sup>From now on, it is convenient to use the dimensionless coordinate  $\rho = \varrho/\varrho_H$ .

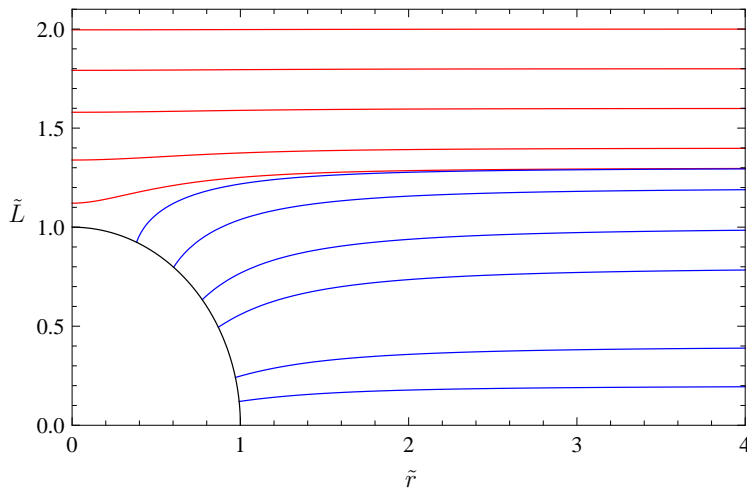


**Figure 4.2:** Embedding function  $\tilde{L}$  versus the radial AdS coordinate  $\tilde{r}$ : (blue) black hole embeddings where the D7-branes fall into the horizon of the black hole. The different curves correspond to the mass parameters  $m = 0.2, 0.4, 0.8, 1, 1.2$  and  $1.3$ . (red) Minkowski embeddings where the D7-branes do not fall into the horizon with  $m = 1.3, 1.4, 1.6, 1.8$  and  $2$ . The change in the topology between the black hole and Minkowski embeddings suggests that there is phase transition in the field theory.

In order to determine the embedding, we have to solve the non-linear equation of motion for the embedding function  $\chi$  and  $L$ , respectively. This is at the moment only possible numerically. We integrate the equation of motion from the interior of the AdS space to its boundary. At the interior the initial conditions may be determined by the asymptotic behavior. This yields

$$\chi(\rho = 1) = \chi_0, \quad \chi'(\rho = 1) = 0 \quad \text{and} \quad \tilde{L}(\tilde{r} = 0) = \tilde{L}_0, \quad \tilde{L}'(\tilde{r} = 0) = 0. \quad (4.61)$$

The numerical results for the embeddings are shown in figure 4.2. The parameter  $\chi_0 = \cos \theta_0$  determines the angle under which the D7-branes fall into the horizon while the parameter  $\tilde{L}_0 > 1$  regulates the distance between the horizon and the D7-branes at  $\tilde{r} = 0$ . The parameters  $\chi_0$  and  $\tilde{L}_0$  are also related to the scaled quark mass  $m$  and the scaled chiral condensate  $\tilde{c}$  (see figure 4.3 and 4.4).

As seen from figure 4.2, there are two different D7-brane embeddings. At large quark mass, the tension of the D7-branes is stronger than the attractive force of the black hole and the D7-branes do not fall into the horizon. These are the Minkowski embeddings. They are similar to the supersymmetric embeddings discussed at zero temperature. For smaller masses the D7-branes fall into the horizon. These are the black hole embeddings. From a geometrical point of view, the two classes of embeddings differ by their topology. The change in the topology suggests that there is also a phase transition in the dual field theory. Since the chiral condensate is multivalued around the critical mass  $m = 1.307$ , we expect that the phase transition is of first order. This phase transition and the critical mass will be clearly seen when we study the thermodynamic contribution of the fundamental fields later.

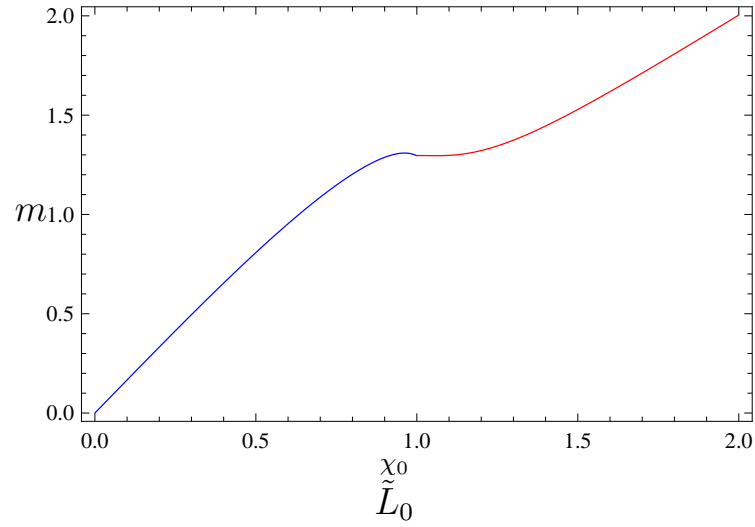


**Figure 4.3:** The dimensionless mass parameter  $m$  as defined in (4.57) and (4.60) versus the horizon value of the black hole embedding  $\chi_0 = \lim_{\rho \rightarrow 1} \chi$  between 0 and 1 and the asymptotic value of the Minkowski embeddings  $L_0 = \lim_{r \rightarrow 0} L$  between 1 and 2. The red curve corresponds to Minkowski embeddings and the blue one to black hole embeddings.

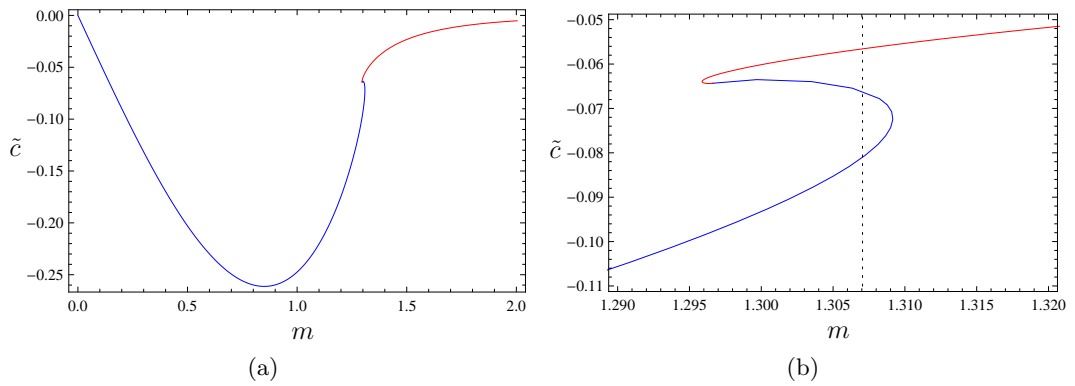


**Figure 4.4:** The dimensionless chiral condensate  $\tilde{c}$  versus the mass parameter  $m$  as defined in (4.57) and (4.60). The red curve corresponds to Minkowski embeddings and the blue one to black hole embeddings. Figure (b) shows the behavior of the chiral condensate near the phase transition marked by the dashed line at  $m \approx 1.307$ . Due to the multivalued behavior, the phase transition is of first order.

### Holographic Renormalization

In order to obtain the thermodynamic quantities, we first have to renormalize the DBI action [173] which determines the contribution of the fundamental fields. As described in section 4.2.1, we introduce a cut-off close to the boundary,  $\rho_{\max} \gg 1$ . The regularized action is then given by

$$I_{\text{DBI}}^{\text{reg}} = \mathcal{N}_\lambda \left( \frac{\rho_{\max}^4}{4} - \frac{m^2 \rho_{\max}^2}{2} + \mathcal{O}(\rho_{\max}^{-2}) \right), \quad (4.62)$$

where the normalization  $\mathcal{N}_\lambda$  is given by

$$\mathcal{N}_\lambda = \frac{T_7 V N_f \text{Vol}(S^3) \varrho_h^4}{4TV} = \frac{\lambda N_c N_f V T^3}{32}. \quad (4.63)$$

The counterterm action is now chosen such that the divergences cancel. In [173] a finite counterterm is introduced to ensure that the on-shell action vanishes for a supersymmetric embedding. The final result is

$$I_{\text{DBI}}^{\text{ct}} = -\frac{\mathcal{N}_\lambda T R^4}{\varrho_h^4} \int dt_E d^3x \sqrt{\gamma} (1 - 2\chi^2 + \chi^4) \Big|_{\rho=\rho_{\max}}, \quad (4.64)$$

where the determinant of the boundary metric  $\gamma$  at  $\rho = \rho_{\max}$  is given by

$$\sqrt{\gamma} = \frac{\varrho_h^4}{4R^4} \rho_{\max}^4 f(\rho_{\max}) \tilde{f}(\rho_{\max}). \quad (4.65)$$

Using the asymptotic behavior of the embedding function (4.57), we obtain the counterterms

$$I_{\text{DBI}}^{\text{ct}} = -\frac{\mathcal{N}_\lambda}{4} \left[ (\rho_{\max}^2 - m^2)^2 - 4mc \right]. \quad (4.66)$$

In order to obtain a finite integral over the radial coordinate  $\rho$  in the DBI action, we include the counterterms in this integral. Then the renormalized Euclidean on-shell action  $I_{\text{ren}}$  may simply be written as [49]

$$\frac{I_{\text{DBI}}^{\text{ren}}}{\mathcal{N}_\lambda} = G(m) - \frac{1}{4} \left[ (\rho_{\min}^2 - m^2)^2 - 4mc \right], \quad (4.67)$$

where  $\rho_{\min}$  determines the minimal value of the coordinate  $\rho$  on the D7-branes, i. e.  $\rho_{\min} = 1$  for black hole embeddings and  $\rho_{\min} = L_0$  for Minkowski embeddings, and

$$G(m) = \int_{\rho_{\min}}^{\infty} d\rho \left( \rho^3 f \tilde{f} (1 - \chi^2) \sqrt{1 - \chi^2 + \rho^2 (\partial_\rho \chi)^2} - (\rho^3 - \rho m^2) \right). \quad (4.68)$$

Note that the integral runs up to infinity since the integral is now finite.

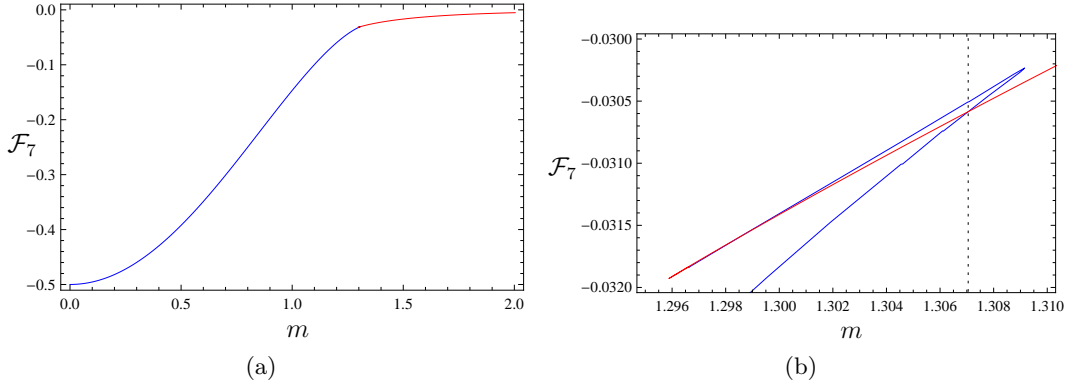


**Figure 4.5:** Free energy  $\mathcal{F}_7$  versus the scaled mass parameter  $m$  as defined in (4.58) at zero density. Figure (b) shows the behavior of the free energy near the phase transition which is located at  $m = 1.307$ . The phase transition is first order since there is a kink in the free energy at the phase transition. The red curve corresponds to Minkowski embeddings and the blue one to black hole embeddings.

## Thermodynamics

We are now prepared to study the thermodynamics of the flavor branes. The contribution of the flavor branes to free energy is given by

$$F_7(T, M_q) = T I_{\text{DBI}}^{\text{ren}} = \frac{\lambda N_c N_f V T^4}{32} \mathcal{F}_7(m), \quad (4.69)$$

with the dimensionless quantity

$$\mathcal{F}_7(m) = \frac{I_{\text{DBI}}^{\text{ren}}}{\mathcal{N}_\lambda} = G(m) - \frac{1}{4} \left[ (\rho_{\text{min}}^2 - m^2)^2 - 4mc \right]. \quad (4.70)$$

In total the free energy of the system  $F$  contains the contribution of the D3-branes  $F_3$  given in (4.43) and the contribution of the D7-branes  $F_7$  given above,

$$F(T, M_q) = F_3(T) + F_7(T, M_q) = -\frac{\pi^2}{8} N_c^2 V T^4 \left( 1 - \frac{\lambda N_f}{4\pi^2 N_c} \mathcal{F}_7(m) \right). \quad (4.71)$$

Since we work in the probe approximation  $N_f \ll N_c$ , we only consider the contribution of order  $N_f/N_c$ . The dependence of the free energy  $F$  on the temperature  $T$  is given by dimensional analysis. However, the dependence on the dimensionless ratio  $m$  of quark mass  $M_q$  to temperature  $T$  is non-trivial and determined by the dimensionless function  $\mathcal{F}_7(m)$ . If the quark mass is very large, i. e.  $m \rightarrow \infty$ , the fundamental degrees of freedom can be integrated out and only the degrees of freedom of the  $\mathcal{N} = 4$  Super-Yang-Mills theory are left. Thus, the free energy  $F$  must coincide with  $F_3$  in this limit, i. e.  $\mathcal{F}_7(m \rightarrow \infty) = 0$ . This can be analytically shown [49, sec. 4.2.2]. In addition, the limit  $m \rightarrow 0$  can also be studied analytically [49, sec. 4.2.1] which leads to  $\mathcal{F}_7(m = 0) = -1/2$ .

Figure 4.5 presents the free energy as calculated above and shows the first order phase transition. There are two branches corresponding to Minkowski and black hole embeddings, which come in from large and small  $m$ , respectively. They intersect at  $m = 1.307$  which marks the phase transition. It is first order since the free energy is not differentiable at the phase transition. Notice that the phase transition occurs in the deconfined phase of the field theory at a temperature  $T_{\text{crit}} > T_{\text{dec}}$  since the black hole background always corresponds to a deconfined theory as discussed in section 4.1.2. The other thermodynamic quantities at zero density and chemical potential may be found in [49].

### 4.3 Physics close to Equilibrium

In this section we study the response of a system due to a small perturbation about the equilibrium. Since the perturbation is small, we may consider only the linear dependence of the response on the perturbation. This framework is known as *linear response theory*.

Let us consider a perturbation sourced by the external field  $\varphi^I(x^\mu)$  which couples to the operators  $\mathcal{O}_I(x^\mu)$ <sup>2</sup>. By this fluctuation the Hamiltonian is modified by a term of the form

$$\delta H = - \int d^d x \mathcal{O}_I(x^\mu) \varphi^I(x^\mu). \quad (4.72)$$

This additional term changes the time evolution of the system. The time evolution operator is given by the time-ordered exponential

$$U(t) = T \exp \left( -i \int_{-\infty}^t dt' \delta H(t') \right), \quad (4.73)$$

which determines the evolution of the expectation value of the operators  $\mathcal{O}_I$ . Expanded to first order in the perturbation, we obtain

$$\begin{aligned} \delta \langle \mathcal{O}_I(t, \mathbf{x}) \rangle &= i \int_{-\infty}^t dt' \langle [\delta H(t'), \mathcal{O}_I(t, \mathbf{x})] \rangle + \mathcal{O}(\delta H^2) \\ &= i \int_{-\infty}^t dt' \int d^d x' \langle [\mathcal{O}_I(t, \mathbf{x}), \mathcal{O}_J(t', \mathbf{x}')] \rangle \varphi^J(t', \mathbf{x}') + \mathcal{O}(\varphi^2) \\ &= \int d^{d+1} y G_{IJ}^R(x^\mu, y^\mu) \varphi^J(y^\mu) + \mathcal{O}(\varphi^2), \end{aligned} \quad (4.74)$$

where in the last equality we used the definition of the *retarded Green's function*,

$$G_{IJ}^R(x, y) = i\theta(x^0 - y^0) \langle [\mathcal{O}_I(x), \mathcal{O}_J(y)] \rangle. \quad (4.75)$$

---

<sup>2</sup>Possible Lorentz indices are suppressed.

It is non-vanishing only in the forward light cone and, therefore, enforces causality. Due to Lorentz invariance, the retarded Green's function only depends on the difference of the two coordinates,  $x - y$ , so that the expectation value  $\delta\langle\mathcal{O}_I\rangle$  is given by a convolution. Due to the convolution theorem, the expression simplifies in Fourier space,

$$\delta\langle\mathcal{O}_I(k)\rangle = G_{IJ}^R(k)\varphi^J(k) + \mathcal{O}(\varphi^2), \quad (4.76)$$

where the Fourier transformed retarded Green's function is given by

$$G_{IJ}^R(k) = \int d^{d+1}x e^{-ikx} G_{IJ}^R(x, 0). \quad (4.77)$$

It is convenient to introduce a weight function  $\mathfrak{R}(k)$  to write the retarded Green's function as

$$G^R(\omega, \mathbf{q}) = \int \frac{d\omega'}{2\pi} \frac{\mathfrak{R}(\omega', \mathbf{q})}{\omega' - \omega + i\epsilon}, \quad (4.78)$$

where the limit  $\epsilon \rightarrow 0^+$  is implied. The weight function  $\mathfrak{R}(\omega', \mathbf{q})$  determines the density of states propagating with energy  $\omega'$ . Therefore,  $\mathfrak{R}$  is called the *spectral function* or *spectral density*. Using the Sokhatsky-Weierstrass theorem and the fact that the spectral function is hermitian, the spectral function can be computed from the retarded Green's function,

$$\mathfrak{R}(k) = i \left( G^R(k) - G^R(k)^\dagger \right). \quad (4.79)$$

The above calculation showed that the response of a system due to a perturbation sourced by  $\phi^J$  is given by the retarded Green's function  $G^R$  at least to linear order in the fluctuation. Therefore, the aim is to calculate the Green's function from the microscopic theory. For strongly coupled systems, the microscopic theory is given by its dual gravity theory, and we need a recipe to determine the retarded Green's function in terms of the gravity fields. We present this recipe in the next section. Afterwards we identify the poles of the Green's functions with the quasinormal modes of the black hole. Quasinormal modes are normalizable fluctuations which describe energy dissipation. Subsequently, we present the Green's functions, the spectral functions and quasinormal modes for the  $\mathcal{N} = 4$  Super-Yang-Mills theory and the flavor branes.

### 4.3.1 Green's Functions from Gravity

In this section we discuss how real-time Green's functions are determined from a gravity calculation at finite temperature by combining the ideas of [174–176]. A possible way is given by the Schwinger-Keldysh formalism. We now review this formalism since it is useful to determine Green's functions from gravity. In the Schwinger-Keldysh formalism, time is considered to be complex. The imaginary time handles finite temperature while the real part corresponds to the real physical time. In order to have a periodic imaginary time with period  $\beta$ , we consider a time

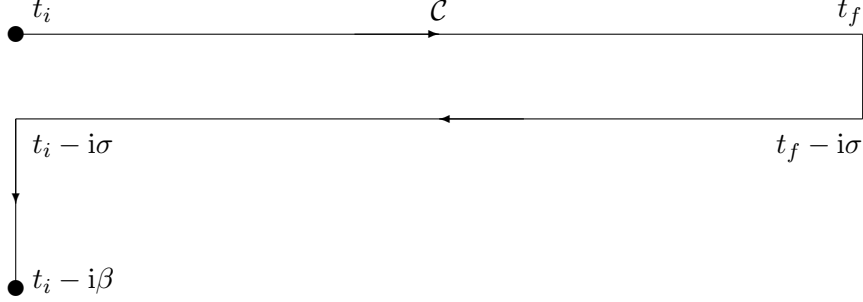


**Figure 4.6:** The Schwinger-Keldysh contour

contour  $\mathcal{C}$  drawn in figure 4.6: It goes from some initial time  $t_i$  first to the final time  $t_f$  along the real axis. Then it runs to  $t_f - i\sigma$  parallel to the imaginary axis. Afterwards it goes backwards parallel to the real axis to  $t_i - i\sigma$ . Finally, it moves again parallel to the imaginary axis to  $t_i - i\beta$ . Since the imaginary time is periodic, we identify the end of the contour with its begin.

Let us now introduce a perturbation sourced by  $\varphi^I(x^\mu)$  on the two real time parts of the contour, i. e.

$$\begin{aligned}\varphi_1^I(t, \mathbf{x}) &= \varphi^I(t, \mathbf{x}), & \mathcal{O}_I^1(t, \mathbf{x}) &= \mathcal{O}_I(t, \mathbf{x}), \\ \varphi_2^I(t, \mathbf{x}) &= \varphi^I(t - i\sigma, \mathbf{x}), & \mathcal{O}_I^2(t, \mathbf{x}) &= \mathcal{O}_I(t - i\sigma, \mathbf{x}),\end{aligned}\tag{4.80}$$

such that the generating functional is given by

$$Z[\varphi_1^I, \varphi_2^J] = \int \mathcal{D}\varphi \exp \left( iS + i \int_{t_i}^{t_f} dt \int d^d x \varphi_1^I(x) \mathcal{O}_I^1(x) - i \int_{t_i}^{t_f} dt \int d^d x \varphi_2^J(x) \mathcal{O}_J^2(x) \right).\tag{4.81}$$

The Schwinger-Keldysh propagators are now given by a second variation of  $\ln Z$  with respect to the source  $\varphi_a^I$ ,

$$G_{IJ}^{ab}(x-y) = i \frac{\delta^2 \ln Z[\varphi_1^I, \varphi_2^J]}{\delta \varphi_a^I(x) \delta \varphi_b^J(y)} = i \begin{pmatrix} \langle T \mathcal{O}_I^1(x-y) \mathcal{O}_J^1(0) \rangle & -\langle \mathcal{O}_I^2(0) \mathcal{O}_J^1(x-y) \rangle \\ -\langle \mathcal{O}_I^2(x-y) \mathcal{O}_J^1(0) \rangle & \langle \bar{T} \mathcal{O}_I^2(x-y) \mathcal{O}_J^2(0) \rangle \end{pmatrix},\tag{4.82}$$

where the time ordering is given by the contour order. Time in the upper part of the contour is normally ordered while in the lower part the order is reversed and denoted by  $\bar{T}$ . In addition, the lower part is considered to be later then the upper part.

In the momentum space, the Schwinger-Keldysh correlators  $G^{ab}$  can be related

to the retarded Green's functions  $G^R$  by

$$G^{11}(k) = \frac{1}{2} \left( G^R(k) + G^R(k)^\dagger \right) + \frac{i}{2} \coth \frac{\beta\omega}{2} \left( G^R(k) - G^R(k)^\dagger \right), \quad (4.83a)$$

$$G^{12}(k) = \frac{ie^{-(\beta-\sigma)\omega}}{1 - e^{-\beta\omega}} \left( G^R(k) - G^R(k)^\dagger \right), \quad (4.83b)$$

$$G^{21}(k) = \frac{ie^{-\sigma\omega}}{1 - e^{-\beta\omega}} \left( G^R(k) - G^R(k)^\dagger \right), \quad (4.83c)$$

$$G^{22}(k) = -\frac{1}{2} \left( G^R(k) + G^R(k)^\dagger \right) + \frac{i}{2} \coth \frac{\beta\omega}{2} \left( G^R(k) - G^R(k)^\dagger \right). \quad (4.83d)$$

For  $\sigma = \beta/2$ , the matrix  $G^{ab}$  is symmetric which makes this choice convenient.

Let us now discuss the gravity side. We consider  $N$  scalar fields  $\Phi^I$  with a general bilinear action,

$$S = \int d^d x \int dz \left[ A_{IJ}(x, z) \partial_M \Phi^I \partial^M \Phi^J + B_{IJ}^M(x, z) \Phi^I \partial_M \Phi^J + C_{IJ}(x, z) \Phi^I \Phi^J \right], \quad (4.84)$$

in an AdS Schwarzschild black hole metric,

$$ds^2 = \frac{R^2}{z^2} \left[ -f(z) dt^2 + d\mathbf{x}^2 + \frac{dz^2}{f(z)} \right] \quad \text{with } f(z) = 1 - \frac{z^4}{z_h^4}. \quad (4.85)$$

We restrict our analysis to the AdS space. Any other direction is integrated out. Inserting the Fourier transform,

$$\Phi^I(x^\mu, z) = \int \frac{d^d k}{(2\pi)^d} \Phi_k^I(z) e^{-ikx}, \quad (4.86)$$

into (4.84), leads to the action for the Fourier modes of the general form

$$S = \int \frac{d^d k}{(2\pi)^d} \int dz \left[ A_{IJ}(k, z) \Phi_{-k}^I \Phi_k^J + B_{IJ}(k, z) \Phi_{-k}^I \Phi_k^J + C_{IJ}(k, z) \Phi_{-k}^I \Phi_k^J \right], \quad (4.87)$$

where the prime denotes a derivative with respect to radial direction  $z$ . Since the matrices  $A, B, C$  are real in real space, we obtain  $A_{IJ}(-k, z) = A_{IJ}(k, z)^*$  in momentum space and equivalent relations for  $B, C$ <sup>3</sup>.

Using the Euler-Lagrange equation, the equations of motion for the Fourier modes are given by

$$-2(A_{IJ} \Phi_k^J)' + (2C_{IJ} - B_{IJ}') \Phi_k^J = 0. \quad (4.88)$$

Asymptotically near the boundary, the Fourier modes have two possible scalings  $\Phi^I(k, z) \approx \phi^I(k) z^{\Delta_-^I} + \tilde{\phi}^I(k) z^{\Delta_+^I}$  with  $\Delta_-^I \leq \Delta_+^I$ . In order to have a finite scaling

<sup>3</sup>Note that the matrices in real space,  $A(x, z), B(x, z), C(x, z)$ , and the matrices in momentum space,  $A(k, z), B(k, z), C(k, z)$ , are not related by a Fourier transformation.

near the boundary, we define  $\Phi^I(z, k) = z^{\Delta_I} \bar{\Phi}^I(z, k) = D^I_J \bar{\Phi}^J(z, k)$ . Close to the horizon, the scaling is  $\bar{\Phi}^I \propto (z_h - z)^\beta$  with  $\beta = \pm i\omega/4\pi T$ . In Minkowskian signature both signs lead to a well behaved solution in contrast to the Euclidean signature, i. e.  $\beta = \pm\omega/4\pi T$ , where only one solution is regular. It seems to be ambiguous which is the right solution in the Minkowskian signature.

This ambiguity can be clarified by studying the black hole in more detail. First we transform the radial coordinate  $(z/z_h)^2 = 2M/\rho$  with  $M = 1/8\pi T$  which leads to the metric

$$\begin{aligned} ds^2 &= \frac{(R\pi T)^2 \rho}{2M} \left[ -f dt^2 + d\mathbf{x}^2 + \left(\frac{2M}{\rho}\right)^3 \frac{4d\rho^2}{f} \right] \quad \text{with } f = 1 - \left(\frac{2M}{\rho}\right)^2 \\ &\stackrel{\rho \approx 2M}{\approx} 2(R\pi T)^2 \left[ -\left(1 - \frac{2M}{\rho}\right) dt^2 + d\mathbf{x}^2 + \left(1 - \frac{2M}{\rho}\right)^{-1} d\rho^2 \right], \end{aligned} \quad (4.89)$$

where in the second line we found the Schwarzschild metric in the near horizon limit. The transformation to the Kruskal coordinates  $U$  and  $V$  is the same as for Schwarzschild black holes,

$$\begin{aligned} U &= -4Me^{-\frac{t-r_*}{4M}} \\ V &= 4Me^{\frac{t+r_*}{4M}} \end{aligned} \quad \text{with } r_* = \rho + 2M \ln \left| \frac{\rho}{2M} - 1 \right|. \quad (4.90)$$

The Kruskal time is defined as  $t_K = U + V$  while the radial coordinate is  $x_K = V - U$ . The Penrose diagram is given in figure 4.7. There are four regions:

**R** with  $U < 0$  and  $V > 0$  in which we worked in the analysis above,

**L** with  $U > 0$  and  $V < 0$  which will be important in the following,

**F** contains the future singularity,

**P** contains the past singularity.

In the quadrants L and R we find a set of mode functions which solve the equations of motion,

$$(u_{k,R,\pm})^I_J = \begin{cases} e^{ikx} (f_{\pm k}(r_*))^I_J & \text{in R} \\ 0 & \text{in L} \end{cases} \quad (u_{k,L,\pm})^I_J = \begin{cases} 0 & \text{in R} \\ e^{ikx} (f_{\pm k}(r_*))^I_J & \text{in L} \end{cases}, \quad (4.91)$$

where near the horizon each element of the matrix  $f_k$  behaves like  $e^{i\omega r_*}$ ,  $(f_k)^I_J = (f_{-k}^*)^I_J$  since  $\Phi^I$  are real scalars and  $\omega = k^0 > 0$ . We may also expand these modes in the Kruskal coordinates. We find that the elements of the matrices  $u_{k,R,+}$  and  $u_{k,L,+}$  are functions of  $U$  while the elements of  $u_{k,R,-}$  and  $u_{k,L,-}$  are functions of  $V$ . The modes depending on  $U$  are outgoing in the R quadrant while the modes depending on  $V$  are ingoing. In the L quadrant the notation is switched.

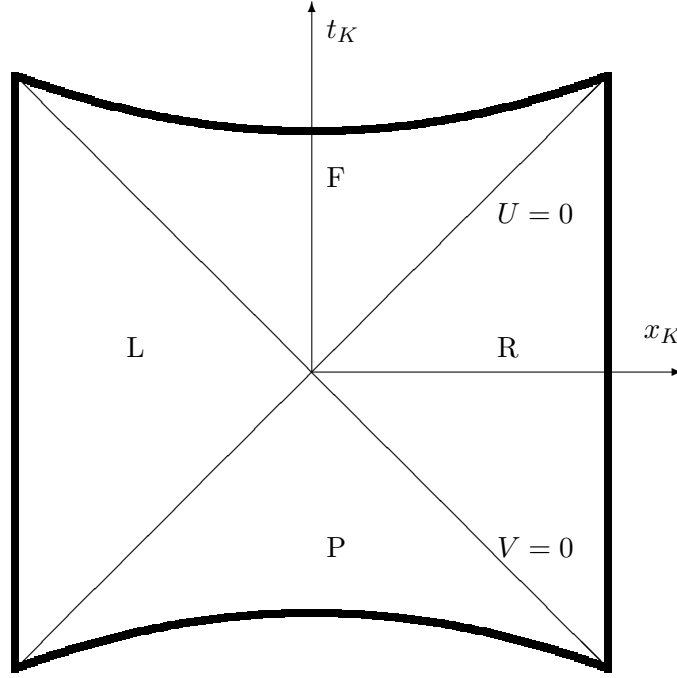


**Figure 4.7:** The Penrose diagram of an AdS black hole

These modes contain positive and negative frequency parts. In order to separate the different frequency modes, we consider the linear combinations that mix the modes on the two quadrants,

$$u_{1,k} = u_{k,R,+} + e^{-\frac{\omega}{2T}} u_{k,L,+}, \quad (4.92a)$$

$$u_{2,k} = u_{k,R,+} + e^{\frac{\omega}{2T}} u_{k,L,+}, \quad (4.92b)$$

$$u_{3,k} = u_{k,R,-} + e^{\frac{\omega}{2T}} u_{k,L,-}, \quad (4.92c)$$

$$u_{4,k} = u_{k,R,-} + e^{-\frac{\omega}{2T}} u_{k,L,-}. \quad (4.92d)$$

$$(4.92e)$$

Let us simplify the mode  $u_{1,k}$  close to the horizon,

$$\begin{aligned} u_{1,k} &\approx \left( e^{-(t-r_*)} \right)_R^{i\omega} + e^{-\frac{\omega}{2T}} \left( e^{-(t-r_*)} \right)_L^{i\omega} \\ &= (2\pi T U e^{i\pi})^{\frac{i\omega}{2\pi T}} + e^{-\frac{\omega}{2T}} (2\pi T U)^{\frac{i\omega}{2\pi T}} \\ &= 2e^{-\frac{\omega}{2T}} (2\pi T)^{\frac{i\omega}{2\pi T}} U^{\frac{i\omega}{2\pi T}} \\ &\propto U^{\frac{i\omega}{2\pi T}}, \end{aligned} \quad (4.93)$$

where we used that  $U < 0$  in R and  $U > 0$  in L. Similarly we find  $u_{4,k} \propto V^{-i\omega/2\pi T}$ . To ensure that these functions are continuous across the horizon, a branch cut must

be placed in the upper halves of the complex  $U$  and  $V$  planes. Thus, these modes are analytic in the lower halves of the complex  $U$  and  $V$  planes and carry positive frequencies. Similarly we may find  $u_{2,k} \propto (U^*)^{i\omega/2\pi T}$  and  $u_{3,k} \propto (V^*)^{-i\omega/2\pi T}$  which are analytic in the upper halves of the complex  $U$  and  $V$  planes. Thus, they carry the negative frequencies. To summarize, we find

$$\begin{aligned} u_{1,k} &: \text{outgoing, positive frequency,} \\ u_{2,k} &: \text{outgoing, negative frequency,} \\ u_{3,k} &: \text{ingoing, negative frequency,} \\ u_{4,k} &: \text{ingoing, positive frequency.} \end{aligned}$$

Now we make contact to the Schwinger-Keldysh formalism discussed above. According to the AdS/CFT dictionary, the two sources  $\phi_{1,2}^I$  are the values of the field at the boundary. Since the Penrose diagram has two boundaries we assume that our field  $\Phi^I$  approaches  $\phi_1^I$  on the boundary of the quadrant R while  $\phi_2^I$  on the boundary of the quadrant L. The general solution can be written as a linear combination of the four modes defined in (4.92). In order to eliminate two of them, we have to specify boundary conditions at the horizon. In order to ensure causality, positive frequency modes should be ingoing at the horizon in the R quadrant, while negative frequency modes should be outgoing at the horizon in the R quadrant. These conditions select out  $u_2$  and  $u_4$  as the only modes, so

$$\bar{\Phi}^I(x, r_*) = \sum_k (u_{2,k})^I{}_J \alpha_k^J + (u_{4,k})^I{}_J \beta_k^J. \quad (4.94)$$

Choosing the matrix  $f_k$  to be normalized  $(f_{\pm k})^I{}_J(r_{*\text{bdy}}) = \delta^I{}_J$ , the boundary conditions become

$$\begin{aligned} \phi_1^I(k) &= \alpha_k^I + \beta_k^I, \\ \phi_2^I(k) &= e^{\frac{\omega}{2T}} \alpha_k^I + e^{-\frac{\omega}{2T}} \beta_k^I, \end{aligned} \quad (4.95)$$

and lead to

$$\begin{aligned} \bar{\Phi}^I(k, r_*)|_R &= ((n+1)(f_k^*)^I{}_J - n(f_k)^I{}_J) \phi_1^J(k) \\ &\quad + \sqrt{n(n+1)}((f_k)^I{}_J - (f_k^*)^I{}_J) \phi_2^J(k) \\ \bar{\Phi}^I(k, r_*)|_L &= \sqrt{n(n+1)}((f_k^*)^I{}_J - (f_k)^I{}_J) \phi_1^J(k) \\ &\quad + ((n+1)(f_k)^I{}_J - n(f_k^*)^I{}_J) \phi_2^J(k), \end{aligned} \quad (4.96)$$

where  $n = (e^{\omega/T} - 1)^{-1}$ .

According to the AdS/CFT dictionary, the Green's functions are determined by the on-shell action. Since we exclusively consider  $\omega > 0$  in the discussion above, we have to restrict the integration in the action to  $\omega > 0$  in order to avoid double

counting, this leads to

$$S = \frac{1}{(2\pi)^d} \int_0^\infty d\omega \int_{\mathbb{R}^{d-1}} d^{d-1}\mathbf{k} \int dz [2\bar{A}_{IJ}^H \bar{\Phi}'_{-k} \bar{\Phi}'_k^J + \bar{B}_{IJ} \bar{\Phi}'_{-k} \bar{\Phi}'_k^J + \bar{B}_{IJ}^\dagger \bar{\Phi}'_{-k} \bar{\Phi}'_k^J + 2C_{IJ}^H \bar{\Phi}'_{-k} \bar{\Phi}'_k^J], \quad (4.97)$$

where now

$$\begin{aligned} \bar{A}^H &= \frac{1}{2} D^\dagger (A + A^\dagger) D, \\ \bar{B} &= D^\dagger B D + 2D'^\dagger A^H D, \\ \bar{C}^H &= \frac{1}{2} D^\dagger (C + C^\dagger) D + D'^\dagger A^H D' + \frac{1}{2} D^\dagger B D' + \frac{1}{2} D'^\dagger B^\dagger D. \end{aligned} \quad (4.98)$$

Using the equations of motion

$$-2(\bar{A}_{IJ}^H \bar{\Phi}'_k^J)' + (\bar{B} - \bar{B}^\dagger)_{IJ} \bar{\Phi}'_k^J + (2C^H - B'^\dagger)_{IJ} \bar{\Phi}'_k^J = 0, \quad (4.99)$$

we obtain the on-shell action<sup>4</sup>

$$S_{\text{on-shell}} = \frac{1}{(2\pi)^d} \int_0^\infty d\omega \int_{\mathbb{R}^{d-1}} d\mathbf{k} \left[ 2\bar{A}_{IJ}^H \bar{\Phi}'_k^J \bar{\Phi}'_{-k}^I + \bar{B}_{IJ}^\dagger \bar{\Phi}'_{-k} \bar{\Phi}'_k^J \right]. \quad (4.100)$$

Defining the retarded and advanced Green's function  $G^R$  and  $G^A$  as

$$\begin{aligned} G^R(k) &= -(2F^\dagger A^H F' + F^\dagger B^\dagger F)_{z=0}, \\ G^A(k) &= -(2F' A^H F^\dagger + F^\dagger B F)_{z=0} = G^R(k)^\dagger, \end{aligned} \quad (4.101)$$

with  $F = f_k^*$ , we obtain

$$\begin{aligned} S_{\text{on-shell}} &= -\frac{1}{2} \int \frac{d^d k}{(2\pi)^d} \left[ \phi_1^I(-k) ((1+n)G_{IJ}^R(k) - nG_{IJ}^A(k)) \phi_1^J(k) \right. \\ &\quad - \phi_2^I(-k) ((1+n)G_{IJ}^A(k) - nG_{IJ}^R(k)) \phi_2^J(k) \\ &\quad + \phi_1^I(-k) \sqrt{n(n+1)} (G_{IJ}^A(k) - G_{IJ}^R(k)) \phi_2^J(k) \\ &\quad \left. + \phi_2^I(-k) \sqrt{n(n+1)} (G_{IJ}^A(k) - G_{IJ}^R(k)) \phi_1^J(k) \right], \end{aligned} \quad (4.102)$$

which leads to the same correlation function as in the field theory calculation (4.83) if  $\sigma = \beta/2$  and confirms our definition of the Green's functions above.

---

<sup>4</sup>In general, the on-shell action is divergent and must be regularized by counterterms as described in 4.2.1.

### Adapting the prescription to numerical solutions

Except for some simple cases, we can only solve the equations of motion for the perturbations numerically. In the following we discuss a prescription to calculate the retarded Green's functions numerically. First we generate  $2N$  solutions of the equations of motion which we now collect in the matrix  $H^I_J(k, z)$  similar to  $(u_{k,R,\pm})^I_J$ . In order to calculate the retarded Green's functions, we need to find the solutions  $u_{4,k} \propto f_k^*$  which are ingoing at the horizon and have positive frequencies,

$$H^I_J(k, z) = (z - z_h)^{-\frac{i\omega}{4\pi T}} \left( e^I_{(J)} + \mathcal{O}(z - z_h) \right), \quad (4.103)$$

where  $e_{(J)}$  are  $N$  linear independent vectors. The other  $N$  possible solutions are discarded since we enforce the ingoing boundary condition. Now the matrix  $F$  which is normalized at the boundary is simply given by  $F(k, z) = H(k, z)H(k, z_{\text{bdy}})^{-1}$  and the retarded Green's functions are given by

$$G^R(k) = - \lim_{z_{\text{bdy}} \rightarrow 0} [2A^H(k, z_{\text{bdy}})H'(k, z_{\text{bdy}})H(k, z_{\text{bdy}})^{-1} + B^\dagger(k, z_{\text{bdy}})]. \quad (4.104)$$

The Green's functions are ill-defined if  $H(k, z_{\text{bdy}})$  is not invertible. The poles of the Green's functions are determined by  $\det[H(k, z_{\text{bdy}})] = 0$  which defines the quasinormal modes of the black hole.

### Quasinormal Modes

Quasinormal modes of black holes are distinct perturbations of black hole solutions. Roughly they can be understood as resonances of the black hole. However, since the energy of the perturbation can leak into the black hole, these fluctuations are not normal modes and, thus, have been dubbed quasinormal. Their corresponding frequencies consist of a real and an imaginary part. As for the damped oscillator, the real part of the frequency essentially determines the energy of the fluctuations, while the imaginary part is responsible for the damping.

In AdS spacetimes the quasinormal modes satisfy the following boundary conditions. At the horizon they are purely ingoing, whereas at the conformal AdS boundary they have an asymptotic behavior that corresponds to a normalizable mode. Thus, they are determined by  $\det[H(k, z_{\text{bdy}})] = 0$ . As we have observed above, the quasinormal frequencies of the dual gravity theory can be identified with the poles of correlation functions in dual thermal gauge theories [177–179].

By the Cauchy integration formula in the complex frequency plane, the Green's function can be written as a sum over the contributions of the different quasinormal modes (see e. g. [180]). Writing the time dependence as  $\exp(-i\omega t)$ , we note that a relaxation towards equilibrium can only happen if all the quasinormal modes lie in the lower half of the complex plane. Following [180, 181] the response caused by an external perturbation  $\varphi(\omega, k)$  can, therefore, be written as a sum over quasinormal frequencies

$$\langle \mathcal{O}(t, k) \rangle = i\theta(t) \sum_n R_n \varphi(\omega_n, k) e^{-i\Omega_n t - \Gamma_n t}, \quad (4.105)$$

where the quasinormal frequencies are  $\omega_n = \Omega_n - i\Gamma_n$  and their residues are  $R_n$ . If the quasinormal frequency comes to lie in the upper half plane, it results in an exponentially growing mode and, therefore, represents an instability of the system.

Since we now have a recipe to calculate Green's functions from gravity, we can discuss the Green's function and the quasinormal mode spectrum of the so far discussed gravity duals, the  $\mathcal{N} = 4$  Super-Yang-Mills theory and the flavor branes, as examples of strongly coupled field theories.

### 4.3.2 Green's Functions of $\mathcal{N} = 4$ Super-Yang-Mills theory

In the  $\mathcal{N} = 4$  Super-Yang-Mills theory, there are two kinds of retarded Green's functions, the R-current correlations  $\langle [J_a^\mu, J_b^\nu] \rangle$  and the energy-momentum tensor correlations  $\langle [T_{\mu\nu}, T_{\lambda\rho}] \rangle$  (see e.g. [179, 182, 183]). The energy-momentum tensor correlations may be computed on the gravity side by considering metric fluctuations about the black brane metric (4.35). We study these correlation in section 4.4.4 where we determine the transport properties of the  $\mathcal{N} = 4$  Super-Yang-Mills theory. For the R-current correlations, we need to consider fluctuations of the gauge field which emerge by gauging the  $SO(6)$  symmetry on the gravity side (see section 3.2).

#### Green's function for the R-current

We now discuss the retarded Green's function of the R-current  $J_a^\mu$ ,

$$G_{a,b}^{\mu,\nu}(k) = -i \int d^4x e^{-ikx} \theta(t) \langle [J_a^\mu(x), J_b^\nu(0)] \rangle. \quad (4.106)$$

In a rotationally invariant theory<sup>5</sup>, the Green's function can be decomposed into transverse and longitudinal parts [179],

$$G_{a,b}^{\mu,\nu}(k) = P_T^{\mu\nu} \Pi_{ab}^T(k) + P_L^{\mu\nu} \Pi_{ab}^L(k). \quad (4.107)$$

Defining  $k_\mu = (\omega, q, 0, 0)$ , we obtain  $G_{a,b}^{ii} = \Pi_{ab}^T$  where  $i$  labels the spatial directions perpendicular to the momentum while the other components are given by the longitudinal part,

$$G_{a,b}^{t,t} = -\frac{q^2}{q^2 - \omega^2} \Pi_{ab}^L, \quad (4.108a)$$

$$G_{a,b}^{t,x} = -\frac{\omega q}{q^2 - \omega^2} \Pi_{ab}^L \quad (4.108b)$$

$$G_{a,b}^{x,x} = -\frac{\omega^2}{q^2 - \omega^2} \Pi_{ab}^L. \quad (4.108c)$$

In the limit  $q \rightarrow 0$ , rotational invariance implies that the two scalar functions coincide,  $\Pi^L = \Pi^T = \Pi$ . The scalar functions  $\Pi^{L,T}$  depend explicitly on the system

<sup>5</sup>The Lorentz symmetry  $SO(3,1)$  is broken to the rotational group  $SO(3)$  by finite temperature.

and have to be determined from the microscopic theory, e. g. the gravity dual of the  $\mathcal{N} = 4$  Super-Yang-Mills theory.

In order to explicitly determine the R-current correlations from a gravity calculation we start with the five-dimensional Yang-Mills action in the black D3-brane metric (4.35),

$$S_{\text{YM}} = -\frac{1}{4g_{\text{YM}}^2} \int d^5x \sqrt{-g} F_{MN}^a F^{aMN}, \quad (4.109)$$

where  $g_{\text{YM}}^2 = 16\pi^2 R/N_c^2$  for the  $\mathcal{N} = 4$  Super-Yang-Mills theory and  $F_{MN}^a = \partial_M A_N^a - \partial_N A_M^a + f^{abc} A_M^b A_N^c$ .  $f^{abc}$  are the structure constants of the Lie algebra  $su(4)$ .

Since we would like to calculate two point functions, it is sufficient to consider linearized perturbations about the background. There is no gauge field in the background. Thus, the gauge field are exclusively given by the perturbation which we label by  $a_M^a$  and the action to second order in the perturbation becomes

$$S_{\text{YM}} = -\frac{1}{4g_{\text{YM}}^2} \int d^5x \sqrt{-g} f_{MN}^a f^{aMN}, \quad (4.110)$$

where  $f_{MN}^a = \partial_M a_N^a - \partial_N a_M^a$ . Since there is no interaction between the fields with different gauge indices, the Green's function will be diagonal in the gauge indices and we will suppress these indices in the following.

In order to get rid of the unphysical degrees of freedom, we have to find the gauge invariant fields. The gauge fields  $A_M^a$  are in the adjoint representation of the  $SU(4)_R$  R-symmetry and transform under  $SU(4)_R$  as

$$\delta_\Lambda A_M^a = \nabla_M \Lambda^a + f^{abc} A_M^b \Lambda^c. \quad (4.111)$$

We work in the gauge where the radial component of the gauge field is zero,  $A_z^a = 0$ . However, this leaves some residual gauge transformations which we also have to fix. We may split the gauge transformations into gauge transformation for the background fields and for the perturbations. The gauge transformations for the background is trivial since there is no background field. For the perturbations we obtain the gauge transformations  $\delta_\lambda a_M = \nabla_M \lambda$  where  $\lambda$  is the gauge transformation linear in the perturbation. Choosing the gauge  $a_z = 0$  leaves the residual gauge transformations  $\lambda(x^\mu)$ . Using the Fourier decomposition

$$\begin{aligned} a_\mu(x^\mu, z) &= \int \frac{d^4k}{(2\pi)^4} e^{ikx} a_\mu(k, z), \\ \lambda(x^\mu, z) &= \int \frac{d^4k}{(2\pi)^4} e^{ikx} \lambda(k, z), \end{aligned} \quad (4.112)$$

where  $k = (\omega, q, 0, 0)$  we can write the residual gauge transformations as

$$\delta_\lambda a_t = -i\omega\lambda, \quad (4.113a)$$

$$\delta_\lambda a_x = iq\lambda, \quad (4.113b)$$

$$\delta_\lambda a_i = 0, \quad (4.113c)$$

Therefore, the gauge invariant fields are  $E_L = qa_t + \omega a_x$  and  $E_T = \omega a_i$  where  $E_L \propto f_{xt}$  ( $E_T \propto f_{it}$ ) can be seen to be the longitudinal (transversal) electric field. This is the expected result since the residual gauge transformation for the fluctuations  $\delta_\lambda a_M = \nabla_M \lambda$  is the same as for an  $U(1)$  field and the electric field is gauge invariant.

By transforming the radial coordinate  $\bar{x} = 1 - z^2/z_h^2$  [184], the equations of motion for the fluctuations become

$$\begin{aligned} 0 &= E_T'' + \frac{f'}{f} E_T' + \frac{\mathfrak{w}^2 - \mathfrak{q}^2}{(1 - \bar{x}f^2)} E_T, \\ 0 &= E_L'' + \frac{\mathfrak{w}^2 f'}{f(\mathfrak{w}^2 - \mathfrak{q}^2 f)} E_L' + \frac{\mathfrak{w}^2 - \mathfrak{q}^2 f}{(1 - \bar{x})f^2} E_L, \end{aligned} \quad (4.114)$$

where the prime denotes a derivative with respect to  $\bar{x}$  and  $\mathfrak{w} = \omega/2\pi T$ ,  $\mathfrak{q} = q/2\pi T$ . For  $q = 0$  the two equations coincide and can be solved analytically [184]. Enforcing the ingoing boundary condition at the horizon  $\bar{x} = 0$ , the solution is given by

$$E = \bar{x}^{-\frac{i\mathfrak{w}}{2}} (2 - \bar{x})^{-\frac{\mathfrak{w}}{2}} (1 - \bar{x})^{\frac{(1+i)\mathfrak{w}}{2}} {}_2F_1 \left( 1 - \frac{(1+i)\mathfrak{w}}{2}, -\frac{(1+i)\mathfrak{w}}{2}; 1 - i\mathfrak{w}; \frac{\bar{x}}{2(\bar{x}-1)} \right), \quad (4.115)$$

where  ${}_2F_1$  is the Gauss hypergeometric function. Using the recipe (4.104), the Green's function is given by

$$\begin{aligned} \Pi(\omega) &= - \left. \frac{\sqrt{-g} g^{zz} g^{ii} \partial_z a}{g_{\text{YM}}^2 a} \right|_{z \rightarrow 0} = \frac{N_c^2 T^2}{8} \lim_{\bar{x} \rightarrow 1} \frac{E'}{E} \\ &= \frac{N_c^2 T^2}{8} \left\{ i\mathfrak{w} + \mathfrak{w}^2 \left[ \psi \left( \frac{(1-i)\mathfrak{w}}{2} \right) + \psi \left( -\frac{(1+i)\mathfrak{w}}{2} \right) \right] \right\}, \end{aligned} \quad (4.116)$$

where  $\psi(z) = \Gamma'(z)/\Gamma(z)$  is the logarithmic derivative of the gamma function  $\Gamma(z)$ .  $\psi(z)$  has poles at  $z = -n$  for  $n \in \mathbb{N}$  which determines the poles of the Green's function to be

$$\mathfrak{w} = n(\pm 1 - i) \quad n \in \mathbb{N}. \quad (4.117)$$

The position of the poles coincides with the quasinormal spectrum of the fluctuations  $E(\bar{x})$  given by the boundary condition  $E(\bar{x} = 1) = 0$ .

Using (4.79) we can determine the spectral function for the R-current [184]

$$\begin{aligned} \mathfrak{R}(\omega) &= -\frac{N_c^2 T^2}{4} \text{Im} \left\{ i\mathfrak{w} + \mathfrak{w}^2 \left[ \psi \left( \frac{(1-i)\mathfrak{w}}{2} \right) + \psi \left( -\frac{(1+i)\mathfrak{w}}{2} \right) \right] \right\} \\ &= -\frac{N_c^2 T^2}{4} \text{Im} \left\{ i\mathfrak{w} + \mathfrak{w}^2 \left[ \psi \left( \frac{(1-i)\mathfrak{w}}{2} \right) - \psi \left( -\frac{(1-i)\mathfrak{w}}{2} \right) \right] \right\} \\ &= \frac{N_c^2 T^2}{4} \frac{\pi \mathfrak{w}^2 \sinh \pi \mathfrak{w}}{\cosh \pi \mathfrak{w} - \cos \pi \mathfrak{w}}, \end{aligned} \quad (4.118)$$

where we used the identities  $\psi(z^*) = \psi(z)^*$  and  $\psi(z) - \psi(-z) = -\pi \cot \pi z - 1/z$ . This analytic results allows to examine various features of the spectral function. For

instance its asymptotics for large and small frequencies can be computed,

$$\Re(\omega) = \frac{\pi N_c^2 T^2 \mathfrak{w}^2}{4} (1 + 2e^{-\pi \mathfrak{w}} \cos \pi \mathfrak{w} + \dots), \quad \mathfrak{w} \rightarrow \infty, \quad (4.119a)$$

$$\Re(\omega) = \frac{\pi N_c^2 T^2 \mathfrak{w}}{4} \left( 1 + \frac{\pi^2 \mathfrak{w}^2}{6} + \dots \right), \quad \mathfrak{w} \rightarrow 0. \quad (4.119b)$$

From the large frequency asymptotic  $\omega \gg T$ , we can read off the zero-temperature result for the spectral function,

$$\Re^{T=0}(\omega) = \frac{N_c^2 \omega^2}{16\pi}. \quad (4.120)$$

Since the theory is conformal at zero temperature, we obtain the conformal result that the spectral function is proportional to  $\omega^{2\Delta-d} = \omega^2$  since the scaling dimension of the R-current is three,  $\Delta = 3$ , in four dimensions,  $d = 4$ . The factor  $N_c^2$  measures the degrees of freedom charged under the R-charge and appears since the R-current is in the adjoint of the gauge group  $SU(N_c)$ . We study the R-current correlations at finite momentum further in section 4.4.4 where we discuss hydrodynamics of the  $\mathcal{N} = 4$  Super-Yang-Mills theory.

### 4.3.3 Green's Functions from Flavor Branes

In this section we discuss the Green's functions of the  $\mathcal{N} = 4$  Super-Yang-Mills theory coupled two  $N_f$  fundamental hypermultiplets given by the flavor branes embedded into the AdS space. For the configuration of a D7-brane probe added to the AdS Schwarzschild black hole background, a first order phase transition occurs between D7-brane probes either staying outside of the horizon or reaching down to it as discussed in section 4.2.3. These two types of embeddings are named Minkowski or black hole embeddings, respectively.

As discussed in [50], the first case corresponds to stable mesons, whereas in the second case the mesons are unstable. For stable mesons, the spectrum has been determined analytically at zero temperature in section 5.2.2. In the second case, the meson excitations may be identified with quasinormal modes and their finite width is related to an ingoing energy boundary condition at the black hole horizon. The spectral functions for this configuration were first studied in [184]. If the temperature is high compared to the quark mass, the quasinormal frequencies lie deep inside the lower complex half plane, and the spectral function is smooth and without noticeable peaks. As the temperature is lowered the quasinormal modes move towards the real axis, producing rather well defined quasiparticle peaks in the spectral function.

In this section I present my own work [3] where we extend the results of the references mentioned before. We determine the first and second quasinormal mode of the fluctuations of the brane. For this purpose we consider the coordinates used in (4.35). Note that here we set the horizon radius  $z_h = 1$ . Frequencies and momenta measured in this metric are related to physical frequencies and momenta by

$(\omega_{ph}, q_{ph}) = \pi T(\omega, q)$ , where  $T$  is the temperature since we explicitly set  $z_h = 1$ . This set of coordinates maps the compact interval  $[0, 1]$  to the distance between the conformal boundary and the black hole horizon. Such a compact radial coordinate is particularly well suited for the calculation of quasinormal modes using the relaxation method as explained in appendix C.4.

In order to determine the DBI action (2.50), we need to calculate the induced metric which is given by

$$\frac{ds_{D7}^2}{R^2} = -\frac{f(z)}{z^2} dt^2 + \left( \frac{1}{z^2 f(z)} - \theta'(z) \right) dz^2 + \frac{1}{z^2} d\mathbf{x}^2 + \sin^2 \theta(z) d\Omega_3^2. \quad (4.121)$$

$\theta(z)$  describes the D7-brane embedding in the AdS-Schwarzschild background and the embedding coordinates are  $\xi^\alpha = (t, \mathbf{x}, z, \alpha_1, \alpha_2, \alpha_3)$  where  $\alpha_i$  are the three angles on the  $S^3$ . To second order in the field strength, the D7-brane Lagrangian can be written in the following way

$$\mathcal{L} = \sqrt{-P[G]} \left[ 1 - \pi^2 \alpha'^2 f_{ab} f^{ab} \right], \quad (4.122)$$

similar to the calculation in the supersymmetric setup (3.44). We again suppress the flavor indices since the different flavors do not interact with each other. From the zero order term, we obtain the background equation of motion

$$\begin{aligned} 0 = & 3 \cos \theta(z) [-1 + z^2 (-1 + z^4) \theta'(z)^2] \\ & - z \sin \theta(z) [(3 + z^4) \theta'(z) + 2z^2 (1 - z^4) (2 - z^4) \theta'(z)^3 - z(-1 + z^4) \theta''(z)]. \end{aligned} \quad (4.123)$$

The brane embedding can be found by integrating this equation from the horizon out to the boundary. As initial conditions one chooses  $\chi_0 = \cos(\theta(1))$  and demands regularity on the horizon. The background field is discussed in section 4.2.3 where  $\chi = \cos(\theta)$ .

We have plotted the mass parameter  $m$  as a function of  $\chi_0 = \cos(\theta(\varrho_h))$  in figure 4.3. The mass is not a single valued function of  $\chi_0$ . Although  $m$  is the physical parameter of the brane embedding, we prefer to quote  $\chi_0$  values instead of  $m$  since much of our investigations will take place in the regime where  $m$  ceases to be single valued. The change in the sign of  $\partial m / \partial \chi_0$  is also suggestive of an instability. Indeed the maximum of  $m = 1.31$  is reached at  $\chi_0 = 0.962$ , which is precisely the value from where an unstable mode appears in the scalar sector of the quasinormal mode spectrum which we will see below.

The second order term produces the Maxwell equation,

$$\partial_\alpha (\sqrt{-P[G]} f^{\alpha\beta}) = 0, \quad (4.124)$$

where  $f_{\alpha\beta} = \partial_\alpha a_\beta - \partial_\beta a_\alpha$ . In order to simplify the calculation, we assume that the fluctuations do not depend on the angles of the  $S^3$ . As in the discussion of the R-current (see 4.3.2), we choose the gauge  $a_z = 0$  and expand  $a_\alpha$  in plane wave modes.

Moreover, if we write the equations in a gauge invariant way using the electric fields in longitudinal  $E_L = q_{ph}a_t + \omega_{ph}a_x$  and transverse direction  $E_T = \omega_{ph}a_T$ , the equations of motion are

$$0 = E_L''(z) + \left[ C(z) + \frac{f'(z)\omega^2}{f(z)(\omega^2 - f(z)q^2)} \right] E_L'(z) + B(z)(\omega^2 - f(z)q^2)E_L(z), \quad (4.125a)$$

$$0 = E_T''(z) + \left[ C(z) + \frac{f'(z)}{f(z)} \right] E_T'(z) + B(z)(\omega^2 - f(z)q^2)E_T(z), \quad (4.125b)$$

with

$$B(z) = \frac{1}{f^2(z)} + \frac{z^2\Theta'(z)^2}{f(z)}, \quad C(z) = -\frac{1}{z} + 2z(-2 + z^4)\Theta'(z)^2.$$

We split our results in two blocks. First we discuss the fluctuations at vanishing momentum and later introduce a finite spatial momentum. Our results are summarized in the following two sections.

### Vanishing momentum

Our analysis produced a considerable amount of data and we will not show all of it because of some redundancy in the results. Technical details on our numerical methods are also deferred to the appendices C.3 and C.4. The idea here is, to have example figures for each case of interest and a listing of all the effects we observe. We also provide a qualitative analysis by studying the correspondent Schrödinger equations (see appendix B.1). The discussion subsection in each of the cases is then devoted to the physically most interesting effects, i. e. the tachyon, diffusion mode, turning point.

**Transverse Vectors** The transverse equation of motion can be written in this simplified form

$$E_T''(z) + A_1(z)E_T'(z) + B(z)(\omega^2 - f(z)q^2)E_T(z) = 0, \quad (4.126)$$

where  $A_1(z) = C(z) + \frac{f'(z)}{f(z)}$ . Close to the boundary of AdS ( $z \rightarrow 0^+$ ), the differential equation reduces to

$$E_T''(z) - \frac{1}{z}E_T'(z) = 0, \quad (4.127)$$

which has the solution  $E_T(z) = \mathcal{A} + \mathcal{B}z^2$ . According the AdS/CFT dictionary,  $\mathcal{A}$  should be zero in order to study the quasinormal states. Close to the horizon ( $z \rightarrow 1^-$ ), the differential equation is given by

$$E_T''(z) + \frac{1}{z-1}E_T'(z) + \frac{\omega^2}{16(z-1)^2}E_T(z) = 0, \quad (4.128)$$

with the solution  $E_T(z) = \mathcal{A}'(1-z)^{i\omega/4} + \mathcal{B}'(1-z)^{-i\omega/4}$ . The ingoing boundary condition is fulfilled by choosing  $\mathcal{A}' = 0$ .

At this point we perform the next transformation  $E_T(z) = (1-z)^{-i\omega/4}y(z)$ , in order to split the ingoing singular part from the regular part of the function. In consequence the function  $y(z)$  must satisfy the boundary conditions  $y(0) = 0$  and  $y(1) = 1$  and the differential equation turns out to be

$$y_t''(z) + [\alpha_1 + i\omega\gamma_1]y_t'(z) + [\alpha_0 + i\omega\beta_1 + \omega^2\beta_2]y_t(z) = 0, \quad (4.129)$$

with

$$\begin{aligned} \alpha_1 &= A_1, & \gamma_1 &= \frac{1}{2(1-z)}, & \alpha_0 &= -q^2 f(z)B(z), \\ \beta_1 &= \frac{1 + A_1(1-z)}{4(1-z)^2}, & \beta_2 &= -\frac{1}{16(1-z)^2} + B(z). \end{aligned}$$

Results for the quasinormal modes of the transverse vectors in this case are shown in figure 4.8.

**Longitudinal Vectors** The equation of motion for longitudinal vectors is given by

$$E_L''(z) + \left[ \frac{A_1(z)(\omega^2 - f(z)q^2) + C_0(z)}{\omega^2 - f(z)q^2} \right] E_L'(z) + B(z)(\omega^2 - f(z)q^2)E_L(z) = 0, \quad (4.130)$$

with  $C_0(z) = q^2 f(z)$ . The asymptotic behavior of this equation is the same as for the transverse equation of motion. If we do the same transformation as above, we obtain

$$y_l''(z) + \left[ \frac{\alpha'_1 + \alpha'_2\omega^2}{\omega^2 - q^2 f(z)} + i\omega\gamma'_1 \right] y_l'(z) + \frac{\alpha'_0 + \beta'_2\omega^2 + \beta'_3\omega^4 + i(\omega\beta'_1 + \omega^3\beta'_4)}{\omega^2 - q^2 f(z)} y_l(z) = 0, \quad (4.131)$$

with

$$\begin{aligned} \alpha'_1 &= C_0(z) - A_1(z)q^2 f(z), & \alpha'_2 &= A_1(z), \\ \gamma'_1 &= \frac{1}{2(1-z)}, & \alpha'_0 &= q^4 f^2(z)B(z), \\ \beta'_1 &= \frac{C_0(1-z) + q^2(A_1(z-1) - 1)f(z)}{4(z-1)^2}, & \beta'_3 &= B(z) - \frac{1}{16(1-z)^2}, \\ \beta'_2 &= \frac{q^2(1 - 32(-1+z)^2 B(z)) f(z)}{16(-1+z)^2}, & \beta'_4 &= \frac{1 + A_1(z)(1-z)}{4(-1+z)^2}. \end{aligned}$$

In the case with  $q = 0$  the differential equations for transverse and longitudinal fluctuations are the same, in consequence their quasinormal spectra coincide, see figure 4.8.

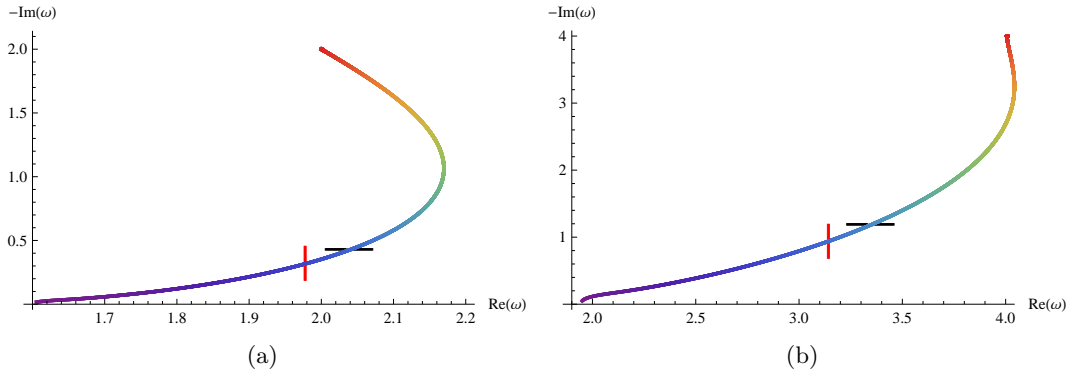


**Figure 4.8:** Location of the first (a) and second (b) quasinormal modes in the complex frequency plane for the *vector* fluctuations at vanishing momentum ( $q = 0$ ) as a function of the embedding  $\chi_0$ . Red color indicates small quark mass, or high temperature, while the temperature decreases towards blue colors. The horizontal (black) dash indicates the frequency at the first order phase transition where the angle is  $\chi_0 = 0.939$ . The vertical (red) dash indicates the frequency at which the embeddings become locally unstable at  $\chi_0 = 0.962$ . The modes are followed down to embeddings with  $\chi_0 = 0.999875$ . These figures are taken from [3].

**Results for vectors** Figure 4.8 shows the first and second quasinormal mode in the complex frequency plane. Starting with zero quark mass, i.e. at high temperature (red color), the imaginary part monotonously decreases with decreasing temperature. This means the corresponding mode becomes more and more stable. In contrast to that the real part of the quasinormal frequency first grows until it reaches a maximum and then decreases as well with decreasing temperature. This maximum in the real part of the quasinormal mode lies above the meson melting transition (indicated by a short horizontal dash). The melting transition takes place at a critical angle  $\chi_0 = 0.939$ . Beyond this value, the Minkowski embeddings are thermodynamically favored, not the black hole embeddings. We have chosen to remain in the so-called *undercooled* phase keeping the black hole embeddings even beyond the transition. This phase is accessible since the meson-melting is a first order transition. So the undercooled phase is metastable. However, we will see in the following section that at a smaller temperature below the melting transition, i.e. a larger angle  $\chi_0^{\text{tachyon}} \approx 0.962$ , this undercooled phase is destabilized by the scalar fluctuation becoming tachyonic. In the figures this is indicated by a red vertical dash.

Exemplary numerical values for the vector quasinormal frequencies at  $q = 0$  are given in table 4.1. We find a remarkable agreement between the values obtained with the two different methods: the relaxation method and the shooting method. The results are in good agreement for all parameter regions and in all the cases we treat in this work. Therefore, we exclusively show results produced with the relaxation method from now on.

	$\chi_0$	Relaxation		Shooting	
		Re $\omega$	Im $\omega$	Re $\omega$	Im $\omega$
1st quasinormal mode	0	2.0000	-2.0000	2.0000	-2.0000
	0.48	2.1075	-1.5973	2.1075	-1.5972
	0.92	2.0656	-0.4853	2.0657	-0.4852
2nd quasinormal mode	0	4.0054	-3.9976	3.9995	-4.0004
	0.48	4.0417	-3.3366	3.9324	-3.3386
	0.92	3.4397	-1.3093	3.4397	-1.3093

**Table 4.1:** Exemplary values for the first and second vector quasinormal mode frequencies at  $q = 0$  for different values of  $\chi_0$  parametrizing the D7-embedding. See figure 4.3 for the relation between  $\chi_0$  and the quark mass  $M_q$ . The first pair of values in each row is obtained from the relaxation method, the second pair stems from requiring the shooting solution to vanish at the AdS boundary. We find a remarkable agreement.

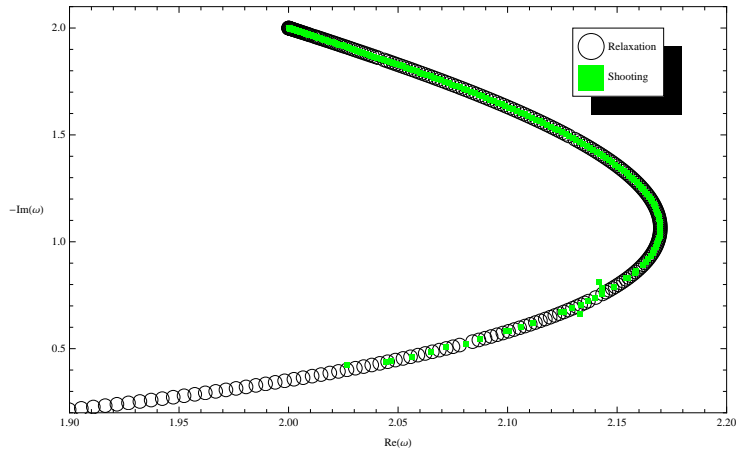


**Figure 4.9:** Shoot and relax: Comparison of the shooting method result (green squares) with the relaxation method results (black circles) for the location of the first transverse vector quasinormal mode at vanishing momentum  $q = 0$ . Along the curves the temperature is varied. Our two methods agree very well. This figure is taken from [3].

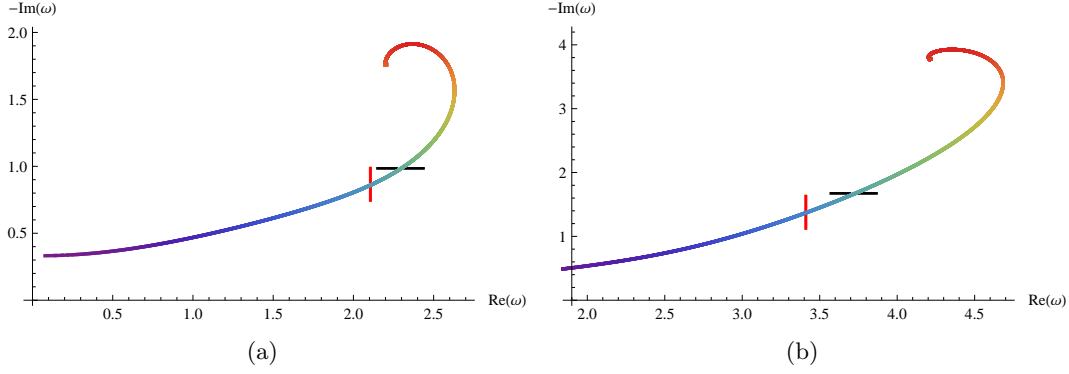


**Figure 4.10:** Location of the first (a) and second (b) quasinormal modes in the complex frequency plane for the *scalar* fluctuations at vanishing momentum ( $q = 0$ ) as a function of the embedding  $\chi_0$ . Red color indicates small quark mass, or high temperature, while the temperature decreases towards blue colors. The horizontal (black) dash indicates the frequency at the phase transition where the angle is  $\chi_0 = 0.939$  whereas the vertical (red) dash indicates the onset of the instability at  $\chi_0 = 0.962$ . These figure are taken from [3].

**Scalar** In the DBI action, we let the  $\theta$ -angle fluctuate and split this fluctuation  $\delta\theta$  into a product of its singular and regular parts  $\delta\theta(z) = (1-z)^{-i\omega/4}zy(z)$ . With this change the ingoing boundary condition at the horizon is translated into  $y(1) = 1^6$  and the Dirichlet condition at the boundary implies  $y(0) = 0$ . The equation of motion for scalar fluctuations then reads

$$y''(z) + [a_1(z) + ic_1(z)\omega]y'(z) + [a_0(z) + ib_1(z)\omega + b_2(z)\omega^2]y(z), \quad (4.132)$$

with

$$\begin{aligned} a_1(z) &= A_1(z) + \frac{2}{z}, & a_0(z) &= \frac{A_1(z)}{z} + A_0(z) - B(z)^2q^2f(z), \\ c_1(z) &= \frac{1}{2(1-z)}, & b_2(z) &= B(z)^2 - \frac{1}{16(1-z)^2}, \\ b_1(z) &= -\frac{(1-A_1(z)(1-z))z-2}{4z(1-z)^2}. \end{aligned}$$

**Results for the scalar** The first and second scalar quasinormal mode at vanishing momentum can be found in figure 4.10. The basic behavior is similar to that of the vector modes. Increasing the quark mass from zero, the real part of the quasinormal frequency again shows a turning behavior moving first to larger values, then to smaller values of  $\text{Re}(\omega)$ . However, in contrast to the vectors, the scalar quasinormal mode frequency also shows a turning behavior in the imaginary part  $\text{Im}\omega$ . This

<sup>6</sup>Notice that the equation for  $y(z)$  is linear and that we can scale  $y$  by an arbitrary constant, therefore, we can always choose the boundary condition at the horizon to be  $y = 1$ .

means that increasing the quark mass, i. e. decreasing the temperature, the corresponding modes first decay faster, then beyond the turning point they decay slower and slower as the mode approaches the real axis. Moreover, the scalar quasinormal modes do not asymptote to the real axis as fast as the vector quasinormal modes do. Instead the scalar quasinormal frequencies even at large masses still have a considerable imaginary part of roughly  $1/2$ . All the values for the scalar modes are in excellent agreement with the ones obtained previously in [50].

The short dash in the figures again shows the location of the known meson melting transition where the initial angle is  $\chi_0 = 0.939$ . Increasing the mass further while staying in the black hole phase, we observe that a scalar quasinormal mode becomes tachyonic. This point is marked by a vertical dash in the figures. Figure 4.11 shows the appearance of an unstable mode explicitly. This particular mode is special since it has vanishing real part but it starts with an extra-ordinary large imaginary part of the quasinormal frequency at zero quark mass. Increasing the quark mass, this purely damped mode moves closer to the real axis until it crosses to become unstable at  $\chi_0 = 0.962$  corresponding to the maximal mass for black hole embeddings of  $m \approx 1.31$ . This particular mode has not been observed in previous studies because at vanishing quark mass it is located very deep in the complex frequency plane near  $\text{Im } \omega \approx -8$ , while for example the first scalar quasinormal mode has  $\text{Im } \omega = -2$  at vanishing quark mass. In principle there could be an infinite tower of such purely imaginary modes, each crossing the real axis at the larger and larger quark mass. However, the accuracy of our numerics proved insufficient to establish additional modes beyond this lowest one. In any case once this mode has crossed the real axis the D7 brane embedding is locally unstable and can not be taken as a (metastable) ground state. This raises the question of what is the true ground state in this regime. It might be that there is another type of D7-brane embedding that is reached somehow by condensation of the scalar mode. Another possibility is that there is simply no locally stable embedding beyond that point.

**Schrödinger potential analysis** Now we present a qualitative analysis of the quasinormal spectrum using the fact that the equations of motion for the fluctuations can be rewritten in the form of the Schrödinger equation (see appendix B.1 for more details),

$$-\partial_{R^*}^2 \psi + V_S \psi = E \psi, \quad (4.133)$$

where  $R^*$  is a tortoise-like coordinate. The Schrödinger potential  $V_S$  determines the energy spectrum  $E$  which is related to the quasinormal spectrum by  $E = \omega^2$ .

At zero momentum, the potentials for the vector and scalar modes are already discussed in [185] and [184], respectively. In figure 4.12 we present the Schrödinger potential for the vector and scalar fluctuations at different quark masses parametrized by  $\chi_0$ . In these plots we observe an infinite wall in the potential at  $R^* = 0$  which corresponds to the AdS boundary. In addition to this wall, the potential for the vector modes develops a step-shape as we increase the quark mass.

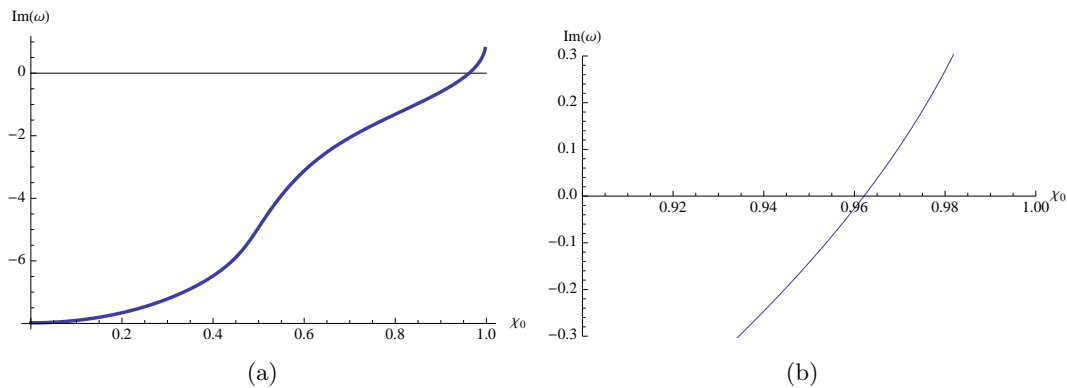


**Figure 4.11:** (a) The plot shows a purely imaginary quasinormal mode at  $q = 0$  as a function of the embedding. (b) Zooming into the region where the *scalar* mode crosses the real axis becoming tachyonic approximately at  $\chi_0 = 0.96221$ . These figures are taken from [3].

In [185] it is shown that the imaginary part of the quasinormal frequency decreases as the step gets longer which is consistent with our result found in figure 4.8.

For the scalar modes a negative well arises in the Schrödinger potential. This well becomes deeper and wider as we increase the quark mass and, therefore, support a ‘bound’ state with  $E < 0$  which corresponds to a tachyonic quasinormal frequency  $\text{Im } \omega > 0$ . The reason why a bound state with negative energy implies an instability is due to the ingoing boundary condition at the horizon. This boundary condition implies that the time-independent part of the mode goes like  $e^{i\omega R^*}$ . Outside the potential well, the mode has to decay exponentially towards the horizon. Combining these two constraints means that  $\omega$  must have a positive imaginary part. Thus, the appearance of the bound state in the Schrödinger picture agrees with the quasinormal frequency crossing the real axis. This well and the ‘bound’ state are studied in [184]. The Schrödinger analysis clearly shows the existence of a tachyonic mode which we already found in figure 4.11.

**Discussion: Tachyon and De-singularization** In this paragraph we discuss why the so-called *undercooled phase* shows unphysical meson spectra which do not approach the known ones in the supersymmetric limit. Further we discuss that finite density cures this behavior by de-singularizing the geometry, i. e. by smoothing out the limiting embedding.

As mentioned above the scalar fluctuation becomes tachyonic once the quark mass parameter has reached its maximum as a function of  $\chi_0$ . It is not to be expected that the region beyond that point contains physically relevant or meaningful signatures. This region contains the limiting embedding which only touches the horizon and geometrically separates Minkowski from black hole embeddings. Here meson spectra had been studied earlier [184, 185]. These meson spectra display a singular behavior in the sense that all the quasinormal modes (first, second, ...)

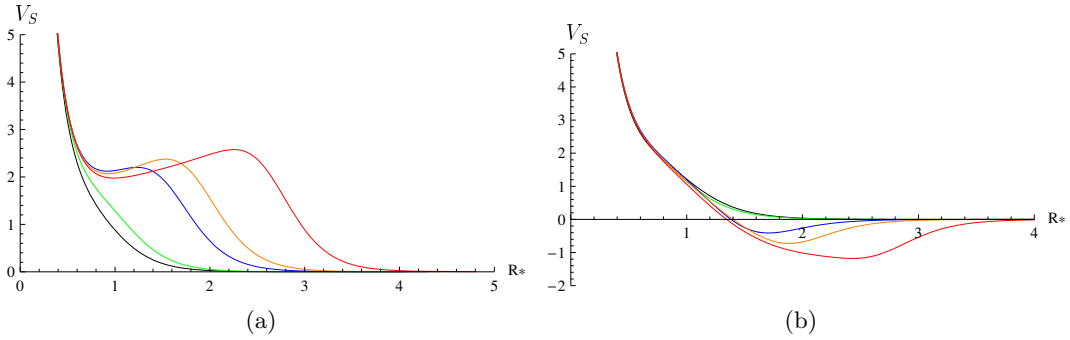


**Figure 4.12:** Schrödinger potential of the *vector* (a) and *scalar* (b) fluctuations for different values of  $\chi_0$ . The different colors correspond to  $\chi_0 = 0$  (black), 0.5 (green), 0.9 (blue), 0.95 (orange), 0.99 (red). These figures are taken from [3].

approach one single “attractor” energy (or frequency) near the limiting embedding. The geometric reason for this is the scaling symmetry for the embeddings in the near-critical region [49]. That scaling symmetry implies that near the critical quark mass (or temperature) there exists no preferred scale on the brane. In this sense there is no scale which could determine the distance between resonances in the brane fluctuations, i. e. between the distinct meson mass resonances, or quasinormal modes equivalently.

At finite fixed baryon density, however, this particular scaling symmetry is broken [72]. Therefore, the chemical potential introduced together with that density does set the scale for the separation between the distinct quasinormal modes. As observed earlier [186] the meson spectrum at finite density approaches the supersymmetric one at low temperatures. In this sense the theory is de-singularized by finite baryon density. We will see this explicitly in the quasinormal mode spectra at finite density in section 5.3.2.

## Finite Momentum

We now turn to the case of non-zero spatial momentum.

**Transverse vectors** We obtain results at finite momentum from the numerical solution of equation (4.126) with distinct non-zero values of  $q$ . Figure 4.13 shows the first of the transverse vector quasinormal modes at different values of the spatial momentum  $q$ . The behavior in the region  $q = 0, \dots, 4$  is very similar to the  $q = 0$  case. Although its trajectory in the complex frequency plane becomes more wavy at larger  $q$ , the first quasinormal mode still starts at quite large real and imaginary parts in order to approach the real axis and smaller real parts when temperature is decreased. Distinct curves for different values of  $q$  within numerical accuracy approach a single limiting value  $\omega_0$  at small temperatures. It is interesting to note that the turning point in  $\text{Re}(\omega)$  mentioned in the previous section for  $q = 0$  disappears

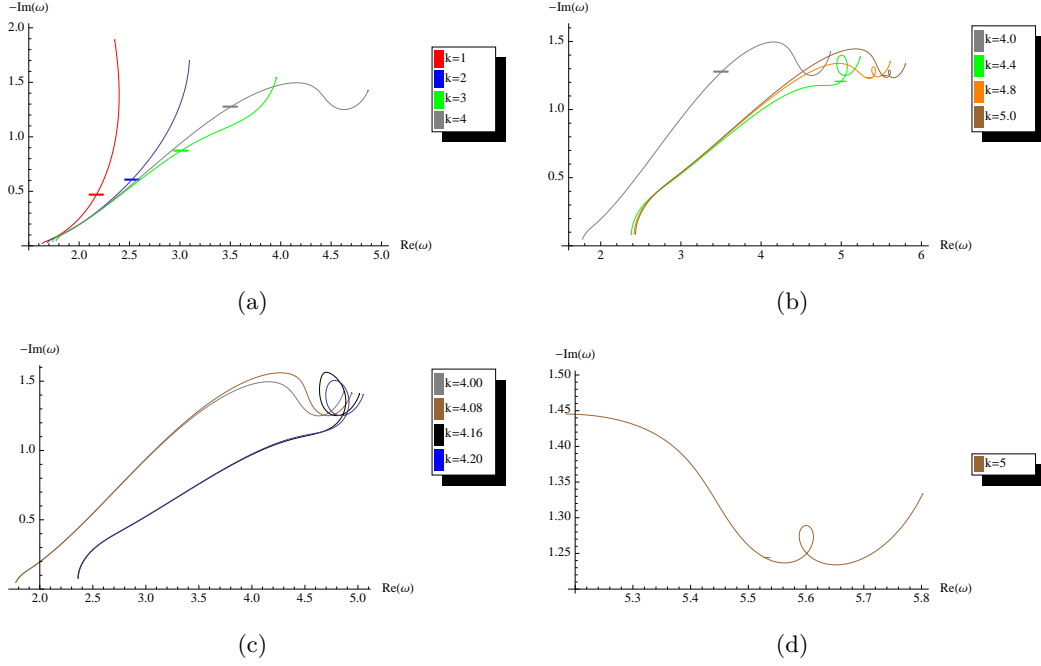


**Figure 4.13:** First quasinormal mode for *transverse vector* fluctuations at different spatial momenta  $q$ . Horizontal short dashes across the curves show the location of the meson melting transition. At  $q \approx 4.16$  a spiral structure appears and the curves also asymptote to a distinct small temperature value from that  $q$  on. Along the curves the quark mass parameter  $\chi_0 = \cos \Theta_0$  is varied. See figure 4.3 for its relation to the quark mass and temperature. These figures are taken from [3].

when  $q$  reaches values between  $q = 1$  and  $q = 2$ .

A quite substantial qualitative change appears at  $q = 4.16$ , where the trajectory of the mode in the frequency plane develops a loop. Also the trajectories at higher  $q$  have this looping behavior. At the same time, these curves with one loop do asymptote to a single small temperature frequency value  $\omega_1$  as well. But this limiting value is distinct from the limiting value which is approached by the low  $q$  curves without the loop, i. e.  $\omega_1 \neq \omega_0$ . This fact suggests that the loop-behavior and the distinct limiting value are somehow related. For the longitudinal vector fluctuations (see figure 4.16) we will explicitly see that this relation generalizes to all fluctuations and to higher loops in this way: All the first quasinormal mode trajectories for scalar and vector fluctuations with  $q < q_n$  have  $n$  loops and they asymptote to a small temperature limit frequency  $\omega_n$  (within numerical accuracy) with  $\omega_{n+1} > \omega_n$ . Note that the loop behavior appears in a physical, thermodynamically preferred phase, i. e. *before* the meson melting transition and also way before the tachyon appears. The loops are absent in the second quasinormal mode as seen from figure 4.15. Nevertheless, the second quasinormal mode also asymptotes to distinct low temperature limits  $\omega_n$  above distinct certain momenta  $q_n$ . Figure 4.14 captures the dispersion

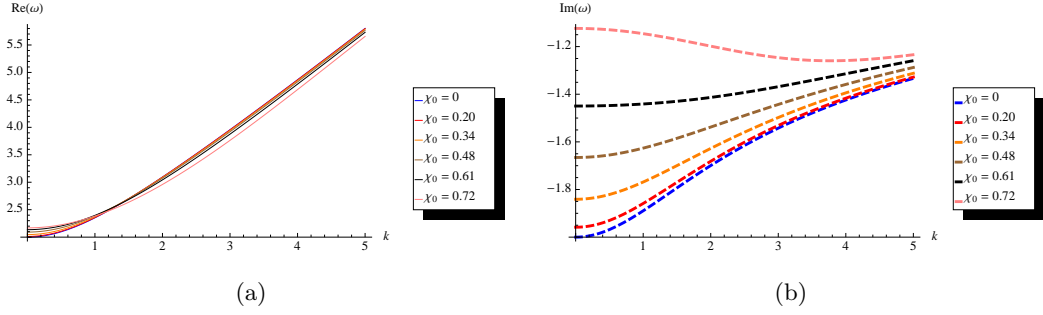


**Figure 4.14:** Dispersion relation for the first *transverse* quasinormal mode at distinct quark masses, or equivalently temperatures, parametrized by the embedding parameter at the horizon,  $\chi_0$ . See figure 4.3 for the relation between  $\chi_0$ , the temperature and quark mass  $M_q$ . These figures are taken from [3].

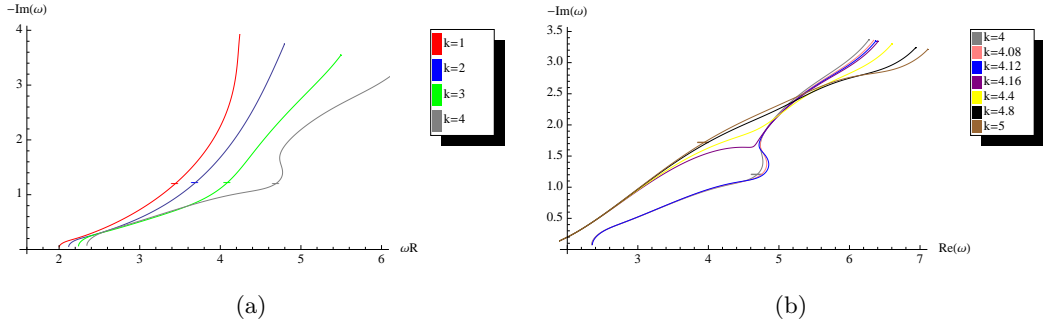


**Figure 4.15:** Second quasinormal mode for *transverse vector* fluctuations at different spatial momenta  $q$ . Horizontal short dashes across the curves show the location of the meson melting transition. There is no spiral structure appearing in contrast to the first quasinormal mode presented in figure 4.13. Along the curves the quark mass parameter  $\chi_0 = \cos \Theta_0$  is varied. See figure 4.3 for its relation to the quark mass and temperature. These figures are taken from [3].

relation of the first transverse vector quasinormal mode at different values of  $\chi_0$ .

**Longitudinal vectors** We obtain results at finite momentum from the numerical solution of equation (4.130) with distinct non-zero values of  $q$ . The behavior of the longitudinal vector quasinormal modes is qualitatively similar to that of the transverse ones discussed above. The mentioned loops in the frequency plane trajectory do appear at smaller values  $q \approx 3.4$  in the longitudinal channel than they do in the transverse one. However, while in the transverse vector case the loops appeared before the meson melting transition, in the longitudinal case the transition takes place before the first loop is terminated as can be seen from the figure 4.16. Just as for the transverse vectors, also the second quasinormal mode of the longitudinal vectors does not have any loops in its complex frequency plane trajectory. The dispersion

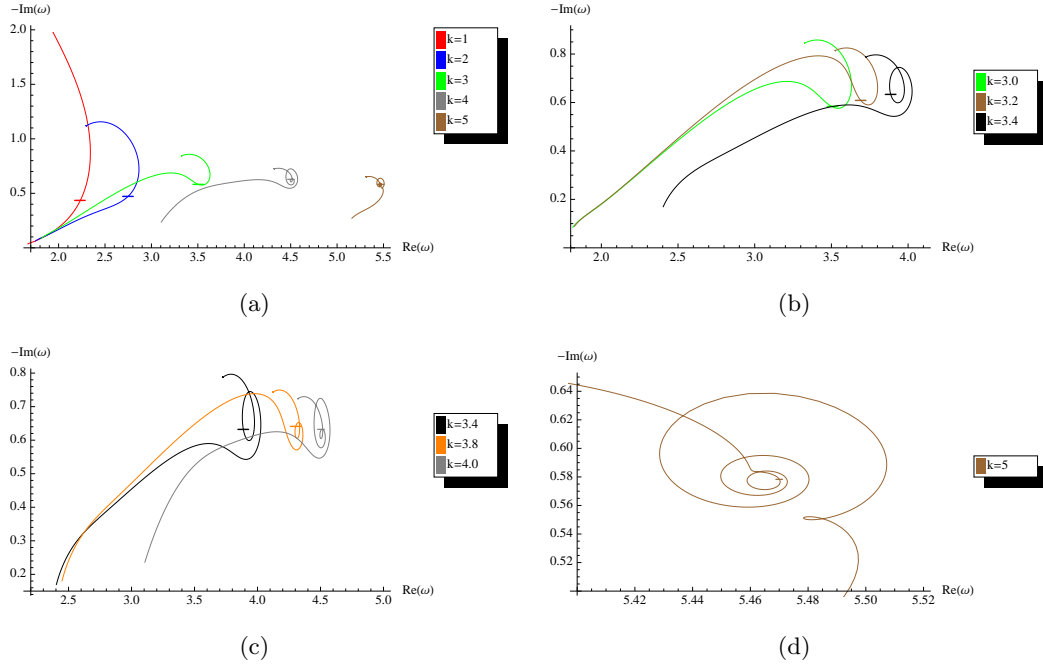


**Figure 4.16:** The first quasinormal mode for *longitudinal vector* fluctuations at distinct values of  $q$ . Along the curves the quark mass parameter  $\chi_0 = \cos \Theta_0$  is varied. See figure 4.3 for its relation to the quark mass and temperature. These figures are taken from [3].

relations for the first quasinormal mode of the longitudinal vector fluctuation is depicted in figure 4.17. Corresponding figures for the second quasinormal mode may be found in the appendix of the original work [3].

**Scalar** We obtain results at finite momentum from the numerical solution of equation (4.132) with distinct non-zero values of  $q$ . The general behavior of the scalar quasinormal modes is qualitatively similar to that of the longitudinal vector quasinormal modes. Figure 4.18 shows the first of the scalar quasinormal modes at momenta between  $q = 1$  and  $q = 5$ . Also in this case the overall behavior is that the real and imaginary parts decrease as temperature is decreased along the curves. At small  $q$ , e.g.  $q = 1$ , there is a turning point present in the real as well as in the imaginary part. These turning points again disappear between  $q = 1$  and  $q = 3$ . Just like for the first of the longitudinal vector quasinormal modes multiple loops form successively for larger values of  $q$ . The meson melting transition appears before the first of the loops has terminated. Again the number of loops seems to be directly related to the low temperature value  $\omega_n$  to which the curves for all  $q > q_n$  asymptote. Dispersion relations for the first scalar quasinormal mode are shown in figure 4.19. The corresponding figures for the second scalar quasinormal mode may be found in the appendix of the original work [3]. Just like for the vectors there are

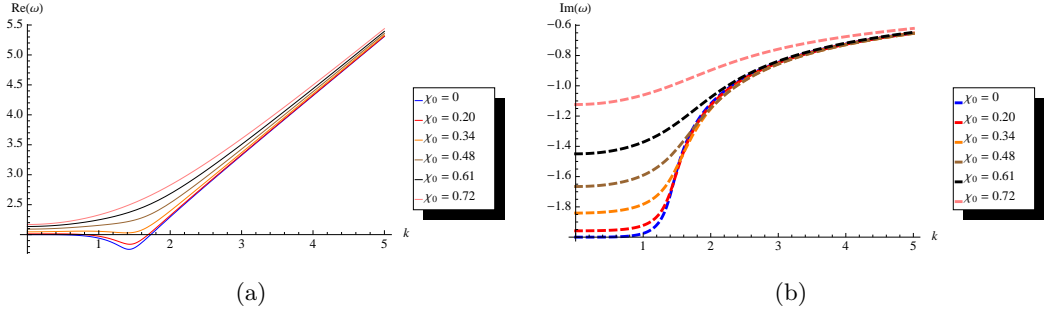


**Figure 4.17:** Dispersion relation for the first quasinormal *longitudinal vector* mode fluctuation at distinct values of the quark mass parameter  $\chi_0$  (see figure 4.3 for its relation to the quark mass at vanishing density). These figures are taken from [3].

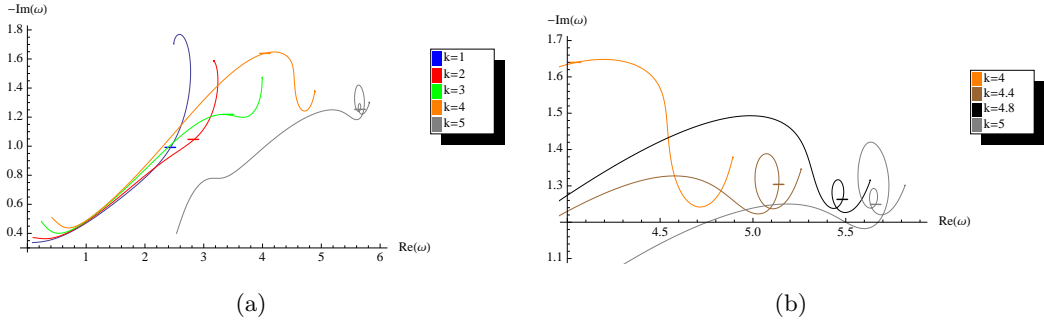


**Figure 4.18:** First *scalar* quasinormal mode at distinct momenta  $q$ . Along the curves the quark mass parameter  $\chi_0 = \cos \Theta_0$  is varied. See figure 4.3 for its relation to the quark mass and temperature. These figures are taken from [3].

also no loops in the second quasinormal mode for the scalars.

**Schrödinger potential analysis** Just as at zero momentum, we compute the effective Schrödinger potential for the scalar and vector fluctuation equations (4.132) and (4.130), (4.126) (see appendix B.1 for more details).

We begin by examining the Schrödinger potential for the scalar fluctuations in figure 4.20. The lowest (red) curve shows the potential at vanishing momentum and density at  $\chi_0 = 0.9999$ . That is near the limiting embedding, far beyond the thermodynamic transition to Minkowski embeddings and far beyond the appearance of the tachyon in the spectrum. The results at smaller  $\chi_0$  are qualitatively the same, but we plot large  $\chi_0$  in order to investigate the tachyon and the reason for the different "attractor" frequencies in that large mass regime. The scalar potential clearly exhibits a wide negative dip in which the tachyonic scalar mode resides, compare figure 4.11. As the momentum is increased, the potential is lifted and the negative dip is narrowed. In this way the lowest possible excitation is pushed towards

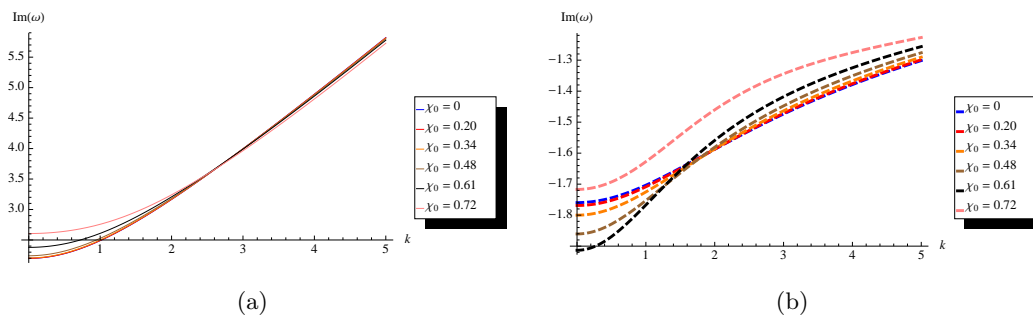


**Figure 4.19:** Dispersion relation for the first *scalar* quasinormal mode at distinct values for the quark mass parameter  $\chi_0$ . See figure 4.3 for its relation to the quark mass. The real part of the quasinormal frequency is shown on the left, the imaginary part on the right. These figures are taken from [3].

more positive energy values becoming non-tachyonic at large momenta. However, the theory is clearly unstable against condensation of the scalar fluctuations already at  $\chi_0 \geq 0.962$  and  $q = 0$ .

In figure 4.21 we zoom out to larger values of the potential. For increasing momentum, a step forms near the boundary. When comparing to figure 4.12 (a), we see that the scalar potential at finite momentum is similar to the vector case at zero momentum. In figure 4.21 the step becomes higher and longer for increasing momentum, while its plateau becomes shorter, i. e. most of the plateau is located near the boundary. Therefore, conceptually the analysis of [185] as discussed at zero momentum applies as in the vector case: When the step becomes longer, the imaginary part of the quasinormal frequencies decreases. This is consistent with our observations in figure 4.18 (compare for example the initial points where  $\chi_0 = 0$  for increasing momenta from curve to curve). The increasing real part of the quasinormal frequency observed in figure 4.18 is due to the fact that the potential step rises closer to the horizon at larger momentum. This narrows the potential and rises the excitation energies.

Turning now to the transverse vector fluctuations, we observe a step potential in figure 4.22. The larger the momentum, the earlier the potential rises towards infinity when approaching the boundary at  $R^* = 0$ . So effectively the boundary moves towards the horizon and the length of the plateau of the potential step becomes shorter. This is different from the scalar modes discussed above. While the imaginary part of the quasinormal frequency decreases for increasing momentum just as in the scalar case, the Schrödinger potential shows a different behavior: For increasing momentum, the Schrödinger potential approaches the shape of a wall. Whereas in the scalar case, the formation of the step is responsible for lowering the imaginary part of the quasinormal frequency, here we expect that the formation of the wall is responsible for a similar decrease of the imaginary part of the quasinormal frequency.

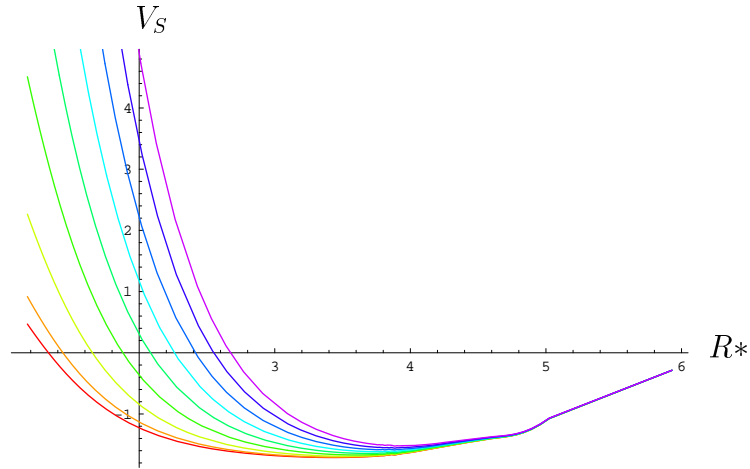


**Figure 4.20:** The *scalar* Schrödinger potential  $V_s$  (zooming in on the minimum of the potential) versus the radial coordinate  $R^*$  defined in section B.1 at increasing momenta  $q = 0, 2, 4, 6, 8, 10, 12, 14, 16$  from bottom to top curve with the quark mass parameter  $\chi_0 = 0.9999$  (see figure 4.3 for its relation to the quark mass). The dip supporting the tachyon narrows. This figure is taken from [3].

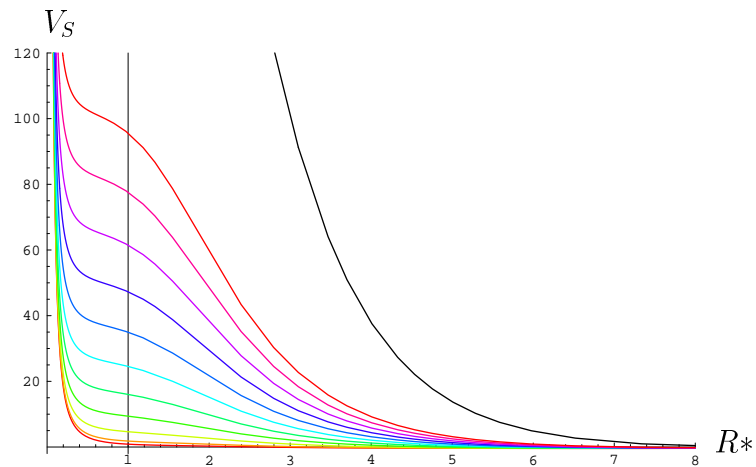


**Figure 4.21:** The *scalar* Schrödinger potential  $V_s$  (zooming out to larger values of the potential) versus the radial coordinate  $R^*$  at increasing momenta  $q = 0, 2, 4, 6, 8, 10, 12, 14, 16, 18, 20, 40$  from bottom to top curve with quark mass parameter  $\chi_0 = 0.9999$  (see figure 4.3 for its relation to the quark mass). A step forms towards the boundary, similar as that for the vectors. The grid line at  $R^* = 1$  serves to guide the eye only. This figure is taken from [3].

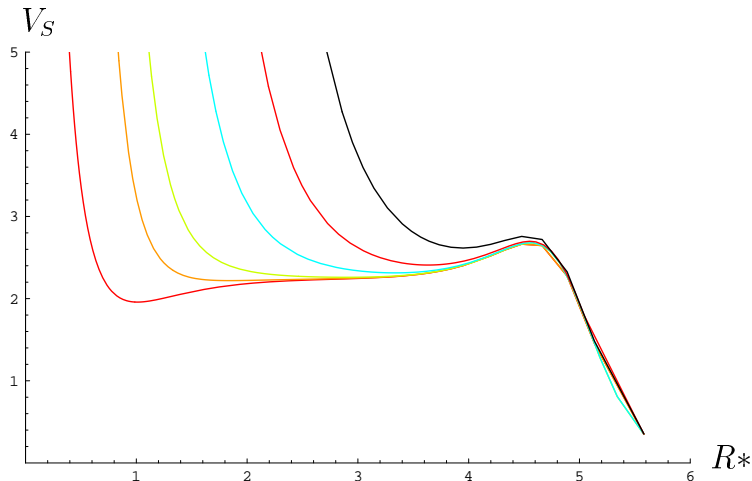


**Figure 4.22:** The *transverse vector* Schrödinger potential  $V_s$  versus the radial coordinate  $R^*$  at increasing momenta  $q = 0, 2, 4, 10, 20, 40$  from bottom to top curve with quark mass parameter  $\chi_0 = 0.9999$  (see figure 4.3 for its relation to the quark mass). The potential step becomes shorter since the potential rises farther and farther away from the boundary  $R^* = 0$ . This figure is taken from [3].

**Discussion:** In this discussion we focus on three distinct physical implications of the quasinormal modes described previously in this section. The longitudinal vector modes tell us when the hydrodynamic approximation breaks down, while the novel purely imaginary scalar mode renders the whole theory unstable as it becomes tachyonic. Both scalar and vector modes asymptote to “attractor” frequencies. This behavior is probably related to a spiraling behavior of the quasinormal mode’s trajectories with changing quark mass or temperature.

**Hydrodynamics to Collisionless Crossover** Contrary to the transverse vector and scalar channel, the longitudinal vector channel also has a hydrodynamic quasinormal mode, i. e. a mode whose dispersion relation does not show a gap at zero momentum,  $\lim_{q \rightarrow 0} \omega(q) = 0$  (see figure 4.23, left). This mode represents diffusion of baryon charge. It is a mode whose frequency is purely imaginary and, therefore, results in a purely damped time evolution without any oscillation. At small momentum the dispersion relation is well approximated by the diffusion kernel  $\omega = -iDq^2$ , as seen in figure 4.23 on the left. We discuss hydrodynamics in more detail in section 4.4. Fitting our numerical data, we can extract the diffusion constant  $D$ . It has been calculated before in the literature in [184, figure 12] (see also figure 4.24), and we checked that our values are consistent with the results there.

On general grounds, one expects that a many body system shows a crossover from a hydrodynamic behavior at long wavelengths to a coherent or collisionless behavior at small wavelengths. In the holographic context, this has first been discussed in an  $AdS_4$  example in [187] by calculating spectral functions. A more direct way

to see this crossover can be obtained by studying the quasinormal mode spectrum. At small momentum the hydrodynamic mode should be the dominant one, i. e. the one with the largest imaginary part. At small wavelengths we expect the dominant modes to have frequencies whose imaginary part is much smaller than their real parts. This means that at large wavelengths the response would be simply an exponential decay, whereas at short wavelengths the response would be a slowly decaying oscillation. In terms of the quasinormal mode spectrum, this implies that the purely imaginary diffusion mode as a function of momentum has to cross the imaginary part of the dispersion relation for the lower non-hydrodynamic modes. Indeed this is what happens for the R-charge and momentum diffusion in the strongly coupled  $\mathcal{N} = 4$  Super-Yang-Mills theory as discussed in [180, 181]. We, therefore, define the crossover from the hydrodynamic regime to the collisionless regime through the momentum at which the imaginary part of the lowest non-hydrodynamic mode crosses the purely imaginary diffusion mode. From that wavelength on, it is the lowest gaped quasinormal mode which dominates the late time response<sup>7</sup>. It should be mentioned that there is at least one other way of how this crossover can be established in terms of quasinormal modes. It could also be that the purely imaginary diffusion mode pairs up with another purely imaginary but non-hydrodynamic mode which allows them to develop real parts as well and to move off the imaginary axis. This seems to be the preferred mechanism for  $AdS_4$  black holes [189] and it also appears on probe D-branes representing defects in the four-dimensional strongly coupled CFT [176, 190]. This crossover has recently also been investigated for AdS black holes in various dimensions in the time domain in [191].

We have numerically determined the crossover point defined above for different embeddings. As seen from the right side of figure 4.23, the crossover moves to higher momenta as the embedding angle  $\chi_0$  is increased. This means that the brane responds to baryon charge fluctuations in a purely absorptive way for smaller and smaller wavelengths as the quark mass is increased, or equivalently as the temperature is decreased. Of course the actual rate of absorption given by the absolute value of the imaginary part of the frequencies decreases with decreasing temperature. Nevertheless, it is somewhat surprising that the crossover towards the collisionless

---

<sup>7</sup>There is a small puzzle related to that. When the prolongation of the hydrodynamic mode to large momenta is constantly increasing, the front velocity computed from it seems to violate causality. As is well-known already the diffusion kernel violates causality because of the  $q^2$  behavior and the extension to larger momenta shows even higher exponents in the dependence on  $q$ . So how does the theory manage to preserve causality? The resolution has been presented in [180]: the residues of the diffusive quasinormal mode vanish for large momenta and, therefore, this mode ceases to exist in the dangerous limit of large  $q$ . On the other hand, one can study the hydrodynamics by fixing a real frequency and then looking for complex roots in the momentum  $q$  as has been done in [188]. The quasinormal frequencies or the complex momenta respectively are roots of infinite order polynomials (or at least of extremely high order polynomials in a truncated approximation of the holographic Green function). Therefore, it is not possible to simply infer the behavior of the complex momentum modes from the quasinormal modes. Indeed as shown in [188], the front velocity of hydrodynamic modes as calculated from the complex momentum roots behaves perfectly causal and approaches 1 to very good numerical accuracy.

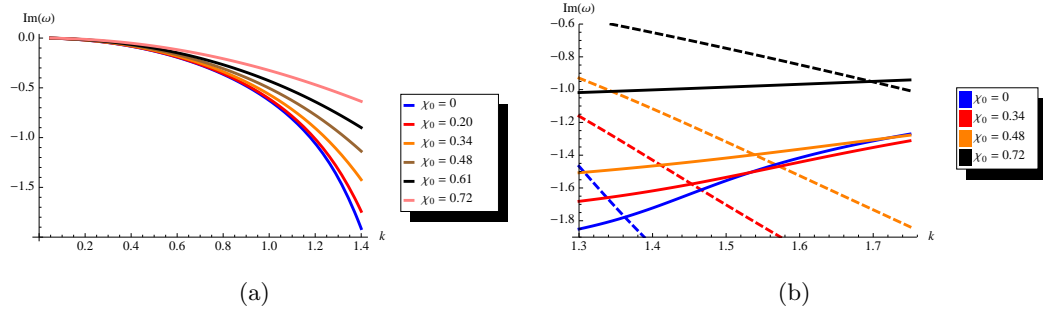


**Figure 4.23:** Left: The dispersion relation for the *diffusion mode* at distinct values for the mass/temperature parameter  $\chi_0$ . See figure 4.3 for its relation to the quark mass. Right: Intersection of the diffusive mode with the imaginary part of the first longitudinal quasinormal mode. The intersection point moves to larger values of  $q$ , but to smaller values of  $\text{Im} \omega$  as the mass/temperature parameter  $\chi_0$  is increased. These figures are taken from [3].

regime takes place at smaller wavelengths for lower temperatures.

**“Attractor” frequencies** Here, we briefly discuss the appearance of spiraling quasinormal mode trajectories and their relation to the “attractor” frequencies found above.

First we should note that in most cases the spirals in the quasinormal mode trajectories occur before the scalar in the spectrum becomes tachyonic. Thus, the spiral is a physical signature on the stable or metastable branch of the theory. However, the “attractor” frequencies to which the trajectories asymptote at large quark mass parameters  $\chi_0 \rightarrow 1$  are located deep in the unstable phase of the theory. Therefore, the “attractor” frequency is no signature of the physical stable sector of the theory. Nevertheless, it would be interesting to understand the apparent direct relation of these “attractor” frequencies and the number of spirals in the quasinormal mode trajectories since the spirals are physical, as noted before.

Note that a spiraling behavior for changing the temperature has been observed in the quark condensate in this system for near-limiting brane embeddings in [49]. There the spirals are due to oscillations of the parameters of the embedding, i. e. the quark mass and the quark condensate. In particular, the asymptotic value  $m$  oscillates. This behavior has only been observed in the near-limiting embeddings. In contrast to that our loops in the quasinormal mode-trajectories appear way above the critical embedding already. Nevertheless, as stated before there is an apparent connection between the number of loops in our quasinormal mode-trajectories and the near-limiting “attractor” frequency. In this way we could argue that at finite momentum we see the near-limiting embedding oscillations reflected already in the non-critical region in spiraling quasinormal mode-trajectories. In other words both the quasinormal mode-loops and the spiraling quark condensate might have the same origin, namely the oscillating embedding parameters which are related to the

mentioned scaling symmetry of the near-limiting embedding [49].

Unfortunately, the Schrödinger potentials at finite momentum but vanishing density close to  $\chi_0 = 1$  in figure 4.20 and 4.22 do not show any distinct feature hinting neither on discrete special frequencies  $\omega_n$  nor on the jumps between them at critical momenta.

**Tachyon: A new hydrodynamic mode** We briefly discuss here the behavior of the scalar mode becoming tachyonic as explained in the previous section. This mode turns into a hydrodynamic mode in a special case.

As expected this scalar mode becomes tachyonic at higher and higher values for the quark mass parameter  $\chi_0$  as the momentum of the excitation is increased. In the parameter space, there is one interesting special point: that is the location  $\chi_0^{crit}$  where the scalar mode becomes tachyonic. Just at this special quark mass/temperature value, this scalar mode develops a hydrodynamic dispersion relation, i. e.  $\lim_{q \rightarrow 0} \omega \rightarrow 0$ . In other words the scalar mode which shows the instability of the system turns into a hydrodynamic mode just at the critical point. This could signal that there is a transition to a new phase. For instance this transition might be similar to the glass transition in supercooled liquids discussed e. g. in [192]. Lastly, there might not exist a new stable ground state since we might be scanning a regime where no stable brane embedding exists besides the thermodynamically preferred Minkowski embedding.

## 4.4 Hydrodynamics

Hydrodynamics is a particular interesting limit where only slowly varying perturbations are considered. Due to the slow variations, the system is locally in thermal equilibrium and is described by the thermodynamic variables such as temperature  $T$ , pressure  $p$ , energy  $E$ , etc. However, these quantities change slowly if we consider different regions of the system.

Formally, hydrodynamics is given as an expansion in small frequency and spatial momentum compared to the mean free path length  $\ell_{mfp}$ , i. e.  $\omega \ell_{mfp} \ll 1$  and  $q \ell_{mfp} \ll 1$ , since the mean free path is the characteristic length scale of an interacting system. This expansion can be seen as an *effective field theory* where the degrees of freedom with large frequency and spatial momentum are integrated out. In general, any effective field theory has undetermined parameters<sup>8</sup>. In hydrodynamics these parameters are named *transport coefficients* since they determine the transport properties of the system. Typical examples for the transport coefficients are the viscosity and the diffusion constant. The first measures the dissipation due to internal motion, i. e. strains, while the second determines the spread of particles from regions of high concentration into the ones of low concentration. As usual in effective field theories if we know the microscopic theory which describes

---

<sup>8</sup>Examples are the Yukawa couplings in the Standard Model.

our system, we may derive the values for these parameters. Thus, we may determine the transport properties of the system. In the context of gauge/gravity duality, we have a microscopic description of a strongly coupled field theory in terms of the dual gravity theory. This gravity theory allows us to calculate values for the transport coefficients.

The transport coefficients can be read off from the Green's functions. Since we exclusively consider slowly varying fluctuations, i. e. small frequency and spatial momentum, the poles of correlation functions closest to the origin are important. More precisely, the modes with a dispersion relation obeying  $\lim_{\mathbf{q} \rightarrow 0} \omega(\mathbf{q}) = 0$  represent the hydrodynamic regime. From these poles we can read off the transport coefficients such as the viscosity or the diffusion constant.

#### 4.4.1 Hydrodynamic Description

We now develop the hydrodynamic description of a system with several conserved currents  $J_a^\mu$  [127, 136]. In addition, there is the conserved energy-momentum tensor  $T^{\mu\nu}$ . These conservation laws are given by

$$\nabla_\mu T^{\mu\nu} = 0, \quad \nabla_\mu J_a^\mu = 0, \quad (4.134)$$

and are the dynamical equations of the hydrodynamic description. In order to specify the system further we need expressions for the energy-momentum tensor and the currents in terms of the local thermodynamic variables.

#### Ideal Fluid

Let us first consider an ideal isotropic fluid which has no dissipation on a background with metric  $g_{\mu\nu}$  in  $d$  dimensions and respects an  $O(d-1)$  rotational symmetry. For the moment we work in the local rest frame such that we can identify the time component of the energy-momentum tensor  $T^{tt}$  with the energy density  $\epsilon = E/V$ , the spatial components  $T^{ii}$  with the pressure  $p$ , and the time component of the currents  $J_a^t$  with the charge density  $\rho_a$ . In general, when the fluid has a velocity  $u_\mu$  with  $u^\mu u_\mu = -1$ , the quantities for an ideal fluid can be written as

$$\begin{aligned} (T^{\mu\nu})_{\text{ideal}} &= \epsilon u^\mu u^\nu + p P^{\mu\nu}, \\ (J_a^\mu)_{\text{ideal}} &= \rho_a u^\mu, \end{aligned} \quad (4.135)$$

where  $P^{\mu\nu} = g^{\mu\nu} + u^\mu u^\nu$  is the projector onto the spatial directions since  $P^{\mu\nu} u_\nu = 0$  and  $P^{\mu\rho} P_{\rho\nu} = P^\mu{}_\nu$ . These relations between the conserved quantities and the local thermodynamic variables are called *constitutive equations*. For a conformal fluid which we usually consider in this thesis, the energy-momentum tensor must be traceless which leads to the equation of state  $\epsilon = (d-1)p$ .

Using the equation of the energy-momentum tensor conservation projected onto the direction of the fluid velocity, the thermodynamic relations  $\epsilon + p = sT + \mu^a \rho_a$  and  $dp = s dT + \rho_a d\mu^a$  where  $s$  is the local entropy density and  $\mu^a$  the chemical

potential associated to the charge density  $\rho_a$  (see chapter 5), we obtain that the entropy current  $(J_s^\mu)_{\text{ideal}} = su^\mu$  of an ideal fluid is conserved. The entropy current measures the variation of the local entropy density. Since it is conserved, there is no entropy production in an ideal fluid.

### Dissipative Fluid

Commonly any fluid which is perturbed should relax back into its equilibrium. This is only possible if dissipation is present and the entropy increases. Thus, we need to include additional terms in the constitutive equations which lead to dissipation,

$$\begin{aligned} (T^{\mu\nu})_{\text{dissipative}} &= (T^{\mu\nu})_{\text{ideal}} + \Pi^{\mu\nu}, \\ (J_a^\mu)_{\text{dissipative}} &= (J_a^\mu)_{\text{ideal}} + \Upsilon_a^\mu. \end{aligned} \quad (4.136)$$

As for the ideal fluid, we require that the time-component of the energy-momentum tensor is the energy density  $\epsilon$ , i. e.  $u_\mu (T^{\mu\nu})_{\text{dissipative}} = -\epsilon u^\nu$ , and the time component of the currents is the charge density  $\rho_a$ , i. e.  $u_\mu (J_a^\mu)_{\text{dissipative}} = -\rho_a$ . These relations are equivalent to demanding that the dissipative contributions are orthogonal to the fluid velocity,

$$u_\mu \Pi^{\mu\nu} = 0, \quad u_\mu \Upsilon_a^\mu = 0, \quad (4.137)$$

and lead to the *Landau frame*. In addition, we have to find expressions for the new terms  $\Pi^{\mu\nu}$ ,  $\Upsilon_a^\mu$  in terms of the fluid velocity and thermodynamic variables. For this purpose we consider the divergence of the entropy current and demand that it must be non-negative. As in the ideal case by using the conservation of the energy-momentum tensor, we derive

$$T \nabla_\mu (su^\mu) = \mu^a \nabla_\mu \Upsilon_a^\mu + u_\nu \nabla_\mu \Pi^{\mu\nu}, \quad (4.138)$$

where now the dissipative terms appear and may lead to an entropy production. Using (4.137) we can rewrite the equation as

$$\nabla_\mu \left( su^\mu - \frac{\mu}{T} \Upsilon^\mu \right) = -\Upsilon_a^\mu \nabla_\mu \frac{\mu^a}{T} - \frac{\Pi^{\mu\nu}}{T} \nabla_\mu u_\nu. \quad (4.139)$$

The left hand side must be the divergence of the entropy current, i. e.  $(J_s^\mu)_{\text{dissipative}} = su^\mu - \frac{\mu^a}{T} \Upsilon_a^\mu$  such that the right hand side has to be positive. Thus, the dissipative part of the energy-momentum tensor must be a linear function of derivatives of the fluid velocity, while the dissipative part of the currents must be a linear function of the derivatives of the chemical potentials,

$$\begin{aligned} \Pi^{\mu\nu} &= -2\eta\sigma^{\mu\nu} - \zeta\theta P^{\mu\nu}, \\ \Upsilon_a^\mu &= -\kappa_{ab} P^{\mu\nu} \nabla_\nu \frac{\mu^b}{T}, \end{aligned} \quad (4.140)$$

where  $\eta$ ,  $\zeta$  and  $\kappa_{ab}$  must be semi-positive definite. The two-tensor of the derivatives of the fluid velocity is decomposed into a symmetric traceless part  $\sigma^{\mu\nu}$  and a trace

part  $\theta$  defined as

$$\begin{aligned}\theta &= P^{\mu\nu}\nabla_\mu u_\nu, \\ \sigma^{\mu\nu} &= \frac{1}{2}P^{\mu\lambda}P^{\nu\rho}(\nabla_\lambda u_\rho + \nabla_\rho u_\lambda) - \frac{1}{d-1}\theta P^{\mu\nu}.\end{aligned}\quad (4.141)$$

These are the possible terms in the hydrodynamic expansion which contain one derivative. The parameters  $\eta$ ,  $\zeta$  and  $\kappa_{ab}$  are the transport coefficients denoted as shear viscosity and bulk viscosity, while  $\kappa_{ab}$  is related to the charge diffusion matrix  $D_{ab}$  if we express the chemical potentials in terms of the charge densities. It is possible to also write down higher order terms in the hydrodynamic expansion (see e.g. [136]). However, in this thesis we will restrict ourselves to the first order expansion. For a conformal fluid with traceless energy-momentum tensor, the bulk viscosity is always zero,  $\zeta = 0$ .

#### 4.4.2 Hydrodynamic Modes

The hydrodynamic description we discussed above leads to three propagating modes: a sound mode, a shear mode and a diffusion mode. These modes give rise to dispersion relations  $\omega(q)$  which we now study. In the following we work in the local rest frame  $u^t = 1$  and choose the spatial momentum along the  $x$  direction which breaks the rotational group down to the little group  $SO(d-2)$ . This allows us to distinguish different fluctuations. The non-trivial helicity one fluctuations which compose the *shear mode* are the momentum  $T^{0i}$  and the stress  $T^{xi}$ , where  $i$  labels the spatial directions orthogonal to the  $x$  direction. Their equations of motion are

$$\begin{aligned}T^{xi} &= -\frac{\eta}{\epsilon + P}\nabla^x T^{ti}, \\ \nabla_t T^{ti} &= -\nabla_x T^{xi}.\end{aligned}\quad (4.142)$$

These two equations can be combined into a diffusion equation for the momentum  $T^{ti}$  with a dispersion relation

$$\omega = -i\frac{\eta}{\epsilon + p}q^2.\quad (4.143)$$

We see that the momentum diffusion constant  $D_m$  is given in terms of thermodynamic quantities and the shear viscosity.

The interesting helicity zero modes are fluctuations of the energy  $\tilde{T}^{tt} = T^{tt} - \epsilon$ , the momentum  $T^{tx}$ , the fluctuations of the pressure  $\tilde{T}^{xx} = T^{xx} - p$ , the charge density  $\rho_a$  and the current  $J^x$ . For the charge density we find again a diffusion equation,  $J^x = -D\nabla^x \rho$ , by combining the charge conservation equation and the definition of the longitudinal current.  $D$  is the *charge diffusion* matrix. Its dispersion relation is  $\omega = -iDq^2$ . For the components of the energy-momentum tensor we obtain

$$\begin{aligned}0 &= \nabla_t \tilde{T}^{tt} + \nabla_x T^{xt}, \\ 0 &= \nabla_t T^{tx} + \nabla_x \tilde{T}^{xx}, \\ \tilde{T}^{xx} &= -\frac{1}{\epsilon + p}\left(\frac{2d-4}{d-1}\eta + \zeta\right)\nabla_x T^{tx}.\end{aligned}\quad (4.144)$$

Using  $\tilde{T}^{xx} = \partial p / \partial \epsilon \tilde{T}^{tt}$ , the equations can be written as

$$\begin{aligned} 0 &= \nabla_t^2 \tilde{T}^{tt} - v_s^2 \nabla_x^2 \tilde{T}^{tt} \\ 0 &= \nabla_t T^{tx} - \frac{1}{\epsilon + p} \left( \frac{2d-4}{d-1} \eta + \zeta \right) \nabla_x^2 T^{tx}, \end{aligned} \quad (4.145)$$

which leads to the dispersion relation

$$\omega = v_s q - \frac{i}{2} \frac{1}{\epsilon + p} \left( \frac{2d-4}{d-1} \eta + \zeta \right) q^2 \quad \text{with } v_s^2 = \frac{\partial P}{\partial \epsilon}. \quad (4.146)$$

We observe that the *speed of sound*  $v_s$  is completely determined by thermodynamic quantities and the *sound attenuation*  $\Gamma$  is given in terms of thermodynamic quantities as well as the shear and bulk viscosity. For a conformal fluid, the sound velocity is constant,  $v_s^2 = 1/(d-1)$ , and the sound attenuation  $\Gamma$  is given in terms of the momentum diffusion constant  $D_m$ ,  $\Gamma = (d-2)/(d-1)D_m$ .

### 4.4.3 Kubo's Formula for Viscosity

As mentioned above, hydrodynamics can be seen as an effective field theory and the transport coefficients can be determined by the microscopic theory. Above we have already seen that the charge diffusion can be extracted from the dispersion relation of the diffusion mode.

In this section we show that the viscosities can be obtained from the low-energy behavior of Green's functions. For this purpose we consider a fluid at rest  $u^t = 1$  in a flat background metric  $\eta_{\mu\nu}$  which has fluctuations  $h_{\mu\nu}$ . Equation (4.140) determines the response of the system due to these metric fluctuations,

$$\Pi^{ij} = -i\omega \left[ \eta h^{ij} + \left( \frac{\eta}{d-1} + \frac{\zeta}{2} \right) h_k^k \delta^{ij} \right], \quad (4.147)$$

at zero spatial momentum,  $q = 0$ . This response can also be calculated by the retarded Green's function (4.77) which allows us to identify

$$\begin{aligned} G_{ij,ij}^R(\omega, 0) &= \int dt d\mathbf{x} e^{i\omega t} \theta(t) \langle [T_{ij}(t, \mathbf{x}), T_{ij}(0, 0)] \rangle \\ &= -i\eta\omega + \mathcal{O}(\omega^2), \quad \text{for } i \neq j, \\ G_{ii,ii}^R(\omega, 0) &= \int dt d\mathbf{x} e^{i\omega t} \theta(t) \langle [T_{ii}(t, \mathbf{x}), T_{ii}(0, 0)] \rangle \\ &= -i\omega \left( \eta + \frac{d-1}{2} \zeta \right) + \mathcal{O}(\omega^2), \end{aligned} \quad (4.148)$$

such that we can write down Kubo's formula for the shear viscosity,

$$\eta = - \lim_{\omega \rightarrow 0} \frac{1}{\omega} G_{ij,ij}^R(\omega, 0) \quad \text{with } i \neq j. \quad (4.149)$$

Since we can calculate Green's functions on the gravity side, this formula allows us to determine the shear viscosity for the dual field theory by a gravity calculation.

#### 4.4.4 Transport in $\mathcal{N} = 4$ Super-Yang-Mills Theory

In the hydrodynamic expansion discussed above, we found transport coefficients which can be determined only if a microscopic theory is available. Since the gauge/gravity duality gives us a microscopic description for strongly coupled field theories, its transport properties are computable. At first we focus on the conformal  $\mathcal{N} = 4$  Super-Yang-Mills theory. The undetermined transport coefficients are the shear viscosity and the  $R$ -charge diffusion constant.

##### $R$ -Charge Diffusion

In order to describe charge diffusion, the charge density  $\rho$  has to fluctuate which corresponds to perturbations of the time component of the gauge  $a_t$  on the gravity side<sup>9</sup>. The field  $a_t$  transforms as a helicity zero mode under the  $SO(2)$  little group and, thus, can couple to any other helicity zero mode. However, at zero charge density there is no coupling to the metric fluctuations, so the field can only couple to the longitudinal gauge field component  $a_x$ . We consider the spatial momentum to be in the  $x$  direction, i. e.  $k^\mu = (\omega, q, 0, 0)$ . The gauge invariant field we have to consider is the longitudinal electric field defined below (4.113). However, it is easier to consider the gauge fields  $a_t$  and  $a_x$  [53]. Their equations of motion in the coordinates defined in (4.35) are

$$0 = a_t'' - \frac{1}{z}a_t' - \frac{1}{f}(\omega q a_x + q^2 a_t), \quad (4.150a)$$

$$0 = a_x'' + \frac{f'}{f}a_x' - \frac{1}{f^2}(\omega q a_t + \omega^2 a_x), \quad (4.150b)$$

$$0 = \omega a_t' + q f a_x', \quad (4.150c)$$

where the prime denotes the derivative with respect to the radial direction  $z$  and we set  $z_h = 1$ . Combining the first and third equation, we obtain

$$a_t''' + \left(\frac{f'}{f} - \frac{1}{z}\right)a_t'' + \left(\frac{1}{z^2} - \frac{f'}{z f} + \frac{\omega^2 - q^2 f}{f^2}\right)a_t' = 0, \quad (4.151)$$

which simplifies to

$$\ddot{a}_t + \left(\frac{\dot{f}}{f} + \frac{1}{u}\right)\dot{a}_t + \left(\frac{\omega^2 - q^2 f}{u f^2}\right)a_t = 0, \quad (4.152)$$

by using the transformation  $u = z^2$  [53]. We can solve this equation in the hydrodynamic limit, i. e.  $\omega \ll 1$  and  $q \ll 1$  by introducing the ansatz

$$\dot{a}_t = (1 - u)^\beta (F_0(u) + \omega F_1(u) + q^2 G_1(u) + \dots). \quad (4.153)$$

<sup>9</sup>In section 4.3.2 we showed that the different flavor fields decouple. The diffusion matrix becomes one constant and we can simply neglect the flavor index.

The index  $\beta$  is determined by enforcing that the other functions are regular. The ingoing boundary condition at the horizon singles out  $\beta = -i\mathfrak{w}/2$ . The equations of motion for the other functions are

$$\ddot{F}_0 + \left( \frac{1}{u} + \frac{\dot{f}}{f} \right) \dot{F}_0 = 0, \quad (4.154a)$$

$$\ddot{F}_1 + \left( \frac{1}{u} + \frac{\dot{f}}{f} \right) \dot{F}_1 = -\frac{i}{2uf}(1+2u)F_0 + \frac{i}{f}(1+u)\dot{F}_0, \quad (4.154b)$$

$$\ddot{G}_1 + \left( \frac{1}{u} + \frac{\dot{f}}{f} \right) \dot{G}_1 = \frac{1}{uf}F_0. \quad (4.154c)$$

The two independent solution to the homogenous equation are a constant  $C$  and  $\log((u^2 - 1)/u^2)$  which is divergent at the horizon, i. e.  $u = 1$ . Thus, we get  $F_0 \equiv C$ . The inhomogenous solution for  $F_1$  and  $G_1$  may be found by integration,

$$F_1 = \frac{iC}{2} \log \frac{2u^2}{1+u}, \quad G_1 = C \log \frac{1+u}{2u}. \quad (4.155)$$

Inserting the first order solution for  $\dot{a}_t$  into (4.150a) and taking the limit  $u \rightarrow 0$  allows us to fix the constant  $C$  in terms of the boundary values of the gauge fields,  $\lim_{u \rightarrow 0} a_t = a_t^0$  and  $\lim_{u \rightarrow 0} a_x = a_x^0$ ,

$$C = -\frac{\mathfrak{q}(\mathfrak{q}a_t^0 + \mathfrak{w}a_x^0)}{\mathfrak{q}^2 - i\mathfrak{w} + \mathcal{O}(\mathfrak{w}^2, \mathfrak{w}\mathfrak{q}^2, \mathfrak{q}^4)} = -\frac{\mathfrak{q}E_L^0}{\mathfrak{q}^2 - i\mathfrak{w} + \mathcal{O}(\mathfrak{w}^2, \mathfrak{w}\mathfrak{q}^2, \mathfrak{q}^4)}. \quad (4.156)$$

The quasinormal mode solution defined by  $E_L^0 = 0$  can only be non-trivial if  $\mathfrak{q}^2 - i\mathfrak{w} = 0$  which determines the dispersion relation  $\omega = -i/(2\pi T)\mathfrak{q}^2$ . Comparing with the dispersion relation for charge diffusion defined in section 4.4.1, we can read off the charge diffusion constant,

$$D = \frac{1}{2\pi T}. \quad (4.157)$$

## Shear Viscosity

The shear viscosity is the other undetermined transport coefficient. It can be determined by Kubo's formula written down in (4.149). In order to determine the Green's function for the energy-momentum tensor, we have to study the off-diagonal metric fluctuations. At zero momentum we can for instance take  $h_{xy}$ . We consider for now a very general setup similar to the one studied in [193] in which we calculate the shear viscosity and find that the result is universal. For this purpose we study gravity coupled to some matter fields given by the Lagrangian  $\mathcal{L}_m$  such that the action becomes

$$S = \int d^{d+1}x \sqrt{-g} \left( \frac{\mathcal{R}}{2\kappa^2} + \mathcal{L}_m \right). \quad (4.158)$$

Notice that there are now higher derivative terms in this action. In general, this action allows for a black hole solution which features an  $SO(d-1)$  rotational symmetry. Its metric including the perturbation  $h_{12}(t, r)$  is given by

$$ds^2 = -c_1^2(r)dt^2 + c_2^2(r)d\mathbf{x}^2 + c_3^2(r)dr^2 + \epsilon h_{12}(t, r)dx^1 dx^2. \quad (4.159)$$

It is more convenient to work with the field  $\psi = 1/2c_2^{-2}h_{12}$  instead of  $h_{12}$ . This field is the only one that transforms as a helicity two mode under the little group. Thus, it cannot couple to any other field present in the system.

The action second order in this fluctuation becomes

$$S^{(2)} = \int d^{d+1}x \sqrt{-g^{(0)}} \left[ \frac{\mathcal{R}^{(2)}}{2\kappa^2} - \frac{1}{2}\psi^2 \left( \frac{\mathcal{R}^{(0)}}{2\kappa^2} + \mathcal{L}_m \right) \right], \quad (4.160)$$

where we used  $\mathcal{R} = \mathcal{R}^{(0)} + \epsilon^2 \mathcal{R}^{(2)}$  and  $\sqrt{-g} = \sqrt{-g^{(0)}}(1 - 1/2\epsilon^2 \psi^2)$ . Einstein's equations at zero order in the fluctuations

$$\mathcal{R}_{MN} - \frac{1}{2}g_{MN}\mathcal{R} = \frac{1}{2}g_{MN}\mathcal{L}_m - \mathcal{K}_{MN} \quad \text{with } \mathcal{K}_{MN} = \frac{\delta \mathcal{L}_m}{\delta g^{MN}} \quad (4.161)$$

lead to the identities

$$\begin{aligned} \frac{\mathcal{R}^{(0)}}{2\kappa^2} + \mathcal{L}_m &= \frac{2}{1-d}(\mathcal{L}_m - \mathcal{K}), \\ \frac{\mathcal{R}_{x^1}^{x^1(0)}}{2\kappa^2} &= \frac{1}{1-d}(\mathcal{L}_m - \mathcal{K}) - \mathcal{K}_{x^1}^{x^1} = \frac{1}{2} \left( \frac{\mathcal{R}^{(0)}}{2\kappa^2} + \mathcal{L}_m \right) - \mathcal{K}_{x^1}^{x^1}. \end{aligned} \quad (4.162)$$

In addition, the Ricci scalar second order in the fluctuation can be expressed as

$$\begin{aligned} \sqrt{-g^{(0)}}\mathcal{R}^{(2)} &= \sqrt{-g^{(0)}} \left[ \frac{1}{2c_1^2}(\partial_t \psi)^2 - \frac{1}{2c_3^2}(\partial_r \psi)^2 \right] \\ &+ \left[ -\partial_t \left( \frac{2c_2^{d-1}c_3}{c_1} \psi \partial_t \psi \right) + \partial_r \left( \frac{2c_2^{d-1}c_1}{c_3} \psi \partial_r \psi + \frac{c_1 c_2^{d-2} c_2'}{c_3} \psi^2 \right) \right] \\ &+ \sqrt{-g^{(0)}}\psi^2 \mathcal{R}_{x^1}^{x^1(0)}, \end{aligned} \quad (4.163)$$

such that the action to second order in the fluctuations simplifies to

$$\begin{aligned} S^{(2)} &= \frac{1}{2\kappa^2} \int d^{d+1}x \left\{ \sqrt{-g^{(0)}} \left[ \frac{1}{2c_1^2}(\partial_t \psi)^2 - \frac{1}{2c_3^2}(\partial_r \psi)^2 \right] \right. \\ &\quad - \left[ \partial_t \left( \frac{2c_2^{d-1}c_3}{c_1} \psi \partial_t \psi \right) - \partial_r \left( \frac{2c_2^{d-1}c_1}{c_3} \psi \partial_r \psi + \frac{c_1 c_2^{d-2} c_2'}{c_3} \psi^2 \right) \right] \\ &\quad \left. - 2\kappa^2 \sqrt{-g^{(0)}}\psi^2 \mathcal{K}_{x^1}^{x^1} \right\}. \end{aligned} \quad (4.164)$$

This result agrees with the result in [193] if  $\mathcal{K}_{x^1}^{x^1} = 0$ . Since we consider isotropic fluids, we expect that  $\mathcal{K}_{x^1}^{x^1} = 0$ . For instance a non-zero result for a kinetic term of a scalar or a gauge field is only achieved if the rotational symmetry is broken. Therefore, we assume from now on that  $\mathcal{K}_{x^1}^{x^1} = 0$  such that the action becomes the action of minimal coupled scalar field

$$S = -\frac{1}{2} \int d^{d+1}x \sqrt{-g^{(0)}} \frac{(\partial\psi)^2}{q}, \quad (4.165)$$

where  $q = 2\kappa^2$  is the coupling constant. There is an additional on-shell boundary contribution from the Gibbons-Hawking term [193],

$$S_{\text{on-shell}} = -\frac{1}{2\kappa^2} \int d^d x \sqrt{-\gamma} \frac{1}{2} g^{(0)rr} \psi \partial_r \psi, \quad (4.166)$$

where  $\gamma$  is the induced boundary metric.

In the Hamiltonian formalism, the equation of motion in Fourier space can be written as [194]

$$\partial_r \Pi = \frac{\sqrt{-g^{(0)}}}{q} g^{(0)rr} g^{(0)\mu\nu} k_\mu k_\nu \psi \quad \text{with} \quad \Pi = -\frac{\sqrt{-g^{(0)}}}{q} g^{(0)rr} \partial_r \psi. \quad (4.167)$$

and using the recipe discussed in section 4.3.1 the Green's function becomes

$$G(k) = \lim_{r \rightarrow \infty} \frac{\Pi(r, k)}{\psi(r, k)}. \quad (4.168)$$

Using Kubo's formula (4.149), the shear viscosity  $\eta$  is given by

$$\eta = \lim_{k_\mu \rightarrow 0} \lim_{r \rightarrow \infty} \frac{\Pi(r, k)}{i\omega \psi(r, k)}. \quad (4.169)$$

Since the profile for  $\Pi$  and  $\omega\psi$  are trivial at low energy [194], i. e.  $\partial_r \Pi = 0 + \mathcal{O}(k^2)$  and  $\partial_r(\omega\psi) = 0 + \mathcal{O}(k)$ , the above expression can also be evaluated at the horizon  $r = r_h$ ,

$$\eta = \lim_{k_\mu \rightarrow 0} \frac{\Pi(r_h, k)}{i\omega \psi(r_h, k)}. \quad (4.170)$$

At the horizon the field  $\psi$  has to satisfy the ingoing boundary condition  $\psi \sim (r - r_h)^{-\frac{i\omega}{4\pi T}}$  where  $1/T = 4\pi \sqrt{g_{rr}^{(0)}/g_{tt}^{(0)}}|_{r=r_h}$  such that the expression for the shear viscosity simplifies to [194]

$$\eta = \frac{1}{q} \sqrt{\frac{-g^{(0)}}{g_{rr} g_{tt}}} \Big|_{r=r_h} = \frac{1}{q} \frac{A}{V}, \quad (4.171)$$

where  $A$  is the area of the horizon and  $V$  is the spatial volume of the dual field theory. For any horizon the entropy density  $s$  is given in terms of the horizon

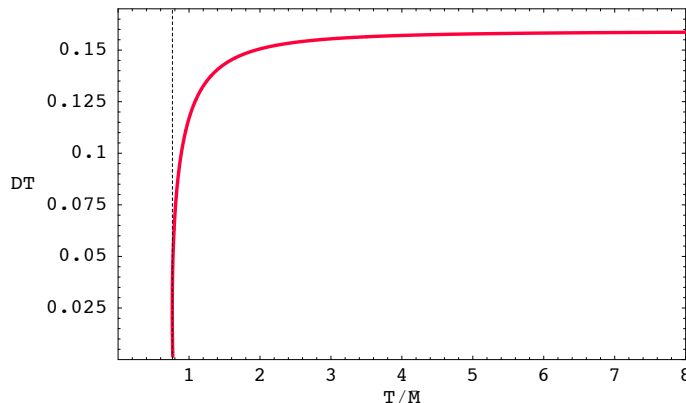


**Figure 4.24:** Flavor diffusion constant  $D$  times the temperature  $T$  versus the temperature  $T/M = m^{-1}$  as defined in (4.58). The dotted line marks the temperature of the phase transition studied in section 4.2.3. For the flat embedding  $m = 0$ , we obtain  $DT = 1/(2\pi)$  which coincides with the result found for  $R$ -charge diffusion (4.157). This figure is taken from [184].

area, i. e.  $s = 2\pi A/(\kappa^2 V)$ . In addition, the coupling  $q$  is given by the gravitational coupling such that the ratio of shear viscosity to entropy density is universal,

$$\frac{\eta}{s} = \frac{1}{4\pi}. \quad (4.172)$$

The assumptions we used here to derive this formula are satisfied for any isotropic fluid which has a dual description in Einstein gravity. As described in section 3.1.1, an Einstein gravity dual describes a large  $N_c$  gauge theory at infinite 't Hooft coupling  $\lambda$ . Since the entropy measures degrees of freedom, the above formula states that for any large  $N$  gauge theory at infinite 't Hooft coupling  $\lambda$ , the shear viscosity per degree of freedom is constant. This is an impressive universal result.

#### 4.4.5 Transport from Flavor Branes

By embedding  $N_f$  flavor branes in the AdS space, we introduce fundamental fields into the dual gauge theory which are charged under a global  $U(N_f)$  flavor symmetry. This introduces flavor charges and, thus, flavor charge diffusion. In order to calculate the diffusion matrix, we study the fluctuations of the dual gauge fields as in the determination of the  $R$ -charge diffusion constant above. The gauge field dual to the flavor charge now lives on the flavor brane. Its embedding changes if we vary the mass of the fundamental fields (see section 4.2.3). Thus, the equations of motion for the gauge field depend on the quark mass which induces a dependence of the diffusion matrix on the quark mass. Since the different flavor fields decouple the diffusion matrix is proportional to the identity matrix. The dispersion relation for the diffusion mode is shown in figure 4.23. Using the dispersion relation  $\omega = -iDq^2$ , we can read off the diffusion constant which is shown in figure 4.24.

# Holography at Finite Baryon and Isospin Chemical Potentials

As described in the previous chapter, gauge/gravity duality is a suitable framework to study strongly coupled systems at finite temperature, such as the quark-gluon plasma. If the system has conserved charges, e.g. the baryon charge in QCD, it is possible to introduce finite chemical potentials for these charges. By varying the chemical potentials, the state of the system may change. An overview of the preferred phases at different values for temperature and chemical potentials is given in the phase diagram. In addition, the real-time response of the system in the different phases can be investigated via gauge/gravity duality.

A sketch of the *QCD phase diagram* is shown in figure 5.1. The critical temperature for the phase transition between the hadronic gas and the quark-gluon plasma is expected to decrease as the baryon chemical potential is increased. Holographically, the same behavior of the deconfinement transition has been observed in [70], where charged AdS black holes have been studied. Also the phase transition from the phase of stable mesons to the phase of unstable mesons behaves like this as discussed in section 5.2.2. The corresponding phase diagram is presented in figure 5.8. The similarity in the phase diagrams is that bound states, hadrons and mesons, melt as the temperature and/or chemical potential is increased. By studying the quasinormal modes which are related to poles of the corresponding Green's functions at finite temperature and finite chemical potential, we can observe how the stable bound states evolve into broad resonances. As presented in section 5.3.1 and 5.3.2 this evolution differs depending on the value of the temperature and chemical potential. We observe an interesting dependence of the location of the poles in the Green's functions on the temperature and the chemical potential. This study has first been done in my own work [3].

A finite chemical potential introduces charge carriers into the systems. Strongly coupled systems with charge carriers are very common in *condensed matter* systems. Important examples are strongly coupled electron systems which are expected to have a rich phase structure. But how can a strongly coupled electron system be de-

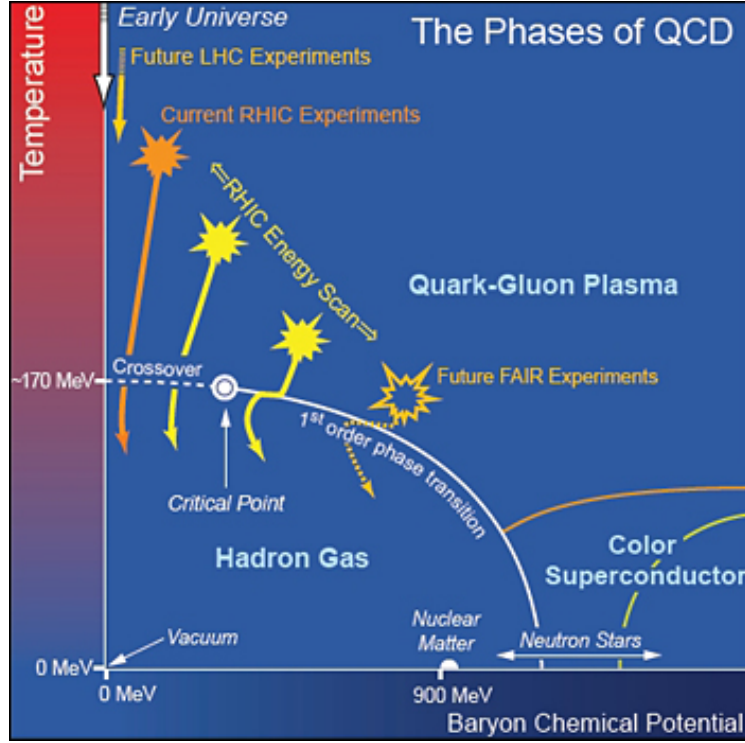


**Figure 5.1:** Expected phase diagram of QCD. The figure is taken from [195].

scribed by a large  $N$  gauge theory? The idea is that the condensed matter system is controlled by an effective field theory in the IR which allows a large  $N$  limit. Several examples are given in [78]. Let us, for instance, consider the three-dimensional Ising model,

$$H = \sum_{\langle ij \rangle} J_{ij} S_i \cdot S_j, \quad (5.1)$$

where  $\langle ij \rangle$  denotes nearest neighbors and  $S_i$  are spin one half degrees of freedom. Now we choose the couplings  $J_{ij}$  to take alternately the values,  $J$  and  $J/g$  with  $J > 0$  and  $g \in [1, \infty)$ . For  $g = 1$ , the model coincides with the antiferromagnetic Heisenberg model with a Néel ordered ground state. Whereas for  $g \rightarrow \infty$  the pairs with coupling  $J$  form spin singlets such that the ground state is given by decoupled dimers. In both cases, fluctuations about the ground state are described by the  $O(N)$  model with  $N = 3$ . Its action is given by

$$S = \int d^3x ((\partial\Phi)^2 + r\Phi^2 + u\Phi^4), \quad (5.2)$$

where  $\Phi$  is an  $N$ -dimensional vector. As QCD, this theory allows an large  $N$  limit. We may use gauge/gravity duality to study these effective field theories for strongly coupled condensed matter systems. We may even assume that gravity models give

rise to new effective field theories which may describe condensed matter systems in the IR.

Especially, gauge/gravity duality is expected to be useful to study systems which contain a *quantum critical point* such as *heavy fermion systems* and *cuprate high  $T_c$  superconductors*. The field theory dual to the extremal Reissner-Nordström black hole is scale invariant in the IR. Therefore, it describes a quantum critical point. Consequently, we assume that the finite temperature Reissner-Nordström black hole characterize the quantum critical region which is in particular exciting. For instance the so far not understood phenomena, known as *non-Fermi liquids* and *high  $T_c$  superconductivity*, are located in this region. The condensed phases which we study in the next chapter are anticipated to be related to high  $T_c$  superconductors. The condensation is triggered by an instability which we obtain by the investigation of the spectral function at large isospin chemical potentials. On the field theory side, this instability is related to Bose-Einstein condensation: The effective mass  $m$  of bosonic fields get lowered due to a chemical potential  $\mu$ , i. e. there is a shift in the mass term  $m^2 \mapsto m^2 - \mu^2$ . When the mass square becomes negative, the field has a runaway potential and starts to condense. A detailed description of this instability is given in section 5.5.

A similar instability can be found if in contrast to an isospin chemical potential, a magnetic field is switched on. This instability has been presented in my own work [7] where the  $SU(2)$  Einstein-Yang-Mills theory is discussed. This analysis is motivated by recent field theory studies within QCD [139–142] where it has been proposed that a strong magnetic field may generate superconductivity in the QCD vacuum. Essentially, in these papers it has been argued that in a strong magnetic field, a gluon-mediated attraction between quarks and antiquarks of different flavor leads to a colorless spin-triplet bound state with quantum numbers of an electrically charged  $\rho^\pm$  meson. These quark-antiquark pairs condense to form a new ground state. Within gauge/gravity duality, a similar result has been obtained in the Sakai-Sugimoto model in [196, 197].

This chapter is organized as follows: In section 5.1 we discuss how chemical potentials can be switched on in field theories with conserved charges. Using the AdS/CFT dictionary, we translate this result into a gravity description which is used in section 5.2. The gravity dual of  $\mathcal{N} = 4$  Super-Yang-Mills theory at finite  $R$ -charge chemical potential is the AdS Reissner-Nordström black hole which is investigated in section 5.2.1. In section 5.2.2 we introduce flavor chemical potentials for the  $\mathcal{N} = 2$  flavored theory. Afterwards the response due to small fluctuations in the flavor fields is discussed in section 5.3. We focus on spectral functions at finite baryon or isospin chemical potential. Especially, we discuss the dependence of the location and the shape of the quasiparticle resonances on the chemical potentials in section 5.3.1. In order to study these structures in more detail at finite baryon chemical potential, we determine the quasinormal mode spectrum of the flavor fields in section 5.3.2. In section 5.4 we collect some results in the hydrodynamic regime.

## 5.1 Field Theory at Finite Chemical Potentials

In addition, to the temperature, we may consider other control parameters. The set of control parameters determines the state of the field theory. If the field theory features conserved currents, we may consider chemical potentials  $\mu^a$  for the corresponding charges  $N_a$ . The chemical potential measures the amount of energy needed to introduce the corresponding particle into the system. As finite temperature allows for fluctuation in the energy of the system, finite chemical potentials introduce fluctuations in their corresponding charge densities. Thus, a system can be found in different states and the density matrix is given by

$$\rho = \frac{e^{-\beta(H - \mu^a N_a)}}{Z_{\text{grand}}}, \quad \text{with } Z_{\text{grand}} = \text{Tr} e^{-\beta(H - \mu^a N_a)}. \quad (5.3)$$

The entropy defined by (4.12) becomes

$$S = \langle -\ln \rho \rangle = \beta (\langle E \rangle - \mu^a \langle N_a \rangle) + \ln Z_{\text{grand}}, \quad (5.4)$$

in the *grand canonical ensemble* which we study here. As in the canonical ensemble, we obtain from this analysis the thermodynamic potential. Here it is the *grand potential*,

$$\Omega(T, V, \mu^a) = \langle E \rangle - TS - \mu^a \langle N_a \rangle = -T \ln Z_{\text{grand}}, \quad (5.5)$$

which is related to the free energy by a Legendre transformation,  $\Omega = F - \mu^a \langle N_a \rangle$ . Using (4.16) the variation of the grand potential becomes

$$d\Omega = -pdV - SdT - N_a d\mu^a. \quad (5.6)$$

Let us now discuss a more suitable way to introduce a chemical potential in the context of gauge/gravity duality. The charges  $N_a$  can be seen as the integral of the time component of the corresponding conserved currents  $J_a^\mu$ . These currents may be coupled to a background gauge fields  $A_\mu^a$ , such that the Hamiltonian of the system gets shifted  $H \rightarrow H - \int d^3x J_a^\mu A_\mu^a$ . If now only the time components of the gauge fields are non-zero and identical to the chemical potentials, i. e.  $A_t^a = \mu^a$ , we obtain the desired shift in the Hamiltonian  $H \rightarrow H - \mu^a N_a$ . Thus, we can describe a system at finite chemical potentials by switching on non-zero time components of the background gauge fields.

This formulation is very suitable in the context of gauge/gravity duality. The currents  $J_a^\mu$ , whose time components are the charge densities, are dual to gauge fields  $A_M^a$  on the gravity side. The leading order terms in the boundary expansion source the currents. Thus, they can be understood as the background gauge fields on the field theory side, while the subleading terms describe the vev of these currents. By switching on only the time component of gauge fields on the gravity side, we can describe chemical potentials by the leading order terms and the charge densities by the subleading terms.

## 5.2 Physics in Equilibrium

As described in the last section, the gravity dual of a field theory at finite chemical potentials has to contain a non-zero time component of the gauge fields dual to the corresponding conserved currents. A well-known gravity solution of this type is the Reissner-Nordström black hole where the black hole is charged. The Reissner-Nordström black hole in an asymptotic AdS space is presented in the next section. In  $AdS_5$  this solution is dual to  $\mathcal{N} = 4$  Super-Yang-Mills with a finite chemical potential for the  $R$ -current. Another system we will study is given by the flavor branes where the time component of the gauge fields on these flavor branes are non-zero. In this system the finite gauge fields induce chemical potentials for the fundamental fields, i. e. quark chemical potentials.

### 5.2.1 AdS Reissner-Nordström Black Hole

Let us now discuss the Reissner-Nordström black hole in asymptotically AdS space. In addition to gravity, there are gauge fields transforming under some gauge group, e. g.  $U(N)$ , such that the system is described by the Einstein-Yang-Mills action. In the following we will specialize to  $(4+1)$ -dimensional asymptotically AdS space and to the gauge group  $U(2)$ . We split the gauge field into an  $SU(2)$  part with field strength tensor

$$F_{\mu\nu}^a = \partial_\mu A_\nu^a - \partial_\nu A_\mu^a + \epsilon^{abc} A_\mu^b A_\nu^c, \quad (5.7)$$

where  $\epsilon^{abc}$  is the total antisymmetric tensor and  $\epsilon^{123} = +1$ , and into a  $U(1)$  part with field strength tensor

$$\mathcal{F}_{\mu\nu} = \partial_\mu A_\nu - \partial_\nu A_\mu. \quad (5.8)$$

In analogy with QCD, we call the  $U(1)$  baryon symmetry and the  $SU(2)$  isospin symmetry. With this split, the Einstein-Yang-Mills action becomes

$$S = \int d^5x \sqrt{-g} \left[ \frac{1}{2\kappa_5^2} (\mathcal{R} - \Lambda) - \frac{1}{4\hat{g}_{\text{MW}}^2} \mathcal{F}_{\mu\nu} \mathcal{F}^{\mu\nu} - \frac{1}{4\hat{g}_{\text{YM}}^2} F_{\mu\nu}^a F^{a\mu\nu} \right], \quad (5.9)$$

where  $\kappa_5$  is the five-dimensional gravitational constant,  $\Lambda = -12/R^2$  is the cosmological constant, with  $R$  being the AdS radius,  $\hat{g}_{\text{MW}}$  the Maxwell and  $\hat{g}_{\text{YM}}$  the Yang-Mills coupling.

The Einstein and Yang-Mills equations derived from the above action are

$$\begin{aligned} \mathcal{R}_{\mu\nu} + \frac{4}{R^2} g_{\mu\nu} &= \kappa_5^2 \left( T_{\mu\nu} - \frac{1}{3} T_\rho^\rho g_{\mu\nu} \right), \\ \nabla_\mu F^{a\mu\nu} &= -\epsilon^{abc} A_\mu^b F^{c\mu\nu}, \\ \nabla_\mu \mathcal{F}^{\mu\nu} &= 0, \end{aligned} \quad (5.10)$$

where the Yang-Mills energy-momentum tensor  $T_{\mu\nu}$  is

$$T_{\mu\nu} = \frac{1}{\hat{g}_{\text{YM}}^2} \left[ F_{\mu\rho}^a F_\nu^{a\rho} - \frac{1}{4} g_{\mu\nu} F_{\sigma\rho}^a F^{a\sigma\rho} \right] + \frac{1}{\hat{g}_{\text{MW}}^2} \left[ \mathcal{F}_{\mu\rho} \mathcal{F}_\nu^\rho - \frac{1}{4} g_{\mu\nu} \mathcal{F}_{\sigma\rho} \mathcal{F}^{\sigma\rho} \right]. \quad (5.11)$$

A known solution of these equations of motion is the AdS Reissner-Nordström black hole,

$$\begin{aligned}\phi(r) &= \mu_I - \frac{q_I}{r^2}, \quad \psi = \mu_B - \frac{q_B}{r^2} \quad \text{with} \quad q_i = \mu_i r_h^2, \\ N(r) &= r^2 - \frac{2m}{r^2} + \frac{2(\alpha_{\text{YM}}^2 q_I^2 + \alpha_{\text{MW}}^2 q_B^2)}{3r^4} \quad \text{with} \quad m = \frac{r_h^4}{2} + \frac{\alpha_{\text{YM}}^2 q_I^2 + \alpha_{\text{MW}}^2 q_B^2}{3r_h^2},\end{aligned}\tag{5.12}$$

where  $\alpha_{\text{MW}} = \kappa_5/\hat{g}_{\text{MW}}$ ,  $\alpha_{\text{YM}} = \kappa_5/\hat{g}_{\text{YM}}$  and  $N$  is the blackening factor in the metric

$$ds^2 = -N(r)dt^2 + \frac{dr^2}{N(r)} + r^2 d\mathbf{x}^2.\tag{5.13}$$

Notice that we set the AdS radius  $R$  to one by using a scaling transformation. The gauge fields are given by

$$\begin{aligned}A &= \phi(r)\tau^3 dt, \\ \mathcal{A} &= \psi(r)dt,\end{aligned}\tag{5.14}$$

where  $\tau^3 = \sigma^3/2i$  with  $\sigma^3$  the third Pauli matrix. The charges  $q_i$  are given in terms of the chemical potentials  $\mu_i$  since we enforce the gauge fields to vanish at the horizon. They must vanish in order to be well-define one forms,  $A = A_t dt$ , since the event horizon can be characterized as a Killing horizon where the Killing vector  $\partial_t$  vanishes [72]. In the field theory we introduce a baryon and isospin chemical potential,  $\mu_B$  and  $\mu_I$ , by the boundary values of the time components of the gauge fields,  $\phi$  and  $\psi$ . We consider the diagonal representations of the gauge group since we can rotate the flavor coordinates until the chemical potential lies in the third isospin direction. This is a gauge choice which breaks the  $SU(2)$  symmetry down to a  $U(1)$  symmetry which leaves  $\tau^3$  invariant. We call this symmetry therefore  $U(1)_3$ .

In the following it will be often convenient to work with dimensionless coefficients by scaling out factors of  $r_h$ . We, thus, define the dimensionless functions  $\tilde{m} = m/r_h^4$ ,  $\tilde{\phi}(r) = \phi(r)/r_h$  and  $\tilde{\psi}(r) = \psi(r)/r_h$ .

## Thermodynamics of $R$ -charge black holes

In this section we extract thermodynamic information from our solutions. The gravity solution describes thermal equilibrium in the boundary field theory. In order to extract thermodynamic quantities from the gravity solution, we use well-established methods of black hole thermodynamics.

The temperature  $T$  in the boundary field theory is identified with the Hawking temperature of the black hole. The Hawking temperature for our black hole solution is given by

$$T = \frac{\kappa}{2\pi} = \frac{r_h}{\pi} \left( 1 - \frac{\alpha_{\text{YM}}^2 \tilde{\mu}_B^2 + \alpha_{\text{MW}}^2 \tilde{\mu}_I^2}{3} \right),\tag{5.15}$$

where  $\kappa = \sqrt{\partial_\mu \xi \partial^\mu \xi}$  is the surface gravity of the black hole, with  $\xi$  being the norm of the timelike Killing vector. In the following we will often convert from the black hole radius  $r_h$  to the temperature  $T$  by inverting the above equation.

The entropy  $S$  of the boundary field theory is identified with the Bekenstein-Hawking entropy of the black hole,

$$S = \frac{2\pi}{\kappa_5^2} A_h = \frac{2V\pi r_h^3}{\kappa_5^2} = \frac{2\pi^4 V T^3}{\kappa_5^2} \left( 1 - \frac{\alpha_{\text{YM}}^2 \tilde{\mu}_I^2 + \alpha_{\text{MW}}^2 \tilde{\mu}_B^2}{3} \right)^{-3}, \quad (5.16)$$

where  $A_h$  is the area of the horizon and  $V$  the spatial volume of the Minkowski space.

The general statement of gauge/gravity duality which relates the field theory partition function to the gravity partition function may be used to calculate the thermodynamic potential of the boundary field theory, i. e. in our case the grand potential,  $\Omega = T I_{\text{on-shell}}$  where  $I_{\text{on-shell}}$  is the on-shell bulk action in Euclidean signature. The Euclidean action  $I$  splits into three parts, a bulk term, a Gibbons-Hawking term and counterterms,

$$I = I_{\text{bulk}} + I_{\text{GH}} + I_{\text{ct}}. \quad (5.17)$$

The counterterms are needed to cancel the divergences of the bulk action and Gibbons-Hawking term which appear on-shell. They are determined by holographic renormalization as described in section 4.2.1. Using the equations of motion, we obtain

$$I_{\text{bulk}}^{\text{on-shell}} = \frac{V}{T\kappa_5^2} r^2 N \Big|_{r=r_{\text{bdy}}}, \quad (5.18)$$

and

$$I_{\text{GH}}^{\text{on-shell}} = -\frac{1}{T\kappa_5^2} \int d^3x \sqrt{\gamma} \nabla_\mu n^\mu = -\frac{V}{\kappa_5^2} N r^3 \left( \frac{N'}{2N} + \frac{3}{r} \right) \Big|_{r=r_{\text{bdy}}}, \quad (5.19)$$

where  $\gamma$  is the induced metric on the  $r = r_{\text{bdy}}$  regulator hypersurface and  $n_\mu dx^\mu = 1/\sqrt{N(r)} dr$  is the outward-pointing normal vector. The only divergence in the bulk action and Gibbons-Hawking term comes from the infinite volume of the asymptotically AdS space, hence, the only non-trivial counterterm is

$$I_{\text{ct}}^{\text{on-shell}} = \frac{3}{T\kappa_5^2} \int d^3x \sqrt{\gamma} = \frac{3V}{\kappa_5^2} r^3 \sqrt{N} \Big|_{r=r_{\text{bdy}}}. \quad (5.20)$$

Finally, the grand potential  $\Omega$  is given by the mass of the black hole  $m$ ,

$$\Omega = T \lim_{r_{\text{bdy}} \rightarrow \infty} I_{\text{on-shell}} = -\frac{Vm}{\kappa_5^2}. \quad (5.21)$$

The baryon chemical potential  $\mu_B$  is simply the boundary value of  $\mathcal{A}_t(r) = \psi(r)$  while the isospin chemical potential  $\mu_I$  is the boundary value of  $A_t^3(r) = \phi(r)$ . The

baryon charge density  $\langle \mathcal{J}_t \rangle$  and isospin charge density  $\langle J_t^3 \rangle$  of the dual field theory may be extracted from the grand potential by

$$\begin{aligned}\langle \mathcal{J}_t \rangle &= -\frac{1}{V} \frac{\partial \Omega}{\partial \mu_B} = \frac{2\alpha_{\text{MW}}^2 q_B}{\kappa_5^2}, \\ \langle J_t^3 \rangle &= -\frac{1}{V} \frac{\partial \Omega}{\partial \mu_I} = \frac{2\alpha_{\text{YM}}^2 q_I}{\kappa_5^2}.\end{aligned}\tag{5.22}$$

The expectation value of the energy-momentum tensor of the dual field theory can be obtained by using (4.48). It is diagonal and the spatial components describing the pressure  $p$  are determined by  $\Omega$ , i. e.  $\Omega = -pV = -V\langle T_{ii} \rangle$  as expected from thermodynamics. In addition, it is traceless as expected for a conformal theory.

**Zero Temperature Limit** It is interesting to study the zero temperature limit of this setup since it can still contain a black hole. Using (5.15), zero temperature is equivalent in choosing the chemical potentials such that  $\alpha_{\text{YM}}^2 \tilde{\mu}_B^2 + \alpha_{\text{MW}}^2 \tilde{\mu}_I^2 = 3$  while  $r_h$  can be still finite. Due to the finite value of the horizon radius, the entropy is also finite and, thus, the ground state of the system must be degenerate. The near horizon geometry of the black hole features an  $AdS_2$  geometry since the blackening factor becomes  $N = 12(r - r_h)^2$  in the limit  $r \rightarrow r_h$ . According to the general conjecture of gauge/gravity duality, the dual field theory contains an one-dimensional conformal field theory, i. e. quantum mechanics, in the IR. Later we will see that this emergent conformal symmetry generates some interesting effects.

### 5.2.2 Flavor Branes and Quark Chemical Potentials

In the context of flavor branes it is possible to introduce chemical potentials for the fundamental fields. In this sense this theory is very similar to QCD where also quark chemical potentials can be considered. In this section we consider  $N_f = 2$  coincident flavor branes which give rise to a  $U(2)$  global flavor symmetry<sup>1</sup>. As in the section above, we split the flavor symmetry in an  $U(1)$  baryon symmetry and an  $SU(2)$  isospin symmetry and use the same notation for the gauge fields.

In [72] a finite baryon chemical potential has been introduced while the isospin chemical potential is still zero. The non-zero time component of the gauge field which induces the chemical potential has a non-trivial effect on the embedding function and the thermodynamics of the system [72, 73, 198–201] as well as on the spectrum of the mesons [186, 202, 203]. The generalization to include also a finite isospin chemical potential has been done in my own work [204] and my diploma thesis. A finite isospin chemical potential has also been introduced in the context of flavor branes in [205, 206].

As described above, we introduce a baryon and isospin chemical potential,  $\mu_B$  and  $\mu_I$ , as the boundary value of the time component of the non-Abelian gauge field

<sup>1</sup>It is also possible to study a different number of D7-branes. Here  $N_f = 2$  is chosen since it is sufficient for the following considerations.

which lives on the D7-branes [72],

$$\mu_B = \lim_{\varrho \rightarrow \varrho_{\text{bdy}}} \mathcal{A}_t(\varrho) \quad \text{and} \quad \mu_I = \lim_{\varrho \rightarrow \varrho_{\text{bdy}}} A_t^3(\varrho). \quad (5.23)$$

Since  $\mathcal{A}_t$  and  $A_t$  depend exclusively on  $\varrho$ , the only non-vanishing components of the background field strength are  $F_{\varrho t} = -F_{t\varrho} = \partial_\varrho A_t$  and  $\mathcal{F}_{\varrho t} = -\mathcal{F}_{t\varrho} = \partial_\varrho \mathcal{A}_t$ . In addition to the gauge fields, there is a scalar field which determines the embedding of the D7-branes (see section 4.2.3).

### DBI Action

The embedding of the flavor branes and the profile of the gauge fields living on these branes are determined by the non-Abelian DBI action (2.52). Here we consider the case with  $p = 7$ ,  $d = 10$  and  $B \equiv 0$ . As at zero chemical potential, the action can be simplified significantly by using the spatial and gauge symmetries present in our setup. However, due to the presents of the non-Abelian gauge field, we must be more careful. As discussed in section 4.2.3, we make use of the spatial rotation symmetry in the 8,9-directions to set  $\phi = 0$  such that  $Q_B^A = \delta_B^A$ . However, the non-Abelian structure of embeddings and gauge fields is still manifest in the pullback appearing in the action (2.52) as

$$\begin{aligned} P_{\alpha\beta}[G] = & g_{\alpha\beta} + (2\pi\alpha')^2 g_{AB} (\partial_\alpha X^A \partial_\beta X^B + i\partial_\alpha X^A [A_\beta, X^B] \\ & + i[A_\alpha, X^A] \partial_\beta X^B - [A_\alpha, X^A] [A_\beta, X^B]) . \end{aligned} \quad (5.24)$$

The only terms coupling the embeddings  $X$  to the gauge fields  $A$  are given by the commutator terms. These commutators vanish due to the following argument: We are free to define the  $\sigma^0 (= \mathbf{1})$  flavor direction to be the direction parallel to the non-vanishing embedding  $X^8$  using the  $U(1) \subset U(N_f)$  gauge symmetry. Now we *choose* our baryonic gauge field to have only a non-vanishing  $A_t^0 \sigma^0 dt$  component. In the dual field theory, this particular choice corresponds to the case in which the baryon charge representation and the mass representation are simultaneously diagonalizable. A different choice is possible and will most likely change the field theory phenomenology. This applies also to the case of non-coincident D $p$ -branes. Finally, we use the remaining gauge symmetry  $SU(N_f) \subset U(N_f)$  to restrict to an isospin gauge field  $A$  along the third flavor direction, i. e.  $A_t^3 \sigma^3 dt$ , without loss of generality. Thus, the only representations appearing in the background are the diagonal elements  $\sigma^0$  and  $\sigma^3$  of  $U(2)$ , which constitute the Cartan subalgebra. By definition these representation matrices commute with each other and, thus, all commutators  $[X, A]$  vanish. In this way we can consistently truncate the non-Abelian DBI action to

$$\begin{aligned} S_{\text{DBI}} = & -T_{D7} \int d^8\xi \text{STr} \left( \sqrt{|\det(G\sigma^0 + 2\pi\alpha' F^{N_f=2})|} \right) \\ = & -T_{D7} \int d^8\xi \sqrt{-G} \text{STr} \left( \sqrt{\sigma^0 + (2\pi\alpha')^2 G^{tt} G^{\varrho\varrho} \left( F_{\varrho t}^{N_f=2} \right)^2} \right), \end{aligned} \quad (5.25)$$

where we set  $G = \mathcal{P}[G]$  and in the second line the determinant is calculated.

Next we determine the square of the non-vanishing components of the field strength tensor, which is by construction diagonal in the flavor space,

$$\begin{aligned} \left(F_{\rho t}^{N_f=2}\right)^2 &= \left[(\mathcal{F}_{\rho t})^2 + (F_{\rho t})^2\right] \sigma^0 + 2\mathcal{F}_{\rho t} F_{\rho t} \sigma^3 \\ &= \text{diag} \left[ (\mathcal{F}_{\rho t} + F_{\rho t})^2, (\mathcal{F}_{\rho t} - F_{\rho t})^2 \right], \end{aligned} \quad (5.26)$$

where we used  $(\sigma^3)^2 = \sigma^0$ . Defining the new fields,

$$X_1 = \mathcal{A}_t + A_t \quad \text{and} \quad X_2 = \mathcal{A}_t - A_t, \quad (5.27)$$

the square of the field strength can be written as

$$\left(F_{40}^{N_f=2}\right)^2 = \text{diag} \left[ (\partial_\rho X_1)^2, (\partial_\rho X_2)^2 \right]. \quad (5.28)$$

Notice that the field  $X_i$  is the gauge field living on the  $i$ th brane. Inserting the metric components, the action (5.25) becomes

$$\begin{aligned} S_{\text{DBI}} &= -T_7 \int d^8 \xi \frac{\sqrt{h_3}}{4} \varrho^3 f \tilde{f} (1 - \chi^2) \\ &\quad \times \left( \sqrt{1 - \chi^2 + \varrho^2 (\partial_\rho \chi)^2 - 2(2\pi\alpha')^2 \frac{\tilde{f}}{f^2} (1 - \chi^2) (\partial_\rho X_1)^2} \right. \\ &\quad \left. + \sqrt{1 - \chi^2 + \varrho^2 (\partial_\rho \chi)^2 - 2(2\pi\alpha')^2 \frac{\tilde{f}}{f^2} (1 - \chi^2) (\partial_\rho X_2)^2} \right). \end{aligned} \quad (5.29)$$

The transformation to the fields  $X_i$  decouple the two branes and we obtain a sum of two Abelian DBI actions. The Abelian actions are known from the pure baryonic case [72]. We, therefore, can use the ideas given there to study our setup in which baryon and isospin charges are switched on simultaneously.

## Quark Densities

The dual operator to the gauge field on the branes is the flavor current (see e. g. [72, Appendix A])

$$J_\mu^a = \bar{\psi} \gamma_\mu \sigma^a \psi + \tilde{\psi}^\dagger \gamma_\mu \sigma^a \tilde{\psi}^\dagger + i \left( q^\dagger \sigma^a \partial_\mu q - (\partial_\mu q)^\dagger \sigma^a q \right) + i \left( \tilde{q} \sigma^a (\partial_t \tilde{q})^\dagger - (\partial_t \tilde{q}) \sigma^a \tilde{q}^\dagger \right). \quad (5.30)$$

According to the AdS/CFT dictionary, the vacuum expectation value for the quark densities,  $n_B$  and  $n_I$ , are given by the variation of the DBI action with respect to the boundary value of the time component of the gauge field,  $\mathcal{A}_t$  and  $A_t$ , respectively. Using the Hamilton-Jacobi theory, the densities can be also read off from the

boundary value of the conjugated momenta which are constants of motion,

$$\begin{aligned} n_B &= \frac{\partial S_{\text{DBI}}}{\partial(\partial_\rho \mathcal{A}_t)} = \frac{\partial S_{\text{DBI}}}{\partial(\partial_\rho X_1)} + \frac{\partial S_{\text{DBI}}}{\partial(\partial_\rho X_2)} = n_1 + n_2, \\ n_I &= \frac{\partial S_{\text{DBI}}}{\partial(\partial_\rho A_i^3)} = \frac{\partial S_{\text{DBI}}}{\partial(\partial_\rho X_1)} - \frac{\partial S_{\text{DBI}}}{\partial(\partial_\rho X_2)} = n_1 - n_2, \end{aligned} \quad (5.31)$$

with

$$\begin{aligned} n_i &= \frac{\partial S_{\text{DBI}}}{\partial(\partial_\rho X_i)} = 2\pi^2 (2\pi\alpha')^2 T_7 \varrho^3 \frac{\tilde{f}^2}{2f} \\ &\quad \times \frac{(1 - \chi^2)^2 \partial_\rho X_i}{\sqrt{1 - \chi^2 + \varrho^2 (\partial_\rho \chi)^2 - 2(2\pi\alpha')^2 \frac{\tilde{f}}{f^2} (1 - \chi^2) (\partial_\rho X_i)^2}}. \end{aligned} \quad (5.32)$$

Since the conjugated momenta are constants of motion, it is convenient to Legendre transform the action (5.29) to eliminate the fields  $X_i$  in favor of the constants  $n_i$ ,

$$\begin{aligned} \tilde{S}_{\text{DBI}} &= S_{\text{DBI}} - \int d^8 \xi \sum_{i=1}^{N_f} \partial_\rho X_i \frac{\delta S_{\text{DBI}}}{\delta(\partial_\rho X_i)} \\ &= -T_7 \int d^8 \xi \frac{1}{4} \varrho^3 f \tilde{f} (1 - \chi^2) \sqrt{1 - \chi^2 + \varrho^2 (\partial_\rho \chi)^2} \\ &\quad \times \sum_{i=1}^{N_f} \sqrt{1 + \frac{8n_i^2}{(2\pi\alpha')^2 T_7^2 \varrho^6 \tilde{f}^3 (1 - \chi^2)^3}}. \end{aligned} \quad (5.33)$$

The gauge fields can be calculated from the Legendre transformed action by  $\partial_\rho X_i = -\delta \tilde{S}_{\text{DBI}} / \delta n_i$ .

### Equations of motion

In order to study this system numerically, it is convenient to introduce dimensionless quantities to write down the equations of motion. For instance the dimensionless gauge fields are given by

$$\tilde{X}_i = \frac{2\pi\alpha'}{\varrho_h} X_i, \quad (5.34)$$

which leads to the dimensionless chemical potentials as their boundary values

$$\tilde{\mu}_i = \frac{2\pi\alpha'}{\varrho_h} = \sqrt{\frac{2}{\lambda}} \frac{\mu_i}{T} \quad \text{and} \quad \frac{\mu_i}{M_q} = \frac{\sqrt{2}\tilde{\mu}_i}{m}. \quad (5.35)$$

Using the Legendre transformed action, they can be obtained by an integration,

$$\tilde{\mu}_i = \tilde{X}_i(\rho_{\min}) + 2\tilde{n}_i \int_{\rho_{\min}}^{\infty} d\rho \frac{f \sqrt{1 - \chi^2 + \varrho^2 (\partial_\rho \chi)^2}}{\sqrt{\tilde{f} (1 - \chi^2) [\varrho^6 \tilde{f}^3 (1 - \chi^2)^3 + 8\tilde{n}_i^2]}}, \quad (5.36)$$

where dimensionless densities  $\tilde{n}_i$  are given by

$$n_i = 2^{-\frac{5}{2}} N_c \sqrt{\lambda} T^3 \tilde{n}_i. \quad (5.37)$$

The equation of motion for the embedding function  $\chi$  can be derived from (5.33) as

$$\begin{aligned} & \partial_\rho \left[ \rho^5 f \tilde{f} (1 - \chi^2) \frac{\partial_\rho \chi}{\sqrt{1 - \chi^2 + \rho^2 (\partial_\rho \chi)^2}} \sum_{i=1}^{N_f} \sqrt{1 + \frac{8\tilde{n}_i^2}{\rho^6 \tilde{f}^3 (1 - \chi^2)^3}} \right] \\ &= - \frac{\rho^3 f \tilde{f} \chi}{\sqrt{1 - \chi^2 + \rho^2 (\partial_\rho \chi)^2}} \left[ [3(1 - \chi^2) + 2\rho^2 (\partial_\rho \chi)^2] \sum_{i=1}^{N_f} \sqrt{1 + \frac{8\tilde{n}_i^2}{\rho^6 \tilde{f}^3 (1 - \chi^2)^3}} \right. \\ & \quad \left. - \frac{24}{\rho^6 \tilde{f}^3 (1 - \chi^2)^3} (1 - \chi^2 + \rho^2 (\partial_\rho \chi)^2) \sum_{i=1}^{N_f} \frac{\tilde{n}_i^2}{\sqrt{1 + \frac{8\tilde{n}_i^2}{\rho^6 \tilde{f}^3 (1 - \chi^2)^3}}} \right]. \end{aligned} \quad (5.38)$$

In addition to the case without isospin density [72], sums over the  $N_f$  different densities appear. Due to these sums, the equation of motion cannot be written down in a more compact form, as done in the Abelian case [72].

### Physical Embeddings

In [72, 198] it is shown that at finite quark density, only black hole embeddings are physical. At finite density the gauge field has a non-trivial profile close to the boundary such that there is a non-vanishing electric field in the radial direction,  $E_\rho = F_{\rho t}$ . Due to Gauss' law, this electric field must be sourced by an electric charge in the bulk. If the brane is connected to the black hole horizon as in the case of black hole embeddings, this charge can be hidden inside the black hole as in the Reissner-Nordström black hole. For large quark masses a spike forms close to the horizon in order to connect the brane with the black hole. Some exemplary embeddings at finite baryon density are presented in figure 5.2.

If the brane is not connected to the black hole as in the case of Minkowski embeddings, this electric charge cannot be present and, therefore, the electric field must be zero. Therefore, only black hole embeddings are allowed at finite densities. For Minkowski embeddings, however, a constant time component of the gauge field is still possible. This leads to a finite chemical potential but zero density. Since a constant gauge field does not change the DBI action, Minkowski embeddings are the same as at zero chemical potential.

Since the global flavor symmetry on the field theory side is mapped to a gauge symmetry in the bulk, we have to make sure that the construction discussed above is gauge invariant. First we fix a gauge by demanding  $A_\rho = 0$  which leaves  $\Lambda(x^\mu)$  as residual gauge symmetries. This naively allows the time component of a gauge field

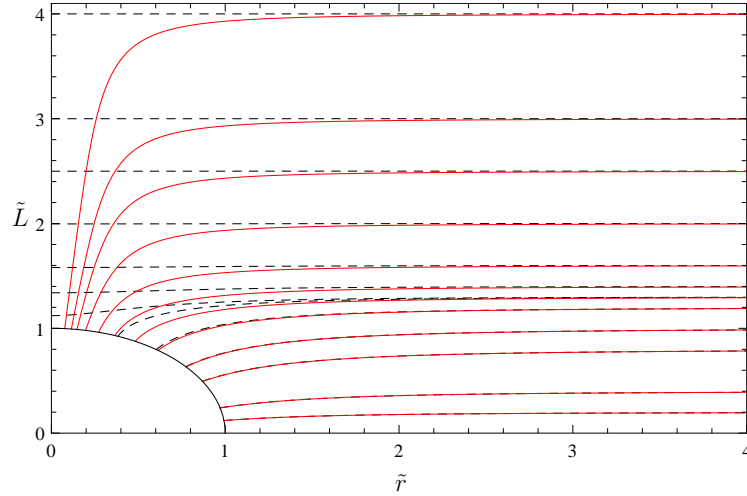


**Figure 5.2:** Embedding function  $\tilde{L}$  of the D7-branes in the AdS black hole background versus the AdS radial coordinate  $\tilde{r}$  for different values of the mass parameter defined in (4.58). The dashed black curves are at zero densities while for the red curves the baryon density  $\tilde{n}_B = 0.1$  is switched on.

to change by  $A_t \rightarrow A_t - \partial_t \Lambda$ . However, for black hole embeddings the time component of the gauge field must be zero at the horizon as discussed for the Reissner-Nordström black hole. Thus, this transformation is not allowed. For the Minkowski embeddings, the constant  $A_t$  gives rise to a Wilson line due to the compact Euclidean time direction and is therefore also gauge invariant.

### Numerical Results for Asymptotic Parameters

In this theory we have three dimensionless physical parameters which determines the state of the system, the quark mass over the temperature  $m$ , the baryon chemical potential over the quark mass  $\mu_B/M_q$  and the isospin chemical potential over the quark mass  $\mu_I/M_q$ . On the other hand there are three “unphysical” parameters: the two densities  $\tilde{n}_B$  and  $\tilde{n}_I$  which are constants of motion and the asymptotic values  $\chi_0$  and  $L_0$  for black hole and Minkowski embedding, respectively. By solving the equations of motion numerically, we obtain a map between the “unphysical” parameters and the physical parameters. Since there is no change for Minkowski embeddings, we refer to section 4.2.3 for the numerical data.

Due to discrete symmetries in the action, some parts of the parameter space are related. For instance the action is invariant under the permutation  $\tilde{n}_1 \leftrightarrow \tilde{n}_2$  which results in the transformation  $\mu_B \mapsto \mu_B$  and  $\mu_I \mapsto -\mu_I$  while the embedding function stays the same. Another symmetry is given by the reflection  $\tilde{n}_i \leftrightarrow -\tilde{n}_i$ . For  $\tilde{n}_1 \leftrightarrow -\tilde{n}_1$  this results in  $\mu_B \mapsto -\mu_I$  and  $\mu_I \mapsto -\mu_B$ , while for  $\tilde{n}_2 \leftrightarrow -\tilde{n}_2$  we obtain  $\mu_B \mapsto \mu_I$  and  $\mu_I \mapsto \mu_B$ . Again the embedding function is invariant under this transformation. These symmetries allows us to restrict the calculation to the

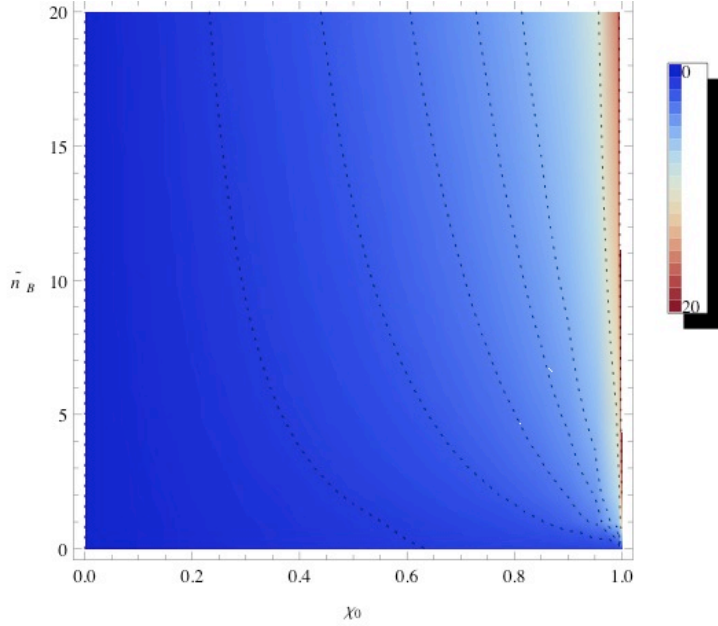


**Figure 5.3:** The dimensionless mass parameter  $m$  as defined in (4.58) versus the embedding parameter  $\chi_0$  and the baryon density  $\tilde{n}_B$  at constant isospin density  $\tilde{n}_I = 0$ . The contours mark the lines of constant  $m = 0, 1, 2, 3, 4, 5, 10, 20$ .

parameters  $0 \leq \tilde{n}_2 \leq \tilde{n}_1$  which leads to  $0 \leq \mu_I \leq \mu_B$ . The other regions can be reconstructed by using the symmetries.

First we study the dependence of the mass parameter  $m$  as defined in (4.58) on the densities  $\tilde{n}_B$ ,  $\tilde{n}_I$  and the embedding parameter  $\chi_0$ . Some exemplary numerical data is presented in figure 5.3 and 5.4. We see that the mass parameter  $m$  strongly depend on the baryon density  $\tilde{n}_B$ , especially at  $\chi_0$  close to one. However, at a fix baryon density  $\tilde{n}_B$ , the dependence of the mass parameter  $m$  on the isospin density  $\tilde{n}_I$  is very weak. As already seen from figure 5.2 at finite density, any value for the mass parameter  $m$  is reachable within the black hole embeddings.

Next we investigate the dependence of the chemical potentials  $\mu_B/M_q$  and  $\mu_I/M_q$  on the densities  $\tilde{n}_B$ ,  $\tilde{n}_I$  and the embedding parameter  $\chi_0$ . Some exemplary numerical data is presented in figure 5.5 and 5.6. We see that the ratios  $\mu_B/M_q$  and  $\mu_I/M_q$  depend strongly on both densities. The value of the ratios in the limit  $m \rightarrow \infty$  can be analytically calculated [72, 204],

$$\begin{aligned}
 \mu_B \rightarrow M_q & \quad \text{and} \quad \mu_I \rightarrow 0 & \quad \text{for } 0 \leq \tilde{n}_I < \tilde{n}_B, \\
 \mu_B \rightarrow 0 & \quad \text{and} \quad \mu_I \rightarrow M_q & \quad \text{for } 0 \leq \tilde{n}_B < \tilde{n}_I, \\
 \mu_B \rightarrow \frac{M_q}{2} & \quad \text{and} \quad \mu_I \rightarrow \frac{M_q}{2} & \quad \text{for } 0 < \tilde{n}_B = \tilde{n}_I.
 \end{aligned} \tag{5.39}$$

From this consideration we obtain a region (large  $m$  and small  $\mu_B + \mu_I$ ) in the phase diagram where the black hole embeddings cannot exist and the Minkowski

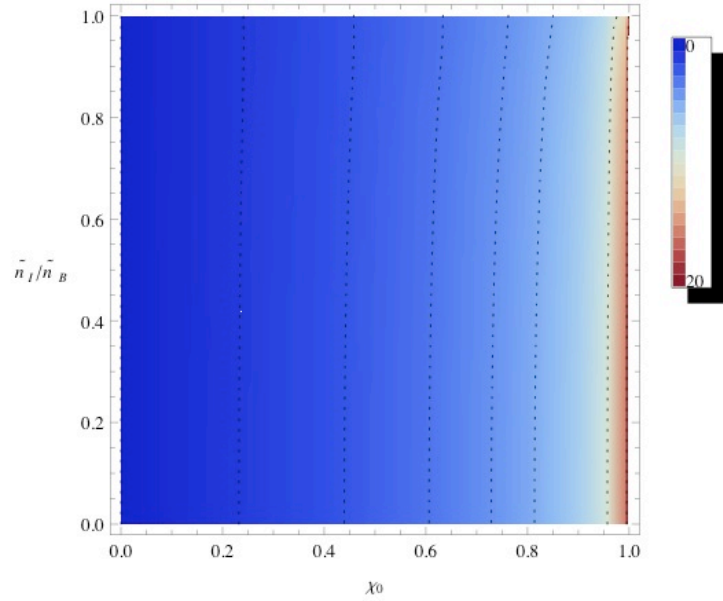


**Figure 5.4:** The dimensionless mass parameter  $m$  as defined in (4.58) versus the embedding parameter  $\chi_0$  and the ratio of the densities  $\tilde{n}_I/\tilde{n}_B$  at constant baryon density  $\tilde{n}_B = 20$ . The contours mark the lines of constant  $m = 0, 1, 2, 3, 4, 5, 10, 20$ .

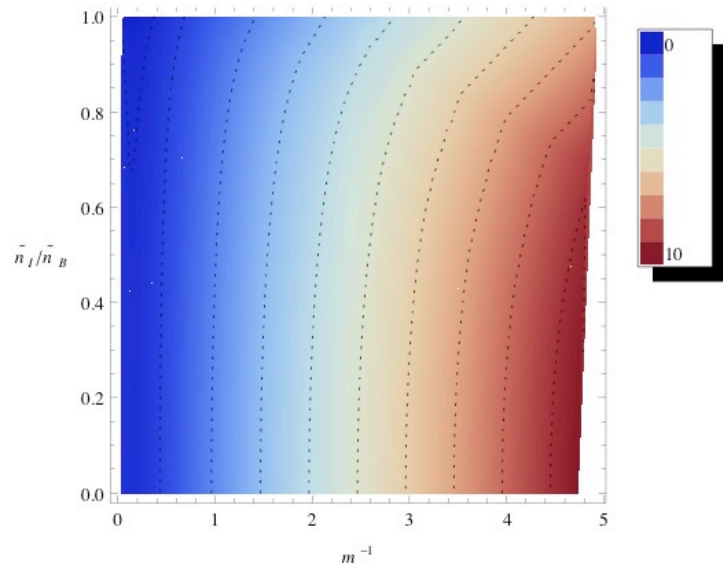


**Figure 5.5:** The dimensionless baryon chemical potential  $\mu_B/M_q$  versus the inverse of the mass parameter  $m^{-1}$  and the ratio of the quark densities  $\tilde{n}_I/\tilde{n}_B$  at constant baryon density  $\tilde{n}_B = 20$ . The contours mark the lines of constant  $\mu_B/M_q = 0.6, 1, 2, 3, 4, 5, 6, 7, 8, 9$ .

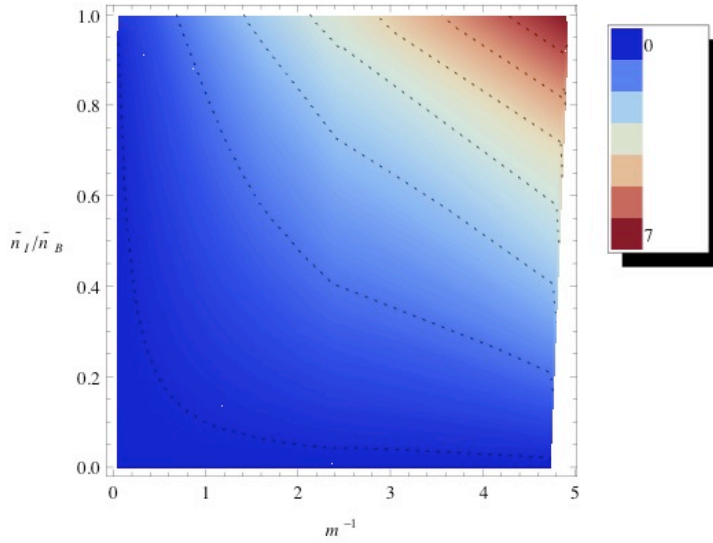


**Figure 5.6:** The dimensionless isospin chemical potential  $\mu_I/M_q$  versus the inverse of the mass parameter  $m^{-1}$  and the ratio of the quark densities  $\tilde{n}_I/\tilde{n}_B$  at constant baryon density  $\tilde{n}_B = 20$ . The contours mark the lines of constant  $\mu_I/M_q = 0.1, 1, 2, 3, 4, 5, 6$ .

embeddings must be favored. Therefore, we expect a phase transition between the black hole and Minkowski embeddings close to the boundary of this region. At zero chemical potential the phase transition is at  $m = 1.307$  as found in section 4.2.3. Below we study the thermodynamics of the system and determine the dependence of the critical mass on the chemical potentials.

## Thermodynamics

In the following we determine the thermodynamics of the system in the grand canonical ensemble. For this purpose we have to evaluate the DBI action on-shell. Since the on-shell action is divergent, we have to use holographic renormalization as described in section 4.2.1. The gauge fields do not generate additional divergences such that the counterterm found in (4.66) is still sufficient. Similar as in (4.67), we rewrite the renormalized on-shell DBI action as

$$\frac{I_{\text{DBI}}^{\text{ren}}}{\mathcal{N}_\lambda} = G(m, \tilde{\mu}) - \frac{1}{4} \left[ (\rho_{\text{min}}^2 - m^2)^2 - 4m\tilde{c} \right], \quad (5.40)$$

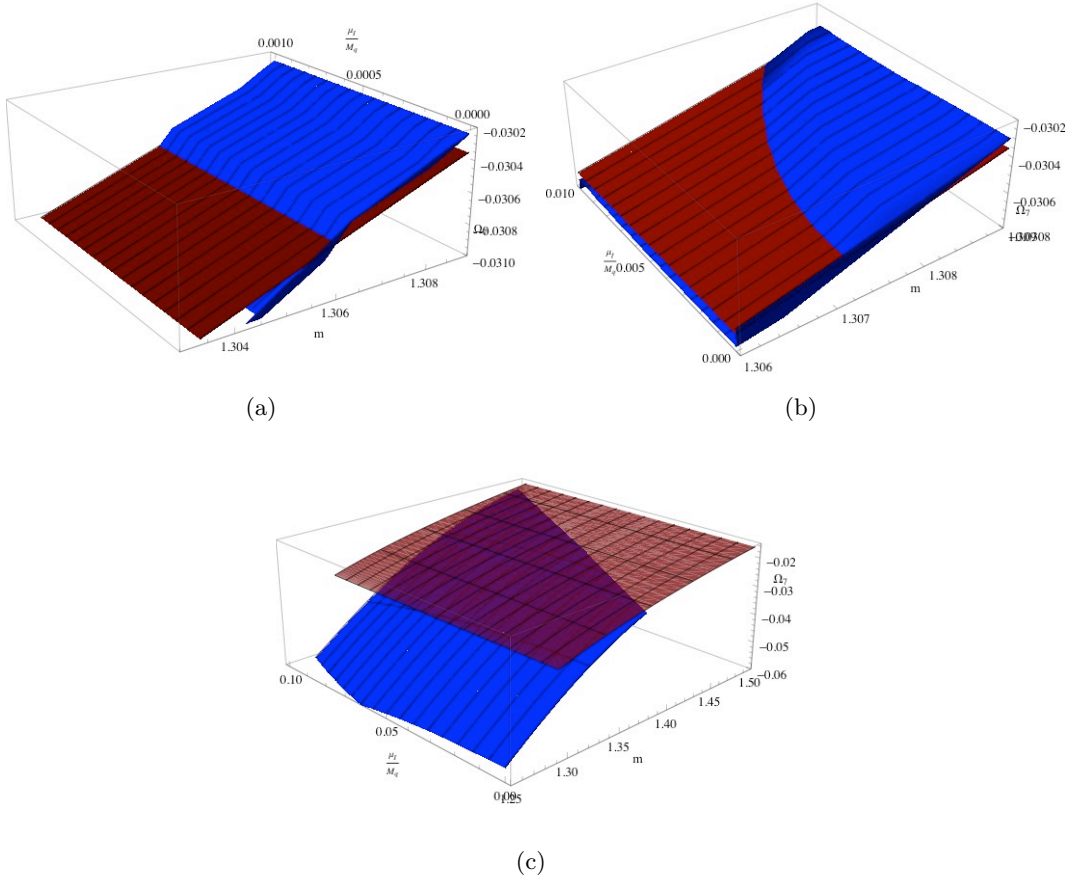


**Figure 5.7:** The dimensionless contribution of the flavor branes to the grand potential  $\mathcal{W}_7$  versus the dimensionless mass parameter  $m$  and the dimensionless isospin chemical potential  $\mu_I/M_q$  at constant baryon chemical potential  $\tilde{\mu}_B = 0.001$  (a),  $0.01$  (b) and  $0.1$  (c) close to the phase transition.

where now

$$G(m, \tilde{\mu}) = \int_{\rho_{\min}}^{\infty} d\rho \left( \rho^3 f \tilde{f} (1 - \chi^2) \sum_{i=1}^{N_f} \sqrt{1 - \chi^2 + \rho^2 (\partial_\rho \chi)^2 - 2 \frac{\tilde{f}}{f^2} (1 - \chi^2) (\partial_\rho \tilde{X}_i)^2} - N_f (\rho^3 - \rho m^2) \right). \quad (5.41)$$

Since we are working in the grand canonical ensemble, the renormalized on-shell DBI action is proportional to the contribution of the flavor branes to the grand potential,

$$\Omega_7(T, M_q, \mu_B, \mu_I) = T I_{\text{DBI}}^{\text{ren}} = \frac{\lambda N_c N_f V_3 T^4}{32} \mathcal{W}_7(m, \tilde{\mu}), \quad (5.42)$$

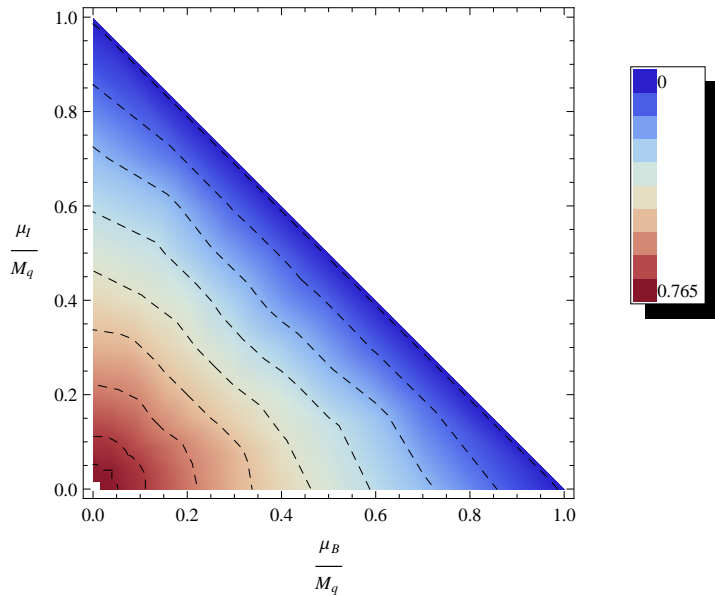


**Figure 5.8:** Phase diagram of the flavor branes in the grand canonical ensemble. The contours mark the line of constant  $m^{-1} = 0.01, 0.1, 0.2, 0.3, 0.4, 0.5, 0.6, 0.7, 0.75$ . For values of  $m^{-1}$  smaller the critical value, the Minkowski embeddings with zero quark densities are favored while bigger values the black hole embeddings with non-zero quark densities are preferred. For  $\mu_B + \mu_I > M_q$  there is no phase transition.

with the dimensionless quantity

$$\mathcal{W}_7(m, \tilde{\mu}) = \frac{1}{N_f} G(m, \tilde{\mu}) - \frac{1}{4} \left[ (\rho_{\min}^2 - m^2)^2 - 4m\tilde{c} \right]. \quad (5.43)$$

In total the grand potential is given by a formula similar to (4.71). The formula (5.43) is especially suitable for black hole embeddings.

However, Minkowski embeddings can be also present and their contribution to the grand potential must be also determined. Since the gauge fields are constant for the Minkowski embeddings and, thus, do not change the on-shell action, the value of the grand potential for Minkowski embeddings at any finite chemical potential is the same as at zero chemical potential and, therefore, equal to the free energy calculated in section 4.2.3.

In figure 5.7 some exemplary numerical data for the dimensionless grand potential is presented. For small chemical potentials  $\mu_B + \mu_I \ll M_q$ , the situation is very similar to the case of zero chemical potential. The grand potential consists out of two branches, one corresponding to black hole embeddings and one to Minkowski embeddings, which overlap. For small values of the mass parameter  $m$ , the black hole embeddings are favored, while for larger values the Minkowski embeddings are preferred. Since the grand potential has a kink at the critical mass, the phase transition is first order as at zero chemical potential. After a critical

value for the chemical potentials is reached, the branches do not overlap anymore (see figure 5.7 (c)). They are smoothly connected such that the phase transition is of higher order. In [207, 208] it is found analytically in the pure baryonic case that the phase transition is third order. At finite isospin chemical potential, the result should be the same. At zero temperature it is also analytically shown in [198] that the phase transition is second order in the pure baryonic case. In this case the phase transition is located at  $\mu_B = M_q$ . This result is in agreement with the field theory expectation: A chemical potential leads to negative mass squared for a charged boson. Thus, if the chemical potential is larger than the mass of the scalar, the scalar becomes unstable and starts to condense. The non-zero vev of the scalar field induces a charge density. At finite isospin chemical potential, the condensation occurs at  $\mu_B + \mu_I \geq M_q$ . The phase diagram for finite baryon and isospin chemical potentials is given in figure 5.8.

## 5.3 Physics close to Equilibrium

In this section we study the response due to small perturbations about the equilibrium. We exclusively consider the flavor branes and are interested in the spectral functions of the flavor fields. At finite chemical potential pronounced peaks appear [186, 202] which are identified with quasiparticles. These quasiparticles are bound states of the flavor fields and are in analogy to QCD called mesons. Later we study the interesting structures emerging in the spectral function in more detail by calculating the corresponding quasinormal mode spectrum. This has first been done in my own work [3].

### 5.3.1 Spectral Functions of Flavor Fields

Here we focus on spectral function of the transverse vector mesons at zero spatial momentum<sup>2</sup> about the equilibrium solution studied above. Due to this vector fluctuations, the gauge fields on the brane contain the additional perturbations  $a_\mu^a$  and  $a_\mu$ ,

$$\begin{aligned}\hat{A}_\mu^a(x, \varrho) &= A_t^3(\varrho)\delta^{a3}\delta_{\mu t} + a_\mu^a(x, \varrho), \\ \hat{\mathcal{A}}_\mu(x, \varrho) &= \mathcal{A}_t(\varrho) + a_\mu(x, \varrho).\end{aligned}\tag{5.44}$$

As discussed before we have to fix a gauge to get rid of unphysical fields. Since we now break the  $SU(2)$  gauge symmetry down to the  $U(1)_3$  symmetry by the non-zero isospin chemical potential, the gauge fixing for the  $SU(2)$  fields is different as in the finite temperature case. For the  $U(1)$  fields, it is the same. Since the background only allows for the gauge transformations generated by  $\Lambda^3$ , the gauge

---

<sup>2</sup>Results at not-zero spatial momentum can be found in [176, 202, 203].

transformations of the fields  $a_\mu^{1,2}$  differs from the one of  $a_\mu^3$ ,

$$\begin{aligned}\delta_\lambda a_\mu^1 &= -\Lambda^3 a_\mu^2 + \lambda^2 A_t^3 \delta_{\mu t} + \nabla_\mu \lambda^1, \\ \delta_\lambda a_\mu^2 &= +\Lambda^3 a_\mu^1 - \lambda^1 A_t^3 \delta_{\mu t} + \nabla_\mu \lambda^2, \\ \delta_\lambda a_\mu^3 &= \nabla_\mu \lambda^3.\end{aligned}\tag{5.45}$$

We see that  $a_\mu^3$  transforms in the adjoint of  $U(1)_3$  while the combination  $E_\mu^\pm = a_\mu^1 \pm i a_\mu^2$  transforms in the (anti-)fundamental of  $U(1)_3$ . At zero spatial momentum, the gauge covariant transverse fields are therefore the adjoint fields  $a_i$ ,  $a_i^3$  and the fundamental fields  $E_i^\pm$ .

Their equations of motion are obtained by the DBI action expanded to second order in these fields. Due to the non-zero background gauge field on the brane, the non-Abelian structure appears to second order in the fluctuations such that an interaction between the gauge fields is present. This induces a meson interaction on the field theory side. The coupling constant for this interaction may be determined by a redefinition of the gauge field, such that the kinetic term of the effective four-dimensional theory has the canonical form, extending the ideas of [39].

Let us now determine this coupling constant which was implicitly used in [186]. This calculation has first been done in my own work [204]. First we consider the eight-dimensional theory determined by the DBI action  $S_{\text{DBI}}^{(2)}$  expanded to second order in the fluctuations  $a$ ,

$$S_{\text{DBI}}^{(2)} = \frac{T_7(2\pi\alpha')^2}{4} \int d^8\xi \sqrt{-\mathcal{G}} \mathcal{G}^{\alpha\alpha'} \mathcal{G}^{\beta\beta'} F_{\alpha'\beta} F_{\beta'\alpha},\tag{5.46}$$

where  $\mathcal{G} = \mathcal{P}[G] + 2\pi\alpha'F$  contains the background fields. To simplify the analysis, we consider only Abelian gauge fields which is sufficient to determine the kinetic term and therefore the coupling constant. Defining the dimensionless coordinate  $\tilde{\rho} = \varrho/R$  and integrating out the contribution of the  $S^3$  where we assume the integral to be trivial, we obtain

$$S_{\text{DBI}}^{(2)} = \frac{T_7(2\pi\alpha')^2 \text{vol}(S_3) R^4}{4} \int d^4x \int d\tilde{\rho} \sqrt{-\mathcal{G}} \mathcal{G}^{\alpha\alpha'} \mathcal{G}^{\beta\beta'} F_{\alpha'\beta} F_{\beta'\alpha}.\tag{5.47}$$

In order to get a four-dimensional effective theory, we have to integrate over the coordinate  $\tilde{\rho}$ . This contribution depends on the geometry induced by the  $\tilde{\rho}$  dependence of the metric factors. However, we expect that it is independent of the 't Hooft coupling  $\lambda$ . We parametrize this contribution by  $\gamma'$ . The kinetic term of the effective theory is then given by

$$S_{\text{DBI}}^{(2)} = \frac{T_7(2\pi\alpha')^2 \text{vol}(S_3) R^4 \gamma'}{4} \int d^4x F_{\mu\nu} F^{\mu\nu}.\tag{5.48}$$

The prefactor may be written as

$$\frac{T_7(2\pi\alpha')^2 \text{vol}(S_3) R^4 \gamma'}{4} = \frac{\lambda}{g_{\text{YM}}^2 \gamma^2},\tag{5.49}$$

where the numerical values independent of the 't Hooft coupling are grouped into the coefficient  $\gamma$ . From this we can read off that a rescaling of the form

$$A \mapsto \frac{\gamma}{\sqrt{\lambda}} A \quad (5.50)$$

casts the Lagrangian into canonical form with a prefactor of  $1/g_{\text{YM}}^2$ . In the following we set  $\gamma = 2\sqrt{2}\pi$  since a numerical calculation has not been performed yet. Using this coupling constant, we can derive the equations of motion for the fluctuations. The detailed calculation can be found in [209, 210].

### Results for Finite Baryon Chemical Potential

For non-zero baryon but zero isospin chemical potential, there is no interaction between the fluctuation and they have the same equation of motion given by

$$E'' + \frac{\partial_\rho[\sqrt{\mathcal{G}}\mathcal{G}^{22}\mathcal{G}^{44}]}{\sqrt{\mathcal{G}}\mathcal{G}^{22}\mathcal{G}^{44}} E' - 4\frac{g_h^4}{R^4} \frac{\mathcal{G}^{00}}{\mathcal{G}^{44}} \mathfrak{w}^2 E = 0, \quad (5.51)$$

where the prime denotes the derivative with respect to  $\rho$ , the upper indices on  $\mathcal{G}$  the elements of  $\mathcal{G}^{-1}$  and  $\mathfrak{w}$  the dimensionless frequency,  $\mathfrak{w} = \omega/(2\pi T)$ . Using the recipe presented in section 4.3.1, the Green's function of the flavor current can be expressed in terms of the gauge fields,

$$G^R(\omega, 0) = \frac{N_f N_c T^2}{8} \lim_{\rho \rightarrow \infty} \left( \rho^3 \frac{\partial_\rho E(\rho)}{E(\rho)} \right). \quad (5.52)$$

Let us now discuss the resulting spectral functions. To emphasize the resonance peaks, we subtract the zero temperature limit of the spectral function

$$\mathfrak{R}_0 = N_f N_c T^2 \pi \mathfrak{w}^2, \quad (5.53)$$

which can be read off from (4.120). The spectral function oscillates around this zero temperature behavior (see figure 5.9 (a)).

We first consider the spectral function at fixed baryon density and vary the mass parameter  $m$ . The numerical results are shown in figure 5.9 (b), (c) and (d). The figures show that an increase of the mass parameter  $m$  from zero to small values results in more and more pronounced peaks in the spectral function. At the same time these maxima change their positions and move to lower frequencies (see figure 5.9 (b)). This behavior is also observed for the case of vanishing baryon density [184]. However, if the mass parameter  $m$  is increased further, the resonances change their direction of motion and move to larger frequencies (see figure 5.9 (c)). Still, the maxima evolve to more and more distinct peaks. Eventually for very large mass parameters  $m$ , the position of the peaks asymptotically reach those frequencies which correspond to the masses of the supersymmetric spectrum (3.55). The formation of a line-like spectrum can be interpreted as the evolution of unstable excitations in

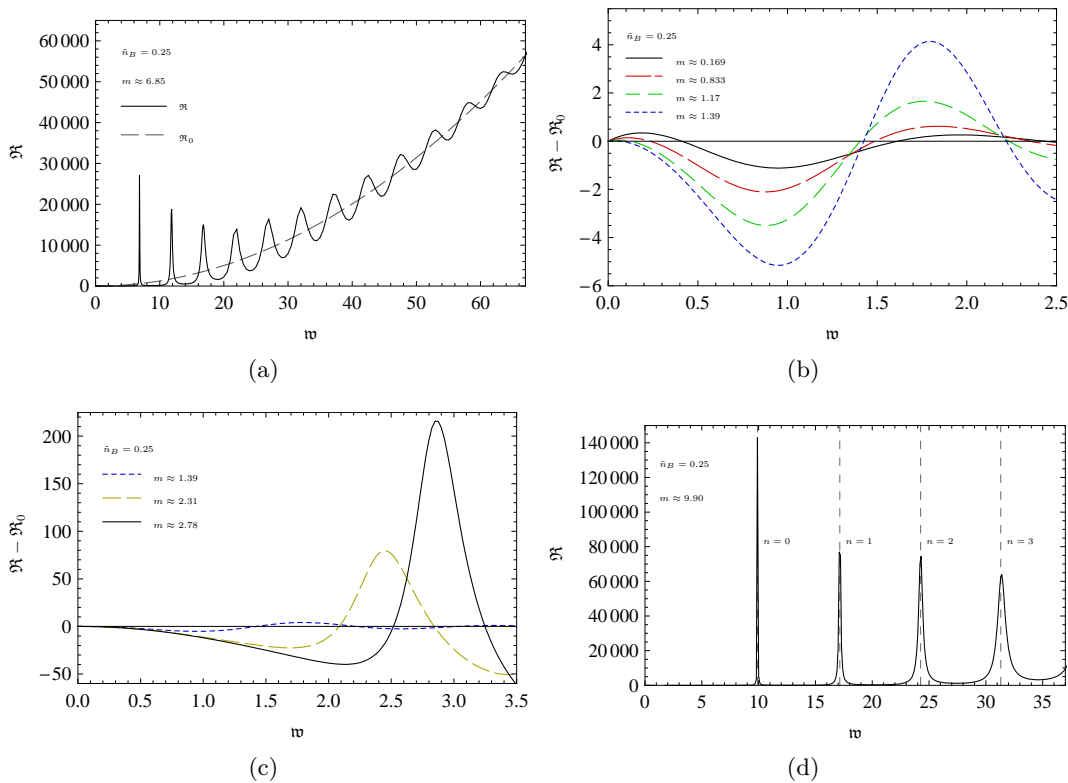


**Figure 5.9:** The spectral function  $\mathfrak{R}$  (in units of  $N_f N_c T^2/4$ ) versus the scaled frequency  $\mathfrak{w} = \omega/(2\pi T)$ : (a) The thermal spectral function  $\mathfrak{R}$  compared to the zero temperature result  $\mathfrak{R}_0$  as defined in (5.53). (b) The peaks in the finite temperature part of the spectral function  $\mathfrak{R} - \mathfrak{R}_0$  grow and move to lower frequencies as we increase the mass parameter  $m$ . (c) After a critical mass is reached the peaks change their direction of motion and move to higher frequencies. However, they still grow and form more and more pronounced maxima. (d) For very large mass parameter  $m$ , a line-like spectrum forms and the peaks reach asymptotically the supersymmetric spectrum defined in (3.55). These plots are taken from [186].

the plasma into quark bound states. These bound states, finally, turn into nearly stable mesons (see figure 5.9 (d)). We study the turning behavior in the next section in more detail when we determine the quasinormal mode spectrum.

Let us now investigate the effects of variations in the baryon density [204]. Spectral functions for various finite baryon density are shown in figure 5.10. At low baryon densities, the position of prominent peaks agree with the supersymmetric mass formula (3.55). Increasing the baryon density leads to a broadening of the peaks which indicates decreasing stability of the mesonic quasiparticle states at increasing baryon density. At the same time the position of the peaks change which indicates a dependence of the meson mass on the baryon density. A further increase of the baryon density leads to the formation of a new structure at  $\mathfrak{w} < 1$ . We discuss this structure together with the results at finite isospin density.

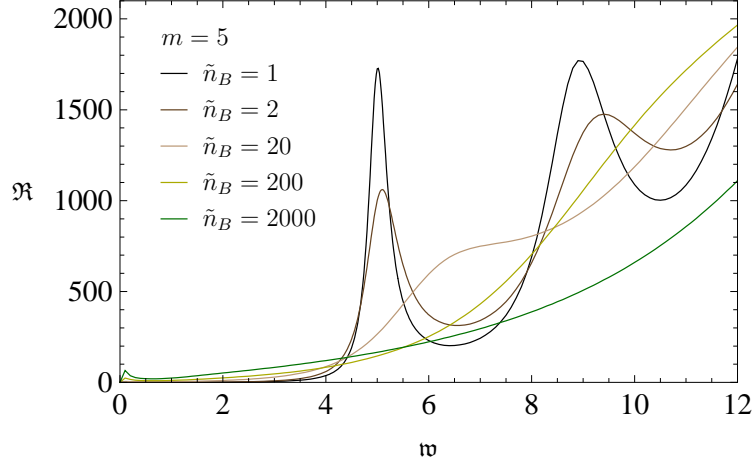


**Figure 5.10:** Spectral functions  $\mathfrak{R}$  for various baryon densities  $\tilde{n}_B$ , again normalized to  $N_f N_c T^2/4$ . The black and brown curves for small baryon densities show quasi-particle states around  $\mathfrak{w} = 5$  and higher excitations. By increasing the baryon density, these excitations disappear. At very high densities a new structure forms at small  $\mathfrak{w}$  (green curve). This figure is taken from [204].

### Results for Finite Isospin Chemical Potential

For non-zero isospin but zero baryon chemical potential, the fluctuations split into two blocks: one transforming in the adjoint and two transforming in the (anti-)fundamental representation as discussed below (5.45). The detailed derivation of their equations of motion can be found in [209, 210]. The result is

$$0 = E^{+''} + \frac{\partial_\rho \left( \sqrt{|\det \mathcal{G}|} \mathcal{G}^{44} \mathcal{G}^{22} \right)}{\sqrt{|\det \mathcal{G}|} \mathcal{G}^{44} \mathcal{G}^{22}} E^{+'} - 4 \frac{\varrho_h^4 \mathcal{G}^{00}}{R^4 \mathcal{G}^{44}} (\mathfrak{w} - \mathfrak{m})^2 E^+, \quad (5.54)$$

$$0 = E^{-''} + \frac{\partial_\rho \left( \sqrt{|\det \mathcal{G}|} \mathcal{G}^{44} \mathcal{G}^{22} \right)}{\sqrt{|\det \mathcal{G}|} \mathcal{G}^{44} \mathcal{G}^{22}} E^{-'} - 4 \frac{\varrho_h^4 \mathcal{G}^{00}}{R^4 \mathcal{G}^{44}} (\mathfrak{w} + \mathfrak{m})^2 E^-, \quad (5.55)$$

$$0 = E^{3''} + \frac{\partial_\rho \left( \sqrt{|\det \mathcal{G}|} \mathcal{G}^{44} \mathcal{G}^{22} \right)}{\sqrt{|\det \mathcal{G}|} \mathcal{G}^{44} \mathcal{G}^{22}} E^{3'} - 4 \frac{\varrho_h^4 \mathcal{G}^{00}}{R^4 \mathcal{G}^{44}} \mathfrak{w}^2 E^3, \quad (5.56)$$

where we have introduced

$$\mathfrak{m} = \frac{\gamma}{2\sqrt{2}\pi} \tilde{A}_0^3(\varrho). \quad (5.57)$$

Here  $\tilde{A}_t^3(\varrho)$  is the dimensionless background gauge field. The quantity  $\mathfrak{m}$  is related to the dimensionful background field  $A_0^3(\rho)$  by  $\mathfrak{m} = \frac{\gamma}{\sqrt{\lambda}} \frac{A_0^3(\rho)}{2\pi T}$ . The equation of motion for the baryonic fluctuation  $a_\mu$  is the same as the one for  $E^3$ . The Green's function is again calculated by (5.52) where we substitute  $E^+, E^-, E^3 \mapsto E$ .

As a result of the finite isospin chemical potential instead of a baryonic one, we end up with three equations of motion for the decoupled fields  $E^+, E^-$  and  $E^3$ .

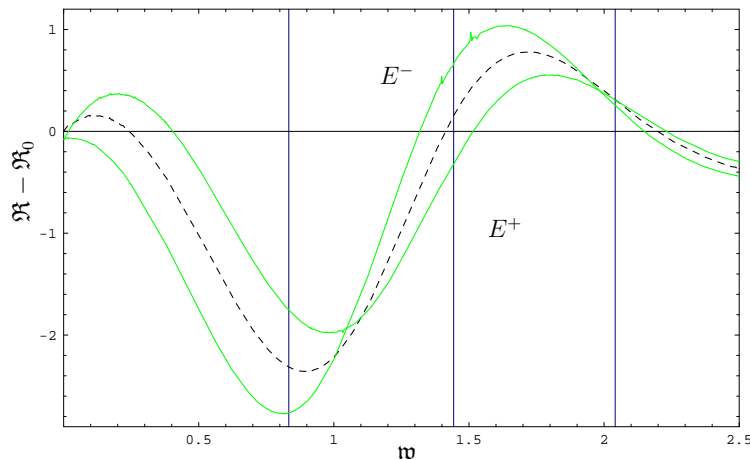


**Figure 5.11:** The finite temperature part of the spectral function  $\mathfrak{R} - \mathfrak{R}_0$  again normalized to  $N_f N_c T^2 / 4$  versus the scaled frequency  $\mathfrak{w} = \omega / (2\pi T)$  at finite isospin density: The dashed curve shows the spectral function of the mode  $E^3$  which is coincident with the mode  $E$  at finite baryon density. The solid curves show the spectral functions of the fields  $E^+$  and  $E^-$  at finite isospin density. The plots are generated for  $m \approx 0.833$  and  $\tilde{n}_I = 0.25$ . The modes  $E^+$  and  $E^-$  split in opposite directions from the baryonic spectral function. This plot is taken from [186].

These equations will have three distinct solutions due to the differences in the last terms of (5.54) to (5.56). Since the difference is a shift in  $\mathfrak{w}$ , one would expect the solutions  $E^+$  and  $E^-$  to be shifted versions of  $E^3$ . However, the shift parameter  $m$  depends on  $\rho$ . The equation of motion for  $E^3$  is identical to the baryonic case which is discussed above.

The three solutions  $E^+$ ,  $E^-$  and  $E^3$  constitute the isospin triplet of mesons which carry isospin charge one. An example is the  $\rho$  meson in QCD [211, 212]. The mode  $E^3$  coincides with the solution in case of a solely baryonic chemical potential, while the other two solutions have peaks in the spectral function at lower and higher values of  $\mathfrak{w}$  (see figure 5.11). The magnitude of this splitting of the spectral lines is determined by the chemical potential.

In the limit of zero frequency  $\mathfrak{w} \rightarrow 0$ , equations (5.54) and (5.55) coincide and will result in identical solutions  $E^+$  and  $E^-$ . In this limit the solution  $E^3$ , though, differs from  $E^+$  and  $E^-$ , by means of the last term. So for small frequencies  $\mathfrak{w}$ , we expect differences between the solutions  $E^3$  and  $E^+$ ,  $E^-$ .

We now investigate the effects of finite isospin density on the spectrum. After solving (5.54) to (5.56) numerically, the correlators may be evaluated as given by (5.52), where  $E$  has to be replaced by  $E^3$ ,  $E^+$  or  $E^-$ . The peaks in the spectral functions again correspond to mesons.

An interesting feature at finite isospin chemical potential is the formation of a new peak in the spectral function in the regime of small  $\mathfrak{w}$  at high density/high chemical potential, see figure 5.12. Notice that compared to the baryonic case the

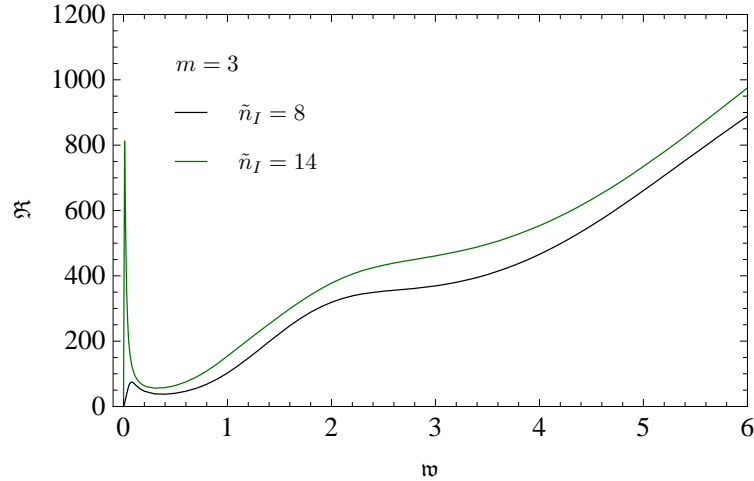


**Figure 5.12:** Spectral function  $\mathfrak{R}$  as calculated from (5.55). A new peak forms at high isospin densities. This figure is taken from [204].

density, at which the new peak forms, is about two orders of magnitude smaller. As in the baryonic case, the excitations related to the supersymmetric spectrum broaden, the corresponding mesons become unstable. In section 5.5 we will see that this new peak triggers an instability of the system. This instability is very general for systems at finite isospin chemical potential. For instance it is also present in the Reissner-Nordström black hole [100].

### 5.3.2 Quasinormal Modes of Flavor Field

Above we found pronounced structures in the spectral function of flavor fields which are interpreted as mesonic quasiparticle resonances. By varying the baryon chemical potential, these structures show an interesting behavior which we would like to study in more detail by investigating the quasinormal mode spectrum. This has been done in my own work [3]. As described in section 4.3.3, we parameterize by  $\chi_0$  instead of  $m$  as well as by density  $\tilde{n}_B$  instead of the chemical potential  $\mu_B$  since  $m$  and  $\mu_B$  are not monotonic functions.

#### Transverse vectors

First we study the quasinormal mode spectrum of transverse vector fluctuations. We aim for an explanation of the turning behavior of the meson mass found in the section above: At large quark mass the meson mass increases proportional to the quark mass  $M_q$  as expected from the formula found in the supersymmetric limit (3.55). Whereas for small quark mass, there exists a region where the meson mass is decreasing when the quark mass is raised.

Figure 5.13 (a) displays the paths of the first quasinormal mode in the complex frequency plane for different densities. The paths are parametrized by the quark

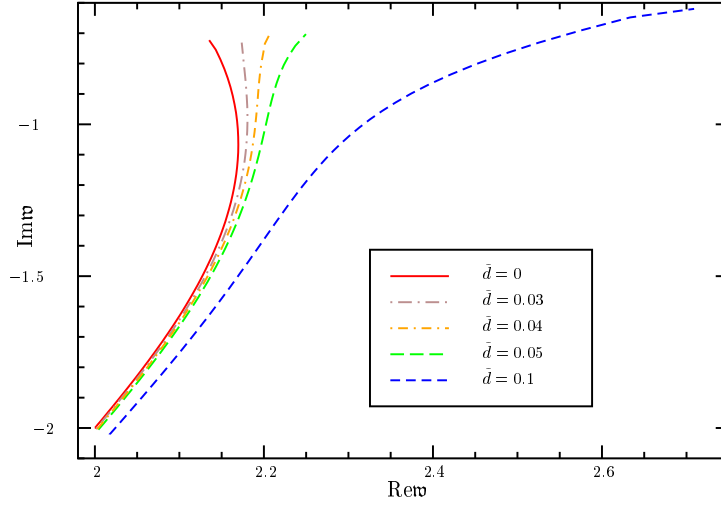


**Figure 5.13:** First *transversal* quasinormal mode for several densities  $\tilde{n}$ . For smaller densities a turning point in the real part occurs, which vanishes as the densities rises. This figure is taken from [3].

mass over temperature ratio. When the quark mass is zero, i.e. our embedding is flat, the quasinormal mode is located near the point  $2(1 - i)$  (cf. (4.117)) and moves towards the real axis as the quark mass increases. For small densities the curves turn around and tend towards smaller real values for larger quark mass. This behavior disappears when we raise the density up to a critical density  $(\tilde{n}_B)_c \approx 0.04$ .

## Scalar

In order to compute the spectral function for scalar modes, we first calculate the pullback of the metric to the D7-branes and expand it in the fluctuations of the embedding variables  $\delta\theta$  and  $\delta\phi$ .  $\delta\theta$  corresponds to the scalar and  $\delta\phi$  to the pseudoscalar excitation. We consider time and  $\rho$  dependence of the fluctuations only, since we stay at zero momentum. The induced metric then reads

$$\begin{aligned}
 ds^2 = & \frac{1}{2} \frac{\rho^2}{R^2} \left( -\frac{f^2}{\tilde{f}} dt^2 + \tilde{f} dx_i^2 \right) + \frac{R^2}{\rho^2} \frac{1 - \chi^2 + \rho^2 \chi'^2}{1 - \chi^2} d\rho^2 + R^2 \sin(\theta + \delta\theta) d\Omega_3 \\
 & - 2R^2 \frac{\chi'}{\sqrt{1 - \chi^2}} \partial_\mu \delta\theta dx^\mu d\rho + R^2 \partial_a \delta\theta \partial_b \delta\theta dx^a dx^b.
 \end{aligned} \tag{5.58}$$

This coincides with the result found in [184] at zero density.

In order to obtain a consistent solution at non-zero density, it is necessary to include fluctuations in the gauge field  $a_t$  since these couple to the fluctuations  $\delta\theta$  of the induced metric on the D7-brane [203]. We may think of the embedding scalar as

being effectively charged which explains its coupling to the gauge field fluctuations<sup>3</sup>. Then the action in this case differs from the action in [184] by the non-vanishing gauge field and gauge field fluctuation terms. The Lagrangian is given by

$$\begin{aligned}
\mathcal{L} \propto & \mathcal{L}_0 + \mathcal{L}_1 + \mathcal{L}_2 - \rho^3 f \tilde{f} a \sqrt{b} \sqrt{1-c} F^{t\varrho} (\delta F_{\varrho t}) - \frac{3}{2} \rho^3 f \tilde{f} \frac{a-bc}{\sqrt{b} \sqrt{1-c}} (\delta\theta)^2 \\
& - \frac{R^4}{r_H^2} \rho \frac{\tilde{f}^2}{f} \frac{a^2}{\sqrt{b} \sqrt{1-c}} (\partial_t \delta\theta)^2 + \frac{1}{2} \rho^5 f \tilde{f} \frac{a^2(a-bc)}{b^{3/2}(1-c)^{3/2}} (\partial_\rho \delta\theta)^2 \\
& + \frac{R^2}{2} \sum_i \mathcal{G}_0^{ii} \chi^2 (\partial_i \delta\phi)^2 + \rho^5 \tilde{f}^{3/2} \chi' \frac{\sqrt{2}}{r_H} \frac{a^2 \sqrt{c}}{b(1-c)^{3/2}} (\delta F_{\varrho t}) (\partial_\rho \delta\theta) \\
& - \rho^3 \tilde{f}^{3/2} \chi \frac{3\sqrt{2}}{r_H} \frac{a\sqrt{c}}{\sqrt{1-c}} (\delta F_{\varrho t}) (\delta\theta) + \frac{1}{4} \rho^3 f \tilde{f} a \sqrt{b} \sqrt{1-c} \sum_{ik} \mathcal{G}_0^{ii} \mathcal{G}_0^{kk} (\delta F_{ik})^2 \\
& - \rho^3 f \tilde{f} a \sqrt{b} \sqrt{1-c} F^{t\varrho} \sum_i \mathcal{G}_0^{ii} \left( -\frac{(1+\delta_{4i}) R^2 \chi'}{\sqrt{a}} \right) (\delta F_{it}) (\partial_i \delta\theta), \tag{5.59}
\end{aligned}$$

where  $\mathcal{L}_0$  is simply the Lagrangian without any fluctuations but non-vanishing density,

$$\mathcal{L}_0 = \rho^3 f \tilde{f} a \sqrt{b} \sqrt{1-c}. \tag{5.60}$$

The boundary terms  $\mathcal{L}_1$  and  $\mathcal{L}_2$  are given by

$$\mathcal{L}_1 = \partial_\rho \left[ -\frac{\rho^5 f \tilde{f} a^{3/2} \chi'}{\sqrt{b} \sqrt{1-c}} (\delta\theta) \right] \quad \text{and} \quad \mathcal{L}_2 = \partial_\rho \left[ -\frac{3}{2} \frac{\rho^5 f \tilde{f} \chi \chi' a}{\sqrt{b} \sqrt{1-c}} (\delta\theta)^2 \right], \tag{5.61}$$

with

$$a = 1 - \chi^2, \quad b = a + \rho^2 \chi'^2, \quad c = \frac{8\tilde{n}_B^2}{\rho^6 \tilde{f}^3 a^3 + 8\tilde{n}_B^2}, \quad \text{so} \quad 1 - c = \frac{\rho^6 \tilde{f}^3 a^3}{\rho^6 \tilde{f}^3 a^3 + 8\tilde{n}_B^2}. \tag{5.62}$$

The equation of motion derived from this action is given by

$$0 = \partial_\rho [A \partial_\rho (\delta\theta)] + B \mathbf{w}^2 (\delta\theta) + C (\delta\theta), \tag{5.63}$$

where

$$\begin{aligned}
A &= \frac{\rho^5 f \tilde{f} (1 - \chi^2)^3}{(1 - \chi^2 + \rho^2 \chi'^2)^{3/2} \sqrt{1 - \frac{8\tilde{n}_B^2}{\rho^6 \tilde{f}^3 (1 - \chi^2)^3 + 8\tilde{n}_B^2}}}, \\
B &= \frac{\rho \tilde{f}^2 (1 - \chi^2)^2}{\sqrt{1 - \chi^2 + \rho^2 \chi'^2} \sqrt{1 - \frac{8\tilde{n}_B^2}{\rho^6 \tilde{f}^3 (1 - \chi^2)^3 + 8\tilde{n}_B^2}}}, \\
C &= \frac{3\rho^3 f \tilde{f} (1 - \chi^2) \sqrt{1 - \frac{8\tilde{n}_B^2}{\rho^6 \tilde{f}^3 (1 - \chi^2)^3 + 8\tilde{n}_B^2}}}{\sqrt{1 - \chi^2 + \rho^2 \chi'^2}} \left[ 1 - 6\chi \left( \rho \frac{f}{\tilde{f}} \chi' + \chi \right) \right]. \tag{5.64}
\end{aligned}$$

<sup>3</sup>The gauge field  $a_t$  and the scalar  $\delta\theta$  transform non-trivially under diffeomorphisms and must therefore be combined to a single physical field.

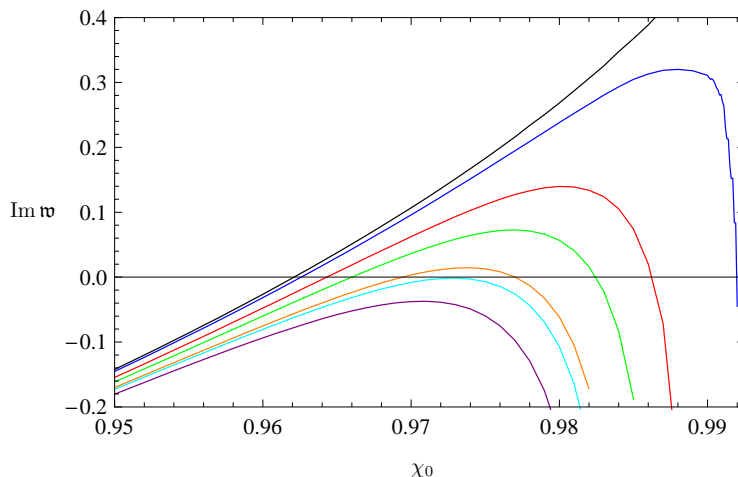


**Figure 5.14:** The *scalar* quasinormal modes with pure imaginary quasinormal frequencies for different densities  $\tilde{n}$ . For densities smaller than the critical density  $(\tilde{n}_B)_c = 0.00315$ , the mode becomes tachyonic in some region of the parameter space. The several colors corresponds to different densities  $\tilde{n}_B = 0$  (black), 0.001 (blue), 0.002 (red), 0.0025 green, 0.003 (orange), 0.00315 (cyan), 0.0035 (purple). This figure is taken from [3].

The gauge field fluctuation is fixed by the constraint equation which is present due to the gauge fixing  $a_\rho = 0$ .

**Results for scalars** First we study the density dependence of the mode with purely imaginary quasinormal frequencies found at zero density in figure 4.11. Our numerical results are shown in figure 5.14. In this figure we observe that the critical parameter  $\chi_0^{\text{crit}}$ , at which the instability occurs, i. e. the quasinormal frequency enters the upper half plane, increases with the density. Thus, we write  $\chi_0^{\text{crit}}(\tilde{n}_B)$ . Also we note that at finite densities the modes become stable again at some larger value for  $\chi_0$ , which we denote by  $\chi_{0,2}^{\text{crit}}(\tilde{n}_B)$ . If we increase the density further, we obtain a critical density  $(\tilde{n}_B)_c = 0.00315$  at which the mode is always stable. Therefore, the system is unstable in the parameter region  $\chi_0^{\text{crit}}(\tilde{n}_B) < \chi_0 < \chi_{0,2}^{\text{crit}}(\tilde{n}_B)$  and  $\tilde{n}_B < (\tilde{n}_B)_c$ . The numerical values can be obtained from figure 5.14. Later we further discuss this mode and relate the instability found to an instability known from thermodynamics.

Let us now consider the behavior of the first quasinormal mode if we vary the baryon density  $\tilde{n}_B$ . In figure 5.15 we present our numerical results. In this figure we observe that for each finite density we find that for large enough  $\chi_0$  the quasinormal frequencies behaves in a similar way. The real part increases while the imaginary part decreases as we increase  $\chi_0$ . For smaller values of  $\chi_0$  we observe three distinct movements of the quasinormal frequencies. For small densities  $\tilde{n}_B < 0.1$  the quasinormal frequency first follows the line of the quasinormal mode corresponding to zero density as we increase the parameter  $\chi_0$ . After a critical value of  $\chi_0$  is reached, the quasinormal frequency leaves this line as the real part of the quasinormal fre-

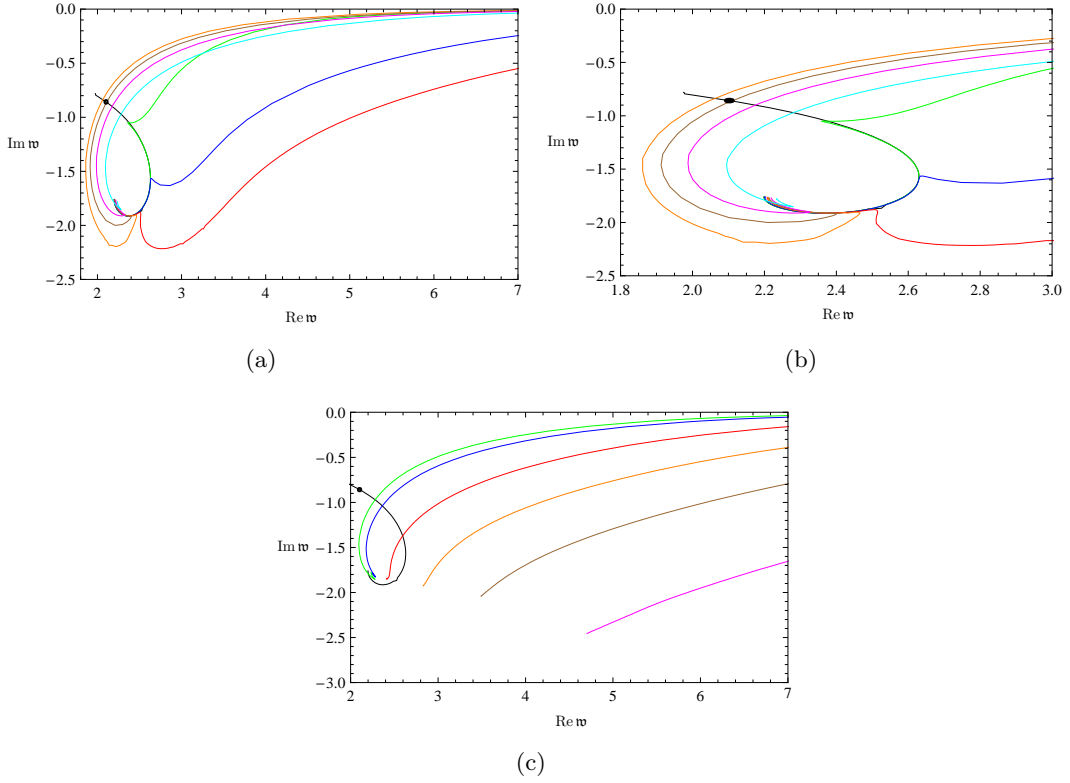


**Figure 5.15:** Dependence of the first *scalar* quasinormal frequency on the density: In (a) and (b) the quasinormal frequencies for small densities  $\tilde{n}_B \leq 0.2$  are shown while in (c) densities up to  $\tilde{n}_B = 5$  are considered. In (a) and (b) the different colors corresponds to distinct densities  $\tilde{n}_B = 0$  (black), 0.01 (green), 0.05 (blue), 0.1 (red), 0.11 (orange), 0.125 (brown), 0.15 (magenta), 0.2 (cyan). In (c) the color coding is  $\tilde{n}_B = 0$  (black), 0.2 (green), 0.25 (blue), 0.5 (red), 1 (orange), 2 (brown), 5 (magenta). In all three plots the black dot marks the critical value of the quark mass/temperature parameter  $\chi_0$  where the instability occurs. These figures are taken from [3].

quency increases monotonically. For slightly larger densities  $0.11 < \tilde{n}_B < 0.2$ , the frequencies also first moves along the line of the quasinormal mode at zero densities but in contrast to the case discussed above the real part of the frequencies now first decreases. For even higher densities  $\tilde{n}_B > 0.2$ , the frequency at  $\chi_0 = 0$  strongly depends on the densities. We find from figure 5.15 (c) that both the real and imaginary part of the quasinormal frequencies at  $\chi_0 = 0$  increase with  $\tilde{n}_B$ . As we increase  $\chi_0$  we find the usual behavior, the real part of the frequency increases while the imaginary part decreases.

## Schrödinger Potential Analysis

In this section we present the Schrödinger potential analysis introduced in section 4.3.3 at finite baryon density. We use this analysis to explain the qualitative movement of the quasinormal frequencies as we change the baryon density.

For the vector fluctuations we observe in figure 5.13 (a) a turning point in the movement of the quasinormal frequencies at low baryon density. The real part of the quasinormal frequencies first increases and later decreases as we increase the mass parameter  $m$ . This turning point disappears as the critical density of  $(\tilde{n}_B)_c = 0.04$  is reached. After a critical quark mass is reached the real part of the quasinormal frequencies always increases while the imaginary part decreases.

Let us now consider the Schrödinger potential which correspond to these quasinormal modes in figure 5.16. A similar analysis has also been done in [202]. In addition to the infinite wall at  $R^* = 0$  which corresponds to the AdS boundary, an additional peak appears in the potential as we increase the quark mass parametrized by  $\chi_0$ . For small densities (see figure 5.16 (a)), this peak slowly grows out of the step-shape potential already observed in section 4.3.3. The step-shape potential is also present at zero density and it is known from the analysis we presented there that the corresponding quasinormal frequencies show the turning point behavior discussed above. Thus, the new feature of the finite density setup is the appearance of the peak at high quark masses. As the peak grows, ‘bound’ states with positive energy can be formed, i. e. the real part of the corresponding quasinormal frequency is always bigger than its imaginary part. Therefore, we find quasiparticle excitations whose masses increase as we increase the quark mass.

If we increase the baryon density, the peak already appears at lower quark mass and can, thus, destroy the step-shape potential (see figure 5.16 (b) and (c)). For instance a step is still observable in the orange and blue curve in figure 5.16 (b), while in figure 5.16 (c) this step is gone. Since the step-shape potential is the reason for the turning point potential, we also find in this analysis a critical baryon density at which the turning point disappears. This critical density agrees with the value found in figure 5.13 (a). For even larger densities (see figure 5.16 (d)), the peak increases even faster, i. e. the real (imaginary) part of the corresponding quasinormal frequencies increase (decrease) even faster.

Let us now consider the scalar fluctuations at finite density which show several distinct features: a tachyonic mode at small densities and three qualitative different movements of the quasinormal frequencies.

From figure 5.14 we know that there exists a parameter region where a scalar mode becomes tachyonic. Especially interesting is that at finite density, the mode is stabilized as the quark mass is increased and that there is a critical density  $(\tilde{n}_B)_c = 0.00315$  at which the mode is always stable. In figure 5.17 we present the Schrödinger potentials of the scalar fluctuations in the relevant density region. As in the case of zero density a negative well appears in the potential. It also first grows as we increase the quark mass (see figure 5.17 (a)). However, as we increase the quark mass further, the well decreases while a peak forms in the potential. After a critical

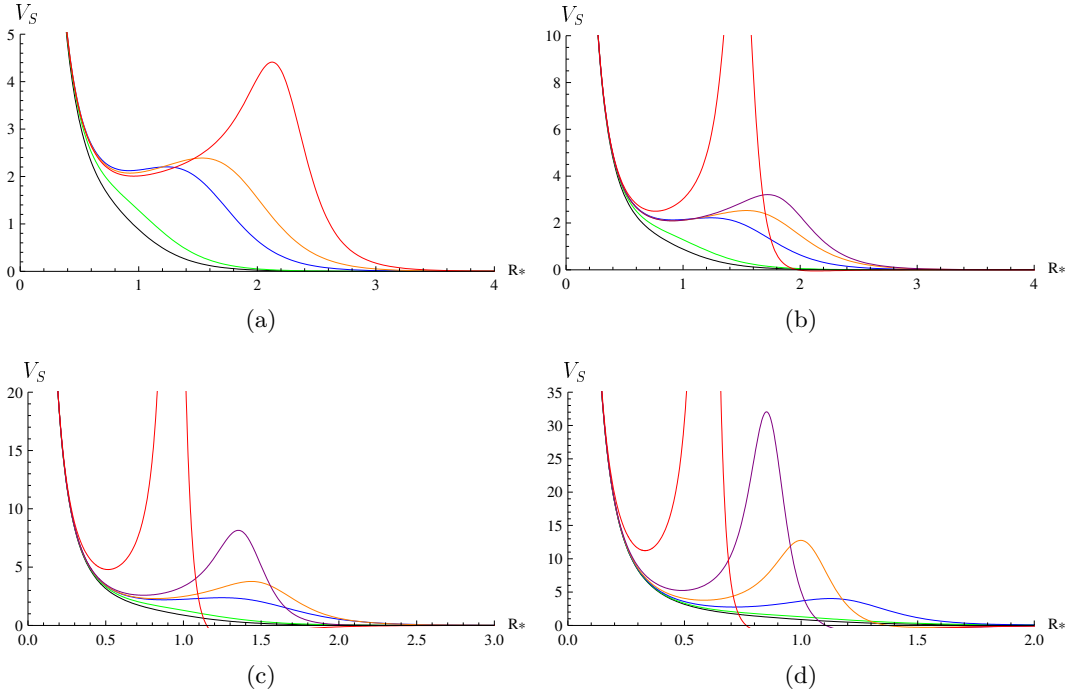


**Figure 5.16:** Schrödinger potential of the *vector* fluctuations at finite baryon density (a)  $\tilde{n}_B = 0.003$ , (b) 0.01, (c) 0.03 and (d) 0.1. The different colors corresponds to distinct quark masses parametrized by  $\chi_0 = 0$  (black), 0.5 (green), 0.9 (blue), 0.95 (orange), 0.97 (purple), 0.99 (red). See figure 5.3 for the relation between  $\chi_0$ , the temperature and the quark mass  $M_q$ . These figures are taken from [3].

quark mass is reached, this well cannot longer support a ‘bound’ state with negative energy, i. e. the imaginary part of the quasinormal frequency becomes negative again. At the critical density  $(\tilde{n}_B)_c = 0.00315$  (see figure 5.17), the potential also shows a negative well. However, this well just reaches a critical depth in order to support a zero energy ‘bound’ state which is due to the zero-point energy (cf. the three-dimensional potential pot know from quantum mechanics).

Now we investigate the Schrödinger potentials which are relevant for the movement of the first quasinormal frequency studied in figure 5.15. These potentials are plotted in figure 5.18. The first observation is that for small densities  $\tilde{n}_B \lesssim 0.15$  (see figure 5.18 (a) and (b)), the potentials at low quark mass agree with the potential at zero density. Thus, also the corresponding quasinormal frequencies must agree which we already found in figure 5.15. At larger densities (see figure 5.18 (c)) even the potential at zero quark mass differs from the one at the zero density such that the corresponding quasinormal frequencies at zero quark mass depend on the density which is consistent with the result found in figure 5.15 (c). As for the vector fluctuations, a peak appears in the potential at finite density as we increase the quark mass. These peak can again support ‘bound’ states which correspond to

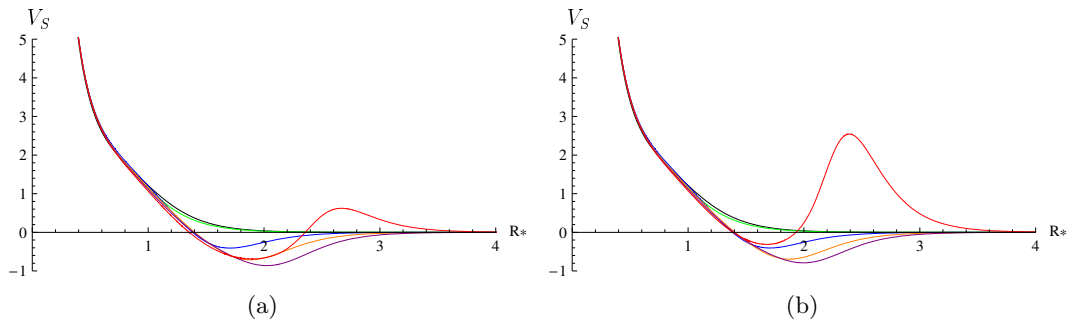


**Figure 5.17:** Schrödinger potential of the *scalar* fluctuations at finite baryon density (a)  $\tilde{n}_B = 0.002$ , (b)  $0.00315$ . The different colors corresponds to distinct quark masses parametrized by  $\chi_0 = 0$  (black),  $0.5$  (green),  $0.9$  (blue),  $0.95$  (orange),  $0.97$  (purple),  $0.99$  (red). See figure 5.3 for the relation between  $\chi_0$ , the temperature and the quark mass  $M_q$ . These figures are taken from [3].

quasiparticle excitations. Thus, the imaginary part of the quasinormal frequencies decreases while the real part increases as we increase the quark mass. This is the overall movement of the quasinormal frequencies which is shown in figure 5.15.

In general, we observe that at finite baryon density a peak appears in the Schrödinger potential as we increase the quark mass. If the peak is high enough, it separates the horizon of the black hole from the AdS boundary. Only a small leak into the black hole is possible due to tunneling. The potential, thus, approaches the one of a Minkowski embedding where the brane does not fall into the horizon of the black hole and, therefore, can support stable normal modes which are calculated in [39] in the supersymmetric limit. In figure 5.19 we explicitly confirm that the Schrödinger potential obtained from the black hole embeddings converges to the potential of the supersymmetric Minkowski embedding<sup>4</sup> with the same mass parameter  $m$  as the mass parameter goes to infinity. This convergence explains that also the quasinormal frequencies approach this supersymmetric mass spectrum if the quark mass is big enough. This behavior has already been found for the vector fluctuations in [186, 202]. We can also understand this convergence if we look at the phase diagram (see figure 5.20). For large quark mass over temperature ratios the equal density lines approach the shaded region where the Minkowski embeddings are preferred. Since the phase transition is third or second order for large quark mass over temperature ratios as it is shown in [207], we also expect a smooth transition from the spectrum of the quasinormal modes obtained from the black hole embeddings to the spectrum of the normal modes obtained from the Minkowski embeddings.

Next we would like to understand the appearance of the peak in terms of the

<sup>4</sup>The Schrödinger potential of a supersymmetric Minkowski embedding is given by [185]

$$V_S = m^2 \left[ 1/4 + 3/8 \left( \tan^2(mR^*/\sqrt{2}) + \cot^2(mR^*/\sqrt{2}) \right) \right].$$

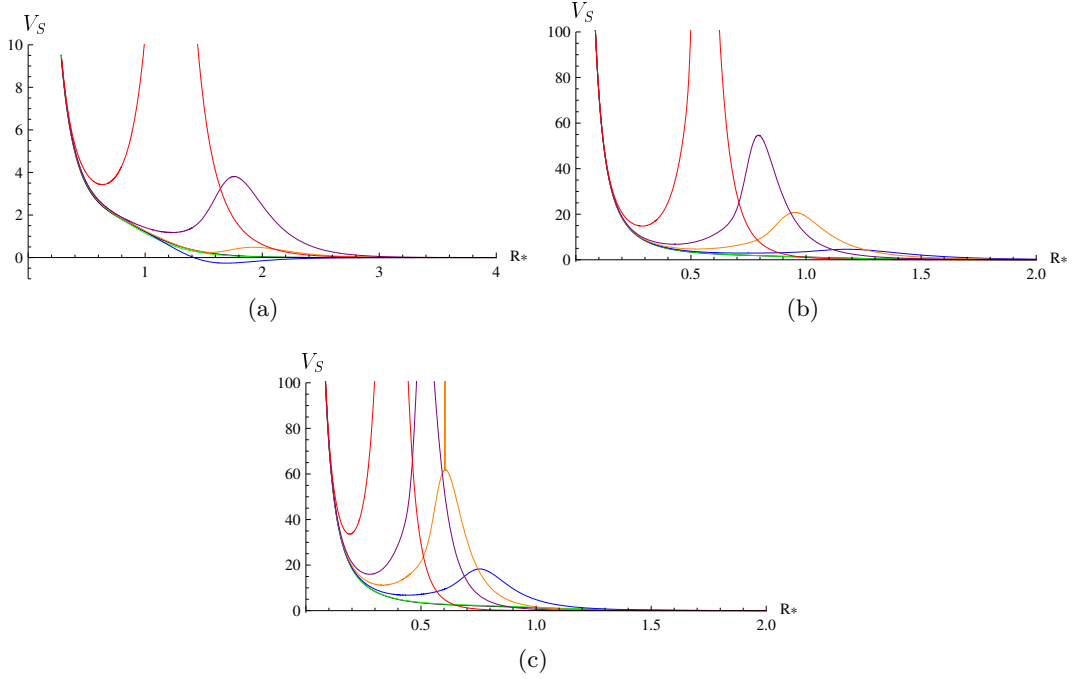


**Figure 5.18:** Schrödinger potential of the *scalar* fluctuations at finite baryon density (a)  $\tilde{n}_B = 0.01$ , (b) 0.15, (c) 0.5. The different colors corresponds to distinct quark masses parametrized by  $\chi_0 = 0$  (black), 0.5 (green), 0.9 (blue), 0.95 (orange), 0.97 (purple), 0.99 (red). See figure 5.3 for the relation between  $\chi_0$ , the temperature and the quark mass  $M_q$ . These figures are taken from [3].

D7-brane embedding. In [72] it was shown that the finite baryon density on the brane is induced by fundamental strings which are stretched from the horizon of the black hole to the D7-brane (see figure 5.2). At large quark masses these strings form a throat close to the horizon. We confirm numerically that the end of this throat and the peak in the Schrödinger potential are located at the same value of the radial coordinate  $\rho$  (see figure 5.21). Therefore, we can interpret this throat as a potential barrier for the fluctuations which becomes bigger as the throat becomes deeper.

### Discussion: Turning Point and Tachyon

We now discuss the turning point in the spectrum of the vector modes and its dependence on the density. For scalars the purely imaginary scalar quasinormal mode reaches into the upper half of the complex plane and, thus, yields a tachyonic excitation, which we also discuss here.

**Turning Point** In this section we discuss why the vector mesons at finite temperature get smaller masses as the quark mass is increased. Further we investigate why there is a turning behavior at finite density.

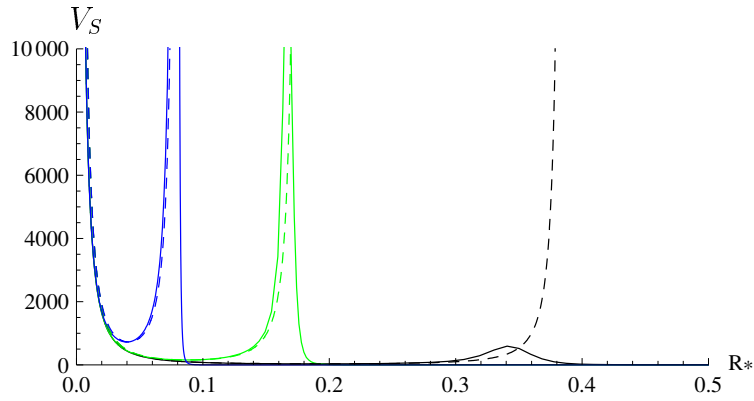


**Figure 5.19:** Comparison of the Schrödinger potential obtained from black hole embeddings (solid lines) and from supersymmetric Minkowski embeddings (dashed lines) at the same quark mass  $m$ . The different colors correspond to different quark masses parametrized by  $\chi_0 = 0.99$  (black),  $0.999$  (green),  $0.9999$  (blue) at a fixed density  $\tilde{n}_B = 0.5$ . See figure 5.3 for the relation between  $\chi_0$ , the temperature and the quark mass  $M_q$ . This figure is taken from [3].

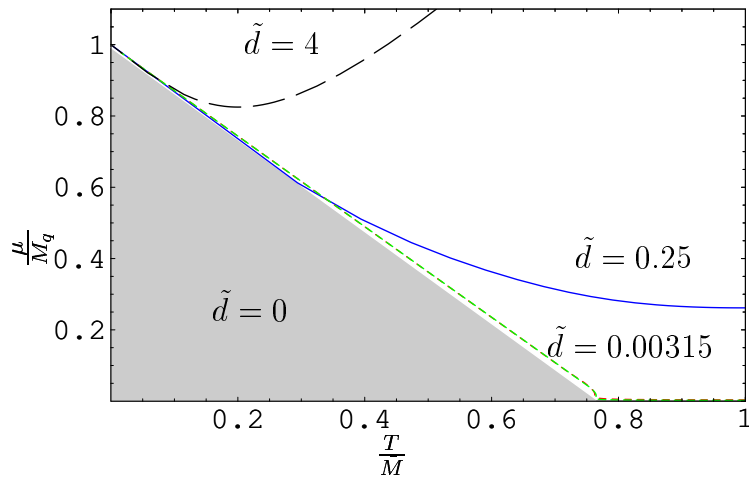


**Figure 5.20:** Sketch of the phase diagram: The chemical potential  $\mu$  divided by the quark mass  $M_q$  is plotted versus the temperature  $T$  divided by  $\bar{M} = 2M_q/\sqrt{\lambda}$ . Two different regions are displayed: The shaded region with vanishing baryon density where Minkowski embeddings are preferred and the region above the transition line with finite baryon density where the black hole embeddings are preferred. Here we work in the second phase. The curves are lines of equal baryon density parametrized by  $\tilde{n}_B$ . This figure is taken from [3].

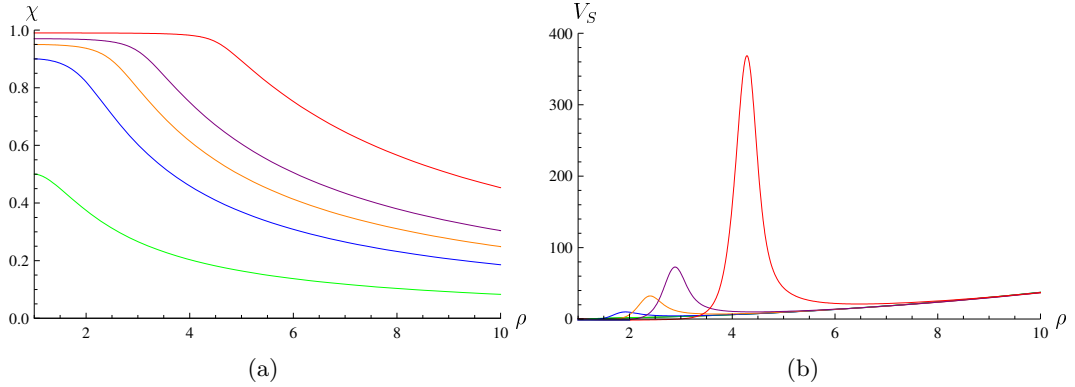


**Figure 5.21:** Comparison of the location of the peak in the Schrödinger potential and the throat in the embedding of the D7-brane. The end of the throat is located where  $\chi$  first changes its value. The different colors corresponds to different quark masses parametrized by  $\chi_0 = 0$  (black), 0.5 (green), 0.9 (blue), 0.95 (orange), 0.97 (purple), 0.99 (red). See figure 5.3 for the relation between  $\chi_0$ , the temperature and the quark mass  $M_q$ . The baryon density is  $\tilde{n}_B = 0.25$ . These figures are taken from [3].

Let us first summarize our results. The D3/D7-system at finite density has two competing geometrical features. One is the formation of a *potential barrier* near the horizon due to the charge located at the horizon. This causes the resonances in the spectral function to become more stable and to move to larger frequency when the quark mass is increased. The second feature is the length of the brane<sup>5</sup> supporting an excitation from the horizon to the boundary. Increasing this length causes the vector meson resonances to move to smaller frequency with increasing quark mass. These two geometrical features compete at finite density while at zero density the potential barrier is absent. In [3, 209] this is explained in greater detail.

The first and as it turns out the more important effect at finite density is the formation of a *potential barrier* near the horizon at  $R^* = \infty$ , see figure 5.19. This barrier effectively cuts off the horizon from the geometry. Only a small part of the wave function "leaks" into the region behind the potential barrier where the black hole is located, that is region *III* in the schematic solution shown in figure 5.22. In this region *III* the Schrödinger potential asymptotically vanishes. Therefore, the solution shown in figure 5.22 first drops to low values in order to diverge only very close to the horizon (not shown in the figure). Region *II* is the finite radial distance covered by the potential barrier. Here the wave function qualitatively drops exponentially. In region *I* the main part of the solution is located between the boundary and the barrier. Here the potential approaches a pot-like form more and more similar to the corresponding potential generated by the Minkowski embedding as the quark mass parameter is increased. As this happens, the black hole fluctuation solu-

<sup>5</sup>Since the AdS-boundary is infinitely far away from the horizon, the length of the brane has to be renormalized by subtracting for example the length of the brane at trivial embedding  $\chi_0 = 0$ .

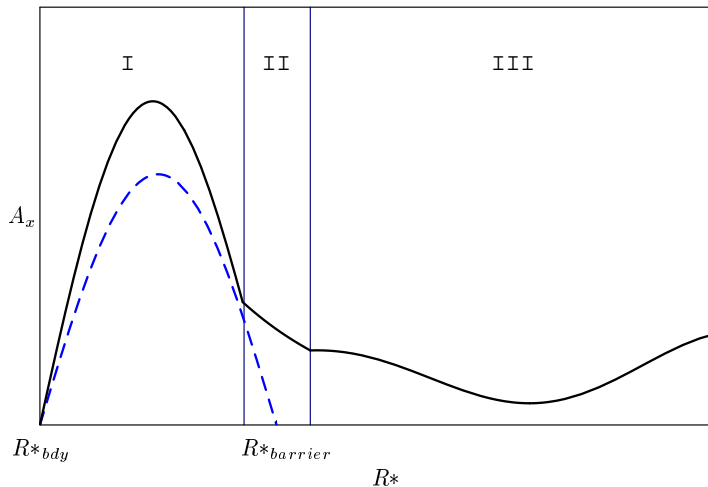


**Figure 5.22:** Schematic outline of the solution to the vector fluctuation equation of motion (5.51). The horizon is located at  $R^* = \infty$  where the wave function diverges, the AdS-boundary is  $R^*_{bdy} = 0$ . The solid black curve shows the solution at finite temperature, density and quark mass, i.e. on a black hole embedding. The dashed blue curve shows the corresponding solution on a Minkowski embedding at the same quark mass. The three regimes correspond to the nature of the potential shown in figure 5.19: I) Minkowski-like, II) potential barrier, III) essentially vanishing potential. This figure is taken from [3].

tion (solid black curve in the schematic plot in figure 5.22) approach the Minkowski solutions (dashed blue curve in the schematic plot in figure 5.22).

As we see from figure 5.21, the potential barrier moves closer to the boundary as the mass parameter  $\chi_0$  is increased. Thus, the potential gets more narrow and the lowest possible excitation is raised to a higher energy, i.e. the real part of the corresponding quasinormal mode is increasing. Furthermore, the barrier becomes higher such that the corresponding excitation becomes more stable, i.e. the imaginary part of the quasinormal frequency decreases. In other words, less of the wave function leaks over the barrier into the black hole.

Let us for simplicity work at vanishing density first. All our considerations will also apply to the finite density case. The heuristic explanation for the left-movement of resonances has to do with the proper length of the D7-brane. At  $\chi_0 = 0$  we have a flat embedding which is the minimal length the brane can have. Increasing the quark mass parameter  $\chi_0$ , the D7-brane becomes “longer”. Therefore, we can imagine a solution supported on the brane to be “stretched” together with the brane, i.e. its effective wavelength increases. Assuming a constant effective speed of light, the effective frequency of this solution has to decrease. In this sense  $\chi_0$  here acts analogously to a damping coefficient  $\gamma$  in a damped harmonic oscillator.<sup>6</sup>

<sup>6</sup> This heuristic picture neglects the fact that the damping of the gravity modes, in general, is a local effect, i.e. it depends on the radial AdS-coordinate (through radially-dependent geometry). Tentatively, we will assume that we can average the damping effects over the radial coordinate and

This leads us to assume that the fluctuation equation of motion on the D7-brane for real values of the frequency  $\mathfrak{w} \in \mathbf{R}$  can effectively be replaced by the equation of motion for a damped harmonic oscillator with an effective eigenfrequency  $\mathfrak{w}_{\text{eff}}$  and with the replacements  $\gamma \rightarrow \gamma(\chi_0)$ , with  $\gamma(\chi_0)$  a monotonous function and  $\mathfrak{w}_0 \rightarrow \mathfrak{w}(\chi_0 = 0)$ . By  $\mathfrak{w}(\chi_0 = 0)$  we mean the effective eigenfrequency corresponding to the solution mainly influenced by the lowest of the quasinormal modes.  $\gamma(\chi_0)$  can be seen as the effective damping coefficient<sup>7</sup>. So an effective solution at finite  $\chi_0$  depend on the reduced eigenfrequency

$$\mathfrak{w}_{\text{eff}}(\chi_0) = \mathfrak{w}_0 \sqrt{1 - \gamma(\chi_0)^2}. \quad (5.65)$$

Since  $0 \leq \gamma(\chi_0) \leq 1$  and  $\gamma(\chi_0)$  is monotonous, the frequency of the solution which has the eigenfrequency  $\mathfrak{w}_0$  at  $\chi_0$  is monotonously decreasing with increasing  $\chi_0$ . So the quark mass parameter  $\chi_0$  effectively acts as a damping coefficient. We might even suspect that the embedding  $\chi(\rho)$  acts as a local damping coefficient depending on the radial location.

Now let us (as a very crude approximation) choose  $\mathfrak{w}_0$  to be the real part of the first vector quasinormal mode on the D7-brane at vanishing  $\chi_0$ . The quasinormal mode is already damped, i. e. it actually has no real eigenfrequency. But let us, nevertheless, follow our recipe and replace the complicated fluctuation equation by the simple damped harmonic oscillator with an effective damping  $\gamma(\chi_0)$  and effective reduced eigenfrequency  $\mathfrak{w}(\chi_0)$  from equation (5.65). The decreasing eigenfrequency  $\mathfrak{w}(\chi_0)$  with increasing  $\chi_0$  effectively explains the left-motion of the resonances in the corresponding spectral functions. Here we have assumed that the lowest resonance peak in the spectral function behaves in the same way (moving to lower frequencies) as the effective eigenfrequency  $\mathfrak{w}_{\text{eff}}(\chi_0)$ . This intuition we get from the fact that in the exact computation both of these frequencies are mainly determined by the behavior of the lowest quasinormal mode.

These considerations shall serve to give an intuition for the behavior of the resonances. To be more precise the resonances are actually influenced by all the quasinormal modes, i. e. by their location in the complex frequency plane *and* by their residues.

**Killing the Tachyon** The scalar tachyon appearing at zero density is stabilized by introducing baryon charge. From a critical density  $(\tilde{n}_B)_c = 0.00315$  on the scalar does not become tachyonic for any value of  $\chi_0$ . Therefore, the finite charge density  $\tilde{n}_B$  cures the instability and *stabilizes the black hole phase of the D3/D7 system*<sup>8</sup>. We have described the scalar quasinormal mode signatures in detail above. The

---

express them globally in an effective damping coefficient independent from the radial coordinate.

<sup>7</sup>This identification of  $\gamma(\chi_0)$  is effective in the sense that the actual quantity appearing in the equation of motion (5.51) is  $\chi(\rho)$  which highly depends on the radial location. So we understand the effective damping  $\gamma(\chi_0)$  to be a constant which averages damping effects over the whole AdS-radius.

<sup>8</sup>Note that there exist Minkowski embeddings with the same chemical potential and the same quark mass, but all states in the Minkowski phase have strictly vanishing density  $\tilde{n}_B = 0$  [72, 73].

mechanisms explaining this effect are discussed with the help of Schrödinger potentials. The negative potential well supporting the tachyon is lifted with increasing charge density. As discussed before the appearance of the tachyon is at non-zero density connected to the black hole to black hole *first order phase transition* taking place at finite densities  $0 < \tilde{n}_B \leq 0.00315$  between two distinct black hole phases. In particular, the tachyon appears on the unstable branch of the free energy diagram of the phase transition. This branch connects two metastable branches as shown in figure 5.23. At the critical density  $(\tilde{n}_B)_c = 0.00315$  both the tachyon and the black hole to black hole phase transition disappear. It is not clear what is the physical ground state below  $(\tilde{n}_B)_c$ . As was argued in [73], the true ground state might be a mixed phase for which the gravity description is not known so far.

We identify the unstable region in which the tachyon is present with an instability related to the first order phase transition found in the thermodynamics of the system. This behavior may be understood by comparing it to the first order phase transition of the well-known van-der-Waals gas, as described for instance in [213]. Figure 5.23 (b) shows the first order phase transition of the van-der-Waals gas, which follows the red line in the  $p$ - $V$ -diagram as obtained from the Maxwell construction. Additionally, there are two metastable branches: One of them reaches from the point where the phase transition begins when increasing the volume to the minimum denoted by the red plus sign in the figure. The second reaches from the maximum denoted by the red cross to the point where the phase transition ends when increasing the volume. The region between the two extrema is unstable since the pressure raises when the volume is increased.

Our calculations show a very similar behavior of the system considered here. We have calculated both the free energy as function of  $m \propto M_q/T$  close to the phase transition (see section 5.2.2), displayed schematically in figure 5.23 (a), and the quasinormal modes for the same range of  $M_q/T$ . Both calculations show a similar structure of stable, metastable and unstable branches, with the numerical values for the boundaries of these branches agreeing up to four digits in both calculations. In particular, in analogy to the van-der-Waals gas, we find that in addition to the stable branches<sup>9</sup>, there are metastable branches close to the phase transition, denoted as overheated and undercooled<sup>10</sup> in figure 5.23 (a). Furthermore, we find an unstable branch which connects these two metastable branches. The metastable phases are stable against fluctuations, while on the unstable branch a tachyonic mode appears in the quasinormal spectrum. In particular, we emphasize that at zero density the limiting embedding which has a conical singularity at the black hole horizon, and is often discussed in the literature, lies clearly deep inside the unstable region. Thus,

---

<sup>9</sup>Note that in [72] it was observed that for a small region of the stable phase in which the mass parameter  $m$  is just slightly larger than the critical one there is a charge instability. This instability is distinct from the instability discussed above. We do not observe this charge instability in our quasinormal mode analysis. This may be due to inadequacy of our numerical methods at large mass over temperature ratios.

<sup>10</sup>In the context of the D3/D7 system, the terms ‘overheated’ and ‘undercooled’ were introduced in [185].

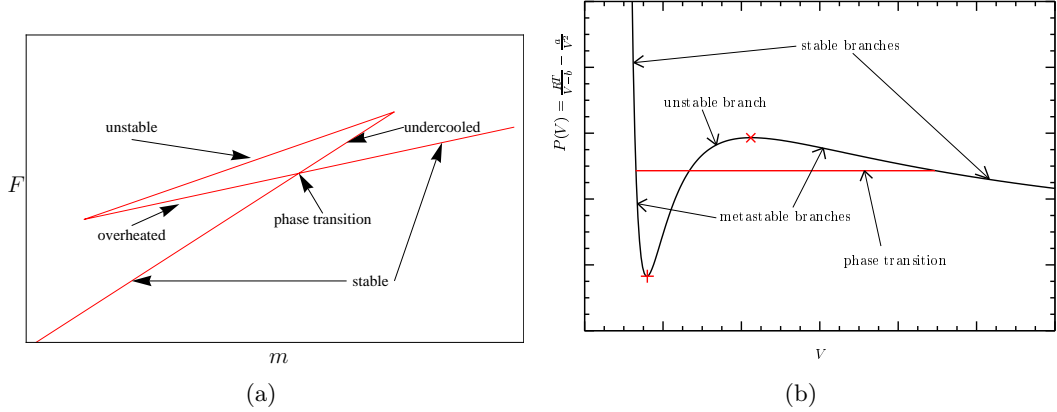


**Figure 5.23:** (a) Sketch of the free energy  $F$  of the flavor fields versus the quark mass over temperature ratio  $m \propto M_q/T$  close to the first order phase transition in the canonical ensemble. (b) Pressure versus volume of the van-der-Waals gas. The red line marks the phase transition which is obtained by the Maxwell construction. Figures are taken from [3].

any observation found by using this embedding should be considered with great care since it does not correspond to a physical state. Furthermore, we should stress that on the field theory side, there exists a stable ground state for any combination of the mass  $m$  and chemical potential  $\mu$ .

## 5.4 Hydrodynamics

In this section we discuss the hydrodynamics for systems with finite chemical potential. The hydrodynamic description discussed in section 4.4 is still valid only the transport coefficients may change. However, the general calculation of the shear viscosity is still possible for the Reissner-Nordström black hole such that we still obtain  $\eta/s = 1/4\pi$ . Since the thermodynamic relation  $\epsilon + P = sT + \mu N$  now contains an additional term due to the finite chemical potential, the momentum diffusion constant is now given by

$$D_m = \frac{\eta}{\epsilon + P} = \frac{1}{4\pi T} \frac{1}{1 + \frac{\mu N}{sT}}. \quad (5.66)$$

The charge diffusion constant for the  $\mathcal{N} = 4$  Super-Yang-Mills theory at finite  $U(1)$  R-charge chemical potential is determined in [214, 215] by using the fluid/gravity correspondence [135, 136],

$$D = \frac{1}{2\pi T} \frac{1 - \frac{Q^4}{4}}{1 + Q^2}, \quad (5.67)$$

where the dimensionless charge density  $Q$  is related to the chemical potential by

$$\frac{\mu}{T} = \frac{4\pi\sqrt{3}Q}{2 - Q^2}. \quad (5.68)$$

The correction term due to the finite density is monotonically decreasing as the density grows and becomes zero at the maximal density given by  $Q = \sqrt{2}$  which corresponds to zero temperature. In contrast to the other transport coefficients, the charge diffusion constant is not given in terms of thermodynamic quantities and is therefore system depending.

## 5.5 Instabilities

In this section we discuss the instabilities present in systems at finite chemical potential. The first observation is that at finite isospin chemical potential the meson resonance split and we have observed the triplet splitting as in figure 5.11. If the chemical potential is increased, the splitting increases and it may happen that the energy of the resonance effectively becomes negative. A negative mass is clearly a signal of an instability and the corresponding field starts to condense. This effect is known as Bose-Einstein condensation.

In order to demonstrate this effect we consider a charged scalar field  $\phi$  at finite chemical potential  $\mu$  given by the time-component of the  $U(1)$  gauge field,  $A_t = \mu$ . The non-zero vev of the gauge field effectively changes the mass term of the scalar field  $\phi$ ,

$$-D_\mu\phi^*D^\mu\phi - m^2\phi^*\phi \rightarrow (\mu^2 - m^2)\phi^*\phi. \quad (5.69)$$

If  $\mu > m$  the mass term is negative and the scalar  $\phi$  starts condensing.

We have already observed this mechanism in the context of gauge/gravity duality in section 5.2.2. There we have obtained a phase transition between the state of zero density, the Minkowski embeddings, and a state at finite density, the black hole embeddings, as we vary the chemical potential. In [73] it is shown that the phase transition happens where the constituent quark mass is equal the quark chemical potential. The critical value for the chemical potential changes with temperature since the constituent quark mass take the interaction into account which changes with temperature.

Let us now come to the instabilities due to the finite isospin chemical potential on the field theory side. We start by considering the global symmetry  $SU(2)$  and pick the chemical potential along the direction of the third Pauli matrix. This breaks the symmetry explicitly down to the  $U(1)_3$  symmetry. The conserved currents  $J_\mu^a$  corresponding to the  $SU(2)$  symmetry, must be now classified according to the residual  $U(1)_3$  symmetry:  $J_\mu^3$  transforms in the adjoint, while  $J_\mu^\pm = J_\mu^1 \pm iJ_\mu^2$  transform in the (anti-)fundamental representation. The currents  $J^\pm$  are charged under the  $U(1)_3$  symmetry and can therefore trigger an instability due to Bose-Einstein condensation. In the following we investigate this instability on the gravity side by studying the quasinormal mode spectrum. An instability is present if a quasinormal mode has a positive imaginary part in our conventions (see for instance (4.105)).

In the following we discuss the quasinormal mode spectrum of the flavor branes at finite isospin chemical potential (5.54) and (5.55) which features an unstable mode. As discussed in 5.3.1 for large isospin densities a new peak forms near the origin.

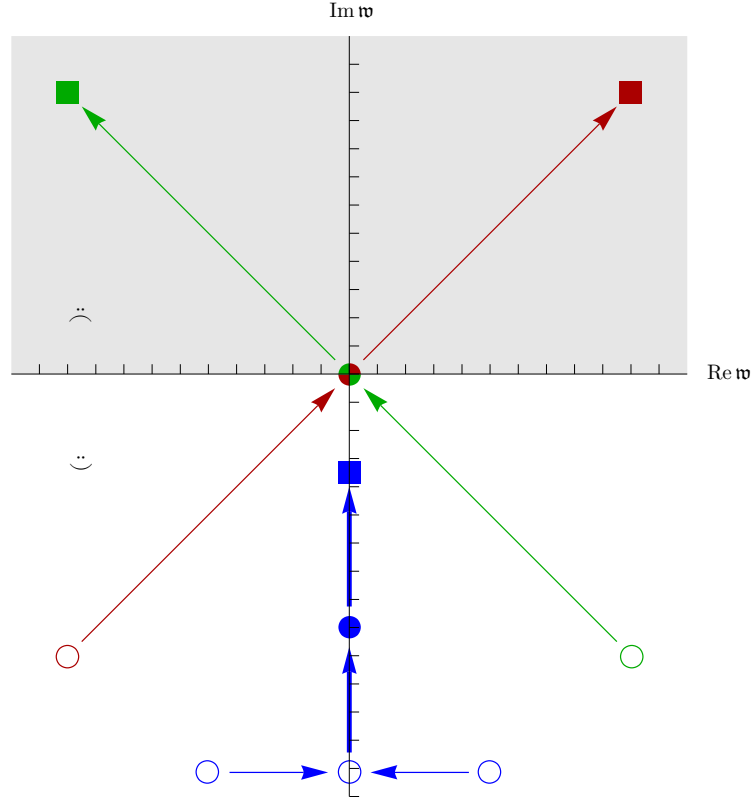


**Figure 5.24:** A sketch of the positions and movements of the quasinormal frequencies under changes of  $\tilde{n}_I$ . Color indicates the function: red =  $E^-$ , green =  $E^+$ , blue =  $E^3$ . The symbols indicate the range of  $\tilde{n}_I$ :  $\circ < (\tilde{n}_I)_{\text{crit}}$ ,  $\bullet = (\tilde{n}_I)_{\text{crit}}$ ,  $\blacksquare > (\tilde{n}_I)_{\text{crit}}$ . Poles in the gray region introduce instabilities. This figure is taken from [204].

This peak is shown in figure 5.12 and originate from a quasinormal mode which is located in the vicinity of the real axis. In figure 5.24 we qualitatively sketch the result from the investigation of the behavior of the quasinormal frequencies closest to the origin of the complex  $\mathbf{w}$ -plane. These modes corresponding to these quasinormal frequencies do *not* produce the peaks corresponding to the supersymmetric spectrum (3.55).

At low densities all quasinormal frequencies are located in the lower half plane. When increasing the isospin density, the quasinormal frequencies of the solutions  $E^\pm$  to (5.54) and (5.55) move towards the origin of the frequency plane. At the same time two poles in the  $E^3$ -correlator move towards each other and merge on the negative imaginary axis, then travel along the axis towards the origin as one single pole. At the critical value of  $\tilde{n}_I$ , the poles corresponding to the quasinormal frequencies of  $E^\pm$  meet at the origin, the poles from  $E^3$  still reside in the lower half plane. This observation matches the discussion below equations (5.54) to (5.56), where we expected  $E^\pm$  to behave similarly at small  $\mathbf{w}$ , while  $E^3$  should differ from this

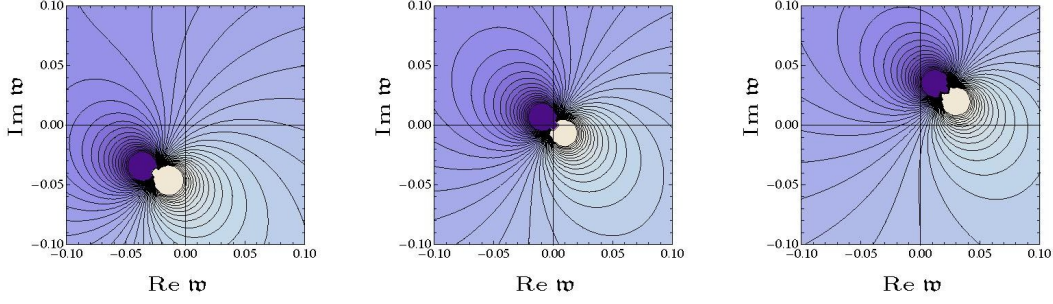


**Figure 5.25:** Contour plot of the imaginary part of the correlator for  $E^-$  around  $\mathfrak{w} = 0$  in the complex  $\mathfrak{w}$ -plane. Left:  $\tilde{n}_I = 10 < (\tilde{n}_I)_{\text{crit}}$ , center:  $\tilde{n}^I = 15.352 = (\tilde{n}_I)_{\text{crit}}$ , right:  $\tilde{n}_I = 20.704 > (\tilde{n}_I)_{\text{crit}}$ . The three graphs were generated for  $m = 3$ , dark shading indicates small values, light shading indicates large values. A pole in the upper half plane introduces an instability. This figure is taken from [204].

behavior. Upon further increasing the isospin density, the quasinormal frequencies  $\omega$  of  $E^\pm$  enter the upper half plane, maintaining their distinct directions and, thus, introduces an instability in the system. Figure 5.25 illustrates the transition of the pole of a quasinormal mode of  $E^-$  from the lower half plane to the upper half plane. The pole of the  $E^3$ -mode does not enter the upper half plane at any value of  $\tilde{n}_I$  we considered. Compare this to the values of  $\tilde{n}_I$  in figure 5.10 and figure 5.12 at which the pole induces visible structures at small  $\mathfrak{w}$ . The same instability is observed for the Reissner-Nordström black hole at finite isospin chemical potential (see e. g. [99, 100]).

In the zero temperature limit, where the Minkowski embedding is flat, we can see this instability in an analytic calculation. Let us for instance consider the gauge field fluctuations about the flat embedding and the constant background gauge field  $A_t^3$ . Due to the non-Abelian interactions, the additional terms  $(A_t^3 a_i^1)^2$  and  $(A_t^3 a_i^2)^2$  appear in the action expanded to second order (3.44). In the basis  $E^\pm = a^1 \pm a^2$ , these terms induce a shift in the frequency  $\omega^2 \mapsto (\omega \mp \gamma/\sqrt{\lambda}\mu_I)^2$  such that the equations of motion for the fluctuation is given by (3.52) where now

$$\tilde{M}^2 = -\frac{2R^4}{L^2} \left( \omega \mp \frac{\gamma}{\sqrt{\lambda}} \mu_I \right)^2. \quad (5.70)$$

Due to the normalization condition, the meson mass  $M$  is then given by

$$M = \frac{2\sqrt{2}\pi M_q}{\sqrt{\lambda}} \left( 1 \mp \frac{\gamma}{2\sqrt{2}\pi} \frac{\mu_I}{M_q} \right) \sqrt{(n+\ell+1)(n+\ell+2)}, \quad (5.71)$$

and we observe the isospin triplet splitting. The meson mass can be negative if  $\mu > M_q$  once we set  $\gamma = 2\sqrt{2}\pi$  and, thus, trigger an instability. In the next chapter we allow the unstable fluctuation to condense which stabilizes the system.

# Condensed Phases and Hairy Black Holes

In both systems, i. e. in the Reissner-Nordström black hole and in the D3/D7 model, we have found the same instability due to a finite isospin chemical potential in the previous chapter. In this chapter we present a way to stabilize these systems.

The basic idea can be summarized as follows: A non-zero vev of the time component of the gauge field  $A_t$  induces a chemical potential on the boundary theory. By fixing a gauge, we can choose the  $SU(2)$  gauge field in the direction of the third Pauli matrix to be non-zero, i. e.  $A_t^3 \neq 0$ . This breaks the  $SU(2)$  symmetry down to an Abelian symmetry denoted as  $U(1)_3$ . Beyond a critical value of the chemical potential, the system becomes unstable against fluctuations of gauge fields pointing in some other direction inside the  $SU(2)$ , for instance  $A_x^1$ , as described in section 5.5. This instability is cured by the condensation of this gauge field  $A_x^1$  which then breaks the  $U(1)_3$  symmetry. In the boundary theory the non-trivial profile of the gauge field  $A_x^1$  induces a vev of the current  $\langle J_x^1 \rangle$ , but no source. Thus, the breaking of the  $U(1)_3$  symmetry is spontaneous, and the order parameter for the transition is given by  $\langle J_x^1 \rangle$ . In general, the  $U(1)_3$  symmetry is global on the field theory side such that the broken phase describes a superfluid. In addition, the rotational group  $SO(3)$  is broken to  $SO(2)$  since the order parameter is a Lorentz vector. Hence, the system is an anisotropic superfluid, a p-wave superfluid. If we weakly gauge the  $U(1)_3$  symmetry, it will describe a superconductor. As mentioned before this may give some insights into high  $T_c$  superconductors. This chapter is based on my own publications [1, 2, 4–6, 8].

Let us now discuss the important result of this chapter. In section 6.1 we study the realization of holographic p-wave superfluid in the  $U(2)$  Einstein-Yang-Mills theory. The unbroken state is described by a charged black hole, the AdS Reissner-Nordström black hole. The phase transition to the superfluid phase in this dual picture is given by the growing of vector hair<sup>1</sup> near the horizon. The vector hair de-

---

<sup>1</sup>The no hair theorem does not apply here since the black hole is in asymptotically AdS space

forms the spacetime such that the solution near the horizon is only  $SO(2)$  invariant. At the boundary the effect of the hair disappears, however, and we obtain asymptotically AdS space. This is the dual picture of spontaneous symmetry breaking since only the IR but not the UV of the theory is influenced. We refer to this new gravity solution as *hairy Reissner-Nordström black hole*.

The Einstein-Yang-Mills theory allows one to change the ratio of gravitational to Yang-Mills coupling,  $\alpha_{\text{YM}} = \kappa_5/\hat{g}_{\text{YM}}$ . On the field theory side, this parameter is related to the ratio of charged degrees of freedom to total degrees of freedom. This identification can be understood as follows: The gravitational coupling  $1/\kappa_5^2$  is related to the central charge which measures the total degrees of freedom (see section 3.1.5), while correlation functions of the Yang-Mills fields are proportional to  $1/\hat{g}_{\text{YM}}^2$  such that  $1/\hat{g}_{\text{YM}}^2$  should count the charged degrees of freedom. This identification is explicitly understood in the D3/D7 setup where the ratio of the gravitational to Yang-Mills coupling is given by  $N_f/N_c$  (see (3.28)).

At zero baryon chemical potential, we map out the phase diagram of the Einstein-Yang-Mills system by varying  $\alpha_{\text{YM}}$  in section 6.1.1. At small  $\alpha_{\text{YM}}$  the phase transition to the superfluid phase is second order, while it becomes first order if  $\alpha_{\text{YM}} > (\alpha_{\text{YM}})_c = 0.365$ . In addition, the critical temperature at which the transition occurs is lowered as  $\alpha_{\text{YM}}$  is increased such that there is quantum phase transition at  $\alpha_{\text{YM}}^{\text{max}} = 0.628$ . A similar phase diagram has been found in Josephson junction arrays [216].

Furthermore, in section 6.4 we embed this system in a string theory setup, the D3/D7 brane intersection, in which we explicitly know the dual field theory (see section 3.2.1). Therefore, we can interpret the condensed phase as a *vector meson condensate*. In QCD-like theories, vector meson condensation is discussed in [217–219]. For pions, similar results have been found within QCD: There are analytical results for small and very large isospin chemical potential using the chiral Lagrangian [220, 221], as well as lattice results [222]. In QCD, the pion condensate is of course the natural state in isospin asymmetric matter. The condensation of a particle sets in if the isospin chemical potential is larger than the mass of this particle (see section 5.5). According to this rule, the pions condense first in QCD since they are the Nambu-Goldstone bosons of the spontaneous chiral symmetry breaking and therefore the lightest particles. However, the dual field theory which we consider is supersymmetric at zero temperature and, thus, chiral symmetry cannot be broken spontaneously. In this supersymmetric theory, the vector and scalar mesons have the same mass at zero temperature (see section 3.2.1). Due to finite temperature effects, the mass of the vector and scalar mesons can become different as we increase the temperature. It is a priori unclear which particle will condense. In D3/D7 model, the vector mesons condense first such that the  $\varrho$  meson condensation state is the physical ground state of our system near the phase transition.

Let us now consider the holographic systems at finite baryon and isospin chemical

---

and not asymptotically flat space.

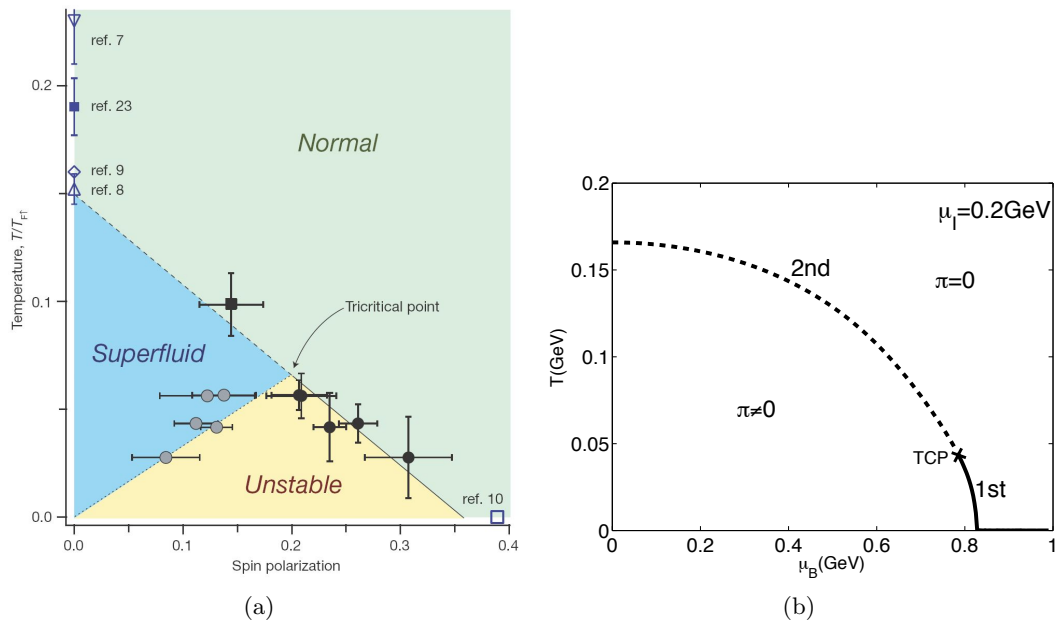


**Figure 6.1:** Phase diagrams of real-world systems: (a) Imbalanced Fermi mixture in the canonical ensemble [223]: The spin polarization is the thermodynamic conjugated variable to the ratio of the chemical potentials favoring the different spins. (b) QCD at finite baryon and isospin chemical potential [211]. In both phase diagrams we observe a superfluid phase at small temperature and small ratio of two chemical potentials. In addition, in both diagrams the phase transition is second order for large temperature and becomes first order at low temperatures. Both diagrams show a first order quantum phase transition.

potential. So two chemical potentials can be tuned. These systems are often called *imbalanced mixtures* since two kinds of particles are present in imbalanced numbers. Examples are imbalanced Fermi mixtures where fermions with spin up and spin down are imbalanced [223], and QCD at finite baryon and isospin chemical potential where for instance up and down quarks are imbalanced [211] (see also [224]). Interestingly the phase diagrams of both these systems are very similar (see figure 6.1). In both systems there is a superfluid state at low temperatures and at certain ratios of the two chemical potentials. In addition, also the order of the phase transition agrees in both examples: At low temperatures (also at zero temperature) the transition is first order, while at higher temperatures the transition becomes second order. Is it possible that there is a universal structure which relates these two different systems?

For the Einstein-Yang-Mills theory (see section 6.1.2) and the D3/D7 model (see section 6.4.2), we can map out the phase diagram by tuning the two control parameters. We find interesting similarities and differences (see figures 6.10 and 6.29 for the phase diagrams). In both cases the critical temperature where the phase transition occurs is finite at zero baryon chemical potential. By increasing the baryon chemical potential, we can tune the critical temperature to zero, and we

obtain a quantum phase transition. However, it is interesting that the details of the phase diagram are very different for the two systems, although they are expected to be dual to very similar field theories. For instance, the local as well as global symmetries match. The differences in the phase diagram are: In the Einstein-Yang-Mills theory (see figure 6.10) the critical temperature is monotonically decreasing as we increase the baryon chemical potential, while in the D3/D7 brane setup (see figure 6.29) the critical temperature first increases as the baryon chemical potential is increased. In addition in the Einstein-Yang-Mills setup, the system exhibits first and second order phase transitions depending on the strength of the back-reaction, while in the D3/D7 brane setup we obtain only second order phase transitions. Thus, the question arises: What is the crucial difference between the systems which induces the different phase transitions?

From the construction there is one obvious difference. In the Einstein-Yang-Mills system, the  $U(1)$  and  $SU(2)$  gauge fields only couple indirectly via the metric. In the field theory this means that the coupling of the currents which are dual to the gauge fields only occurs due to gluon loops. In the D3/D7 brane setup, these loops are neglected due to the probe approximation. In this case the field theory currents directly interact with each other. These interactions are induced by the non-linear terms of the DBI action. Due to this difference, it is reasonable that the phase transitions may be different. The different couplings of the gauge fields to each other may lead to different RG flows and therefore to different IR physics which lead to differences in the phase diagram.

In addition, we find an interesting difference in the origin of the quantum critical point in these systems. In the Einstein-Yang-Mills setup we can pinpoint the origin of the instability to the violation of the Breitenlohner-Freedman bound in an IR  $AdS_2$  region. This  $AdS_2$  region shows up as the near horizon region of the extremal Reissner-Nordström black hole. According to the AdS/CFT dictionary, the dual field theory, thus, contains a one-dimensional CFT in the IR (see figure 6.10). It is also important that the IR dimension of the dual operator depends on the ratio of the chemical potentials, such that the dimension can be tuned to an unstable value. In [225] it is argued that the violation of the Breitenlohner-Freedman bound will lead to a BKT-like phase transition. A common feature for this kind of transition seems to be the turning point in the phase diagram, such that the critical temperature slowly goes to zero as the ratio of baryon to isospin chemical potential is increased. In contrast to this behavior, the critical temperature in the D3/D7 brane setup goes to zero linearly. In this second model we do not obtain a violation of the Breitenlohner-Freedman bound in the IR, since the IR dimension of the dual operator does not depend on the ratio of the chemical potentials. Therefore, we expect that the quantum phase transition is second order with mean field exponents.

A similar difference occurs for the phase transition of chiral symmetry breaking via magnetic catalysis [226, 227], if we compare this transition for the D3/D5 brane setup to the same transition for the D3/D7 brane setup [228, 229]. In the D3/D5 model, the quantum phase transition is BKT-like, while in the D3/D7 model it is

second order. Here the difference between the two systems is more obvious: In the D3/D5 model both control parameters, the magnetic field and the baryon density, have mass dimension two. In the D3/D7 model, the magnetic field still has mass dimension two, but the baryon density has now mass dimension three, so that the dimensions of the control parameters do not match. It is expected that the BKT-like transition only occurs if the two control parameters have the same dimension (see [230–233]). This is in contrast to field theories with two chemical potentials where the dimensions of the two control parameters match independently of the spacetime dimensions. This is a great advantage since these systems always satisfy the necessary condition for a BKT-like transition. However, this condition cannot be sufficient as our result in the D3/D7 brane setup shows.

Comparing the phase diagrams obtained in our models (see figure 6.10 and 6.29) with the one obtained in imbalanced Fermi mixtures [223] and QCD at finite baryon and isospin chemical potential [211] (see figure 6.1), we see some similarities. In all cases the critical temperature is finite if the second control parameter, in our case the baryon chemical potential, is zero. By increasing the second control parameter we can tune the critical temperature to zero and we obtain a quantum phase transition. This seems to be a universal behavior for systems with two control parameters. However, in imbalanced Fermi mixtures and QCD at finite baryon and isospin chemical potential shown in figure 6.1, the order of the phase transition is different from that in our models. In the models of figure 6.1, the phase transition is second order at large temperatures and becomes first order at low temperatures. On the other hand, in the holographic models this is different: For large back-reaction the behavior in the Einstein-Yang-Mills system is completely opposite. The phase transition is first order at large temperatures and becomes continuous at small temperatures. Also for small back-reaction, we find a continuous quantum phase transition instead of a discontinuous one.

The difference in the order of the quantum phase transition may be related to the different behavior of the normal phase at zero temperature. For instance, the BKT-like transition in the Einstein-Yang-Mills setup is possible since the theory is conformal in the IR and the IR dimension of the dual operator depends on  $\mu_B/\mu_I$ . In [225] a BKT-like transition has been discussed in conformal field theories. The transition may occur if two fixed points of the  $\beta$ -function annihilate. The Einstein-Yang-Mills setup is the only one considered here which is conformal in the IR with tunable IR dimension of the dual operator, unlike both the models of figure 6.1 and the D3/D7 setup, such that a different order of the phase transition is plausible. In the D3/D7 probe brane setup we do not observe any change in the order of the phase transition which is always second order. Therefore, by comparing the different models, we conclude that the order of the phase transition is not universal and depends on the precise form of the interaction.

Moreover, we study the response of the holographic systems due to small fluctuations at zero baryon chemical potential in section 6.2 and 6.5. In both systems we determined the *conductivity* perpendicular to the condensate of the spontaneously

broken  $U(1)$  and find the well-known features of superconductors: There is an *energy gap* in the frequency-depending conductivity and a delta peak at zero frequency. The strength of the delta peak is given by the *superfluid density*. In addition, we find the Nambu-Goldstone bosons in the Green's function of the currents  $J_{\pm}^{\perp}$  which are charged under the spontaneously broken  $U(1)$ . These Nambu-Goldstone bosons generate rotations of the order parameter in real space.

In the Einstein-Yang-Mills setup (see section 6.2), we also investigate fluctuations of the metric which are dual to perturbations of the energy-momentum tensor on the field theory side. By exploring these fluctuations, we find the thermoelectric effect perpendicular to the condensate. The *thermoelectric effect* is the phenomenon that the electric and heat current mix since charged object transport charge as well as energy. This effect has already been studied for holographic s-wave superfluids [78, 95]. Due to the anisotropy, the fluctuations of the metric couple to the fluctuations of the gauge fields. This generates some additional phenomena. For instance we find an effect similar to the *flexoelectric effect* which is known from nematic liquid crystals. Liquid crystals consist of molecules with non-zero dipole moment (see e.g. [234]). A direction can be preferred by the dipoles. In this anisotropic phase, a strain can lead to effective polarization of the liquid and an electric field applied to the liquid can lead to a stress. This is the first appearance of this effect in the context of gauge/gravity duality. The most important result, however, is that the ratio of shear viscosity to entropy density can be *non-universal* for an anisotropic fluid.

In an anisotropic fluid, the transport coefficients depend on the direction, i.e. they are tensors. The p-wave superfluid is transversely symmetric, i.e. the system has an  $SO(2)$  symmetry and we can use this symmetry to reduce the tensors to the minimal amount of independent quantities. For instance, the viscosity which relates the stress  $T^{\mu\nu}$  in a fluid with the strain  $\nabla_{\lambda}u_{\rho} + \nabla_{\rho}u_{\lambda}$  given in terms of the four velocity of the fluid  $u_{\mu}$  is parametrized by a rank four tensor  $\eta^{\mu\nu\lambda\rho}$  (see e.g. [234, 235]). Using the symmetry we find two independent shear viscosities, in contrast to only one in the isotropic case, i.e.  $SO(3)$  symmetry.

Via Kubo's formula (4.149), the shear viscosity can be obtained from the transversely polarized fluctuation given by, for instance,  $\nabla_y u_z + \nabla_z u_y$  for a momentum in  $x$  direction. In the isotropic case, this mode is unique since any momentum can be rotated into the  $x$  direction by the  $SO(3)$  rotational symmetry. In the transversely symmetric case, two momenta, one along and one perpendicular to the favored direction, e.g. the  $x$  direction, must be considered. Thus, there are two shear modes. If the momentum is along the favored direction, the situation is similar to the isotropic case and the strain is again  $\nabla_y u_z + \nabla_z u_y$ . However, if the momentum is perpendicular to the favored direction say in  $y$  direction, the situation changes dramatically. Now the little group is given by the discrete group  $\mathbb{Z}_2$  and the strain is given by  $\nabla_x u_z + \nabla_z u_x$ . Since the shear viscosity can be evaluated at zero momentum, we can characterize the fluctuations with respect to the full symmetry group which is in the transversely symmetric case  $SO(2)$ . The first fluctuation  $\nabla_y u_z + \nabla_z u_y$  is a helicity

two state as in the isotropic case. The ratio of shear viscosity to entropy density for this mode is universal. The second fluctuation  $\nabla_x u_z + \nabla_z u_x$ , however, transform as helicity one state under the rotational symmetry. Therefore, the universality is lost since this mode can couple to other helicity one modes present in the system. The coupling generates non-trivial dynamics which lead to a non-universal behavior of the shear viscosity (see figure 6.16 and 6.17). This is the first time that a non-universal result for the ratio of shear viscosity to entropy density is found in the context of gauge/gravity duality for a field theory dual to Einstein gravity without additional contributions to the gravity action. It has been known so far that the universality is lost if finite  $N_c$  and/or coupling  $\lambda$  is considered for instance by adding a Gauss-Bonnet term to the gravity action (see e. g. [57, 58]).

## 6.1 Hairy Reissner-Nordström Black Hole

### Action and equations of motion

In this section we consider the  $U(2)$  Einstein-Yang-Mills (EYM) theory in  $(4 + 1)$ -dimensional asymptotically AdS space. The action is given in (5.9). The  $U(2)$  gauge field is again split into an  $SU(2)$  part with field strength tensor as defined in (5.7) and an  $U(1)$  part with field strength tensor given in (5.8). The Einstein and Yang-Mills equations derived from this action are presented in (5.10). Following [100], to construct charged black hole solutions with a vector hair we choose a gauge field ansatz

$$\begin{aligned} A &= \phi(r)\tau^3 dt + w(r)\tau^1 dx, \\ \mathcal{A} &= \psi(r)dt. \end{aligned} \tag{6.1}$$

The motivation for this ansatz is as follows: In the field theory we introduce a baryon and isospin chemical potential by the the boundary values of the time components of the gauge fields,  $\phi$  and  $\psi$ . This breaks the  $U(2)$  symmetry down to a diagonal  $U(1)$  which is generated by  $\tau^3$ . We denote this  $U(1)$  as  $U(1)_3$ . In order to study the transition to the superfluid state, we allow solutions with non-zero  $\langle J_x^1 \rangle$  such that we include the dual gauge field  $A_x^1 = w$  in the gauge field ansatz. Since we consider only isotropic and time-independent solutions in the field theory, the gauge fields exclusively depend on the radial coordinate  $r$ . With this ansatz the Yang-Mills energy-momentum tensor defined in (5.11) is diagonal. Solutions with  $\langle J_x^1 \rangle \neq 0$  also break the spatial rotational symmetry  $SO(3)$  down to  $SO(2)$ <sup>2</sup> such that our metric ansatz will respect only  $SO(2)$ . In addition, the system is invariant under the  $\mathbb{Z}_2$  parity transformation  $P_{\parallel} : x \rightarrow -x$  and  $w \rightarrow -w$ . Furthermore, given that the Yang-Mills energy-momentum tensor is diagonal, a diagonal metric is consistent.

---

<sup>2</sup>Note that the finite temperature and chemical potential already break the Lorentz group down to  $SO(3)$ .

Following [236], our metric ansatz is

$$ds^2 = -N(r)\sigma(r)^2 dt^2 + \frac{1}{N(r)} dr^2 + r^2 f(r)^{-4} dx^2 + r^2 f(r)^2 (dy^2 + dz^2), \quad (6.2)$$

with  $N(r) = -2m(r)/r^2 + r^2/R^2$ .

Inserting our ansatz into the Einstein and Yang-Mills equations leads to six equations of motion for  $m(r)$ ,  $\sigma(r)$ ,  $f(r)$ ,  $\phi(r)$ ,  $w(r)$ ,  $\psi(r)$  and one constraint equation from the  $rr$  component of the Einstein equations. The dynamical equations may be written as

$$\begin{aligned} m' &= \frac{\alpha_{\text{YM}}^2 r f^4 w^2 \phi^2}{6N\sigma^2} + \frac{r^3(\alpha_{\text{YM}}^2 \phi'^2 + \alpha_{\text{MW}}^2 \psi'^2)}{6\sigma^2} + N \left( \frac{r^3 f'^2}{f^2} + \frac{\alpha_{\text{YM}}^2 r f^4 w'^2}{6} \right), \\ \sigma' &= \frac{\alpha_{\text{YM}}^2 f^4 w^2 \phi^2}{3rN^2\sigma} + \sigma \left( \frac{2r f'^2}{f^2} + \frac{\alpha_{\text{YM}}^2 f^4 w'^2}{3r} \right), \\ f'' &= -\frac{\alpha_{\text{YM}}^2 f^5 w^2 \phi^2}{3r^2 N^2 \sigma^2} + \frac{\alpha_{\text{YM}}^2 f^5 w'^2}{3r^2} - f' \left( \frac{3}{r} - \frac{f'}{f} + \frac{N'}{N} + \frac{\sigma'}{\sigma} \right), \\ \phi'' &= \frac{f^4 w^2 \phi}{r^2 N} - \phi' \left( \frac{3}{r} - \frac{\sigma'}{\sigma} \right), \\ w'' &= -\frac{w \phi^2}{N^2 \sigma^2} - w' \left( \frac{1}{r} + \frac{4f'}{f} + \frac{N'}{N} + \frac{\sigma'}{\sigma} \right), \\ \psi'' &= -\psi' \left( \frac{3}{r} - \frac{\sigma'}{\sigma} \right). \end{aligned} \quad (6.3)$$

The equations of motion are invariant under five scaling transformations (invariant quantities are not shown),

$$\begin{aligned} (I) \quad & \sigma \rightarrow \lambda\sigma, \quad \phi \rightarrow \lambda\phi, \quad \psi \rightarrow \lambda\psi, \\ (II) \quad & f \rightarrow \lambda f, \quad w \rightarrow \lambda^{-2}w, \\ (III) \quad & r \rightarrow \lambda r, \quad m \rightarrow \lambda^4 m, \quad w \rightarrow \lambda w, \quad \phi \rightarrow \lambda\phi, \quad \psi \rightarrow \lambda\psi, \\ (IV) \quad & r \rightarrow \lambda r, \quad m \rightarrow \lambda^2 m, \quad R \rightarrow \lambda R, \quad \phi \rightarrow \lambda^{-1}\phi, \quad \psi \rightarrow \lambda^{-1}\psi, \\ & \alpha_{\text{YM}} \rightarrow \lambda\alpha_{\text{YM}}, \quad \alpha_{\text{MW}} \rightarrow \lambda\alpha_{\text{MW}}, \\ (V) \quad & \psi \rightarrow \lambda\psi, \quad \alpha_{\text{MW}} \rightarrow \lambda^{-1}\alpha_{\text{MW}}, \end{aligned} \quad (6.4)$$

where in each case  $\lambda$  is some real positive number. We use (I) and (II) to set the boundary values of both  $\sigma$  and  $f$  to one, so that the metric will be asymptotically *AdS*. Also we can use (III) to set  $r_h$  to one, but we will keep it as a bookkeeping device. We use (IV) to set the *AdS* radius  $R$  to one. The relation (V) allows us to set  $\alpha_{\text{MW}} = 1$  by rescaling the baryon chemical potential, i.e. we can relate states with different baryon chemical potentials in different theories characterized by  $\alpha_{\text{MW}}$  to each other.

A known solution of the equations of motion is the *AdS* Reissner-Nordström black hole as discussed in section 5.2.1. In order to obtain solutions in the superfluid

phase, i. e.  $w(r) \neq 0$ , we have to resort to numerics. We will solve the equations of motion using a shooting method. We will vary the values of functions near the horizon until we find solutions with suitable values near the AdS boundary. We, thus, need the asymptotic forms of the solutions near the horizon  $r = r_h$  and near the boundary  $r \rightarrow \infty$ .

Near the horizon, we expand all fields in powers of  $\epsilon_h = r/r_h - 1 \ll 1$  with some constant coefficients. Three of these coefficients can be fixed as follows: We determine  $r_h$  by the condition  $N(r_h) = 0$  which gives  $m(r_h) = r_h^4/2$ . Additionally, the time components of the gauge fields must be zero to obtain well-defined one-forms (see for example discussion below (5.14)), i. e.  $\phi(r_h) = 0$  and  $\psi(r_h) = 0$ . The equations of motion then impose relations among the other coefficients. A straightforward exercise shows that only five coefficients are independent,

$$\left\{ \sigma_0^h, f_0^h, w_0^h, \phi_1^h, \psi_1^h \right\}, \quad (6.5)$$

where the subscript denotes the order of  $\epsilon_h$ . All other near-horizon coefficients are determined in terms of these five independent coefficients.

Near the boundary, we expand all fields in powers of  $\epsilon_b = (r_h/r)^2 \ll 1$  with some constant coefficients. Again the equations of motion impose relations on these coefficients. There are seven independent coefficients

$$\left\{ m_0^b, \phi_0^b, \phi_1^b, \psi_0^b, \psi_1^b, w_1^b, f_2^b \right\}, \quad (6.6)$$

where here the subscript denotes the power of  $\epsilon_b$ . All other near-boundary coefficients are determined in terms of these seven independent coefficients. We used the scaling symmetries (6.4) to set  $\sigma_0^b = f_0^b = 1$ . Our solutions will also have  $w_0^b = 0$  since we do not want to source the operator  $J_x^1$  in the dual field theory, i. e. the  $U(1)_3$  symmetry will be spontaneously broken. In our shooting method we choose a value of  $\phi_0^b = \mu_I$ , the isospin chemical potential, and of  $\psi_0^b = \mu_B$ , the baryon chemical potential, and then vary the five independent near-horizon coefficients until we find a solution which produces the desired values at the boundary.

In the following it will be often convenient to work with dimensionless coefficients by scaling out factors of  $r_h$ . We, thus, define the dimensionless functions  $\tilde{m}(r) = m(r)/r_h^4$ ,  $\tilde{\phi}(r) = \phi(r)/r_h$ ,  $\tilde{\psi}(r) = \psi(r)/r_h$  and  $\tilde{w}(r) = w(r)/r_h$ , while  $f(r)$  and  $\sigma(r)$  are already dimensionless.

## Thermodynamics

In this section we extract thermodynamic information from our solutions by using the well-known methods of black hole thermodynamics as we have already done for the Reissner-Nordström black hole solution in section 5.2.1. In this section we present the changes in the thermodynamic quantities due to the new fields  $w(r)$ ,  $\sigma(r)$ ,  $f(r)$ .

The temperature  $T$  in the boundary field theory is identified with the Hawking temperature of the black hole. The Hawking temperature for our black hole solutions is given by

$$T = \frac{\kappa}{2\pi} = \frac{r_h \sigma_0^h}{\pi} \left( 1 - \frac{\alpha_{\text{YM}}^2 (\tilde{\phi}_1^h)^2 + \alpha_{\text{MW}}^2 (\tilde{\psi}_1^h)^2}{12 (\sigma_0^h)^2} \right), \quad (6.7)$$

where  $\kappa = \sqrt{\partial_\mu \xi \partial^\mu \xi}$  is the surface gravity of the black hole, with  $\xi$  being the norm of the timelike Killing vector, and in the second equality we write  $T$  in terms of the near-horizon coefficients. In the following we will often convert from the black hole radius  $r_h$  to the temperature  $T$  by inverting the above equation.

The entropy  $S$  of the boundary field theory is identified with the Bekenstein-Hawking entropy of the black hole. For our ansatz we obtain

$$S = \frac{2\pi}{\kappa_5^2} A_h = \frac{2V\pi r_h^3}{\kappa_5^2} = \frac{2\pi^4 V T^3}{\kappa_5^2 (\sigma_0^h)^3} \left( 1 - \frac{\alpha_{\text{YM}}^2 (\tilde{\phi}_1^h)^2 + \alpha_{\text{MW}}^2 (\tilde{\psi}_1^h)^2}{12 (\sigma_0^h)^2} \right)^{-3}, \quad (6.8)$$

where  $A_h$  is the area of the horizon and  $V$  the spatial volume of the Minkowski space.

The grand potential is determined by the Euclidean on-shell action as described in section 5.2.1. We, therefore, analytically continue to Euclidean signature and compactify the time direction with period  $1/T$ . We denote the Euclidean action as  $I$  and its on-shell value as  $I_{\text{on-shell}}$ . Since our solutions are always static, we can integrate out the time direction which produces an overall factor of  $1/T$ . In order to simplify the expressions, we define  $\tilde{I} = I/T$ . From now on we refer to  $\tilde{I}$  as the action.  $\tilde{I}$  splits into three parts, a bulk term, a Gibbons-Hawking term and counterterms,

$$\tilde{I} = \tilde{I}_{\text{bulk}} + \tilde{I}_{\text{GH}} + \tilde{I}_{\text{ct}}. \quad (6.9)$$

Using the equations of motion and our ansatz, we obtain the bulk term

$$\tilde{I}_{\text{bulk}}^{\text{on-shell}} = \frac{V}{\kappa_5^2} \frac{1}{2f^2} r N \sigma (r^2 f^2)' \Big|_{r=r_{\text{bdy}}}, \quad (6.10)$$

and the Euclidean Gibbons-Hawking term

$$\tilde{I}_{\text{GH}}^{\text{on-shell}} = -\frac{V}{\kappa_5^2} N \sigma r^3 \left( \frac{N'}{2N} + \frac{\sigma'}{\sigma} + \frac{3}{r} \right) \Big|_{r=r_{\text{bdy}}}. \quad (6.11)$$

The counterterm is the same as for the Reissner-Nordström black hole solution presented in (5.20). Finally, the grand potential  $\Omega$  is given by

$$\Omega = \lim_{r_{\text{bdy}} \rightarrow \infty} \tilde{I}_{\text{on-shell}}. \quad (6.12)$$

The baryon chemical potential  $\mu_B$  is simply the boundary value of  $\mathcal{A}_t(r) = \psi(r)$  while the isospin chemical potential  $\mu_I$  is the boundary value of  $A_t^3(r) = \phi(r)$ . The baryon charge density  $\langle \mathcal{J}_t \rangle$  and isospin charge density  $\langle J_t^3 \rangle$  of the dual field theory may be extracted from the on-shell action  $\tilde{I}_{\text{on-shell}}$  by

$$\begin{aligned} \langle \mathcal{J}_t \rangle &= \frac{1}{V} \lim_{r_{\text{bdy}} \rightarrow \infty} \frac{\delta \tilde{I}_{\text{on-shell}}}{\delta \mathcal{A}_t(r_{\text{bdy}})} \\ &= -\frac{2\pi^3 \alpha_{\text{MW}}^2 T^3}{\kappa_5^2 (\sigma_0^h)^3} \left( 1 - \frac{\alpha_{\text{YM}}^2 (\tilde{\phi}_1^h)^2 + \alpha_{\text{MW}}^2 (\tilde{\psi}_1^h)^2}{12 (\sigma_0^h)^2} \right)^{-3} \tilde{\psi}_1^b, \\ \langle J_t^3 \rangle &= \frac{1}{V} \lim_{r_{\text{bdy}} \rightarrow \infty} \frac{\delta \tilde{I}_{\text{on-shell}}}{\delta A_t^3(r_{\text{bdy}})} \\ &= -\frac{2\pi^3 \alpha_{\text{YM}}^2 T^3}{\kappa_5^2 (\sigma_0^h)^3} \left( 1 - \frac{\alpha_{\text{YM}}^2 (\tilde{\phi}_1^h)^2 + \alpha_{\text{MW}}^2 (\tilde{\psi}_1^h)^2}{12 (\sigma_0^h)^2} \right)^{-3} \tilde{\phi}_1^b. \end{aligned} \quad (6.13)$$

Similarly, the current density  $\langle J_x^1 \rangle$  is

$$\begin{aligned} \langle J_x^1 \rangle &= \frac{1}{V} \lim_{r_{\text{bdy}} \rightarrow \infty} \frac{\delta \tilde{I}_{\text{on-shell}}}{\delta A_x^1(r_{\text{bdy}})} \\ &= -\frac{2\pi^3 \alpha_{\text{YM}}^2 T^3}{\kappa_5^2 (\sigma_0^h)^3} \left( 1 - \frac{\alpha_{\text{YM}}^2 (\tilde{\phi}_1^h)^2 + \alpha_{\text{MW}}^2 (\tilde{\psi}_1^h)^2}{12 (\sigma_0^h)^2} \right)^{-3} \tilde{w}_1^b. \end{aligned} \quad (6.14)$$

The expectation value of the energy-momentum-tensor of the dual field theory may be determined by (4.48), here we find

$$\begin{aligned} \langle T_{tt} \rangle &= \frac{3\pi^4 T^4}{\kappa_5^2 (\sigma_0^h)^4} \left( 1 - \frac{\alpha_{\text{YM}}^2 (\tilde{\phi}_1^h)^2 + \alpha_{\text{MW}}^2 (\tilde{\psi}_1^h)^2}{12 (\sigma_0^h)^2} \right)^{-4} \tilde{m}_0^b, \\ \langle T_{xx} \rangle &= \frac{\pi^4 T^4}{\kappa_5^2 (\sigma_0^h)^4} \left( 1 - \frac{\alpha_{\text{YM}}^2 (\tilde{\phi}_1^h)^2 + \alpha_{\text{MW}}^2 (\tilde{\psi}_1^h)^2}{12 (\sigma_0^h)^2} \right)^{-4} (\tilde{m}_0^b - 8f_2^b), \\ \langle T_{yy} \rangle = \langle T_{zz} \rangle &= \frac{\pi^4 T^4}{\kappa_5^2 (\sigma_0^h)^4} \left( 1 - \frac{\alpha_{\text{YM}}^2 (\tilde{\phi}_1^h)^2 + \alpha_{\text{MW}}^2 (\tilde{\psi}_1^h)^2}{12 (\sigma_0^h)^2} \right)^{-4} (\tilde{m}_0^b + 4f_2^b). \end{aligned} \quad (6.15)$$

Notice that the energy-momentum tensor is still diagonal such that the momentum is zero even in the superfluid phase where the current  $\langle J_x^1 \rangle$  is non-zero. This result

is guaranteed by our ansatz for the gauge fields which implies a diagonal Yang-Mills energy-momentum tensor and a diagonal metric.

For  $\tilde{m}_0^b = 1/2 + (\alpha_{\text{YM}}^2 \tilde{\mu}_I^2 + \alpha_{\text{MW}}^2 \tilde{\mu}_B^2)/3$ ,  $\sigma_0^h = 1$ ,  $\tilde{\phi}_1^h = 2\tilde{\mu}_I$ ,  $\tilde{\psi}_1^h = 2\tilde{\mu}_B$ ,  $f_2^b = 0$ ,  $\tilde{\phi}_b^0 = \tilde{\mu}_I$ , and  $\tilde{\psi}_b^0 = \tilde{\mu}_B$  we recover the correct thermodynamics for the Reissner-Nordström black hole, which preserves the  $SO(3)$  rotational symmetry. For instance, we find that  $\langle T_{xx} \rangle = \langle T_{yy} \rangle = \langle T_{zz} \rangle$  and  $\Omega = -\langle T_{yy} \rangle V$ . For solutions with non-zero  $\langle J_x^1 \rangle$ , the  $SO(3)$  symmetry is spontaneously broken to  $SO(2)$  and we find  $\langle T_{xx} \rangle \neq \langle T_{yy} \rangle = \langle T_{zz} \rangle$ . Just using the equations above, we also find

$$\Omega = -V \langle T_{yy} \rangle. \quad (6.16)$$

This suggests the identification of  $\langle T_{yy} \rangle$  as the pressure  $p$ . However, due to the breaking of the  $SO(3)$  symmetry  $\langle T_{xx} \rangle$  is not the pressure  $p$  but most also contain terms which are non-zero in the broken phase, i. e. terms which contain the order parameter  $\langle J_1^x \rangle$ . For instance, it may be written as

$$\langle T_{xx} \rangle = p + \Delta \langle J_1^x \rangle \langle J_1^x \rangle, \quad (6.17)$$

where  $\Delta$  is a measure for the breaking of the rotational symmetry and is given by

$$\Delta = -\frac{3\kappa_5^2}{\alpha_{\text{YM}}^2 \pi^2 T^2} \left( 1 - \frac{\alpha_{\text{YM}}^2 (\tilde{\phi}_1^h)^2 + \alpha_{\text{MW}}^2 (\tilde{\psi}_1^h)^2}{12 (\sigma_0^h)^2} \right)^2 \frac{f_2^b}{(\tilde{w}_1^b)^2}. \quad (6.18)$$

Using this identification we can write down the energy-momentum tensor for the dual field theory in equilibrium in a covariant form,

$$\langle T^{\mu\nu} \rangle = \epsilon u^\mu u^\nu + p P^{\mu\nu} + \Delta P^\mu{}_\lambda P^\nu{}_\rho \langle J_a^\lambda \rangle \langle J_a^\rho \rangle, \quad (6.19)$$

where  $\epsilon = \langle T^{tt} \rangle$  is the energy density and  $P^{\mu\nu} = u^\mu u^\nu + \eta^{\mu\nu}$  is the projector to the space perpendicular to the velocity  $u^\mu$  (see section 4.4.1).

Since the energy-momentum tensor is traceless, the dual field theory is scale invariant and describes a conformal fluid. Therefore, the only physical parameters in the dual field theory are the ratios  $\mu_B/T$ ,  $\mu_I/T$  and  $\mu_B/\mu_I$ . Since only two of them are independent from each other, we choose  $\mu_I/T$  and  $\mu_B/\mu_I$  to determine the physical state of the boundary field theory in what follows.

### 6.1.1 Results at Zero Baryon Chemical Potential

In this section we present our numerical results at zero baryon chemical potential<sup>3</sup>. We scanned through values of  $\alpha_{\text{YM}}$  from  $\alpha_{\text{YM}} = 0.032$  to  $\alpha_{\text{YM}} = 0.548$ . Typical solutions for the metric and gauge field functions are presented in figure 6.2. The solutions for other values of  $\alpha_{\text{YM}}$  are qualitatively similar. Notice that all boundary conditions are met: at the horizon  $\tilde{\phi}(r)$  vanishes, and at the boundary  $f_0^b = \sigma_0^b = 1$  and  $\tilde{w}_0^b = 0$ .

<sup>3</sup>Note that we sometimes just write  $\alpha$  instead of  $\alpha_{\text{YM}}$ .

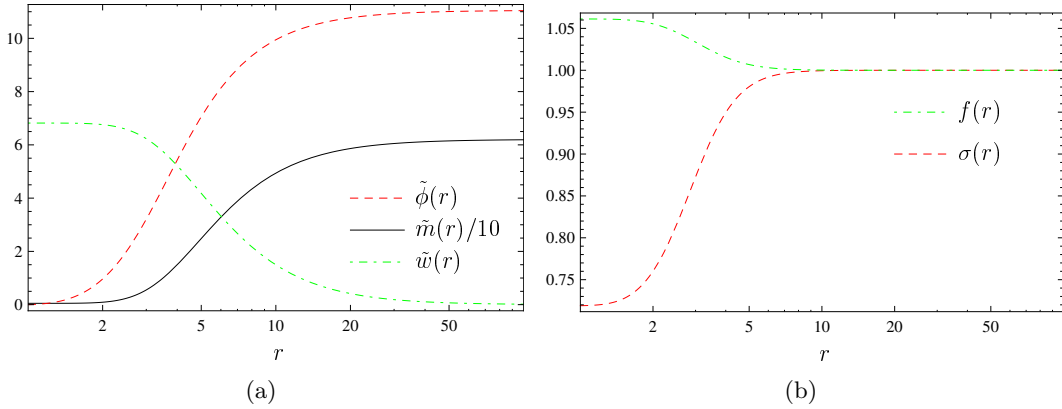


**Figure 6.2:** (a) The dimensionless gauge field components  $\tilde{\phi}(r)$  (red dashed) and  $\tilde{w}(r)$  (green dot-dashed) and the dimensionless metric function  $\tilde{m}(r)$ , scaled down by a factor of 10, (black solid) versus the AdS radial coordinate  $r$  for  $\alpha_{\text{YM}} = 0.316$  at  $T \approx 0.45T_c$ . (b) The dimensionless metric functions  $\sigma(r)$  (red dashed) and  $f(r)$  (green dot-dashed) versus the AdS radial coordinate  $r$  for  $\alpha_{\text{YM}} = 0.316$  at  $T \approx 0.45T_c$ . These figures are taken from [4].

For every value of  $\alpha_{\text{YM}}$  that we use, we find Reissner-Nordström solutions for all temperatures, and for sufficiently low temperatures we always find additional solutions, with nonzero  $w(r)$ , that are thermodynamically preferred to the Reissner-Nordström solution. In other words, for every value of  $\alpha_{\text{YM}}$  that we use, we find a phase transition, at some temperature  $T_c$ , in which a charged black hole grows vector hair, which on the field theory side is interpreted as a p-wave superfluid phase transition. Our numerical results show that the phase transition is second order for  $\alpha_{\text{YM}} < (\alpha_{\text{YM}})_c$  and first order for  $\alpha_{\text{YM}} > (\alpha_{\text{YM}})_c$  where  $(\alpha_{\text{YM}})_c \approx 0.365 \pm 0.001$ .

For example, for  $\alpha_{\text{YM}} = 0.316 < (\alpha_{\text{YM}})_c$ , we only find solutions with  $\langle J_1^x \rangle = 0$  until a temperature  $T_c$  where a second set of solutions, with nonzero  $\langle J_1^x \rangle$ , appears. Figure 6.3 shows that  $\langle J_1^x \rangle$  rises continuously from zero as we decrease  $T$  below  $T_c$ . Figure 6.4 (a) shows the grand potential  $\Omega$ , divided by  $\pi^4 V T_c^4 / \kappa_5^2$ , versus the rescaled temperature  $T/T_c$  for  $\alpha_{\text{YM}} = 0.316$ . The blue solid curve in Figure 6.4 (a) comes from solutions with  $\langle J_1^x \rangle = 0$  and the red dashed curve comes from solutions with  $\langle J_1^x \rangle \neq 0$ . We see clearly that at  $T < T_c$  the states with  $\langle J_1^x \rangle \neq 0$  have the lower  $\kappa_5^2 \Omega / (\pi^4 V T_c^4)$  and hence are thermodynamically preferred. We, thus, conclude that a phase transition occurs at  $T = T_c$ . The nonzero  $\langle J_1^x \rangle$  indicates spontaneous breaking of  $U(1)_3$  and of  $SO(3)$  rotational symmetry down to  $SO(2)$ , and hence is an order parameter for the transition. Figure 6.4 (b) shows the entropy  $S$ , divided by  $2\pi^4 V T_c^3 / \kappa_5^2$ , versus the rescaled temperature  $T/T_c$  for  $\alpha_{\text{YM}} = 0.316$ . The blue solid curve and the red dashed curve have the same meaning as in Figure 6.4 (a). Here we see that  $\kappa_5^2 S / (2\pi^4 V T_c^3)$  is continuous but has a kink, i. e. a discontinuous first derivative, clearly indicating a second order transition. For other values of  $\alpha_{\text{YM}} < (\alpha_{\text{YM}})_c$ , the figures are qualitatively similar.

A good question concerning these second order transitions is: what are the

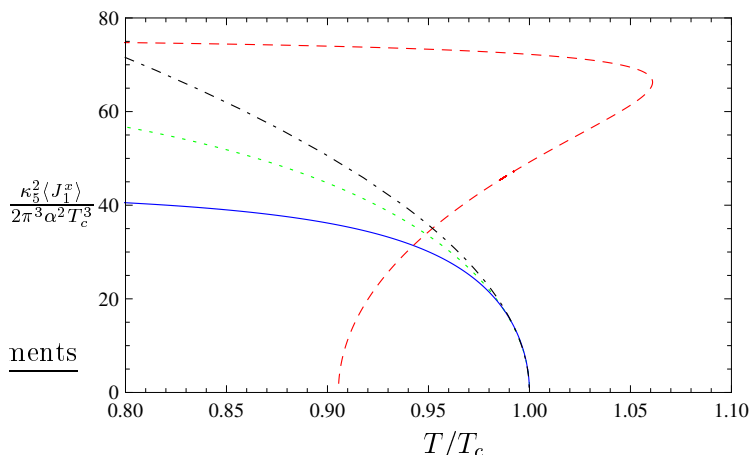


**Figure 6.3:** The order parameter  $\langle J_1^x \rangle$ , multiplied by  $\kappa_5^2/(2\pi^3\alpha_{\text{YM}}^2 T_c^3)$ , versus the rescaled temperature  $T/T_c$  for different  $\alpha_{\text{YM}}$ :  $\alpha_{\text{YM}} = 0.032 < (\alpha_{\text{YM}})_c$  (green dotted),  $\alpha_{\text{YM}} = 0.316 < (\alpha_{\text{YM}})_c$  (blue solid) and  $\alpha_{\text{YM}} = 0.447 > (\alpha_{\text{YM}})_c$  (red dashed). The black dot-dashed curve is the function  $a(1 - T/T_c)^{1/2}$  with  $a = 160$ . The green dotted curve is scaled up by a factor of 8 while the red dashed curve is scaled down by a factor of 5 such that  $a$ , which depends on  $\alpha_{\text{YM}}$ , coincides for the green dotted and blue solid curves. If we decrease  $T$  toward  $T_c$ , entering the figure from the right, we see that the blue solid and the green dotted curves rise continuously and monotonically from zero at  $T = T_c$ , signaling a second order phase transition. The close agreement with the black dot-dashed curve suggests that these grow from zero as  $(1 - T/T_c)^{1/2}$ . In the  $\alpha_{\text{YM}} = 0.447$  case, the red dashed curve becomes multi-valued at  $T = 1.061 T_c$ . In this case, at  $T = T_c$ , the value of  $\kappa_5^2 \langle J_1^x \rangle / (2\pi^3 \alpha_{\text{YM}}^2 T_c^3)$  jumps from zero to the upper part of the red dashed curve, signaling a first order transition. This figure is taken from [4].

critical exponents? In the probe limit,  $\alpha_{\text{YM}} = 0$ , an analytic solution for the gauge fields exists for  $T$  near  $T_c$  [102], which was used in [128] to show that for  $T \lesssim T_c$ ,  $\langle J_1^x \rangle \propto (1 - T/T_c)^{1/2}$ . In other words, in the probe limit the critical exponent for  $\langle J_1^x \rangle$  takes the mean-field value  $1/2$ . Does increasing  $\alpha_{\text{YM}}$  change the critical exponent? Our numerical evidence suggests that the answer is no: for all  $\alpha_{\text{YM}} < (\alpha_{\text{YM}})_c$ , we appear to find  $\langle J_1^x \rangle \propto (1 - T/T_c)^{1/2}$  (see Figure 6.3).

As  $\alpha_{\text{YM}}$  increases past  $(\alpha_{\text{YM}})_c = 0.365 \pm 0.001$ , we see a qualitative change in the thermodynamics. Consider for example  $\alpha_{\text{YM}} = 0.447$ . Here again we only find solutions with  $\langle J_1^x \rangle = 0$  down to some temperature where *two* new sets of solutions appear, both with nonzero  $\langle J_1^x \rangle$ . In other words, three states are available to the system: one with  $\langle J_1^x \rangle = 0$  and two with nonzero  $\langle J_1^x \rangle$ . Figure 6.3 shows that as we cool the system,  $\langle J_1^x \rangle$  becomes multi-valued at  $T = 1.061 T_c$ . To determine which state is thermodynamically preferred, we compute the grand potential  $\Omega$ . Figure 6.5 (a) shows  $\kappa_5^2 \Omega / (\pi^4 V T_c^4)$  versus  $T/T_c$ . The blue solid curve and the red dashed curve have the same meanings as in Figure 6.4. We immediately see the characteristic “swallowtail” shape of a first order phase transition. If we decrease  $T$ , entering the figure along the blue solid curve from the right, we reach the temper-

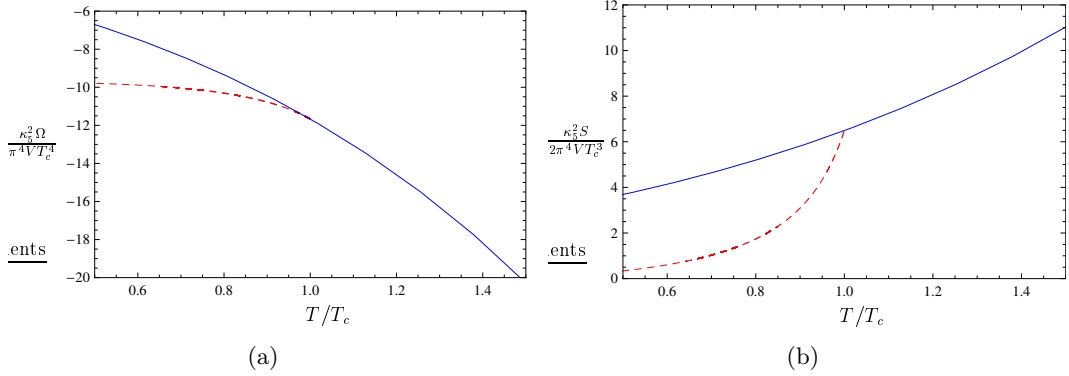


**Figure 6.4:** (a) The dimensionless grand potential  $\kappa_5^2 \Omega / (\pi^4 V T_c^4)$  versus the rescaled temperature  $T/T_c$  for  $\alpha_{\text{YM}} = 0.316$ . The blue solid curve comes from solutions with  $\langle J_1^x \rangle = 0$  while the red dashed curve comes from solutions with nonzero  $\langle J_1^x \rangle$ . For  $T > T_c$ , we have only the blue curve, but when  $T \leq T_c$  the red dashed curve appears and has the lower grand potential, indicating a phase transition at  $T = T_c$ . The grand potential is continuous and differentiable at  $T = T_c$ . (b) The dimensionless entropy  $\kappa_5^2 S / (2\pi^4 V T_c^3)$  versus  $T/T_c$  for  $\alpha_{\text{YM}} = 0.316$ . The blue solid and red dashed curves have the same meaning as in (a). The entropy is continuous but not differentiable at  $T = T_c$ , indicating a second order transition. These figures are taken from [4].

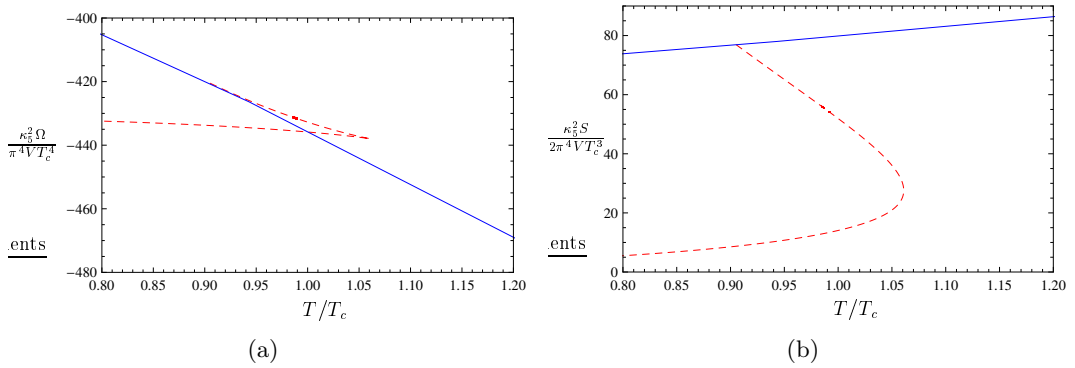


**Figure 6.5:** (a) The dimensionless grand potential  $\kappa_5^2 \Omega / (\pi^4 V T_c^4)$  versus the rescaled temperature  $T/T_c$  for  $\alpha_{\text{YM}} = 0.447$ . The blue solid and red dashed curves have the same meanings as in Figure 6.4. For  $T > T_c$  we have only the blue solid curve. At  $T = 1.061 T_c$ , the red dashed curve appears and the grand potential becomes multi-valued. When  $T \leq T_c$  the red dashed curve has the lowest grand potential, indicating a phase transition at  $T = T_c$ . The grand potential is continuous but not differentiable at  $T = T_c$ , signaling a first order transition. (b) The dimensionless entropy  $\kappa_5^2 S / (2\pi^4 V T_c^3)$  versus  $T/T_c$  for  $\alpha_{\text{YM}} = 0.447$ . The entropy is not continuous at  $T = T_c$ , but rather jumps from the blue solid curve to the lowest branch of the red dashed curve, indicating a first order transition. These figures are taken from [4].

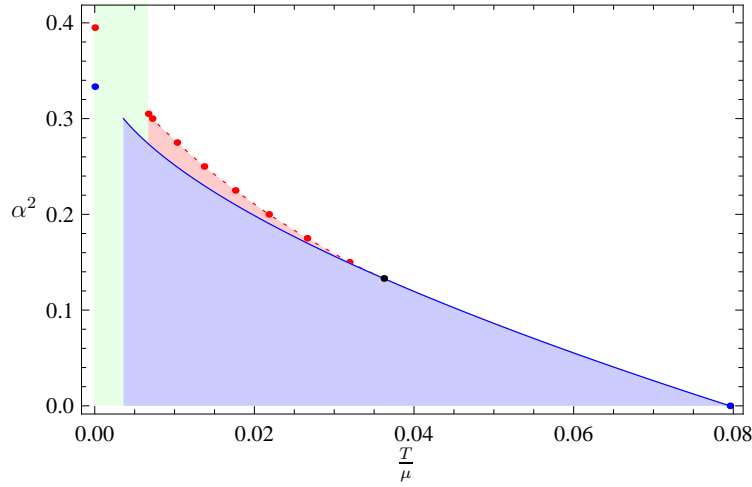


**Figure 6.6:** The phase structure of the theory: In the blue and red region the broken phase is the thermodynamically preferred phase while in the white region the Reissner-Nordström black hole is the ground state. In the blue region the Reissner-Nordström black hole is unstable and the transition from the white to the blue region is second order. In the red region the Reissner-Nordström black hole is still stable. The transition from the white to the red region is first order. The black dot determines the critical point where the order of the phase transition changes. In the green region we cannot trust our numerics. This figure is taken from [8].

ature  $T = 1.061 T_c$  where the new solutions appear (as the red dashed curve). The blue solid curve still has the lowest  $\kappa_5^2 \Omega / (\pi^4 V T_c^4)$  until  $T = T_c$  (by definition). If we continue reducing  $T$  below  $T_c$ , then the red curve has the lowest  $\kappa_5^2 \Omega / (\pi^4 V T_c^4)$ . The transition is clearly first order:  $\kappa_5^2 \Omega / (\pi^4 V T_c^4)$  has a kink at  $T = T_c$ . We can also see from the entropy that the transition is first order. Figure 6.5 (b) shows  $\kappa_5^2 S / (2\pi^4 V T_c^3)$  versus  $T/T_c$ . The entropy, like the grand potential, is multi-valued, and jumps discontinuously from the blue solid curve to the lowest part of the red dashed curve at  $T = T_c$ , indicating a first order transition.

Notice that a crucial difference between  $\alpha_{\text{YM}} < (\alpha_{\text{YM}})_c$  (second order) and  $\alpha_{\text{YM}} > (\alpha_{\text{YM}})_c$  (first order) is that for  $\alpha_{\text{YM}} > (\alpha_{\text{YM}})_c$  the critical temperature  $T_c$  is not simply the temperature at which  $\langle J_1^x \rangle$  becomes nonzero. We need more information to determine  $T_c$  when  $\alpha_{\text{YM}} > (\alpha_{\text{YM}})_c$ , for example we can study the grand potential  $\Omega$  as described above.

A good question is: how does increasing  $\alpha_{\text{YM}}$  change  $T_c$ ? We find that the critical temperature decreases as we increase the parameter  $\alpha_{\text{YM}}$ . The quantitative dependence of the critical temperature on the parameter  $\alpha_{\text{YM}}$  is given in figure 6.6. The broken phase is thermodynamically preferred in the blue and red region while in the white region the Reissner-Nordström black hole is favored. The Reissner-Nordström black hole is unstable in the blue region and the phase transition from the white to the blue region is second order. In the red region, the Reissner-Nordström black hole is still stable, however, the state with non-zero condensate is preferred.

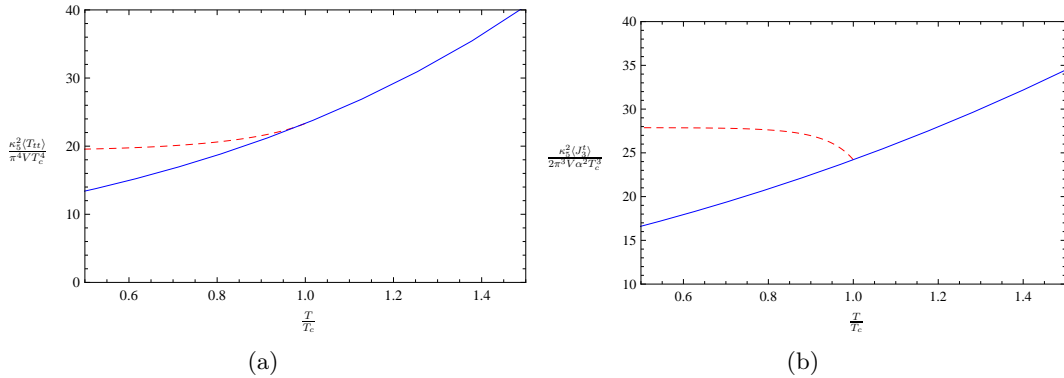


**Figure 6.7:** The energy density  $\langle T_{tt} \rangle$  (a) and the charge density  $\langle J_3^t \rangle$  (b) over the reduced temperature  $T/T_c$  for  $\alpha_{\text{YM}} = 0.316$ . The blue solid line is the solution without a condensate and the red dashed line the solution with  $\langle J_x^1 \rangle \neq 0$  below  $T_c$ .

The transition from the white to the red region is first order. In the green region we cannot trust our numerics. At zero temperature, the data is obtained below. In the probe limit,  $\alpha_{\text{YM}} = 0$ , we have the analytic result from [128] that  $T_c/\mu = 1/4\pi \approx 0.0796$ .

In figure 6.7 we plot the energy density  $\langle T_{tt} \rangle$  and isospin charge density  $\langle J_3^t \rangle$  versus the reduced temperature, respectively. We see that in both cases there is one solution for temperatures above  $T_c$  and two for temperatures below  $T_c$ . The solution with condensate (red dashed line) is the thermodynamically preferred one.

### Solutions at Zero Temperature

In this section we determine the critical value for  $\alpha_{\text{YM}}$  for which the Reissner-Nordström solution is unstable against perturbation in  $w$  and the value of  $\alpha_{\text{YM}}$  for which the hairy black hole is thermodynamically preferred at zero temperature. Since the phase transition is first order at zero temperature, the two values for  $\alpha_{\text{YM}}$  do not agree. In this analysis we follow the idea of [119, 123].

The Reissner-Nordström black hole at zero temperature is discussed in section 5.2.1. For fluctuations  $w(r)$  about this zero temperature black hole background, we find, in the limit  $r \rightarrow r_h$ , the equation of motion

$$w'' + \frac{2}{r - r_h} w' + \frac{1}{12(r - r_h)^2 \alpha_{\text{YM}}^2} w = 0. \quad (6.20)$$

This is the equation of motion for a scalar field with mass  $m_{\text{eff}}^2 = -1/12\alpha_{\text{YM}}^2$  in the emergent  $AdS_2$  near horizon region. This fluctuation is unstable if the effective mass is smaller than the Breitenlohner-Freedman bound  $m_{\text{BF}}^2 = -1/4$  in  $AdS_2$ <sup>4</sup>.

<sup>4</sup>Note that at the boundary the geometry is  $AdS_5$  where the Breitenlohner-Freedman bound is  $-4$ .

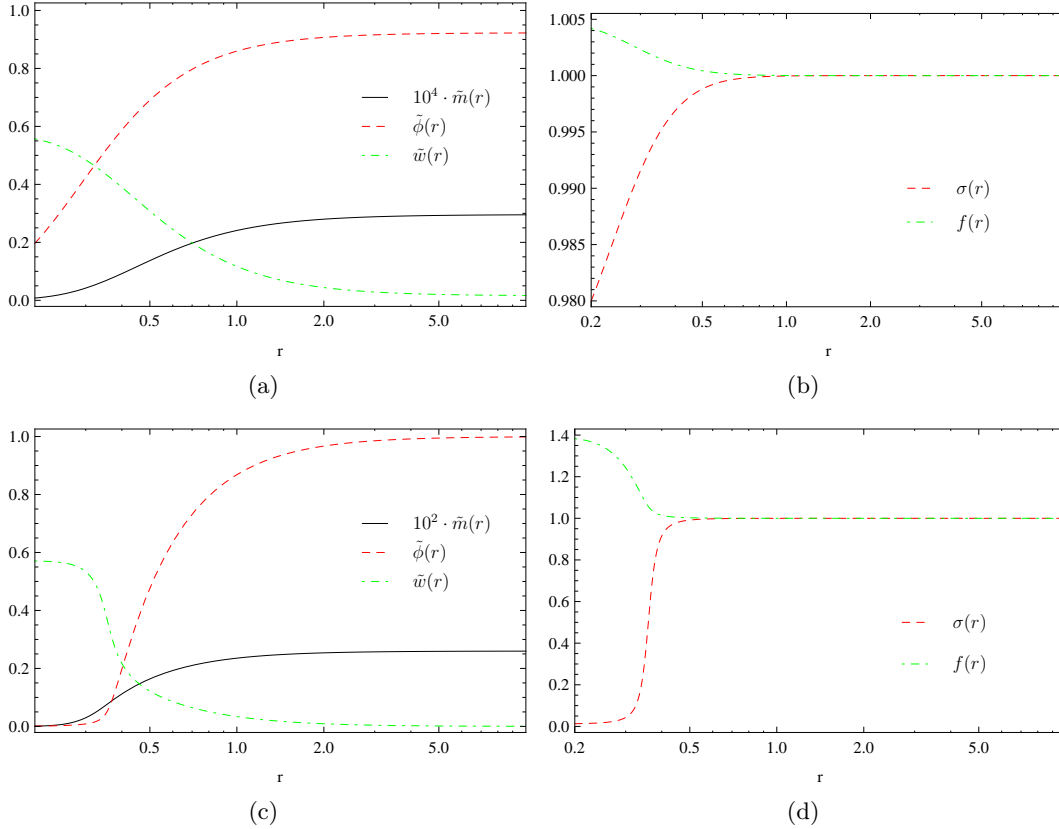


**Figure 6.8:** The dimensionless field configuration at zero temperature for  $\alpha_{\text{YM}} = 0.1$  (above) and  $\alpha_{\text{YM}} = 0.628$  (below) versus the AdS radial coordinate  $r$ : The fields describe a domain wall. The thickness of this domain wall decreases as the ratio of the coupling constants  $\alpha_{\text{YM}}$  is increased. As seen in the lower figures for large  $\alpha_{\text{YM}}$ , the domain wall approaches the form of the extremal Reissner-Nordström black hole with  $r_h \approx 0.3$ .

Therefore, the condition for an instability is

$$\alpha_{\text{YM}}^2 < \frac{1}{3}. \quad (6.21)$$

Let us now investigate the zero temperature solutions with hair numerically. It is consistent with our numerical results (see figure 6.4 and 6.5) to assume that the entropy is zero at zero temperature. This means the superfluid state has no degeneracy<sup>5</sup>. The only possibility to satisfy zero entropy at zero temperature is that the horizon size goes to zero,  $r_h = 0$ . Therefore, we cannot reach zero temperature in our numerics since there  $r_h$  is fixed to one. However, we may confirm whether our numerical solutions seem to converge to zero temperature solution. For this purpose we have to find the zero temperature solutions in our conventions.

<sup>5</sup>Note that the extremal Reissner-Nordström black hole has non-zero entropy and the ground state is degenerate.

We choose the following ansatz, which is consistent with our numerics, near  $r = 0$

$$\begin{aligned}\phi &\sim \phi_1(r), & w &\sim w_0 + w_1(r), \\ N &\sim r^2 + N_1(r), & m &\sim m_1(r), \\ \sigma &\sim \sigma + \sigma_1(r), & f &\sim f_0 + f_1(r),\end{aligned}\tag{6.22}$$

such that all fields with index one go to zero at  $r = 0$ , e.g.  $\phi_1(r) \rightarrow 0$  as  $r \rightarrow 0$ . Solving the equations of motion near the horizon lead the asymptotic forms,

$$\begin{aligned}\phi &\sim \phi_0 \sqrt{\frac{\beta}{r}} e^{-\frac{\beta}{r}}, & w &\sim w_0 \left(1 - \frac{\phi_0^2}{4\sigma_0^2 \beta} r e^{-\frac{2\beta}{r}}\right), \\ f &\sim f_0 \left(1 - \frac{\alpha^2 \beta \phi_0^2}{12\sigma_0^2} \frac{e^{-\frac{2\beta}{r}}}{r^3}\right), & \sigma &\sim \sigma_0 \left(1 + \frac{\alpha^2 \beta^2 \phi_0^2}{6\sigma_0^2} \frac{e^{-\frac{2\beta}{r}}}{r^4}\right), \\ N &\sim r^2 - \frac{\alpha^2 \beta^2 \phi_0^2}{3\sigma_0^2} \frac{e^{-\frac{2\beta}{r}}}{r^2},\end{aligned}\tag{6.23}$$

with  $\beta = f_0^2 w_0$ . Using these asymptotic forms we can integrate the equations of motion numerically towards the boundary. Some exemplary numerical results are presented in figure 6.8. These numerical solution describe a domain wall as first discussed in [115]. Since the solution does not contain a black hole the charge is located in the bulk. As we see from the numerical solution the region which contains the charge, i.e. the region where the gauge field changes rapidly, is very small and defines the domain wall. As we increase the coupling constant  $\alpha_{\text{YM}}$  the domain wall narrows and approaches the form of the extremal Reissner-Nordström black hole [123]. The maximal value for  $\alpha_{\text{YM}}$  for which a hairy solution is possible is given by  $\alpha_{\text{YM}}^{\text{max}} = 0.628$ .

### 6.1.2 Results at Finite Isospin and Baryon Chemical Potential

Let us now consider the influence of the baryon chemical potential on the phase transition to the superfluid phase. We first map out the phase diagram of the  $U(2)$  EYM theory at finite temperature, baryon and isospin chemical potential for different values of the coupling constant  $\alpha_{\text{YM}}$ . We start our discussion for small  $\alpha_{\text{YM}}$ . Our numerical results are shown in figure 6.9 and are confirmed by an analytic calculation at  $\alpha_{\text{YM}} = 0$  presented below. In the blue region the order parameter  $\langle J_x^1 \rangle$  is non-zero and the system is in the superfluid phase while in the white region the order parameter  $\langle J_x^1 \rangle$  is zero and the system is in the normal phase. We observe that the phase boundary moves monotonically to lower temperatures compared to the isospin chemical potential  $T/\mu_I$  as we increase the baryon chemical compared to the isospin chemical potential  $\mu_B/\mu_I$ . The order of the phase transition does not depend on the baryon chemical potential and stays second order. At a critical value for the ratio of baryon to isospin chemical potential  $(\mu_B/\mu_I)_c$  we obtain a quantum critical point at zero temperature. Later we determine this critical ratio analytically. Its value can be found in (6.29).

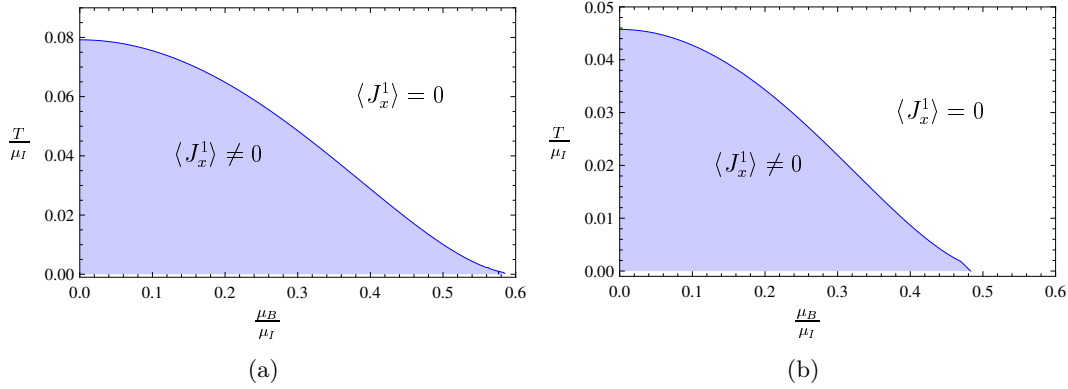


**Figure 6.9:** The phase diagram of the  $U(2)$  Einstein Yang-Mills theory at finite temperature  $T$ , baryon  $\mu_B$  and isospin chemical potential  $\mu_I$  for  $\alpha_{\text{YM}} = 0.001$  (a) and  $\alpha_{\text{YM}} = 0.1$  (b): In the blue region the order parameter  $\langle J_x^1 \rangle$  is non-zero and the system is in the superfluid phase while in the white region the order parameter  $\langle J_x^1 \rangle$  is zero and the system is in the normal phase. These figures are taken from [6].

By increasing  $\alpha_{\text{YM}}$  the area of the superfluid phase in the phase diagram decreases but the shape of the phase diagram stays the same until we reach a critical value for  $\alpha_{\text{YM}}$ . Beyond the critical value  $(\alpha_{\text{YM}})_{c,1} = 0.365 \pm 0.001$  we know from the discussion at zero baryon chemical potential that the phase transition to the superfluid phase becomes first order. If we now increase the baryon chemical potential, we find a critical point where the phase transition becomes second order again (for a sketch see figure 6.10 (b)). The phase transition at zero temperature is still continuous and therefore a quantum critical point. If we increase  $\alpha_{\text{YM}}$ , the critical point describing the change of the phase transition from first to second order moves to larger values of the ratio of baryon to isospin chemical potential. We find a critical value of  $\alpha_{\text{YM}}$  where the zero temperature phase transition becomes first order and the quantum critical point disappears. Its value is given by  $(\alpha_{\text{YM}})_{c,2} = 0.492 \pm 0.008$ . For  $\alpha_{\text{YM}}$  above this value, the phase transition is always first order (for a sketch see figure 6.10 (c)).

### Solutions at Zero Temperature

In this section we consider the system exclusively at zero temperature. From the phase diagrams presented above we see that for large baryon compared to isospin chemical potential the system is in the normal state. Since the normal state is described by a Reissner-Nordström black hole, the zero temperature limit is an extremal Reissner-Nordström black hole. Zero temperature is given by fixing the isospin chemical potential (see section 5.2.1),

$$\mu_I = \frac{\sqrt{3r_h^2 - \mu_B^2 \alpha_{\text{MW}}^2}}{\alpha_{\text{YM}}}. \quad (6.24)$$

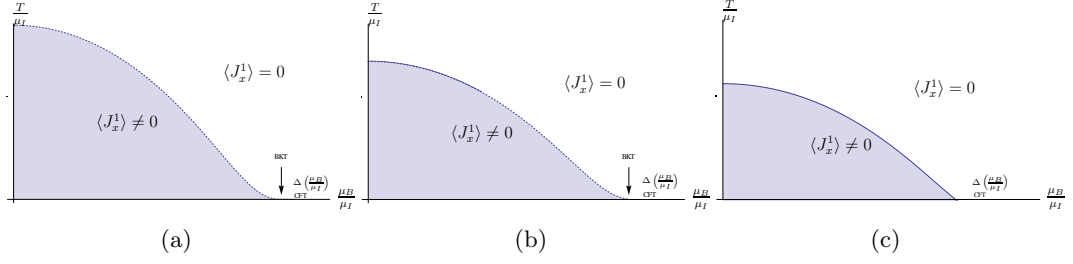


**Figure 6.10:** Sketch of the phase diagrams for the Einstein-Yang-Mills system for different strength of the back-reaction: In the white region the system is in the normal phase while in the blue region it is in the superfluid phase. The solid line marks a first order phase transition and the dotted line a second order phase transition. In the normal phase at zero temperature the dual field theory contains an emergent one-dimensional CFT in the IR and the IR dimension of the operator depends on the ratio of the chemical potentials. For small back-reaction (a), the phase transition is second order for finite temperatures and we expect the quantum phase transition to be BKT-like. For intermediate back-reaction (b), there is a first order phase transition at large temperatures. At low temperatures the behavior is as for small back-reaction. For large back-reaction (c), the phase transition is always first order. Also the quantum phase transition is first order. These figures are taken from [6].

The full solution in the near-horizon region which features an  $AdS_2$  geometry is given by

$$\begin{aligned}
 ds^2 &= -12\xi^2 dt^2 + \frac{d\xi^2}{12\xi^2} + r_h^2 d\mathbf{x}^2, \\
 \phi &= \frac{2\sqrt{3r_h^2 - \mu_B^2 \alpha_{\text{MW}}^2}}{\alpha_{\text{YM}} r_h} \xi, \quad \psi = \frac{2\mu_B}{r_h} \xi,
 \end{aligned} \tag{6.25}$$

where  $\xi = r - r_h$ . According to the AdS/CFT dictionary, the dual field theory contains a one-dimensional CFT in the IR. Let us now consider this theory as we decrease the baryon chemical potential. From our numerical solutions we expect a phase transition towards a superfluid phase with non-zero vev  $\langle J_x^1 \rangle$ . This phase transition should be triggered by an instability in the normal state. In order to obtain this instability, we consider fluctuations of the gauge field  $w(r)$  which is dual to the current  $J_x^1$  about the extremal Reissner-Nordström background [237]. The equation of motion for this fluctuation is given by

$$w'' + \frac{2}{\xi} w' + \frac{3r_h^2 - \mu_B^2 \alpha_{\text{MW}}^2}{36\alpha_{\text{YM}}^2 r_h^2 \xi^2} w = 0, \tag{6.26}$$

where the prime denotes a derivative with respect to  $\xi$ . This equation is the equation of motion for a scalar field in  $AdS_2$  with effective negative mass squared  $m_{\text{eff}}^2 = -\frac{3r_h^2 - \mu_B^2 \alpha_{\text{MW}}^2}{36\alpha_{\text{YM}}^2 r_h^2}$ . Thus, according to the AdS/CFT dictionary, the IR dimension of the dual operator can be tuned by changing the baryon chemical potential. Hence,

the fluctuation is stable until the mass is below the Breitenlohner-Freedman bound  $m_{\text{eff}}^2 = -1/4$ .<sup>6</sup> In our case, the bound is given by

$$\frac{\sqrt{3r_h^2 - \mu_B^2 \alpha_{\text{MW}}^2}}{6\alpha_{\text{YM}} r_h} \leq \frac{1}{2}. \quad (6.27)$$

From this equation we may determine the baryon chemical potential at which the bound is saturated,

$$\mu_B = \frac{r_h \sqrt{3 - 9\alpha_{\text{YM}}^2}}{\alpha_{\text{MW}}}. \quad (6.28)$$

With equation (6.24), we may determine the ratio between the baryon and the isospin chemical potential at which the Breitenlohner-Freedman bound is saturated. This ratio determines the point at which the system becomes unstable,

$$\left(\frac{\mu_B}{\mu_I}\right)_c = \frac{\sqrt{1 - 3\alpha_{\text{YM}}^2}}{\sqrt{3} \alpha_{\text{MW}}}. \quad (6.29)$$

Thus, the Reissner-Nordström black hole may be unstable if  $\alpha_{\text{YM}} < 1/\sqrt{3}$  and a quantum critical point may exist if in addition  $\alpha_{\text{MW}}$  is non-zero. This confirms our intuition obtained from our numerical results that at a given ratio of the baryon to isospin chemical potential a phase transition to a superfluid phase occurs. Unfortunately, this calculation only determines the value for the ratio of baryon to isospin chemical potential where the system becomes unstable and not the phase boundary in general. For a continuous phase transition, the two values coincide while for a first order phase transition, the transition always occurs before the instability is reached. Thus, only for  $\alpha_{\text{YM}} \leq (\alpha_{\text{YM}})_{c,2}$  the phase boundary which is a quantum critical point and the critical value obtained here coincide. In [225] it is argued that the violation of the Breitenlohner-Freedman bound leads to a BKT-like transition.

Naively, we may assume that the superfluid phase is non-degenerate at zero temperature and the entropy is zero. In the gravity dual this is translated to a zero horizon radius of the black hole. The solution with zero horizon radius differs from the zero temperature solutions described by the extremal limit of the AdS Reissner-Nordström black hole with finite horizon size. Similarly to (6.22), we choose the following ansatz which is consistent with the numerical results near  $r = 0$ , namely

$$\begin{aligned} \phi &\sim \phi_1(r), & \psi &\sim \psi_1(r), & w &\sim w_0 + \omega_1(r), & N &\sim r^2 + N_1(r), \\ m &\sim m_1(r), & \sigma &\sim \sigma_0 + \sigma_1(r), & f &\sim f_0 + f_1(r). \end{aligned} \quad (6.30)$$

Inserting the ansatz above in (6.3) and solving the equations of motion near the horizon  $r = 0$ , we obtain exclusively the same solutions as at zero baryon chemical potential,  $\psi \equiv 0$ . It is important to note that a zero entropy solution is only

---

<sup>6</sup>Note that at the boundary the geometry is  $AdS_5$  where the Breitenlohner-Freedman bound is  $-4$ .

consistent with  $\psi$  being zero, i. e. no baryon chemical potential. Thus, the domain walls we can construct from this asymptotics always have zero baryon chemical potential and coincide with the one found above. At finite baryon chemical potential we expect a solution which interpolates between the domain wall solutions at zero baryon chemical potential and the extremal Reissner-Nordström solution in the normal phase. This solution should always contain a black hole with finite horizon radius. Therefore, its entropy increases with the baryon chemical potential. By dimensional analysis we obtain  $S \propto V\mu_B^3$ .

### The Semi-Probe Limit

In this section we study the EYM system taking just the back-reaction of the  $U(1)$  Maxwell field into account, i. e.  $\alpha_{\text{YM}} = 0$ . We refer to this limit as the semi-probe limit. From equation (6.29) we observe that there is the possibility of a quantum critical point at  $\mu_B/\mu_I = 1/\sqrt{3}\alpha_{\text{MW}}$  in this limit. In addition, the equations of motion (6.3) simplify significantly and we can obtain an analytical solution if we restrict ourselves to small baryon chemical potential  $\mu_B$  and small condensate  $\langle J_x^1 \rangle$ . The equations of motion in the semi-probe limit read

$$\begin{aligned} m' &= \frac{\alpha_{\text{MW}}^2 r^3 \psi'^2}{6}, & \psi'' &= -\frac{3}{r} \psi', \\ w'' &= -\frac{w\phi^2}{N^2} - w' \left( \frac{1}{r} + \frac{N'}{N} \right), & \phi'' &= \frac{w^2 \phi}{r^2 N} - \phi' \left( \frac{3}{r} \right), \end{aligned} \quad (6.31)$$

since  $\sigma = f = 1$  if the back-reaction of the  $SU(2)$  Yang-Mills field is neglected. The equation for  $m$  and  $\psi$  can be integrated directly,

$$\begin{aligned} m &= \frac{r_h^4}{2} + \frac{\alpha_{\text{MW}}^2 \mu_B^2 r_h^2}{3} \left( 1 - \frac{r_h^2}{r^2} \right), \\ \psi &= \mu_B \left( 1 - \frac{r_h^2}{r^2} \right). \end{aligned} \quad (6.32)$$

Thus, we are left with the two equations of motion for the  $SU(2)$  gauge fields in the given Reissner-Nordström background. By solving these equations numerically we can map out the phase diagram for  $\alpha_{\text{YM}} = 0$  (see figure 6.11). The phase diagram looks similar to the one where a small back-reaction of the  $SU(2)$  fields is included (see figure 6.9).

**The expansion** In the limit of small  $\mu_B$  and small  $\langle J_x^1 \rangle$ , we can solve the equations of motion for  $\phi$  and  $w$  analytically. For the case  $\mu_B = 0$ , this has already been done in [128]. Similarly to [137], the solutions here are obtained as a double expansion in  $\mu_B$  and  $\langle J_x^1 \rangle$  which are chosen to be proportional to the expansion parameters  $\delta$  and  $\epsilon$ , respectively. More precisely, we choose  $\delta \equiv \tilde{\mu}_B = \tilde{\psi}(\infty)$  and  $\epsilon \equiv \tilde{w}_1^b \propto \langle J_x^1 \rangle$

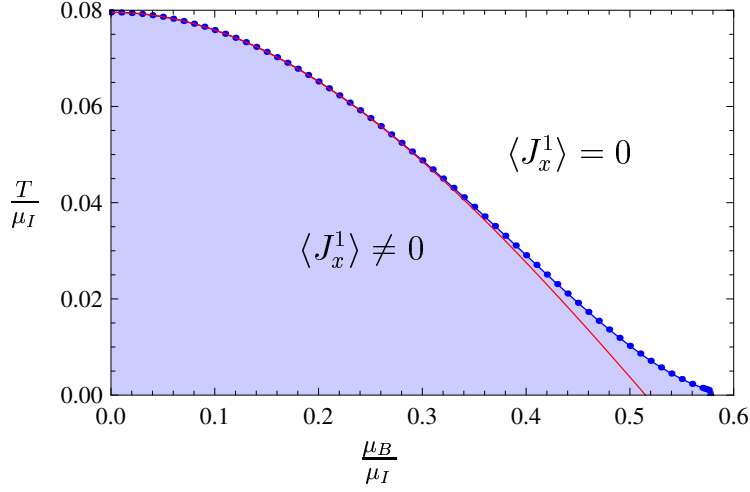


**Figure 6.11:** Phase diagram in the semi-probe limit: We compare the numerical data for the phase boundary (blue dots) with the analytic result (red line). We obtain a nice agreement for small baryon chemical potential where our approximation is valid. This figure is taken from [6].

from (6.14) where the tilde denotes dimensionless quantities which can be obtained by using (6.4) to set  $R = r_h = 1$ . We make the following ansatz for  $\tilde{\phi}$  and  $\tilde{w}$

$$\begin{aligned}
\tilde{\phi}(r) &= \phi_{0,0}(r) + \delta^2 \phi_{2,0}(r) + \delta^4 \phi_{4,0}(r) + \mathcal{O}(\delta^6) \\
&\quad + \epsilon^2 (\phi_{0,2}(r) + \delta^2 \phi_{2,2}(r)) + \mathcal{O}(\delta^4 \epsilon^2) \\
&\quad + \epsilon^4 \phi_{0,4}(r) + \mathcal{O}(\delta^2 \epsilon^4) \\
&\quad + \mathcal{O}(\epsilon^6), \\
\tilde{w}(r) &= \epsilon (w_{0,1}(r) + \delta^2 w_{2,1}(r) + \delta^4 w_{4,1}(r)) + \mathcal{O}(\delta^6 \epsilon) \\
&\quad + \epsilon^3 (w_{0,3}(r) + \delta^2 w_{2,3}(r)) + \mathcal{O}(\delta^4 \epsilon^3) \\
&\quad + \epsilon^5 w_{0,5}(r) + \mathcal{O}(\delta^2 \epsilon^5).
\end{aligned} \tag{6.33}$$

Inserting the ansatz (6.33) into (6.31), we can construct a solution order by order in  $\delta$  and  $\epsilon$ . The possible solutions are restricted by certain boundary conditions. At the horizon  $r = 1$ , we demand that  $\tilde{\phi}$  vanishes while  $\tilde{w}$  has to be regular. At the boundary,  $\tilde{w}$  is fixed to the expectation value  $\langle J_x^1 \rangle \propto \epsilon$  (6.14) while the isospin chemical potential  $\tilde{\mu}_I$  associated to  $\tilde{\phi}$  receives finite corrections in  $\delta$  and  $\epsilon$ .

The coefficient functions to lowest order,

$$\begin{aligned}
\phi_{0,0}(r) &= 4 \left( 1 - \frac{1}{r^2} \right), \\
w_{0,1}(r) &= \frac{r^2}{(1+r^2)^2},
\end{aligned} \tag{6.34}$$

have already been known from [102], while the coefficients in the pure  $\epsilon$  expansion,

that is with  $\delta = 0$ , were first computed in [128]. To order  $\epsilon^4$ , they read

$$\begin{aligned}\phi_{0,2}(r) &= \mu_{I0,2} \left(1 - \frac{1}{r^2}\right) + \frac{5 + 7r^2 - 9r^4 - 3r^6}{96r^2(1+r^2)^3}, \quad \mu_{I0,2} = \frac{71}{6,720}, \\ w_{0,3}(r) &= \frac{39 - 331r^2 - 819r^4 - 369r^6 + 156r^2(1+r^2)^3 \ln(1 + \frac{1}{r^2})}{20,160(1+r^2)^5}, \\ \phi_{0,4}(r) &= \mu_{I0,4} \left(1 - \frac{1}{r^2}\right) + \Phi_{0,4}(r), \quad \mu_{I0,4} = \frac{13(-4,015,679 + 5,147,520 \ln(2))}{75,866,112,000},\end{aligned}\tag{6.35}$$

where  $\Phi_{0,4}(r)$  is a complicated function of  $r$  which we do not write down explicitly here. The  $\mu_{Im,n}$  are determined by the regular boundary condition of  $\tilde{w}$  at the horizon  $r = 1$  and describe corrections to the critical isospin chemical potential  $\tilde{\mu}_I = 4$  at  $\delta^m \epsilon^n$  orders. The lowest order coefficient functions in the pure  $\delta$  expansion read

$$\begin{aligned}\phi_{2,0}(r) &= \mu_{I2,0} \left(1 - \frac{1}{r^2}\right), \quad \mu_{I2,0} = \frac{4}{9} \alpha_{\text{MW}}^2 (-17 + 24 \ln(2)), \\ \phi_{4,0}(r) &= \mu_{I4,0} \left(1 - \frac{1}{r^2}\right), \\ \mu_{I4,0} &= \frac{2}{243} \alpha_{\text{MW}}^2 [-5,495 + 864 \pi^2 \ln(2) + 192 \ln(2) (61 + 12 \ln(2)^2 - \ln(8)) \\ &\quad - 13,824 \text{Li}_3(1 - i) - 13,824 \text{Li}_3(1 + i) + 12 \zeta(3)].\end{aligned}\tag{6.36}$$

For small baryon chemical potential  $\tilde{\mu}_B = \delta$ , the critical isospin chemical potential for the phase transition will be corrected as

$$\tilde{\mu}_I^c(\delta) = 4 + \mu_{I2,0} \delta^2 + \mu_{I4,0} \delta^4 + \mathcal{O}(\delta^6).\tag{6.37}$$

This determines the phase boundary between the superfluid and the normal phase. We compare this analytic result with our numerical results in figure 6.11.

The lowest order coefficient functions in mixed orders read

$$\begin{aligned}\phi_{2,2}(r) &= \mu_{I2,2} \left(1 - \frac{1}{r^2}\right) + \Phi_{2,2}(r), \\ \mu_{I2,2} &= \frac{(680,573 + 29,820 \pi^2 - 404,232 \ln(2) - 1,406,160 \ln(2)^2) \alpha_{\text{MW}}^2}{6,350,400}, \\ w_{2,1}(r) &= \alpha_{\text{MW}}^2 \left( \frac{13 + r^2 (7 + 6r^2 - 4 \pi^2 (1 + r^2) + 24(1 + r^2) \ln(2)^2)}{9(1 + r^2)^3} \right. \\ &\quad + \frac{4(3 - 20r^2 + 3r^4) \ln(r)}{9(1 + r^2)^2} - \frac{2(3 + 3r^4 + 4r^2(-5 + \ln(64))) \ln(1 + r^2)}{9(1 + r^2)^2} \\ &\quad \left. - \frac{16r^2 \ln(r)^2}{3(1 + r^2)^2} - \frac{8r^2 (\text{Li}_2(-r^2) + \text{Li}_2(1 - r^2) - 2 \text{Li}_2(\frac{1}{2}(1 - r^2)))}{3(1 + r^2)^2} \right),\end{aligned}\tag{6.38}$$

where  $\Phi_{2,2}(r)$  is a complicated function of  $r$  which we do not show explicitly here.

**The free energy** Using the results from the last section, we compute the contribution to the free energy up to order  $\delta^m \epsilon^n$  for  $m + n \leq 4$  from the gauge field term in the on-shell action

$$\begin{aligned} S &= -\frac{1}{4g_{\text{YM}}^2} \int d^5x \sqrt{-g} F_{AB}^a F^{aAB} \\ &= \frac{\beta V r_h^4}{2g_{\text{YM}}^2} \int_1^\infty dr \left( r^3 (\partial_r \tilde{\phi})^2 - r \tilde{N}(r) (\partial_r \tilde{w})^2 + \frac{r}{\tilde{N}(r)} (\tilde{\phi} \tilde{w})^2 \right) \\ &= \frac{\beta V r_h^4}{2g_{\text{YM}}^2} \left( r^3 \tilde{\phi} (\partial_r \tilde{\phi}) \Big|_{r \rightarrow \infty} - \int_1^\infty dr r \tilde{N}(r) (\partial_r \tilde{w})^2 \right), \end{aligned} \quad (6.39)$$

where  $V$  is the spatial volume of the field theory and  $\beta = 1/T$  is the inverse temperature. In the  $\alpha_{\text{YM}} \rightarrow 0$  limit, only  $\psi(r)$  contributes to the back-reaction which is described by

$$\tilde{N}(r) = r^2 - \frac{1}{r^2} - \frac{2(r^2 - 1)}{3r^4} \alpha_{\text{MW}}^2 \delta^2, \quad (6.40)$$

where the expansion parameter  $\delta \equiv \tilde{\mu}_B$  is chosen to be small.

For the background with vanishing condensate, i.e.  $\omega(r) = 0$ , and

$$\tilde{\phi}(r) = \frac{r^2 - 1}{r^2} (4 + \mu_{I0,2} \epsilon^2 + \mu_{I0,4} \epsilon^4 + \mu_{I2,0} \delta^2 + \mu_{I4,0} \delta^4 + \mu_{I2,2} \delta^2 \epsilon^2), \quad (6.41)$$

the on-shell action is

$$\begin{aligned} S_{\text{vac}} &= \frac{\beta V r_h^4}{g_{\text{YM}}^2} \left[ 16 + 8\mu_{I0,2} \epsilon^2 + (\mu_{I0,2}^2 + 8\mu_{I0,4}) \epsilon^4 + 8\mu_{I2,0} \delta^2 + (\mu_{I2,0}^2 + 8\mu_{I4,0}) \delta^4 \right. \\ &\quad \left. + 2(\mu_{I0,2} \mu_{I2,0} + 4\mu_{I2,2}) \delta^2 \epsilon^2 + \mathcal{O}(\delta^p \epsilon^q) \right], \end{aligned} \quad (6.42)$$

for  $p + q = 6$ .

For the background where  $w \neq 0$  has condensed, the on-shell action reads

$$\begin{aligned} S_{\text{sf}} &= \frac{\beta V r_h^4}{g_{\text{YM}}^2} \left[ 16 + 8\mu_{I0,2} \epsilon^2 + \left( \mu_{I0,2}^2 + 8\mu_{I0,4} + \frac{71}{215,040} \right) \epsilon^4 + 8\mu_{I2,0} \delta^2 \right. \\ &\quad \left. + (\mu_{I2,0}^2 + 8\mu_{I4,0}) \delta^4 + 2(\mu_{I0,2} \mu_{I2,0} + 4\mu_{I2,2}) \delta^2 \epsilon^2 + \mathcal{O}(\delta^p \epsilon^q) \right]. \end{aligned} \quad (6.43)$$

The difference in the values of the two on-shell actions is

$$\beta \Delta p = S_{\text{vac}} - S_{\text{sf}} = \frac{\beta V r_h^4}{4g_{\text{YM}}^2} \left( -\frac{71}{53,760} \epsilon^4 + \mathcal{O}(\delta^p \epsilon^q) \right). \quad (6.44)$$

This result is known from [128] which remains robust in our back-reacted background. The grand potential is minus the value of the on-shell action times the temperature, hence the quantity  $\Delta p$  determines the difference in the grand potential between the normal and superfluid phase. In this case, the grand potential of the superfluid state is the smaller one because  $\Delta p < 0$ , and this implies the stability of the superfluid phase.

For small  $\epsilon$  and small  $\delta$ , we have  $\epsilon^4 \sim (\tilde{\mu}_I - \tilde{\mu}_I^c(\delta))^2$ . Using (III) in (6.4) to restore dimensions by taking  $\lambda = r_h \sim T$  (6.7), the dimensionless  $\tilde{\mu}_I$  will be replaced by  $\frac{\mu_I}{r_h} \sim \frac{\mu_I}{T}$  and, thus, we have  $\epsilon^2 \sim (T_c(\delta) - T)$ . The cancelation of the term proportional to  $\delta^2 \epsilon^2$  in the free energy difference suggests that the phase transition stays second order with mean field exponents as we increase the baryon chemical potential which coincides with our numerical result.

## 6.2 Fluctuations About the Hairy Black Hole

In this section we study the response of the holographic p-wave superfluid described by the hairy black hole under small perturbations. We exclusively study the system at zero baryon chemical potential<sup>7</sup>. On the gravity side, these perturbations are given by fluctuations of the metric  $h_{MN}(x^\mu, r)$  and the gauge field  $a_M^a(x^\mu, r)$ . Thus, we study in total 14 physical modes: 5 from the massless graviton in 5 dimensions and  $3 \times 3$  from the massless vectors in 5 dimensions. Due to time and spatial translation invariance in the Minkowski directions, the fluctuations can be decomposed in a Fourier decomposition,

$$\begin{aligned} h_{MN}(x^\mu, r) &= \int \frac{d^4 k}{(2\pi)^4} e^{ik_\mu x^\mu} \hat{h}_{MN}(k^\mu, r), \\ a_M^a(x^\mu, r) &= \int \frac{d^4 k}{(2\pi)^4} e^{ik_\mu x^\mu} \hat{a}_M^a(k^\mu, r). \end{aligned} \tag{6.45}$$

To simplify notations we drop the hat on the transformed fields which we use from now on if not stated otherwise.

### 6.2.1 Characterization of Fluctuations and Gauge Fixing

In general, we have to introduce two spatial momenta: one longitudinal to the condensate  $k_\parallel$  and one perpendicular to the condensate  $k_\perp$ , i. e.  $k^\mu = (\omega, k_\parallel, k_\perp, 0)$ . Introducing the momentum perpendicular to condensate breaks the remaining rotational symmetry  $SO(2)$  down the discrete  $\mathbb{Z}_2$  parity transformation  $P_\perp: k_\perp \rightarrow -k_\perp$  and  $x_\perp \rightarrow -x_\perp$ . Thus, introducing this momentum forbids the usual classification of the fluctuations in different helicity states of the little group since the symmetry group just consists of discrete groups at best  $P_\parallel \times P_\perp$ . We do not study this case further. However, a momentum exclusively in the direction longitudinal to

<sup>7</sup>Note that we sometimes just write  $\alpha$  instead of  $\alpha_{YM}$ .

	dynamical fields	constraints	# physical modes
helicity 2	$h_{yz}, h_{yy} - h_{zz}$	none	2
helicity 1	$h_{ty}, h_{xy}; a_y^a$	$h_{yr}$	4
	$h_{tz}, h_{xz}; a_z^a$	$h_{zr}$	4
helicity 0	$h_{tt}, h_{xx}, h_{yy} + h_{zz}, h_{xt}; a_t^a, a_x^a$	$h_{tr}, h_{xr}, h_{rr}; a_r^a$	4

**Table 6.1:** Classifications of the fluctuations according to their transformation under the little group  $SO(2)$ . The constraints are given by the equations of motion for the fields which are set to zero due the fixing of the gauge freedom:  $a_r^a \equiv 0$  and  $h_{rM} \equiv 0$ . The number of physical modes is obtained by the number of dynamical fields minus the number of constraints. Due to  $SO(2)$  invariance the fields in the first and second line of the helicity one fields can be identified.

the condensate or zero spatial momentum preserves the  $SO(2)$  rotational symmetry such that we can classify the fluctuations according to their transformation under this  $SO(2)$  symmetry (see table 6.1). The modes of different helicity decouple from each other. The momentum longitudinal to the condensate, however, break the longitudinal parity invariance  $P_{\parallel}$ .

In order to obtain the physical modes of the system, we have to fix the gauge freedom. We choose a gauge where  $a_r^a \equiv 0$  and  $h_{Mr} \equiv 0$  such that the equations of motion for these fields become constraints. These constraints fix the unphysical fluctuations in each helicity sector and allow only the physical modes to fluctuate. The physical modes may be constructed by enforcing them to be invariant under the residual gauge transformations,  $\delta a_r^a = 0$  and  $\delta h_{Mr} = 0$  (see appendix B.2),

$$\begin{aligned} \text{helicity two: } \Xi &= g^{yy} h_{yz}, h_{yy} - h_{zz}, \\ \text{helicity one: } \Psi &= g^{yy} (\omega h_{xy} + k_{\parallel} h_{ty}); a_y^a, \end{aligned} \quad (6.46)$$

and helicity zero:

$$\begin{aligned} \Phi_1 &= \xi_y, \\ \Phi_2 &= a_t^1 + \frac{i\omega}{\phi} a_t^2 + \frac{ik(\omega^2 - \phi^2)}{(k^2 - w^2)\phi} a_x^2 + \frac{w(\omega^2 - \phi^2)}{(k^2 - w^2)\phi} a_x^3, \\ \Phi_3 &= \xi_x - \frac{k^2 N \sigma^2 f^4}{\omega^2 r^2} \xi_t + \frac{2k}{\omega} \xi_{tx}, \\ \Phi_4 &= a_x^1 + \frac{k}{\omega} a_t^1 - \frac{1}{2} w \xi_x - \frac{w'}{\phi'} a_t^3 + \frac{\phi w'}{2\phi'} \xi_t - \frac{k(\omega^2 w' + w\phi\phi')}{\omega(k^2 - w^2)\phi'} a_x^3 \\ &\quad - i \frac{\omega^2 w w' + k^2 \phi \phi'}{\omega \phi' (k^2 - w^2)} a_x^2, \end{aligned} \quad (6.47)$$

with

$$\xi_y = g^{yy} h_{yy}, \quad \xi_x = g^{xx} h_{xx}, \quad \xi_t = g^{tt} h_{tt}, \quad \xi_{tx} = g^{xx} h_{tx}. \quad (6.48)$$

### 6.2.2 Equations of Motion, On-shell Action and Correlators

In the following we will focus on the response exclusively due to time dependent perturbations, i. e.  $k^\mu = (\omega, 0, 0, 0)$ . In this case in addition to the  $SO(2)$  symmetry,  $P_{\parallel}$  parity is conserved which allows us to decouple some of the physical modes in the different helicity blocks. In this section we write down the equations of motion for the fluctuations, determine the on-shell action and vary the on-shell action with respect to the fluctuations to obtain the retarded Green's functions  $G$  of the stress-energy tensor  $T^{\mu\nu}$  and the currents  $J_a^\mu$ ,

$$\begin{aligned} G^{\mu\nu,\rho\sigma}(k) &= -i \int dt d^3x e^{-ikx} \theta(t) \langle [T^{\mu\nu}(t, \mathbf{x}), T^{\rho\sigma}(0, 0)] \rangle, \\ G_{a,b}^{\mu,\nu}(k) &= -i \int dt d^3x e^{-ikx} \theta(t) \langle [J_a^\mu(t, \mathbf{x}), J_b^\nu(0, 0)] \rangle, \\ G_a^{\mu\nu\rho}(k) &= -i \int dt d^3x e^{-ikx} \theta(t) \langle [T^{\mu\nu}(t, \mathbf{x}), J_a^\rho(0, 0)] \rangle, \\ G_a^{\rho\mu\nu}(k) &= -i \int dt d^3x e^{-ikx} \theta(t) \langle [J_a^\rho(t, \mathbf{x}), T^{\mu\nu}(0, 0)] \rangle. \end{aligned} \quad (6.49)$$

$T^{\mu\nu}$  and  $J_a^\mu$  are the full stress-energy tensor and current, respectively. Thus, they include the equilibrium parts, which we from now on call  $\langle T^{\mu\nu} \rangle$  and  $\langle J_a^\mu \rangle$ , as well as the corresponding dissipative parts which arise due to the inclusion of fluctuations in our model. In the following we split the analysis into the different helicity blocks.

#### Helicity two mode

First we look at the non-trivial helicity two mode displayed in table 6.1. If we expand the action (5.9) up to second order in the fluctuations, this mode decouples from every other field. Therefore, it can be written as a minimal coupled scalar with the equation of motion

$$\Xi'' + \left( \frac{1}{r} + \frac{4r}{N} - \frac{r\alpha_{\text{YM}}^2 \phi'^2}{3N\sigma^2} \right) \Xi' + \frac{\omega^2}{N^2\sigma^2} \Xi = 0. \quad (6.50)$$

The contribution from this mode to the on-shell action is

$$\begin{aligned} \tilde{S}_{\text{helicity } 2}^{\text{on-shell}} &= \frac{1}{\kappa_5^2} \int \frac{d^4k}{(2\pi)^4} \left\{ r^3 N \sigma \left[ \left( \frac{3}{2\sqrt{N}} - \frac{1}{r} + \frac{f'}{2f} - \frac{N'}{4N} - \frac{\sigma'}{2\sigma} \right) \Xi^2 \right. \right. \\ &\quad \left. \left. - \frac{1}{4} \Xi \Xi' \right] \right\}_{r=r_{\text{bdy}}}, \end{aligned} \quad (6.51)$$

which is divergent as we send  $r_{\text{bdy}} \rightarrow \infty$ . The divergence can be cured by holographic renormalization (see appendix B.3). The renormalized on-shell action is

$$\mathcal{S}_{\text{helicity } 2}^{\text{on-shell}} = \frac{r_h^4}{\kappa_5^2} \int \frac{d^4k}{(2\pi)^4} \left[ \Xi_0^b \Xi_2^b - \frac{1}{2} \left( \tilde{m}_0^b + 4f_2^b - \frac{1}{32} \tilde{\omega}^4 \right) \left( \Xi_0^b \right)^2 \right], \quad (6.52)$$

where  $\tilde{\omega} = \omega/r_h$  is the dimensionless frequency,  $\Xi_0^b$  and  $\Xi_2^b$  are defined similar to the quantities in (6.6) and  $\Xi_0^b \Xi_2^b$  is a short form for  $\Xi_0^b(\omega) \Xi_2^b(-\omega)$ . Now we use the recipe discussed in section 4.3.1 to compute the Green's function of this component. The response due to the perturbation  $h_{yz}$  is given by

$$\langle T^{yz} \rangle(\omega) = \frac{\delta S_{\text{helicity 2}}^{\text{on-shell}}}{\delta \Xi_0^b(-\omega)} = G^{yz,yz}(\omega) \Xi_0^b(\omega), \quad (6.53)$$

with

$$G^{yz,yz}(\omega) = \left( \frac{2r_h^4}{\kappa_5^2} \frac{\Xi_2^b(\omega)}{\Xi_0^b(\omega)} - \langle \mathcal{T}_{yy} \rangle + \frac{1}{32} \omega^4 \right), \quad (6.54)$$

where  $\langle \mathcal{T}_{yy} \rangle$  is the equilibrium contribution given by the pressure  $p$ . As we will see in section 6.3.2, the Green's function of this helicity mode will lead to a shear viscosity component with universal behavior, i. e.  $\eta_{yz}/s = 1/4\pi$ .

### Helicity one modes

Now we look at the helicity one modes displayed in table 6.1. Again we obtain their equations of motion by expanding the action (5.9) up to second order in the fluctuations and varying it with respect to the corresponding fields. The equations of motion are

$$0 = a_y^{3''} + \left( \frac{1}{r} - \frac{2f'}{f} + \frac{N'}{N} + \frac{\sigma'}{\sigma} \right) a_y^{3'} + \left( \frac{\omega^2}{N^2 \sigma^2} - \frac{f^4 w^2}{r^2 N} - \frac{2\alpha_{\text{YM}}^2 \phi'^2}{N \sigma^2} \right) a_y^3, \quad (6.55a)$$

$$0 = \Psi_t' + \frac{2\alpha_{\text{YM}}^2 \phi'}{r^2 f^2} a_y^3, \quad (6.55b)$$

and

$$0 = \Psi_x'' + \left( \frac{1}{r} + \frac{4r}{N} + \frac{6f'}{f} - \frac{r\alpha_{\text{YM}}^2 \phi'^2}{3N\sigma^2} \right) \Psi_x' + \frac{2\alpha_{\text{YM}}^2 w'}{r^2 f^2} a_y^{1'} + \frac{\omega^2}{N^2 \sigma^2} \Psi_x \\ + \frac{2i\alpha_{\text{YM}}^2 \omega w \phi}{r^2 f^2 N^2 \sigma^2} a_y^2 - \frac{2\alpha_{\text{YM}}^2 w \phi^2}{r^2 f^2 N^2 \sigma^2} a_y^1, \quad (6.56a)$$

$$0 = a_y^{1''} + \left( \frac{1}{r} - \frac{2f'}{f} + \frac{N'}{N} + \frac{\sigma'}{\sigma} \right) a_y^{1'} - f^6 w' \Psi_x' + \left( \frac{\omega^2}{N^2 \sigma^2} + \frac{\phi^2}{N^2 \sigma^2} \right) a_y^1 \\ - \frac{2i\omega \phi}{N^2 \sigma^2} a_y^2, \quad (6.56b)$$

$$0 = a_y^{2''} + \left( \frac{1}{r} - \frac{2f'}{f} + \frac{N'}{N} + \frac{\sigma'}{\sigma} \right) a_y^{2'} + \left( \frac{\omega^2}{N^2 \sigma^2} + \frac{\phi^2}{N^2 \sigma^2} - \frac{f^4 w^2}{r^2 N} \right) a_y^2 \\ + \frac{2i\omega \phi}{N^2 \sigma^2} a_y^1 - \frac{i\omega f^6 w \phi}{N^2 \sigma^2} \Psi_x. \quad (6.56c)$$

where  $\Psi_t = g^{yy} h_{ty}$  and  $\Psi_x = g^{yy} h_{xy}$ . Note that due to the parity  $P_{\parallel}$ , the helicity one modes split into two blocks where the modes of the first block are even while

the modes of the second block are odd under  $P_{\parallel}$ . In the first block there is only one physical mode  $a_y^3$  while the value of the other field  $\Psi_t$  is given by the constraint (6.55b). This can also be seen in the gauge invariant fields (6.46) since  $h_{ty}$  drop out for  $k_{\parallel} = 0$ . The other three physical modes appear in the second block where  $\Psi_x = \Psi$  for  $k_{\parallel} = 0$ .

The contribution from these modes to the on-shell action is

$$\begin{aligned} \tilde{S}_{\text{helicity } 1}^{\text{on-shell}} &= \frac{1}{\kappa_5^2} \int \frac{d^4 k}{(2\pi)^4} \left\{ \frac{r^5 f^2}{4\sigma} \Psi_t \Psi_t' - \frac{1}{4} r^3 f^6 N \sigma \Psi_x \Psi_x' \right. \\ &\quad - \frac{r \alpha_{\text{YM}}^2 N \sigma}{2 f^2} \left( a_y^1 a_y^{1'} + a_y^2 a_y^{2'} + a_y^3 a_y^{3'} \right) + \frac{3 r^4 f^2}{2 \sigma} \left( 1 - \frac{r}{\sqrt{N}} \right) \Psi_t^2 \\ &\quad + \frac{r^3 f^6 N \sigma}{2} \left( \frac{3}{\sqrt{N}} - \frac{2}{r} - \frac{2 f'}{f} - \frac{N'}{2 N} - \frac{\sigma'}{\sigma} \right) \Psi_x^2 \\ &\quad \left. + \frac{r \alpha_{\text{YM}}^2 f^4 N \sigma w'}{2} a_y^1 \Psi_x - \frac{r^3 \alpha_{\text{YM}}^2 \phi'}{2 \sigma} a_y^3 \Psi_t \right\} \Big|_{r=r_{\text{bdy}}}, \end{aligned} \quad (6.57)$$

which is again divergent<sup>8</sup>. The renormalized on-shell action is given by

$$\begin{aligned} S_{\text{helicity } 1}^{\text{on-shell}} &= \frac{r_h^4}{\kappa_5^2} \int \frac{d^4 k}{(2\pi)^4} \left\{ (\Psi_x)_0^b (\Psi_x)_2^b + \alpha_{\text{YM}}^2 \left[ (\tilde{a}_y^1)_0^b (\tilde{a}_y^1)_1^b + (\tilde{a}_y^2)_0^b (\tilde{a}_y^2)_1^b + (\tilde{a}_y^3)_0^b (\tilde{a}_y^3)_1^b \right] \right. \\ &\quad - \frac{1}{2} \left( \tilde{m}_0^b - 8 f_4^b - \frac{1}{32} \tilde{\omega}^4 \right) \left( (\Psi_x)_0^b \right)^2 - \frac{3}{2} \tilde{m}_0^B \left( (\Psi_t)_0^b \right)^2 - \frac{1}{4} \alpha_{\text{YM}}^2 \tilde{\omega}^2 (\tilde{a}_y^3)_0^{b^2} \\ &\quad - \frac{1}{4} \alpha_{\text{YM}}^2 (\tilde{\mu}_I^2 + \tilde{\omega}^2) \left[ (\tilde{a}_y^1)_0^{b^2} + (\tilde{a}_y^2)_0^{b^2} \right] + i \alpha_{\text{YM}}^2 \tilde{\omega} \tilde{\mu}_I (\tilde{a}_y^1)_0^b (\tilde{a}_y^2)_0^b \\ &\quad \left. + \alpha_{\text{YM}}^2 \left[ 2 \tilde{\phi}_1^b (\tilde{a}_y^3)_0^b (\Psi_t)_0^b - \tilde{w}_1^b (\tilde{a}_y^1)_0^b (\Psi_x)_0^b \right] \right\}, \end{aligned} \quad (6.58)$$

where  $\tilde{a}_\mu^a = r_h a_\mu^a$  is dimensionless. We obtain the response of the system due to the fluctuations  $a_y^3$  and  $h_{ty}$  by variation of the on-shell action,

$$\begin{pmatrix} \langle J_3^y \rangle(\omega) \\ \langle T^{ty} \rangle(\omega) \end{pmatrix} = \begin{pmatrix} \frac{\delta S_{\text{helicity } 1}^{\text{on-shell}}}{\delta (a_y^3)_0^b(-\omega)} \\ \frac{\delta S_{\text{helicity } 1}^{\text{on-shell}}}{\delta (\Psi_t)_0^b(-\omega)} \end{pmatrix} = \begin{pmatrix} G_{3,3}^{y,y}(\omega) & G_3^{yty}(\omega) \\ G^{tyy}_3(\omega) & G^{ty,ty}(\omega) \end{pmatrix} \begin{pmatrix} (a_y^3)_0^b(\omega) \\ (\Psi_t)_0^b(\omega) \end{pmatrix}, \quad (6.59)$$

with

$$\begin{pmatrix} G_{3,3}^{y,y}(\omega) & G_3^{yty}(\omega) \\ G^{tyy}_3(\omega) & G^{ty,ty}(\omega) \end{pmatrix} = \begin{pmatrix} \frac{\alpha_{\text{YM}}^2 r_h^2}{\kappa_5^2} \left( \frac{2 (\tilde{a}_y^3)_1^b(\omega)}{(\tilde{a}_y^3)_0^b(\omega)} - \frac{\tilde{\omega}^2}{2} \right) & -\langle \mathcal{J}_3^t \rangle \\ -\langle \mathcal{J}_3^t \rangle & -\langle \mathcal{I}_{tt} \rangle \end{pmatrix}. \quad (6.60)$$

<sup>8</sup>Note that the contribution of the on-shell action is zero at the horizon since we can set  $\Psi_t$  to zero there.

This result agrees with the result obtain in the holographic s-wave superfluids [78,95] and, therefore, the breaking of the rotational symmetry has no effect on this subset of fluctuations. The coupling between the current  $J_3^y$  and the momentum  $T_{ty}$  is called the thermoelectric effect which we will study in the next section.

The response due to the fluctuations  $a_y^1$ ,  $a_y^2$  and  $h_{xy}$  is given by

$$\begin{pmatrix} \langle J_1^y \rangle(\omega) \\ \langle J_2^y \rangle(\omega) \\ \langle T^{xy} \rangle(\omega) \end{pmatrix} = \begin{pmatrix} \frac{\delta S_{\text{helicity 1}}^{\text{on-shell}}}{\delta (a_y^1)_0^b(-\omega)} \\ \frac{\delta S_{\text{helicity 1}}^{\text{on-shell}}}{\delta (a_y^2)_0^b(-\omega)} \\ \frac{\delta S_{\text{helicity 1}}^{\text{on-shell}}}{\delta (\Psi_x)_0^b(-\omega)} \end{pmatrix} = \begin{pmatrix} G_{1,1}^{y,y}(\omega) & G_{1,2}^{y,y}(\omega) & G_1^{yxy}(\omega) \\ G_{2,1}^{y,y}(\omega) & G_{2,2}^{y,y}(\omega) & G_2^{yxy}(\omega) \\ G^{xyy}_1(\omega) & G^{xyy}_2(\omega) & G^{xy,xy}(\omega) \end{pmatrix} \begin{pmatrix} (a_y^1)_0^b(\omega) \\ (a_y^2)_0^b(\omega) \\ (\Psi_x)_0^b(\omega) \end{pmatrix}, \quad (6.61)$$

where the matrix of the Green's functions is given by

$$\begin{pmatrix} \frac{\alpha_{\text{YM}}^2 r_h^2}{\kappa_5^2} \left( 2 \frac{(\tilde{a}_y^1)_1^b(\omega)}{(\tilde{a}_y^1)_0^b(\omega)} - \frac{\tilde{\mu}_I^2 + \tilde{\omega}^2}{2} \right) & \frac{\alpha_{\text{YM}}^2 r_h^2}{\kappa_5^2} \left( 2 \frac{(\tilde{a}_y^1)_1^b(\omega)}{(\tilde{a}_y^2)_0^b(\omega)} + i\tilde{\omega}\tilde{\mu}_I \right) & -\frac{\langle \mathcal{J}_1^x \rangle}{2} + 2 \frac{\alpha_{\text{YM}}^2 r_h^3}{\kappa_5^2} \frac{(\tilde{a}_y^1)_1^b(\omega)}{(\Psi_x)_0^b(\omega)} \\ \frac{\alpha_{\text{YM}}^2 r_h^2}{\kappa_5^2} \left( 2 \frac{(\tilde{a}_y^2)_1^b(\omega)}{(\tilde{a}_y^1)_0^b(\omega)} - i\tilde{\omega}\tilde{\mu}_I \right) & \frac{\alpha_{\text{YM}}^2 r_h^2}{\kappa_5^2} \left( 2 \frac{(\tilde{a}_y^2)_1^b(\omega)}{(\tilde{a}_y^2)_0^b(\omega)} - \frac{\tilde{\mu}_I^2 + \tilde{\omega}^2}{2} \right) & 2 \frac{\alpha_{\text{YM}}^2 r_h^3}{\kappa_5^2} \frac{(\tilde{a}_y^2)_1^b(\omega)}{(\Psi_x)_0^b(\omega)} \\ -\frac{\langle \mathcal{J}_1^x \rangle}{2} + 2 \frac{r_h^3}{\kappa_5^2} \frac{(\Psi_x)_2^b(\omega)}{(\tilde{a}_y^1)_0^b(\omega)} & 2 \frac{r_h^3}{\kappa_5^2} \frac{(\Psi_x)_2^b(\omega)}{(\tilde{a}_y^2)_0^b(\omega)} & \frac{r_h^4}{\kappa_5^2} \left( 2 \frac{(\Psi_x)_2^b(\omega)}{(\Psi_x)_0^b(\omega)} + \frac{1}{32} \tilde{\omega}^4 \right) - \langle \mathcal{T}_{xx} \rangle \end{pmatrix}. \quad (6.62)$$

Due to the breaking of the rotational symmetry we see a new coupling between the currents  $J_{1,2}^y$  and the stress tensor  $T_{xy}$  in this subset of the fluctuations. This new coupling generates some interesting new physical effect: it induces a non-universal behavior of the ratio of shear viscosity to entropy density and a flexoelectric effect known from nematic crystals. We will study these effects in the next section.

## 6.3 Transport Properties of the Hairy Black Hole

In this section we extract the transport properties of the holographic p-wave superfluid from the correlation functions presented in the previous section. We split our analysis into distinct transport phenomena. However, let us first discuss anisotropic fluids.

### 6.3.1 General Remarks on Viscosity in Anisotropic Fluids

In general, viscosity refers to the dissipation of energy due to any internal motion [127]. For an internal motion which describes a general translation or a general rotation, the dissipation is zero. Thus, the dissipation depends on the gradient of the velocities  $u^\mu$  only in the combination  $u_{\mu\nu} = \frac{1}{2}(\nabla_\mu u_\nu + \nabla_\nu u_\mu)$ , and we may define a general dissipation function  $\Xi = \frac{1}{2}\eta^{\mu\nu\lambda\rho}u_{\mu\nu}u_{\lambda\rho}$ , where  $\eta^{\mu\nu\lambda\rho}$  defines the viscosity tensor [235]. Its symmetries are given by

$$\eta^{\mu\nu\lambda\rho} = \eta^{\nu\mu\lambda\rho} = \eta^{\mu\nu\rho\lambda} = \eta^{\lambda\rho\mu\nu}. \quad (6.63)$$

The part of the stress tensor which is dissipative due to viscosity is defined by

$$\Pi^{\mu\nu} = -\frac{\partial \Xi}{\partial u_{\mu\nu}} = -\eta^{\mu\nu\lambda\rho} u_{\lambda\rho}. \quad (6.64)$$

We consider a fluid in the rest frame of the normal fluid  $u^t = 1$ . To satisfy the condition of the Landau frame  $u_\mu \Pi^{\mu\nu} = 0$ , the stress energy tensor and thus the viscosity has non-zero components only in the spatial directions  $i, j = \{x, y, z\}$ . In general, only 21 independent components of  $\eta_{ijkl}$  appear in the expressions above.

For an isotropic fluid, there are only two independent components which are usually parametrized by the shear viscosity  $\eta$  and the bulk viscosity  $\zeta$ . The dissipative part of the stress tensor becomes  $\Pi^{ij} = -2\eta(u^{ij} - \frac{1}{3}\delta^{ij}u_i^l) - \zeta u_i^l \delta^{ij}$  which is the well-known result (see section 4.4.1).

In a transversely isotropic fluid, there are five independent components of the tensor  $\eta^{ijkl}$ . For concreteness, we choose the symmetry axis to be along the  $x$ -axis. The non-zero components are given by

$$\begin{aligned} \eta^{xxxx} &= \zeta_x - 2\lambda, & \eta^{yyyy} &= \eta^{zzzz} = \zeta_y - \frac{\lambda}{2} + \eta_{yz}, \\ \eta^{xxyy} &= \eta^{xxzz} = \lambda, & \eta^{yyzz} &= \zeta_y - \frac{\lambda}{2} - \eta_{yz}, \\ \eta^{yzyz} &= \eta_{yz}, & \eta^{xyxy} &= \eta^{xzzx} = \eta_{xy}. \end{aligned} \quad (6.65)$$

The non-zero off-diagonal components of the stress tensor are given by

$$\begin{aligned} \Pi^{xy} &= -2\eta_{xy}u_{xy}, & \Pi^{xz} &= -2\eta_{xy}u_{xz}, \\ \Pi^{yz} &= -2\eta_{yz}u_{yz}. \end{aligned} \quad (6.66)$$

So far, we only considered the contribution to the stress tensor due to the dissipation via viscosity and found the terms in the constitutive equation which contain the velocity of the normal fluid  $u_\mu$ . In general, also terms depending on the derivative of Nambu-Goldstone boson fields  $v_\mu = \partial_\mu \varphi$ , on the superfluid velocity and on the velocity of the director may contribute to the dissipative part of the stress tensor. Here the director is given by the vector pointing in the preferred direction. However, these terms do not contribute to the off-diagonal components of the energy-momentum tensor for the following reasons: (1) a shear viscosity due to the superfluid velocity leads to a non-positive divergence of the entropy current [127, 238] and (2) no rank two tensor can be formed out of degrees of freedom of the director if the gradients of the director vanish [239]. In our case the second argument is fulfilled since the condensate is homogeneous and the fluctuations depend only on time. These degrees of freedom will generate additional transport coefficients, but they do not change the shear viscosities. Thus, we can write Kubo's formulae similar to (4.149) which determine the shear viscosities in terms of the stress energy correlation functions.

### 6.3.2 Universal Shear Viscosity

Let us start by considering the helicity two mode  $h_{yz}$ . It is well-known that, in the isotropic case, the corresponding component of the energy-momentum tensor may be written as<sup>9</sup>

$$\langle T^{yz} \rangle = -(p + i\omega\eta_{yz})h_{yz}. \quad (6.67)$$

Using (6.66) we see that this result is still correct in the transversely symmetric case we are studying here. The result also agrees with our gravity calculation (6.54)<sup>10</sup>. Thus, the shear viscosity is given by the Kubo formula (4.149),

$$\eta_{yz} = -\lim_{\omega \rightarrow 0} \frac{1}{\omega} \text{Im} (G^{yz,yz}) = -\lim_{\omega \rightarrow 0} \frac{1}{\omega} \frac{2r_h^4}{\kappa_5^2} \frac{\Xi_2^b(\omega)}{\Xi_0^b(\omega)}. \quad (6.68)$$

In the following we show that we can apply the proof for the universal result for the ratio of the shear viscosity to entropy density described in [194]. In the  $\omega \rightarrow 0$  limit the equation of motion (6.50) corresponds to  $\partial_r \Pi = 0$ , with  $\Pi$  the conjugate momentum to the field  $\Xi = g^{yy}h_{yz}$ . This is the decisive condition needed to apply the proof of the universality discussed in section 4.4.4. Therefore, we conclude that here we obtain the universal result for the ratio of shear viscosity to entropy density,

$$\frac{\eta_{yz}}{s} = \frac{1}{4\pi}. \quad (6.69)$$

In this subset we do not see any effect of the rotational symmetry breaking since the fluctuation  $h_{yz}$  is transverse to the condensate.

### 6.3.3 Thermoelectric Effect Perpendicular to the Condensate

Now we relate the results of (6.59) to the thermoelectric effect on the field theory side. We begin with the well-known connection between electric  $\langle J_3^\perp \rangle = \langle J^\perp \rangle$  and thermal  $\langle Q^\perp \rangle = \langle T^{t\perp} \rangle - \mu_I \langle J^\perp \rangle$  transport perpendicular to the condensate direction (see e. g. [78, 79, 95] for the same calculation for holographic s-wave superfluids), i. e.

$$\begin{pmatrix} \langle J^\perp \rangle \\ \langle Q^\perp \rangle \end{pmatrix} = \begin{pmatrix} \sigma^{\perp\perp} & T\alpha^{\perp\perp} \\ T\alpha^{\perp\perp} & T\bar{\kappa}^{\perp\perp} \end{pmatrix} \begin{pmatrix} E_\perp \\ -(\nabla_\perp T)/T \end{pmatrix}, \quad (6.70)$$

where the electric field  $E_\perp$  and the thermal gradient  $-\nabla_\perp T/T$  need to be related to the background values of the gauge field  $(a_\perp^3)_0^b$  and the metric  $(\Psi_t)_0^b$ . This identification has been done in [78],

$$\begin{aligned} E_\perp &= i\omega \left( (a_\perp^3)_0^b + \mu_I (\Psi_t)_0^b \right), \\ -\frac{\nabla_\perp T}{T} &= i\omega (\Psi_t)_0^b. \end{aligned} \quad (6.71)$$

<sup>9</sup>Note that  $g^{\mu\nu} = \eta^{\mu\nu} - h^{\mu\nu}$ .

<sup>10</sup>We do not see an  $\omega^4$ -term as in (6.54) in the linear hydrodynamic description since this term corresponds to higher order term with four derivatives.

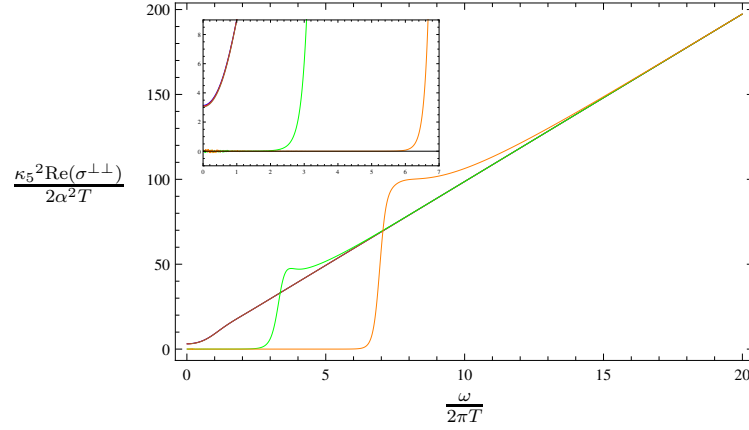


**Figure 6.12:** Real part of the conductivity  $\text{Re}(\sigma^{\perp\perp})$  over the frequency  $\omega/(2\pi T)$  for  $\alpha_{\text{YM}} = 0.032$ . The color coding is as follows: blue  $T = \infty$ , red  $T = 1.34T_c$ , brown  $T = 1.00T_c$ , green  $T = 0.40T_c$ , orange  $T = 0.19T_c$ . Note that the three curves with the highest temperature, blue, red and brown, are nearly on top of each other. The agreement of the curves in the  $\omega \rightarrow 0$  limit is due to the small change in the strength of the Drude peak with temperature. Below  $T_c$ , the superfluid contribution to the delta peak at  $\omega = 0$  is turned on, and we obtain larger deviations from the  $T = \infty$  curve since the area below the curves has to be the same for all temperatures (sum rule). Furthermore, the value for  $\omega \rightarrow 0$  clearly asymptotes to 0 with decreasing temperature. This figure is taken from [8].

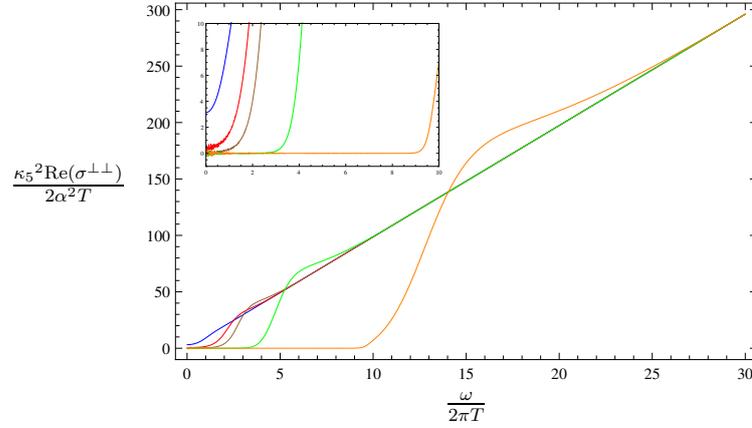


**Figure 6.13:** Real part of the conductivity  $\text{Re}(\sigma^{\perp\perp})$  over the frequency  $\omega/(2\pi T)$  for  $\alpha_{\text{YM}} = 0.316$ . The color coding is as follows: blue  $T = \infty$ , red  $T = 1.00T_c$ , brown  $T = 0.88T_c$ , green  $T = 0.50T_c$ , orange  $T = 0.19T_c$ . In this plot we see that the Drude peak has already a much stronger dependence on the temperature than in the  $\alpha_{\text{YM}} = 0.032$  case, since the blue and the red curve can be clearly distinguished. Below  $T_c$  the contributions of the superfluid phase to the delta peak leads again to a tendency of the curve to vanish for frequencies in the gap region since the area below the curves have to be the same for all temperatures (sum rule). This figure is taken from [8].

Putting all together and comparing the relation of the electric and thermal transport to the corresponding equations for  $\langle J^y \rangle$  and  $\langle T^{ty} \rangle$  in (6.59), we can identify the transport matrix of (6.70),

$$\begin{aligned}\sigma^{\perp\perp} &= -\frac{iG_{3,3}^{\perp,\perp}}{\omega} = -\frac{\alpha_{\text{YM}}^2 r_h}{\kappa_5^2} \frac{i}{\tilde{\omega}} \left( \frac{2(\tilde{a}_\perp^3)_1^b}{(\tilde{a}_\perp^3)_0^b} - \frac{\tilde{\omega}^2}{2} \right), \\ T\alpha^{\perp\perp} &= -\frac{i}{\omega} \left( G_3^{\perp,t\perp} - \mu_I G_{3,3}^{\perp,\perp} \right) = \frac{i}{\omega} \langle \mathcal{J}_3^t \rangle - \mu_I \sigma^{\perp\perp}, \\ T\bar{\kappa}^{\perp\perp} &= -\frac{i}{\omega} \left( G^{t\perp,t\perp} + \mu_I^2 G_{3,3}^{\perp,\perp} \right) = \frac{i}{\omega} \langle \mathcal{I}_{tt} \rangle + \mu_I^2 \sigma^{\perp\perp}.\end{aligned}\tag{6.72}$$

These results are in agreement with [78]. The coupling between thermal and electrical transport is well-known in condensed matter physics, since the charge carriers (electron or holes) transport charge as well as heat. In this subset we do not observe any effect of the breaking of the rotational symmetry since all the fields are in the transverse direction to the condensate.

In figure 6.12, 6.13 and 6.14 we plot our numerical results for  $\text{Re}(\sigma^{\perp\perp})$  versus the frequency  $\omega/(2\pi T)$  for different values of  $\alpha_{\text{YM}}$ , namely  $\alpha_{\text{YM}} = 0.032 < (\alpha_{\text{YM}})_c$ ,  $\alpha_{\text{YM}} = 0.316 \lesssim (\alpha_{\text{YM}})_c$  and  $\alpha_{\text{YM}} = 0.447 > (\alpha_{\text{YM}})_c$ , respectively. For large frequencies, i. e.  $\omega \gg 2\pi T$ , the conductivity asymptotically has a linear dependence on the frequency as obtained from (4.120),

$$\text{Re}(\sigma^{\perp\perp}) \rightarrow \frac{\alpha_{\text{YM}}^2}{\kappa_5^2} \pi \omega \quad \text{for} \quad \omega \gg 2\pi T.\tag{6.73}$$

For small temperatures, i. e.  $T < T_c$ , we see a gap opening up at small frequencies. The size of the gap increases as the temperature is decreased. This is the expected energy gap we know from superconductors. The gap ends at a frequency  $\omega_g$  with a sharp increase of the conductivity. Beyond the gap the conductivity at small temperature, i. e.  $T < T_c$ , is larger than the corresponding value at large temperature, i. e.  $T > T_c$ , such that the small temperature conductivities approach the asymptotic behavior (6.73) from above (cf. [100] and section 6.5).

The value of  $\text{Re}(\sigma^{\perp\perp})$  at  $\omega = 0$  approaches zero with decreasing temperature. When we go below  $T_c$ , the tendency for this part of the conductivity to vanish increases. Nevertheless, we still find finite values even below  $T_c$ , i. e. these values seem to be suppressed but not identically vanishing (c.f. [95]). In [119] it is shown that in the limit  $T \rightarrow 0$  there is a hard gap, i. e. the value for the conductivity becomes zero. Finally, we observe that an increase in  $\alpha_{\text{YM}}$  leads to a stronger suppression of the real part of the conductivity in the gap region.

Due to the sum rule for the conductivity, i. e. the frequency integral over the real part of the conductivity is constant for all temperatures, a delta peak has to form at zero frequency which contains the ‘‘missing area’’ of the gap region. The strength of the delta peak has two contributions: the first is proportional to the superfluid density  $n_s$ ,  $\text{Re}(\sigma^{\perp\perp}) \sim \alpha_{\text{YM}}^2/\kappa_5^2 \pi n_s \delta(\omega)$  and appears only for temperatures below

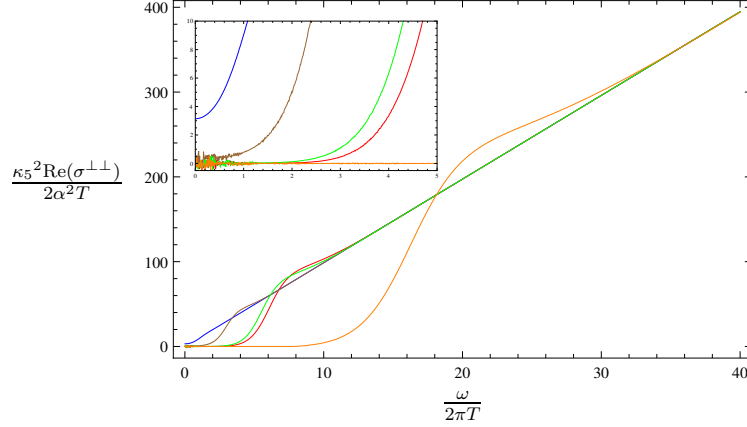


**Figure 6.14:** Real part of the conductivity  $\text{Re}(\sigma^{\perp\perp})$  over the frequency  $\omega/(2\pi T)$  for  $\alpha_{\text{YM}} = 0.447$ . The color coding is as follows: blue  $T = \infty$ , brown  $T = 1.95T_c$ , green  $T = 1.00T_c$ , red  $T = 0.91T_c$ , orange  $T = 0.34T_c$ . Again we see the same tendency as before for the curve to vanish at  $\omega \rightarrow 0$  for decreasing temperatures. The strength of the Drude peak has a strong dependence on the temperatures since the blue and the brown curve are quite far apart (both curves were computed for temperatures above  $T_c$ ). This figure is taken from [8].

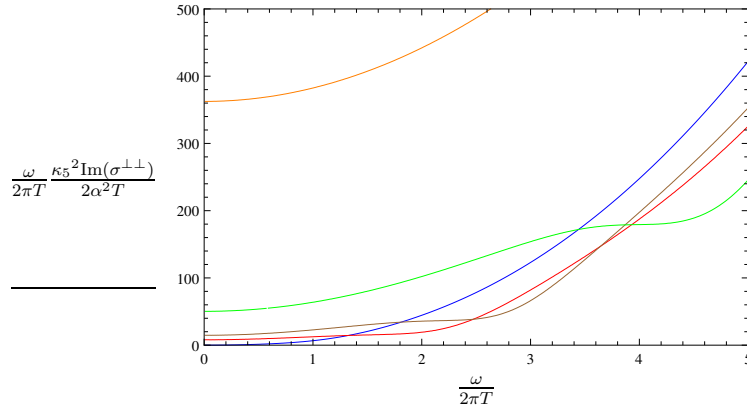


**Figure 6.15:** Imaginary part of the conductivity  $\omega \text{Im}(\sigma^{\perp\perp})$  over the frequency  $\omega/(2\pi T)$  for  $\alpha_{\text{YM}} = 0.316$ . The color coding is as follows: blue  $T = \infty$ , red  $T = 1.00T_c$ , brown  $T = 0.88T_c$ , green  $T = 0.50T_c$ , orange  $T = 0.19T_c$ . The curves in this plot have a constant value for  $\frac{\omega}{2\pi T} \rightarrow 0$ , which is determined by the delta peak in the real part of the conductivity by the Kramers-Kronig relation. The values for this constant are, in the same order as the temperatures above: 0, 8.0, 14.7, 50.3 and 362.4. Note that we already see a finite value for  $T = 1.00T_c$ , this is due to the Drude peak. Below  $T_c$  the values at  $\omega = 0$  are due to two contributions, first the Drude peak, as before, and second due to the superfluid density. This figure is taken from [8].

$T_c$ . The second contribution is a consequence of translation invariance of our system, the Drude peak, and appears for all temperatures.

The delta peak is observed in the imaginary part of the conductivity by using the Kramers-Kronig relation (see [95]),

$$\text{Im}(\sigma^{\perp\perp}) \simeq \frac{A_D(\alpha_{\text{YM}}, T)}{\omega} + \frac{A_s(\alpha_{\text{YM}})}{\omega} \left(1 - \frac{T}{T_c}\right), \quad (6.74)$$

for  $T \lesssim T_c$ , with  $A_s(\alpha_{\text{YM}}) \left(1 - \frac{T}{T_c}\right) \propto n_s$  and  $A_D$  parametrizing the contribution from the Drude peak. In figure 6.15 we present the imaginary part of the conductivity  $\omega \text{Im}(\sigma^{\perp\perp})$  versus the frequency  $\omega/(2\pi T)$  for  $\alpha_{\text{YM}} = 0.316$  and different temperatures. We see that  $\omega \text{Im}(\sigma^{\perp\perp})$  takes finite values for  $\omega \rightarrow 0$  and  $T < \infty$ . The finite values above  $T_c$  are due to the Drude peak, i.e. the  $A_D$  part of (6.74). Below  $T_c$  we see a further contribution from the superfluid density. By analyzing the temperature dependence of  $\lim_{\omega \rightarrow 0} \omega \text{Im}(\sigma^{\perp\perp})$ , we get a smooth curve, which is, however, not differentiable at  $T_c$  for  $\alpha_{\text{YM}} \leq (\alpha_{\text{YM}})_c$ , i.e. it behaves as equation (6.74) anticipated. However, for  $\alpha_{\text{YM}} > (\alpha_{\text{YM}})_c$  we see a jump at  $T_c$  as consequence of the jump in the condensate. Furthermore,  $A_D$  and  $A_s$  have a non trivial dependence on  $\alpha_{\text{YM}}$ . Finally, as expected, there is an increase in the superfluid density with decreasing temperature.

### 6.3.4 Non-Universal Shear Viscosity and Flexoelectric Effect

Now let us study the remaining three components of the helicity one modes,  $\langle J_1^\perp \rangle$ ,  $\langle J_2^\perp \rangle$  and  $\langle T^{x\perp} \rangle$  as given by (6.61). We first focus on  $\langle T^{x\perp} \rangle$ , which for  $(a_y^1)_0^b, (a_y^2)_0^b = 0$  can be translated into the following dual field theory behavior

$$\langle T^{x\perp} \rangle = -\langle \mathcal{T}_{xx} \rangle h_{x\perp} - i\omega \eta_{x\perp} h_{x\perp}, \quad (6.75)$$

where  $\eta_{x\perp}$  is the second shear viscosity which is present in a transversal isotropic fluid and with  $\langle \mathcal{T}_{xx} \rangle$  as defined in (6.17). Here we see again that we can apply the Kubo formula (4.149) to determine the shear viscosity  $\eta_{x\perp}$ ,

$$\eta_{x\perp} = -\lim_{\omega \rightarrow 0} \frac{1}{\omega} \text{Im} \left( G^{x\perp, x\perp} \right). \quad (6.76)$$

This shear viscosity has a non-trivial temperature dependence even in the large  $N_c$  and large  $\lambda$  limit and is therefore not universal. In figure 6.16 we compare our numerical results for the ratio of the shear viscosity  $\eta_{x\perp}$  to the entropy density  $s$  with the universal behavior of the shear viscosity  $\eta_{yz}$  for different values of  $\alpha_{\text{YM}}$ . We see that in the normal phase  $T \geq T_c$ , the two shear viscosities coincide as required in an isotropic fluid. In addition, the ratio of shear viscosity to entropy density is universal. In the superfluid phase  $T < T_c$ , the two shear viscosities deviate from each other and  $\eta_{x\perp}$  is non-universal. However, it is exciting that  $\eta_{x\perp}/s \geq 1/4\pi$ , such that the KSS bound on the ratio of shear viscosity to entropy density [56] is still valid.

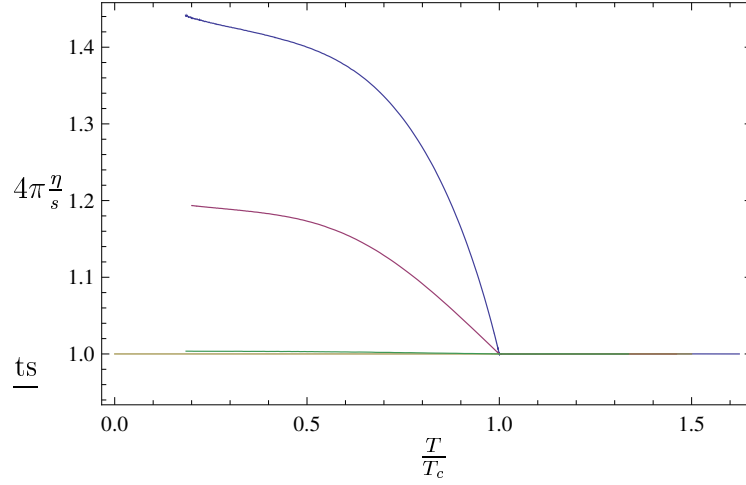


**Figure 6.16:** Ratio of shear viscosities  $\eta_{yz}$  and  $\eta_{x\perp}$  to entropy density  $s$  over the reduced temperature  $T/T_c$  for different values of the ratio of the gravitational coupling constant to the Yang-Mills coupling constant  $\alpha_{\text{YM}}$ . The color coding is as follows: In yellow,  $\eta_{yz}/s$  for all values of  $\alpha_{\text{YM}}$ ; while the curve for  $\eta_{x\perp}/s$  is plotted in green for  $\alpha_{\text{YM}} = 0.032$ , red for  $\alpha_{\text{YM}} = 0.224$  and blue for  $\alpha_{\text{YM}} = 0.316$ . The shear viscosities coincide and are universal in the normal phase  $T \geq T_c$ . However, in the superfluid phase  $T < T_c$ , the shear viscosity  $\eta_{yz}$  has the usual universal behavior while the shear viscosity  $\eta_{x\perp}$  is non-universal. This figure is taken from [5].

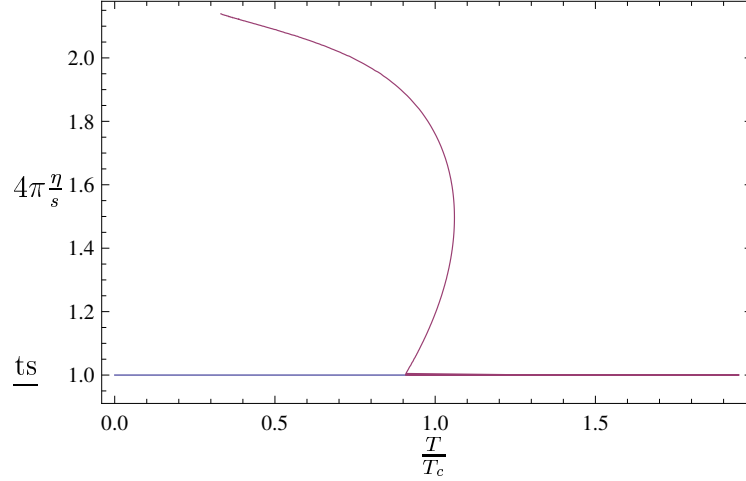


**Figure 6.17:** Ratio of shear viscosities  $\eta_{yz}$  (blue) and  $\eta_{x\perp}$  (red) to entropy density  $s$  over the reduced temperature  $T/T_c$  for  $\alpha_{\text{YM}} = 0.447$ , which is larger than the critical value where the phase transition becomes first order: The shear viscosities coincide in the normal phase  $T \geq T_c$  and are universal. In the superfluid phase  $\eta_{x\perp}$  is non-universal. Close to the phase transition, it is multivalued as expected for a first order phase transition. This figure is taken from [5].

The difference between the two viscosities in the superfluid phase is controlled by  $\alpha_{\text{YM}}$ . In the probe limit where  $\alpha_{\text{YM}} = 0$ , the shear viscosities also coincide in the superfluid phase. By increasing the back-reaction of the gauge fields, i. e. rising  $\alpha_{\text{YM}}$ , the deviation between the shear viscosities becomes larger in the superfluid phase as shown in figure 6.16. If  $\alpha_{\text{YM}}$  is larger than the critical value  $(\alpha_{\text{YM}})_c = 0.365$  found in section 6.1 (see figure 6.6) where the phase transition to the superfluid phase becomes first order, the shear viscosities are also multivalued close to the phase transition as seen in figure 6.17. Since there is a maximal  $\alpha_{\text{YM}}$  denoted by  $(\alpha_{\text{YM}})_{\text{max}} = 0.628$  for which the superfluid phase exists (see figure 6.6), we expect that the deviation of the shear viscosity  $\eta_{x\perp}$  from its universal value is maximal for this  $(\alpha_{\text{YM}})_{\text{max}}$ . Unfortunately, numerical calculations for large values of  $\alpha_{\text{YM}}$  are very challenging such that we cannot present satisfying numerical data for this region. It is interesting that also the deviations due to  $\lambda$  and  $N_c$  corrections are bounded. In this case the bound is determined by causality [240].

For  $\alpha_{\text{YM}}$  smaller than the critical value where the phase transition is second order, we may study the critical behavior of the ratio of the shear viscosities to entropy density close to the phase transition. Due to universality,  $\eta_{yz}/s$  is constant and does not change on both sides of the phase transition, while  $\eta_{xy}/s$  is only constant in the normal phase, but has a different critical behavior in the superfluid phase. Let us consider the critical exponent related to  $\eta_{xy}/s$  and its dependence on  $\alpha_{\text{YM}}$ . From our numerical data we obtain the critical behavior

$$1 - 4\pi \frac{\eta_{xy}}{s} \propto \left(1 - \frac{T}{T_c}\right)^\beta \quad \text{with} \quad \beta = 1.00 \pm 3\% \quad (6.77)$$

in the superfluid phase close to the phase transition. It is interesting that the critical exponent  $\beta$  does not change with  $\alpha_{\text{YM}}$ . This result has been confirmed by an analytic calculation for small  $\alpha_{\text{YM}}$  in [241].

The non-universality of the shear viscosity can be understood in the following way. For the  $\eta_{x\perp}$  component, the equation of motion (6.56a) in the  $\omega \rightarrow 0$  limit includes also non-vanishing source terms besides the derivative of the conjugate momentum  $\Pi_x$  of  $\Psi_x$ , i. e.  $\partial_r \Pi_x = \text{source}$ . This is in contrast to equation of motion which leads to the  $\eta_{yz}$  component. Note that the source term depends on the condensate  $w$  and the fluctuation  $a_\perp^1$  and vanishes if the condensate  $w$  vanishes. Hence, as we confirm numerically in figure 6.16, when the condensate is absent (i. e. for the  $T > T_c$  case) we obtain again the universal result, since in this case the same proof as described above for the helicity two mode applies.

For  $h_{x\perp} = 0$ , we obtain flavor charge transport, i. e. a flavor field  $a_\perp^{1,2}$  generates a flavor current  $\langle J_{1,2}^\perp \rangle$ . In the unbroken phase it is useful to combine the fields  $a_\perp^{1,2}$  in the way  $a_\perp^\pm = a_\perp^1 \pm ia_\perp^2$  since they transform in the fundamental representation of the  $U(1)_3$  symmetry and are complex conjugate to each other. To make contact to the unbroken phase, we also use this definition in the broken phase.

We also use the definition for the currents  $\langle J_\pm \rangle = 1/2 (\langle J_1 \rangle \pm i \langle J_2 \rangle)$ , such that

the full transport matrix becomes

$$\begin{pmatrix} \langle J_+^\perp \rangle \\ \langle J_-^\perp \rangle \\ \langle T^{x\perp} \rangle \end{pmatrix} = \begin{pmatrix} G_{+,+}^{\perp,\perp} & G_{+,-}^{\perp,\perp} & G_+^{\perp x\perp} \\ G_{-,+}^{\perp,\perp} & G_{-,-}^{\perp,\perp} & G_-^{\perp x\perp} \\ G^{x\perp}_+ & G^{x\perp}_- & -\langle T_{xx} \rangle - i\omega\eta_{x\perp} \end{pmatrix} \begin{pmatrix} a_+^\perp \\ a_-^\perp \\ h_{x\perp} \end{pmatrix}, \quad (6.78)$$

where the flavor conductivities are given by

$$\begin{aligned} G_{\pm,\pm}^{\perp,\perp}(\omega) &= \frac{1}{4} \left[ G_{1,1}^{\perp,\perp}(\omega) + G_{2,2}^{\perp,\perp}(\omega) \mp i \left( G_{1,2}^{\perp,\perp}(\omega) - G_{2,1}^{\perp,\perp}(\omega) \right) \right] \\ &= \frac{\alpha_{\text{YM}}^2 r_h^2}{2\kappa_5^2} \left( \frac{(\tilde{a}_\perp^1)^b(\omega)}{(\tilde{a}_\perp^1)^b(\omega)} + \frac{(\tilde{a}_\perp^2)^b(\omega)}{(\tilde{a}_\perp^2)^b(\omega)} \right. \\ &\quad \left. - \frac{(\tilde{\mu}_I \mp \tilde{\omega})^2}{2} \mp i \left( \frac{(\tilde{a}_y^1)^b(\omega)}{(\tilde{a}_y^2)^b(\omega)} - \frac{(\tilde{a}_y^2)^b(\omega)}{(\tilde{a}_y^1)^b(\omega)} \right) \right), \\ G_{\pm,\mp}^{\perp,\perp}(\omega) &= \frac{1}{4} \left[ G_{1,1}^{\perp,\perp}(\omega) - G_{2,2}^{\perp,\perp}(\omega) \pm i \left( G_{1,2}^{\perp,\perp}(\omega) + G_{2,1}^{\perp,\perp}(\omega) \right) \right] \\ &= \frac{\alpha_{\text{YM}}^2 r_h^2}{2\kappa_5^2} \left( \frac{(\tilde{a}_\perp^1)^b(\omega)}{(\tilde{a}_\perp^1)^b(\omega)} - \frac{(\tilde{a}_\perp^2)^b(\omega)}{(\tilde{a}_\perp^2)^b(\omega)} \pm i \left( \frac{(\tilde{a}_y^1)^b(\omega)}{(\tilde{a}_y^2)^b(\omega)} + \frac{(\tilde{a}_y^2)^b(\omega)}{(\tilde{a}_y^1)^b(\omega)} \right) \right), \quad (6.79) \\ G^{x\perp}_\pm(\omega) &= \frac{1}{2} \left[ G^{x\perp}_1(\omega) \mp i G^{x\perp}_2(\omega) \right] \\ &= -\frac{\langle \mathcal{J}_1^x \rangle}{4} + \frac{r_h^3}{\kappa_5^2} \left( \frac{(\Psi_x)_2^b(\omega)}{(\tilde{a}_y^1)^b(\omega)} \mp i \frac{(\Psi_x)_2^b(\omega)}{(\tilde{a}_y^2)^b(\omega)} \right), \\ G^{\perp x\perp}_\pm(\omega) &= \frac{1}{2} \left[ G_1^{\perp x\perp}(\omega) \pm i G_2^{\perp x\perp}(\omega) \right] \\ &= -\frac{\langle \mathcal{J}_1^x \rangle}{4} + \frac{\alpha_{\text{YM}}^2 r_h^3}{\kappa_5^2} \left( \frac{(\tilde{a}_y^1)^b(\omega)}{(\Psi_x)_0^b(\omega)} \pm i \frac{(\tilde{a}_y^2)^b(\omega)}{(\Psi_x)_0^b(\omega)} \right). \end{aligned}$$

First note that for  $\mu_I = 0$  where the  $SU(2)$  symmetry is restored, i. e.  $a^1 \equiv a^2$ , the Green's function is diagonal and  $G_{+,+}^{\perp,\perp} = G_{-,-}^{\perp,\perp} = G_{3,3}^{\perp,\perp}$ . In the unbroken phase,  $G_{+,-}^{\perp,\perp} = G_{-,+}^{\perp,\perp} \equiv 0$  is still valid for  $\mu_I \neq 0$ , since the  $a^\pm$  do not couple to each other, while  $G_{+,+}^{\perp,\perp} \neq G_{-,-}^{\perp,\perp}$  for  $\mu_I \neq 0$ . In the unbroken as well as in the broken phase we find

$$\begin{aligned} G_{-,-}^{\perp,\perp}(\omega) &= G_{+,+}^{\perp,\perp}(-\omega)^*, & G_{+,-}^{\perp,\perp}(\omega) &= G_{-,+}^{\perp,\perp}(-\omega)^*, \\ G_+^{\perp x\perp}(\omega) &= G_-^{\perp x\perp}(-\omega)^* & \text{and} & \quad G^{x\perp}_+(\omega) = G^{x\perp}_-(-\omega)^*, \end{aligned} \quad (6.80)$$

as expected since  $a^1(\omega) = (a^1(-\omega))^*$ ,  $a^2(\omega) = (a^2(-\omega))^*$  and  $\Psi_x(\omega) = (\Psi_x(-\omega))^*$ .

In figure 6.18 we plot the real and imaginary parts of  $G_{\pm,\pm}^{\perp,\perp}(\omega)$ . We see in figure 6.18(c) and 6.18(d), showing  $\text{Im}(G_{\pm,\pm}^{\perp,\perp})$ , that for temperatures  $T > T_c$ , the

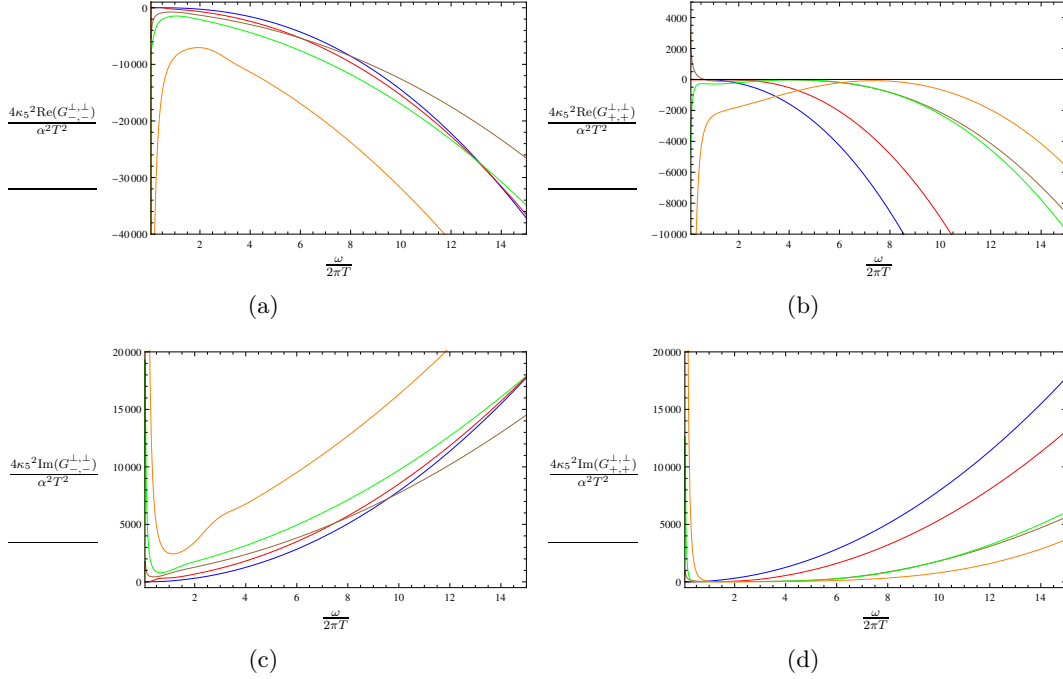


**Figure 6.18:** These plots show the real and imaginary part of the correlators  $G_{\pm,\pm}^{\perp,\perp}$  versus the reduced frequency  $\omega/(2\pi T)$  for  $\alpha_{\text{YM}} = 0.316$  at different temperatures:  $T = \infty$  blue line,  $T = 3.02T_c$  red line,  $T = 1.00T_c$  brown line,  $T = 0.88T_c$  green line and  $T = 0.50T_c$  orange line. These figures are taken from [8].

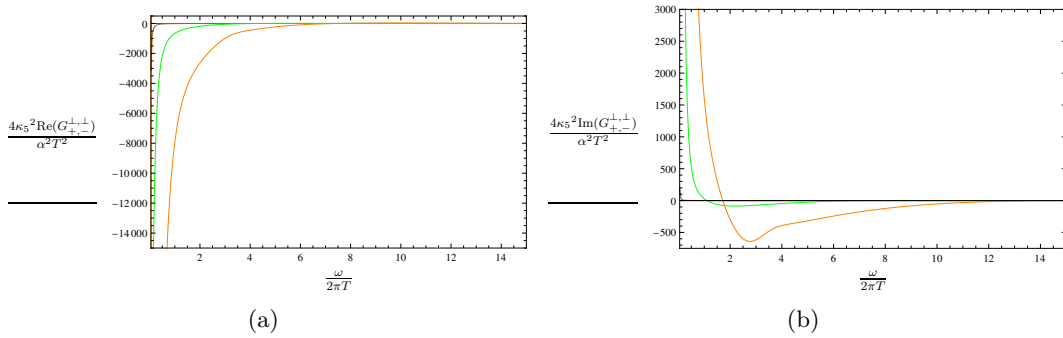


**Figure 6.19:** These plots show the real and imaginary part of the correlator  $G_{+,-}^{\perp,\perp}$  versus the reduced frequency  $\omega/(2\pi T)$  for  $\alpha_{\text{YM}} = 0.316$  at different temperatures:  $T = \infty$  blue line,  $T = 3.02T_c$  red line,  $T = 1.00T_c$  brown line,  $T = 0.88T_c$  green line and  $T = 0.50T_c$  orange line. The curves for the temperatures above  $T_c$  are exactly zero for all frequencies. These figures are taken from [8].

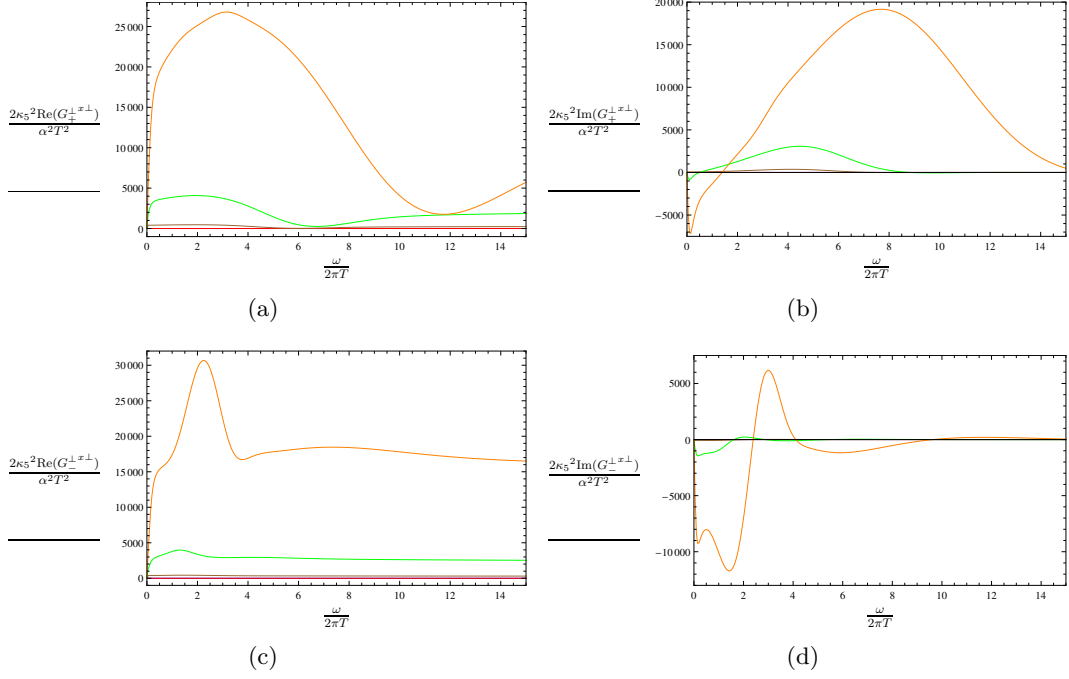


**Figure 6.20:** These plots show the real and imaginary part of the correlators  $G_{\pm}^{\perp x \perp}$  versus the reduced frequency  $\omega/(2\pi T)$  for  $\alpha_{\text{YM}} = 0.316$  at different temperatures:  $T = \infty$  blue line,  $T = 3.02T_c$  red line,  $T = 1.00T_c$  brown line,  $T = 0.88T_c$  green line and  $T = 0.50T_c$  orange line. The curves for the temperatures above  $T_c$  are exactly zero for all frequencies. These figures are taken from [8].

quasinormal modes tend towards the origin (in these plots we see their projection on the real axis) (see e. g. [100] and section 5.5). For  $T \leq T_c$  we see a pole at the origin which is due to the massless Nambu-Goldstone modes. These Nambu-Goldstone modes are related to rotations of the director  $\langle \mathcal{J}_x^1 \rangle$  in real space which are generated by the fluctuations  $a_{\perp}^1$ <sup>11</sup>. Furthermore, as expected for large frequencies, the Green's function grows proportional to  $\omega^2$  in the  $\pm\pm$  components as for the correlator  $G_{3,3}^{\perp,\perp}$ . In figure 6.18 the correlators for the different temperatures do not seem to have the same asymptotic behavior. However, in the present case we have contribution from terms such as  $\omega\mu_I$ , i. e. of first order in  $\omega$ , which are not existent in the  $G_{3,3}^{\perp,\perp}$  component. Hence, to see that all correlators have the same limit, larger values of  $\omega$  have to be considered. Even not present in our figures we verified numerically that the asymptotics of the correlators at different temperatures agree. A more detailed study of this sector in the probe approximation is in preparation [242].

In figure 6.19 we plot  $G_{+,-}^{\perp,\perp}(\omega)$ . We see that this correlator vanishes since the  $a^{\pm}$  do not couple in the unbroken phase. Furthermore, below  $T_c$ , a pole at  $\omega = 0$

<sup>11</sup>The other Nambu-Goldstone mode is related to the change of the phase of the condensate and correspond to the fluctuation  $a_x^2$  which shows up in the helicity zero sector.

due to the Nambu-Goldstone mode appears. We do not show  $G_{-,+}^{\perp,\perp}(\omega)$  since  $G_{+,-}^{\perp,\perp}$  and  $G_{-,+}^{\perp,\perp}$  look alike. Nevertheless, there is a difference between them in the broken phase. The difference arises from the contributions to the correlators due to the mixed terms,  $G_{1,2}^{\perp,\perp}$  and  $G_{2,1}^{\perp,\perp}$ , in the corresponding equation in (6.79). However, these are suppressed in relation to  $G_{1,1}^{\perp,\perp}$ , which contains the Goldstone mode in the broken phase.

Finally, in figure 6.20 we show  $G_{\pm}^{\perp x\perp}(\omega)$ . Note that the contribution of  $\langle \mathcal{J}_1^x \rangle$  to the real parts of the correlators is not included in the corresponding plots since it just shifts the curves by a constant. Furthermore, we have that  $\text{Im}(G_{\pm}^{\perp x\perp}) = \text{Im}(G^{x\perp\perp})$  and  $\text{Re}(G_{\pm}^{\perp x\perp}) - \text{const} = \text{Re}(G^{x\perp\perp})$ , i. e. there is a constant offset between the real parts of these correlators. We expect that this constant offset is generated by the term  $(\Psi_x)_2^b(\omega)/(\tilde{a}_y^1)_0^b(\omega)$  which may be constant in the limit  $\omega \rightarrow 0$  since  $a_y^1$  has a normal mode at  $\omega = 0$  and the subleading term of  $\Psi_x$  is probably not sourced. An analytic calculation similar to [241] may confirm this claim. In the unbroken phase these correlators vanish since the differential equations of the corresponding fields decouple. In the broken phase the correlators present a rich structure, which we cannot fully address at present. However, it seems that the coupling between the  $a_{\perp}^{\pm}$  flavor fields and the strain  $h_{x\perp}$  generates new quasiparticles which appear as bumps in the curves.

In addition to the flavor conductivity and the shear viscosity, we obtain a coupling between the stress  $\langle T^{x\perp} \rangle$  and the flavor fields  $a_{\perp}^{\pm}$  as well as the currents  $\langle J_{\pm}^{\perp} \rangle$  and the strain  $h_{x\perp}$  described in (6.78). This coupling introduces an effect which is named flexoelectric effect in nematic crystals [234] and only appears in fluids with broken rotational symmetry. We have a current  $\langle \mathcal{J}_1^x \rangle$  in a favored direction in the background which interacts with the flavor fields  $a_{\perp}^{\pm}$ . This interaction induces a force on the current which pushes the current in its perpendicular direction generating the stress  $\langle T^{x\perp} \rangle$ . In the similar way, a strain  $h_{x\perp}$  introduces an inhomogeneity in the current  $\langle \mathcal{J}_1^x \rangle$  resulting in a flavor field  $a_{\perp}^{\pm}$  which generates the currents  $\langle J_{\pm}^{\perp} \rangle$ .

## 6.4 Holographic Vector Meson Condensation

In this section we investigate the flavor branes which is a string theory realization of the model studied above. We consider  $N_f$  coincident D7-branes in asymptotically  $AdS_5 \times S^5$  spacetime which is the near-horizon geometry of a stack of D3-branes (see section 3.2.1). In order to study the dual field theory at finite temperature, we consider a black hole in the bulk. The embedding of the D7-branes in this background is studied in section 4.2.3. In addition, we introduce a baryon and isospin chemical potential as discussed in section 5.2.2. In section 5.5 we have seen that this configuration is unstable and have argued that a condensation should occur in order to stabilize the systems. Therefore, we allow the gauge field  $A_x^1$  to be non-zero. To obtain an isotropic and time-independent configuration in the field theory, the gauge field  $A_x^1$  only depends on  $\rho$ . This leads to a similar ansatz for the gauge

field as in the Einstein-Yang-Mills theory,

$$A = (\mathcal{A}_t(\varrho)\sigma^0 + A_t^3(\varrho)\sigma^3) dt + A_x^1(\varrho)\sigma^1 dx. \quad (6.81)$$

With this ansatz, the field strength tensor on the D7-branes has the following non-zero components,

$$\begin{aligned} F_{\varrho x}^1 &= -F_{x\varrho}^1 = \partial_\varrho A_x^1, \\ F_{tx}^2 &= -F_{xt}^2 = \frac{\gamma}{\sqrt{\lambda}} A_t^3 A_x^1, \\ F_{\varrho t}^3 &= -F_{t\varrho}^3 = \partial_\varrho A_t^3, \\ F_{\varrho t}^0 &= -F_{t\varrho}^0 = \partial_\varrho \mathcal{A}_t = \mathcal{F}_{\varrho t} = -\mathcal{F}_{t\varrho}. \end{aligned} \quad (6.82)$$

The DBI action determines the shape of the brane embeddings as well as the configuration of the gauge fields on these branes. We consider the case of  $N_f = 2$  coincident D7-branes for which the non-Abelian DBI action (2.52) has to be used. As described in section 5.2.2 we can use the symmetries of our setup to simplify the action. In the present case the action becomes

$$\begin{aligned} S_{\text{DBI}} &= -T_{D7} \int d^8\xi \text{STr} \sqrt{|\det(G + 2\pi\alpha' F)|} \\ &= -T_{D7} \int d^8\xi \sqrt{-G} \text{STr} \left[ 1 + G^{tt} G^{\varrho\varrho} \left( (F_{\varrho t}^3)^2 (\sigma^3)^2 + 2F_{\varrho t}^3 \mathcal{F}_{\varrho t} \sigma^3 \sigma^0 \right. \right. \\ &\quad \left. \left. + (\mathcal{F}_{\varrho t})^2 (\sigma^0)^2 \right) + G^{xx} G^{\varrho\varrho} (F_{\varrho x}^1)^2 (\sigma^1)^2 + G^{tt} G^{xx} (F_{tx}^2)^2 (\sigma^2)^2 \right]^{\frac{1}{2}}, \end{aligned} \quad (6.83)$$

where in the second line the determinant is calculated. Due to the symmetrized trace, all commutators between the matrices  $\sigma^i$  vanish. It is known that the symmetrized trace prescription in the DBI action is only valid up to fourth order in  $\alpha'$  [149, 150]. However, the corrections to the higher order terms are suppressed by  $N_f^{-1}$  [147] (see also [190]).

#### 6.4.1 Results at Zero Baryon Chemical Potential

Here we use two different approaches to evaluate the non-Abelian DBI action (6.83) for zero baryon chemical potential. First, we modify the symmetrized trace prescription by omitting the commutators of the generators  $\sigma^i$  and then setting  $(\sigma^i)^2 = \mathbb{1}$ . This prescription makes the calculation of the full DBI action feasible. Second, we expand the non-Abelian DBI action to fourth order in the field strength  $F$ .

### Adapted symmetrized trace prescription

Using the adapted symmetrized trace prescription defined above, the action becomes

$$\begin{aligned} S_{\text{DBI}} &= -T_7 N_f \int d^8 \xi \sqrt{-G} \left[ 1 + G^{tt} G^{\varrho\varrho} (F_{\varrho t}^3)^2 + G^{xx} G^{\varrho\varrho} (F_{\varrho x}^1)^2 + G^{tt} G^{xx} (F_{tx}^2)^2 \right]^{\frac{1}{2}} \\ &= -\frac{T_7 N_f}{4} \int d^8 \xi \varrho^3 f \tilde{f} (1 - \chi^2) \Upsilon(\rho, \chi, \tilde{A}), \end{aligned} \quad (6.84)$$

with

$$\begin{aligned} \Upsilon(\rho, \chi, \tilde{A}) &= \left[ 1 - \chi^2 + \rho^2 (\partial_\rho \chi)^2 - \frac{2\tilde{f}}{f^2} (1 - \chi^2) (\partial_\rho \tilde{A}_t^3)^2 + \frac{2}{f} (1 - \chi^2) (\partial_\rho \tilde{A}_x^1)^2 \right. \\ &\quad \left. - \frac{2\gamma^2}{\pi^2 \rho^4 f^2} (1 - \chi^2 + \rho^2 (\partial_\rho \chi)^2) (\tilde{A}_t^3 \tilde{A}_x^1)^2 \right]^{\frac{1}{2}}, \end{aligned} \quad (6.85)$$

where the dimensionless quantities  $\rho = \varrho/\varrho_H$  and  $\tilde{A} = (2\pi\alpha')A/\varrho_H$  are used. In order to obtain first order equations of motion for the gauge fields which are easier to solve numerically, we perform a Legendre transformation. Similarly as in section 5.2.2, we calculate the conjugate momenta  $p_t^3$  and  $p_x^1$  of the gauge fields  $A_t^3$  and  $A_x^1$ ,

$$p_t^3 = \frac{\delta S_{\text{DBI}}}{\delta (\partial_\varrho A_t^3)}, \quad p_x^1 = \frac{\delta S_{\text{DBI}}}{\delta (\partial_\varrho A_x^1)}. \quad (6.86)$$

In contrast to the discussion in section 5.2.2 with  $A_x^1 \equiv 0$ , the conjugate momenta are not constant anymore but depend on the radial coordinate  $\varrho$  due to the non-Abelian term  $A_t^3 A_x^1$  in the DBI action. For the dimensionless momenta  $\tilde{p}_t^3$  and  $\tilde{p}_x^1$  defined as

$$\tilde{p} = \frac{p}{2\pi\alpha' N_f T_{D7} \varrho_H^3}, \quad (6.87)$$

we get

$$\tilde{p}_t^3 = \frac{\rho^3 \tilde{f}^2 (1 - \chi^2)^2 \partial_\rho \tilde{A}_t^3}{2f \Upsilon(\rho, \chi, \tilde{A})}, \quad \tilde{p}_x^1 = -\frac{\rho^3 f (1 - \chi^2)^2 \partial_\rho \tilde{A}_x^1}{2\Upsilon(\rho, \chi, \tilde{A})}. \quad (6.88)$$

Note that in contrast to the definition of the conjugate momenta in (5.37), the definition here differs by a factor of  $N_f^{-1}$ . Finally, the Legendre-transformed action is given by

$$\begin{aligned} \tilde{S}_{\text{DBI}} &= S_{\text{DBI}} - \int d^8 \xi \left[ (\partial_\varrho A_t^3) \frac{\delta S_{\text{DBI}}}{\delta (\partial_\varrho A_t^3)} + (\partial_\varrho A_x^1) \frac{\delta S_{\text{DBI}}}{\delta (\partial_\varrho A_x^1)} \right] \\ &= -\frac{T_{D7} N_f}{4} \int d^8 \xi \varrho^3 f \tilde{f} (1 - \chi^2) \sqrt{1 - \chi^2 + \rho^2 (\partial_\rho \chi)^2} V(\rho, \chi, \tilde{A}, \tilde{p}), \end{aligned} \quad (6.89)$$

with

$$V(\rho, \chi, \tilde{A}, \tilde{p}) = \left[ \left( 1 - \frac{2\gamma^2}{\pi^2 \rho^4 f^2} (\tilde{A}_t^3 \tilde{A}_x^1)^2 \right) \left( 1 + \frac{8(\tilde{p}_t^3)^2}{\rho^6 \tilde{f}^3 (1-\chi^2)^3} - \frac{8(\tilde{p}_x^1)^2}{\rho^6 \tilde{f} f^2 (1-\chi^2)^3} \right) \right]^{\frac{1}{2}}. \quad (6.90)$$

Then the first order equations of motion for the gauge fields and their conjugate momenta are

$$\begin{aligned} \partial_\rho \tilde{A}_t^3 &= \frac{2f \sqrt{1-\chi^2 + \rho^2 (\partial_\rho \chi)^2}}{\rho^3 \tilde{f}^2 (1-\chi^2)^2} \tilde{p}_t^3 W(\rho, \chi, \tilde{A}, \tilde{p}), \\ \partial_\rho \tilde{A}_x^1 &= -\frac{2\sqrt{1-\chi^2 + \rho^2 (\partial_\rho \chi)^2}}{\rho^3 f (1-\chi^2)^2} \tilde{p}_x^1 W(\rho, \chi, \tilde{A}, \tilde{p}), \\ \partial_\rho \tilde{p}_t^3 &= \frac{\tilde{f}(1-\chi^2) \sqrt{1-\chi^2 + \rho^2 (\partial_\rho \chi)^2} c^2}{2\pi^2 \rho f W(\rho, \chi, \tilde{A}, \tilde{p})} (\tilde{A}_x^1)^2 \tilde{A}_t^3, \\ \partial_\rho \tilde{p}_x^1 &= \frac{\tilde{f}(1-\chi^2) \sqrt{1-\chi^2 + \rho^2 (\partial_\rho \chi)^2} c^2}{2\pi^2 \rho f W(\rho, \chi, \tilde{A}, \tilde{p})} (\tilde{A}_t^3)^2 \tilde{A}_x^1, \end{aligned} \quad (6.91)$$

with

$$W(\rho, \chi, \tilde{A}, \tilde{p}) = \sqrt{\frac{1 - \frac{2\gamma^2}{\pi^2 \rho^4 f^2} (\tilde{A}_t^3 \tilde{A}_x^1)^2}{1 + \frac{8(\tilde{p}_t^3)^2}{\rho^6 \tilde{f}^3 (1-\chi^2)^3} - \frac{8(\tilde{p}_x^1)^2}{\rho^6 \tilde{f} f^2 (1-\chi^2)^3}}}. \quad (6.92)$$

For the embedding function  $\chi$  we get the second order equation of motion

$$\begin{aligned} \partial_\rho \left[ \frac{\rho^5 \tilde{f} (1-\chi^2) (\partial_\rho \chi)}{\sqrt{1-\chi^2 + \rho^2 (\partial_\rho \chi)^2}} V \right] &= -\frac{\rho^3 \tilde{f} \chi}{\sqrt{1-\chi^2 + \rho^2 (\partial_\rho \chi)^2}} \left[ [3(1-\chi^2) + 2\rho^2 (\partial_\rho \chi)^2] V \right. \\ &\quad \left. - \frac{24(1-\chi^2 + \rho^2 (\partial_\rho \chi)^2)}{\tilde{f}^3 \rho^6 (1-\chi^2)^3} W \left( (\tilde{p}_t^3)^2 - \frac{\tilde{f}^2}{f^2} (\tilde{p}_x^1)^2 \right) \right]. \end{aligned} \quad (6.93)$$

We solve the equations numerically and determine the solution by integrating the equations of motion from the horizon at  $\rho = 1$  to the boundary at  $\rho = \infty$ . The initial conditions may be determined by the asymptotic expansion of the gravity fields near the horizon

$$\begin{aligned} \tilde{A}_t^3 &= \frac{c_0}{\sqrt{(1-\chi_0^2)^3 + c_0^2}} (\rho-1)^2 + \mathcal{O}((\rho-1)^3), \\ \tilde{A}_x^1 &= b_0 + \mathcal{O}((\rho-1)^3), \\ \tilde{p}_t^3 &= c_0 + \frac{\gamma^2 b_0^2 c_0}{8\pi^2} (\rho-1)^2 + \mathcal{O}((\rho-1)^3), \\ \tilde{p}_x^1 &= \mathcal{O}((\rho-1)^3), \\ \chi &= \chi_0 - \frac{3\chi_0(1-\chi_0^2)^3}{4[(1-\chi_0^2)^3 + c_0^2]} (\rho-1)^2 + \mathcal{O}((\rho-1)^3), \end{aligned} \quad (6.94)$$

where the terms in the expansions are arranged according to their order in  $\rho-1$ . For the numerical calculation we consider the terms up to sixth order in  $\rho-1$ . The three independent parameter  $\{b_0, c_0, \chi_0\}$  may be determined by field theory quantities defined via the asymptotic expansion of the gravity fields near the boundary,

$$\begin{aligned}
\tilde{A}_t^3 &= \tilde{\mu}_I && - \frac{\tilde{n}_t^3}{\rho^2} && + \mathcal{O}(\rho^{-4}), \\
\tilde{A}_x^1 &= && - \frac{\tilde{n}_x^1}{\rho^2} && + \mathcal{O}(\rho^{-4}), \\
\tilde{p}_t^3 &= \tilde{n}_t^3 && && + \mathcal{O}(\rho^{-4}), \\
\tilde{p}_x^1 &= -\tilde{n}_x^1 && + \frac{\gamma^2 \tilde{\mu}^2 \tilde{n}_x^1}{4\pi^2 \rho^2} && + \mathcal{O}(\rho^{-4}), \\
\chi &= && \frac{m}{\rho} && + \frac{\tilde{c}}{\rho^3} + \mathcal{O}(\rho^{-4}).
\end{aligned} \tag{6.95}$$

There are five independent parameters  $\{\tilde{\mu}_I, \tilde{n}_t^3, \tilde{n}_x^1, m, \tilde{c}\}$ . According to the AdS/CFT dictionary,  $\mu_I$  is the isospin chemical potential. The parameters  $\tilde{n}$  are related to the vev of the flavor currents  $J$  by (5.37) where the additional factor of  $N_f$  has to be considered.  $m$  and  $\tilde{c}$  are identified with the bare quark mass  $M_q$  and the quark condensate  $\langle \bar{\psi}\psi \rangle$  defined in (4.58). There are two independent physical parameters, e.g.  $m$  and  $\mu_I$ , in the grand canonical ensemble. With the constraint  $\tilde{A}_x^1|_{\rho \rightarrow \infty} = 0$  and the two independent physical parameters, we may fix the three independent parameters of the near-horizon asymptotics and obtain a solution to the equations of motion.

### Expansion of the DBI action

We now outline the second approach which we use. Expanding the action (6.83) to fourth order in the field strength  $F$  yields

$$S_{\text{DBI}} = -T_{D7} N_f \int d^8 \xi \sqrt{-G} \left[ 1 + \frac{\mathcal{T}_2}{2} - \frac{\mathcal{T}_4}{8} + \dots \right], \tag{6.96}$$

where  $\mathcal{T}_i$  consists of the terms with order  $i$  in  $F$ . To calculate the  $\mathcal{T}_i$ , we use the following results for the symmetrized traces

$$\begin{aligned}
2\sigma : \quad \text{STr} \left[ (\sigma^i)^2 \right] &= N_f, \\
4\sigma : \quad \text{STr} \left[ (\sigma^i)^4 \right] &= N_f, \quad \text{STr} \left[ (\sigma^i)^2 (\sigma^j)^2 \right] = \frac{N_f}{3},
\end{aligned} \tag{6.97}$$

where the indices  $i, j$  are distinct. Notice that the symmetrized trace of terms with unpaired  $\sigma$  matrices vanish, e. g.  $\text{STr}[\sigma^i \sigma^j] = N_f \delta^{ij}$ . The  $\mathcal{T}_i$  are given by

$$\begin{aligned}
\mathcal{T}_2 &= (2\pi\alpha')^2 \left[ G^{tt} G^{\rho\rho} (F_{\rho t}^3)^2 + G^{xx} G^{\rho\rho} (F_{\rho x}^1)^2 + G^{tt} G^{xx} (F_{tx}^2)^2 \right] \\
&= -\frac{2\tilde{f}H}{f^2} (\partial_\rho \tilde{A}_t^3)^2 + \frac{2H}{\tilde{f}} (\partial_\rho \tilde{A}_x^1)^2 - \frac{2\gamma^2}{\rho^4 f^2 \pi^2} (\tilde{A}_t^3 \tilde{A}_x^1)^2, \\
\mathcal{T}_4 &= (2\pi\alpha')^4 \left[ (G^{tt} G^{\rho\rho})^2 (F_{\rho t}^3)^4 + (G^{xx} G^{\rho\rho})^2 (F_{\rho x}^1)^4 + (G^{tt} G^{xx})^2 (F_{tx}^2)^4 \right. \\
&\quad + \frac{2}{3} G^{tt} G^{xx} (G^{\rho\rho})^2 (F_{\rho t}^3)^2 (F_{\rho x}^1)^2 + \frac{2}{3} (G^{tt})^2 G^{xx} G^{\rho\rho} (F_{\rho t}^3)^2 (F_{tx}^2)^2 \\
&\quad \left. + \frac{2}{3} G^{tt} (G^{xx})^2 G^{\rho\rho} (F_{\rho x}^1)^2 (F_{tx}^2)^2 \right] \\
&= \frac{4\tilde{f}^2 H^2}{f^4} (\partial_\rho \tilde{A}_t^3)^4 + \frac{4H^2}{\tilde{f}^2} (\partial_\rho \tilde{A}_x^1)^4 + \frac{4\gamma^4}{\rho^8 f^4 \pi^4} (\tilde{A}_t^3 \tilde{A}_x^1)^4 - \frac{8H^2}{3f^2} (\partial_\rho \tilde{A}_t^3)^2 (\partial_\rho \tilde{A}_x^1)^2 \\
&\quad + \frac{8\tilde{f}H\gamma^2}{3\rho^4 f^4 \pi^2} (\partial_\rho \tilde{A}_t^3)^2 (\tilde{A}_t^3 \tilde{A}_x^1)^2 - \frac{8H\gamma^2}{3\rho^4 \tilde{f} f^2 \pi^2} (\partial_\rho \tilde{A}_x^1)^2 (\tilde{A}_t^3 \tilde{A}_x^1)^2,
\end{aligned} \tag{6.98}$$

with

$$H = \frac{1 - \chi^2}{1 - \chi^2 + \rho^2 (\partial_\rho \chi)^2}. \tag{6.99}$$

In order to perform the Legendre transformation of the above action, we determine the conjugate momenta as in (6.86). However, we cannot easily solve these equations for the derivative of the gauge fields since we obtain two coupled equations of third degree. Thus, we directly calculate the equations of motion for the gauge fields on the D7-branes. The equations are given by

$$\begin{aligned}
\partial_\rho \left[ \sqrt{-G} \left( \frac{2\tilde{f}H}{f^2} (\partial_\rho \tilde{A}_t^3) + \frac{2\tilde{f}^2 H^2}{f^4} (\partial_\rho \tilde{A}_t^3)^3 - \frac{2H^2}{3f^2} (\partial_\rho \tilde{A}_x^1)^2 (\partial_\rho \tilde{A}_t^3) \right. \right. \\
\left. \left. + \frac{2\tilde{f}\gamma^2 H}{3f^4 \rho^4 \pi^2} (\partial_\rho \tilde{A}_t^3) (\tilde{A}_t^3 \tilde{A}_x^1)^2 \right) \right] &= \frac{2\gamma^2 \sqrt{-G}}{\pi^2 \rho^4 f^2} \left[ \tilde{A}_t^3 (\tilde{A}_x^1)^2 + \frac{\gamma^2}{\pi^2 \rho^4 f^2} (\tilde{A}_t^3)^3 (\tilde{A}_x^1)^4 \right] \\
+ \frac{\tilde{f}H}{3f^2} (\partial_\rho \tilde{A}_t^3)^2 \tilde{A}_t^3 (\tilde{A}_x^1)^2 - \frac{H}{3\tilde{f}} (\partial_\rho \tilde{A}_x^1)^2 \tilde{A}_t^3 (\tilde{A}_x^1)^2, \\
\partial_\rho \left[ \sqrt{-G} \left( \frac{2H}{\tilde{f}} (\partial_\rho \tilde{A}_x^1) - \frac{2H^2}{\tilde{f}^2} (\partial_\rho \tilde{A}_x^1)^3 + \frac{2H^2}{3f^2} (\partial_\rho \tilde{A}_t^3)^2 (\partial_\rho \tilde{A}_x^1) \right. \right. \\
\left. \left. + \frac{2\gamma^2 H}{3\pi^2 \rho^4 f^2 \tilde{f}} (\partial_\rho \tilde{A}_x^1) (\tilde{A}_t^3 \tilde{A}_x^1)^2 \right) \right] &= -\frac{2\gamma^2 \sqrt{-G}}{\pi^2 \rho^4 f^2} \left[ (\tilde{A}_t^3)^2 \tilde{A}_x^1 + \frac{\gamma^2}{\pi^2 \rho^4 f^2} (\tilde{A}_t^3)^4 (\tilde{A}_x^1)^3 \right. \\
\left. + \frac{\tilde{f}H}{3f^2} (\partial_\rho \tilde{A}_t^3)^2 (\tilde{A}_t^3)^2 \tilde{A}_x^1 - \frac{H}{3\tilde{f}} (\partial_\rho \tilde{A}_x^1)^2 (\tilde{A}_t^3)^2 \tilde{A}_x^1 \right],
\end{aligned} \tag{6.101}$$

$$\begin{aligned}
\partial_\rho \left[ \frac{\rho^5 f \tilde{f} (1 - \chi^2) (\partial_\rho \chi)}{\sqrt{1 - \chi^2 + \rho^2 (\partial_\rho \chi)^2}} \left( 1 - \frac{\varrho_H^2}{R^2} \frac{2\rho^2 (1 - \chi^2)}{1 - \chi^2 + \rho^2 (\partial_\rho \chi)^2} \left[ \frac{1}{2} \frac{\partial \mathcal{T}_2}{\partial G^{ee}} - \frac{1}{8} \frac{\partial \mathcal{T}_4}{\partial G^{ee}} \right] \right. \right. \\
\left. \left. + \frac{\mathcal{T}_2}{2} - \frac{\mathcal{T}_4}{8} \right) \right] = - \frac{\rho^3 f \tilde{f} \chi}{\sqrt{1 - \chi^2 + \rho^2 (\partial_\rho \chi)^2}} \left[ (3(1 - \chi^2) + 2\rho^2 (\partial_\rho \chi)^2) \left( 1 + \frac{\mathcal{T}_2}{2} - \frac{\mathcal{T}_4}{8} \right) \right. \\
\left. + \frac{\varrho_H^2}{R^2} \frac{2\rho^4 (1 - \chi^2) (\partial_\rho \chi)^2}{1 - \chi^2 + \rho^2 (\partial_\rho \chi)^2} \left( \frac{1}{2} \frac{\partial \mathcal{T}_2}{\partial G^{ee}} - \frac{1}{8} \frac{\partial \mathcal{T}_4}{\partial G^{ee}} \right) \right], \tag{6.102}
\end{aligned}$$

with

$$\begin{aligned}
\frac{\partial \mathcal{T}_2}{\partial G^{ee}} &= \frac{2R^2}{\varrho_H^2 \rho^2} \left[ -\frac{\tilde{f}}{f^2} (\partial_\rho \tilde{A}_t^3)^2 + \frac{1}{\tilde{f}} (\partial_\rho \tilde{A}_x^1)^2 \right], \\
\frac{\partial \mathcal{T}_4}{\partial G^{ee}} &= \frac{2R^2}{\varrho_H^2 \rho^2} \left[ \frac{4\tilde{f}^2 H}{f^4} (\partial_\rho \tilde{A}_t^3)^4 + \frac{4H}{\tilde{f}^2} (\partial_\rho \tilde{A}_x^1)^4 - \frac{8H}{3f^2} (\partial_\rho \tilde{A}_t^3)^2 (\partial_\rho \tilde{A}_x^1)^2 \right. \\
&\quad \left. + \frac{4\gamma^2 \tilde{f}}{3\rho^4 f^4 \pi^2} (\partial_\rho \tilde{A}_t^3)^2 (\tilde{A}_t^3 \tilde{A}_x^1)^2 - \frac{4\gamma^2}{3\rho^4 \tilde{f} f^2 \pi^2} (\partial_\rho \tilde{A}_x^1)^2 (\tilde{A}_t^3 \tilde{A}_x^1)^2 \right]. \tag{6.103}
\end{aligned}$$

We solve these equations by using the same strategy as in the adapted symmetrized trace prescription discussed above. We integrate the equations of motion from the horizon at  $\rho = 1$  to the boundary at  $\rho = \infty$  numerically. The initial conditions may be determined by the asymptotic behavior of the gravity fields near the horizon

$$\begin{aligned}
\tilde{A}_t^3 &= a_2 (\rho - 1)^2 + \mathcal{O}((\rho - 1)^3), \\
\tilde{A}_x^1 &= b_0 + \mathcal{O}((\rho - 1)^3), \\
\chi &= \chi_0 + \frac{3(a_2^4 + 4a_2^2 - 8)\chi_0}{4(3a_2^4 + 4a_2^2 + 8)} (\rho - 1)^2 + \mathcal{O}((\rho - 1)^3). \tag{6.104}
\end{aligned}$$

For the numerical calculation we use the asymptotic expansion up to sixth order. As in the adapted symmetrized trace prescription, there are again three independent parameters  $\{a_2, b_0, \chi_0\}$ . Since we have not performed a Legendre transformation, we trade the independent parameter  $c_0$  in the asymptotics of the conjugate momenta  $\tilde{p}_t^3$  in the symmetrized trace prescription with the independent parameter  $a_2$  (cf. asymptotics in equation (6.94)). However, the three independent parameters may again be determined in field theory quantities which are defined by the asymptotics of the gravity fields near the boundary

$$\begin{aligned}
\tilde{A}_t^3 &= \mu_I - \frac{\tilde{n}_t^3}{\rho^2} + \mathcal{O}(\rho^4), \\
\tilde{A}_x^1 &= -\frac{\tilde{n}_x^1}{\rho^2} + \mathcal{O}(\rho^4), \\
\chi &= \frac{m}{\rho} + \frac{\tilde{c}}{\rho^3} + \mathcal{O}(\rho^4). \tag{6.105}
\end{aligned}$$

The independent parameters  $\{\mu_I, \tilde{n}_t^3, \tilde{n}_x^1, m, \tilde{c}\}$  are given by field theory quantities as presented in (5.37) and (4.58). The independent parameters in both prescriptions are the same and we can use the same strategy to solve the equations of motion.

### Field Theory Interpretation

The dual field theory of the flavor branes is given by a  $(3+1)$ -dimensional  $\mathcal{N} = 2$  supersymmetric  $SU(N_c)$  Yang-Mills theory, consisting of a  $\mathcal{N} = 4$  gauge multiplet as well as  $N_f$  massive  $\mathcal{N} = 2$  supersymmetric hypermultiplets  $(q_i, \psi_i)$  as described in section 3.2.1. Here we consider exclusively two flavors, i. e.  $N_f = 2$ . The flavor degrees of freedom are denoted as  $u$  and  $d$ . If the masses of the two flavor degrees are degenerate, the theory has a global  $U(2)$  flavor symmetry, whose overall  $U(1)_B$  subgroup can be identified with the baryon number.

We consider the theory at finite isospin chemical potential  $\mu_I$ , which is introduced as the source of the operator

$$J_t^3 \propto \bar{\psi} \sigma^3 \gamma_t \psi + q \sigma^3 \partial_t q = n_u - n_d, \quad (6.106)$$

where  $n_{u/d}$  is the charge density of the isospin fields,  $(q_u, q_d) = \phi$  and  $(\psi_u, \psi_d) = \psi$ .  $\sigma^i$  are the Pauli matrices. A non-zero vev  $\langle J_t^3 \rangle$  introduces an isospin density. The isospin chemical potential  $\mu_I$  explicitly breaks the  $U(2) \simeq U(1)_B \times SU(2)_I$  flavor symmetry down to  $U(1)_B \times U(1)_3$ , where  $U(1)_3$  is generated by the unbroken generator  $\sigma^3$  of the  $SU(2)_I$ . Under the  $U(1)_3$  symmetry the fields with index  $u$  and  $d$  have positive and negative charge, respectively.

However, the theory is unstable at large isospin chemical potential as discussed in section 5.5. In the following we show that the new phase is stabilized by a non-vanishing vacuum expectation value of the current component

$$J_x^1 \propto \bar{\psi} \sigma^1 \gamma_x \psi + q \sigma^1 \partial_x q = \bar{\psi}_u \gamma_x \psi_d + \bar{\psi}_d \gamma_x \psi_u + \text{bosons}. \quad (6.107)$$

This current component breaks both the  $SO(3)$  rotational symmetry as well as the remaining Abelian  $U(1)_3$  flavor symmetry spontaneously. The rotational  $SO(3)$  is broken down to  $SO(2)_3$ , which is generated by rotations around the  $x$  axis. Due to the non-vanishing vev for  $J_x^1$ , flavor charged vector mesons condense and form a superfluid. Let us emphasize that we do not describe a color superconductor on the field theory side, since the condensate is a gauge singlet.

### Stringy Interpretation

Now we give a string theory interpretation, i. e. a geometrical picture, of the formation of the new phase. We show that the system is stabilized by dynamically generating a non-zero vev of the current component  $J_x^1$  dual to the gauge field  $A_x^1$  on the brane. Moreover, we find a geometrical picture of the condensation mechanism which forms the condensate  $\langle J_x^1 \rangle$ .

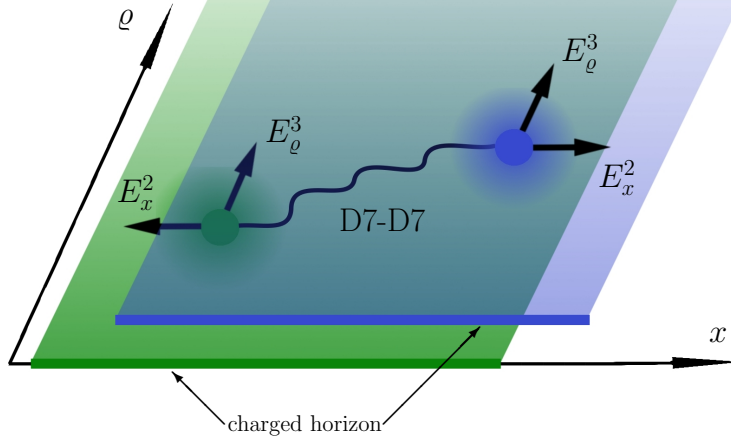


**Figure 6.21:** Sketch of our string setup: The figure shows the two coincident D7 branes stretched from the black hole horizon to the boundary as a green and a blue plane, respectively. Strings spanned from the horizon of the AdS black hole to the D7-branes induce a charge at the horizon (see section 5.2.2). However, above a critical charge density, the strings charging the horizon recombine to D7-D7 strings. These D7-D7 strings are shown in the figure. Whereas the fundamental strings stretched between the horizon and the D7-brane are localized near the horizon, the D7-D7 strings propagate into the bulk balancing the flavorelectric and gravitational, i. e. tension forces (see text). Thus, these D7-D7 strings distribute the isospin charges along the AdS radial coordinate, leading to a stable configuration of reduced energy. This configuration of D7-D7 strings corresponds to a superfluid condensate.

Let us first describe the unstable configuration in absence of the field  $A_x^1$ . As known from section 5.2.2, the non-zero field  $A_t^3$  is induced by fundamental strings which are stretched from the D7-brane to the horizon of the black hole. In the subsequent we call these strings ‘horizon strings’. Since the tension of these strings would increase as they move to the boundary, they are localized at the horizon, i. e. the horizon is effectively charged under the isospin charge given by (6.106). By increasing the horizon string density, the isospin charge on the D7-brane at the horizon and therefore the energy of the system grows. In section 5.5, the critical density has been found beyond which this setup becomes unstable. In this case, the strings would prefer to move towards the boundary due to the repulsive force on their charged endpoints generated by the flavorelectric field  $E_\rho^3 = F_{\rho t}^3 = \partial_\rho A_t^3$ .

The setup is now stabilized by the new non-zero field  $A_x^1$ . This field is induced by D7-D7 strings moving in the  $x$  direction. This movement of the strings may be interpreted as a current in  $x$  direction which induces the magnetic field  $B_{x\rho}^1 = F_{x\rho}^1 = -\partial_\rho A_x^1$ . Moreover, the non-Abelian interaction between the D7-D7 strings and the horizon strings induces a flavorelectric field  $E_x^2 = F_{xt}^2 = \gamma/\sqrt{\lambda} A_t^3 A_x^1$ .

From the profile of the gauge fields and their conjugate momenta (see figure 6.22), we obtain the following: For  $A_x^1 = 0$ , i. e. in the normal phase ( $T \geq T_c$ ), the isospin density  $\tilde{n}_t^3$  is exclusively generated at the horizon by the horizon strings. This can

also be understood by the profile of the conjugate momenta  $p_t^3$  (see figure 6.22 (c)). We interpret  $p_t^3(\rho^*)$  as the isospin charge located between the horizon at  $\rho = 1$  and a fictitious boundary at  $\rho = \rho^*$ . In the normal phase, the momentum  $p_t^3$  is constant along the radial direction  $\rho$  (see figure 6.22(c), blue curve) and therefore the isospin density is exclusively generated at the horizon. In the superconducting phase where  $A_x^1 \neq 0$ , i. e.  $T < T_c$ , the momentum  $p_t^3$  is not constant anymore. Its value increases monotonically towards the boundary and asymptotes to  $\tilde{n}_t^3$  (see figure 6.22(c), red curve). Thus, the isospin charge is also generated in the bulk and not only at the horizon. This decreases the isospin charge at the horizon and stabilizes the system.

Now we describe the string dynamics which distributes the isospin charge into the bulk. Since the field  $A_x^1$  induced by the D7-D7 strings is non-zero in the superfluid phase, these strings must be responsible for stabilizing this phase. In the normal phase, there are only horizon strings. In the superfluid phase, some of these strings recombine to form D7-D7 strings which correspond to the non-zero gauge field  $A_x^1$  and carry isospin charge<sup>12</sup>. There are two forces acting on the D7-D7 strings, the flavorelectric force induced by the field  $E_\varrho^3$  and the gravitational force between the strings and the black hole. The flavorelectric force points to the boundary while the gravitational force points to the horizon. The gravitational force is determined by the change in the effective string tension, which contains the  $\varrho$  dependent warp factor. The position of the D7-D7 strings is determined by the equilibrium of these two forces. Therefore, the D7-D7 strings propagate from the horizon into the bulk and distribute the isospin charge.

Since the D7-D7 strings induce the field  $A_x^1$ , they also generate the density  $\tilde{n}_x^1$  dual to the condensate  $\langle J_x^1 \rangle$ . This density  $\tilde{n}_x^1$  is proportional to the D7-D7 strings located in the bulk, in the same way as the density  $\tilde{n}_t^3$  counts the strings which carry isospin charge. This suggests that we can also interpret  $p_x^1(\rho^*)$  as the number of D7-D7 strings which are located between the horizon at  $\rho = 1$  and the fictitious boundary at  $\rho = \rho^*$ . The momentum  $p_x^1$  is always zero at the horizon and increases monotonically in the bulk (see figure 6.22 (d)). Thus, there are no D7-D7 strings at the horizon.

The double importance of the D7-D7 strings is given by the fact that they are both responsible for stabilizing the superfluid phase by lowering the isospin charge density, as well as being the dual of the superfluid density since they break the  $U(1)_3$  symmetry.

## Thermodynamics and Phase Transition

Let us now study the thermodynamics of the fundamental matter sector which is dual to the thermal contributions of the D7-branes. As discussed in section 4.2.3, the thermodynamical potential, i. e. in the grand canonical ensemble the grand potential

---

<sup>12</sup>Note that the D7-D7 strings are of the same order as the horizon strings, namely  $N_f/N_c$ , since they originate from the DBI action [198].

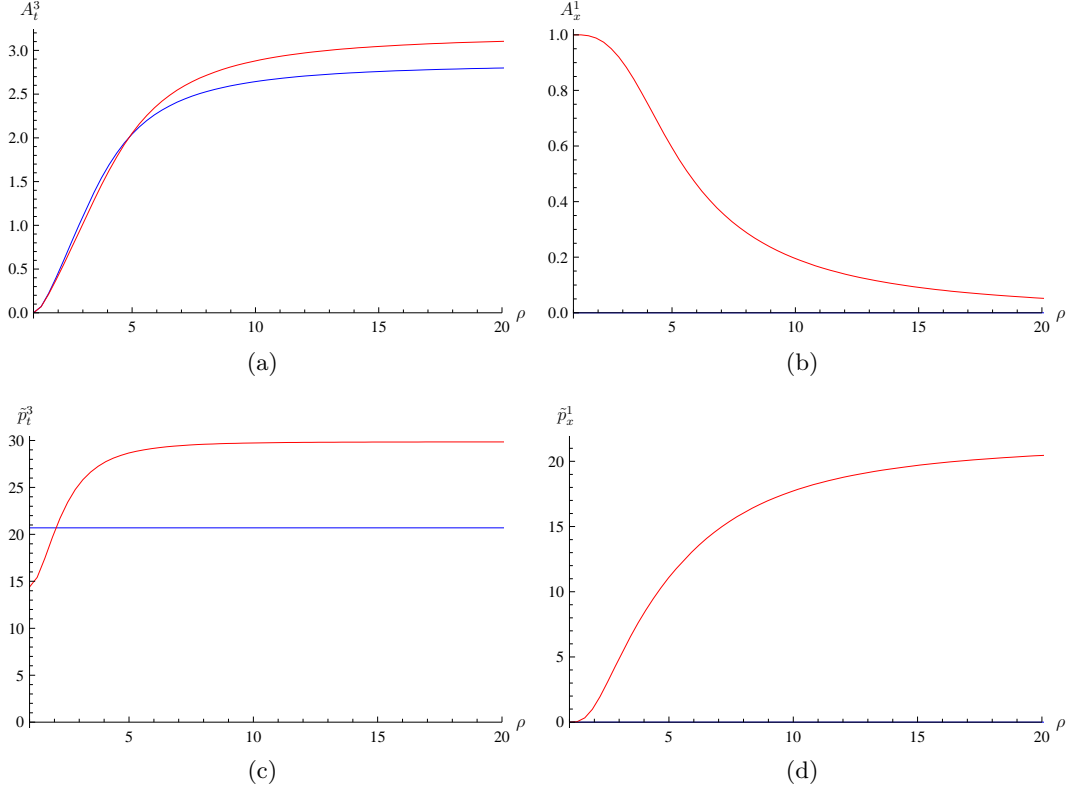


**Figure 6.22:** Profiles of the relevant dimensionless gauge fields  $\tilde{A}$  on the D7-branes and their dimensionless conjugate momenta  $\tilde{p}$  versus the dimensionless AdS radial coordinate  $\rho$  near the horizon at  $\rho = 1$ . The different curves correspond to the temperature  $T = T_c$  (blue) and  $T \approx 0.9T_c$  (red). The plots are obtained at zero quark mass  $m = 0$  and by using the adapted symmetrized trace prescription. Similar plots may also be obtained at finite mass  $m \neq 0$  and by using the DBI action expanded to fourth order in  $F$ . These plots show the same features: (a) The gauge field  $\tilde{A}_t^3$  increases monotonically towards the boundary. At the boundary, its value is given by the dimensionless isospin chemical potential  $\tilde{\mu}_I$ . (b) The gauge field  $\tilde{A}_x^1$  is zero for  $T \geq T_c$ . For  $T < T_c$ , its value is non-zero at the horizon and decreases monotonically towards the boundary where its value has to be zero. (c) The conjugate momentum  $\tilde{p}_t^3$  of the gauge field  $\tilde{A}_t^3$  is constant for  $T \geq T_c$ . For  $T < T_c$ , its value increases monotonically towards the boundary. Its boundary value is given by the dimensionless isospin density  $\tilde{n}_t^3$ . (d) The conjugate momentum  $\tilde{p}_x^1$  of the gauge field  $\tilde{A}_x^1$  is zero for  $T \geq T_c$ . For  $T < T_c$ , its value increases monotonically towards the boundary. Its boundary value is given by the dimensionless density  $-\tilde{n}_x^1$  which is dual to the order parameter. These figures are taken from [2].

$\Omega$ , is proportional to the Euclidean on-shell DBI action,

$$\Omega = TI_{\text{on-shell}}. \quad (6.108)$$

To calculate the thermal contributions of the D7-branes  $\Omega_7$ , we have to determine the Euclidean version of the DBI action (6.83) on-shell.

**Adapted symmetrized trace prescription** Now we calculate the Euclidean on-shell action using the adapted symmetrized trace prescription. First we perform a Wick rotation in the time direction. Next we renormalize the action by adding appropriate counterterms  $I_{\text{ct}}$ . Since no additional divergences occur in this setup, the counterterms are given by (4.66) and the renormalized Euclidean on-shell action  $I_R$  may simply be written as

$$\frac{I_R}{\mathcal{N}_\lambda} = G(m, \tilde{\mu}) - \frac{1}{4} \left[ (\rho_{\min}^2 - m^2)^2 - 4mc \right], \quad (6.109)$$

where  $\rho_{\min}$  determines the minimal value of the coordinate  $\rho$  on the D7-branes, i. e.  $\rho_{\min} = 1$  for black hole embeddings which we consider exclusively here, and

$$G(m, \tilde{\mu}) = \int_{\rho_{\min}}^{\infty} d\rho \left( \rho^3 f \tilde{f} (1 - \chi^2) \Upsilon(\rho, \chi, \tilde{A}) - (\rho^3 - \rho m) \right). \quad (6.110)$$

In figure 6.23 we plot the dimensionless grand potential  $\mathcal{W}_7$  defined as

$$\Omega_7 = TI_R = \frac{\lambda N_f N_c V_3 T^4}{32} \mathcal{W}_7. \quad (6.111)$$

**Expansion of the DBI action** The thermodynamical behavior in the case of the expanded DBI action may be determined in the same way as for the adapted symmetrized trace prescription. As mentioned above, counterterms are needed to regularize the action and do not depend on the gauge fields on the brane. For vanishing gauge fields on the brane, the action calculated using the adapted symmetrized trace prescription and the action expanded in field strength  $F$  coincide. Thus, the counterterms are also the same. For the renormalized Euclidean action we obtain

$$\frac{I_R}{\mathcal{N}_\lambda} = G(m, \tilde{\mu}) - \frac{1}{4} \left[ (\rho_{\min}^2 - m^2)^2 - 4mc \right], \quad (6.112)$$

where

$$G(m, \tilde{\mu}) = \int_{\rho_{\min}}^{\infty} d\rho \left[ \sqrt{-G} \left( 1 + \frac{\mathcal{T}_2}{2} - \frac{\mathcal{T}_4}{8} \right) - (\rho^3 - \rho m) \right], \quad (6.113)$$

with  $\mathcal{T}_2$  and  $\mathcal{T}_4$  as defined in equations (6.96) and (6.98). In figure 6.25 we plot the dimensionless grand potential  $\mathcal{W}_7$  obtained by the action expanded to fourth order in  $F$  and defined as

$$\Omega_7 = TI_R = \frac{\lambda N_f N_c V_3 T^4}{32} \mathcal{W}_7. \quad (6.114)$$

**Thermodynamical consistency** In the following we confirm that both definitions of the grand potential, (6.111) and (6.114), give consistent thermodynamics. For this purpose, we have to vary the grand potential with respect to the thermodynamical variables. In the gravity setup this variation is induced by a variation of the gravity fields. Here we only consider a variation of the gauge field  $A_\mu^a$  since the variation of the embedding function  $\chi$  is the same as in [72]. Using the equations of motion, the variation of the dimensionless grand potential with respect to the gauge field  $A_\mu^a$  reduces to a boundary term,

$$\begin{aligned} \delta\mathcal{W}_7 &= \left[ \frac{\partial\mathcal{L}}{\partial(\partial_\rho\tilde{A}_t^3)}\delta\tilde{A}_t^3 + \frac{\partial\mathcal{L}}{\partial(\partial_\rho\tilde{A}_x^1)}\delta\tilde{A}_x^1 \right]_{\rho_{\min}}^{\infty} \\ &= \tilde{p}_t^3(\rho_{\min})\delta\tilde{A}_t^3(\rho_{\min}) + \tilde{p}_x^1(\rho_{\min})\delta\tilde{A}_x^1(\rho_{\min}) \\ &\quad - \tilde{p}_t^3(\infty)\delta\tilde{A}_t^3(\infty) - \tilde{p}_x^1(\infty)\delta\tilde{A}_x^1(\infty). \end{aligned} \quad (6.115)$$

Here  $\mathcal{L}$  is given by the integrand of the grand potential. Using the asymptotic behavior of the gauge fields (6.94), (6.95), (6.104) (6.95), the contribution of the fields  $\tilde{A}_x^1$  and  $\tilde{p}_x^1$  vanishes and the result coincides with [72],

$$\delta\mathcal{W}_7 = -\tilde{p}_t^3(\infty)\delta\tilde{A}_t^3(\infty) = -\tilde{n}_t^3\delta\tilde{\mu}. \quad (6.116)$$

Therefore, we confirm that  $\Omega_7$  is the thermodynamical potential in the grand canonical ensemble, namely the grand potential. We also see that the density  $\tilde{n}_x^1$  is not a thermodynamical variable.

**Results & Comparison of the two prescriptions** We now compare the results obtained by evaluating the non-Abelian DBI action using the adapted symmetrized trace prescription or the expansion to fourth order.

Figure 6.23 shows that for non-zero gauge field  $A_x^1$ , a phase transition occurs. The presence of this phase transition does not depend on the prescription used, as seen from the comparison of the potential derived using the adapted symmetrized trace prescription (see figure 6.24) with the results derived from the expanded DBI action (see figure 6.25). The transition is second order since the grand potential is smooth at the phase transition.

The temperature scale in the massless case is defined by

$$\frac{T}{T_c} = \frac{(\tilde{\mu}_I)_c}{\tilde{\mu}_I}, \quad (6.117)$$

where  $(\tilde{\mu}_I)_c \approx 2.85$  as obtained from the adapted symmetrized trace prescription. For the expanded DBI action, we equivalently obtain  $\tilde{\mu}_c \approx 2.48$ . In the massive case we fix a quark mass  $M_q$ , then a chemical potential  $\mu_I$  measured in units of  $M_q$ . Thus, the temperature scale is defined as

$$\frac{T}{T_c} = \frac{m_c}{m}, \quad (6.118)$$

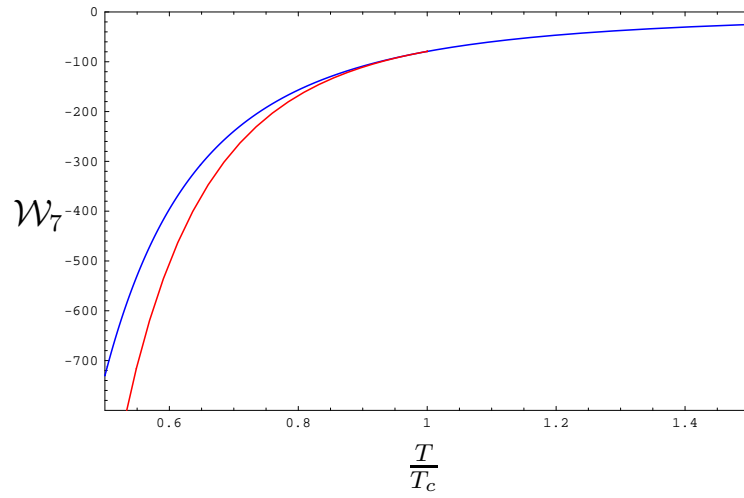


**Figure 6.23:** The dimensionless grand canonical potential  $\mathcal{W}_7$  calculated using the adapted symmetrized trace prescription versus temperature at zero quark mass  $M_q = 0$ : For  $T < T_c$  the superfluid phase (red line) is thermodynamically preferred over the normal phase (blue line). This figure is taken from [2].

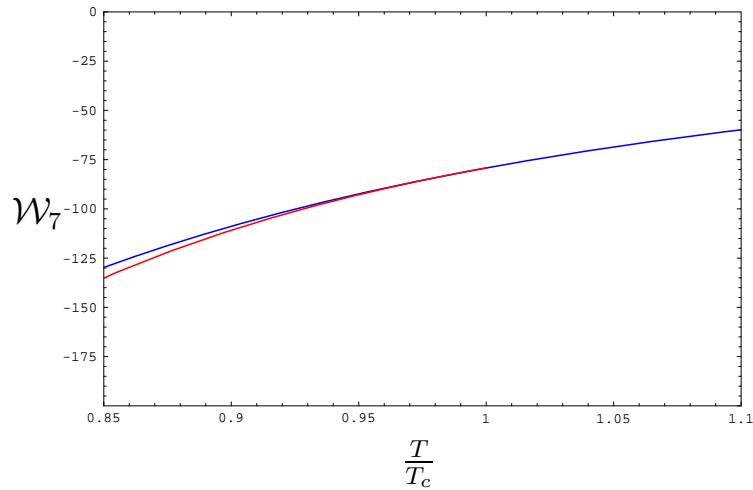


**Figure 6.24:** Same as figure 6.23 close to the phase transition. This figure is taken from [2].

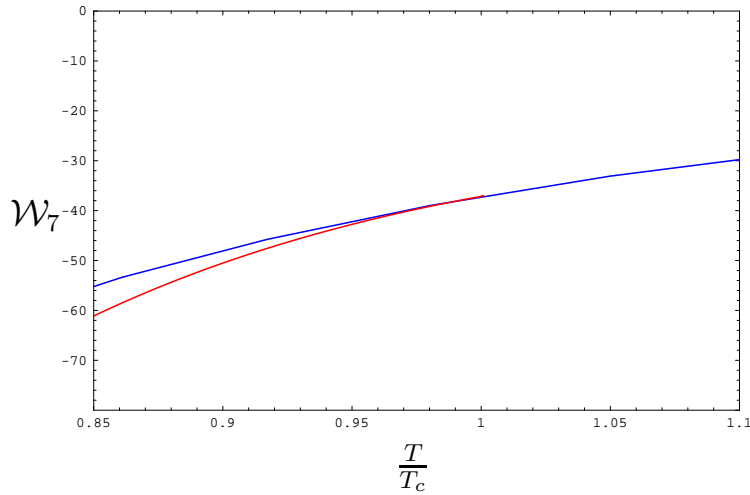


**Figure 6.25:** Grand canonical potential computed from the expanded DBI action at vanishing quark mass  $M_q = 0$ . The qualitative behavior is in agreement with the results from the adapted symmetrized trace prescription (see figure 6.24). This figure is taken from [2].

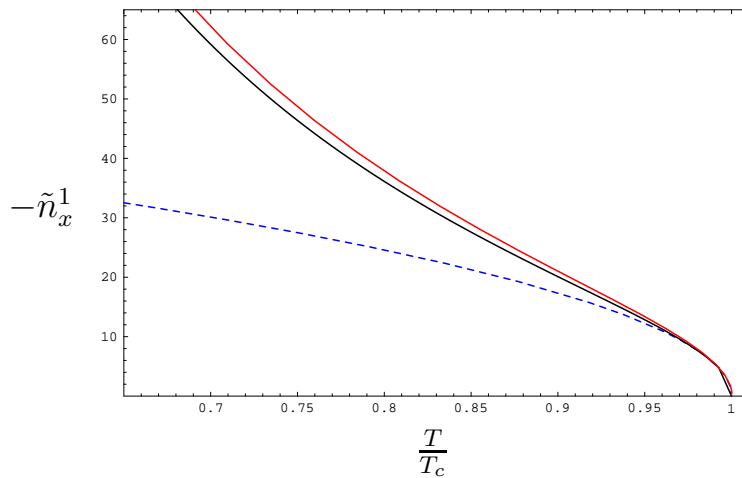


**Figure 6.26:** The order parameter  $\tilde{n}_x^1$  defined in (6.95) and obtained from the adapted symmetrized trace prescription versus temperature  $T$ : The case of vanishing quark mass (red curve) shows the same behavior near  $T_c$  as that at finite mass where  $\mu/M_q = 3$  is fixed. In both cases the order parameter vanishes with a critical exponent of  $1/2$ . This is visualized by the fit  $55(1 - T/T_c)^{1/2}$  (dashed blue curve). This figure is taken from [2].

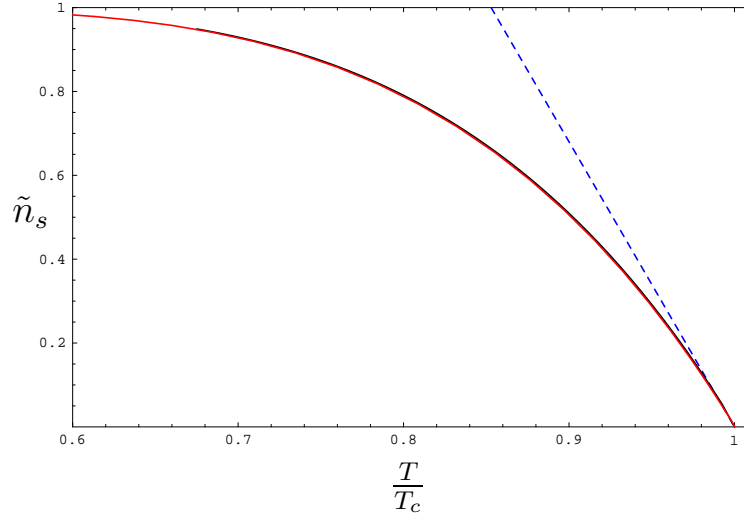


**Figure 6.27:** Superfluid density  $\tilde{n}_s = (\tilde{n}_t^3 - c_0)/\tilde{n}_t^3$  versus temperature  $T$ : In both, the massless (red curve) and the massive case at  $\mu/M_q = 3$  (blue curve), the superfluid density  $\tilde{n}_s$  vanishes linearly at the critical temperature. This is visualized by the fit  $6.8(1 - T/T_c)$  (dashed blue curve). This figure is taken from [2].

where  $m_c$  is the value of the mass parameter at which the phase transition occurs.

From the behavior of the order parameter  $\tilde{n}_x^1$ , see figure 6.26, near the critical temperature, we obtain the critical exponent of the transition to be  $1/2$ , which coincides with the result obtained from mean field theory. It is determined numerically from a fit within 10 percent accuracy, see blue dashed curve in figure 6.26. This exponent is independent from the quark mass as seen from the black curve at  $\mu/M_q = 3$  shown in figure 6.26. We have also confirmed numerically that the critical exponent of the order parameter  $\tilde{n}_x^1$  does not depend on the prescription (adapted symmetrized trace or expanded DBI).

We define the density of superfluid density  $\tilde{n}_s$  in the following way

$$\tilde{n}_s = \frac{\tilde{p}_t^3(\rho_B) - \tilde{p}_t^3(\rho_H)}{\tilde{p}_t^3(\rho_B)} = \frac{\tilde{n}_t^3 - c_0}{\tilde{n}_t^3}. \quad (6.119)$$

This identification was suggested in [100]. Beyond the arguments given there, we have the advantage of exactly knowing the dual field theory interpretation and having a string picture. The numerator of equation (6.119) counts the isospin charges present in the bulk excluding those localized at the black hole horizon  $p_t^3(\rho_H) = c_0$ . Following the ideas described in the paragraph about the string interpretation above, these charges may be identified with the D7-D7 strings in the bulk, which are dual to the superfluid condensate. As expected from Ginzburg-Landau theory, this superfluid density  $\tilde{n}_s$  vanishes linearly at  $T_c$  in massive and massless cases regardless of the prescription chosen, see figure 6.27.

To summarize, our thermodynamical results in a phase diagram, we obtain figure 6.28. The choice of the calculational method – adapted symmetrized trace or

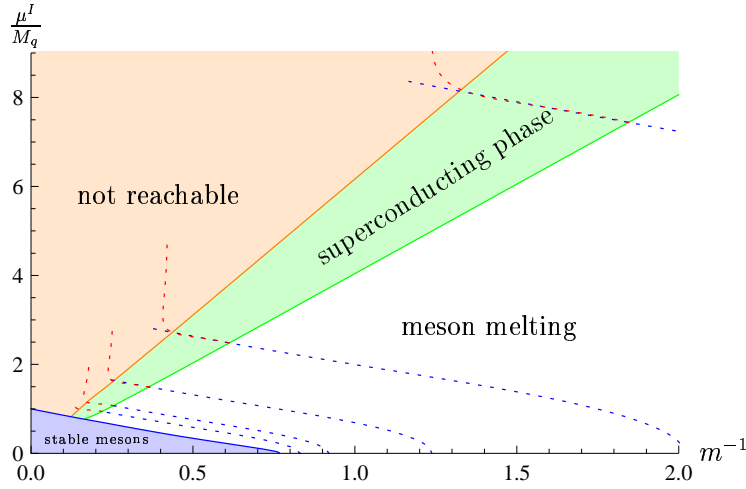


**Figure 6.28:** Phase diagram for fundamental matter with mass  $m = 2M_q/(\sqrt{\lambda}T)$  obtained with the adapted symmetrized trace prescription: The blue and white regions are the same as in figure 5.8, while the green region determined the superfluid phase. The dotted curves correspond to lines at finite mass, i. e. constant  $\chi_0$ . These curves are parametrized by the density  $\tilde{n}_t^3$ . Along the blue curves the field  $A_x^1$  is zero, while along the red ones the field  $A_x^1$  is non-zero. The endpoints of the red curves determine the second order phase transition to the superfluid phase. The dotted, red curves diverge inside the superfluid phase since the back-reaction of the condensate on the background is not considered. This divergence determines the boundary of the orange region which is not reachable without back-reaction. This figure is taken from [2].

expansion of the DBI to fourth order – does not change the qualitative structure of the phase diagram. The blue phase indicates the known region of stable mesons surviving the deconfinement transition. It is separated from the white meson melting region by the meson melting transition (blue line), see section 4.2.3 and 5.2.2. Above a critical isospin density marked by the green line, a superfluid phase forms. At even higher isospin density, our approach, which does not include the back-reaction of the D7-brane, gives diverging order parameters, signaling the breakdown of this approach. This particular region is indicated by orange color. Note that this behavior is well-known to occur in systems without back-reaction. In our case, the gauge fields on the D7-brane grow arbitrarily large close to zero temperature. This behavior will be cured by including the back-reaction, i. e. the contribution of the gauge fields to the total energy-momentum tensor. This back-reaction is for instance considered in the Einstein-Yang-Mills theory discussed in section 6.1.

#### 6.4.2 Results at Finite Baryon and Isospin Chemical Potential

We now consider, in addition to the finite isospin chemical potential, a finite baryon chemical potential. At zero baryon chemical potential, we used two different approaches to evaluate the non-Abelian DBI action (6.83): The modified symmetrized

trace prescription and expansion of the non-Abelian DBI action to fourth order in the field strength  $F$ . We obtained the same physical properties for the two approaches.

We expect that the adapted symmetrized trace prescription also captures the relevant physics at finite baryon chemical potential such that we exclusively use the adapted symmetrized trace prescription in this section. Using this prescription, the action becomes

$$S_{\text{DBI}} = -\frac{T_{D7}}{4} \int d^8\xi \varrho^3 f \tilde{f} (1 - \chi^2) \left( \Upsilon_1(\rho, \chi, \tilde{A}) + \Upsilon_2(\rho, \chi, \tilde{A}) \right), \quad (6.120)$$

with

$$\begin{aligned} \Upsilon_i(\rho, \chi, \tilde{A}) = & \left[ 1 - \chi^2 + \rho^2 (\partial_\rho \chi)^2 - \frac{2\tilde{f}}{f^2} (1 - \chi^2) \left( \partial_\rho \tilde{X}_i \right)^2 + \frac{2}{f} (1 - \chi^2) \left( \partial_\rho \tilde{A}_x^1 \right)^2 \right. \\ & \left. - \frac{\gamma^2}{2\pi^2 \rho^4 f^2} (1 - \chi^2 + \rho^2 (\partial_\rho \chi)^2) \left( (\tilde{X}_1 - \tilde{X}_2) \tilde{A}_x^1 \right)^2 \right]^{\frac{1}{2}}, \end{aligned} \quad (6.121)$$

where again the dimensionless quantities  $\rho = \varrho/\varrho_h$  and  $\tilde{A} = (2\pi\alpha')A/\varrho_h$  are used. The fields  $X_1 = \mathcal{A}_t + A_t^3$  and  $X_2 = \mathcal{A}_t - A_t^3$  are the gauge fields on the  $i$ th brane. In section 5.2.2 it is shown that the non-Abelian DBI action with  $A_x^1 = 0$  decouples into two Abelian DBI actions in terms of these new gauge fields  $X_i$ .

We perform a Legendre transformation as in the previous section. The conjugate momenta of the gauge fields  $X_i$  and  $A_x^1$  as defined in (6.86) and (6.87) where now  $\tilde{p} \mapsto N_f \tilde{p}$  are given by

$$\begin{aligned} \tilde{p}_i &= \frac{\rho^3 \tilde{f}^2 (1 - \chi^2)^2 \partial_\rho \tilde{X}_i}{2f \Upsilon_i(\rho, \chi, \tilde{A})}, \\ \tilde{p}_x^1 &= -\frac{\rho^3 f (1 - \chi^2)^2 \partial_\rho \tilde{A}_x^1}{2} \left( \frac{1}{\Upsilon_1(\rho, \chi, \tilde{A})} + \frac{1}{\Upsilon_2(\rho, \chi, \tilde{A})} \right). \end{aligned} \quad (6.122)$$

Finally, the Legendre-transformed action is given by (6.89) now with

$$\begin{aligned} V(\rho, \chi, \tilde{A}, \tilde{p}) &= \left( 1 - \frac{\gamma^2}{2\pi^2 \rho^4 f^2} \left( (\tilde{X}_1 - \tilde{X}_2) \tilde{A}_x^1 \right)^2 \right)^{\frac{1}{2}} \\ &\times \left[ \left( \sqrt{1 + \frac{8(\tilde{p}_1)^2}{\rho^6 \tilde{f}^3 (1 - \chi^2)^3}} + \sqrt{1 + \frac{8(\tilde{p}_2)^2}{\rho^6 \tilde{f}^3 (1 - \chi^2)^3}} \right)^2 \right. \\ &\left. - \frac{8(\tilde{p}_x^1)^2}{\rho^6 \tilde{f} f^2 (1 - \chi^2)^3} \right]^{\frac{1}{2}}. \end{aligned} \quad (6.123)$$

This action agrees with the one for finite baryon and isospin chemical potential (5.33) after  $\tilde{p}_x^1 \rightarrow 0$  and with the one for the superfluid state at pure isospin chemical

potential (6.89) after  $\tilde{p}_1 \rightarrow -\tilde{p}_2$  and  $\tilde{p}_x^1 \rightarrow N_f \tilde{p}_x^1$ . The change in  $\tilde{p}_x^1$  has to be done such that the definitions agree in both cases.

Then the first order equations of motion for the gauge fields and their conjugate momenta are

$$\begin{aligned}
\partial_\rho \tilde{X}_i &= \frac{2f\sqrt{1-\chi^2+\rho^2(\partial_\rho\chi)^2}}{\rho^3\tilde{f}^2(1-\chi^2)^2} \tilde{p}_i W(\rho, \chi, \tilde{A}, \tilde{p}) U_i(\rho, \chi, \tilde{A}, \tilde{p}), \\
\partial_\rho \tilde{A}_x^1 &= -\frac{2\sqrt{1-\chi^2+\rho^2(\partial_\rho\chi)^2}}{\rho^3 f(1-\chi^2)^2} \tilde{p}_x^1 W(\rho, \chi, \tilde{A}, \tilde{p}), \\
\partial_\rho \tilde{p}_{1/2} &= \pm \frac{\tilde{f}(1-\chi^2)\sqrt{1-\chi^2+\rho^2(\partial_\rho\chi)^2}\gamma^2}{8\pi^2\rho f W(\rho, \chi, \tilde{A}, \tilde{p})} \left(\tilde{A}_x^1\right)^2 (\tilde{X}_1 - \tilde{X}_2), \\
\partial_\rho \tilde{p}_x^1 &= \frac{\tilde{f}(1-\chi^2)\sqrt{1-\chi^2+\rho^2(\partial_\rho\chi)^2}\gamma^2}{8\pi^2\rho f W(\rho, \chi, \tilde{A}, \tilde{p})} \left(\tilde{X}_1 - \tilde{X}_2\right)^2 \tilde{A}_x^1,
\end{aligned} \tag{6.124}$$

with

$$\begin{aligned}
U_i(\rho, \chi, \tilde{A}, \tilde{p}) &= \frac{\sqrt{1 + \frac{8(\tilde{p}_1)^2}{\rho^6 \tilde{f}^3(1-\chi^2)^3}} + \sqrt{1 + \frac{8(\tilde{p}_2)^2}{\rho^6 \tilde{f}^3(1-\chi^2)^3}}}{\sqrt{1 + \frac{8(\tilde{p}_i)^2}{\rho^6 \tilde{f}^3(1-\chi^2)^3}}}, \\
W(\rho, \chi, \tilde{A}, \tilde{p}) &= \sqrt{\frac{1 - \frac{\gamma^2}{2\pi^2\rho^4 f^2} \left((\tilde{X}_1 - \tilde{X}_2)\tilde{A}_x^1\right)^2}{\left(\sqrt{1 + \frac{8(\tilde{p}_1)^2}{\rho^6 \tilde{f}^3(1-\chi^2)^3}} + \sqrt{1 + \frac{8(\tilde{p}_2)^2}{\rho^6 \tilde{f}^3(1-\chi^2)^3}}\right)^2 - \frac{8(\tilde{p}_x^1)^2}{\rho^6 \tilde{f}^2(1-\chi^2)^3}}}.
\end{aligned} \tag{6.125}$$

For the embedding function  $\chi$  we get the second order equation of motion

$$\begin{aligned}
\partial_\rho \left[ \frac{\rho^5 f \tilde{f}(1-\chi^2)(\partial_\rho\chi)V}{\sqrt{1-\chi^2+\rho^2(\partial_\rho\chi)^2}} \right] &= -\frac{\rho^3 f \tilde{f} \chi}{\sqrt{1-\chi^2+\rho^2(\partial_\rho\chi)^2}} \left\{ [3(1-\chi^2) + 2\rho^2(\partial_\rho\chi)^2] V \right. \\
&\quad \left. - \frac{24(1-\chi^2+\rho^2(\partial_\rho\chi)^2)}{\rho^6 \tilde{f}^3(1-\chi^2)^3} W \left[ (\tilde{p}_1)^2 U_1 + (\tilde{p}_2)^2 U_2 - \frac{\tilde{f}^2}{f^2} (\tilde{p}_x^1)^2 \right] \right\}.
\end{aligned} \tag{6.126}$$

We solve the equations of motion numerically by integrating them again from the horizon at  $\rho = 1$  to the boundary  $\rho = \infty$ . The initial conditions may be determined

by the asymptotic expansion of the gravity fields near the horizon

$$\begin{aligned}
\tilde{X}_i &= \frac{b_i}{(1-\chi_0^2)^{\frac{3}{2}} B_i} (\rho-1)^2 + \mathcal{O}((\rho-1)^3), \\
\tilde{A}_x^1 &= a + \mathcal{O}((\rho-1)^3), \\
\tilde{p}_{1/2} &= b_{1/2} \pm \frac{\gamma^2 a^2}{32\pi^2} \left( \frac{b_1}{B_1} - \frac{b_2}{B_2} \right) (B_1 + B_2) (\rho-1)^2 + \mathcal{O}((\rho-1)^3), \\
\tilde{p}_x^1 &= + \mathcal{O}((\rho-1)^3), \\
\chi &= \chi_0 - \frac{3\chi_0}{4B_1 B_2} (\rho-1)^2 + \mathcal{O}((\rho-1)^3),
\end{aligned} \tag{6.127}$$

with

$$B_i = \sqrt{1 + \frac{b_i^2}{(1-\chi_0^2)^3}}.$$

The terms in the asymptotic expansions are arranged according to their order in  $(\rho-1)$ . There are four independent parameters  $\{a, b_1, b_2, \chi_0\}$  which have to be determined. In order to obtain the field theory quantities we determine the asymptotic expansion of the gravity fields near the AdS boundary

$$\begin{aligned}
\tilde{X}_i &= \tilde{\mu}_i - \frac{\tilde{n}_i}{\rho^2} + \mathcal{O}(\rho^{-4}), \\
\tilde{A}_x^1 &= + \frac{\tilde{n}_x^1}{2\rho^2} + \mathcal{O}(\rho^{-4}), \\
\tilde{p}_i &= \tilde{n}_i + \mathcal{O}(\rho^{-4}), \\
\tilde{p}_x^1 &= \tilde{n}_x^1 - \frac{\gamma^2 \tilde{n}_x^1 (\tilde{\mu}_1 - \tilde{\mu}_2)^2}{8\pi^2 \rho^2} + \mathcal{O}(\rho^{-4}), \\
\chi &= \frac{m}{\rho} + \frac{c}{\rho^3} + \mathcal{O}(\rho^{-4}).
\end{aligned} \tag{6.128}$$

Note that the factor of two in  $\tilde{A}_x^1$  is consistent with the earlier definitions in section 6.4.1 since here we have a different definition of the conjugate momenta (factor  $N_f$ ). In this asymptotic expansion, we find seven independent parameters  $\{\tilde{\mu}_i, \tilde{n}_i, \tilde{n}_x^1, m, c\}$ . Using the transformation of the gauge field from  $\tilde{X}_i$  to  $\tilde{A}_t$  and  $\tilde{A}_t^3$ , the independent parameters of the gauge fields  $X_i, \{\tilde{\mu}_i, \tilde{n}_i\}$ , may be translated into the baryon and isospin chemical potential and densities as defined in (5.31).  $m$  and  $c$  to the bare quark mass  $M_q$  and the quark condensate  $\langle \bar{\psi}\psi \rangle$  as defined in (4.58). There are three independent physical parameters, e.g.  $m, \mu_B$  and  $\mu_I$  in the grand canonical ensemble. The asymptotic expansion close to the horizon has four independent solutions. These parameters may be fixed by choosing the three independent physical parameters, i.e. the state in the field theory and by the constraint that  $\tilde{A}_x^1$  goes to zero at the boundary, i.e. the  $U(1)_3$  symmetry is spontaneously broken. We use a standard shooting method to determine the parameters at the horizon.

### Thermodynamics

As at zero baryon chemical potential we determine the grand potential in terms of the on-shell action. The final result just differs by the definition of the function  $G$ . Here we get

$$I_R = \frac{\lambda N_c N_f V_3 T^3}{32} \left( \frac{G(m, \tilde{\mu})}{N_f} - \frac{1}{4} [(\rho_{\min}^2 - m^2)^2 - 4mc] \right), \quad (6.129)$$

with

$$G(m, \tilde{\mu}) = \int_{\rho_{\min}}^{\infty} d\rho \left[ \rho^3 f \tilde{f} (1 - \chi^2) \left( \Upsilon_1(\rho, \chi, \tilde{A}) + \Upsilon_2(\rho, \chi, \tilde{A}) \right) - N_f (\rho^3 - \rho m) \right]. \quad (6.130)$$

**Phase transition and phase diagram** We expect that a phase transition occurs between a normal fluid phase and a superfluid phase. At zero baryon chemical potential we have seen in section 6.4.1 that the phase transition from the normal phase to the superfluid phase is second order with mean field exponents. Now we consider the phase transition at non-zero baryon chemical potentials.

First we map out the phase diagram of the given theory with zero quark mass  $m = 0$ . The phase diagram is shown in figure 6.29. As we increase the baryon chemical potential the transition temperature to the superfluid phase first increases. Then for  $\mu_B/\mu_I \gtrsim 0.4$  the transition temperature monotonically decreases to zero as the baryon chemical potential grows. We can show numerically that the phase transition is always second order, and hence we obtain a quantum critical point. Below we will show numerically that the transition temperature is zero at  $\mu_B/\mu_I \approx 1.23$ .

### Zero temperature solutions and quantum critical point

In this section we study the D3/D7-brane setup at zero temperature. The zero temperature limit is given by  $\rho_h \rightarrow 0$ , i. e.  $f = \tilde{f} = 1$ . The induced metric on the D7-branes may now be written in  $(L, r)$  coordinates (see equation (4.53)),

$$ds^2 = \frac{r^2 + L^2}{2R^2} (-dt^2 + d\mathbf{x}^2) + \frac{R^2}{r^2 + L^2} (1 + (\partial_r L)^2) dr^2 + \frac{R^2 r^2}{r^2 + L^2} d\Omega_3^2. \quad (6.131)$$

The square root of the metric is now

$$\sqrt{-G} = \frac{\sqrt{h_3}}{4} r^3 \sqrt{1 + (\partial_r L)^2}, \quad (6.132)$$

and using the adapted symmetrized trace prescription, the DBI action becomes

$$S_{\text{DBI}} = -T_{D7} \int d\xi^8 \frac{r^3}{4} \left[ \Xi_1(\tilde{r}, \tilde{L}, \tilde{A}) + \Xi_2(\tilde{r}, \tilde{L}, \tilde{A}) \right], \quad (6.133)$$

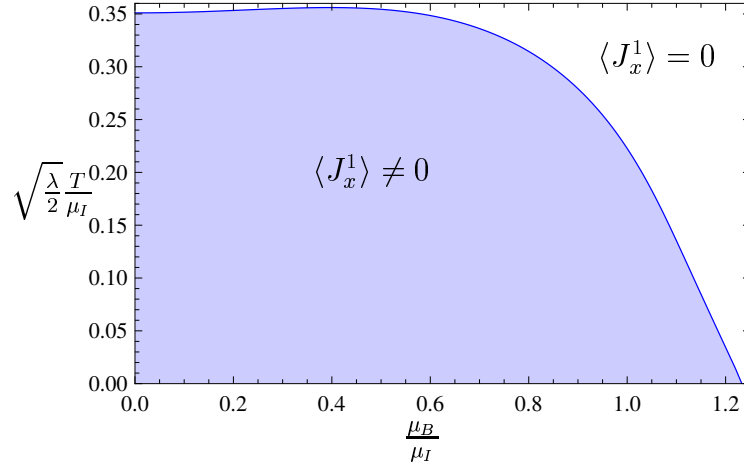


**Figure 6.29:** The phase diagram for fundamental matter in thermal strongly coupled  $\mathcal{N} = 2$  SYM theory at zero quark mass with  $\mu_I$  the isospin chemical potential,  $\mu_B$  the baryon chemical potential,  $T$  the temperature and  $\lambda$  the 't Hooft coupling: In the blue region the order parameter  $\langle J_x^1 \rangle$  is non-zero and the system is in the superfluid phase while in the white region the order parameter  $\langle J_x^1 \rangle$  is zero and the system is in the normal phase. This figure is taken from [6].

with

$$\Xi_i(\tilde{r}, \tilde{L}, \tilde{A}) = \left[ 1 + (\partial_{\tilde{r}} \tilde{L})^2 - 2(\partial_{\tilde{r}} \tilde{X}_i)^2 + 2(\partial_{\tilde{r}} \tilde{A}_x^1)^2 - \frac{\gamma^2}{2\pi^2(\tilde{r}^2 + \tilde{L}^2)^2} (1 + (\partial_{\tilde{r}} \tilde{L})^2) \left( (\tilde{X}_1 - \tilde{X}_2) \tilde{A}_x^1 \right)^2 \right]^{\frac{1}{2}}, \quad (6.134)$$

where the dimensionless quantities are now defined by

$$\tilde{r} = \frac{r}{R}, \quad \tilde{L} = \frac{L}{R}, \quad \tilde{A} = \frac{2\pi\alpha'}{R} A. \quad (6.135)$$

In the normal phase, i. e.  $A_x^1 \equiv 0$ , the equations of motion for the gauge fields  $X_i$  for the massless embedding  $L = 0$ ,

$$\partial_{\tilde{r}} \tilde{X}_i = \frac{2\tilde{n}_i}{\sqrt{\tilde{r}^6 + 8\tilde{n}_i^2}}, \quad (6.136)$$

can be solved analytically [198]. The solution expressed in terms of incomplete Beta functions is given by

$$\tilde{X}_i(\tilde{r}) = \frac{\tilde{n}_i^{\frac{1}{3}}}{6} B \left( \frac{\tilde{r}^6}{8\tilde{n}_i^2 + \tilde{r}^6}; \frac{1}{6}, \frac{1}{3} \right). \quad (6.137)$$

From the asymptotic form near the boundary, we can read off the chemical potential and the density (see equation (6.128)),

$$\tilde{X}_i = \frac{\tilde{n}_i^{\frac{1}{3}} 2\sqrt{\pi} \gamma \left(\frac{7}{6}\right)}{\sqrt{3} \gamma \left(\frac{2}{3}\right)} - \frac{\tilde{n}_i}{\tilde{r}^2} + \dots \quad (6.138)$$

In the normal fluid phase, we may now consider fluctuations  $E_x^\pm = A_x^1 \pm iA_x^2$  as in section 5.5 and look for an instability which may lead to a phase transition. For the flat embedding  $L = 0$ , the equation of motion for the fluctuation  $E_x^\pm$  at zero momentum is given by

$$\frac{d^2 \tilde{E}_x^\pm(\tilde{r})}{d\tilde{r}^2} + \frac{F'(\tilde{r})}{F(\tilde{r})} \frac{d\tilde{E}_x^\pm(\tilde{r})}{d\tilde{r}} + \frac{8}{\tilde{r}^4} \left( \tilde{\omega} \pm \frac{\gamma}{4\sqrt{2}\pi} (\tilde{X}_1 - \tilde{X}_2) \right)^2 \tilde{E}_x^\pm(\tilde{r}) = 0, \quad (6.139)$$

with  $\tilde{\omega} = \sqrt{\frac{\lambda}{2}} \alpha' \omega$  coming from the ansatz  $A_x^i(\tilde{r}, t) = A_x^i(\tilde{r}) e^{-i\omega t}$ . The analytical expression for  $\tilde{X}_i(\tilde{r})$  is given in (6.137) and

$$F(\tilde{r}) = \tilde{r}^3 \left( \frac{1}{\sqrt{1 - 2(\partial_{\tilde{r}} \tilde{X}_1)^2}} + \frac{1}{\sqrt{1 - 2(\partial_{\tilde{r}} \tilde{X}_2)^2}} \right). \quad (6.140)$$

The system is unstable if the imaginary part of the quasinormal frequency is positive. For a massless embedding  $L \equiv 0$ , we find this instability at  $\mu_B/\mu_I \approx 1.23$ .

**What is the origin of the instability?** In the back-reacted Einstein-Yang-Mills theory, we see that the instability of the extremal Reissner-Nordström black hole which triggers the phase transition to the superfluid phase can be related to the violation of the Breitenlohner-Freedman bound of the field  $A_x^1$  in the near horizon geometry of the black hole. This near horizon geometry features an  $AdS_2$  factor (see section 6.1.2). Here we investigate the instability in the D3/D7 brane setup at zero temperature. In the following we show that in contrast to the back-reacted Einstein-Yang-Mills system, the instability in the brane setup cannot be related to the violation of the Breitenlohner-Freedman bound in the far IR, i. e. the fluctuation of the field  $A_x^1$  does not become unstable in the far IR. In this system we expect that the instability occurs in the bulk.

Let us now consider a fluctuation  $A_x^1$  about the solution in the normal phase given by equation (6.137) for zero quark mass, i. e.  $L \equiv 0$ . The equation of motion for this fluctuation is given by

$$(\tilde{A}_x^1)'' + \frac{F'(\tilde{r})}{F(\tilde{r})} (\tilde{A}_x^1)' + \frac{\gamma^2 (\tilde{X}_1 - \tilde{X}_2)^2}{4\pi^2 \tilde{r}^4} \tilde{A}_x^1 = 0. \quad (6.141)$$

As for the Einstein-Yang-Mills theory we consider the equation of motion in the far IR. Since there is no horizon at zero temperature in the brane setup, the expansion

is around  $\tilde{r} = 0$ . The equation of motion becomes trivial,  $\partial_{\tilde{r}}^2 \tilde{A}_x^1 = 0$ , if we expand to first order only. Thus,  $\tilde{A}_x^1/r$  satisfies the equation of motion of a massless scalar in  $AdS_2$ . In contrast to the EYM setup, the mass cannot be tuned by changing a UV quantity and the Breitenlohner-Freedman bound can never be violated<sup>13</sup>. Hence, the fluctuation is stable in the IR. We expect that the instability observed by the numerical study of the quasinormal modes above occurs along the flow. Thus, the origin of the instability in this brane setup is different compared to the one in the back-reacted Einstein-Yang-Mills system studied in section 6.1.2.

## 6.5 Fluctuations About the Vector Condensate

In this section we consider the response of the vector meson condensate due to small fluctuations exclusively at zero baryon chemical potential. Since we work here in the probe approximation, the metric fluctuations decouple and we only have to consider the gauge field fluctuations. The full gauge field  $\hat{A}$  on the D7-branes consists of the background field  $A$  and fluctuations  $a$ ,

$$\hat{A} = A_t^3 \tau^3 dt + A_x^1 \tau^1 dx + a_\mu^a \tau^a dx^\mu, \quad (6.142)$$

where  $\tau^a$  are the  $SU(2)$  generators. The linearized equations of motion for the fluctuations  $a$  are obtained by expanding the DBI action in  $a$  to second order. We will analyze the fluctuations  $a_\perp^3$  and  $E_\perp^+ = a_\perp^1 + ia_\perp^2$ ,  $E_\perp^- = a_\perp^1 - ia_\perp^2$ .

Including these fluctuations, the DBI action reads

$$S_{\text{DBI}} = -T_7 \int d^8 \xi \text{STr} \sqrt{\det [G + (2\pi\alpha') \hat{F}]}, \quad (6.143)$$

with the non-Abelian field strength tensor

$$\hat{F}_{\mu\nu}^a = F_{\mu\nu}^a + \check{F}_{\mu\nu}^a, \quad (6.144)$$

where the background is collected in

$$F_{\mu\nu}^a = 2\partial_{[\mu} A_{\nu]}^a + \frac{\gamma}{\sqrt{\lambda}} f^{abc} A_\mu^b A_\nu^c, \quad (6.145)$$

and all terms containing fluctuations in the gauge field are summed in

$$\check{F}_{\mu\nu}^a = 2\partial_{[\mu} a_{\nu]}^a + \frac{\gamma}{\sqrt{\lambda}} f^{abc} a_\mu^b a_\nu^c + \frac{\gamma}{\sqrt{\lambda}} f^{abc} (A_\mu^b a_\nu^c + a_\mu^b A_\nu^c). \quad (6.146)$$

Index anti-symmetrization is always defined with a factor of two in the following way  $\partial_{[\mu} A_{\nu]} = (\partial_\mu A_\nu - \partial_\nu A_\mu)/2$ .

<sup>13</sup>We thank K. Jensen for pointing this out.

### 6.5.1 Adapted Symmetrized Trace Prescription

In this section we use the adapted symmetrized trace prescription to determine the fluctuations about the background we discussed above. To obtain the linearized equations of motion for the fluctuations  $a$ , we expand the action (6.143) to second order in fluctuations,

$$S^{(2)} = -T_7 \int d^8\xi \text{STr} \left[ \sqrt{-\mathcal{G}} + \frac{(2\pi\alpha')}{2} \sqrt{-\mathcal{G}} \mathcal{G}^{MN} \check{F}_{NM} - \frac{(2\pi\alpha')^2}{4} \sqrt{-\mathcal{G}} \mathcal{G}^{MM'} \check{F}_{M'N} \mathcal{G}^{NN'} \check{F}_{N'M} + \frac{(2\pi\alpha')^2}{8} \sqrt{-\mathcal{G}} (\mathcal{G}^{MN} \check{F}_{NM})^2 \right]. \quad (6.147)$$

As before, we collect the metric and gauge field background in the tensor  $\mathcal{G} = G + (2\pi\alpha')F$ . Using the Euler-Lagrange equation, we get the linearized equation of motion for fluctuations  $a_K^d$  in the form

$$0 = \partial_L \text{STr} \left[ \sqrt{-\mathcal{G}} \tau^d \left\{ \mathcal{G}^{[KL]} + (2\pi\alpha') \left( \mathcal{G}^{M[K} \mathcal{G}^{L]N} + \frac{1}{2} \mathcal{G}^{MN} \mathcal{G}^{[KL]} \right) \check{F}_{NM} \right\} \right] - \text{STr} \left[ \frac{\gamma}{\sqrt{\lambda}} f^{abd} \tau^a \sqrt{-\mathcal{G}} \left\{ \mathcal{G}^{[KL]} (a + A)_L^b + (2\pi\alpha') \left( \mathcal{G}^{M[K} \mathcal{G}^{L]N} + \frac{1}{2} \mathcal{G}^{MN} \mathcal{G}^{[KL]} \right) \check{F}_{NM} A_L^b \right\} \right]. \quad (6.148)$$

Note that the linearized version of the fluctuation field strength used in equation (6.148) is given by

$$\check{F}_{MN}^a = 2\partial_{[M} a_{N]}^a + \frac{\gamma}{\sqrt{\lambda}} f^{abc} (A_M^b a_N^c + a_M^b A_N^c) + \mathcal{O}(a^2). \quad (6.149)$$

In our specific case the background tensor in its covariant form is given by

$$\mathcal{G}_{MN} = G_{MN} \tau^0 + (2\pi\alpha') \left( 2\partial_\rho A_t^3 \delta_{\rho[M} \delta_{N]t} \tau^3 + 2\partial_\rho A_x^1 \delta_{\rho[M} \delta_{N]x} \tau^1 + 2\frac{\gamma}{\sqrt{\lambda}} A_t^3 A_x^1 \delta_{t[M} \delta_{N]x} \tau^2 \right). \quad (6.150)$$

Inversion yields the contravariant form needed to compute the explicit equations of motion. The inverse of  $\mathcal{G}$  is defined as  $\mathcal{G}^{MN} \mathcal{G}_{NM'} = \delta_{M'}^M \tau^0$ <sup>14</sup>. The non-zero components of  $\mathcal{G}^{MN}$  are as follows: The diagonal elements are given by

$$\mathcal{G}^{tt} = G^{tt} \frac{1 + G^{xx} G^{\rho\rho} (\partial_\rho \tilde{A}_x^1)^2}{N}, \quad \mathcal{G}^{xx} = G^{xx} \frac{1 + G^{tt} G^{\rho\rho} (\partial_\rho \tilde{A}_t^3)^2}{N}, \quad (6.151)$$

$$\mathcal{G}^{\rho\rho} = G^{\rho\rho} \frac{1 - \frac{2\gamma^2}{\pi^2 \rho^4 f^2} (\tilde{A}_x^1 \tilde{A}_t^3)^2}{N},$$

<sup>14</sup>We calculate the inverse of  $\mathcal{G}$  by ignoring the commutation relation of the  $\tau$ 's because of symmetrized trace. It is important that  $\tau^a \tau^b$  must not be simplified to  $\epsilon^{abc} \tau^c$  since symmetrization is not the same.

where the other diagonal elements are just  $\mathcal{G}^{ii} = G^{ii}$ . The off-diagonal elements read

$$\begin{aligned}
\mathcal{G}^{x\varrho} &= G^{\varrho\varrho} \frac{G^{xx}(\partial_\rho \tilde{A}_x^1)\tau^1 - \frac{2\sqrt{2}\gamma}{\pi\rho^4 f^2} \frac{R^2}{\varrho_h^2} \tilde{A}_x^1 \tilde{A}_t^3 (\partial_\rho \tilde{A}_t^3)\tau^2 \tau^3}{N}, \\
\mathcal{G}^{\varrho x} &= G^{\varrho\varrho} \frac{-G^{xx}(\partial_\rho \tilde{A}_x^1)\tau^1 - \frac{2\sqrt{2}\gamma}{\pi\rho^4 f^2} \frac{R^2}{\varrho_h^2} \tilde{A}_x^1 \tilde{A}_t^3 (\partial_\rho \tilde{A}_t^3)\tau^2 \tau^3}{N}, \\
\mathcal{G}^{tx} &= \frac{4R^2}{\varrho_h^2 \rho^4 f^2} \frac{\frac{\sqrt{2}\gamma}{2\pi} \tilde{A}_x^1 \tilde{A}_t^3 \tau^2 + \frac{R^2}{\varrho_h^2} G^{\varrho\varrho} (\partial_\rho \tilde{A}_x^1) (\partial_\rho \tilde{A}_t^3) \tau^1 \tau^3}{N}, \\
\mathcal{G}^{xt} &= \frac{4R^2}{\varrho_h^2 \rho^4 f^2} \frac{-\frac{\sqrt{2}\gamma}{2\pi} \tilde{A}_x^1 \tilde{A}_t^3 \tau^2 + \frac{R^2}{\varrho_h^2} G^{\varrho\varrho} (\partial_\rho \tilde{A}_x^1) (\partial_\rho \tilde{A}_t^3) \tau^1 \tau^3}{N}, \\
\mathcal{G}^{t\varrho} &= G^{tt} G^{\varrho\varrho} \frac{(\partial_\rho \tilde{A}_t^3)\tau^3 - \frac{\sqrt{2}\gamma}{2\pi} \frac{\varrho_H^2}{R^2} G^{xx} \tilde{A}_x^1 \tilde{A}_t^3 (\partial_\rho \tilde{A}_x^1)\tau^1 \tau^2}{N}, \\
\mathcal{G}^{\varrho t} &= G^{tt} G^{\varrho\varrho} \frac{-(\partial_\rho \tilde{A}_t^3)\tau^3 - \frac{\sqrt{2}\gamma}{2\pi} \frac{\varrho_H^2}{R^2} G^{xx} \tilde{A}_x^1 \tilde{A}_t^3 (\partial_\rho \tilde{A}_x^1)\tau^1 \tau^2}{N}.
\end{aligned} \tag{6.152}$$

The denominator  $N$  is given by

$$N = 1 + G^{xx} G^{\varrho\varrho} (\partial_\rho \tilde{A}_x^1)^2 + G^{tt} G^{\varrho\varrho} (\partial_\rho \tilde{A}_t^3)^2 - \frac{2\gamma^2}{\pi^2 \rho^4 f^2} (\tilde{A}_x^1 \tilde{A}_t^3)^2. \tag{6.153}$$

**Fluctuations in  $a_\perp^3$ :** For the fluctuation  $a_\perp^3$  with zero spatial momentum, we obtain the equation of motion

$$\begin{aligned}
0 &= (a_\perp^3)'' + \frac{\partial_\rho H}{H} (a_\perp^3)' - \left[ \frac{4\varrho_h^4}{R^4} \left( \frac{\mathcal{G}^{xx}}{\mathcal{G}^{\varrho\varrho}} (\mathbf{m}_x^1)^2 + \frac{\mathcal{G}^{tt}}{\mathcal{G}^{\varrho\varrho}} \mathbf{w}^2 \right) \right. \\
&\quad \left. - 16 \frac{\partial_\rho \left( \frac{H}{\rho^4 f^2} \tilde{A}_t^3 (\partial_\rho \tilde{A}_t^3) (\mathbf{m}_x^1)^2 \right)}{H \left( 1 - \frac{2c^2}{\pi^2 \rho^4 f^2} (\tilde{A}_x^1 \tilde{A}_t^3)^2 \right)} \right] a_\perp^3,
\end{aligned} \tag{6.154}$$

with

$$\mathbf{m}_x^1 = \frac{\gamma}{2\sqrt{2}\pi} \tilde{A}_x^1, \quad H = \sqrt{\mathcal{G}} G^{xx} \mathcal{G}^{\varrho\varrho}. \tag{6.155}$$

**Fluctuations in  $E_{\perp}^{\pm} = a_{\perp}^1 \pm ia_{\perp}^2$ :** For the fluctuations  $E_{\perp}^{\pm}$  and  $E_{\perp}^{\mp}$  with zero spatial momentum, we obtain the coupled equations of motion

$$\begin{aligned}
0 = & (E_{\perp}^+)' + \frac{\partial_{\rho} H}{H} (E_{\perp}^+)' - \frac{4\varrho_h^4}{R^4} \left[ \frac{\mathcal{G}^{tt}}{\mathcal{G}^{\varrho\varrho}} (\mathfrak{w} - \mathfrak{m}_t^3)^2 + \frac{\mathcal{G}^{\{tx\}}}{\mathcal{G}^{\varrho\varrho}} \mathfrak{m}_x^1 \mathfrak{w} \right] E_{\perp}^+ \\
& + \frac{4\varrho_h^4}{R^4} \left[ \frac{\mathcal{G}^{\{tx\}}}{\mathcal{G}^{\varrho\varrho}} \mathfrak{m}_x^1 \mathfrak{m}_t^3 + \frac{R^2}{4\varrho_h^2} \frac{\partial_{\rho} [\sqrt{-\mathcal{G}} G^{\perp\perp} \mathcal{G}^{\{x\varrho\}} \mathfrak{m}_x^1]}{H} - \frac{\mathcal{G}^{xx}}{2\mathcal{G}^{\varrho\varrho}} (\mathfrak{m}_x^1)^2 \right] (E_{\perp}^+ - E_{\perp}^-) \\
& + \frac{4\varrho_h^2}{R^2} \frac{\mathcal{G}^{\{t\varrho\}}}{\mathcal{G}^{\varrho\varrho}} \mathfrak{w} (E_{\perp}^-)' + \frac{2\varrho_h^2}{R^2} \frac{\partial_{\rho} [\sqrt{-\mathcal{G}} G^{\perp\perp} \mathcal{G}^{\{t\varrho\}} (\mathfrak{w} + \mathfrak{m}_t^3)]}{H} E_{\perp}^-,
\end{aligned} \tag{6.156}$$

$$\begin{aligned}
0 = & (E_{\perp}^-)' + \frac{\partial_{\rho} H}{H} (E_{\perp}^-)' + \frac{4\varrho_h^4}{R^4} \left[ -\frac{\mathcal{G}^{tt}}{\mathcal{G}^{\varrho\varrho}} (\mathfrak{w} + \mathfrak{m}_t^3)^2 + \frac{\mathcal{G}^{\{tx\}}}{\mathcal{G}^{\varrho\varrho}} \mathfrak{m}_x^1 \mathfrak{w} \right] E_{\perp}^- \\
& - \frac{4\varrho_h^4}{R^4} \left[ \frac{\mathcal{G}^{\{tx\}}}{\mathcal{G}^{\varrho\varrho}} \mathfrak{m}_x^1 \mathfrak{m}_t^3 + \frac{R^2}{4\varrho_h^2} \frac{\partial_{\rho} [\sqrt{-\mathcal{G}} G^{\perp\perp} \mathcal{G}^{\{x\varrho\}} \mathfrak{m}_x^1]}{H} - \frac{\mathcal{G}^{xx}}{2\mathcal{G}^{\varrho\varrho}} (\mathfrak{m}_x^1)^2 \right] (E_{\perp}^+ - E_{\perp}^-) \\
& - \frac{4\varrho_h^2}{R^2} \frac{\mathcal{G}^{\{t\varrho\}}}{\mathcal{G}^{\varrho\varrho}} \mathfrak{w} (E_{\perp}^+)' - \frac{2\varrho_h^2}{R^2} \frac{\partial_{\rho} [\sqrt{-\mathcal{G}} G^{\perp\perp} \mathcal{G}^{\{t\varrho\}} (\mathfrak{w} - \mathfrak{m}_t^3)]}{H} E_{\perp}^+,
\end{aligned} \tag{6.157}$$

where index symmetrization is defined as  $\mathcal{G}^{\{MN\}} = (\mathcal{G}^{MN} + \mathcal{G}^{NM})/2$  and

$$\mathfrak{m}_t^3 = \frac{\gamma}{2\sqrt{2}\pi} \tilde{A}_t^3. \tag{6.158}$$

### 6.5.2 Expansion of the DBI Action

In this section we determine the equation of motion for the fluctuation  $a_{\perp}^3$  in the background determined by the DBI action expanded to fourth order in  $F$ . To obtain the quadratic action in the field  $a_{\perp}^3$ , we first have to expand the DBI action (6.143) to fourth order in the full gauge field strength  $\hat{F}$ , and expand the result to second order in  $a_{\perp}^3$ . Due to the symmetries of our setup, the equation of motion for the fluctuation  $a_{\perp}^3$  at zero spatial momentum decouples from the other equations of motion, such that we can write down an effective Lagrangian for the fluctuation  $a_{\perp}^3$ .

This effective Lagrangian is given by

$$\begin{aligned}
\mathcal{L}_{\text{eff}}^{a_2^3} = & \sqrt{-G} \text{STr} \left[ \frac{1}{2} G^{\perp\perp} G^{\rho\rho} (\check{F}_{\perp\rho}^3)^2 (\sigma^3)^2 + \frac{1}{2} G^{tt} G^{\perp\perp} (\check{F}_{t\perp}^3)^2 (\sigma^3)^2 \right. \\
& + \frac{1}{2} G^{\perp\perp} G^{xx} (\check{F}_{\perp x}^2)^2 (\sigma^2)^2 + \frac{1}{4} G^{xx} G^{\rho\rho} (F_{x\rho}^1)^2 \left[ G^{tt} G^{\perp\perp} (\check{F}_{t\perp}^3)^2 (\sigma^3 \sigma^1)^2 \right. \\
& \left. - G^{\perp\perp} G^{\rho\rho} (\check{F}_{\perp\rho}^3)^2 (\sigma^3 \sigma^1)^2 - G^{\perp\perp} G^{xx} (\check{F}_{\perp x}^2)^2 (\sigma^2 \sigma^1)^2 \right] \\
& + \frac{1}{4} G^{tt} G^{xx} (F_{tx}^2)^2 \left[ G^{\perp\perp} G^{\rho\rho} (\check{F}_{\perp\rho}^3)^2 (\sigma^3 \sigma^2)^2 - G^{tt} G^{\perp\perp} (\check{F}_{t\perp}^3)^2 (\sigma^3 \sigma^2)^2 \right. \\
& \left. - G^{\perp\perp} G^{xx} (\check{F}_{\perp x}^2)^2 (\sigma^2)^4 \right] + \frac{1}{4} G^{tt} G^{\rho\rho} (F_{t\rho}^3)^2 \left[ G^{\perp\perp} G^{xx} (\check{F}_{\perp x}^2)^2 (\sigma^3 \sigma^2)^2 \right. \\
& \left. - G^{tt} G^{\perp\perp} (\check{F}_{t\perp}^3)^2 (\sigma^3)^4 - G^{\perp\perp} G^{\rho\rho} (\check{F}_{\perp\rho}^3)^2 (\sigma^3)^4 \right] \\
& + G^{tt} G^{\perp\perp} G^{xx} G^{\rho\rho} \left[ (F_{x\rho}^1)(F_{t\rho}^3)(\check{F}_{t\perp}^3)(\check{F}_{\perp x}^2) \sigma^1 \sigma^2 (\sigma^3)^2 \right. \\
& \left. - (F_{tx}^2)(F_{t\rho}^3)(\check{F}_{\perp\rho}^3)(\check{F}_{\perp x}^2) (\sigma^2 \sigma^3)^2 \right] \\
& \left. - G^{tt} G^{\perp\perp} G^{xx} G^{\rho\rho} (F_{tx}^2)(F_{x\rho}^1)(\check{F}_{t\perp}^3)(\check{F}_{\perp\rho}^3) \sigma^1 \sigma^2 (\sigma^3)^2 \right]. \tag{6.159}
\end{aligned}$$

Using the results for the symmetrized traces (6.97), the effective Lagrangian simplifies to

$$\begin{aligned}
\mathcal{L}_{\text{eff}}^{a_2^3} = & \sqrt{-G} \left[ \frac{1}{2} G^{\perp\perp} G^{\rho\rho} (\check{F}_{\perp\rho}^3)^2 + \frac{1}{2} G^{tt} G^{\perp\perp} (\check{F}_{t\perp}^3)^2 + \frac{1}{2} G^{\perp\perp} G^{xx} (\check{F}_{\perp x}^2)^2 \right. \\
& + \frac{1}{6} G^{xx} G^{\rho\rho} (F_{x\rho}^1)^2 \left[ G^{tt} G^{\perp\perp} (\check{F}_{t\perp}^3)^2 - G^{\perp\perp} G^{\rho\rho} (\check{F}_{\perp\rho}^3)^2 - G^{\perp\perp} G^{xx} (\check{F}_{\perp x}^2)^2 \right] \\
& + \frac{1}{2} G^{tt} G^{\rho\rho} (F_{t\rho}^3)^2 \left[ \frac{1}{3} G^{\perp\perp} G^{xx} (\check{F}_{\perp x}^2)^2 - \frac{1}{2} G^{\perp\perp} G^{\rho\rho} (\check{F}_{\perp\rho}^3)^2 - \frac{1}{2} G^{tt} G^{\perp\perp} (\check{F}_{t\perp}^3)^2 \right] \\
& + \frac{1}{2} G^{tt} G^{xx} (F_{tx}^2)^2 \left[ -\frac{1}{3} G^{tt} G^{\perp\perp} (\check{F}_{t\perp}^3)^2 - \frac{1}{2} G^{\perp\perp} G^{xx} (\check{F}_{\perp x}^2)^2 + \frac{1}{3} G^{\perp\perp} G^{\rho\rho} (\check{F}_{\perp\rho}^3)^2 \right] \\
& \left. - \frac{2}{3} G^{tt} G^{\perp\perp} G^{xx} G^{\rho\rho} (F_{tx}^2)(F_{t\rho}^3)(\check{F}_{\perp\rho}^3)(\check{F}_{\perp x}^2) \right]. \tag{6.160}
\end{aligned}$$

The equation of motion for  $a_{\perp}^3$  with zero spatial momentum determined by the Euler-Lagrange equation is given by

$$\begin{aligned}
0 = & (a_{\perp}^3)'' + \frac{\partial_{\rho} \mathcal{H}}{\mathcal{H}} (a_{\perp}^3)' - \frac{\rho_h^4}{R^4} \left[ 4 \left( \frac{\mathcal{H}^{tt}}{\mathcal{H}^{\rho\rho}} \mathbf{m}^2 + \frac{\mathcal{H}^{xx}}{\mathcal{H}^{\rho\rho}} (\mathbf{m}_x^1)^2 \right) \right. \\
& \left. + \frac{8}{3} \frac{\partial_{\rho} [\sqrt{-G} G^{tt} G^{\perp\perp} G^{xx} G^{\rho\rho} \check{A}_t^3 (\partial_{\rho} \check{A}_t^3) (\mathbf{m}_x^1)^2]}{\mathcal{H}} \right] a_{\perp}^3, \tag{6.161}
\end{aligned}$$

where

$$\begin{aligned}
\mathcal{H} &= \sqrt{-G} G^{\perp\perp} \mathcal{H}^{\varrho\varrho} . \\
\mathcal{H}^{tt} &= G^{tt} \left[ 1 + \frac{1}{3} G^{xx} G^{\varrho\varrho} (\partial_\rho \tilde{A}_x^1)^2 - \frac{1}{2} G^{tt} G^{\varrho\varrho} (\partial_\rho \tilde{A}_t^3)^2 - \frac{1}{3} \frac{\varrho_h^4}{R^4} G^{tt} G^{xx} \left( \frac{\gamma}{\sqrt{2}} \tilde{A}_x^1 \tilde{A}_t^3 \right)^2 \right] , \\
\mathcal{H}^{xx} &= G^{xx} \left[ 1 - \frac{1}{3} G^{xx} G^{\varrho\varrho} (\partial_\rho \tilde{A}_x^1)^2 - \frac{1}{3} G^{tt} G^{\varrho\varrho} (\partial_\rho \tilde{A}_t^3)^2 - \frac{1}{2} \frac{\varrho_h^4}{R^4} G^{tt} G^{xx} \left( \frac{\gamma}{\sqrt{2}} \tilde{A}_x^1 \tilde{A}_t^3 \right)^2 \right] , \\
\mathcal{H}^{\varrho\varrho} &= G^{\varrho\varrho} \left[ 1 - \frac{1}{3} G^{xx} G^{\varrho\varrho} (\partial_\rho \tilde{A}_x^1)^2 - \frac{1}{2} G^{tt} G^{\varrho\varrho} (\partial_\rho \tilde{A}_t^3)^2 + \frac{1}{3} \frac{\varrho_h^4}{R^4} G^{tt} G^{xx} \left( \frac{\gamma}{\sqrt{2}} \tilde{A}_x^1 \tilde{A}_t^3 \right)^2 \right] .
\end{aligned} \tag{6.162}$$

We introduce the factors  $\mathcal{H}^{MN}$  to emphasize the similarity to the equation of motion obtained by the adapted symmetrized trace prescription (6.154).

### 6.5.3 Results and Comparison of the Two Prescriptions

#### Conductivity

We calculate the frequency-dependent conductivity  $\sigma(\omega)$  using Kubo's formula,

$$\sigma(\omega) = \frac{i}{\omega} G_{3,3}^{\perp\perp}(\omega, q = 0) , \tag{6.163}$$

where  $G_{3,3}^{\perp\perp}$  is the retarded Green function of the current  $J_3^\perp$  dual to the fluctuation  $a_\perp^3$ , which we calculate using the method obtained in section 4.3.1. The current  $J_3^\perp$  is the analog to the electric current since it is charged under the  $U(1)_3$  symmetry. In real space it is transverse to the condensate. Since this fluctuation is the only one which transforms as a vector under the  $SO(2)$  rotational symmetry, it decouples from the other fluctuations of the system.

The real part of the frequency-dependent conductivity  $\text{Re } \sigma(\omega)$  is presented in figure 6.30, 6.31, 6.32, 6.34. It shows the appearance and growth of a gap as we increase the condensate  $\tilde{n}_x^1$ . The conductivity gap originates in a pseudo gap already present right above  $T_c$ , as can be seen for example from the red curve in figure 6.30. By pseudo gap we mean a well-defined gap in the conductivity at low frequency in which the conductivity is not identically zero [243]. Both calculational prescriptions – the adapted symmetrized trace prescription and the expansion of the DBI action to fourth order in the field strength – yield qualitatively very similar results as can be seen by comparing figures 6.32 and 6.34. As a further distinct effect when using the adapted symmetrized trace prescription, figure 6.30, 6.31, 6.32 show prominent peaks which we interpret as mesonic excitations below. Increasing the quark mass  $M_q$  from zero to a finite value, these meson peaks become sharper, i. e. more quasiparticle-like. This is reminiscent of results for condensed matter systems where prominent quasiparticle peaks appear (e. g. [244]). In figure 6.31 at fixed  $\mu/M_q = 3$ , the sharp

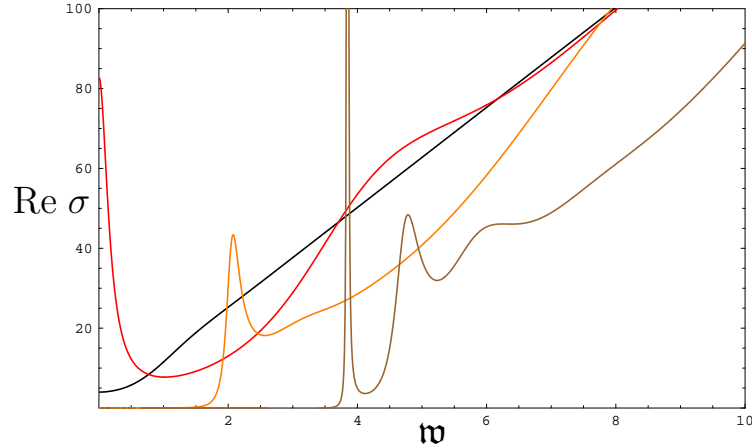


**Figure 6.30:** Real part of conductivity,  $\text{Re } \sigma$ , in units of  $N_f N_c T / (16\pi)$  versus the dimensionless frequency  $\omega = \omega / (2\pi T)$  for massless quarks computed from the adapted symmetrized trace prescription. Distinct curves correspond to  $T/T_c = \infty$  (black), 1 (red), 0.5 (orange) and 0.28 (brown). By decreasing the temperature below the critical one, a gap where the conductivity is approximately zero appears which is a characteristic feature of a superconductor. In addition, prominent peaks arise. This figure is taken from [2].

resonances are also present inside the gap. In contrast to the adapted symmetrized trace prescription, from the expanded DBI action we obtain less prominent peaks as seen from figure 6.34. In the conductivity obtained from the DBI action expanded to fourth order, the peaks do not appear until we approach small temperatures. We expect that the terms higher order in the field strength dominate the generation of the peaks and therefore the generation of the meson mass. If the higher order terms discussed here are included, we presume that the quasinormal modes which generate these peaks move closer to the real axis.

Using the Kramers-Kronig relation, which connects the real and imaginary part of the complex conductivity, we find a delta peak at  $\omega = 0$  in the real part of the conductivity,  $\text{Re } \sigma(\omega) \sim \pi n_s \delta(\omega)$ . The corresponding  $n_s/\omega$ -behavior in the imaginary part is visualized in figure 6.33. As expected from Ginzburg-Landau theory, our numerics show that the superconducting density  $n_s$  vanishes linearly at the critical temperature,  $n_s \propto (1 - T/T_c)$  for  $T \approx T_c$ . This field theory definition of the superconducting density  $n_s$  yields a quantity with the same linear scaling near  $T_c$  as found in our bulk definition (6.119) of the superfluid density  $\tilde{n}_s$ . This confirms that these two quantities may be identified. Our numerics indeed indicate that  $\tilde{n}_s$  and  $n_s$  are proportional to each other.

Note that for translation invariant systems at finite density, there is a delta peak in the real part of the conductivity even in a normal conducting phase since the charge carriers cannot lose their momentum as seen in section 6.3.3. This peak is called Drude peak. In our system, however, the charge carriers can dissipate their momentum, although our system is translation invariant [245, 246]. The adjoint

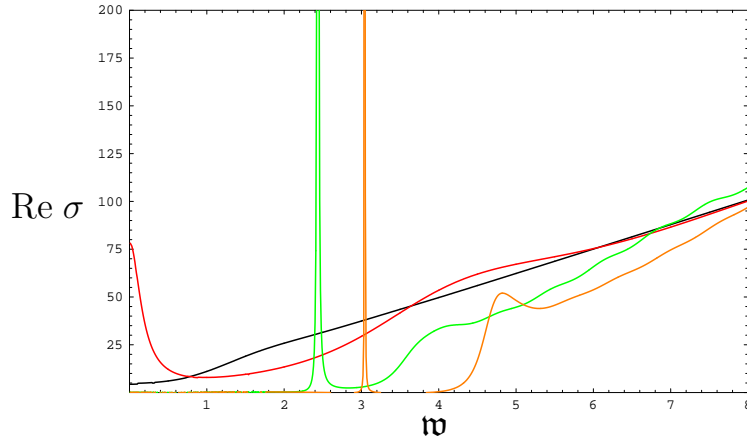


**Figure 6.31:** Real part of conductivity,  $\text{Re } \sigma$ , in units of  $N_f N_c T / (16\pi)$  versus the dimensionless frequency  $\mathfrak{w} = \omega / (2\pi T)$  for massive quarks at fixed  $\mu / M_q = 3$  computed from the adapted symmetrized trace prescription. Distinct curves correspond to  $T / T_c = 10$  (black), 1 (red), 0.6 (green) and 0.5 (orange). As in figure 6.30 a gap appears. Moreover, we observe a prominent peak inside the gap where the conductivity is approximately zero in the green and orange curves. This figure is taken from [2].

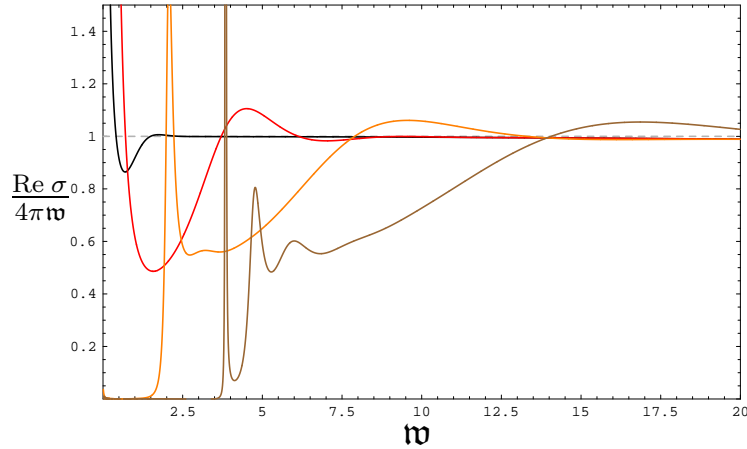


**Figure 6.32:** Scaled real part of conductivity  $\text{Re } \sigma / (4\pi \mathfrak{w})$  in units of  $N_f N_c T / (16\pi)$  versus the dimensionless frequency  $\mathfrak{w} = \omega / (2\pi T)$  for massive quarks at fixed  $\mu / M_q = 3$  computed from the adapted symmetrized trace prescription. Distinct curves correspond to  $T / T_c = 10$  (black), 1 (red), 0.5 (orange) and 0.28 (brown). This figure has been scaled to asymptote to a constant in order to show similarity to the lower-dimensional cases computed from  $AdS_4$  and to show common asymptotics. This figure is taken from [2].

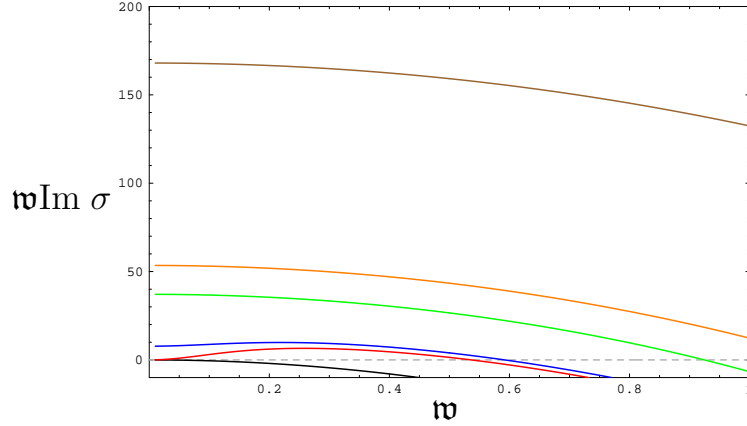


**Figure 6.33:** Scaled imaginary part of conductivity  $w\text{Im}\sigma$  in units of  $N_f N_c T / (16\pi)$  versus the dimensionless frequency  $w = \omega / (2\pi T)$  for massless quarks computed from the adapted symmetrized trace prescription. Distinct curves correspond to  $T/T_c = \infty$  (black), 1 (red), 0.9 (blue), 0.6 (green), 0.5 (orange) and 0.28 (brown). This figure has been scaled to asymptote to a constant at  $w = 0$ . This constant determines the superconducting density  $n_s$ . This figure is taken from [2].

degrees of freedom can transfer momentum at order  $N_c^2$  while the fundamental degrees of freedom only at order  $N_c$ . The adjoint degrees of freedom effectively act as a heat sink into which the flavor fields can dissipate their momentum. Thus, we do not observe a Drude peak in our system.

## Spectral Functions

In order to identify the prominent peaks in the conductivity in terms of field theory quantities as meson resonances, we examine the spectral functions  $\mathfrak{R} = -2\text{Im}G^R$  which are related to the corresponding conductivities by (6.163). Due to this relation the prominent peaks in the conductivity correspond to the prominent peaks in the spectral function, see figure 6.35. As discussed in section 4.3.3 the resonances appearing in the spectral functions of vector fields in the bulk correspond to vector meson excitations in the dual field theory. Moving to higher quark mass parameter  $m = 2.842$  and chemical potential  $\tilde{\mu}_I = 3.483$  near the meson melting transition, we compare the resulting spectrum, see figure 6.36 to the supersymmetric mass formula obtained in (3.55). The prominent peaks clearly approach the supersymmetric line spectrum from above. The same behavior was found in figure 5.9, where vector mesons were considered also close to the meson melting transition. Note that the accuracy of our numerics becomes insufficient at larger frequencies around  $w \approx 15$ <sup>15</sup>.

<sup>15</sup>The frequency range of validity of our fluctuation numerics increases with quark mass. However, the numerics for the background become worse at large quark masses.

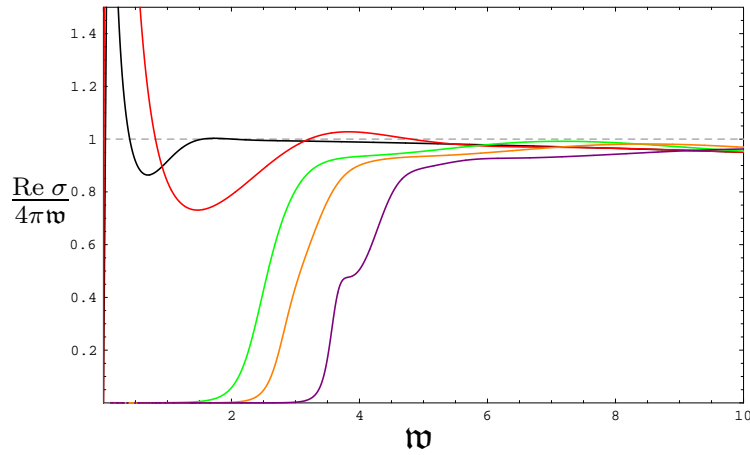


**Figure 6.34:** Scaled real part of conductivity  $\text{Re } \sigma / (4\pi\omega)$  in units of  $N_f N_c T / (16\pi)$  versus the dimensionless frequency  $\omega = \omega / (2\pi T)$  for massless quarks computed from the expanded DBI action. Distinct curves correspond to  $T/T_c = \infty$  (black), 1 (red), 0.6 (green), 0.5 (orange) and 0.39 (purple). This figure has been scaled to asymptote to a constant in order to show similarity to the lower-dimensional cases computed from  $AdS_4$  and to show common asymptotics. This figure is taken from [2].

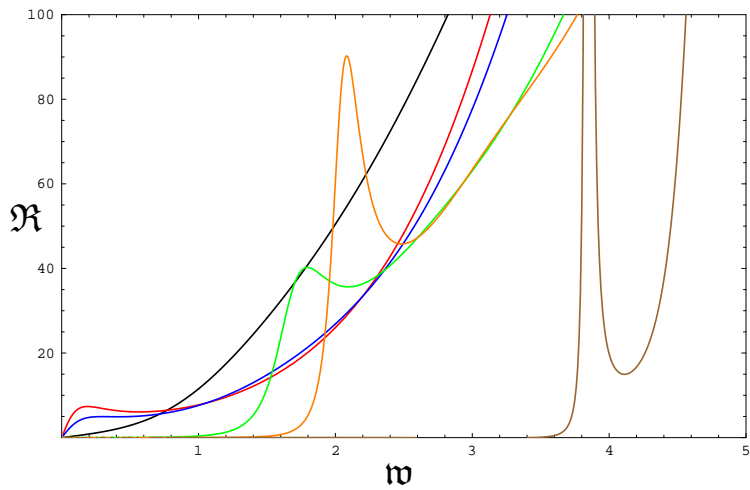


**Figure 6.35:** The spectral function  $\mathfrak{R}$  in units of  $N_f N_c T^2 / 8$  versus the dimensionless frequency  $\omega = \omega / (2\pi T)$  for massless quarks  $M_q = 0$ . The distinct curves corresponds to different temperature (for color coding see figure 6.33). When decreasing the temperature, peaks which correspond to mesonic quasiparticles emerge. This figure is taken from [2].

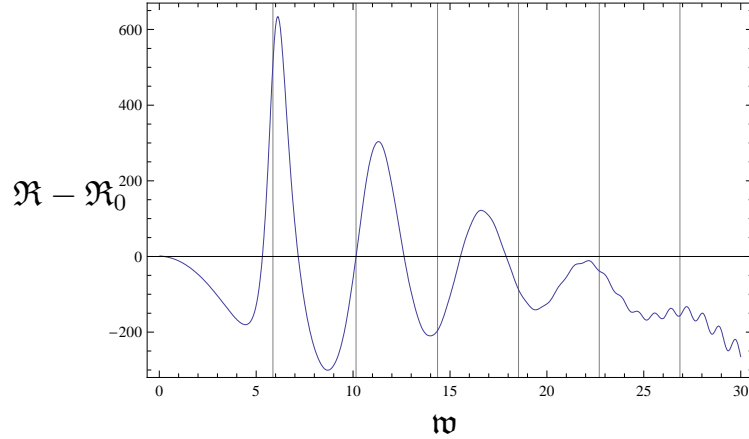


**Figure 6.36:** Finite temperature part of the spectral function  $\mathfrak{R} - \mathfrak{R}_0$  with  $\mathfrak{R}_0 = 4\pi\mathfrak{w}^2$  in units of  $N_f N_c T^2/8$  versus the dimensionless frequency  $\mathfrak{w} = \omega/(2\pi T)$  at finite mass  $m = 2.842$  and chemical potential  $\tilde{\mu} = 3.483$ . The grey lines correspond to the supersymmetric mass spectrum calculated in (3.55). This figure is taken from [2].

### Comments on Stability

As shown in figure 6.37, our setup is stable with respect to the fluctuations  $E_{\perp}^+$  and  $E_{\perp}^-$ . Furthermore, figure 6.37 shows that the quasinormal modes of higher excitations  $n > 1$  move to larger frequencies and closer to the real axis. This corresponds to the formation of stable massive mesons. Such a behavior is known in gauge/gravity duality for mesons which are built from massive quarks (see figure 5.9). Thus, we observe a dynamical mass generation for the mesons as described in the following.

### Dynamical Mass Generation

In this section we discuss dynamical mass generation on the field theory and on the gravity side. For this issue, it is important to distinguish between the cases where the broken symmetry is global or local in the boundary field theory.

**Field theory observation** The superfluid condensate breaks the  $U(1)_3$  symmetry spontaneously in the field theory living on the AdS boundary. According to the Goldstone theorem, this generates one massless Nambu-Goldstone boson in the boundary field theory. Let us now discuss the two different cases:

**Local  $U(1)_3$  symmetry:** If the broken symmetry is gauged, the Nambu-Goldstone boson is eaten by the gauge field  $A^3$  charged under the spontaneously broken  $U(1)_3$  symmetry. In conventional superconductors this mechanism gives mass to the photons which implies the Meissner-Ochsenfeld effect.

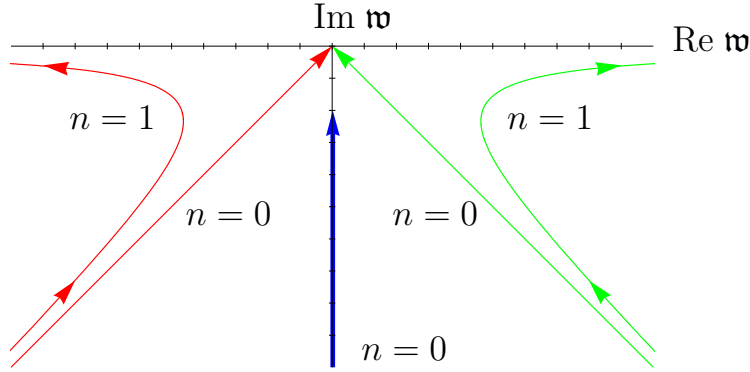


**Figure 6.37:** Movement of quasinormal modes under changes of the temperature  $T$ : The different colors indicate the different fluctuations  $E_{\perp}^{+}$  (red),  $E_{\perp}^{-}$  (green) and  $a_{\perp}^3$  (blue). The higher excitations of the fields  $E_{\perp}^{+}$  and  $E_{\perp}^{-}$  behave as excitations with a non-zero quark mass. This indicates a dynamical generation of the meson mass. This figure is taken from [1].

**Global  $U(1)_3$  symmetry:** If the broken symmetry is global, there is no dynamical gauge field which eats the Nambu-Goldstone boson. Thus, the Nambu-Goldstone boson remains present in the spectrum. Since this is the case in our setup, we need to identify this Nambu-Goldstone boson in the spectrum. In general, the Nambu-Goldstone boson corresponds to the phase of the condensate which parametrizes the coset space  $U(1)_3/\mathbb{Z}_2$ . In our setup, the fluctuations  $E_{\perp}^{+}$  and  $E_{\perp}^{-}$  defined above (6.156) are charged under the  $U(1)_3$  symmetry such that the Nambu-Goldstone boson can be found in these fluctuations (see figure 6.37).

Although in our case the broken symmetry is global, we, nevertheless, observe dynamical mass generation as seen for instance in figures 6.35 and 6.37. Therefore, in our setup, a more subtle mechanism than the ordinary Higgs mechanism generates the meson masses dynamically. Let us explain this mechanism in the dual gravity setup.

**Gravity explanation** According to the AdS/CFT dictionary, a global symmetry in the boundary field theory is mapped to a local symmetry in the gravity theory. Thus, the  $SU(2)$  symmetry of the two D7-branes is local in the gravity theory. In this paper we find new solutions to the equations of motion with non-vanishing gauge field components  $A_t^3$  and  $A_x^1$ . Since the gravity action is unchanged and therefore still  $SU(2)$  invariant, these non-zero components break the  $SU(2)$  gauge symmetry spontaneously which generates in total three Nambu-Goldstone bosons. They are eaten by the gauge fields which then become massive. Let us now discuss the corresponding mass terms in more detail.

First we consider a non-zero  $SU(2)$  isospin chemical potential  $A_t^3$  which generates the mass term  $(A_t^3)^2 (a^{1,2})^2$  for the fluctuations  $a^{1,2}$ . This new term shifts the quadratic fluctuation term in the action, i. e. its energy by the value of the field  $A_t^3$ .

For the spectral function of the dual field theory this results in a shift of the meson resonance peaks, see figure 5.9.

Second we consider the non-zero gauge field component  $A_x^1$  which generates a mass term  $(A_x^1)^2(a^3)^2$  for the fluctuation  $a^3$ . We expect that this mass term shifts the quasinormal frequencies of this system in the complex plane. That results in generation and shift of the resonance peaks in the spectral function as well as generation of the gap structure in the conductivity. To make more precise statements, the spectrum of quasinormal modes needs to be studied in presence of these fields.



# Conclusion and Outlook

In this thesis several applications of gauge/gravity duality to real-world phenomena have been presented. In particular, we have concentrated on strongly coupled systems at finite temperature and finite chemical potentials which we have described by the  $U(2)$  Einstein-Yang-Mills theory and the D3/D7 brane model. In the following my own results on which this thesis is based are summarized.

## 7.1 Quasinormal Modes of Massive Charged Flavors

Our extensive study of the quasinormal modes of the D3/D7-brane system in section 4.3.3 and 5.3.2 has revealed some interesting relations between previously known and unknown phenomena. As a main result, we have shown that the system is completely stable above the critical baryon density  $(\tilde{n}_B)_c = 0.00315$  as long as the isospin chemical potential is zero. This means that the spectrum of scalar excitations does *not* contain any tachyonic mode. Also in this regime, the spectrum of mesonic excitations in the field theory – corresponding directly to distinct quasinormal modes – is de-singularized at low temperature or large quark mass through the explicit breaking of a scaling symmetry near the limiting embedding. For instance the different meson excitations behave in accordance with the mass formula derived for the supersymmetric case [39]. Furthermore, for the regime below the critical density, i. e. for  $\tilde{n}_B < 0.00315$ , we have established the connection between the black hole to black hole phase transition at finite charge density on the one hand and the tachyonic scalar on the other. Using the Schrödinger formulation of the problem we have explained the movement of scalar and vector quasinormal modes in the complex frequency plane in great detail. A universal feature of all Schrödinger potentials at finite charge density is that they develop a barrier near the black hole horizon which hides the horizon and the black hole from the boundary. Consequently, the dissipation decreases with increasing density and the quasinormal modes asymptote to a normal mode behavior. This behavior has also been observed in [118] in a setup where a black hole in  $AdS_4$  develops scalar hair, i. e. there is also a charge density

distributed near the horizon.

At vanishing baryon density but finite momentum, we found a critical wavelength at which the hydrodynamic approximation explicitly breaks down. Below that wavelength the system at late times is no longer governed by hydrodynamics but by (propagating) collisionless modes only. A few unresolved issues remain for zero baryon density. In that case we found a spiraling behavior of the first quasinormal mode's trajectory for both scalars and vectors. The number,  $n$ , of loops appears to be directly related to what we coined "attractor" frequencies  $\omega_n$  to which all QNM-trajectories asymptote if their momentum  $k_n$  lies in a certain momentum regime  $k_{n-1} < k_n \leq k_{n+1}$ . A direct relation remains unknown. In the same case we found that a scalar becomes tachyonic at low enough temperature. This instability might give rise to a condensation process or more generally to a phase transition as suggested by the hydrodynamic behavior of the scalar mode where it just becomes tachyonic. It is interesting to ask what the new phase could be and if it exists at all.

The methods which we have developed in these studies can be reused to study other systems. For instance the following study relies on these techniques.

## 7.2 Black Hole Instabilities

We have found an interesting instability of black holes in asymptotically AdS spacetimes. In particular, we consider the  $SU(2)$  Einstein-Yang-Mills theory. If we neglect the back-reaction of the gauge fields on the background metric, a solution of the equations of motion is given by an asymptotically Schwarzschild black hole.

In addition, we turn on a magnetic field  $F_{xy} = B\tau^3$ , where  $\tau^3$  is one of the three generators of  $SU(2)$ . By investigating the fluctuations of the gauge field around the Schwarzschild black hole, we find in [7] that the system becomes unstable above a critical value  $\mathfrak{B}_c \approx 5.15$  of the magnetic field. In particular, we identify the quasinormal mode which crosses the real axis into the upper half plane. This result can be confirmed in two different ways. First, we calculate an effective action for the fluctuations and show that these fluctuations get a negative mass squared, which drops below the Breitenlohner-Freedman bound for large enough magnetic fields. Second, we rewrite the equations of motion into a Schrödinger-like wave equation with an effective potential  $V_s$  and show that  $V_s$  has a bound state for large enough magnetic fields. The bound state signals the instability of the system.

Note that here we have turned on a magnetic field for one of the three generators of  $SU(2)$  and not for a  $U(1)$  gauge group. One might think that this is not so common in gauge/gravity duality. However, as we now discuss, a similar structure [196, 197] also arises in the Sakai-Sugimoto model [247]. To see this, let us consider the Sakai-Sugimoto setup with two flavors (with electric charges  $q_1$  and  $q_2$ ). The flavor degrees of freedom are described by two pairs of  $D8/\overline{D8}$ -branes. Part of the dynamics of the flavor degrees of freedom is therefore given by a non-Abelian gauge theory with gauge group  $U(2)_L \times U(2)_R$ . Note that the gauge group on the gravity side corresponds to the dual flavor symmetry on the field theory side. In the Sakai-Sugimoto model

the electromagnetic gauge group with generator  $Q = \text{diag}(q_1, q_2)$  is realized as a subgroup of  $U(2)_L \times U(2)_R$ . Thus, in the case  $q_1 \neq q_2$ , the magnetic field  $\mathcal{B}_{\text{em}}$  has a baryon and isospin component, i. e.

$$Q\mathcal{B}_{\text{em}} = \frac{q_1 + q_2}{2}\mathcal{B}_{\text{em}}\mathbb{1} + \frac{q_1 - q_2}{2}\mathcal{B}_{\text{em}}\tau_3. \quad (7.1)$$

Although we aim to study the effect of the  $U(1)$  magnetic field  $\mathcal{B}_{\text{em}}$ , we have to consider a non-vanishing magnetic field for the isospin component. Note that already in [196,197], evidence was given that the vacuum at zero temperature is unstable for large enough magnetic fields. The results presented here indicate that such an instability arises not only in the Sakai-Sugimoto model but also in the simplest possible toy model at finite temperature for which we can explicitly study the quasinormal modes.

This instability gives rise to interesting questions: What is the true ground state of the system and what are its properties? Is it a superfluid state? Can we realize this ad hoc toy model in string theory, e. g. in the D3/D7 brane model? By addressing these questions, we expect in particular to obtain further information about the QCD vacuum instability at finite  $B$  field discussed in [139–142]. As our results suggest, a more general form of this instability may occur also at finite temperature in non-confining field theories.

## 7.3 Holographic p-wave Superfluids

The investigation of holographic p-wave superfluids is the central point of this thesis. My results are presented in [1, 2, 4–6, 8] and in chapter 6 of this thesis. To conclude these studies, we summarize the main results.

### 7.3.1 Hairy Black Hole Solution

We have studied asymptotically AdS charged black holes in  $(4 + 1)$ -dimensional  $SU(2)$  Einstein-Yang-Mills theory with back-reaction of the gauge fields in [4]. Our numerical solutions show that as the temperature decreases the black holes grow vector hair. Via gauge/gravity duality, this process appears as a phase transition to a p-wave superfluid state in a strongly-coupled dual field theory. We have shown that the order of the phase transition depends on the strength of the back-reaction: For small back-reaction, the transition is second order, while for larger values the transition is first order. By increasing the strength of the back-reaction, the transition temperature can be tuned to zero such that we obtain a first order quantum phase transition.

### 7.3.2 Holographic Vector Meson Condensate

In [1, 2] we have found the first holographic realization of superfluidity which is embedded in string theory. Due to the string theory embedding, the dual field

theory action is known explicitly. This is a big advantage compared to the bottom-up models. For instance we may interpret this new state as a  $\varrho$  meson superfluid on the field theory side. On the string theory side, the condensation process corresponds to a recombination of strings which leads to a thermodynamically favored configuration. From a technical point of view, we compare two different approaches for evaluating the non-Abelian DBI action involved (expansion to fourth order and a new modified trace evaluation procedure which we propose) and find the same physical results in both approaches, at least qualitatively.

### 7.3.3 Holographic Superfluidity in Imbalanced Mixtures

In [6] we have considered holographic models of field theories with global  $U(2)$  symmetry. The  $U(2)$  symmetry allows us to switch on two chemical potentials: a baryon and an isospin chemical potential. Holographically, we have realized the global  $U(2)$  symmetry in two different ways: first by a  $U(2)$  Einstein-Yang-Mills theory and second by the D3/D7 brane setup with two coincident D7-branes. We have mapped out the phase diagrams for both systems and found interesting similarities and differences which we have already discussed in the introduction of chapter 6.

It would be interesting to study the origin of these differences in the phase diagrams in more detail. For example a detailed analysis of how the order of the phase transition can be changed by varying the form of the interaction would be attractive. In addition, the study of back-reaction effects in the D3/D7 model may lead to a new behavior in the phase diagrams. Furthermore, it is important to establish a full understanding of the instability mechanism in the D3/D7 brane setup and its difference to the violation of the Breitenlohner-Freedman bound found in the Einstein-Yang-Mills theory. This may lead to a characterization of the universality classes of quantum phase transitions.

### 7.3.4 Transport in Anisotropic Superfluids

In [5, 8] we have studied transport phenomena in holographic p-wave superfluids constructed in the  $SU(2)$  Einstein-Yang-Mills theory. We have classified the perturbations about equilibrium according to their transformation properties under the symmetry group. At zero momentum there is an  $SO(2)$  symmetry remaining which allows us to divide the perturbations into different helicity sectors: helicity two, one and zero states. While the helicity two state is trivial and leads to the universal ratio of shear viscosity to entropy density, the helicity one states are non-trivial. They mix under the RG flow. Due to a  $\mathbb{Z}_2$  parity, this sector splits into two blocks. In the first block we have found the thermoelectric effect transversal to the direction favored by the condensate. In the second block we have obtained two interesting new phenomena: a non-universal shear viscosity and a flexoelectric effect. These two effects are due to the anisotropy of our system.

Anisotropic fluids have been studied in particular in the context of nematic crystals whose hydrodynamic description is given in [234, 239]. In our study, we have

initiated the connection of the hydrodynamic description of anisotropic fluids with gauge/gravity duality. The results we have obtained so far are in agreement with this description, i.e. the transport coefficients which we have found here can be related to the ones in [239]. However, since we have not studied the helicity zero modes in full detail, we have not yet described all transport properties. In particular, the thermoelectric effect along the condensate as well as the coefficients  $\zeta_x$ ,  $\zeta_y$  and  $\lambda$  described in section 6.3.1 are still missing. It would be interesting to study these coefficients in detail. This study may also lead to a covariant hydrodynamic description of anisotropic superfluids.

In addition, several interesting questions are still not answered: What is the fluid's response to nonzero superfluid velocities? In similar systems, sufficiently large superfluid velocities also changed the transition from second to first order [93, 248]. What is the speed of sound, which need *not* be the same in all directions since rotational symmetry is broken, or the speeds of second and fourth sounds?

Furthermore, analytic results close to the phase transition can be found for small values of back-reaction [241]. On the one hand, this analytic approach allows for a detailed study of the transport coefficients close to the phase transition. On the other hand, it also permits us to use the fluid/gravity correspondence [135, 136] to obtain the full hydrodynamic description of the system directly from gravity. It would be interesting to follow this line of thought further.

## 7.4 Outlook

Let us now discuss some general developments to which gauge/gravity duality may contribute in the future.

### 7.4.1 Critical Phenomena

Critical phenomena describe the physics at critical points, e.g. second order phase transitions. At these critical points, some observables behave as e.g.  $(T - T_c)^\alpha$  when the critical temperature  $T_c$  is approached.  $\alpha$  is named critical the exponent. Interestingly, the critical exponents take the same value for very different physical systems. They are believed to be universal. For static observables, e.g. the order parameter, the critical exponents can be calculated by Landau theory. However, the critical exponents for dynamical observables, e.g. viscosity, are still under debate.

Since gauge/gravity duality is a suitable framework to describe dynamical processes, we can especially look at these critical exponents in holographic models which feature a critical point. The critical exponents can be explicitly calculated and compared to the general classification of the dynamical critical phenomena developed in [249]. An example is the critical behavior of the non-universal shear viscosity in the p-wave superfluid discussed in section 6.3.4. Detailed studies of critical phenomena in the  $\mathcal{N} = 4$  Super-Yang-Mills theory and in the  $\mathcal{N} = 2^*$  theory can be found in [250–252]. These explicit studies contradict the general theory of [249]. There-

fore, the general classification of critical phenomena is not complete and should be enlarged to incorporate the new universality classes. In the same sense, the new BKT-like transition which has been discovered recently [225] should also be included. In the future, gauge/gravity considerations should make it possible to understand these universality classes or to discover yet unknown ones.

### 7.4.2 Hydrodynamics

As we have learned in the recent years, gauge/gravity duality is very powerful to describe hydrodynamics. These studies have increased in number since the discovery of the fluid/gravity correspondence [135, 136]. Einstein's equation together with regularity requirements turn in to the equations of motions of the boundary fluid with specific values for the transport coefficients. By using these techniques, new transport coefficients have been revealed and analyzed (see e.g. [214, 215, 253]). In this sense, more transport coefficients may still be discovered. Especially in anisotropic fluids, e.g. holographic p-wave superfluids, improvements may still be possible.

### 7.4.3 Universality

The most famous universality in gauge/gravity duality, is the universal value of the shear viscosity to entropy ratio. A reasonable question to ask is now: Are there other values which share a similar universality? Interestingly, for superconductors there is an empirical law, called Homes' Law [254, 255], which universally relates the superfluid density at zero temperature to the dc conductivity at the critical temperature. So far, the relation is not understood theoretically. Can gauge/gravity duality help to shed light on this law? Maybe. By using sum rules and the Drude formula, it can be shown that the relation is based on a time scale which universally scales with the critical temperature. The idea is now to calculate several time scales holographically and compare their scaling. For instance the diffusion constants we discussed in (4.157), (5.66) and (5.67) define time scales. Unfortunately, the charge diffusion constants at finite chemical potential (5.66) and (5.67) do not scale in the right way, strictly speaking. However, the deviation is not that big and it may still agree with the data. Accordingly, it seems to be worth following this line of thought further.

To conclude, gauge/gravity duality is a powerful tool for analyzing different real-world phenomena. Thus, we believe that it will give answers to multiple questions in the future. Moreover, holography has also uncovered several new interesting phenomena and more are expected. So, keep exploring.

## Acknowledgments

First of all, I would like to express my gratitude to Johanna Erdmenger for her tremendous efforts in supervising my work during the last years. I am very thankful for her patience, permanent help and the willingness to discuss problems and achievements at any time which lead to a very stimulating and solitary atmosphere in our work group.

Furthermore, I would like to thank Dieter Lüst not only for working through this thesis as an interested second referee, but primarily for providing brilliant working conditions in his groups at the Max-Planck-Institut für Physik (Werner-Heisenberg-Institut) and at Ludwig-Maximilians-Universität in Munich. Especially, I would like to include the opportunity to visit a vast amount of different workshops and conferences which enriched my time as a Ph.D. student.

I also thank the International Max Planck Research School (IMPRS) for providing various useful seminars and promoting interchange among the Ph.D. students.

Moreover, I am thankful to Martin Ammon, Viviane Grass, Constantin Greubel, Matthias Kaminski, Karl Landsteiner, Hai Ngo, Andy O'Bannon, Francisco Peña-Benitez, Felix Rust, Migael Strydom and Hansjörg Zeller for valuable discussions and fruitful collaborations.

I am grateful to Alex Buchel, Aleksey Cherman, Veselin Filev, Michael Haack, Sebastian Halter, Carlos Hoyos, Kristan Jensen, Junji Jia, Andreas Karch, Elias Kiritsis, Pavel Kovtun, Shu Lin, Javier Mas, John McGreevy, Rene Meyer, Steffen Müller, Robert Myers, Makoto Natsuume, Chris Pagnutti, Giuseppe Policastro, Mark Van Raamsdonk, Mukund Rangamani, Anton Rebhan, Jonathan Shock, Dam Son, Stephan Steinfurt, Javier Tarrío, Efstratios Tsatis, Amos Yarom, Jan Zaanen and Andrew Zayakin for valuable suggestions and discussions.

I also thank my colleagues, especially, Martin Ammon, Jochen Baumann, Sophia Borowka, Veselin Filev, Jan Germer, Peter Graf, Viviane Grass, Constantin Greubel, Sebastian Halter, Daniel Härtl, Johannes Held, Matthias Kaminski, Phillip Kostka, Clemens Kießig, Ananda Landwehr, Shu Lin, Jonas Lindert, Rene Meyer, Steffen Müller, Andy O'Bannon, Thorsten Rahn, Felix Rust, Oliver Schlotterer, Jonathan Schock, Katja Seidel, Martin Spinrath, Stephan Steinfurt, Migael Strydom and Hansjörg Zeller for sharing many pleasant moments during the last few years.

I am tankful to Johanna Erdmenger, Sebastian Halter, Johannes Held, Steffen Müller, Jonathan Schock, Stephan Steinfurt, Migael Strydom and Hansjörg Zeller for many comments on the manuscript.

Finally, I would like to thank my family, in particular, my parents and my friends for their continuous support and understanding.



## CHAPTER A

# Conventions

### A.1 Units

Throughout this thesis we work in the natural units in which the speed of light  $c$ , Planck's constant  $\hbar$  as well as Boltzmann's constant  $k_B$  are set to one.

### A.2 Convention for Indices

In this thesis we use the following convention for indices:

$A, B, \dots$	Indices for an internal direction, i. e. on $S^5$ or $S^3$	
$M, N, \dots$	10 or 26-dimensional spacetime indices	
$\mathcal{A}, \mathcal{B}, \dots$	Indices for an transverse space of a D-brane	
$\alpha, \beta, \dots$	Indices on a D-brane	(A.1)
$\mu, \nu, \dots$	$d$ -dimensional Minkowski indices	
$a, b, \dots$	Indices labeling the gauge group generators	
$i, j, \dots$	$d - 1$ -dimensional spatial indices if not stated otherwise	



# General Procedures

## B.1 Schrödinger Potentials

This appendix shows how to compute the effective potentials, i. e. the Schrödinger potentials for the scalar and vector fluctuations on the D7-brane. In order to do so the linearized fluctuation equations of motion have to be rewritten in terms of a new radial coordinate  $R^*$ . This procedure has been described before (e. g. in [184], [185]), nevertheless, we include it here for completeness. For convenience, we stick to the notation made use of in [184], and we compute all Schrödinger potentials in the  $\rho$ -coordinates introduced in section 4.2.3.

We are not interested in the higher angular excitations on the  $S^3$ , so we separate the fluctuations according to  $\phi(\rho, S^3) = (\rho - 1)^{-i\mathfrak{w}} y(\rho) \Phi(S^3)$ . Let us consider exclusively fluctuations without angular momentum on the  $S^3$ , i. e.  $\Phi(S^3) = 1$ . All the linearized vector and scalar fluctuation equations of motion are second order ordinary differential equations and can be rewritten in the form

$$-\frac{H_0}{H_1} \partial_\rho [H_1 \partial_\rho y(\rho)] + [\mathfrak{k}^2 H_2 + H_\theta] y(\rho) = \mathfrak{w}^2 y(\rho), \quad (\text{B.1})$$

where  $H_0$ ,  $H_1$ ,  $H_2$  and  $H_\theta$  are in general functions of  $\rho$  and depend on the particular field fluctuation considered.  $H_\theta$  only appears in the scalar fluctuations. For *transverse vector* fluctuations we have

$$H_0 = -\frac{G^{\rho\rho}}{G^{tt}}, \quad H_1 = \sqrt{-G} G^{\rho\rho} G^{xx}, \quad (\text{B.2})$$

$$H_2 = -\frac{G^{zz}}{G^{tt}}, \quad H_\theta = 0. \quad (\text{B.3})$$

For *longitudinal vector* fluctuations we have

$$H_0 = -\frac{G^{\rho\rho}}{G^{tt}}, \quad H_1 = \sqrt{-G} G^{\rho\rho} G^{zz}, \quad (\text{B.4})$$

$$H_2 = -\frac{G^{zz}}{G^{tt}}, \quad H_\theta = 0. \quad (\text{B.5})$$

For *scalar* fluctuations the equations of motion do not take such a simple general form in terms of metric components since the metric itself contains scalar fluctuations. So we choose to write explicitly

$$H_0 = -\frac{f^2 \rho^4 (1 - \chi^2)}{8 \tilde{f} (1 - \chi^2 + \rho^2 \chi'^2)}, \quad (\text{B.6})$$

$$H_1 = \frac{f \tilde{f} \rho^5 (1 - \chi^2)^3}{(1 - \chi^2 + \rho^2 \chi'^2)^{3/2}} \sqrt{1 + \frac{8 \tilde{d}^2}{\tilde{f}^3 \rho^6 (1 - \chi^2)^3}}, \quad (\text{B.7})$$

$$H_\theta = \frac{3 f^2 \tilde{f}^2 \rho 8 (1 - \chi^2)^2 \left[ \tilde{f}^3 \rho^6 (1 - \chi^2)^3 + 8 \tilde{d}^2 (1 - 6 \chi^2) - 144 \tilde{d}^2 f^3 \tilde{f} \rho^9 \chi \chi' (1 - \chi^2)^2 \right]}{8 \left[ \tilde{f}^3 \rho^6 (1 - \chi^2)^3 + 8 \tilde{d}^2 \right]^2}, \quad (\text{B.8})$$

where we do not include  $H_2$  since the above coefficients are computed in the case of vanishing momentum  $\mathfrak{k} = 0$  but at finite density  $\tilde{d}$ . At finite momentum and at vanishing density we have  $H_2 = f^2/\tilde{f}^2$  in addition to the  $\tilde{d} \rightarrow 0$  limits of  $H_0$ ,  $H_1$  and  $H_\theta$  from (B.6). At finite momentum *and* density the scalar fluctuations couple to the vector fluctuations. We will not address this complication in this work.

In any case we can substitute  $y(\rho) = h\psi$  in equation (B.1) to obtain

$$-H_0 \psi'' - H_0 \left( 2 \frac{h'}{h} + \frac{H_1'}{H_1} \right) \psi' + \left[ \mathfrak{k}^2 H_2 + H_\theta - H_0 \left( \frac{h''}{h} + \frac{H_1'}{H_1} \frac{h'}{h} \right) \right] \psi = \mathfrak{w}^2 \psi. \quad (\text{B.9})$$

Introducing the new radial coordinate

$$R_* = \int_{\rho}^{\infty} d\tilde{\rho} / \sqrt{H_0(\tilde{\rho})}, \quad (\text{B.10})$$

we can rewrite the first term  $-H_0 \psi'' = -\partial_{R_*}^2 \psi + H_0' \psi' / 2$ . The special choice of  $h = H_0^{1/4} / H_1^{1/2}$  eliminates all the terms containing  $\psi'$ . Thus, the fluctuation equation of motion, finally, assumes Schrödinger form,

$$-\partial_{R_*}^2 \psi + V_S \psi = E \psi, \quad (\text{B.11})$$

with the effective energy  $E = \mathfrak{w}^2$  and the Schrödinger potential given by

$$V_S = -H_0 \left( \frac{h''}{h} + \frac{H_1'}{H_1} \frac{h'}{h} \right) + \mathfrak{k}^2 H_2 + H_\theta. \quad (\text{B.12})$$

From this general formula the specific scalar, longitudinal and transversal vector Schrödinger potentials may be obtained by substituting for  $H_0$ ,  $H_1$ ,  $H_2$ ,  $H_\theta$ ,  $h$  using the corresponding values from equations (B.6), (B.4) and (B.2), respectively.

## B.2 Constructing the Gauge Covariant Fields

In this section we exemplarily present how gauge covariant fields are constructed. In this example we look at the fluctuations about the hairy black hole which are considered in section 6.2.

### B.2.1 Residual Gauge Transformations

The transformations we have to look at are diffeomorphisms and  $SU(2)$  gauge transformations. On the one hand, we demand that the fields be diffeomorphism invariant, i. e.

$$\delta_\Sigma \Phi = \mathcal{L}_\Sigma \Phi = 0. \quad (\text{B.13})$$

$\mathcal{L}_\Sigma$  is the Lie derivative along  $\Sigma$ , i. e.

$$\begin{aligned} \mathcal{L}_\Sigma g_{MN} &= \nabla_M \Sigma_N + \nabla_N \Sigma_M = \partial_M \Sigma_N + \partial_N \Sigma_M - 2\Gamma_{MN}^P \Sigma_P, \\ \mathcal{L}_\Sigma A_M^a &= \Sigma^P \nabla_P A_M^a + A_P^a \nabla_M \Sigma^P = \Sigma^P \partial_P A_M^a + A_P^a \partial_M \Sigma^P, \end{aligned} \quad (\text{B.14})$$

with  $\Gamma_{MN}^P$  being the Christoffel symbol.

On the other hand they have to be invariant under the  $SU(2)$ ,

$$\Phi \rightarrow M(\Lambda)\Phi = \Phi, \quad (\text{B.15})$$

with  $M(\Lambda)$  being the  $SU(2)$  transformation matrices, this is equivalent to

$$\delta_\Lambda \Phi = 0. \quad (\text{B.16})$$

$\Phi$  stands for the physical modes in our system and is composed of the helicity 0 fields  $\xi_{tx}$ ,  $\xi_t$ ,  $\xi_x$ ,  $\xi_y$ ,  $a_x^a$  and  $a_t^a$ , with  $a = 1, 2, 3$ . The invariance of  $\Phi$  under the above transformations translates into

$$\delta\Phi = (\delta_\Sigma + \delta_\Lambda)\Phi = \sum_{a=1}^3 (\tau_a \delta a_x^a + \tau_{3+a} \delta a_t^a) + \tau_7 \delta \xi_{tx} + \tau_8 \delta \xi_t + \tau_9 \delta \xi_x + \tau_{10} \delta \xi_y = 0, \quad (\text{B.17})$$

with  $\tau_i$  being  $r$  dependent coefficients.

### Diffeomorphism Invariance

Let us look at the invariance under diffeomorphisms. We begin by defining

$$\begin{aligned} \hat{g}_{MN} &= g_{MN} + h_{MN}, \\ \hat{A}_M^a &= A_M^a + a_M^a. \end{aligned} \quad (\text{B.18})$$

Furthermore, note that  $\Sigma_M$  (and later on  $\Lambda$ ) are of the same order as the fluctuations.

Through the gauge choice,  $h_{Mr} = 0$ , we can determine the form of  $\Sigma_M$  up to some constants, because

$$\begin{aligned} \mathcal{L}_\Sigma \hat{g}_{Mr} &= 0 \\ \Rightarrow \partial_M \Sigma_r + \partial_r \Sigma_M - 2\Gamma_{Mr}^P \Sigma_P &= 0. \end{aligned} \quad (\text{B.19})$$

Note that we just need the Christoffel symbols to zeroth order in fluctuations, i. e. the background Christoffel symbols. They are

$$\begin{aligned} \Gamma_{rr}^r &= \frac{c_4'}{c_4}, & \Gamma_{tr}^t &= \frac{c_1'}{c_1}, & \Gamma_{xr}^x &= \frac{c_2'}{c_2}, & \Gamma_{yr}^y &= \frac{c_3'}{c_3}, \\ \Gamma_{tt}^r &= \frac{c_1 c_1'}{c_4^2}, & \Gamma_{xx}^r &= -\frac{c_2 c_2'}{c_4^2} & \text{and} & & \Gamma_{yy}^r &= -\frac{c_3 c_3'}{c_4^2}, \end{aligned} \quad (\text{B.20})$$

with

$$ds^2 = g_{MN} dx^M dy^N = -c_1(r)^2 dt^2 + c_2(r)^2 dx^2 + c_3(r)^2 (dy^2 + dz^2) + c_4(r)^2 dr^2. \quad (\text{B.21})$$

We get 4 equations (+1 for the  $z$  component which is exactly the same as the one for the  $y$  component), which read

$$0 = -i\omega \Sigma_r + \Sigma_t' - 2\frac{c_1'}{c_1} \Sigma_t, \quad (\text{B.22a})$$

$$0 = ik \Sigma_r + \Sigma_x' - 2\frac{c_2'}{c_2} \Sigma_x, \quad (\text{B.22b})$$

$$0 = \Sigma_y' - 2\frac{c_3'}{c_3} \Sigma_y, \quad (\text{B.22c})$$

$$0 = 2\Sigma_r' - 2\frac{c_4'}{c_4} \Sigma_r. \quad (\text{B.22d})$$

We work in momentum space, i. e. the ansatz used is

$$\Sigma_M(t, x, r) = \int d^4x e^{ik_\mu x^\mu} \Sigma(\omega, k, r), \quad (\text{B.23})$$

with  $k^\mu = (\omega, k, 0, 0)$ . The solutions to the equations above are

$$\begin{aligned} \Sigma_t(\omega, k, r) &= K_t c_1^2 + i\omega K_r c_1^2 A, \quad \text{with } A = \int dr \frac{c_4}{c_1^2}, \\ \Sigma_x(\omega, k, r) &= K_x c_2^2 - ik K_r c_2^2 B, \quad \text{with } B = \int dr \frac{c_4}{c_2^2}, \\ \Sigma_y(\omega, k, r) &= K_y c_3^2, \\ \Sigma_r(\omega, k, r) &= K_r c_4, \end{aligned} \quad (\text{B.24})$$

with  $K_i$  being constants. Using these solutions in the remaining equations  $\delta_\Sigma \xi_i$ , we get

$$\begin{aligned}\delta_\Sigma \xi_t &= \frac{2i\omega}{c_1^2} \Sigma_t, \\ \delta_\Sigma \xi_x &= \frac{2ik}{c_2^2} \Sigma_x, \\ \delta_\Sigma \xi_y &= 0, \\ \delta_\Sigma \xi_{tx} &= -\frac{i\omega}{c_2^2} \Sigma_x + \frac{ik}{c_2^2} \Sigma_t.\end{aligned}\tag{B.25}$$

Here we see already that  $\xi_y$  is a physical mode.

Applying the same procedure to the gauge fields, i. e.  $\delta_\Sigma a_\mu^a = \mathcal{L}_\Sigma \hat{A}_\mu^a$ , it results in

$$\begin{aligned}\delta_\Sigma a_x^1 &= \frac{w'}{c_4^2} \Sigma_r + \frac{ikw}{c_2^2} \Sigma_x, \\ \delta_\Sigma a_t^3 &= \frac{\phi'}{c_4^2} \Sigma_r + \frac{i\omega\phi}{c_1^2} \Sigma_t.\end{aligned}\tag{B.26}$$

The Lie derivatives of the remaining components vanish.

### $SU(2)$ Gauge Invariance

This transformation only affects the gauge fields, therefore, we do not have to take care about the metric fluctuations here. A field in the adjoint  $SU(2)$  representation transform under the  $SU(2)$  as

$$\delta_\Lambda a_M^a = \nabla_M \Lambda^a(t, x, r) + \epsilon^{abc} A_M^b \Lambda^c.\tag{B.27}$$

Again we constrain the possible  $\Lambda^a$  by using the gauge choice  $a_r^a = 0$ , i. e.

$$\begin{aligned}0 &= \delta_\Lambda a_r^a = \nabla_r \Lambda^a(t, x, r) = \partial_r \Lambda^a(t, x, r) \\ \Rightarrow \Lambda^a(t, x, r) &= \Lambda^a(t, x).\end{aligned}\tag{B.28}$$

We choose the ansatz  $\Lambda^a(t, x) = \int d^4x e^{ik_\mu x^\mu} \Lambda^a(\omega, k)$  with  $k^\mu = (\omega, k, 0, 0)$  to calculate  $\delta_\Lambda a_\mu^a$ . Note that by using the definition above of  $k^\mu$ , the  $y$  and  $z$  components do not mix with the rest and we can forget about them. We end up with

$$\begin{aligned}\delta_\Lambda a_x^1 &= ik\Lambda^1, & \delta_\Lambda a_t^1 &= -i\omega\Lambda^1 - \phi\Lambda^2, \\ \delta_\Lambda a_x^2 &= ik\Lambda^2 - w\Lambda^3, & \delta_\Lambda a_t^2 &= -i\omega\Lambda^2 + \phi\Lambda^1, \\ \delta_\Lambda a_x^3 &= ik\Lambda^3 + w\Lambda^2, & \delta_\Lambda a_t^3 &= -i\omega\Lambda^3.\end{aligned}\tag{B.29}$$

## B.2.2 Physical Fields

Inserting everything into equation (B.17) results in 6 equations, due to the fact that  $\Sigma_t, \Sigma_x, \Sigma_r, \Lambda^1, \Lambda^2$  and  $\Lambda^3$  are independent. The equations are

$$\begin{aligned}
0 &= ik\tau_1 - i\omega\tau_4 + \phi\tau_5, \\
0 &= ik\tau_2 + w\tau_3 - \phi\tau_4 - i\omega\tau_5, \\
0 &= -w\tau_2 + ik\tau_3 - i\omega\tau_6, \\
0 &= -i\omega\tau_7 + 2ik\tau_9 + ikw\tau_1, \\
0 &= 2i\omega\tau_8 + ik\frac{c_1^2}{c_2^2}\tau_7 + i\omega\phi\tau_6, \\
0 &= w'\tau_1 + \phi'\tau_6.
\end{aligned} \tag{B.30}$$

The four physical fields,  $\Phi_i = \sum_{i=1}^{10} \tau_i \cdot$  (Helicity 0 fields), we get by solving above equations, are

$$\begin{aligned}
\Phi_1 &= \xi_y, \\
\Phi_2 &= a_t^1 + \frac{i\omega}{\phi} a_t^2 + \frac{ik(\omega^2 - \phi^2)}{(k^2 - w^2)\phi} a_x^2 + \frac{w(\omega^2 - \phi^2)}{(k^2 - w^2)\phi} a_x^3, \\
\Phi_3 &= \xi_x - \frac{k^2 c_1^2}{\omega^2 c_2^2} \xi_t + \frac{2k}{\omega} \xi_{tx}, \\
\Phi_4 &= a_x^1 + \frac{k}{\omega} a_t^1 - \frac{1}{2} w \xi_x - \frac{w'}{\phi'} a_t^3 + \frac{\phi w'}{2\phi'} \xi_t - \frac{k(\omega^2 w' + w\phi\phi')}{\omega(k^2 - w^2)\phi'} a_x^3 \\
&\quad - i \frac{\omega^2 w w' + k^2 \phi \phi'}{\omega \phi' (k^2 - w^2)} a_x^2.
\end{aligned} \tag{B.31}$$

## B.3 Holographic Renormalization

The goal we are pursuing in this section is to find covariant counterterms which can be subtracted from the action (6.51) and (6.57) in order to make it finite. We follow the lead of [169, 256] to perform the holographic renormalization.

### B.3.1 Asymptotic Behavior

In this section we look at the behavior of the fields at the horizon and at the boundary. We want to calculate real-time retarded Green's functions [174, 220], i. e. at the horizon, besides regularity<sup>1</sup>, we have to fulfill the incoming boundary condition. For this purpose we plug in the ansatz,

$$F(r)|_{r \rightarrow r_H} = \epsilon_h^\beta \sum_{i \geq 0} \epsilon_h^i F_i^h, \quad \text{with} \quad \epsilon_h = \frac{r}{r_h} - 1, \tag{B.32}$$

<sup>1</sup>Even with all fluctuations switched on, there is no need for a further constraint besides  $\phi(r_H) = 0$  at the horizon to guarantee regularity.

for the behavior of the fields near the horizon, into the equations of motion (6.50), (6.55) and (6.56). It turns out that, as expected, we obtain two possibilities for  $\beta$ , namely

$$\beta = \pm i \frac{\omega}{4\pi T}, \quad (\text{B.33})$$

with  $T$  being the temperature. As said before, we choose the solution with the “−” sign which corresponds to the incoming boundary condition. Note that the other solution represents the outgoing boundary condition.

Our ansatz at the boundary is similar to the one used for the background calculation in section 6.1. However, here we have to add a logarithmic term to get a consistent solution (c.f. [169]). Therefore we use

$$F(r)|_{r \rightarrow r_{\text{bdy}}} = \sum_{i \geq 0} \epsilon_b^i \left( F_i^b + \frac{1}{2} \hat{F}_i^b \ln \epsilon_b \right), \quad \text{with} \quad \epsilon_b = \left( \frac{r_h}{r} \right)^2. \quad (\text{B.34})$$

Let us now use the above expansions for the helicity one states. In the case of the equations (6.55), we have 3 independent expansion coefficients at the boundary (4 free parameters from the 2 second order differential equations minus 1 free parameter due to the constraint). We choose them to be  $(a_y^3)_0^b$ ,  $(a_y^3)_1^b$  and  $(\Psi_t)_0^b$ . At the horizon we have already halved the independent parameters by choosing the incoming boundary condition. From the remaining two parameters, we can get rid of one by using the constraint equation (6.55b). Therefore, we are left with one free parameter at the horizon, we choose  $(a_y^3)_0^h$ . When solving these equations numerically, we set  $(a_y^3)_0^h = 1$  and scan through different values of  $\omega$ .

We can perform similar considerations for the second part (equations (6.56)). In this case it is even simpler. We do not have any constraint, just three fields and their corresponding equations of motion. Therefore at the boundary we have six independent parameters, namely  $(a_y^1)_0^b$ ,  $(a_y^1)_1^b$ ,  $(a_y^2)_0^b$ ,  $(a_y^2)_1^b$ ,  $(\Psi_x)_0^b$  and  $(\Psi_x)_2^b$ . At the horizon we have  $(\Psi_x)_0^h$ ,  $(a_y^1)_0^h$ ,  $(a_y^2)_0^h$ . Note that, as before, we have already fixed three free parameters at the horizon by choosing the incoming boundary condition. Again by choosing the values for all fields at the horizon, the system is fully determined.

Notice that the same is true for the helicity 2 state. We have again 2 independent components at the boundary, namely  $(\Xi)_0^b$  and  $(\Xi)_2^b$  which are fixed by the incoming boundary condition and  $(\Xi)_0^h$  at the horizon. Therefore, as before, the equation is fully determined.

In the following we state the first few non-vanishing coefficients of the expansion at the boundary of the different fields. We need them later on to determine divergences in the on-shell action and to calculate the Green’s function. The explicit

form of the dependent coefficients are

$$(\hat{a}_y^1)_1^b = \frac{1}{2} \left[ \tilde{\omega}^2 (a_y^1)_0^b - 2i\tilde{\omega}\tilde{\mu} (a_y^2)_0^b + \tilde{\mu}^2 (a_y^1)_0^b \right], \quad (\text{B.35a})$$

$$(\hat{a}_y^2)_1^b = \frac{1}{2} \left[ \tilde{\omega}^2 (a_y^2)_0^b + 2i\tilde{\omega}\tilde{\mu} (a_y^1)_0^b + \tilde{\mu}^2 (a_y^2)_0^b \right], \quad (\text{B.35b})$$

$$(\hat{a}_y^3)_1^b = \frac{1}{2} \tilde{\omega}^2 (a_y^3)_0^b, \quad (\text{B.35c})$$

$$(\Xi)_1^b = \frac{1}{4} \tilde{\omega}^2 (\Xi)_0^b, \quad (\hat{\Xi})_2^b = \frac{1}{16} \tilde{\omega}^4 (\Xi)_0^b, \quad (\text{B.35d})$$

$$(\Psi_t)_2^b = -\alpha^2 \tilde{\phi}_2^b (\tilde{a}_y^3)_0^b, \quad (\hat{\Psi}_t)_3^b = -\frac{\alpha^2 \tilde{\omega}^2}{3} \tilde{\phi}_2^b (\tilde{a}_y^3)_0^b, \quad (\text{B.35e})$$

$$(\Psi_x)_1^b = \frac{1}{4} \tilde{\omega}^2 (\Psi_x)_0^b, \quad (\hat{\Psi}_x)_2^b = \frac{1}{16} \tilde{\omega}^4 (\Psi_x)_0^b. \quad (\text{B.35f})$$

Note that  $\mu \equiv \phi_0^b$  and  $\phi_1^b$  are the expansion coefficients of  $\phi(r)$  at the boundary.

We do not state the expansion at the horizon since there is no additional information to equation (B.32), and the explicit form of the non-independent coefficients is very long.

### B.3.2 Counterterms

By inserting the expansions (B.34) into (6.51) and (6.57), we obtain

$$\begin{aligned} \frac{\mathcal{L}_{r_b}}{r_h^4} = & (\Xi)_0^b (\Xi)_2^b + \left( -2f_2^b - \frac{\tilde{m}_0^b}{2} \right) (\Xi)_0^{b^2} + (\Psi_x)_0^b (\Psi_x)_2^b + \left( 4f_2^b - \frac{\tilde{m}_0^b}{2} \right) (\Psi_x)_0^{b^2} \\ & - \frac{3}{2} \tilde{m}_0^b (\Psi_t)_0^{b^2} + \alpha^2 \left[ (\tilde{a}_y^1)_0^b (\tilde{a}_y^1)_1^b + (\tilde{a}_y^2)_0^b (\tilde{a}_y^2)_1^b + (\tilde{a}_y^3)_0^b (\tilde{a}_y^3)_1^b \right] \\ & - \frac{1}{4} \alpha^2 \tilde{\mu}^2 \left[ (\tilde{a}_y^1)_0^{b^2} + (\tilde{a}_y^2)_0^{b^2} \right] + \alpha^2 \left[ -\tilde{w}_2^b (\tilde{a}_y^1)_0^b (\Psi_x)_0^b + 2\tilde{\phi}_2^b (\tilde{a}_y^3)_0^b (\Psi_t)_0^b \right] \\ & + i\alpha^2 \tilde{\omega} \tilde{\mu} (\tilde{a}_y^1)_0^b (\tilde{a}_y^2)_0^b \\ & + \left( \frac{1}{8} \epsilon_b \tilde{\omega}^2 + \frac{1}{64} \tilde{\omega}^4 + \frac{1}{32} \tilde{\omega}^4 \ln \epsilon_b \right) \left[ (\Psi)_0^{b^2} + (\Psi_x)_0^{b^2} \right] \\ & - \left( \frac{1}{4} \alpha^2 \tilde{\omega}^2 - \frac{1}{4} \alpha^2 \tilde{\omega}^2 \ln \epsilon_b \right) \left[ (\tilde{a}_y^1)_0^{b^2} + (\tilde{a}_y^2)_0^{b^2} + (\tilde{a}_y^3)_0^{b^2} \right] \\ & + \frac{1}{4} \alpha^2 \tilde{\mu}^2 \ln \epsilon_b \left[ (\tilde{a}_y^1)_0^{b^2} + (\tilde{a}_y^2)_0^{b^2} \right] \\ & - i\alpha^2 \tilde{\omega} \tilde{\mu} (\tilde{a}_y^1)_0^b (\tilde{a}_y^2)_0^b \ln \epsilon_b \Big|_{r=r_{\text{bdy}}}. \end{aligned} \quad (\text{B.36})$$

Note that  $S_{\text{on-shell}} = \frac{1}{\kappa_2^2} \int \frac{d^4 k}{(2\pi)^4} \mathcal{L}_{r_b}$  with  $r = r_{\text{bdy}} \gg 1$ . Moreover, as before, the first field expansion coefficient is always a field of  $-k$  and the second of  $k$ , e.g.

$(\Xi)_0^b(-k)(\Xi)_2^b(k)$ . It is obvious from the last few lines of (B.36) that we have to add counter terms to the on-shell action  $S_{\text{on-shell}}$  to take the divergences in  $r$  into account.

The terms that have to be considered are the ones in (B.36) with explicit  $r$  dependence,

$$\begin{aligned} & \left( \frac{1}{8} \epsilon_b \tilde{\omega}^2 + \frac{1}{32} \tilde{\omega}^4 \ln \epsilon_b \right) \left[ (\Xi)_0^{b^2} + (\Psi_x)_0^{b^2} \right], \\ & \frac{1}{4} \alpha^2 \ln \epsilon_b \left\{ \tilde{\omega}^2 \left[ (\tilde{a}_y^1)_0^{b^2} + (\tilde{a}_y^2)_0^{b^2} + (\tilde{a}_y^3)_0^{b^2} \right] + \tilde{\mu}^2 \left[ (\tilde{a}_y^1)_0^{b^2} + (\tilde{a}_y^2)_0^{b^2} \right] \right\} \quad \text{and} \\ & - i \alpha^2 \tilde{\omega} \tilde{\mu} (\tilde{a}_y^1)_0^b (\tilde{a}_y^2)_0^b \ln \epsilon_b \end{aligned}$$

First we need the induced metric  $\gamma$  on the  $r = r_{\text{bdy}}$  plane. The induced metric is defined by

$$\gamma_{\mu\nu} = \frac{\partial x^M}{\partial \tilde{x}^\mu} \frac{\partial x^N}{\partial \tilde{x}^\nu} g_{MN}(r) \Big|_{r=r_{\text{bdy}}}, \quad (\text{B.37})$$

resulting in

$$ds_{r_{\text{bdy}}}^2 = -N(r_{\text{bdy}}) \sigma(r_{\text{bdy}})^2 dt^2 + \frac{r_{\text{bdy}}^2}{f(r_{\text{bdy}})^4} dx^2 + r_{\text{bdy}}^2 f(r_{\text{bdy}})^2 (dy^2 + dz^2). \quad (\text{B.38})$$

We do not literally derive the covariant counter terms. However, by looking at the counter terms calculated in [256], we get an idea how they should look like, namely some combinations of  $R[\gamma]$ ,  $R_{\mu\nu}[\gamma]$  and  $F_{\mu\nu}^a$ . The first two are the Ricci scalar and Ricci tensor on the induced surface respectively, the latter is the field strength tensor on that surface. Possible covariant combinations of the three terms are  $\sqrt{-\gamma}R[\gamma]$ ,  $\sqrt{-\gamma}R^{\mu\nu}[\gamma]R_{\mu\nu}[\gamma]$  and  $\sqrt{-\gamma}F_{\mu\nu}^a F^{a\mu\nu}$ . Now let's have a look at their expansion for  $r \gg 1$ .

$$\begin{aligned} \sqrt{-\gamma}R[\gamma] \Big|_{r \gg 1} &= \frac{r^2 \omega^2}{2} \left[ (\Xi)_0^{b^2} + (\Psi_x)_0^{b^2} \right], \\ \sqrt{-\gamma}R^{\mu\nu}[\gamma]R_{\mu\nu}[\gamma] \Big|_{r \gg 1} &= \frac{\omega^4}{2} \left[ (\Xi)_0^{b^2} + (\Psi_x)_0^{b^2} \right] \quad \text{and} \\ \sqrt{-\gamma}F_{\mu\nu}^a F^{a\mu\nu} \Big|_{r \gg 1} &= -2 \left\{ \omega^2 \left[ (a_y^1)_0^{b^2} + (a_y^2)_0^{b^2} + (a_y^3)_0^{b^2} \right] \right. \\ & \quad \left. + \mu^2 \left[ (a_y^1)_0^{b^2} + (a_y^2)_0^{b^2} \right] - 4i\omega\mu (a_y^1)_0^b (a_y^2)_0^b \right\}. \end{aligned} \quad (\text{B.39})$$

Therefore, by adding the real space action,

$$S_{\text{ct}} = - \int d^4x \sqrt{-\gamma} \left( \frac{1}{4} R[\gamma] + \frac{1}{16} R^{\mu\nu}[\gamma] R_{\mu\nu}[\gamma] \ln \epsilon_b - \frac{\alpha^2}{8} F_{\mu\nu}^a F^{a\mu\nu} \ln \epsilon_b \right) \Big|_{r=r_{\text{bdy}}}, \quad (\text{B.40})$$

to the action  $S_{\text{on-shell}}$  (6.51) and (6.57), we get a divergence-free theory (up to the second order in the fluctuations) for  $r_{\text{bdy}} \gg 1$ , i. e. also the real time Green's functions are divergence free. The renormalized  $r_{\text{bdy}} \gg 1$  Lagrangian is then given in (6.52) and (6.58).

# Numerical Recipes for Holography

In this chapter we discuss some numerical procedures which are commonly used in the context of gauge/gravity duality and so in this thesis.

## C.1 Numerics for Flavor Branes at Finite Temperature

Here the numerical procedure to determine the embedding as well as the thermodynamics of the D3/D7 brane model at finite temperature is presented. We discuss its realization in *Mathematica*.

### Definitions

First we define the equations of motion in the coordinates  $\{L, r\}$ ,

$$\text{eqL} = \partial_r((1 - 1/(r^2 + L[r]^2))^4 r^3 L'[r] / \text{Sqrt}[1 + (L'[r])^2]) - 8r^3 L[r] / (r^2 + L[r]^2)^5 \text{Sqrt}[1 + (L'[r])^2];$$

and  $\{\chi, \rho\}$  coordinates,

$$\begin{aligned} f &:= 1 - 1/\rho^4; \\ ft &:= 1 + 1/\rho^4; \\ \text{eq}\chi &= \partial_\rho(\rho^5 ft (1 - \chi[\rho]^2) \chi'[\rho] / \text{Sqrt}[1 - \chi[\rho]^2 + \rho^2 \chi'[\rho]^2]) \\ &\quad + \rho^3 ft \chi[\rho] / \text{Sqrt}[1 - \chi[\rho]^2 + \rho^2 \chi'[\rho]^2] ((3(1 - \chi[\rho]^2) + 2\rho^2 \chi'[\rho]^2))); \end{aligned}$$

Second we define several parameters:

- IR and UV cutoffs (initial and final value for the integration)

$$\begin{aligned} r_{\text{init}} &:= 10^{-5}; \\ r_{\text{final}} &:= 10^3; \\ \rho_{\text{init}} &:= 1 + 10^{-5}; \end{aligned}$$

```
 $\rho$ final:=10^3;
```

- Discrete step distance and exit condition for the Newton method (see below)

```
eps:=10^(-4);  
error:=10^(-5);
```

- Parameter range of  $\chi_0$

```
 $\chi$ 0start:=0;  
 $\chi$ 0end:=0.9999;  
 $\chi$ 0step:=0.0001;
```

- Parameter range of  $L_0$

```
L0start:=1.0001;  
L0end:=2;  
L0step:=0.0001;
```

and distribute the definitions in order to allow for parallel computing,

```
DistributeDefinitions[rinit, rfinal,  $\rho$ init,  $\rho$ final, eps, error, L0start, L0end,  
L0step,  $\chi$ 0start,  $\chi$ 0end,  $\chi$ 0step];
```

Next we define the asymptotic expansion for  $L$  and  $\chi$ ,

```
asymL = m + c(1/r^2 - 1/rfinal^2);  
asym $\chi$  = m(1/ $\rho$  - 1/ $\rho$ final) + c(1/ $\rho$ ^3 - 1/ $\rho$ final^3);
```

```
DistributeDefinitions[asymL, asym $\chi$ ];
```

and the integrands to determine the free energy,

```
intL:=r^3(1 - 1/(r^2 + L[r]^2)^4)Sqrt[1 + (L'[r])^2]  
+ (r + L[r]L'[r])(m^2 - (r^2 + L[r]^2));
```

```
intχ:=ρ^3(1-1/ρ^8)(1-χ[ρ]^2)Sqrt[1-χ[ρ]^2+ρ^2(χ'[ρ])^2]
      -ρ^3+ρm^2;
```

```
DistributeDefinitions[intL, intχ];
```

## Numerics

After the definitions we now discuss the numerics which are split into two functions. The first handles the calculation in the  $\{L, r\}$  coordinates,

```
CalcL[L0.]:=Module[{eq, sol, ri, LL, reffit, nrp, step, l, g, asym, mt, ms,
  ct, cs, cutoff, rcut, rstep, int, Gs, Fs},
```

First we solve the equation of motion and save the result in **LL**

```
eq = {eqL == 0, L[ri] == L0, L'[ri] == 0}/.ri -> rinit;
sol = NDSolve[eq, L, {r, rinit, rfinal}, AccuracyGoal -> 20];
LL = L/.sol[[1]];
```

Next we determine the asymptotic parameters by a fit. The result are saved in **ms** and **cs**. For this purpose we generate a list of points out of the numerical solution. Here we use **nrp=100** points separated along the radial direction by **step=10**,

```
l = Table[{(rfinal - step * nrp) + i * step, LL[(rfinal - nrp * step) + i * step]},
  {i, 1, nrp}];
asym = asymL/.m -> mt/.c -> ct;
g = FindFit[l, asym, {mt, ct}, r];
ms = mt/.g;
cs = ct/.g;
```

Next we calculate the function  $G(m)$  which determines the thermodynamics. In order to improve the convergence of the integral we introduce a cutoff **cutoff = 10<sup>-5</sup>** and determine the radial coordinate **rcut** at which the integrand is smaller than this cutoff,

```
rcut = 10;
rstep = 1;
```

```
int = intL/.L -> LL/.m -> ms;
```

```
While[Abs[int/.r->rcut] > cutoff, rcut+=rstep; If[rcut > rfinal, rcut = rfinal;
```

```
Break[];];];
```

Then we integrate from the initial value to the cutoff,

```
Gs = NIntegrate[int, {r, rinit, rcut}, AccuracyGoal -> 10, MaxRecursion -> 30];
Fs = Gs - 1/4((L0^2 - ms^2)^2 - 4mscs);
```

The function returns the initial value  $L_0$ , asymptotic values  $m$ ,  $c$ , the function  $G$  and the dimensionless free energy  $\mathcal{F}$ ,

```
{L0, ms, cs, Gs, Fs}
];
```

There is a similar function that handles the calculation in the  $\{\chi, \rho\}$  coordinates,

```
CalcChi[chi0_] := Module[{eq, sol, rho, cchi, rendfit, nrp, step, l, g, asym, mt, ms, cs, ct,
  cutoff, rhoCut, rhoStep, int, Gs, Fs},
```

First we solve the equation of motion and save the result in  $c\chi$

```
eq = {eqchi == 0, chi[rho] == chi0, chi'[rho] == 0}/.rho -> rhoinit;
sol = NDSolve[eq, chi, {rho, rhoinit, rhoFinal}, AccuracyGoal -> 20];
cchi = chi/.sol[[1]];
```

Next we determine the asymptotic parameters by a fit. The result are saved in  $ms$  and  $cs$ ,

```
nrp = 100;
step = 10;
```

```
(*fit*)
```

```
l = Table[{{{(rhoFinal - step * nrp) + i * step} Sqrt[1 - (cchi[(rhoFinal - nrp * step)
  + i * step])^2], ((rhoFinal - nrp * step) + i * step) cchi[(rhoFinal - nrp * step)
  + i * step]}}, {i, 1, nrp}];
asym = asymL/.m -> mt/.c -> ct;
g = FindFit[l, asym, {mt, ct}, r];
ms = mt/.g;
cs = ct/.g;
```

Next we determine the thermodynamics,

```
cutoff = 10^(-5);
rhoCut = 10;
```

```

 $\rho$ step = 1;

int = int $\chi$ /. $\chi$   $\rightarrow$  c $\chi$ /. $m$   $\rightarrow$  ms;

While[Abs[int/. $\rho$   $\rightarrow$   $\rho$ cut] > cutoff,  $\rho$ cut +=  $\rho$ step; If[ $\rho$ cut >  $\rho$ final,
   $\rho$ cut =  $\rho$ final; Break[];];
Gs = NIntegrate[int, { $\rho$ ,  $\rho$ init,  $\rho$ cut}, AccuracyGoal  $\rightarrow$  10, MaxRecursion  $\rightarrow$  30];

Fs = Gs - 1/4((1 - ms^2)^2 - 4mscs);

```

The function returns the initial value  $\chi_0$ , the asymptotic parameters  $m$ ,  $c$ , the function  $G$  and the dimensionless free energy  $\mathcal{F}$ ,

```

{ $\chi_0$ , ms, cs, Gs, Fs}
];

```

The definition of the functions are shared in order to allow for parallel computations,

```

DistributeDefinitions[CalcL, Calc $\chi$ ];

```

By using the functions defined above we generate the relevant data for each initial value  $L_0$  and  $\chi_0$ , respectively. We parallelize the computation. The result are saved in the tables **tabsolL** and **tabsol $\chi$** ,

```

tabsolL = ParallelTable[CalcL[L0], {L0, L0start, L0end, L0step}];
tabsol $\chi$  = ParallelTable[Calc $\chi$ [ $\chi_0$ ], { $\chi_0$ ,  $\chi_0$ start,  $\chi_0$ end,  $\chi_0$ step}];

SetSharedVariable[tabsolL, tabsol $\chi$ ];

```

We may save and load the data by using **Export** and **Import**,

```

SetDirectory["/home/pcl332/pkerner/thesis/numerics/finiteT"];

Export["tabsolL.dat", tabsolL];
Export["tabsolchi.dat", tabsol $\chi$ ];

tabsolL = Import["tabsolL.dat", "Table"];
tabsol $\chi$  = Import["tabsolchi.dat", "Table"];

```

### Find the First Order Phase Transition

In the following an algorithm which finds the critical value of a first order phase transition is discussed. For this purpose we restrict the tables calculated above to the region of interest [*mstart*, *mend*]. We scan the tables and generated a new list with an equal distance *mstep*. The values are allowed to differ by *merror*.

```
mstart:=1.25;
mend:=1.35;
mstep:=0.0001;
merror:=0.0001;
```

```
DistributeDefinitions[mstart, mend, mstep, merror];
```

```
tabredL = Block[{ftemp},
ftemp[mt_][{par_, ms_, cs_, Gs_, Fs_}] := Module[{temp},
temp = {};
If[Abs[mt - ms] < merror, temp = {ms, Fs};];
temp
];
DistributeDefinitions[ftemp];
ParallelTable[Flatten[ftemp[mt]/@tabsoL], {mt, mstart, mend, mstep}]
];
```

```
tabredχ = Block[{ftemp},
ftemp[mt_][{par_, ms_, cs_, Gs_, Fs_}] := Module[{temp},
temp = {};
If[Abs[mt - ms] < merror, temp = {ms, Fs};];
temp
];
DistributeDefinitions[ftemp];
ParallelTable[Flatten[ftemp[mt]/@tabsoχ], {mt, mstart, mend, mstep}]
];
```

This allows us to calculate the difference in the dimensionless free energy for each point in the region of interest,

```
tabdiff = Table[If[Length[tabredL[[i]]] > 1&&
Length[tabredχ[[i]]] > 1, {tabredL[[i, 1], tabredL[[i, 2]] - tabredχ[[i, 2]]},
{}, {i, 1, Length[tabredL]}];
```

Now we only need to find the point at which the difference is smaller than

```

Error:=10(-5);

listtransition = Flatten[Block[{ftemp},
ftemp[{ms_, Fs_]:=Module[{temp},
temp = {};
If[Abs[Fs] < Error, temp = ms;];
temp
];
ftemp[{}]:=Module[{}, {}];

ftemp/@tabdiff
]]

```

The resulting points are  $\{1.30691, 1.30702, 1.30712, 1.30722\}$  which leads to critical value  $m = 1.307$ .

### Plot of Embedding Functions

Here some functions which are useful to plot the embedding functions are presented:

```

CalcL[L0_]:=Module[{eq, sol, LL},
eq = {eqL == 0, L[ri] == L0, L'[ri] == 0}/.ri -> rinit;
sol = NDSolve[eq, L, {r, rinit, rfinal}, AccuracyGoal -> 20];
LL = L/.sol[[1]]
];

Calcχ[χ0_]:=Module[{eq, sol, cχ},
eq = {eqχ == 0, χ[ρi] == χ0, χ'[ρi] == 0}/.ρi -> ρinit;
sol = NDSolve[eq, χ, {ρ, ρinit, ρfinal}, AccuracyGoal -> 20];
cχ = χ/.sol[[1]]
];

```

determine the solution of the equations of motion for the initial value  $L_0$  and  $\chi_0$ , respectively.

```

FindL0[m_, L0init_]:=Module[{mt1, mt2, L0},
L0 = L0init;
While[1 == 1,
mt1 = CalcL[L0][rfinal];
mt2 = CalcL[L0 + eps][rfinal];
L0=(m - mt1)eps/(mt1 - mt2);
If[Abs[mt1 - m] < error, Break[]];
];

```

```
{mt1, L0}
]
```

```
Findχ0[m., χ0init.]:=Module[{mt1, mt2, χ0},
χ0 = χ0init;
While[1 == 1,
mt1 = ρfinalCalcχ[χ0][ρfinal];
mt2 = ρfinalCalcχ[χ0 + eps][ρfinal];
χ0=(m - mt1)eps/(mt1 - mt2);
If[Abs[mt1 - m] < error, Break[]];
];
{mt1, χ0}
]
```

determine the initial value  $L_0$  and  $\chi_0$ , respectively, for a given mass  $m$ .

```
PlotL[m., L0init., rstart., rend.]:=Module[{L0, eq, sol, LL},
L0 = FindL0[m, L0init][[2]];

LL = CalcL[L0];

Plot[LL[r], {r, rstart, rend}, PlotRange → {{rstart, rend}, {L0, m}},
AxesOrigin → {rstart, L0}, PlotStyle → Red, Frame → True,
FrameLabel → {"r", "L"}, RotateLabel → False]
]

Plotχ[m., χ0init., rstart., rend.]:=Module[{χ0, eq, sol, cχ},
χ0 = Findχ0[m, χ0init][[2]];

cχ = Calcχ[χ0];

ParametricPlot[{Sqrt[ρ^2 - (ρcχ[ρ])^2], ρcχ[ρ]}, {ρ, rstart, rend},
PlotRange → {{rstart, rend}, {0, m}}, AxesOrigin → {rstart, 0},
PlotStyle → Blue, Frame → True, FrameLabel → {"r", "L"},
RotateLabel → False]
]
```

plot the embedding function  $L$  and  $\chi$  between **rstart** and **rend** in the coordinates  $\{r, L\}$ . The figure 4.2 is generated by

```
plotemb = Block[{ploth, rplotend},
ploth = Plot[Sqrt[1 - x^2], {x, 0, 1}, PlotStyle → Black];
rplotend = 4;
```

```

Minkowskiemb = Table[PlotL[x, x, rinit, rplotend], {x, {1.3, 1.4, 1.6, 1.8, 2}}];
Blackemb = Table[Plotχ[x, 2x/3, ρinit, 10], {x, {0.2, 0.40, 0.8, 1, 1.20, 1.3}}];
Show[Minkowskiemb, Blackemb, plot, PlotRange → {{0, rplotend}, {0, 2.1}},
     AxesOrigin → {0, 0}]
]

```

## C.2 Numerics for Flavor Branes at Finite Chemical Potentials

Let us now discuss the situation where in addition to the temperature, the chemical potential are switched on. We reuse the *Mathematica* notebook discussed above. Here we just mention the changes in the notebook in order handle the finite chemical potentials. The equation of motion for the embedding function *emχ* is now given by (5.38) and the integrand to determine the thermodynamics *intχ* is given by (5.41). Additional definitions are need to determine the gauge fields,

```

intX:=2ntfSqrt[1 - χ[ρ]^2 + ρ^2χ'[ρ]^2]/Sqrt[ft(1 - χ[ρ]^2)
(ρ^6ft^3(1 - χ[ρ]^2)^3 + 8nt^2)];

```

In the actual numerical procedure now called *Calχ[χ0-, n1-, n2-]*, we also have to include some parts which deal with the chemical potentials. After the mass parameter *m* and the chiral condensate  $\tilde{c}$  are determined by the fit, we evaluate the integrals which lead to the grand potential and the chemical potentials in a similar way as in the notebook discussed above.

```

cutoff = 10^(-4);
ρcut = 10;
ρstep = 1;

```

```

dX1t = intX/.nt → n1/.χ → cχ;
dX2t = intX/.nt → n2/.χ → cχ;

```

```

int = intχ/.χ → cχ/.m → ms/.dX1 → dX1t/.dX2 → dX2t;

```

```

mcor = (int/.ρ->ρfinal)/ρfinal;
int = int - ρmcor;

```

```

While[Abs[int/.ρ->ρcut] > cutoff, ρcut+=ρstep; If[ρcut > ρfinal,
  ρcut = ρfinal; Break[;,];];
Gs = NIntegrate[int, {ρ, ρinit, ρcut}, AccuracyGoal → 10,

```

```

MaxRecursion → 30}];

ρcut = 10;
While[Abs[dX1t/.ρ->ρcut] > cutoff, ρcut+=ρstep; If[ρcut > ρfinal,
  ρcut = ρfinal; Break[];]];
mu1s = NIntegrate[dX1t, {ρ, ρinit, ρcut}, AccuracyGoal → 10,
  MaxRecursion → 30];

ρcut = 10;
While[Abs[dX2t/.ρ->ρcut] > cutoff, ρcut+=ρstep; If[ρcut > ρfinal,
  ρcut = ρfinal; Break[];]];
mu2s = NIntegrate[dX2t, {ρ, ρinit, ρcut}, AccuracyGoal → 10,
  MaxRecursion → 30];

Omegas = 1/2Gs - 1/4((1 - ms^2)^2 - 4mcs);

```

The function returns the initial value  $\chi_0$ , the asymptotic parameters of the embedding function  $m$ ,  $\tilde{c}$ , the chemical potentials  $\tilde{\mu}_B$ ,  $\tilde{\mu}_I$ , the densities  $\tilde{n}_B$ ,  $\tilde{n}_I$  the function  $G(m, \tilde{\mu})$  and the grand potential  $\mathcal{W}_7$

```

{χ0, ms, cs, 1/2(mu1s + mu2s), 1/2(mu1s - mu2s), n1 + n2, n1 - n2, Gs,
  Omegas}
];

```

## Newton Method to Find Physical State

Since we are working in the grand canonical ensemble where the temperature and the chemical potentials are fixed, we need a procedure which determines the corresponding parameters  $\chi_0$ ,  $\tilde{n}_1$  and  $\tilde{n}_2$ . For this purpose we use the discrete Newton Method

$$x_{n+1} = x_n - \epsilon(f(x_n + \epsilon e_i) - f(x_n))^{-1} f(x_n) \quad (\text{C.1})$$

which converges to the next zero of  $f$ , i. e.  $x_n \rightarrow x$  with  $f(x) = 0$ . In *Mathematica* it looks like,

```

Calcχgrand[m_, muB_, muI_, χ0start_, n1start_, n2start_] :=
  Module[{x, dx, y, dy, yend},
    x = {χ0start, n1start, n2start};
    yend = {m, muB, muI};
    y = Calcχred[x] - yend;
    While[Abs[y[[1]]] > error || Abs[y[[2]]] > error || Abs[y[[3]]] > error,

```

```

dx = Table[x, {i, 1, 3}];
For[i = 1, i ≤ 3, i++, dx[[i, i]] += eps; ];
y = Calc $\chi$ red[x] - yend;
dy = Transpose[Map[Calc $\chi$ red, dx] - {y, y, y}];
x = x - epsInverse[dy].y;
];
x
];

```

Here **Calc** $\chi$ **red** is a reduced version of **Calc** $\chi$  where only  $m$ ,  $\mu_B$  and  $\mu_I$  are calculated. In **dx** the discrete steps ( $x + \epsilon e_i$ ) are calculated such that **dy** is given by the matrix  $f(x + \epsilon e_i) - f(x)$ .

This Newton method can always be used to fix the independent parameters at the horizon by the constraints on the boundary. These constraints have to be satisfied to obtain a physical solution. The other numerical results presented in this thesis are obtained with similar algorithms.

### C.3 Shooting Method

We now discuss an improved shooting method for solving the equation of motion for the fluctuations at complex frequencies. The problem arises when using the standard method for solving the equations of motion by just numerically integrating the differential equation.

As an example for the failure of this naive method we look at figure C.1 which shows the spectral function for the transverse vector modes for vanishing quark mass and vanishing density. Note here that we use the dimensionless frequency  $\mathfrak{w} = \omega/(2\pi T)$ . The line of poles found at  $\text{Im } \mathfrak{w} = -1$  is definitely not correct since in [182] the pole-structure of the very same configuration was analytically determined to be

$$\mathfrak{w} = n(1 - i) \quad \text{for } n \in \mathbb{N}_0 . \quad (\text{C.2})$$

It turns out that the numerical errors hide the quasi-normal modes behind this „wall“ at  $\text{Im } \mathfrak{w} = -1$ . This wall could be misinterpreted as a branch cut.

The problem is that the equations of motion we have investigated are not regular at the horizon where the initial conditions are imposed. One, therefore, splits the solution in a regular and regulating part  $E(\rho) = (\rho - 1)^{-i\mathfrak{w}} F(\rho)$  by computing its Frobenius expansion near the horizon. Nevertheless, we have to move the starting point for the numerical integration slightly away from the real horizon to, say  $\rho = 1.00001$  where we choose this value so close to 1 that we can expect only small deviations from the exact solution. However, for values of  $\text{Im } \mathfrak{w} \leq -1$  the boundary condition yields

$$(\rho - 1)^{-i\mathfrak{w}} = (1 \times 10^{-5})^{\text{Im } \mathfrak{w} - i\text{Re } \mathfrak{w}} . \quad (\text{C.3})$$

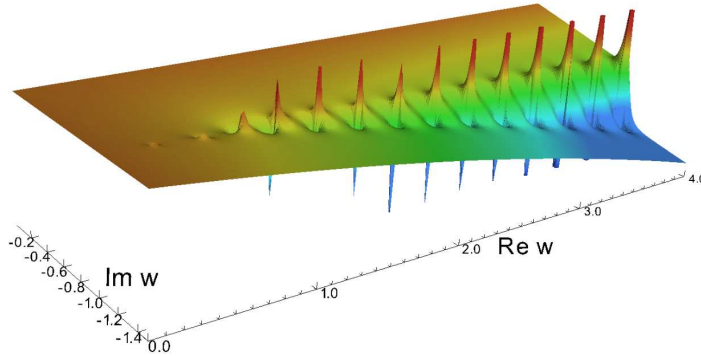


**Figure C.1:** Breakdown of the standard numerical techniques at  $\text{Im } \omega \lesssim -1$ . A series of spikes can be seen, being a firmly erroneous solution in view of the analytic result (C.2). This problem will be solved by means of our improved method, discussed in the text. This figure is taken from [3].

This is problematic when  $\text{Im } \omega$  is smaller than  $-1$ , the initial condition is becoming large, leading to round off errors. These change the value of the fluctuation at infinity dramatically and are responsible for the invalid results of the spectral function in the specific region.

The cure is to shift the starting point for the numerical integration away from the horizon and, thus, dealing with not so small values in the basis of (C.3), resulting in better numerical initial conditions. Of course, the error from starting the integration further away from the horizon has to be compensated. This is simply done, by calculating the asymptotics of the gauge field fluctuations in the vector case, or the embedding deviations in the scalar case at the horizon to higher order.

When reimplementing the numerical integration with a starting value of e.g.  $\rho = 1.1$  and the new asymptotics, the numerical aberration is prevented successfully and one can gain insight farther into the complex  $\omega$ -plane.

A look at the results shows what can be achieved with this more sophisticated method. A comparison between the surface plot of the old method (figure C.1) and the improved one (figure C.2) reveals that the expected pole structure can now be seen clearly. In fact, it can be checked that the position of the poles agrees with the analytical result (C.2) very well.

## C.4 Relaxation Method

The determination of quasinormal frequencies can be understood as a particular case of a two-point boundary value problem. A common numerical method for solving such problems is the shooting method, where one solves the differential equations with varying boundary conditions at one boundary and searches for a solution that

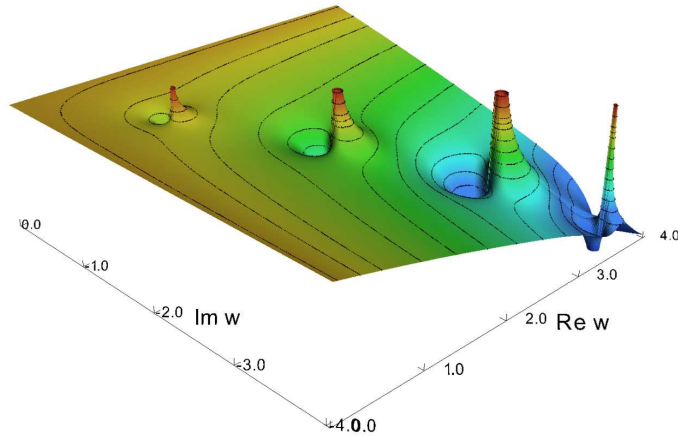


**Figure C.2:** With the improved method nearly four poles can be resolved for vanishing density  $\tilde{d} = 0$  and massless quarks  $m = 0$ . For the computation of the initial values the expansion in the fluctuation equation were evaluated up to eleventh order. As can be seen, the location of the poles fits the analytical solution (C.2) very well. This figure is taken from [3].

approximates the wanted boundary condition at the other boundary within some numerical error. We describe that method in appendix C.3.

A different approach is provided by the relaxation method which allows to fix the correct boundary values on both boundaries. Since this method is less frequently used we give a short outline below<sup>1</sup>.

The method is based on replacing the differential equations by a system of finite-difference equations (FDE) on a discrete grid. Starting from an ansatz solution obeying the correct boundary conditions, one varies the value of the dependent variables at each point *relaxing* to the configuration which provides an approximate solution for the FDE within some given numerical error. In our case, we convert our second order complex ODE into a set of four first order equations by separating real and imaginary parts of the dependent variables.

More generally we can consider a set of  $\tilde{N}$  first order ODE's

$$\frac{dy_i(x)}{dx} = g_i(x, y_1, \dots, y_{\tilde{N}}; \lambda) , \quad (\text{C.4})$$

where each dependent variable  $y_i(x)$  depends on the others and itself, on the independent variable  $x$  and possibly on additional parameters, like  $\lambda$  above. In our case this (complex) parameter is the quasinormal frequency. These extra parameters can

<sup>1</sup>A more detailed exposition can be found in [257].

be embedded into the problem by writing trivial differential equations for them

$$\begin{cases} y_{N+j} & \equiv \lambda_j , \\ \frac{dy_{N+j}}{dx} & = 0 , \text{ since it is constant .} \end{cases} \quad (\text{C.5})$$

We assume that there are  $n$  additional parameters and include them from now on into the set of dependent variables  $y_1, \dots, y_N$ ,  $N = \tilde{N} + n$ .

The solution to the problem involves  $N \times M$  values, for the  $N$  dependent variables in a grid of  $M$  points. We also have to fix  $N$  boundary conditions for the dependent variables.

The system is discretized as usual

$$x \rightarrow \frac{1}{2}(x_k + x_{k-1}) , \quad y \rightarrow \frac{1}{2}(y_k + y_{k-1}) , \quad (\text{C.6})$$

for points in the bulk. One may arrange the whole set of  $y_i$ 's in a column vector  $\mathbf{y}_k = (y_1, \dots, y_N)_k^T$ , where the subscript  $k$  refers to evaluation at the point  $x_k$ ,  $k = 1, \dots, M$ . With this matrix notation, the system (C.4) can be written as

$$0 = \mathbf{E}_k \equiv \mathbf{y}_k - \mathbf{y}_{k-1} - (x_k - x_{k-1}) \mathbf{g}_k(x_k, x_{k-1}, \mathbf{y}_k, \mathbf{y}_{k-1}) , \quad k = 2, \dots, M , \quad (\text{C.7})$$

where the  $\mathbf{E}_k$  are the aforementioned FDE's. These are the equations that we need to fulfill. Notice there are  $N$  equations at  $M-1$  points, so the remaining  $N$  equations are supplied by the boundary conditions. We will set  $n_1$  of them on the left at  $x_1$ , called  $\mathbf{E}_1$ , and the rest  $n_2 = N - n_1$  at  $x_M$ , called  $\mathbf{E}_{M+1}$ .

Now we take a trial solution that nearly solves the FDE's  $\mathbf{E}_k$ . By shifting each solution  $\mathbf{y}_k \rightarrow \mathbf{y}_k + \Delta \mathbf{y}_k$  and Taylor expanding in the shift, one obtains the relation

$$0 = \mathbf{E}_k(\mathbf{y} + \Delta \mathbf{y}) \simeq \mathbf{E}_k(\mathbf{y}_k, \mathbf{y}_{k-1}) + \sum_{n=1}^N \frac{\partial \mathbf{E}_k}{\partial y_{n,k-1}} \Delta y_{n,k-1} + \sum_{n=1}^N \frac{\partial \mathbf{E}_k}{\partial y_{n,k}} \Delta y_{n,k} , \quad (\text{C.8})$$

$$\Rightarrow -E_{j,k} = \sum_{n=1}^N \left( S_{j,n} \Delta y_{n,k-1} \right) + \sum_{n=N+1}^{2N} \left( S_{j,n} \Delta y_{n-N,k} \right) . \quad (\text{C.9})$$

This allows to find the  $\Delta \mathbf{y}_k$  that improve the solution. First we merge the two differentials

$$S_{j,n} = \frac{\partial E_{j,k}}{\partial y_{n,k-1}} , \quad S_{j,n+N} = \frac{\partial E_{j,k}}{\partial y_{n,k}} , \quad n = 1, \dots, N , \quad (\text{C.10})$$

in a  $N \times 2N$  matrix, for each bulk grid position  $x_k$ . For the boundaries the expressions follow equally

$$-E_{j,1} = \sum_{n=1}^N S_{j,n} \Delta y_{n,1} = \sum_{n=1}^N \frac{\partial E_{j,1}}{\partial y_{n,1}} \Delta y_{n,1} , \quad j = n_2 + 1, \dots, N , \quad (\text{C.11})$$

$$-E_{j,M+1} = \sum_{n=1}^N S_{j,n} \Delta y_{n,M} = \sum_{n=1}^N \frac{\partial E_{j,M+1}}{\partial y_{n,M}} \Delta y_{n,M} , \quad j = 1, \dots, n_2 , \quad (\text{C.12})$$

where  $n$  runs in both from 1 to  $N$ . The whole  $(NM \times NM)$  matrix  $S$  possesses a block diagonal structure. In fact, since for reasonable systems  $N \ll M$ ,  $S$  is a sparse matrix. This allows the usage of computer packages in which the solution of linear systems with sparse matrices can be done in a very efficient way. The actual solution can now be found by an iterative process until a desired accuracy is achieved. As measure for the discrepancy of an approximate solution to the actual solution we used

$$\text{err} = \frac{1}{MN} \sum_{k=1}^M \sum_{j=1}^N \left| \frac{\Delta y[j][k]}{\text{scalevar}[j]} \right| < \text{conv} , \quad (\text{C.13})$$

where  $\text{scalevar}[j]$  is an associated scale for each of the dependent variables (e.g. the value at the midpoint or so). The idea is that when that averaged value of the shift to get a better solution is smaller than  $\text{conv}$ , we accept the former values we had as the actual solution. In our computations we set  $\text{conv} = 10^{-6}$ .

In order to obtain the correct boundary conditions, we have used the  $z$  coordinate system where the horizon lies at  $z = 1$  and the boundary at  $z = 0$ . We split off the ingoing boundary condition on the horizon according to  $\Phi(z) = (1 - z)^{-i\omega/4} y(z)$ . Demanding  $y(1) = 1$  and  $y(0) = 0$  gives four real boundary conditions. Since in total we have, however, six dependent variables, counting also the real and imaginary part of the quasinormal frequency we need two more boundary conditions. We found it convenient to expand the function  $y(z)$  in a Taylor series at the horizon and compute also  $y'(1)$  which provides the additional two real boundary conditions.



# Bibliography

- [1] M. Ammon, J. Erdmenger, M. Kaminski, and P. Kerner, *Superconductivity from gauge/gravity duality with flavor*, Phys. Lett. **B680** (2009) 516–520, arXiv:0810.2316.
- [2] M. Ammon, J. Erdmenger, M. Kaminski, and P. Kerner, *Flavor Superconductivity from Gauge/Gravity Duality*, JHEP **10** (2009) 067, arXiv:0903.1864.
- [3] J. Erdmenger, C. Greubel, M. Kaminski, P. Kerner, K. Landsteiner, and F. Pena-Benitez, *Quasinormal modes of massive charged flavor branes*, JHEP **03** (2010) 117, arXiv:0911.3544.
- [4] M. Ammon, J. Erdmenger, V. Grass, P. Kerner, and A. O’Bannon, *On Holographic p-wave Superfluids with Back-reaction*, Phys. Lett. **B686** (2010) 192–198, arXiv:0912.3515.
- [5] J. Erdmenger, P. Kerner, and H. Zeller, *Non-universal shear viscosity from Einstein gravity*, Phys.Lett. **B699** (2011) 301–304, arXiv:1011.5912.
- [6] J. Erdmenger, V. Grass, P. Kerner, and T. H. Ngo, *Holographic Superfluidity in Imbalanced Mixtures*, JHEP **1108** (2011) 037, arXiv:1103.4145.
- [7] M. Ammon, J. Erdmenger, P. Kerner, and M. Strydom, *Black Hole Instability Induced by a Magnetic Field*, Phys.Lett. **B706** (2011) 94–99, arXiv:1106.4551.
- [8] J. Erdmenger, P. Kerner, and H. Zeller, *Transport in Anisotropic Superfluids: A Holographic Description*, arXiv:1110.0007.
- [9] C. Burgess and G. Moore, *The Standard Model: A Primer*. Cambridge University Press, 2007.
- [10] **ATLAS Collaboration** Collaboration, C. Sbarra, *ATLAS status and latest results*, PoS **BORMIO2011** (2011) 055.
- [11] S. Weinberg, *The Quantum Theory of Fields: Foundations*. Cambridge University Press, 2002.

- [12] S. Weinberg, *The Quantum Theory of Fields: Modern Applications*. Cambridge University Press, 2001.
- [13] S. Carroll, *An Introduction to general Relativity, Spacetime and Geometry*. Addison Wesley, 2004.
- [14] J. D. Bekenstein, *Entropy bounds and black hole remnants*, Phys.Rev. **D49** (1994) 1912–1921, arXiv:gr-qc/9307035.
- [15] G. 't Hooft, *Dimensional reduction in quantum gravity*, arXiv:gr-qc/9310026.
- [16] L. Susskind, *The World as a hologram*, J.Math.Phys. **36** (1995) 6377–6396, arXiv:hep-th/9409089.
- [17] L. Susskind and J. Lindesay, *An Introduction to Black Holes, Information and the Stringtheory Revolution: The Holographic Universe*. World Scientific publishing Co. Pte. Ltd., 2006.
- [18] J. Jackson, *Classical Electrodynamics*. John Wiley & Sons, INC., 2001.
- [19] H. Georgi and S. L. Glashow, *Unity of All Elementary-Particle Forces*, Phys. Rev. Lett. **32** (Feb, 1974) 438–441.
- [20] D. Lüst and S. Theisen, *Lectures on string theory*. Lecture notes in physics. Springer-Verlag, 1989.
- [21] J. Polchinski, *String Theory I: An Introduction to the Bosonic String*. Cambridge University Press, 2005.
- [22] J. Polchinski, *String Theory II: Superstring Theory and Beyond*. Cambridge University Press, 2005.
- [23] B. Zwiebach, *A first course in string theory*. Cambridge University Press, 2004.
- [24] T. Thiemann, *Lectures on loop quantum gravity*, Lect. Notes Phys. **631** (2003) 41–135, arXiv:gr-qc/0210094.
- [25] J. M. Maldacena, *The large  $N$  limit of superconformal field theories and supergravity*, Adv. Theor. Math. Phys. **2** (1998) 231–252, arXiv:hep-th/9711200.
- [26] D. J. Gross and F. Wilczek, *Ultraviolet Behavior of Non-Abelian Gauge Theories*, Phys. Rev. Lett. **30** (1973) 1343–1346.
- [27] H. D. Politzer, *Reliable Perturbative Results for Strong Interactions?*, Phys. Rev. Lett. **30** (1973) 1346–1349.

- [28] J. G. Bednorz and K. A. Müller, *Possible high  $T_c$  superconductivity in the Ba-La-Cu-O system*, Zeitschrift für Physik B Condensed Matter **64** (1986) 189–193. 10.1007/BF01303701.
- [29] P. Coleman, *Heavy Fermions: electrons at the edge of magnetism*, eprint arXiv:cond-mat/0612006 (Nov., 2006) arXiv:arXiv:cond-mat/0612006.
- [30] W. Ketterle and M. W. Zwierlein, *Making, probing and understanding ultracold Fermi gases*, Nuovo Cimento Rivista Serie **31** (May, 2008) 247–422, arXiv:0801.2500.
- [31] M. Reece, *The status of AdS/QCD*, AIP Conf.Proc. **1343** (2011) 117–122.
- [32] J. Erlich, E. Katz, D. T. Son, and M. A. Stephanov, *QCD and a holographic model of hadrons*, Phys.Rev.Lett. **95** (2005) 261602, arXiv:hep-ph/0501128.
- [33] A. Karch, E. Katz, D. T. Son, and M. A. Stephanov, *Linear confinement and AdS/QCD*, Phys.Rev. **D74** (2006) 015005, arXiv:hep-ph/0602229.
- [34] A. Karch and E. Katz, *Adding flavor to AdS/CFT*, JHEP **06** (2002) 043, arXiv:hep-th/0205236.
- [35] J. Erdmenger, N. Evans, I. Kirsch, and E. Threlfall, *Mesons in Gauge/Gravity Duals - A Review*, Eur. Phys. J. **A35** (2008) 81–133, arXiv:0711.4467.
- [36] J. Erdmenger, N. Evans, and J. Grosse, *Heavy-light mesons from the AdS/CFT correspondence*, JHEP **0701** (2007) 098, arXiv:hep-th/0605241.
- [37] J. Erdmenger, K. Ghoroku, and I. Kirsch, *Holographic heavy-light mesons from non-Abelian DBI*, JHEP **0709** (2007) 111, arXiv:0706.3978.
- [38] C. Nunez, A. Paredes, and A. V. Ramallo, *Unquenched flavor in the gauge/gravity correspondence*, Adv.High Energy Phys. **2010** (2010) 196714, arXiv:1002.1088.
- [39] M. Kruczenski, D. Mateos, R. C. Myers, and D. J. Winters, *Meson spectroscopy in AdS/CFT with flavour*, JHEP **07** (2003) 049, arXiv:hep-th/0304032.
- [40] J. Babington, J. Erdmenger, N. J. Evans, Z. Guralnik, and I. Kirsch, *Chiral symmetry breaking and pions in non-supersymmetric gauge / gravity duals*, Phys. Rev. **D69** (2004) 066007, arXiv:hep-th/0306018.
- [41] E. V. Shuryak, *What RHIC experiments and theory tell us about properties of quark-gluon plasma?*, Nucl. Phys. **A750** (2005) 64–83, arXiv:hep-ph/0405066.

- [42] E. Shuryak, *Strongly Coupled Quark-Gluon Plasma: The Status Report*, arXiv:hep-ph/0608177.
- [43] E. Witten, *Anti-de Sitter space and holography*, Adv.Theor.Math.Phys. **2** (1998) 253–291, arXiv:hep-th/9802150.
- [44] E. Witten, *Anti-de Sitter space, thermal phase transition, and confinement in gauge theories*, Adv. Theor. Math. Phys. **2** (1998) 505–532, arXiv:hep-th/9803131.
- [45] R. C. Myers and S. E. Vazquez, *Quark Soup al dente: Applied Superstring Theory*, Class. Quant. Grav. **25** (2008) 114008, arXiv:0804.2423.
- [46] F. Karsch, *Lattice QCD at high temperature and density*, Lect. Notes Phys. **583** (2002) 209–249, arXiv:hep-lat/0106019.
- [47] S. S. Gubser, I. R. Klebanov, and A. W. Peet, *Entropy and Temperature of Black 3-Branes*, Phys. Rev. **D54** (1996) 3915–3919, arXiv:hep-th/9602135.
- [48] I. Kirsch, *Generalizations of the AdS/CFT correspondence*, Fortsch. Phys. **52** (2004) 727–826, arXiv:hep-th/0406274.
- [49] D. Mateos, R. C. Myers, and R. M. Thomson, *Thermodynamics of the brane*, JHEP **05** (2007) 067, arXiv:hep-th/0701132.
- [50] C. Hoyos-Badajoz, K. Landsteiner, and S. Montero, *Holographic Meson Melting*, JHEP **04** (2007) 031, arXiv:hep-th/0612169.
- [51] D. T. Son and A. O. Starinets, *Viscosity, Black Holes, and Quantum Field Theory*, Ann. Rev. Nucl. Part. Sci. **57** (2007) 95–118, arXiv:0704.0240.
- [52] G. Policastro, D. T. Son, and A. O. Starinets, *The shear viscosity of strongly coupled  $N = 4$  supersymmetric Yang-Mills plasma*, Phys. Rev. Lett. **87** (2001) 081601, arXiv:hep-th/0104066.
- [53] G. Policastro, D. T. Son, and A. O. Starinets, *From AdS/CFT correspondence to hydrodynamics*, JHEP **09** (2002) 043, arXiv:hep-th/0205052.
- [54] P. Kovtun, D. T. Son, and A. O. Starinets, *Holography and hydrodynamics: Diffusion on stretched horizons*, JHEP **10** (2003) 064, arXiv:hep-th/0309213.
- [55] A. Buchel and J. T. Liu, *Universality of the shear viscosity in supergravity*, Phys. Rev. Lett. **93** (2004) 090602, arXiv:hep-th/0311175.
- [56] P. Kovtun, D. T. Son, and A. O. Starinets, *Viscosity in strongly interacting quantum field theories from black hole physics*, Phys. Rev. Lett. **94** (2005) 111601, arXiv:hep-th/0405231.

- [57] A. Buchel, R. C. Myers, and A. Sinha, *Beyond  $\eta/s = 1/4\pi$* , JHEP **03** (2009) 084, arXiv:0812.2521.
- [58] S. Cremonini, *The Shear Viscosity to Entropy Ratio: A Status Report*, Mod. Phys. Lett. **B25** (2011) 1867–1888, arXiv:1108.0677.
- [59] **PHENIX Collaboration** Collaboration, A. Adare *et al.*, *Energy Loss and Flow of Heavy Quarks in Au+Au Collisions at  $s(NN)^{1/2} = 200$ -GeV*, Phys.Rev.Lett. **98** (2007) 172301, arXiv:nucl-ex/0611018.
- [60] S. S. Gubser and A. Karch, *From gauge-string duality to strong interactions: A Pedestrian's Guide*, Ann.Rev.Nucl.Part.Sci. **59** (2009) 145–168, arXiv:0901.0935.
- [61] J. Casalderrey-Solana, H. Liu, D. Mateos, K. Rajagopal, and U. A. Wiedemann, *Gauge/String Duality, Hot QCD and Heavy Ion Collisions*, arXiv:1101.0618.
- [62] S. S. Gubser, S. S. Pufu, and A. Yarom, *Entropy production in collisions of gravitational shock waves and of heavy ions*, Phys.Rev. **D78** (2008) 066014, arXiv:0805.1551.
- [63] P. M. Chesler and L. G. Yaffe, *Horizon formation and far-from-equilibrium isotropization in supersymmetric Yang-Mills plasma*, Phys. Rev. Lett. **102** (2009) 211601, arXiv:0812.2053.
- [64] S. Lin and E. Shuryak, *Grazing Collisions of Gravitational Shock Waves and Entropy Production in Heavy Ion Collision*, Phys.Rev. **D79** (2009) 124015, arXiv:0902.1508.
- [65] **ATLAS Collaboration** Collaboration, M. Spousta, *Jet Reconstruction and Jet Quenching in Heavy Ion Collisions at ATLAS*, arXiv:1106.1604.
- [66] S. S. Gubser, S. S. Pufu, F. D. Rocha, and A. Yarom, *Energy loss in a strongly coupled thermal medium and the gauge-string duality*, arXiv:0902.4041.
- [67] N. Evans and A. Tedder, *A Holographic model of hadronization*, Phys.Rev.Lett. **100** (2008) 162003, arXiv:0711.0300.
- [68] N. Evans, J. French, K. Jensen, and E. Threlfall, *Hadronization at the AdS wall*, Phys.Rev. **D81** (2010) 066004, arXiv:0908.0407.
- [69] L. McLerran and R. D. Pisarski, *Phases of cold, dense quarks at large  $N(c)$* , Nucl.Phys. **A796** (2007) 83–100, arXiv:0706.2191.
- [70] A. Chamblin, R. Emparan, C. V. Johnson, and R. C. Myers, *Holography, thermodynamics and fluctuations of charged AdS black holes*, Phys.Rev. **D60** (1999) 104026, arXiv:hep-th/9904197.

- [71] N. Horigome and Y. Tani, *Holographic chiral phase transition with chemical potential*, JHEP **0701** (2007) 072, arXiv:hep-th/0608198.
- [72] S. Kobayashi, D. Mateos, S. Matsuura, R. C. Myers, and R. M. Thomson, *Holographic phase transitions at finite baryon density*, JHEP **02** (2007) 016, arXiv:hep-th/0611099.
- [73] D. Mateos, S. Matsuura, R. C. Myers, and R. M. Thomson, *Holographic phase transitions at finite chemical potential*, JHEP **11** (2007) 085, arXiv:0709.1225.
- [74] G. Torrieri, S. Lottini, I. Mishustin, and P. Nicolini, *The Phase diagram in  $T - \mu - N_c$  space*, arXiv:1110.6219.
- [75] S. Sachdev, *Quantum Phase Transitions*. Cambridge University Press, 1999.
- [76] S. Sachdev, *Where is the quantum critical point in the cuprate superconductors?*, arXiv:0907.0008.
- [77] S. Sachdev, *Condensed matter and AdS/CFT*, arXiv:1002.2947.
- [78] S. A. Hartnoll, *Lectures on holographic methods for condensed matter physics*, Class. Quant. Grav. **26** (2009) 224002, arXiv:0903.3246.
- [79] C. P. Herzog, *Lectures on Holographic Superfluidity and Superconductivity*, J.Phys.A **A42** (2009) 343001, arXiv:0904.1975.
- [80] J. McGreevy, *Holographic duality with a view toward many-body physics*, Adv.High Energy Phys. **2010** (2010) 723105, arXiv:0909.0518.
- [81] M. Ammon, *Gauge/gravity duality applied to condensed matter systems*, Fortsch.Phys. **58** (2010) 1123–1250.
- [82] S. A. Hartnoll, C. P. Herzog, and G. T. Horowitz, *Building a Holographic Superconductor*, Phys. Rev. Lett. **101** (2008) 031601, arXiv:0803.3295.
- [83] H. Liu, J. McGreevy, and D. Vegh, *Non-Fermi liquids from holography*, Phys.Rev. **D83** (2011) 065029, arXiv:0903.2477.
- [84] M. Cubrovic, J. Zaanen, and K. Schalm, *String Theory, Quantum Phase Transitions and the Emergent Fermi-Liquid*, Science **325** (2009) 439–444, arXiv:0904.1993.
- [85] T. Faulkner, H. Liu, J. McGreevy, and D. Vegh, *Emergent quantum criticality, Fermi surfaces, and AdS(2)*, Phys.Rev. **D83** (2011) 125002, arXiv:0907.2694.
- [86] S. A. Hartnoll, J. Polchinski, E. Silverstein, and D. Tong, *Towards strange metallic holography*, JHEP **1004** (2010) 120, arXiv:0912.1061.

- [87] T. Faulkner and J. Polchinski, *Semi-Holographic Fermi Liquids*, JHEP **1106** (2011) 012, arXiv:1001.5049.
- [88] L. Huijse and S. Sachdev, *Fermi surfaces and gauge-gravity duality*, Phys.Rev. **D84** (2011) 026001, arXiv:1104.5022.
- [89] M. Cubrovic, Y. Liu, K. Schalm, Y.-W. Sun, and J. Zaanen, *Spectral probes of the holographic Fermi groundstate: dialing between the electron star and AdS Dirac hair*, Phys.Rev. **D84** (2011) 086002, arXiv:1106.1798.
- [90] N. Iqbal, H. Liu, and M. Mezei, *Lectures on holographic non-Fermi liquids and quantum phase transitions*, arXiv:1110.3814.
- [91] G. T. Horowitz, *Introduction to Holographic Superconductors*, arXiv:1002.1722.
- [92] S. S. Gubser, *Breaking an Abelian gauge symmetry near a black hole horizon*, Phys. Rev. **D78** (2008) 065034, arXiv:0801.2977.
- [93] C. P. Herzog, P. K. Kovtun, and D. T. Son, *Holographic model of superfluidity*, Phys. Rev. **D79** (2009) 066002, arXiv:0809.4870.
- [94] G. T. Horowitz and M. M. Roberts, *Holographic Superconductors with Various Condensates*, Phys. Rev. **D78** (2008) 126008, arXiv:0810.1077.
- [95] S. A. Hartnoll, C. P. Herzog, and G. T. Horowitz, *Holographic Superconductors*, JHEP **12** (2008) 015, arXiv:0810.1563.
- [96] K. Maeda, M. Natsuume, and T. Okamura, *Universality class of holographic superconductors*, Phys.Rev. **D79** (2009) 126004, arXiv:0904.1914.
- [97] S. Franco, A. Garcia-Garcia, and D. Rodriguez-Gomez, *A general class of holographic superconductors*, JHEP **04** (2010) 092, arXiv:0906.1214.
- [98] F. Aprile and J. G. Russo, *Models of Holographic superconductivity*, Phys. Rev. **D81** (2010) 026009, arXiv:0912.0480.
- [99] S. S. Gubser, *Colorful horizons with charge in anti-de Sitter space*, Phys. Rev. Lett. **101** (2008) 191601, arXiv:0803.3483.
- [100] S. S. Gubser and S. S. Pufu, *The gravity dual of a p-wave superconductor*, JHEP **11** (2008) 033, arXiv:0805.2960.
- [101] F. Benini, C. P. Herzog, R. Rahman, and A. Yarom, *Gauge gravity duality for d-wave superconductors: prospects and challenges*, JHEP **1011** (2010) 137, arXiv:1007.1981.
- [102] P. Basu, J. He, A. Mukherjee, and H.-H. Shieh, *Superconductivity from D3/D7: Holographic Pion Superfluid*, JHEP **11** (2009) 070, arXiv:0810.3970.

- [103] F. Denef and S. A. Hartnoll, *Landscape of superconducting membranes*, Phys. Rev. **D79** (2009) 126008, arXiv:0901.1160.
- [104] S. S. Gubser, C. P. Herzog, S. S. Pufu, and T. Tesileanu, *Superconductors from Superstrings*, Phys.Rev.Lett. **103** (2009) 141601, arXiv:0907.3510.
- [105] J. P. Gauntlett, J. Sonner, and T. Wiseman, *Holographic superconductivity in M-Theory*, Phys.Rev.Lett. **103** (2009) 151601, arXiv:0907.3796.
- [106] S. S. Gubser, S. S. Pufu, and F. D. Rocha, *Quantum critical superconductors in string theory and M-theory*, Phys.Lett. **B683** (2010) 201–204, arXiv:0908.0011.
- [107] J. P. Gauntlett, J. Sonner, and T. Wiseman, *Quantum Criticality and Holographic Superconductors in M-theory*, JHEP **1002** (2010) 060, arXiv:0912.0512.
- [108] F. Aprile, D. Rodriguez-Gomez, and J. G. Russo, *p-wave Holographic Superconductors and five-dimensional gauged Supergravity*, JHEP **1101** (2011) 056, arXiv:1011.2172.
- [109] A. Donos and J. P. Gauntlett, *Superfluid black branes in  $AdS_4 \times S^7$* , JHEP **1106** (2011) 053, arXiv:1104.4478.
- [110] E. Nakano and W.-Y. Wen, *Critical magnetic field in a holographic superconductor*, Phys. Rev. **D78** (2008) 046004, arXiv:0804.3180.
- [111] T. Albash and C. V. Johnson, *A Holographic Superconductor in an External Magnetic Field*, JHEP **09** (2008) 121, arXiv:0804.3466.
- [112] T. Albash and C. V. Johnson, *Phases of Holographic Superconductors in an External Magnetic Field*, arXiv:0906.0519.
- [113] M. Montull, A. Pomarol, and P. J. Silva, *The Holographic Superconductor Vortex*, Phys.Rev.Lett. **103** (2009) 091601, arXiv:0906.2396.
- [114] K. Maeda, M. Natsuume, and T. Okamura, *Vortex lattice for a holographic superconductor*, Phys.Rev. **D81** (2010) 026002, arXiv:0910.4475.
- [115] S. S. Gubser and F. D. Rocha, *The gravity dual to a quantum critical point with spontaneous symmetry breaking*, Phys. Rev. Lett. **102** (2009) 061601, arXiv:0807.1737.
- [116] S. S. Gubser and A. Nellore, *Low-temperature behavior of the Abelian Higgs model in anti-de Sitter space*, JHEP **04** (2009) 008, arXiv:0810.4554.
- [117] S. S. Gubser and A. Nellore, *Ground states of holographic superconductors*, Phys.Rev. **D80** (2009) 105007, arXiv:0908.1972.

- [118] G. T. Horowitz and M. M. Roberts, *Zero Temperature Limit of Holographic Superconductors*, JHEP **11** (2009) 015, arXiv:0908.3677.
- [119] P. Basu, J. He, A. Mukherjee, and H.-H. Shieh, *Hard-gapped Holographic Superconductors*, Phys. Lett. **B689** (2010) 45–50, arXiv:0911.4999.
- [120] J.-W. Chen, Y.-J. Kao, and W.-Y. Wen, *Peak-Dip-Hump from Holographic Superconductivity*, Phys.Rev. **D82** (2010) 026007, arXiv:0911.2821.
- [121] T. Faulkner, G. T. Horowitz, J. McGreevy, M. M. Roberts, and D. Vegh, *Photoemission 'experiments' on holographic superconductors*, JHEP **1003** (2010) 121, arXiv:0911.3402.
- [122] S. S. Gubser, F. D. Rocha, and P. Talavera, *Normalizable fermion modes in a holographic superconductor*, JHEP **1010** (2010) 087, arXiv:0911.3632.
- [123] S. S. Gubser, F. D. Rocha, and A. Yarom, *Fermion correlators in non-abelian holographic superconductors*, JHEP **1011** (2010) 085, arXiv:1002.4416.
- [124] M. Ammon, J. Erdmenger, M. Kaminski, and A. O'Bannon, *Fermionic Operator Mixing in Holographic p-wave Superfluids*, JHEP **1005** (2010) 053, arXiv:1003.1134.
- [125] F. Benini, C. P. Herzog, and A. Yarom, *Holographic Fermi arcs and a d-wave gap*, Phys.Lett. **B701** (2011) 626–629, arXiv:1006.0731.
- [126] A. Damascelli, Z. Hussain, and Z.-X. Shen, *Angle-resolved photoemission studies of the cuprate superconductors*, Rev. Mod. Phys. **75** (Apr, 2003) 473–541.
- [127] L. D. Landau and E. M. Lifshitz, *Course of Theoretical Physics, Volume 6, Fluid Mechanics*. Pergamon Press, 1959.
- [128] C. P. Herzog and S. S. Pufu, *The Second Sound of SU(2)*, JHEP **04** (2009) 126, arXiv:0902.0409.
- [129] A. Yarom, *Fourth sound of holographic superfluids*, JHEP **07** (2009) 070, arXiv:0903.1353.
- [130] I. Amado, M. Kaminski, and K. Landsteiner, *Hydrodynamics of Holographic Superconductors*, JHEP **0905** (2009) 021, arXiv:0903.2209.
- [131] C. P. Herzog and A. Yarom, *Sound modes in holographic superfluids*, Phys. Rev. **D80** (2009) 106002, arXiv:0906.4810.
- [132] J. Bhattacharya, S. Bhattacharyya, and S. Minwalla, *Dissipative Superfluid dynamics from gravity*, JHEP **1104** (2011) 125, arXiv:1101.3332.

- [133] C. P. Herzog, N. Lisker, P. Surowka, and A. Yarom, *Transport in holographic superfluids*, JHEP **1108** (2011) 052, arXiv:1101.3330.
- [134] J. Bhattacharya, S. Bhattacharyya, S. Minwalla, and A. Yarom, *A Theory of first order dissipative superfluid dynamics*, arXiv:1105.3733.
- [135] S. Bhattacharyya, V. E. Hubeny, S. Minwalla, and M. Rangamani, *Nonlinear Fluid Dynamics from Gravity*, JHEP **0802** (2008) 045, arXiv:0712.2456.
- [136] M. Rangamani, *Gravity and Hydrodynamics: Lectures on the fluid-gravity correspondence*, Class.Quant.Grav. **26** (2009) 224003, arXiv:0905.4352.
- [137] C. P. Herzog, *An Analytic Holographic Superconductor*, Phys. Rev. **D81** (2010) 126009, arXiv:1003.3278.
- [138] A. Rebhan and D. Steineder, *Violation of the Holographic Viscosity Bound in a Strongly Coupled Anisotropic Plasma*, arXiv:1110.6825.
- [139] M. Chernodub, *Superconductivity of QCD vacuum in strong magnetic field*, Phys.Rev. **D82** (2010) 085011, arXiv:1008.1055.
- [140] M. Chernodub, *Electromagnetically superconducting phase of QCD vacuum induced by strong magnetic field*, AIP Conf.Proc. **1343** (2011) 149–151, arXiv:1011.2658.
- [141] M. Chernodub, *Spontaneous electromagnetic superconductivity of vacuum in strong magnetic field: evidence from the Nambu–Jona-Lasinio model*, Phys.Rev.Lett. **106** (2011) 142003, arXiv:1101.0117.
- [142] M. Chernodub, *Can nothing be a superconductor and a superfluid?*, PoS **FACESQCD** (2010) 021, arXiv:1104.4404.
- [143] G. F. Chew and S. C. Frautschi, *Principle of Equivalence for all Strongly Interacting Particles within the S-Matrix Framework*, Phys. Rev. Lett. **7** (Nov, 1961) 394–397.
- [144] L. Susskind, *Dual-symmetric theory of hadrons.—I*, Il Nuovo Cimento A (1965-1970) **69** (1970) 457–496. 10.1007/BF02726485.
- [145] D. Friedan, *Nonlinear Models in  $2 + \epsilon$  Dimensions*, Phys. Rev. Lett. **45** (Sep, 1980) 1057–1060.
- [146] J. Polchinski, *Dirichlet Branes and Ramond-Ramond Charges*, Phys. Rev. Lett. **75** (Dec, 1995) 4724–4727.
- [147] N. R. Constable, R. C. Myers, and O. Tafjord, *The noncommutative bion core*, Phys. Rev. **D61** (2000) 106009, arXiv:hep-th/9911136.
- [148] R. C. Myers, *Dielectric-branes*, JHEP **12** (1999) 022, arXiv:hep-th/9910053.

- [149] A. Hashimoto and W. Taylor, *Fluctuation spectra of tilted and intersecting D-branes from the Born-Infeld action*, Nucl. Phys. **B503** (1997) 193–219, arXiv:hep-th/9703217.
- [150] A. A. Tseytlin, *On non-abelian generalisation of the Born-Infeld action in string theory*, Nucl. Phys. **B501** (1997) 41–52, arXiv:hep-th/9701125.
- [151] C. V. Johnson, *D-brane primer*, arXiv:hep-th/0007170.
- [152] E. D'Hoker and D. Z. Freedman, *Supersymmetric gauge theories and the AdS/CFT correspondence*, arXiv:hep-th/0201253.
- [153] G. t Hooft, *A planar diagram theory for strong interactions*, Nuclear Physics B **72** (1974), no. 3, 461 – 473.
- [154] O. Aharony, S. S. Gubser, J. M. Maldacena, H. Ooguri, and Y. Oz, *Large N field theories, string theory and gravity*, Phys. Rept. **323** (2000) 183–386, arXiv:hep-th/9905111.
- [155] S. S. Gubser, I. R. Klebanov, and A. M. Polyakov, *Gauge theory correlators from non-critical string theory*, Phys. Lett. **B428** (1998) 105–114, arXiv:hep-th/9802109.
- [156] D. Gabor, *A New Microscopic Principle*, Nature **161** (1948) 777–778.
- [157] K. Pilch and N. P. Warner,  *$N = 2$  supersymmetric RG flows and the IIB dilaton*, Nucl. Phys. **B594** (2001) 209–228, arXiv:hep-th/0004063.
- [158] J. Polchinski and M. J. Strassler, *The string dual of a confining four-dimensional gauge theory*, arXiv:hep-th/0003136.
- [159] A. Karch and L. Randall, *Open and closed string interpretation of SUSY CFT's on branes with boundaries*, JHEP **0106** (2001) 063, arXiv:hep-th/0105132.
- [160] O. DeWolfe, D. Z. Freedman, and H. Ooguri, *Holography and defect conformal field theories*, Phys.Rev. **D66** (2002) 025009, arXiv:hep-th/0111135.
- [161] J. Erdmenger, Z. Guralnik, and I. Kirsch, *Four-dimensional superconformal theories with interacting boundaries or defects*, Phys.Rev. **D66** (2002) 025020, arXiv:hep-th/0203020.
- [162] N. R. Constable, J. Erdmenger, Z. Guralnik, and I. Kirsch, *Intersecting D-3 branes and holography*, Phys.Rev. **D68** (2003) 106007, arXiv:hep-th/0211222.
- [163] P. Breitenlohner and D. Z. Freedman, *Positive Energy in anti-De Sitter Backgrounds and Gauged Extended Supergravity*, Phys. Lett. **B115** (1982) 197.

- [164] P. Breitenlohner and D. Z. Freedman, *Stability in Gauged Extended Supergravity*, *Annals Phys.* **144** (1982) 249.
- [165] M. Abramowitz and I. Stegun, *Handbook of Mathematical Functions*. Dover Publications, Inc., New York, 1970.
- [166] I. Kirsch, *Spectroscopy of fermionic operators in AdS/CFT*, *JHEP* **0609** (2006) 052, arXiv:hep-th/0607205.
- [167] S. W. Hawking and D. N. Page, *Thermodynamics of black holes in anti-de Sitter space.*, *Communications in Mathematical Physics* **87** (1982) 577–588.
- [168] T. Schafer and D. Teaney, *Nearly Perfect Fluidity: From Cold Atomic Gases to Hot Quark Gluon Plasmas*, *Rept. Prog. Phys.* **72** (2009) 126001, arXiv:0904.3107.
- [169] K. Skenderis, *Lecture notes on holographic renormalization*, *Class. Quant. Grav.* **19** (2002) 5849–5876, arXiv:hep-th/0209067.
- [170] L. Susskind and E. Witten, *The Holographic bound in anti-de Sitter space*, arXiv:hep-th/9805114.
- [171] C. Burgess, N. Constable, and R. C. Myers, *The Free energy of  $N=4$  superYang-Mills and the AdS / CFT correspondence*, *JHEP* **9908** (1999) 017, arXiv:hep-th/9907188.
- [172] V. Balasubramanian and P. Kraus, *A stress tensor for anti-de Sitter gravity*, *Commun. Math. Phys.* **208** (1999) 413–428, arXiv:hep-th/9902121.
- [173] A. Karch, A. O’Bannon, and K. Skenderis, *Holographic renormalization of probe D-branes in AdS/CFT*, *JHEP* **04** (2006) 015, arXiv:hep-th/0512125.
- [174] D. T. Son and A. O. Starinets, *Minkowski-space correlators in AdS/CFT correspondence: Recipe and applications*, *JHEP* **09** (2002) 042, arXiv:hep-th/0205051.
- [175] C. P. Herzog and D. T. Son, *Schwinger-Keldysh propagators from AdS/CFT correspondence*, *JHEP* **03** (2003) 046, arXiv:hep-th/0212072.
- [176] M. Kaminski, K. Landsteiner, J. Mas, J. P. Shock, and J. Tarrío, *Holographic Operator Mixing and Quasinormal Modes on the Brane*, *JHEP* **02** (2010) 021, arXiv:0911.3610.
- [177] G. T. Horowitz and V. E. Hubeny, *Quasinormal modes of AdS black holes and the approach to thermal equilibrium*, *Phys.Rev.* **D62** (2000) 024027, arXiv:hep-th/9909056.

- [178] D. Birmingham, I. Sachs, and S. N. Solodukhin, *Conformal field theory interpretation of black hole quasi-normal modes*, Phys. Rev. Lett. **88** (2002) 151301, arXiv:hep-th/0112055.
- [179] P. K. Kovtun and A. O. Starinets, *Quasinormal modes and holography*, Phys. Rev. **D72** (2005) 086009, arXiv:hep-th/0506184.
- [180] I. Amado, C. Hoyos-Badajoz, K. Landsteiner, and S. Montero, *Hydrodynamics and beyond in the strongly coupled  $N=4$  plasma*, JHEP (2008) 133, arXiv:0805.2570.
- [181] I. Amado, C. Hoyos-Badajoz, K. Landsteiner, and S. Montero, *Residues of Correlators in the Strongly Coupled  $N=4$  Plasma*, Phys. Rev. **D77** (2008) 065004, arXiv:0710.4458.
- [182] A. Nunez and A. O. Starinets, *AdS/CFT correspondence, quasinormal modes, and thermal correlators in  $N = 4$  SYM*, Phys. Rev. **D67** (2003) 124013, arXiv:hep-th/0302026.
- [183] P. Kovtun and A. Starinets, *Thermal spectral functions of strongly coupled  $N=4$  supersymmetric Yang-Mills theory*, Phys.Rev.Lett. **96** (2006) 131601, arXiv:hep-th/0602059.
- [184] R. C. Myers, A. O. Starinets, and R. M. Thomson, *Holographic spectral functions and diffusion constants for fundamental matter*, JHEP **11** (2007) 091, arXiv:0706.0162.
- [185] A. Paredes, K. Peeters, and M. Zamaklar, *Mesons versus quasi-normal modes: undercooling and overheating*, JHEP **05** (2008) 027, arXiv:0803.0759.
- [186] J. Erdmenger, M. Kaminski, and F. Rust, *Holographic vector mesons from spectral functions at finite baryon or isospin density*, Phys. Rev. **D77** (2008) 046005, arXiv:0710.0334.
- [187] C. P. Herzog, P. Kovtun, S. Sachdev, and D. T. Son, *Quantum critical transport, duality, and M-theory*, Phys. Rev. **D75** (2007) 085020, arXiv:hep-th/0701036.
- [188] I. Amado, C. Hoyos-Badajoz, K. Landsteiner, and S. Montero, *Absorption Lengths in the Holographic Plasma*, JHEP **09** (2007) 057, arXiv:0706.2750.
- [189] A. S. Miranda, J. Morgan, and V. T. Zanchin, *Quasinormal modes of plane-symmetric black holes according to the AdS/CFT correspondence*, JHEP **11** (2008) 030, arXiv:0809.0297.
- [190] R. C. Myers and M. C. Wapler, *Transport Properties of Holographic Defects*, JHEP **12** (2008) 115, arXiv:0811.0480.

- [191] J. Morgan, V. Cardoso, A. S. Miranda, C. Molina, and V. T. Zanchin, *Gravitational quasinormal modes of AdS black branes in d spacetime dimensions*, JHEP **09** (2009) 117, arXiv:0907.5011.
- [192] P. G. Debenedetti and F. H. Stillinger, *Supercooled liquids and the glass transition*, Nature (2001).
- [193] P. Benincasa, A. Buchel, and R. Naryshkin, *The shear viscosity of gauge theory plasma with chemical potentials*, Phys. Lett. **B645** (2007) 309–313, arXiv:hep-th/0610145.
- [194] N. Iqbal and H. Liu, *Universality of the hydrodynamic limit in AdS/CFT and the membrane paradigm*, Phys. Rev. **D79** (2009) 025023, arXiv:0809.3808.
- [195] RHIC [http://www.bnl.gov/today/story.asp?ITEM\\_NO=1870](http://www.bnl.gov/today/story.asp?ITEM_NO=1870).
- [196] N. Callebaut, D. Dudal, and H. Verschelde, *Holographic study of rho meson mass in an external magnetic field: Paving the road towards a magnetically induced superconducting QCD vacuum?*, PoS **FACESQCD** (2010) 046, arXiv:1102.3103.
- [197] N. Callebaut, D. Dudal, and H. Verschelde, *Holographic rho mesons in an external magnetic field*, arXiv:1105.2217.
- [198] A. Karch and A. O’Bannon, *Holographic Thermodynamics at Finite Baryon Density: Some Exact Results*, JHEP **11** (2007) 074, arXiv:0709.0570.
- [199] S. Nakamura, Y. Seo, S.-J. Sin, and K. P. Yogendran, *Baryon-charge Chemical Potential in AdS/CFT*, Prog. Theor. Phys. **120** (2008) 51–76, arXiv:0708.2818.
- [200] S. Nakamura, Y. Seo, S.-J. Sin, and K. P. Yogendran, *A new phase at finite quark density from AdS/CFT*, J. Korean Phys. Soc. **52** (2008) 1734–1739, arXiv:hep-th/0611021.
- [201] A. Karch, D. T. Son, and A. O. Starinets, *Zero Sound from Holography*, arXiv:0806.3796.
- [202] R. C. Myers and A. Sinha, *The fast life of holographic mesons*, JHEP **06** (2008) 052, arXiv:0804.2168.
- [203] J. Mas, J. P. Shock, J. Tarrio, and D. Zoakos, *Holographic Spectral Functions at Finite Baryon Density*, JHEP **09** (2008) 009, arXiv:0805.2601.
- [204] J. Erdmenger, M. Kaminski, P. Kerner, and F. Rust, *Finite baryon and isospin chemical potential in AdS/CFT with flavor*, JHEP **11** (2008) 031, arXiv:0807.2663.

- [205] J. Erdmenger, M. Kaminski, and F. Rust, *Isospin diffusion in thermal AdS/CFT with flavor*, Phys. Rev. **D76** (2007) 046001, arXiv:0704.1290.
- [206] R. Apreda, J. Erdmenger, N. Evans, and Z. Guralnik, *Strong coupling effective Higgs potential and a first order thermal phase transition from AdS/CFT duality*, Phys. Rev. **D71** (2005) 126002, arXiv:hep-th/0504151.
- [207] T. Faulkner and H. Liu, *Condensed matter physics of a strongly coupled gauge theory with quarks: some novel features of the phase diagram*, arXiv:0812.4278.
- [208] P. Benincasa, *Universality of Holographic Phase Transitions and Holographic Quantum Liquids*, arXiv:0911.0075.
- [209] M. Kaminski, *Holographic quark gluon plasma with flavor*, Fortsch. Phys. **57** (2009) 3–148, arXiv:0808.1114.
- [210] F. Rust, *In-medium effects in the holographic quark-gluon plasma*, Adv.High Energy Phys. **2010** (2010) 564624, arXiv:1003.0187.
- [211] L.-y. He, M. Jin, and P.-f. Zhuang, *Pion superfluidity and meson properties at finite isospin density*, Phys. Rev. **D71** (2005) 116001, arXiv:hep-ph/0503272.
- [212] S. Chang, J. Liu, and P. Zhuang, *Nucleon mass splitting at finite isospin chemical potential*, Chin. Phys. Lett. **25** (2008) 55–57, arXiv:nucl-th/0702032.
- [213] K. Binder, *Theory of first-order phase transitions*, Reports on Progress in Physics **50** (1987), no. 7, 783–859.
- [214] J. Erdmenger, M. Haack, M. Kaminski, and A. Yarom, *Fluid dynamics of R-charged black holes*, JHEP **01** (2009) 055, arXiv:0809.2488.
- [215] N. Banerjee, J. Bhattacharya, S. Bhattacharyya, S. Dutta, R. Loganayagam, *et al.*, *Hydrodynamics from charged black branes*, JHEP **1101** (2011) 094, arXiv:0809.2596.
- [216] R. Fazio and H. van der Zant, *Quantum phase transitions and vortex dynamics in superconducting networks*, Physics Reports **355** (2001), no. 4, 235 – 334.
- [217] G. E. Brown and M. Rho, *Scaling effective Lagrangians in a dense medium*, Phys. Rev. Lett. **66** (1991) 2720–2723.
- [218] F. Sannino and W. Schafer, *Relativistic massive vector condensation*, Phys. Lett. **B527** (2002) 142–148, arXiv:hep-ph/0111098.

- [219] F. Sannino, *General structure of relativistic vector condensation*, Phys. Rev. **D67** (2003) 054006, arXiv:hep-ph/0211367.
- [220] D. T. Son and M. A. Stephanov, *QCD at finite isospin density*, Phys. Rev. Lett. **86** (2001) 592–595, arXiv:hep-ph/0005225.
- [221] D. T. Son and M. A. Stephanov, *QCD at finite isospin density: From pion to quark antiquark condensation*, Phys. Atom. Nucl. **64** (2001) 834–842, arXiv:hep-ph/0011365.
- [222] J. B. Kogut and D. K. Sinclair, *Lattice QCD at finite isospin density at zero and finite temperature*, Phys. Rev. **D66** (2002) 034505, arXiv:hep-lat/0202028.
- [223] Y.-i. Shin, C. H. Schunck, A. Schirotzek, and W. Ketterle, *Phase diagram of a two-component Fermi gas with resonant interactions*, Nature **451** (2008) 689–693.
- [224] M. Chernodub and A. Nedelin, *Phase diagram of chirally imbalanced QCD matter*, Phys.Rev. **D83** (2011) 105008, arXiv:1102.0188.
- [225] D. B. Kaplan, J.-W. Lee, D. T. Son, and M. A. Stephanov, *Conformality Lost*, Phys. Rev. **D80** (2009) 125005, arXiv:0905.4752.
- [226] V. G. Filev, C. V. Johnson, R. C. Rashkov, and K. S. Viswanathan, *Flavoured large  $N$  gauge theory in an external magnetic field*, JHEP **10** (2007) 019, arXiv:hep-th/0701001.
- [227] J. Erdmenger, R. Meyer, and J. P. Shock, *AdS/CFT with Flavour in Electric and Magnetic Kalb-Ramond Fields*, JHEP **12** (2007) 091, arXiv:0709.1551.
- [228] N. Evans, A. Gebauer, K.-Y. Kim, and M. Magou, *Phase diagram of the  $D3/D5$  system in a magnetic field and a BKT transition*, Phys.Lett. **B698** (2011) 91–95, arXiv:1003.2694.
- [229] N. Evans, A. Gebauer, K.-Y. Kim, and M. Magou, *Holographic Description of the Phase Diagram of a Chiral Symmetry Breaking Gauge Theory*, JHEP **03** (2010) 132, arXiv:1002.1885.
- [230] K. Jensen, A. Karch, D. T. Son, and E. G. Thompson, *Holographic Berezinskii-Kosterlitz-Thouless Transitions*, Phys. Rev. Lett. **105** (2010) 041601, arXiv:1002.3159.
- [231] S. S. Pal, *Quantum phase transition in a  $Dp$ - $Dq$  system*, Phys. Rev. **D82** (2010) 086013, arXiv:1006.2444.
- [232] K. Jensen, *More Holographic Berezinskii-Kosterlitz-Thouless Transitions*, Phys. Rev. **D82** (2010) 046005, arXiv:1006.3066.

- [233] N. Evans, K. Jensen, and K.-Y. Kim, *Non Mean-Field Quantum Critical Points from Holography*, Phys.Rev. **D82** (2010) 105012, arXiv:1008.1889.
- [234] P. de Gennes, *The Physics of Liquid Crystals*. Oxford University Press, 1974.
- [235] L. D. Landau and E. M. Lifshitz, *Course of Theoretical Physics, Volume 7, Theory of Elasticity*. Pergamon Press, 1959.
- [236] R. Manvelyan, E. Radu, and D. H. Tchrakian, *New AdS non Abelian black holes with superconducting horizons*, Phys. Lett. **B677** (2009) 79–87, arXiv:0812.3531.
- [237] N. Iqbal, H. Liu, M. Mezei, and Q. Si, *Quantum phase transitions in holographic models of magnetism and superconductors*, Phys.Rev. **D82** (2010) 045002, arXiv:1003.0010.
- [238] C. Pujol and D. Davesne, *Relativistic dissipative hydrodynamics with spontaneous symmetry breaking*, Phys. Rev. **C67** (2003) 014901, arXiv:hep-ph/0204355.
- [239] F. M. Leslie, *Some Constitutive Equations For Anisotropic Fluids*, The Quarterly Journal of Mechanics and Applied Mathematics **19** (1966), no. 3, 357–370.
- [240] A. Buchel and R. C. Myers, *Causality of Holographic Hydrodynamics*, JHEP **08** (2009) 016, arXiv:0906.2922.
- [241] P. Basu and J.-H. Oh, *Analytic Approaches to An-Isotropic Holographic Superfluids*, arXiv:1109.4592.
- [242] S. Barisch, M. Haack, S. Nampuri, and G. Policastro, *to appear*,.
- [243] M. M. Roberts and S. A. Hartnoll, *Pseudogap and time reversal breaking in a holographic superconductor*, JHEP **08** (2008) 035, arXiv:0805.3898.
- [244] M. Tinkham, *The electromagnetic properties of superconductors*, Rev. Mod. Phys. **46** (Oct, 1974) 587–596.
- [245] A. Karch and A. O’Bannon, *Metallic AdS/CFT*, JHEP **09** (2007) 024, arXiv:0705.3870.
- [246] A. Karch, A. O’Bannon, and E. Thompson, *The Stress-Energy Tensor of Flavor Fields from AdS/CFT*, JHEP **04** (2009) 021, arXiv:0812.3629.
- [247] T. Sakai and S. Sugimoto, *Low energy hadron physics in holographic QCD*, Prog.Theor.Phys. **113** (2005) 843–882, arXiv:hep-th/0412141.
- [248] P. Basu, A. Mukherjee, and H.-H. Shieh, *Supercurrent: Vector Hair for an AdS Black Hole*, Phys. Rev. **D79** (2009) 045010, arXiv:0809.4494.

- [249] P. C. Hohenberg and B. I. Halperin, *Theory of Dynamic Critical Phenomena*, Rev. Mod. Phys. **49** (1977) 435–479.
- [250] A. Buchel and C. Pagnutti, *Transport at criticality*, Nucl.Phys. **B834** (2010) 222–236, arXiv:0912.3212.
- [251] A. Buchel, *Critical phenomena in  $N=4$  SYM plasma*, Nucl.Phys. **B841** (2010) 59–99, arXiv:1005.0819.
- [252] A. Buchel and C. Pagnutti, *Critical phenomena in  $N=2^*$  plasma*, Phys.Rev. **D83** (2011) 046004, arXiv:1010.3359.
- [253] D. T. Son and P. Surowka, *Hydrodynamics with Triangle Anomalies*, Phys.Rev.Lett. **103** (2009) 191601, arXiv:0906.5044.
- [254] C. C. Homes, S. V. Dordevic, M. Strongin, D. A. Bonn, R. Liang, W. N. Hardy, S. Komiyama, Y. Ando, G. Yu, N. Kaneko, X. Zhao, M. Greven, D. N. Basov, and T. Timusk, *A universal scaling relation in high-temperature superconductors*, Nature **430** (July, 2004) 539–541, arXiv:arXiv:cond-mat/0404216.
- [255] J. Zaanen, *Superconductivity: Why the temperature is high*, Nature **430** (2004) 512–513.
- [256] B. Sahoo and H.-U. Yee, *Electrified plasma in AdS/CFT correspondence*, JHEP **11** (2010) 095, arXiv:1004.3541.
- [257] W. H. Press, S. A. Teukolsky, W. T. Vetterling, and B. P. Flannery, *Numerical Recipes*. Cambridge University Press; 3 edition, 2007. <http://www.nr.com>.